On the measurement of fracture toughness to understand the cracking resistance of Advanced High Strength Steel sheets

David Frómeta Gutiérrez

Doctoral thesis

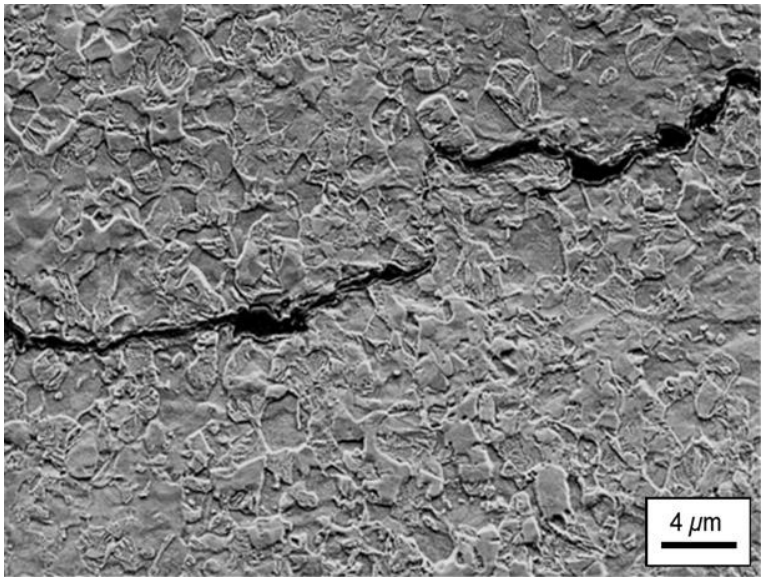

UNIVERSITAT POLITÈCNICA DE CATALUNYA
BARCELONATECH
Escola d'Enginyeria de Barcelona Est

eurecat

On the measurement of fracture toughness to understand the cracking resistance of Advanced High Strength Steel sheets

David Frómeta Gutiérrez

Thesis by compendium of publications submitted to Universitat Politècnica de Catalunya in partial fulfilment of the requirements for the degree of Doctor of Philosophy

Thesis supervisor

Jessica Calvo Muñoz

Thesis supervisor

Daniel Casellas i Padró

UNIVERSITAT POLITÈCNICA DE CATALUNYA
BARCELONATECH
Escola d'Enginyeria de Barcelona Est

eurecat

To my brother, Daniel, who always believed in me

Abstract

Automotive designers are constantly facing new challenges to meet the more and more stringent safety and CO_2 emission legislations. Concerning the latter, vehicle lightweighting has become one of the main goals of the automotive industry, not only to reduce fuel consumption in fuel-powered cars but also to enhance the battery range in electric vehicles. At the same time, weight reduction cannot be attained at the expense of passenger's safety in case of a crash. Hence, it is important to select the best-suited strategies to find the optimum balance between weight reduction and crashworthiness. In this sense, Advanced High Strength Steels (AHSS) have been positioned as one of the most effective solutions to this demand. AHSS present very high strength and high crash performance, which allows reducing vehicle mass while maintaining the safety of the occupants. These outstanding mechanical properties have promoted their widespread implementation for structural and crash-relevant automobile components. However, the application of AHSS have introduced new challenges related to their limited ductility and cracking resistance. Premature cracking during edge forming operations (edge cracking) or the occurrence and propagation of cracks under impact loading are some of the common cracking related issues in processing and implementation of AHSS.

To face these problems, the development of new approaches to properly characterize the cracking resistance of AHSS has become unavoidable since conventional failure criteria based on uniaxial tensile properties and forming limit curves fail to describe cracking related phenomena. In this thesis, a fracture mechanics-based approach is proposed to rationalize and understand the crack initiation and propagation resistance of AHSS. Results have been correlated with edge cracking resistance and crash behaviour of a broad range of advanced high strength sheet steels.

Fracture toughness is evaluated in the frame of fracture mechanics through different testing methods, such as the essential work of fracture, the *J*-integral and the Kahn-type tear tests. The relationship between the obtained fracture toughness parameters as well as the limitations of the different methods have been discussed. High-resolution video extensometry and Digital Image Correlation (DIC) techniques were used to investigate the fracture behaviour of the different steels. Edge cracking resistance is characterized by standard hole expansion tests and DIC-assisted hole tension tests. Crashworthiness is assessed through laboratory impact resistance tests. The influence of microstructural constituents on the crack propagation resistance of AHSS is also assessed.

The results show that fracture toughness, in particular the specific essential work of fracture (w_e), is a suitable material property to understand the cracking behaviour of AHSS and rank the material's resistance to different crack-related failures, such as edge fracture or crack propagation during a crash event. These conclusions are based on the good correlation established between w_e and the results from edge cracking and impact resistance tests. On the other hand, the experimental observations show that w_e can be used to discern the role of microstructural constituents on the fracture behaviour of AHSS. It is pointed out that proper microstructural design cannot be only focused on tensile properties since they do not inform about cracking resistance.

According to all the experimental findings, the fracture toughness is considered as a relevant material property for AHSS design and performance classification. In line with this, a new classification system, considering global ductility and fracture toughness, is proposed for a more comprehensive description of the overall formability and fracture behaviour of AHSS.

Resumen

Los diseñadores de automóviles se enfrentan constantemente a nuevos desafíos para cumplir con las cada vez más estrictas legislaciones de seguridad y emisiones de CO_2. Con respecto a esto último, el aligeramiento de los vehículos se ha convertido en uno de los principales objetivos de la industria automotriz, no solo para reducir el consumo en los automóviles de combustión interna, sino también para mejorar la autonomía de los vehículos eléctricos. Al mismo tiempo, la reducción de peso no se puede lograr a expensas de la seguridad del pasajero en caso de accidente. Por lo tanto, es importante seleccionar las estrategias más adecuadas para encontrar el equilibrio óptimo entre reducción de peso y resistencia al impacto. En este sentido, los aceros avanzados de alta resistencia (AHSS) se han posicionado como una de las soluciones más efectivas. Los AHSS presentan una elevada resistencia y un buen comportamiento en caso de impacto, lo que permite reducir el peso del vehículo manteniendo la seguridad de los ocupantes. Estas excepcionales propiedades mecánicas han contribuido a su extensa implementación en componentes estructurales y de seguridad en el automóvil. Sin embargo, estos aceros también han introducido nuevos problemas relacionados con su limitada ductilidad y resistencia la fisuración, como la aparición prematura de fisuras durante el conformado (*edge cracking*) o la generación de fisuras durante el impacto.

Para hacer frente a estos problemas, se ha hecho inevitable el desarrollo de nuevos enfoques para caracterizar la resistencia a la fisuración de los AHSS, ya que los criterios convencionales basados en ensayos de tracción y curvas límite de conformabilidad no son adecuados. En esta tesis doctoral se propone un enfoque basado en la mecánica de la fractura para explicar este tipo de fracturas relacionadas con la resistencia a la iniciación y propagación de grietas en el material. Con este fin, se investiga la correlación entre las mediciones de tenacidad de fractura y la resistencia al *edge cracking* y el comportamiento en caso de impacto en una amplia gama de chapas de acero avanzado de alta resistencia.

La tenacidad de fractura se evalúa en el marco de la mecánica de la fractura mediante distintos métodos como el trabajo esencial de fractura, la integral *J* o los ensayos tipo Kahn y se discute la relación entre los parámetros obtenidos, así como las limitaciones de los diferentes métodos. Se utilizan técnicas de video de alta resolución y correlación de imágenes digitales para investigar el comportamiento de fractura de los diferentes aceros. La resistencia *edge cracking* se caracteriza mediante ensayos de expansión de orificios (*hole expansion tests*). La resistencia al impacto se evalúa mediante ensayos de impacto de laboratorio. Finalmente, se analiza brevemente la influencia de la microestructura en la resistencia a la propagación de grietas de los AHSS.

Los resultados muestran que la tenacidad de fractura, en concreto el trabajo esencial de fractura (w_e) es una herramienta útil para comprender fenómenos de fisuración en los AHSS. Estas conclusiones se basan en la buena correlación establecida entre w_e y los resultados de las pruebas de resistencia al impacto y al *edge cracking*. Por otro lado, las observaciones experimentales muestran el gran potencial del parámetro w_e para discernir el efecto de la microestructura en la resistencia a la fractura de los AHSS. Se destaca que el diseño microestructural no debe centrarse sólo en las propiedades de tracción, ya que éstas no aportan información sobre la resistencia a la propagación de fisuras.

De acuerdo con esto, la tenacidad de fractura se considera una propiedad del material relevante para el diseño y clasificación de los AHSS y se propone un nuevo método de clasificación para una descripción más completa de la conformabilidad y la resistencia a la fractura de los aceros AHSS.

Preface

This dissertation is presented to fulfil the requirements for obtaining the degree of Doctor in Materials Science and Engineering at Universitat Politècnica de Catalunya. This research work has been carried out at the Unit of Metallic and Ceramic Materials of Eurecat, Centre Tecnològic de Catalunya under the supervision of Dr Daniel Casellas and Dr Jessica Calvo from September 2016 to June 2020.

This thesis is presented as a compendium of articles published in international journals and conferences. The document is composed of six chapters and two appendices including the papers published as a result of the work performed during the thesis period.

Chapter 1 offers a complete introduction to advanced high strength steels (AHSS) and fracture mechanics. In this chapter, the current state-of-the art in sheet metal forming and fracture resistance characterization is reviewed and the main fracture mechanics concepts used in this work are defined. Chapter 2 describes the main objectives and scope of the thesis. In Chapter 3, the materials investigated and the main experimental techniques are described. Chapter 4 summarizes the main results obtained in the appended papers. Additional findings of interest not included in the publications are also shown. The discussion of the results is presented in Chapter 5. Finally, Chapter 6 shows the main conclusions reached in this thesis work and propose future research lines.

Appendix A includes the articles published in scientific journals. One of the appended papers (Paper IV) is under review at the time of presenting this thesis. Paper I addresses the applicability of the different fracture mechanics testing procedures to characterize the fracture resistance of thin AHSS sheets. In Paper II, fracture toughness measurements are used to understand the edge fracture resistance of AHSS and a new classification map for AHSS performance is proposed. Paper III investigates the correlation between fracture toughness measurements and the cracking behaviour of AHSS under axial impact conditions and establishes a new methodology for crash resistance estimation. Finally, Paper IV discusses the influence of microstructure on the cracking resistance of two industrially processed high strength dual phase steels.

Appendix B is composed of four conference papers. Paper A to Paper C are part of the main body of the thesis work. Paper A describes an industrial case study where the proposed methodology is used to explain the fracture problems presented by a serial production automotive component. Paper B and Paper C investigate the correlation between crack propagation resistance and fracture performance (edge cracking, bendability, etc.) of several AHSS grades, evaluated by different experimental methods (hole expansion tests, hole tension tests, V-bending tests). Finally, in Paper D, a new rapid notching procedure for shet metal specimens is presented. The method is validated in four AHSS grades and the results are used in this work to discuss the influence of the notch preparation method on fracture toughness measurements.

Acknowledgements

Of course, the completion of this thesis work would not have been possible without the collaboration and support of many people. First of all, I would like to thank my supervisors, Dr Daniel Casellas and Dr Jessica Calvo, for their good advice and support throughout the thesis work. Especially to Dr Casellas for guiding this research from the very beginning and giving me the opportunity to initiate this PhD adventure. I would also like to express my thanks to all my colleagues of the Unit of Metallic and Ceramic Materials of Eurecat who have participated, in one way or another, in the execution of this thesis work. Thanks to Toni Lara, for your trust and for sharing your knowledge and expertise, which has definitely contributed to my personal and professional growth. Thanks to Dr Sílvia Molas for your teachings and good advice, as well as for your continuous support and implication. Thanks also to Sergi Parareda, for your indispensable collaboration in the design of experiments and the extended and interesting discussions on fracture mechanics. Finally, I want to thank Dr Nuria Cuadrado, Laura Grifé, Anna Payà, Anna Barrero and all the laboratory staff for supporting the experimental work. *A tots, moltes gràcies!*

I would also like to thank the support of the industrial partners involved in this work, especially to voestalpine Stahl, ArcelorMittal and Centro Ricerche Fiat (CRF), for their high interest and implication. Special thanks to voestalpine Stahl for performing the impact resistance tests presented in this research, which are an important part of the thesis work. Thanks to Dr Johannes Rehrl, Dr Clemens Suppan and Dr Patrick Larour from voestalpine for their collaboration in the preparation of the manuscripts and the interesting discussions. Also thanks to Dr. Thomas Dieudonné from ArcelorMittal for his active participation in the final part of this thesis.

The major part of this research has been performed in the frame of European funded research projects. So, I would like to thank and acknowledge the funded received by the European Commission under the Research Fund for Coal and Steel (RFCS Tough-sheet, RFCS Crash&Tough) and the EU-Horizon 2020 (FormPlanet) funding programs.

I also would like to thank Dr Oriol Vallcorba, researcher of the Powder Diffraction beamline (BL04-MSPD) at ALBA Synchrotron, for performing the X-ray powder diffraction measurements and supporting data post-processing.

Finally, I would like to thank my family and friends. *A mis padres por su preocupación, ayuda y apoyo incondicional y sobre todo a ti, Tatiana, por estar ahí en los momentos más difíciles, por tu apoyo, por tus ánimos, por hacer que este largo y difícil camino sea más llevadero, por todo… Gracias*.

List of publications

Appended publications

Paper I. D. Frómeta, S. Parareda, A. Lara, S. Molas, D. Casellas, P. Jonsén, J. Calvo. Identification of fracture toughness parameters to understand the fracture resistance of advanced high strength sheet steels. *Engineering Fracture Mechanics* 229 (2020) 106949.

Paper II. D. Frómeta, A. Lara, L. Grifé, T. Dieudonné, P. Dietsch, J. Rehrl, C. Suppan, D. Casellas, J. Calvo. Fracture resistance of advanced high strength steel sheets for automotive applications. *Metallurgical and Materials Transactions A,* Accepted manuscript.

Paper III. D. Frómeta, A. Lara, S. Molas, D. Casellas, J. Rehrl, C. Suppan, P. Larour, J. Calvo, On the correlation between fracture toughness and crash resistance of advanced high strength steels, *Engineering Fracture Mechanics* 205 (2019) 319-332

Paper IV. D. Frómeta, N. Cuadrado, J. Rehrl, C. Suppan, T. Dieudonné, P. Dietsch, J. Calvo, D. Casellas. Microstructural effects on fracture toughness of ultra-high strength dual phase sheet steels. Submitted to *Materials Science and Engineering A* (under review).

Other appended works

Paper A. D. Frómeta, M. Tedesco, J. Calvo, A. Lara, S. Molas, D. Casellas. Assessing edge cracking resistance in AHSS automotive parts by the Essential Work of Fracture methodology, *J. Phys.: Conf. Ser.* 896 (2017) 012102.

Paper B. D. Frómeta, A. Lara, S. Parareda and D. Casellas. Evaluation of Edge Formability in High Strength Sheets Through a Fracture Mechanics Approach. *AIP Conference Proceedings* 2113 (2019) 160007.

Paper C. D. Frómeta, A. Lara, B. Casas, D. Casellas. Fracture toughness measurements to understand local ductility of advanced high strength steels. *IOP Conf. Ser.: Mater. Sci. Eng.* 651 (2019) 012071

Paper D. D Frómeta, A. Lara, S. Parareda, L. Grifé, D. Casellas. New tool to evaluate the fracture resistance of thin high strength metal sheets. *IOP Conf. Ser.: Mater. Sci. Eng.* 967 (2020) 012088.

Table of Contents

List of figures

List of tables

List of symbols and abbreviations

Symbols

a	crack length
α_{Fmax}	bending angle at maximum force from V-bending tests according to VDA 238-100
A_{pl}	plastic area under load-displacement curve
β	plastic zone shape factor
δ_5	crack opening displacement measured over an initial gauge length of 5 mm
δ_c	critical crack opening displacement
d_f	displacement at fracture (EWF tests)
E	Young's modulus
ε_{ij}	strain tensor
ε_u	true uniform strain
$\varepsilon_{f\,HTT}$	true major strain at fracture at the hole edge in HTT specimens
$\varepsilon_{f\,KTT}$	true major strain at fracture at the notch tip in KTT specimens
Γ	integration path of the contour integral
G	Energy release rate
J	J-integral
J_i	J-integral at crack initiation
J_c	J-integral near the onset of stable crack propagation
K	stress intensity factor
K_{IC}	mode I plane strain fracture toughness
l_0	initial ligament length
M_s	Martensite start temperature
n	strain hardening exponent
P	applied load
R curve	crack growth resistance curve
ψ	crack tip opening angle
ρ	notch root radius
σ_{ij}	stress tensor
σ_Y	effective yield strength
σ_{YS}	yield strength
σ_{UTS}	ultimate tensile strength
σ_f	fracture stress
t_0	initial thickness
t_f	specimen thickness after fracture
Ti	traction vector components
T_R	Tearing modulus
u_p	actual plastic displacement
w	strain energy density
W	Specimen width
W_f	total work of fracture
W_e	essential work of fracture
W_p	non-essential plastic work
w_f	total specific work of fracture
w_f^i	specific work of fracture initiation
w_e	specific essential work of fracture
w_e^i	specific essential work of fracture initiation
w_p	non-essential specific plastic work

Abbreviations

AHSS	advanced high strength steel
BCC	body-centred cubic
CI	crash index

CIDR	crash index decreasing rate
CP	complex phase steel
CT	compact tension specimen
CTOA	crack tip opening angle
CTOD	crack tip opening displacement
DCT	Disk-shaped Compact Tension specimen
DENT	double edge notched tension specimen
DIC	digital image correlation
DP	dual phase steel
EBSD	electron backscatter diffraction
EDM	electrical discharge machining
EPFM	elastic plastic fracture mechanics
EWF	essential work of fracture
ESIS	European structural integrity society
FB	ferritic bainitic steel
FCC	face-centred cubic
FLC	forming limit curve
FLD	forming limit diagram
FPZ	fracture process zone
HER	hole expansion ratio
HET	hole expansion test
HSLA	high strength low alloyed steel
HTT	hole tension test
KTT	Kahn-type tear tests
LOM	light optical microscope
MS	martensitic steel
PHS	press hardened steel
Q&P	quenching and partitioning steel
RA	retained austenite
SEM	scanning electron microscopy
SENB	single edge notched bending specimen
SENT	single edge notched tension specimen
TBF	TRIP-aided bainitic ferritic steel
TE	total elongation
TRIP	transformation induced plasticity steel
TTS	true thickness strain from uniaxial tensile tests
TTS_{DENT}	true thickness strain from DENT specimens
TTS_{HER}	true thickness strain from HET specimens
TWIP	twinning induced plasticity steel
TYR	tear strength to yield strength ratio
UE	uniform elongation
UIE	unit initiation energy
UPE	unit propagation energy
UTS	ultimate tensile strength

Chapter 1

Introduction

1.1 Advanced High Strength Steels

1.1.1. Definition and applications

The advanced high strength steels (AHSS) family includes a vast variety of high-performance multiphase steels. These steels are characterized by their complex multiphase microstructures and excellent mechanical properties, which make them especially suitable for structural and safety-related auto body components [1]. Their higher strength and enhanced impact performance compared to conventional steels allow reducing the vehicle mass while improving the safety of the occupants, which is essential to satisfy the more and more stringent safety and fuel consumption regulations [1, 2]. These characteristics, together with the affordability of the manufacturing processes, are the key reasons that have motivated the widespread implementation of AHSS in passenger's cars. As a reference, a modern vehicle can have up to 56% of AHSS in the body structure (Figure 1.1) and it is expected that this percentage is increased up to 61% in near future vehicles [3].

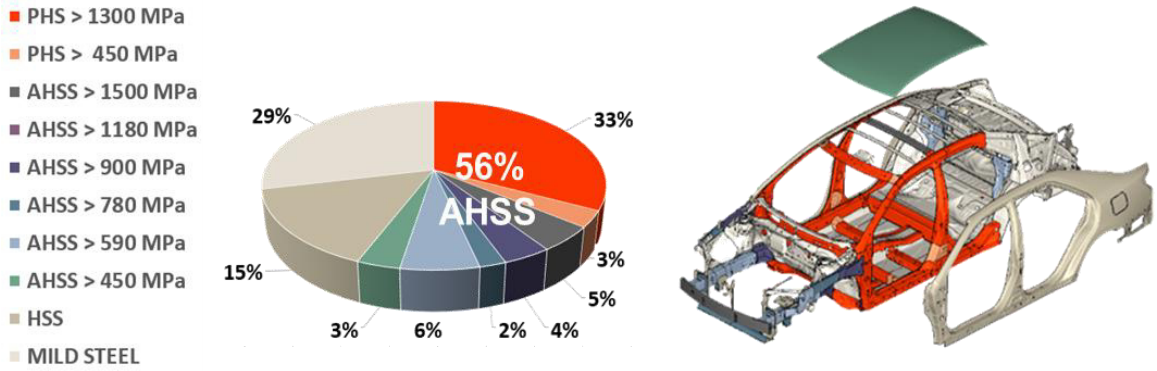

Figure 1.1. Implementation of AHSS in the body structure of a modern car. Reference for a NAFTA mid-size sedan. Source: ArcelorMittal

According to a 2015 market study, AHSS have become the fastest growing materials for automotive applications [4]. As shown in Figure 1.2 left, the average usage of AHSS in North American light passenger vehicles experienced a continuous increase of 7-8% from 2012 to 2015, surpassing the estimations of previous studies [4]. This study forecasts a similar growth rate from 2015 to 2025. The rapid growth of AHSS compared to other metallic materials for automobile body structures is also illustrated in Figure 1.2 right. The figure shows a significant increase in the use of bake hardenable steels and AHSS from 2007 to 2015, in replacement of an important part of conventional mild steels.

1.1.2. Classification

The great demands of the automotive industry have multiplied the research efforts towards the development of novel AHSS concepts in order to meet the increasingly exigent performance targets. As a result, a large number of AHSS grades with complex and unique microstructures,

carefully adjusted by controlling the chemical compositions and the thermomechanical processing routes, have been developed in the last two decades.

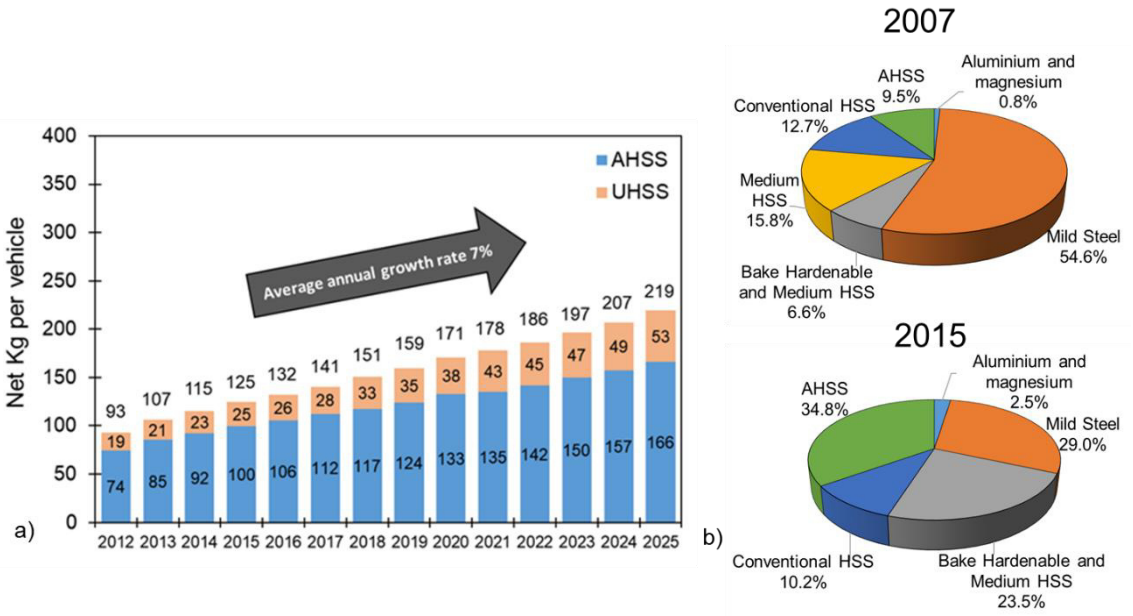

Figure 1.2. a) Average AHSS utilization in North America light passenger cars. Forecasts from 2015 to 2025. Image adapted from [4]. **b)** Body and closure metallic material content by type. Image adapted from [1].

In general, AHSS can be divided into three big groups or generations: 1st, 2nd and 3rd generation AHSS. Dual-Phase (DP), Complex Phase (CP), Martensitic (MS), Press-hardened (PHS) or Hot formed (HF), and Transformation-Induced Plasticity (TRIP) steels are part of the 1st generation of AHSS. This generation is characterized by showing better formability than single-phase high strength low alloyed (HSLA) steels of similar strength [5]. The 2nd generation of AHSS includes Twinning-Induced Plasticity (TWIP) and austenitic stainless steels. These steels present very high strength and extremely high ductility when compared to the 1st generation of AHSS. However, their production complexity and elevated costs, together with other problems of delayed cracking and poor weldability, have limited their application [6]. The 3rd generation was developed to cover the gap between the 1st and the 2nd generation of AHSS. 3rd generation AHSS present superior strength and enhanced formability than 1st generation AHSS but at significantly lower production costs [1]. Such AHSS family comprises steels with ultrafine microstructural constituents, such as martensite or bainite, produced in non-equilibrium conditions, in combination with retained austenite (RA) [7-9]. Bainite and martensite contribute to increasing the strength, whereas the stress-induced transformation of RA (TRIP effect) contributes to further optimize ductility and strength [9]. Some of the steels developed under this classification are TBF (TRIP-aided bainitic ferritic) and Q&P (quenching and partitioning) steels. Other 3rd generation TRIP-assisted steels, such as medium-Mn [9,10] or δ-TRIP steels [11], and nanoprecipitation steels [12] are currently under development.

Figure 1.3 illustrates the wide range of mechanical properties covered by AHSS in the well-known strength-ductility diagram for steels (also known as “banana” plot). The main characteristics of the above mentioned AHSS, in terms of microstructure, thermomechanical process and mechanical properties are described below.

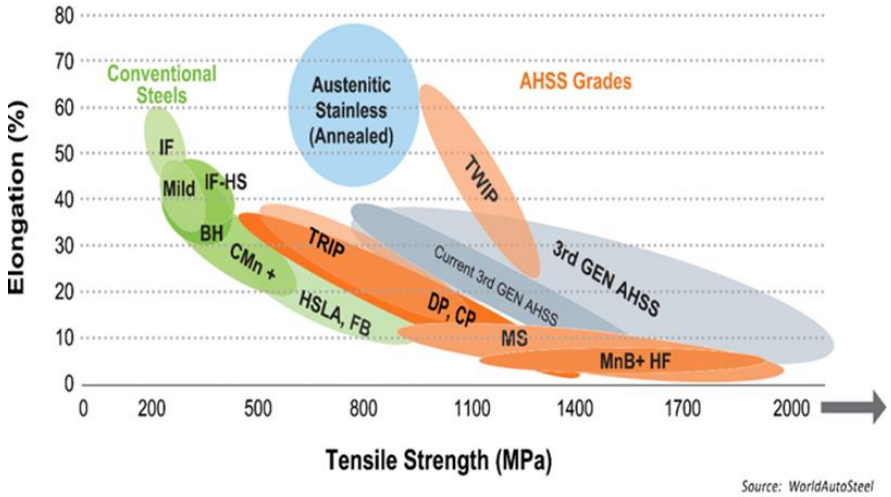

Figure 1.3. Strength ductility diagram for various types type of steels, including conventional and AHSS grades [1]

1.1.2.1. Dual Phase

Dual phase (DP) steels have a microstructure basically consisting of a soft ferritic matrix with hard martensite islands embedded (Figure 1.4a). They are produced by controlled cooling from the austenite phase (Figure 1.4b, DP1) or from the ferrite + austenite phase (Figure 1.4b, DP2) to transform some austenite to ferrite before a rapid cooling transforms the remaining austenite to martensite. Due to the production process, a small amount of other secondary phases, such as bainite or retained austenite, can also be present in different proportions [13-15].

DP steels are characterized by showing high strength, low yield strength to tensile strength (YS/TS) ratio, high strain hardening and high ductility compared to high strength low-alloy steels [1,15]. The strength level of DP steels is mainly governed by the martensite volume fraction (typical martensite volume fractions are in the range of 20-50% for tensile strengths of 600-1200 MPa). Their high strain hardening is caused by the strain gradients between the soft ferritic matrix and the hard martensite islands during forming, which generate dislocations pile-ups (geometrically necessary dislocations) in the soft matrix to accommodate the plastic incompatibility between the two phases [16]. Such deformation mechanism contributes to increase the work-hardening rate and to delay the onset of localized necking, thus improving the formability. Nevertheless, DP steels are known to be more sensitive to edge fractures [17,18] and show rather low hole expansion capacity [18-20].

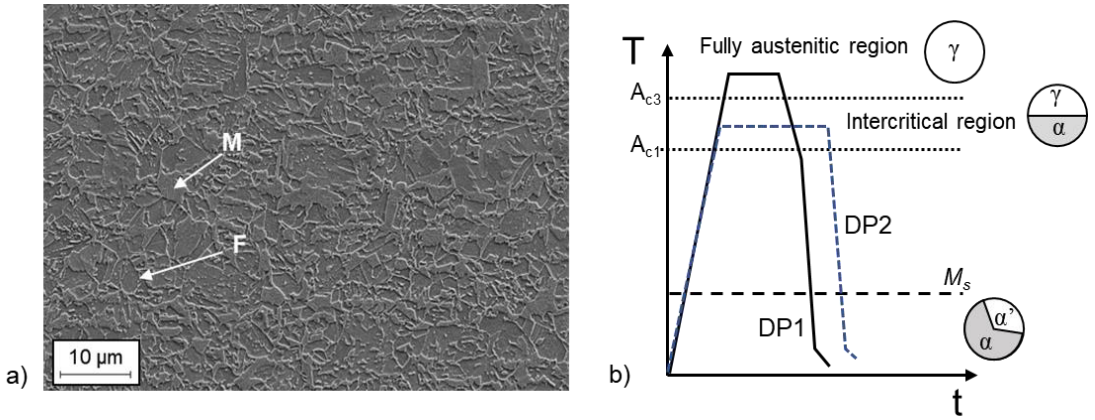

Figure 1.4. a) Typical microstructure of DP steels (SEM micrograph). F: ferrite; M: martensite **b)** Time-temperature cycle applied to obtain the DP microstructure. M_s: martensite start temperature.

1.1.2.2. Complex Phase

The microstructure of complex phase (CP) steels consists of ferrite, bainite, martensite and tempered martensite (Figure 1.5a). CP steels are produced by intercritical annealing followed by fast cooling to a temperature above *Ms*, where it is isothermally held for some time followed by cooling to room temperature (Figure 1.5b). During the first cooling, the intercritical austenite transforms to bainite, and the austenite remaining after the isothermal holding transforms to martensite after the final cooling step [21].

These steels are characterized by high yield strength to tensile strength ratio and low strain hardening. Compared to DP, CP steels exhibit higher yield strengths at equal tensile strengths (≥800 MPa) and lower elongation. On the other hand, they have a great energy absorption capacity, good hole expansion and excellent bendability, which makes them especially suitable for crash-resistant parts [20-22].

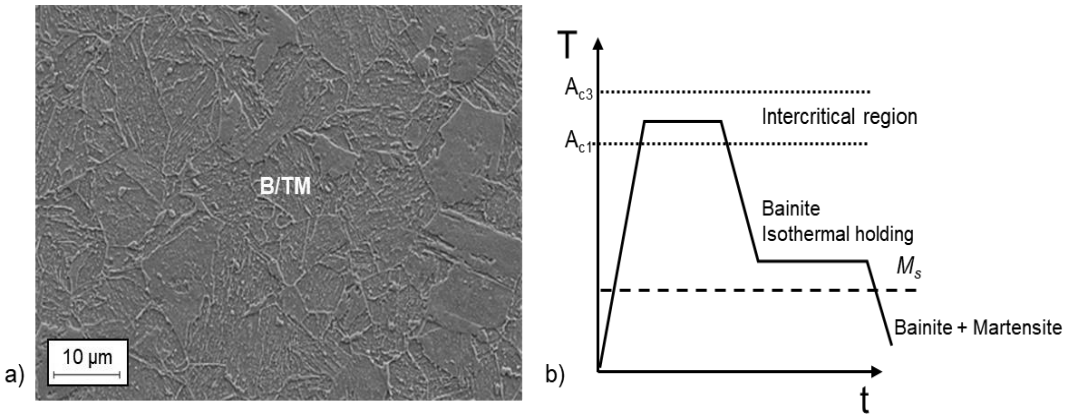

Figure 1.5. a) Microstructure of a CP steel (SEM micrograph). B: bainite; TM: tempered martensite **b)** Time-temperature cycle applied to obtain the CP microstructure.

1.1.2.3. TRIP

Transformation-induced plasticity (TRIP) steels have a primarily ferritic matrix with some amounts of bainite and a significant retained austenite (RA) volume fraction (5-20%). Figure 1.6a shows the microstructure of a TRIP steel with a tensile strength of 800 MPa. TRIP steels are produced using a heat treatment similar to that of CP grades (Figure 1.5b). The higher carbon and manganese content of these steels contributes to stabilizing the RA at room temperature [1, 9] and the addition of silicon or aluminium, helps to suppress carbide formation during bainitic transformation. The suppression of carbide formation in the austenite facilitates the carbon enrichment of austenite and increases its stability at room temperature [22]. The bainitic holding time and temperature determine the amount of bainite, as well as the amount and stability of RA.

The main advantage of TRIP steels is their increased ductility and strain hardening compared to DP steels of similar strength level (Figure 1.6b). Their high formability and work hardening rates are attributed to the austenite to martensite transformation during deformation (TRIP effect). The beneficial influence of the TRIP effect in mechanical properties is associated with the formation of additional mobile dislocations in ferrite in the vicinity of strain-induced martensite, which increases work hardening and delays the onset of necking. Due to the accompanying volume change, the shear strain leads to an additional increase of the dislocation density. With further straining the fresh formed strain-induced martensite generates more geometrically necessary

dislocations [9]. The additional strain hardening provides TRIP steels enhanced ductility and strength.

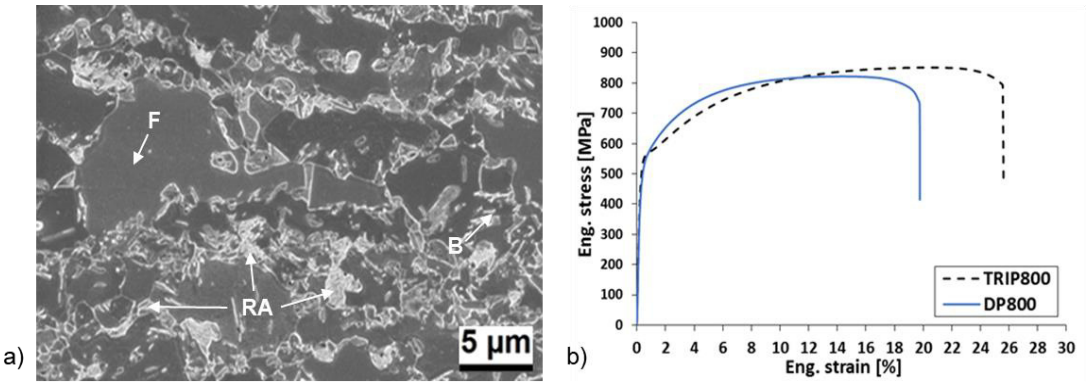

Figure 1.6. a) Microstructure of TRIP steel. F: ferrite; B: bainite; RA: retained austenite. **b)** Engineering stress-strain curves for DP and TRIP steel of similar strength.

1.1.2.4. Ferritic-Bainitic steel

Ferritic-Bainitic (FB) steels are a variation of DP steels. They have a ferritic matrix with bainite as a secondary phase in substitution of martensite (Figure 1.7a). The thermal cycle for processing FB steels is similar to that of CP steels (Figure 1.5b). The isothermal holding time determines the amount of bainite present in the final microstructure. Increasing the isothermal holding time increases the bainite volume fraction and decreases the amount of martensite formed during the final cooling step [23]. FB steels show slightly lower strength values and lower strain hardening than ferrite-martensite DP steels. They cover a tensile strength range of approximately 500–900 MPa, with total elongation values from 10 to 30% (Figure 1.7b). The main advantage of FB steels with respect to DP and TRIP steels is the improved edge stretchability. This makes FB steels especially suitable for applications where high stretch flangeability or hole expansion capability is required.

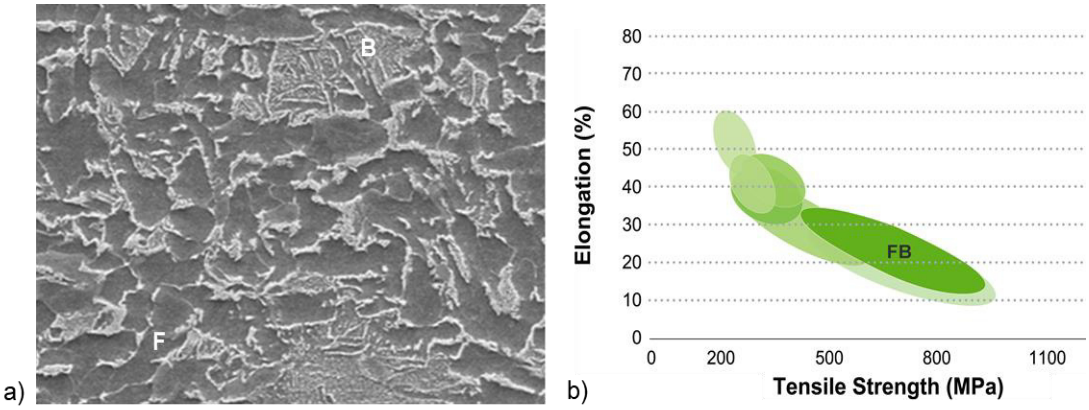

Figure 1.7. a) Microstructure of a FB 450/600 [1]. F: ferrite; B: bainite. b) Tensile strength-elongation diagram showing the range of mechanical properties covered by FB steels [1].

1.1.2.5. Martensitic steel

Martensitic steels (MS) are characterized by a martensitic matrix containing small amounts of ferrite and/or bainite (Figure 1.8a). They are produced by quenching at very high cooling rates

from the austenite region. The hard martensitic matrix provides very high yield and tensile strength (up to 1700 MPa) and lower elongation. Post quench tempering treatments improve ductility maintaining high strength. Generally, this kind of steels presents low stretch flangeability and fracture toughness. They are ideal for components of the passenger compartment where high resistance to intrusion is required.

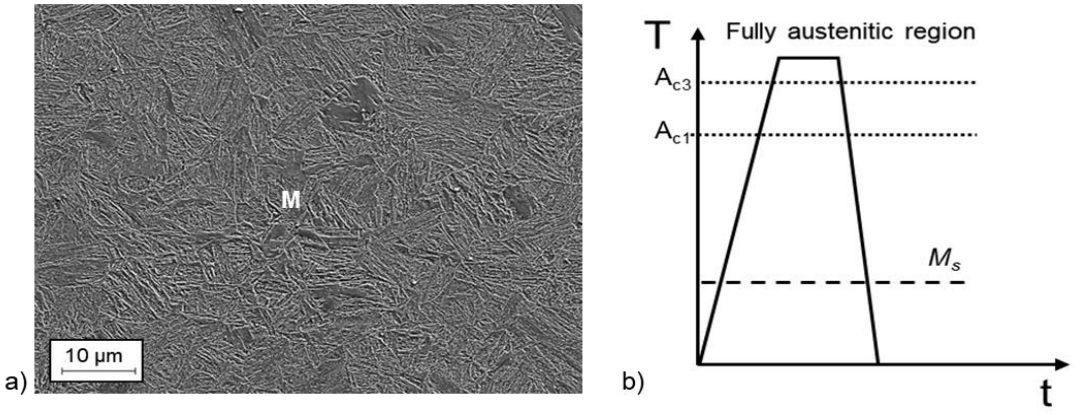

Figure 1.8. a) Microstructure of a MS (SEM micrograph). M: martensite. **b)** Time-temperature cycle applied to obtain martensitic microstructures.

1.1.2.6. Press Hardened steels

Press hardened steels (PHS) are extensively used in body-in-white applications, especially for structural components with high anti-intrusion requirements (impact beams, bumper beams, A- and B-pillars, etc.). The press-hardening technique, also known as hot stamping, takes advantage of low flow stress of boron-alloyed steel (22MnB5) in the austenitic phase at elevated temperature and allows the manufacturing of parts with ultrahigh strength and minimum springback issues [24]. The process is schematized in Figure 1.9. The blanks are austenitized at temperatures between 900 and 950 °C for 4 to 10 min inside a furnace and subsequently transferred to a cooled die via an automated transfer system. The blanks are formed at high temperature (650-850 ºC) in a single stroke and cooled down under pressure for a specific amount of time (5-15 s). During this period, the formed part is quenched in the closed die at a cooling rate of 50 to 100 °C/s. The total cycle time for transferring, stamping, and cooling in the die is 15 to 25 s [24].

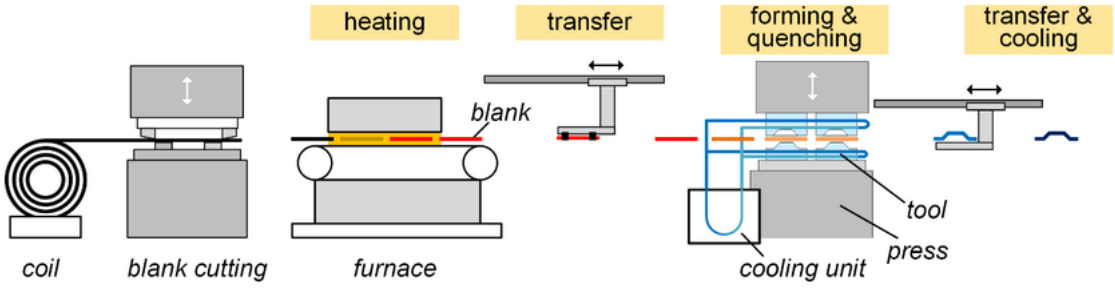

Figure 1.9. Schematic representation of the press hardening process [25].

Usually, the final microstructure is martensite (Figure 1.10a) with high ultimate tensile strength (1400-1700 MPa) and yield strength (1000-1200 MPa). However, as shown in Figure 1.10b-d, a wide range of final microstructures and mechanical properties can be obtained by controlling the cooling rate in the quenching process [26].

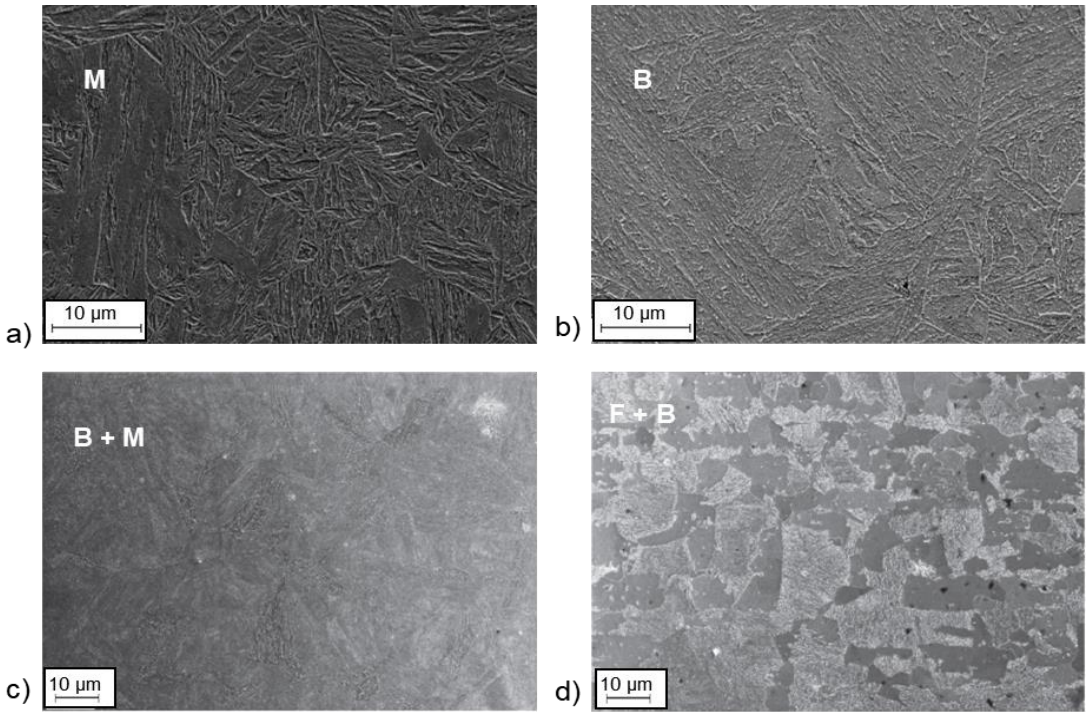

Figure 1.10. SEM micrographs of different press-hardened microstructures**. a)** martensite**, b)** bainite**, c)** bainite + martensite and **d)** ferrite + bainite [26]

1.1.2.7. TWIP

Twinning-Induced plasticity (TWIP) steels present a fully austenitic microstructure at room temperature (Figure 1.11), caused by their high manganese content (15-30%). Additional alloying elements such as Si and/or Al are needed to obtain the high strength and large uniform elongation associated with the strain-induced twinning. Al increases the stacking-fault energy (SFE) and, therefore, suppresses the austenite to martensite transformation so that the formation of deformation twins is favoured [27]. In contrast, Si decreases the SFE and sustains austenite to martensite transformation during cooling and deformation [28]. The main deformation mechanisms in TWIP steel are dislocation glide and deformation twinning. Mechanical twins are formed due to the low stacking fault energy. The formation of deformation-induced twins, gradually reduces the dislocation mean free path (Figure 1.11), resulting in a very high strain hardening rate due to the dynamic Hall-Petch effect. This high strain hardening rate allows for the combination of higher strengths and higher uniform elongations [27].

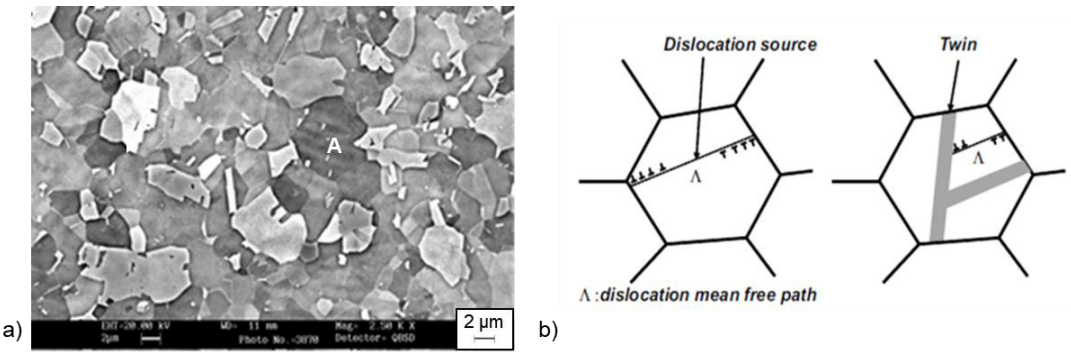

Figure 1.11. a) Microstructure of TWIP steels. A: austenite. **b)** Illustration of the dynamical Hall-Petch effect [27].

1.1.2.8. TRIP-assisted bainitic ferritic

TRIP-assisted bainitic ferritic (TBF) steels present a multiphase matrix, basically consisting of ferrite and bainite, with significant amounts of metastable RA (5-15%). The replacement of the soft single-phase matrix present in 1st generation TRIP steels by harder ferrite/bainite matrix, allows attaining higher strengths, whereas the good ductility and formability are maintained thanks to the TRIP effect. Figure 1.12a shows the microstructure of a TBF steel. The thermal cycle applied for the production of TBF steels is shown in Figure 1.12b. After full austenitization, the material is cooled down to the overageing temperature (usually about 400°C), at which the isothermal bainitic transformation takes place. The steel composition should contain Si and/or Al in order to prevent the carbide formation in the RA.

TBF steels generally exhibit great strain hardening and large elongation values (both uniform and fracture) which makes them suitable for forming operations involving global deformation, such as deep drawing. However, their DP-like microstructures usually show limited local formability (hole expansion, edge stretching) compared to more homogeneous CP-type microstructures [20].

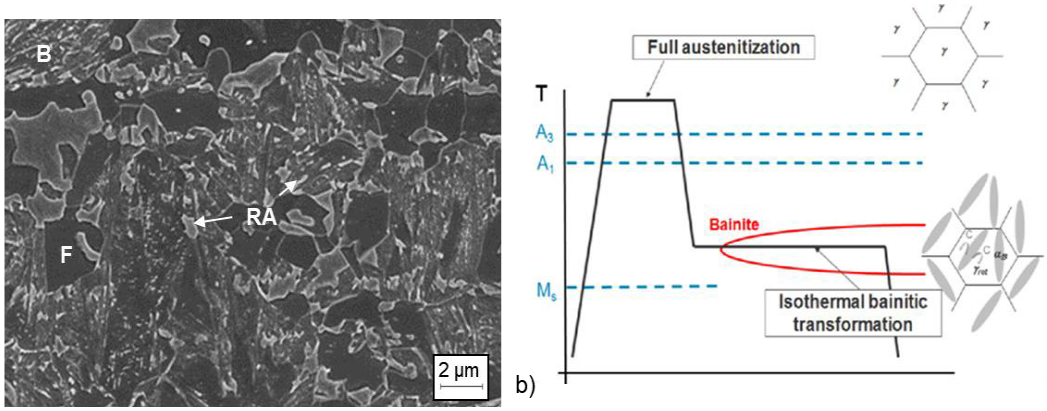

Figure 1.12. SEM micrograph of TBF steel. B: bainite, F: Ferrite; RA: retained austenite. **b)** Thermal cycle for TBF production [9].

1.1.2.9. Quenched and partitioned

The microstructure of quenched and partitioned (Q&P) steels consists of a tempered martensite/lower bainite matrix (ferrite can be also present in case of partial austenitization) and metastable RA (Figure 1.13a). The Q&P process involves quenching to a temperature (T_Q) under the *Ms* temperature, followed by a 'partitioning' treatment either at the initial quench temperature or above. This partitioning step is designed to enrich the remaining untransformed austenite with carbon, escaping from the supersaturated martensite, thus stabilizing RA at room temperature [29, 30].

The presence of hard martensite instead of bainitic ferrite promotes higher strength levels than the ones attained for TBF steels but lower elongation. The more homogeneous CP-like microstructure of Q&P steels makes them more suitable for forming operations with localized deformation, such as bending or edge stretching. These steels represent a good option for anti-intrusion structural parts.

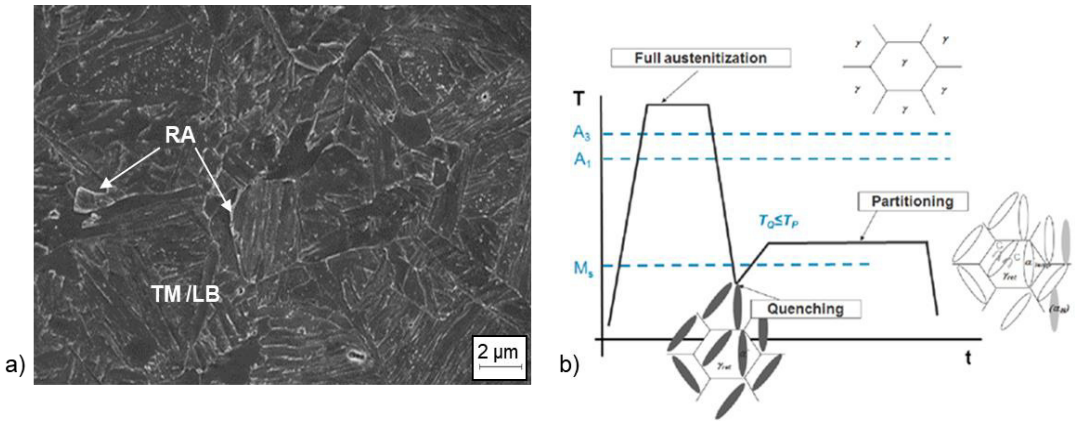

Figure 1.13. a) Microstructure of Q&P steel. RA: retained austenite; TM: tempered martensite; LB: lower bainite. **b)** Schematic representation of the quenching and partitioning process [9].

1.1.2.10. Medium Mn steels

The first investigations on the development of medium-Mn TRIP steels were carried out by Miller in 1972 [31]. The microstructural constituents of Fe–0.11C–5.7Mn consisted of ferrite and 29 vol.% austenite with a tensile strength of 878 MPa and a total elongation of 34%. Motivated by this success, recent research has focused on medium-Mn alloy design to obtain optimum strength and ductility combinations [32-37]. Medium Mn TRIP steels contain typically from 5-7 wt-% Mn. Their microstructure consists of an ultrafine-grained ferritic matrix with a grain size typically less than 1μm, and a high volume fraction of RA, usually up to 30 vol.-% (Figure 1.14a). The tensile strength of these steels commonly exceeds 1000 MPa along with total elongations in the range of 25 – 40 %.

The refined microstructure of medium Mn TRIP steels is obtained by the austenite-reverted-transformation (ART) annealing process (Figure 1.14b). The ART treatment is performed by reheating a strip with initial martensitic microstructure to a certain temperature (Intercritical annealing temperature, T_{IA}) between Ac1 and Ac3 to allow the formation of austenite, followed by quenching to room temperature. C and Mn diffuse from martensite to austenite during isothermal holding, contributing to the strong hardenability of austenite. In addition, Mn segregation at the martensite/austenite interface promotes the growth of austenite [38].

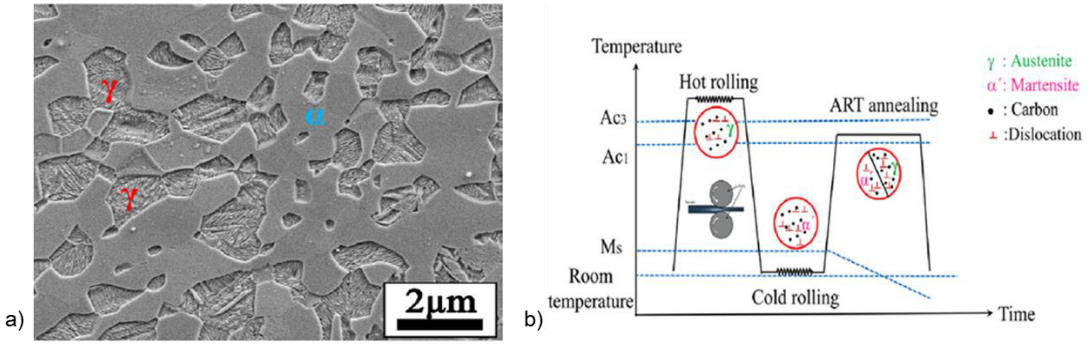

Figure 1.14. a) SEM micrograph of a medium Mn TRIP steel with a chemical composition of Fe–7Mn–0.14C–0.23Si [38]. **b)** processing routine of austenite reverted transformation (ART) annealing applied for the production of ultrafine-grained medium-Mn TRIP steels [38].

1.1.2.11. δ-TRIP

The so-called δ-TRIP steels are a novel concept of TRIP-assisted steel. These steels have a multiphase microstructure consisting of δ-ferrite, bainitic ferrite and RA (Figure 1.15). They have a typical chemical composition of 0.3 - 0.4 wt-% C, 2 - 6 wt-% Al, 0.2 - 0.8 wt-% Si and 0.5 - 1.6 wt-% Mn [39]. The high aluminium addition makes possible a density reduction of up to approximately 5% without sacrificing the Young's modulus [40]. δ-TRIP steels have excellent mechanical properties with tensile strengths of around 800-1000 MPa and elongations between 25- 40% [39-42].

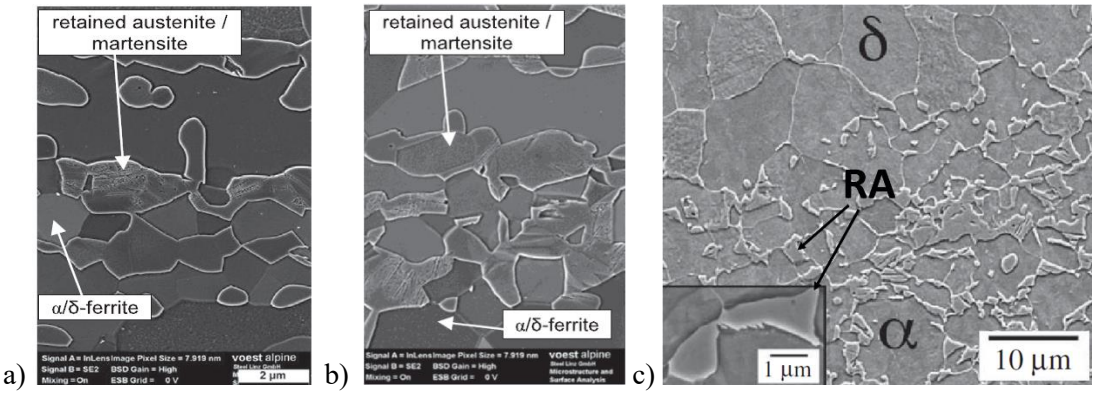

Figure 1.15. SEM micrographs of: a) Fe-0.4C-1.5Mn-5.2Al [39], b) Fe-0.4C-2.5Mn-5.2Al [39] and c) Fe-0.39C-0.5Mn-3.8Al [41].

1.2 Global and local formability

The continuous development of new complex multiphase AHSS grades has led to the need for alternative formability and fracture performance classification criteria. Owing to their complex microstructures and limited ductility compared to mild steels, AHSS are more susceptible to the occurrence of cracks during cold forming (edge cracking, limited hole expansion ability, etc. [43-45]) or in situations of severe deformation such as in crash scenario [46-49].

Unfortunately, this kind of fractures cannot be described by traditional ductility and formability definitions based on elongation values from uniaxial tensile tests and limit strains from Forming Limit Curves (FLC), as has been evidenced by several authors [43-51]. Therefore, extensive research is currently being conducted on the identification of different material parameters for a better description of the overall formability and fracture resistance of AHSS.

In the last years, different approaches have been proposed and an increasing interest has arisen in the classification of AHSS according to their global and local formability [52]. The term “global” is used to define the deformation modes where relatively large regions of material are deformed simultaneously (stretch forming, drawing, etc.) and strain localization occurs due to the application of a uniform deformation. Therefore, global formability refers to the material’s resistance against the formation of localized necking. On the other hand, “local” formability is more related to the fracture resistance of the material when the deformation is applied in a localized zone (tight-radius bending, stretch flanging, hole expansion, etc.).

1.2.1. Global formability

Global formability can be described by classical uniaxial tensile parameters (true uniform strain, elongation at fracture, n-value) and FLCs. The true uniform strain (ε_u) is the true strain value corresponding to the percent uniform elongation (*UE*) in a conventional uniaxial tensile stress-strain curve (Figure 1.16a), and it is calculated according to Equation (1):

$$\varepsilon_u = \ln(1 + \frac{UE}{100}) \tag{1}$$

The *UE* corresponds to the elongation at the ultimate tensile strength (*UTS*). Before the *UE*, the deformation is homogeneously distributed throughout the tensile specimen. When the *UTS* is reached, the deformation starts to localize over a length of the order of the specimen width ("diffuse necking") [54]. For materials that follow a power-law relationship between stress and strain (Equation (2)):

$$\sigma = \mathrm{K}\,\varepsilon^n \tag{2}$$

where σ is the true stress, ε is the true strain and *K* and *n* are two material constants (strength coefficient and strain hardening exponent, respectively); it is found that the corresponding strain at the onset of necking (ε_u) is equal to the strain hardening exponent [55]:

$$\varepsilon_u = n \tag{3}$$

Accordingly, both parameters ε_u and *n* inform about the material's ability to uniformly distribute the strains and are used to describe the global ductility of a material; the higher they are, the higher the global ductility.

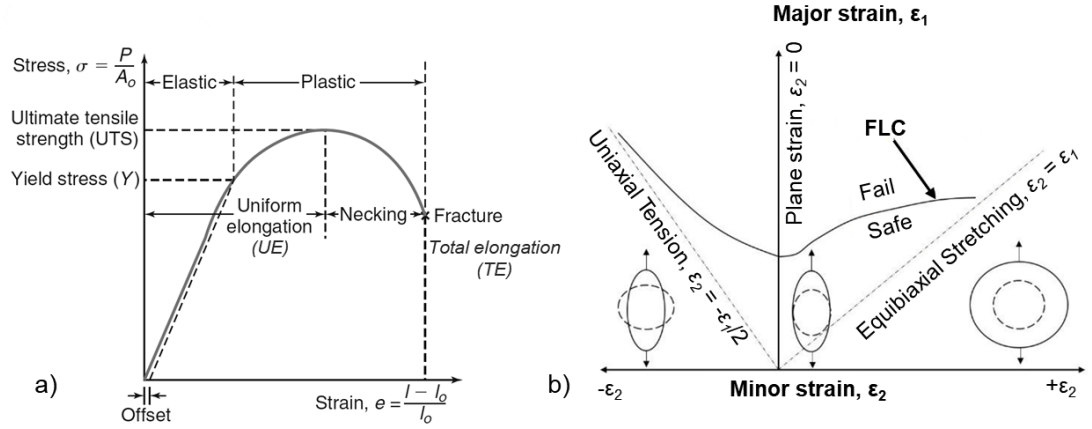

Figure 1.16. a) Typical stress-strain curve obtained from a uniaxial tensile test [53]. **b)** Schematic representation of an FLC [56].

The FLC defines the deformation limits of a material for multiple strain paths, represented by different combinations of major (ε_1) and minor (ε_2) strains in the so-called Forming Limit Diagram (FLD, Figure 1.16b). These critical strains represent the onset of localized necking and determine the limits below which safety margins are calculated. The strain points below the FLC correspond to the safe zone, where the sheet metal can be formed without risk of localized necking. The points located above the FLC indicate risk of failure.

The FLC is evaluated by means of Nakajima or Marciniak (Figure 1.17) tests with different specimen geometries to generate the different strain paths (between uniaxial and equibiaxial tension). The experimental procedure is described in the ISO 12004 standard [57]. Different works have shown that the FLC can be predicted from uniaxial tensile properties and sheet thickness [58, 59].

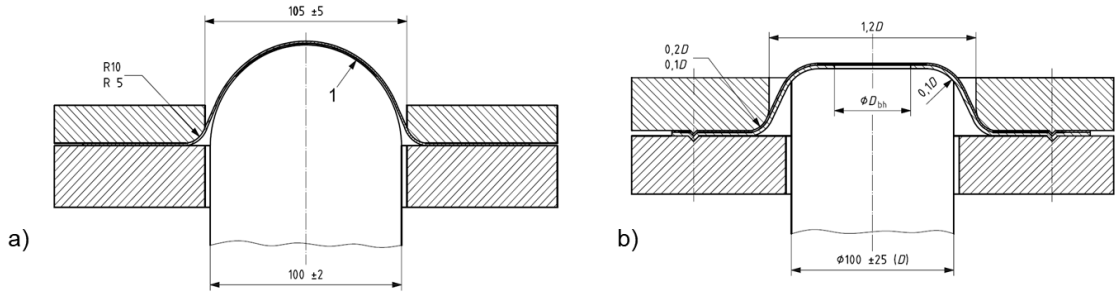

Figure 1.17. a) Geometry of the punch used for Nakajima tests. **b)** Tool used for Marciniak tests [57].

1.2.2. Local formability

Local formability fractures generally occur in absence of significant necking or thinning prior to failure, such as, for example, edge fractures or shear fractures during tight-radius stretch bending. Therefore, they cannot be predicted through conventional global ductility approaches based on necking instability. Hole expansion tests and 3-point V-bending tests are currently the most extended experimental techniques to characterize the resistance of AHSS to some of these local ductility-related failures. Alternatively, some authors have proposed different parameters based on the measurement of local fracture strains in uniaxial tensile and notched specimens to classify the local formability of AHSS in a more objective manner.

1.2.2.1. Hole expansion tests

The Hole Expansion Test (HET) according to ISO 16630 [60] is established as a standard procedure for evaluating the edge fracture resistance of AHSS sheets. The HET consists in punching a hole in a flat sheet sample and then, by using a conical tool, expand the hole until a through-thickness edge crack is observed (Figure 1.18a). The obtained result is the Hole Expansion Ratio (HER), which is determined according to Equation (4):

$$HER\ (\%) = \left[\frac{D_h - D_0}{D_0}\right] x100 \tag{4}$$

where D_h is the hole diameter when the first through-thickness crack is observed and D_0 is the initial diameter of the punched hole. The HER is used as a representative measure of the edge cracking sensitivity of the material (the lower the HER the greater the edge cracking sensitivity) and it has become one of the most important parameters for local formability assessment. However, the HER is not a material property and its reliability is often put into question because of the large data scattering and the poor repeatability found in some research works and round-robin tests [61,62].

1.2.2.2. V-bending tests

V-bending tests according to VDA 238-100 [63] have become a common practice to assess the bendability of AHSS sheets. The test consists of submitting a rectangular flat sheet sample to

plastic deformation by bending until a crack appears. Punch displacement and force are recorded during the test. The test is stopped when there is a load drop of 30-60 N after the maximum force, depending on the sheet thickness and the type of material. To avoid the influence of springback in post-test bending angle measurements, different analytical expressions are used to evaluate the bending angle indirectly from the punch displacement. The bendability of the materials is characterized by the bending angle at maximum force, α_{Fmax}. Figure 1.18b shows the experimental setup for the determination of the α_{Fmax} from V-bending tests according to VDA 238-100.

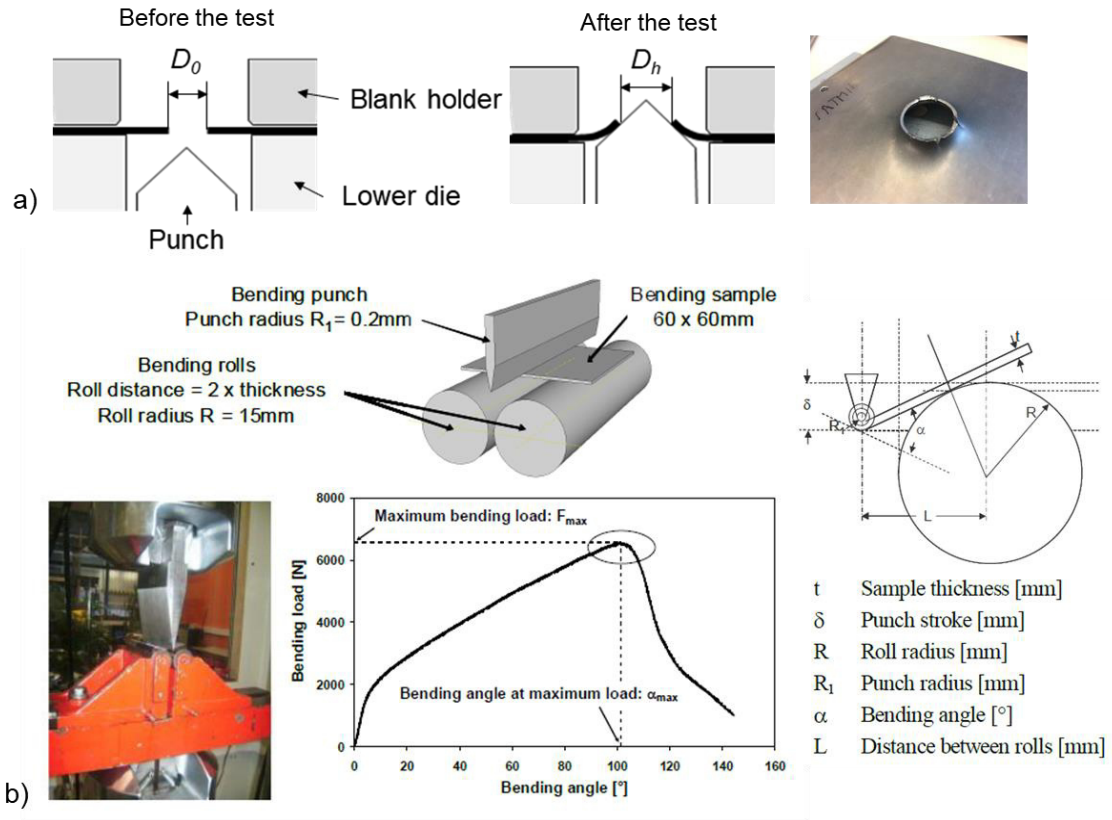

Figure 1.18. a) Experimental procedure of the HET and HET sample after the test. **b)** Experimental setup for the 3-point V-bending tests according to VDA 238-100 at voestalpine Stahl [47].

1.2.2.3. Local fracture strain measurements

Hance and Davenport proposed the use of the True Fracture Strain (*TFS*) as a relative index of local formability [52]. The *TFS* is calculated from the reduction of area at fracture of uniaxial tensile specimens as follows:

$$TFS = \ln\left(\frac{A_0}{A_f}\right) \tag{5}$$

A_0 is the cross-section area of the tensile specimen before testing and A_f is the area at fracture. A_f is given by

$$A_f = w_f \cdot t_f \tag{6}$$

where w_f and t_f are, respectively, the width and the thickness at fracture. For specimens with original rectangular cross-sections, and assuming a parabolic fracture surface, the ASTM E8 [64] recommends calculating the thickness at fracture as indicated in Equation (7):

$$t_f = \frac{1}{6}(t_1 + 4t_2 + t_3) \quad (7)$$

where t_1 and t_3 are the thicknesses at the corners, and t_2 is the thickness at mid-width (Figure 1.19).

Other authors have alternatively suggested the use of the reduction of area at fracture in tensile testing (*Z-value,* Equation (8)) or the true thickness strain at fracture (*TTS,* Equation (9)), as local formability indicators [65, 66].

$$Z = \frac{A_0 - A_f}{A_f} \quad (8)$$

$$TTS = \ln(\frac{t_0}{t_f}) \quad (9)$$

t_o is the initial sheet thickness and A_0, A_f and t_f are described above.

Different works have shown a quite good correlation between these local formability parameters and HER values from ISO 16630 HET [65-67].

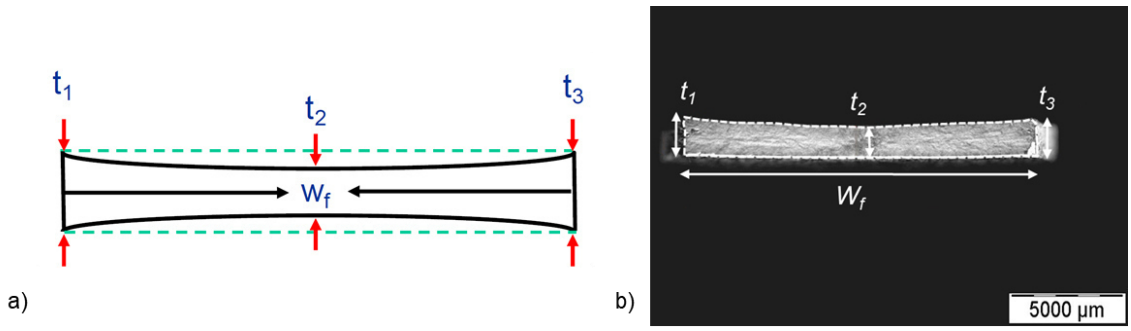

Figure 1.19. a) Schematic representation of the parabolic fracture surface profile of a uniaxial tensile specimen with rectangular cross-section [52]. **b)** Fracture surface of a flat sheet tensile specimen. Microscope image.

1.2.3. Global vs local formability maps

Recently, a novel global/local formability map concept was introduced by Hance and Davenport [52]. This diagram (also known as "Hance diagram") represents the true fracture strain (TFS) as a function of the true uniform strain (ε_u) (Figure 1.20a). The ratio between the TFS and ε_u (TFS/ ε_u) gives an estimate of the formability characteristics of AHSS. Materials with higher ε_u have better performance in stretch forming and global formability modes, whereas materials with higher *TFS* are expected to behave better in local forming operations. Following the proposal of Hance, Heibel et al. introduced an alternative global/local formability classification diagram, using the true thickness strain (*TTS* or ε_{3f}) instead of the *TFS* (Figure 1.20b) [66].

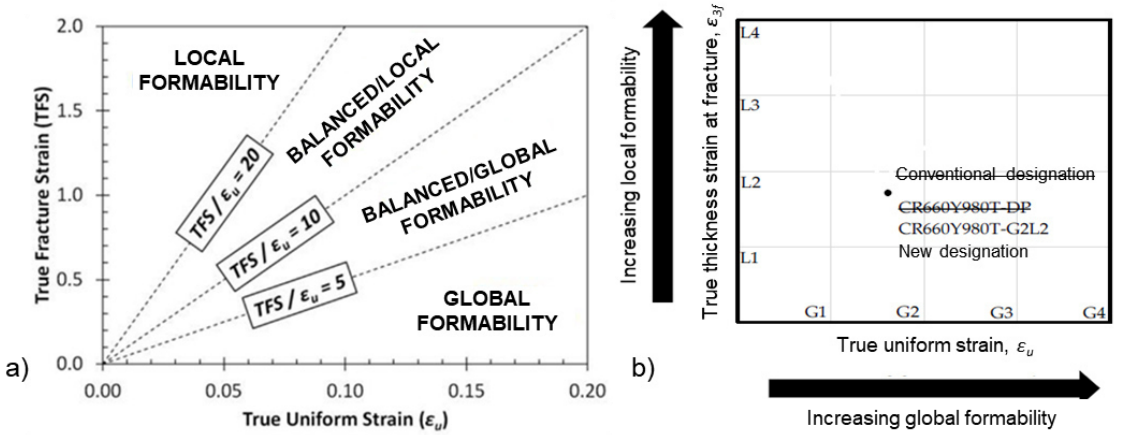

Figure 1.20. Local/global formability maps for AHSS classification. Global (G) formability is represented by the true uniform strain (εu) from uniaxial tensile tests. Local (L) formability is expressed in terms of **a)** True Fracture Strain (TFS) [52] and **b)** True thickness strain at fracture (ε_{3f}) [66].

1.3 Local formability and crack-related failures

This section describes two of the main fracture problems related to the local formability and cracking resistance of AHSS, the edge cracking and the crack formation under impact loading, and how they are addressed. Even though, as mentioned in the previous section, several approaches and material parameters have been proposed to describe this kind of fractures, it is a recurrent problem that it is not completely solved yet. Rather on the contrary, with the development of steel grades with increasingly higher strengths, these fractures are more and more frequent, becoming a real concern to automotive part manufacturers and limiting the applicability of some AHSS grades. Therefore, large efforts are still being devoted to the identification of the most appropriate material properties to rationalize these crack-related failures.

1.3.1 Edge cracking

Automotive part manufacturers frequently report the presence of unexpected cracks in sheared, trimmed or punched edges in stamped components (Figure 1.21). These edge fractures are one of the most important failure modes related to the local formability of AHSS. Edge cracking occurs at strain levels much lower than the deformation limits determined by conventional FLCs [43,45,68]. Furthermore, elongation values from tensile tests are not suitable either to classify the edge cracking sensitivity of AHSS, since materials showing greater elongation may show poorer edge cracking resistance [20]. Therefore, several alternative characterization methods have been developed for edge formability prediction and material ranking. The ISO 16630 Hole Expansion Test (HET) is the most commonly used test to evaluate the edge cracking sensitivity of AHSS. However, as mentioned before, these tests present some limitations to obtain reliable results and extrapolate the edge cracking test results to real stamped parts. To overcome such experimental uncertainties and improve the accuracy of edge cracking prediction, additional experimental techniques based on Digital Image Correlation (DIC) measurements have been recently proposed. Hole tension tests (HTT), biaxial Nakajima or Marciniak hole expansion tests and edge-fracture tensile tests are some examples of the tests developed for edge formability characterization [62, 69-73]. Based on their good correlation with the HER, local ductility parameters from uniaxial tensile tests (*TFS*, *TTS*, Z-value) are also often used as indicators of edge cracking resistance [65-67]. Nevertheless, in spite of all these efforts, at the present, there are no reliable failure criteria to accurately predict edge cracking of AHSS.

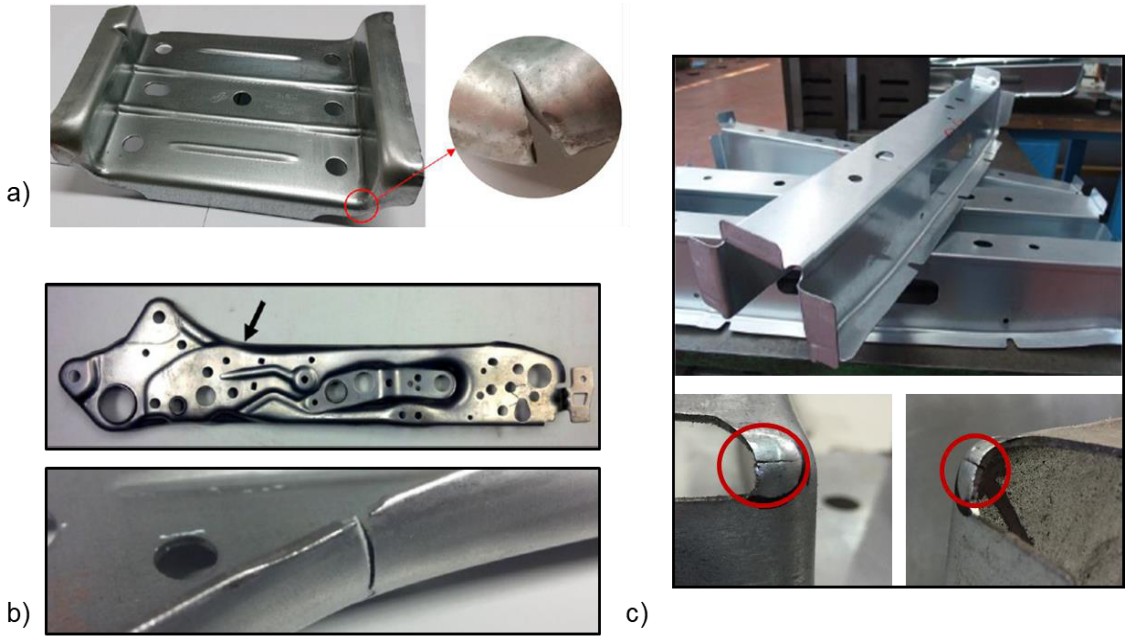

Figure 1.21. Examples of edge cracking in cold formed automotive components**. a)** body in white stamped part. Material: DP600 [45]. **b)** Automotive seat component. Material: DP980 [67]. **c)** Under seat beam made of DP980. Images courtesy of Centro Ricerche Fiat (CRF).

Edge formability is mainly influenced by two factors: the edge quality (amount of damage introduced in the edge during cutting) and the damage tolerance of the material. During shearing, blanking or punching, several defects such as microcracks, voids or surface irregularities are introduced in the edge surface (Figure 1.22) [74-76]. Such defects act as crack nucleation sites which propagate through the sheet thickness during the subsequent forming processes (edge stretching, hole expansion, etc.) and cause the fracture of the part [76]. The amount of damage depends on several parameters of the cutting process: cutting/punching clearance [77-79], cutting tool condition [79], etc. On the other hand, the formability of the sheared edge depends on the material's resistance against the propagation of cracks from initial defects, i.e. on its fracture toughness [76].

Different research works have established a direct relationship between fracture toughness and edge formability of high strength steel sheets [20, 23, 76, 80]. The work of Takahashi et al. [76] discussed the edge flangeability of different hot rolled high strength steels using a fracture mechanics approach and found a linear correlation between the fracture toughness (J_c) and the HER. Fonstein et al. [23] observed that the increase in the HER of a cold rolled steel with different bainite contents could be explained by an increase in the crack propagation resistance, measured in the frame of fracture mechanics. Similar conclusions can be extracted from the works of Casellas et al. [20] and Yoon et al. [80], where fracture toughness is proposed as the key property governing the edge cracking resistance of AHSS. This approach, based on fracture mechanics, is further investigated and discussed in this thesis work.

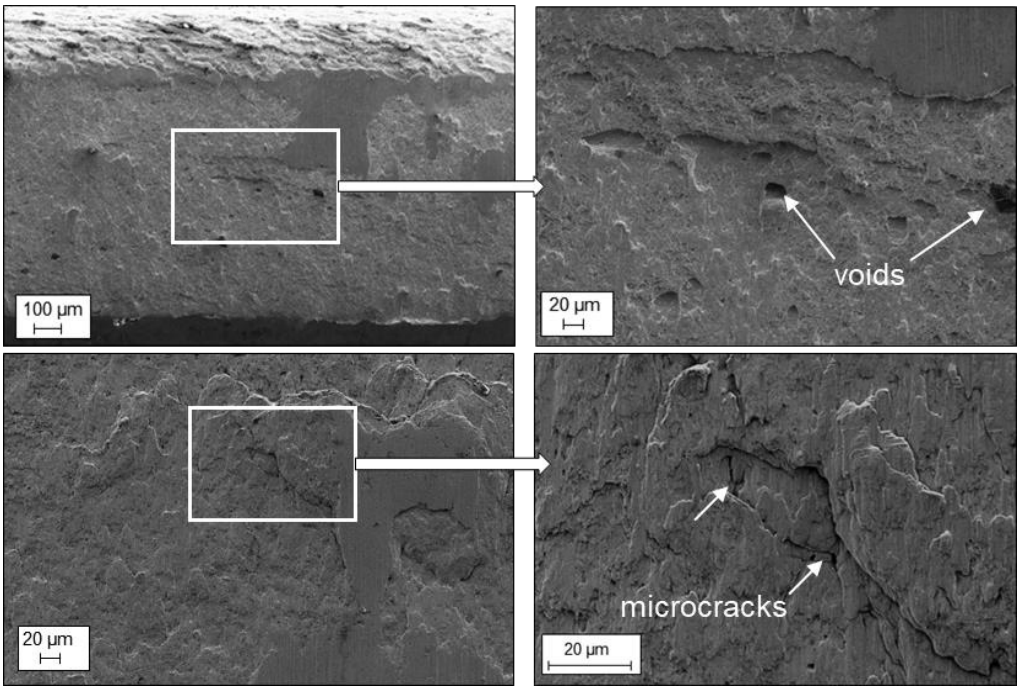

Figure 1.22. SEM images of the surface of two mechanically sheared edges. CP steel (upper row) and DP steel (lower row).

1.3.1 Crash fracture behaviour

The main application of AHSS in the automobile is directed to the design of structural parts and safety components. Therefore, the characterization of the material performance under crash conditions is one of the most critical aspects for automakers and steel product developers.

The main crash energy management areas in a vehicle are two: the crumple zone and the passenger compartment (Figure 1.23). The requirements and expected safety performance for these zones are very different. The crumple zone is designed to absorb the maximum possible energy during a crash event. Thus, the materials selected for this area should be materials that combine high strength and toughness. On the other hand, the passenger compartment is enclosed in a safety cage that must be rigid and prevent any deformation or intrusions that can compromise structural integrity. The passenger compartment requires materials with very high strength.

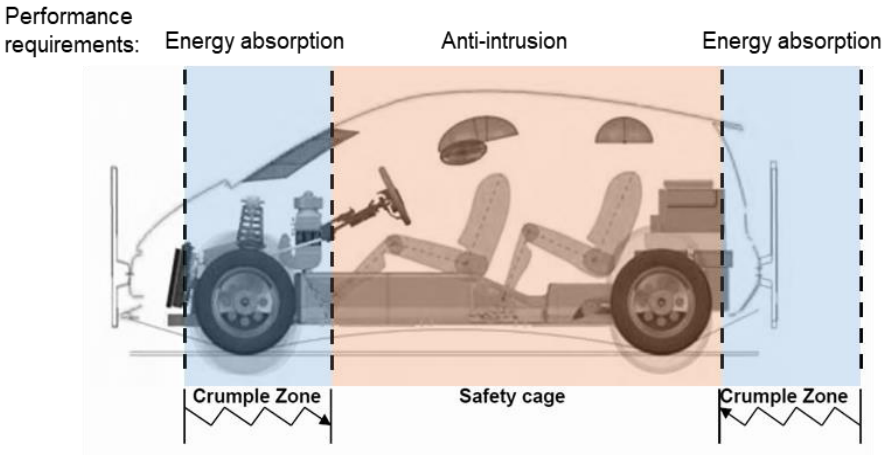

Figure 1.23. Main crash energy management areas in a vehicle. Adapted from [1].

To characterize the crash energy absorption and anti-intrusion characteristics of AHSS, two main laboratory tests are currently used in the automotive industry, axial impact tests and bending (or side) impact tests, respectively (Figure 1.24). However, these tests are expensive and time-consuming. Moreover, the results are very sensitive to the experimental setup and the crash sample geometry. This can provide contradictory crash failure behaviours for the same material with different test coupon design and makes difficult the comparison of results [81]. Thus, aimed at improving material selection and optimizing new material design, several attempts have been made to develop alternative small-scale tests and material parameters for crash resistance estimation. V-bending tests according to VDA 238-100 [63] are state of the art to characterize AHSS crash bendability [47-49, 82]. Other approaches based on plane strain fracture strain measurements from V-bending or notched specimens have been also found to be useful for ranking the crash folding ability of AHSS and PHS [48, 83]. Nevertheless, an additional complexity emerges from the crash failure behaviour of very high strength steels (UTS > 800 MPa), which is strongly affected by the nucleation and propagation of cracks (Figure 1.25). Consequently, these parameters are not accurate enough to describe the overall crash resistance of AHSS, since they do not take into account the non-negligible energy spent in crack propagation. Larour et al suggested that the overall crash failure behaviour of AHSS and PHS was mainly dominated by the bendability (resistance to crack initiation) and the fracture toughness (how rapid these cracks propagate through the material). The relationship between fracture toughness and the cracking behaviour of AHSS under impact loading is other of the main points analysed in the present project.

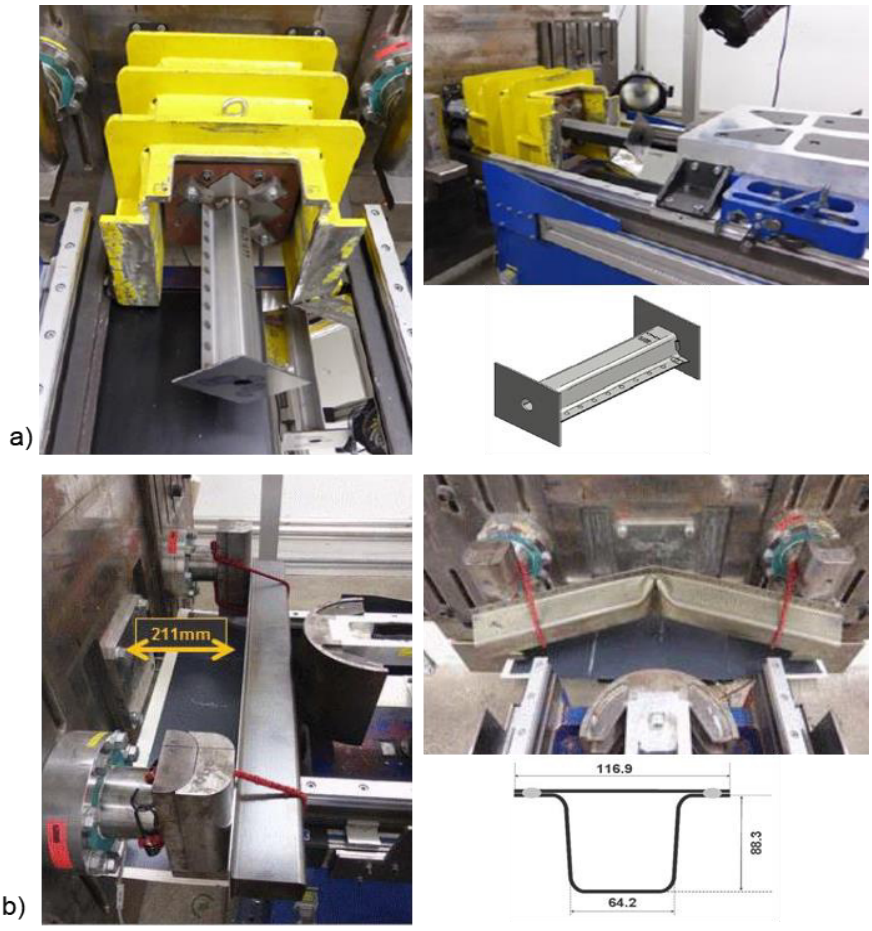

Figure 1.24. Experimental setup and specimen geometry for laboratory impact resistance tests at voestalpine Stahl: **a)** axial impact tests [81]. **b)** bending impact tests [82].

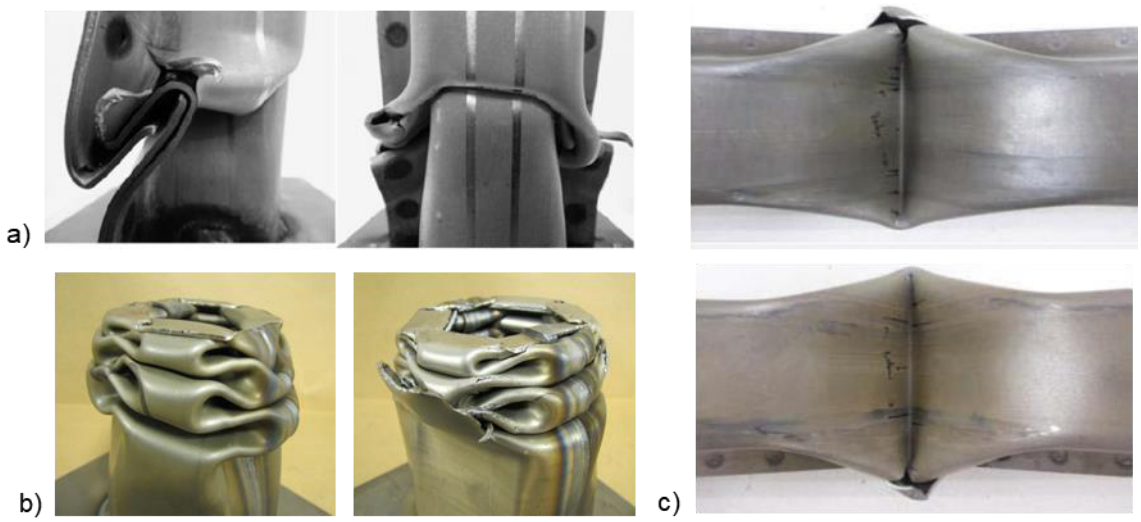

Figure 1.25. Examples of cracks in axial (a, b) and bending (c) crash tested samples of AHSS and PHS. Images from: **a)** [81], **b**) [49] and **c)** [82]

1.4 Fracture toughness of advanced high strength steels

The fracture toughness, from a fracture mechanics point of view, is the property that controls the crack initiation and propagation resistance of a material. It is important to differentiate this definition from the conventional use of the term 'toughness', referring to the area under the stress-strain curve of a uniaxial tensile test or the product of the ultimate tensile strength by the total elongation (UTSxTE), which is not suitable to describe the material resistance in the presence of pre-existing cracks or defects.

Fracture toughness is considered as a key design parameter for engineering applications where structural integrity is of primary importance, such as pipelines in oil and gas industries, nuclear plants, pressure vessels, aeronautics, etc. However, until the rise of AHSS, the fracture toughness has not been considered to be relevant to automotive designers due to the large ductility of conventional mild steels. This fact, together with the complexity of fracture mechanics testing and the absence of affordable standard procedures for fracture toughness characterization of thin metal sheets have generated a gap of knowledge in this field.

However, due to the increasingly demanding performance requirements and the frequent occurrence of fractures related to the crack initiation and propagation resistance in AHSS, the knowledge on the fracture toughness properties of high strength metal sheets has become unavoidable. As a sign of the growing interest in this topic, the number of research works related to the fracture toughness of AHSS has significantly increased in the last years [20, 26, 80, 84-91]. Nevertheless, there is still some confusion about which are the most appropriate testing methods for characterizing the fracture toughness of thin high strength metal sheets and how they can be used to understand the cracking resistance of AHSS.

Some of the basic fracture mechanics concepts and the main experimental techniques for fracture toughness characterization of ductile sheet materials are reviewed below.

1.4.1. Introduction to fracture mechanics

Fracture mechanics is the discipline that evaluates the conditions under which a structural component can break due to the existence and growth of a crack in the component. Fracture mechanics covers a broad field of disciplines, from materials science to engineering applications, passing through applied mechanics (Figure 1.26). Materials science addresses the fracture itself at atomistic level and the evolution of the fracture process considering grains, impurities, etc., what is key to understand the behaviour of a crack in a determined stress-strain field. Applied mechanics is found one step beyond and is responsible to characterize and quantify the parameters that describe the crack resistance of the material. In order to successfully use fracture mechanics in engineering applications, it is important to have some knowledge on all these disciplines.

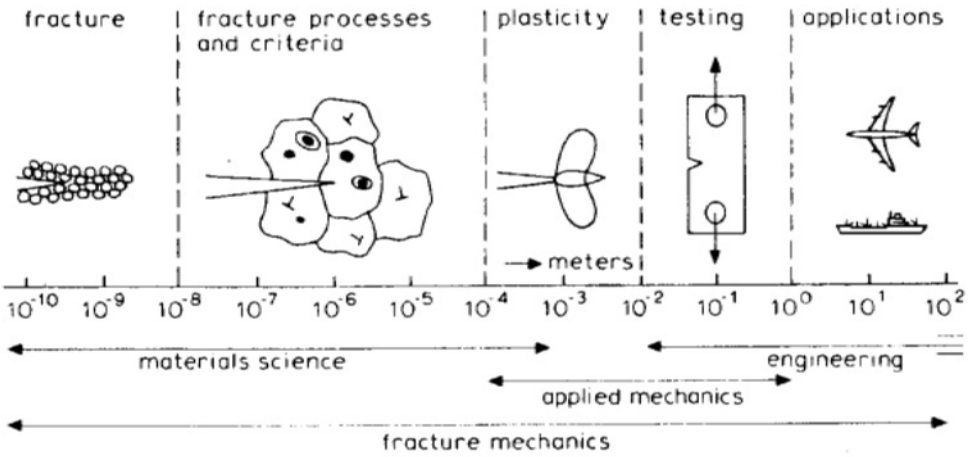

Figure 1.26. Science and engineering fields covered by fracture mechanics [92].

In materials with high sensitivity to the presence of cracks or defects, like the case of high strength materials with high yield strength and moderated ductility, engineering fracture mechanics is a useful tool to complement the conventional design criteria based on tensile strength, yield strength or buckling stress. It was developed mainly in the 20th century from the works of Griffith [93] and Inglis [94]. Such authors set the bases for the Linear Elastic Fracture Mechanics (LEFM), which was firmly established in the 1950s. Later, at the end of the 1960s, LEFM was extended to non-linear problems from the works of Rice [95, 96] and Hutchinson [97], giving rise to the development of the Elastic-Plastic Fracture Mechanics (EPFM).

1.4.2. Linear Elastic Fracture Mechanics

The application of LEFM is only valid when there is no significant deformation before the fracture, like is the case of very brittle materials such as glass or ceramics. Griffith established the link between the fracture and the size of the defects, analysing the stresses in an elliptical crack [93]. He developed an energetic approach based on the first law of thermodynamics, using a simple energy balance. According to his theory, a crack is unstable and the fracture takes place when the energetic change associated with the crack growth is sufficient to overcome the material surface energy. However, Griffith's model is only applicable to ideally brittle solids, since the energy of fracture comes exclusively from the surface energy of the material. The theory assumed that the fracture strength was limited by the existence of initial cracks and that brittle materials contain elliptical microcracks, which introduce high stress concentrations near their tips. He

developed a relationship between crack length (a), surface energy connected with traction-free crack surfaces (2γ), and applied stress (σ), which is given by Equation (10).

$$\sigma^2 = \frac{2\gamma E}{\pi a} \tag{10}$$

Where *E* is the Young's modulus.

Nevertheless, it was found that the energy required for fracture was much greater for most engineering materials. In 1948, Irwin [98] and Orowan [99] independently presented an extension to Griffith's theory, proposing that the total energy required for crack growth comes from surface energy and an irreversible plastic work close to the crack tip. This approach allowed to extend Griffith's model to ductile materials. The criterion was that the strain energy release rate, *G,* must be larger than the critical work, *Gc*, which is required to create a new unit crack area.

Using Westergaards' method to analyse stresses and displacements at the crack tip, Irwin showed that the stress field in the area of the crack tip is completely determined by a quantity *K,* called the stress intensity factor, as follows [100]:

$$\sigma_{ij} = \frac{K f_{ij}(\theta)}{\sqrt{2\pi r}} \tag{11}$$

The relation between *G* and *K* is described in Equation (12):

$$G = \frac{K^2}{E'} \tag{12}$$

Where $E'=E$ for plane stress and $E' = E/(1-\nu^2)$ for plane strain and ν being the Poisson's ratio.

1.4.3. Loading modes

There are three primary modes of crack loading (Figure 1.27), Mode I, Mode II and Mode III. In Mode I loading (opening), the principal load is applied normal to the crack plane and tends to open the crack. Mode II (in-plane shear) involves a shear loading that tends to slide the crack faces in the direction parallel to the primary crack dimension. Mode III (out-of-plane shear) loading or tearing mode involves a shear load sliding the crack faces in the direction perpendicular to the primary crack dimension.

A cracked body can experience any of these loading modes or a combination of two or three modes. However, loading Mode I is the most used one for stress analysis of cracks since it is the predominant loading mode in engineering applications and most crack failures occur under this opening mode.

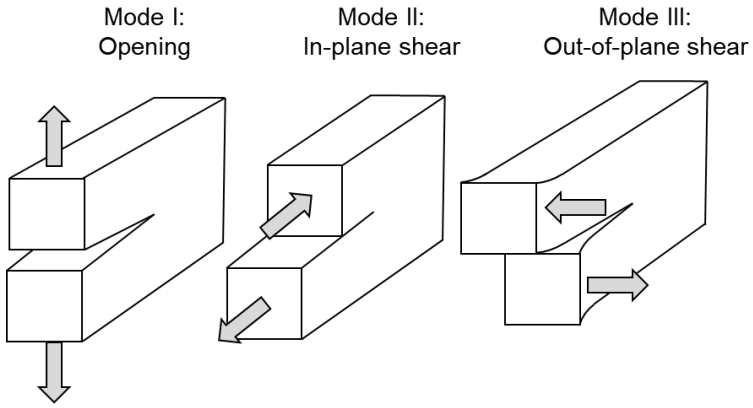

Figure 1.27. Loading modes that can be applied to a crack

1.4.4. Crack tip triaxiality: plane stress vs plane strain

As illustrated in Figure 1.28, the stress triaxiality at the crack tip varies along the thickness direction. In the mid-thickness of the cracked plate, the material at the crack tip tries to deform in the x (crack advance direction) and z (thickness direction) axes but it is constrained by the surrounding material. This generates a high stress triaxiality (plane strain) in the mid-thickness. The stress in the thickness direction, σ_{zz}, is gradually reduced to zero towards the outer free-surfaces (Figure 1.28 right), resulting in a biaxial stress state (plane stress).

The difference in plastic constraint between the mid-thickness and the outer surface has a direct influence on the size of the plastic zone surrounding the crack tip, which gradually decreases from the plane stress region (outer surface) to the mid-thickness in plane strain (Figure 1.29).

The relative size of the plastic zone, r_p, respect to the plate dimensions determines the dominating stress state at the crack tip. When the plastic zone is large compared to the plate thickness ($r_p/B >$ 0.5), such as the case of thin plates, the material at the crack tip can deform in the thickness direction. In this case, plane stress conditions prevail. On the other hand, if the plastic zone is relatively small ($r_p/B < 0.02$), the deformation in the thickness direction is constrained and the crack tip is in a plane strain condition. In the intermediate range between the two conditions, a mixed plane stress/plane strain mode occurs at the crack tip [103].

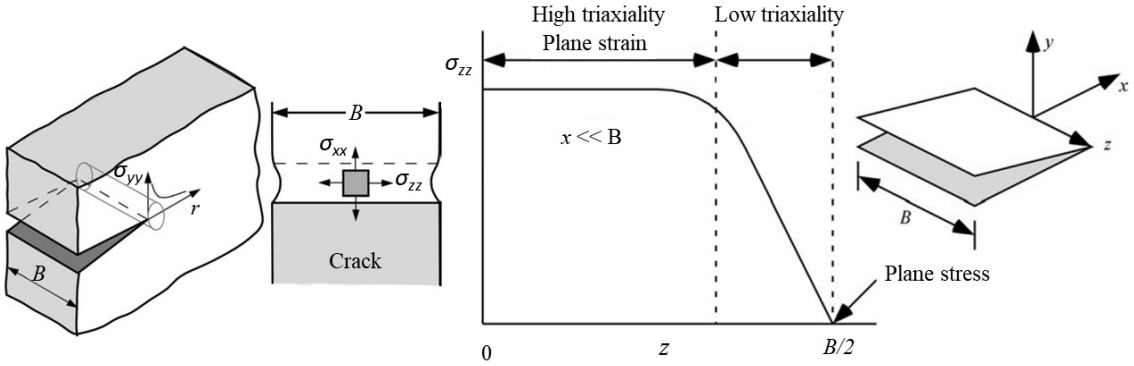

Figure 1.28. Three-dimensional deformation at the crack tip of a cracked plate subjected to in-plane loading (left) and schematic variation of transverse stress through the thickness at a point near the crack tip (right) [101].

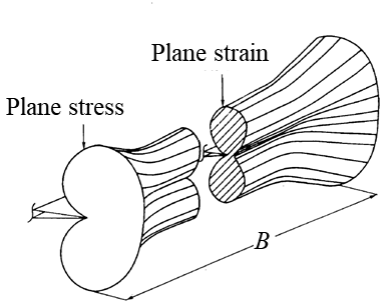

Figure 1.29. Three-dimensional plastic zone at the crack tip in a finite plate [102].

1.4.5. Influence of thickness on fracture toughness

The stress intensity factor, K, allows determining the conditions under which the material fractures. The condition for fracture is that the stress intensity factor reaches a critical level, K_c, which represents the fracture toughness of the material. As observed in Figure 1.30a, K_c depends on specimen thickness until a plateau is reached for a determined thickness (t_c). Above this thickness value, fracture toughness becomes insensitive to the specimen thickness and it is designated with the symbol K_{Ic}. K_{Ic} is referred to as the plane strain fracture toughness in loading mode I and it is a size-independent material property.

On the other hand, in the thickness-dependent region, K_c reaches a maximum value for a relatively low thickness (t_o). Below t_0, plane stress conditions prevail and toughness tends to decrease with decreasing specimen thickness. Above t_0, a mixed plane stress/plane strain mode occurs and toughness decreases as thickness increase until it reaches the thickness t_c.

The influence of thickness on fracture toughness is related to the relative portions of flat and shear fracture (Figure 1.30b). Very thin sheets typically exhibit a 45º shear fracture (slant fracture). When increasing thickness, the fracture shows a combination of shear fracture in the outer surfaces and flat fracture in the central region (tunnelling effect). For further thickness increase, flat fracture mechanisms, associated with plane strain conditions, dominate and thickness has no significant influence on toughness.

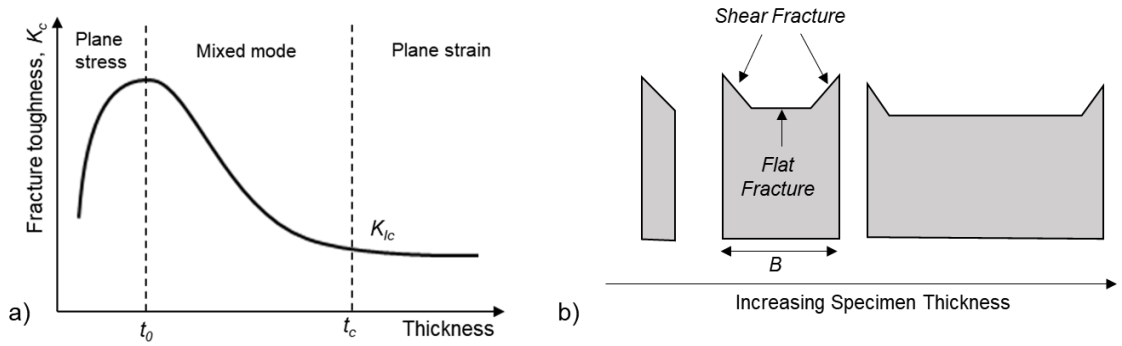

Figure 1.30. a) Thickness-dependence of fracture toughness. b) Effect of specimen thickness on ductile fracture surface morphology. Redrawn from [101].

1.4.6. Fracture toughness evaluation in the frame of linear elastic fracture mechanics

Many efforts have been dedicated to the standardization of experimental methodologies to properly evaluate the plane strain critical stress intensity factor, K_{Ic}, through reproducible and

reliable tests. The most extended and applied standard is the ASTM E399 [104]. Different specimen geometries are proposed in this standard, being the most used the Compact Tension (CT) and the Single Edge Notched Bending (SENB) geometries (Figure 1.31).

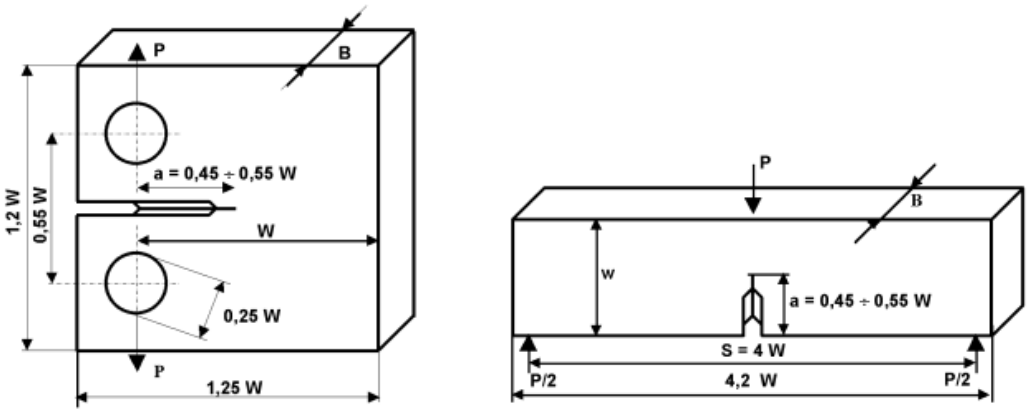

Figure 1.31. Standardized specimens for fracture toughness determination: CT specimen (left) and SENB specimen (right) [105]

In order to achieve a sharp crack with the minimum radius possible the standard recommends introducing fatigue pre-cracks in the notched specimens. After that, the specimens are tested and the load (P) as a function of the Crack Opening Displacement (COD) is recorded. The stress intensity factors for such geometries is given by Equation (13)

$$K_I = \frac{P}{B\sqrt{W}} f\left(\frac{c}{W}\right) \tag{13}$$

Where $f\left(\frac{c}{W}\right)$ is a geometrical factor that depends on specimen geometry.
Some constraints are required to guarantee the plane strain conditions. It is proposed that the crack length, c, the ligament, b, and the specimen thickness, B, must be, at least, fifty times larger than the radius of the plastic zone in plane strain.

$$c, b, B \geq 2.5\left(\frac{K_{IC}}{\sigma_{ys}}\right)^2 \tag{14}$$

Table 1.1 shows characteristic fracture toughness values for different materials.

Table 1.1. Fracture toughness values for different materials [105].

Material	$\boldsymbol{\sigma_{ys}}$ $\boldsymbol{MPa}$	$\boldsymbol{K_{IC}}$ $\boldsymbol{MPa\sqrt{m}}$	$\boldsymbol{Minimum\ thickness, mm}$
Maraging steel	1500	100	12
Low carbon steel	240	200	1750
304	300	180	900
Al 7075-T651	550	31	8
Al 2024-T3	400	34	18
Ti alloy 6Al-4V	1100	40	4
Ti alloy 4Al-4Mo-2Sn-0.5Si	950	70	13,5

1.4.7. Elastic-Plastic Fracture Mechanics

When considerable plastic deformation occurs before fracture and the size of the crack-tip plastic zone is comparable to the crack length or specimen dimensions, LEFM is no longer valid. In such case, elastic-plastic fracture mechanics (EPFM) allows characterizing the stress state at the crack tip using plastic properties such as yield strength and hardening coefficient. Thus, EPFM can be considered an extension of LEFM. The parameters used to describe the crack-tip conditions in elastic-plastic materials are described below.

1.4.7.1. Crack Tip Opening Displacement

During fracture toughness tests with high-toughness structural steels, Wells [106] observed that plastic deformation had blunted the crack tip before the fracture. The degree of crack blunting increased with increasing the toughness of the material. Consequently, Wells proposed the opening at the crack tip as a parameter to characterize the fracture toughness when LEFM is no longer applicable. Such parameter is known as the crack tip opening displacement (CTOD) and it is represented by the symbol δ (Figure 1.32).

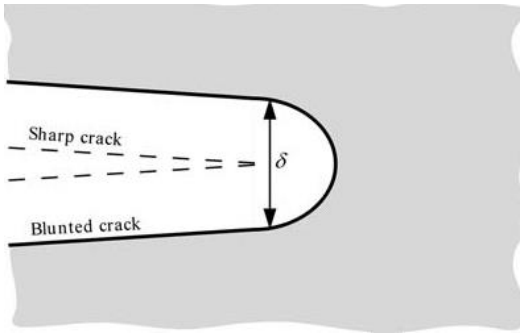

Figure 1.32. Initially sharp crack blunts before fracture due to plastic deformation, causing the displacement δ in the crack tip (CTOD) [101].

The CTOD criterion establishes that the Mode I crack initiation occurs when the CTOD reaches a critical value, $\delta = \delta_c$. δ_c can be used as a design parameter to predict the failure of a cracked structure.

Wells [106] performed an approximate analysis that related CTOD to the stress intensity factor in the limit of small-scale yielding. Using Irwin's plastic zone model, the CTOD can be calculated as follows [107]:

$$\delta = \frac{4}{\pi E}\frac{K_I}{\sigma_{ys}}^2 \tag{15}$$

where E is the Young's modulus, K_I is the stress intensity factor in mode I and σ_{YS} is the yield stress.

By definition, the CTOD is the opening displacement at the sharp crack tip (Figure 1.32). However, alternative definitions have been proposed. The most common alternative definition was proposed by Rice [95], which defined the CTOD as the displacement at the intersection of a 90° vertex originated at the tip of the blunted crack with the crack faces (Figure 1.33). This definition is commonly used to determine the CTOD in finite element simulations.

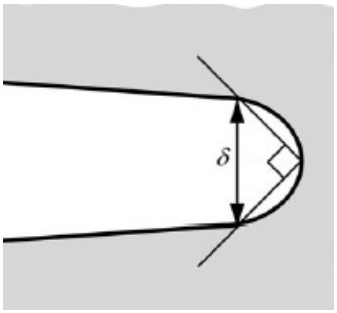

Figure 1.33. CTOD defined as the displacement at the intersection of a 90° vertex with the crack faces [101].

1.4.7.2. Crack Tip Opening Angle

Together with the CTOD, the Crack Tip Opening Angle (CTOA) is often used to describe the stable crack growth of ductile materials. The CTOA (ψ) is defined as the relative angle of the crack surfaces at a given distance (r_0) behind the current crack tip (Figure 1.34). It can be calculated as follows:

$$CTOA = \psi = 2tan^{-1}\left(\frac{\delta_0}{2r_0}\right) \tag{16}$$

where δ_0 is the crack opening displacement at the distance r_o.

The CTOA reaches a steady value during the stable crack propagation. This critical CTOA (ψ_c) is used to define the stable crack propagation resistance of ductile materials.

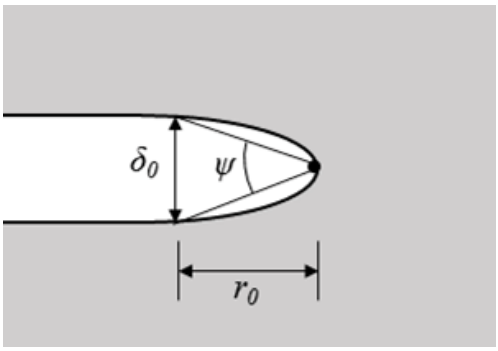

Figure 1.34. CTOA (ψ) definition.

1.4.7.3. J-integral

The *J*-integral concept was introduced by Rice [95] to characterize the crack tip strain fields in nonlinear elastic materials. Since, in most cases, the monotonic loading behaviour of a nonlinear elastic and an elastic-plastic material is identical, Rice idealized the plastic deformation as nonlinear elastic behaviour and applied the deformation plasticity theory to the analysis of a crack in an elastic-plastic material. Then, he showed that the nonlinear energy release rate *J* could be written as a path independent contour integral:

$$J = \int_{\Gamma} \left(wdy - T_i \frac{\delta u}{\delta x} ds\right) \tag{17}$$

where Γ is an arbitrary contraclockwise path around the crack tip (Figure 1.35), w is the strain energy density, T_i are the components of the traction vector, defined according to the outward normal along Γ ($T_i=\sigma_{ij}n_j$), u is the displacement vector and ds is an element of arc length along Γ. The strain energy density w is defined according to Equation (18):

$$w = \int_0^{\varepsilon_{ij}} \sigma_{ij}\varepsilon_{ij} \tag{18}$$

where σ_{ij} and ε_{ij} are the stress and strain tensors, respectively.

The works of Hutchinson [97] and Rice and Rosengren [96] related the *J-integral* parameter to the crack tip stress fields in nonlinear materials (HRR singularity). Thus, it can be considered as both an energy parameter and a stress intensity parameter.

The parameter J is a more general version of energy release rate, G. For the case of a linear elastic material $J=G$.

$$J = \frac{K^2}{E'} \tag{19}$$

This energy release rate definition was used in the early works of Begley and Landes [108, 109] to experimentally measure J in elastic-plastic materials. Since these first experimental works, J , in particular the critical J value at the onset of stable crack propagation, J_c, has been the most extended parameter to evaluate the fracture toughness of ductile materials.

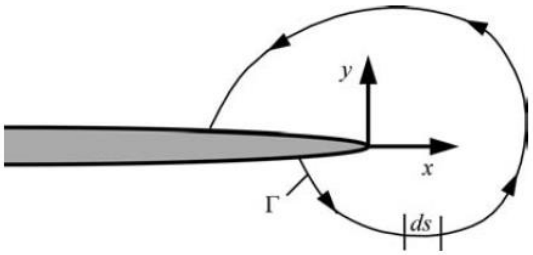

Figure 1.35. Arbitrary contour around the tip of a crack [101].

1.4.7.4. Relationship between J and CTOD

The relationship between J and the CTOD was proposed by Rice [95] and later revised by Shih [110], among others. Shih evaluated the displacements at the crack tip implied by the HRR solution and related the displacement at the crack tip to J and flow properties:

$$\delta = d_n \frac{J}{\sigma_{YS}} \tag{20}$$

where d_n is a constant depending on σ_{YS}/E and the strain hardening exponent, n [110].

This relation between J and δ shows that these two parameters are both valid for characterizing the crack-tip conditions of elastic-plastic materials.

1.4.8. Fracture toughness evaluation in the frame of elastic-plastic fracture mechanics

Different methodologies are available to characterize the fracture toughness of ductile materials within the frame of EPFM. The most extended methodology is the measurement of the *J-integral*

and CTOD as described in ASTM E1820 [111]. However, this standard is intended for characterizing the plane-strain fracture toughness of metallic materials. Thus, the size requirements described are too restrictive and cannot be satisfied with thin sheets. To characterize the stable crack propagation resistance of thin sheet materials under plane stress conditions, there are alternative standards such as the ASTM E2472 [112] or the ISO 22889 [113]. These standards propose the use of the CTOA and the crack opening displacement δ_5 for characterizing fracture toughness.

On the other hand, alternative faster and simpler methods, like the Kahn-type tear tests and the Essential Work of Fracture (EWF) methodology, are also commonly used to evaluate the fracture toughness of thin sheet materials.

The experimental procedures of the main elastic-plastic fracture mechanics testing methods are briefly described below.

1.4.8.1. J-integral and CTOD

The ASTM E1820 [111] describes in detail the specimens and tests characteristics for the evaluation of fracture toughness of metallic materials using the parameters, *J* and CTOD (δ). The standard establishes two procedures: a basic procedure for the direct evaluation of a single *J* or CTOD value and a procedure to determine the fracture toughness resistance (R) curve (*J*-R curve).

The basic procedure allows obtaining a single fracture toughness value such as J_{Ic} or δ_{Ic}. Multiple specimens are used to evaluate *J* at crack initiation, J_{Ic}. The initial and final crack sizes are measured by optical measurements. On the other hand, the resistance curve procedure uses an elastic unloading procedure to obtain a *J* or CTOD-based resistance curve from a single specimen. In this procedure, the crack length is measured from compliance and is verified by optical measurements. Specimens recommended are the CT, the SENB and the Disk-shaped Compact Tension specimen (DCT).

In materials showing a rising R curve behaviour, *Jc* has shown to be a very conservative parameter to evaluate the fracture toughness and, thus, the complete *J-R* curve must be determined. An example of a *J*-R curve determination with a CT specimen is shown in Figure 1.36 The specimen is loaded and is subjected to successive partial unloadings. The slopes provide a measure of the elastic stiffness of the specimen, which decreases as the crack grows and allows estimating the crack length in different points during the test.

The *J* values are calculated for the different points along the P- δ curve. For the evaluation of *J* is necessary the value of the area A_{pl}. Such area represents the area under the load vs displacement curve for the load and unload of a hypothetic crack length $a=a_i+\Delta a$, where a_i is the initial crack length and Δa the crack extension. Thus, the hypothetic load slope for m_5 is lower than the initial slope m_i.

The *J* value can be determined by:

$$J = J_{el} + J_{pl} \tag{21}$$

where J_{el} and J_{pl} are the elastic and the plastic component of *J*, respectively and are given by:

$$J_{el} = \frac{K^2(1-\vartheta^2)}{E} \tag{22}$$

$$J_{pl} = \frac{\eta A_{pl}}{B(W-a)} \tag{23}$$

where $\eta = 2 + \frac{0{,}522\ (W-a)}{B}$ for the CT specimen, B and W are the specimen thickness and width respectively and a is the crack size.

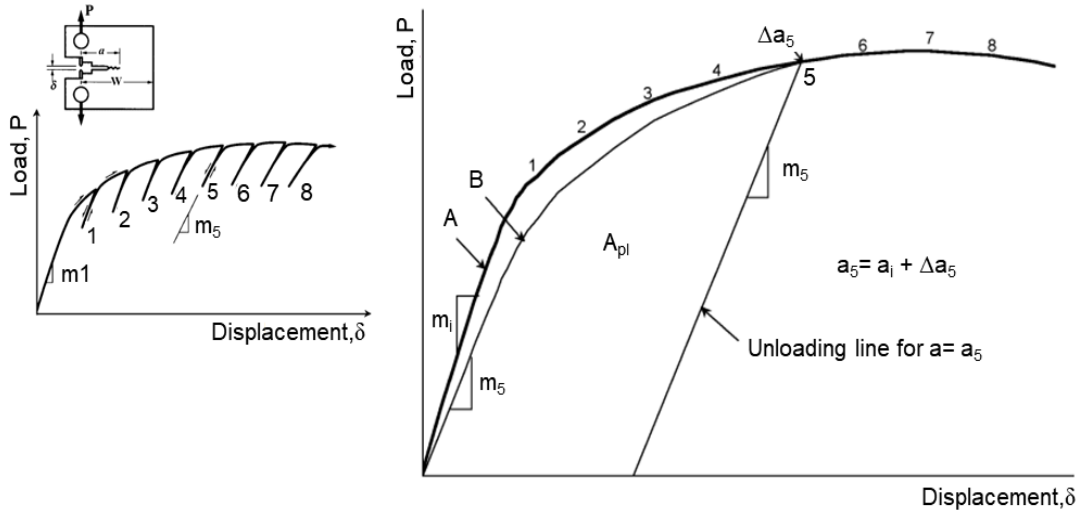

Figure 1.36. *J* determination through partial unloadings following the compliance method [105].

The *J* values are plotted against the crack extension, Δa, in order to obtain the *J*-*R* curve (Figure 1.37).

The process for the construction of the *J*-R curve is described as follows:

A construction line is drawn with slope $2\sigma_Y$, where:

$$\sigma_y = \frac{\sigma_{ys}+\sigma_{UTS}}{2} \tag{24}$$

Such slope represents the initial slope caused by the blunting of the crack tip. Two exclusion lines parallel to the construction line are plotted at 0.15 mm and 1.5 mm. The data points lying between these two lines define the *J*-R curve. The J_Q value, which characterizes the fracture toughness at the onset of the crack propagation is determined by the intersection of the *J*-R curve with a third line, parallel to the exclusion lines, drawn at 0,2 mm. The boundary J_{limit} is given by the smaller of the following:

$$J_{max} = b_0\ \sigma_y/10 \tag{25}$$

or

$$J_{max} = B\,\sigma_y/10 \tag{26}$$

Where b_o is the distance from the original crack front to the back edge of the specimen, i.e. the initial ligament length, and B is the thickness of the specimen. The maximum crack extension capacity for a specimen is:

$$\Delta a_{max} = 0.25\,b_0 \tag{27}$$

In order that J_Q can be considered as the size-independent plane-strain fracture toughness, J_{Ic}, the following conditions must be satisfied:

$$B, b_0 > 10\,\frac{J_Q}{\sigma_Y} \tag{28}$$

The same procedure is used to evaluate de δ-R curve and the critical CTOD, δ_c. The value of δ for each crack extension is derived from J using the relationship expressed in Equation (20).

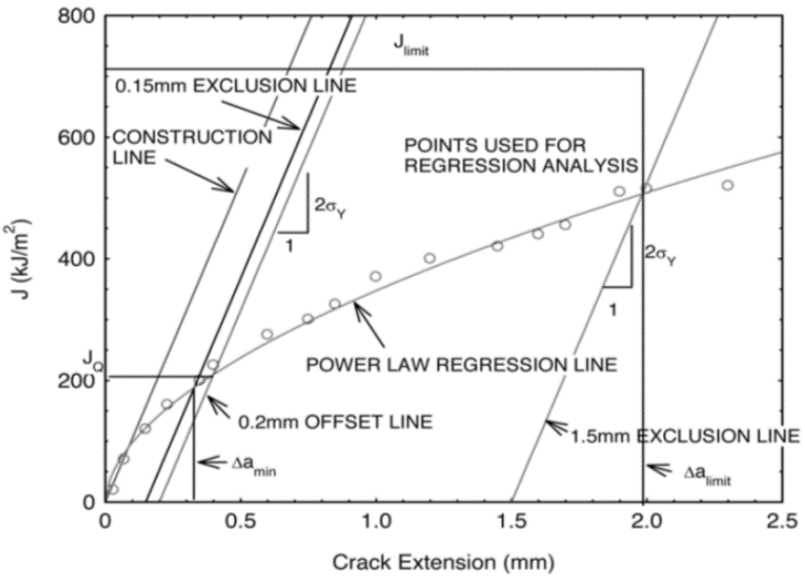

Figure 1.37. J values against crack extension for the J-R curve determination [111].

Some reported J_{Ic} values for different ductile materials are shown in Table 1.2.

Table 1.2. J_{IC} values for different materials

Material	***Thickness (mm)***	***J_{IC} (KJ/m²)***
Martensitic stainless steel [114]	25.4	266
30CrNi2MoVA [115]	8	143
High strength martensitic steel-420 HB [116]	12.5	34
High strength martensitic steel-270 HB [116]	12.5	140
High strength martensitic steel-305 HB [116]	12.5	175

As mentioned before, the ASTM E1820 cannot be directly applied to thin sheet materials because of its specimen size requirements. However, if the thickness limitations are disregarded, it is possible to use the *J*-integral procedure to evaluate the *J*-R curve of ductile sheet materials [117]. Some authors have used alternative specimen geometries and J-integral expressions to evaluate the critical *J* value at crack initiation (J_c) of thin metal sheets [84, 88, 118, 119].

Reported J_c values for thin metal are shown in Table 1.3.

Table 1.3. Published J_c values for metal sheets.

Material	*Thickness (mm)*	J_C (KJ/m^2)
Low C steel (no specific %C) [118]	2.0	510
TRIP steel (8% austenite vol. fraction) [84]	0.9	225
TRIP steel (24% austenite vol. fraction) [84]	0.9	45
Aluminium 6082 T0 [119]	1.0-6.0	50-150
TWIP steel [88]	1.45	250
Dual-Phase steel [88]	1.85	100
Quenching & Partitioning steel [88]	1.0	65

1.4.8.2. CTOA and δ_5

The ISO 22889 [113] standard specifies the experimental procedure for determining the crack opening displacement, δ_5 and the crack tip opening angle, ψ in thin compact and middle-crack tension specimens. δ_5 is the relative displacement of the crack surfaces normal to the original crack plane at the crack tip, measured on the specimen surface over an initial gauge length of 5 mm. The δ_5 results are expressed in terms of a resistance curve (δ_5-R).

The standard defines ψ as the relative angle of the crack surfaces measured at 1 mm from the current crack tip. The critical CTOA, ψ_c, is expressed in terms of a constant value achieved after a certain amount of crack extension. Figure 1.38 shows an example of the specimen geometry and the procedure for determining ψ_c.

The CTOA is directly measured on the specimen surface with the aid of an optical microscope or a digital image correlation equipment. The CTOA values are represented as a function of the crack extension, as illustrated in Figure 1.38. After the initiation of propagation, the CTOA gradually decreases until it reaches a steady value during stable tearing. The average of the CTOA values in this constant region corresponds to the ψ_c. The maximum amount of crack extension, Δa_{max}, is given by:

$$\Delta a_{max} = (W - a_0) - 4B \tag{29}$$

where W is the specimen with, a_0 is the initial crack length and B is the specimen thickness. The minimum amount of crack extension, Δa_{min}, is that for which the CTOA reaches the constant value.

Alternative methods for CTOA determination are proposed in the ISO 22889, such as post-test microtopography measurements, finite element analysis and indirect determination using δ_5.

Table 1.4 shows published values of ψ_c for different sheet materials.

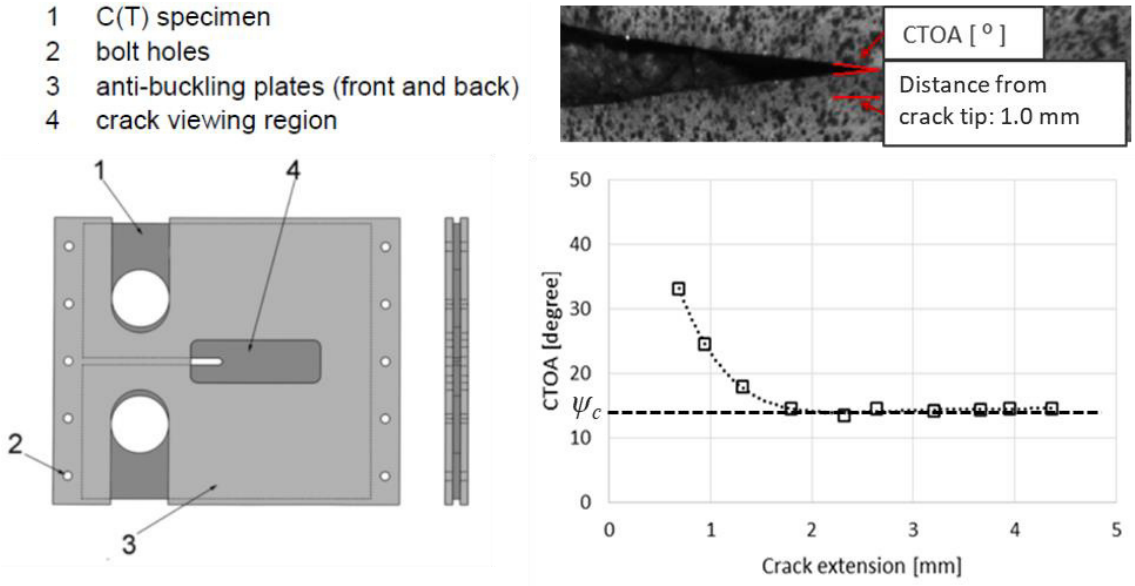

Figure 1.38. Compact tension specimen with an anti-buckling system [113] (left) and example of CTOA and ψ_c determination by direct optical measurements (right).

Table 1.4. ψ_c values for different sheet materials.

Material	***Thickness (mm)***	***ψc (°)***
AA2024-T3 [120]	2.3	5.8
AA 5083 [121]	3.0	5
Interstitial free high strength (IFHS) steel [122]	1.0	12
Dual Phase steel 780 [123]	1.6	8.6
Dual Phase steel 980 [123]	1.94	3.6
API 5L X65 pipe steel [124]	6.0	20

1.4.8.3. Kahn-type tear tests

The Kahn-type tear test was developed by Kaufman and Knoll [125] to characterize the notch resistance of thin aluminium sheets. The test consists in pulling at constant speed a sharp notched specimen and record the load as a function of the displacement. Figure 1.39 shows the typical load-displacement curve of these tests. The Unit Initiation Energy, *UIE*, represents the notch resistance to nucleate a crack and is calculated from the area under the curve at maximum load. The Unit Propagation Energy, *UPE*, represents the crack propagation resistance of the material. The ASTM B871 [126] standard describes the experimental procedure for obtaining the *UIE* and *UPE* in thin aluminium alloy sheet products. The UPE is the primary result of the test and it can be used as a relative fracture toughness indicator. Some works have shown a good correlation between *UPE* and K_{Ic} [125, 127].

The method has been used in many research works to characterize the toughness of aluminium alloys [125,127-130] and high strength steels [131,132]. Table 1.5 shows some reported values of *UIE* and *UPE* for different aluminium alloys and steels.

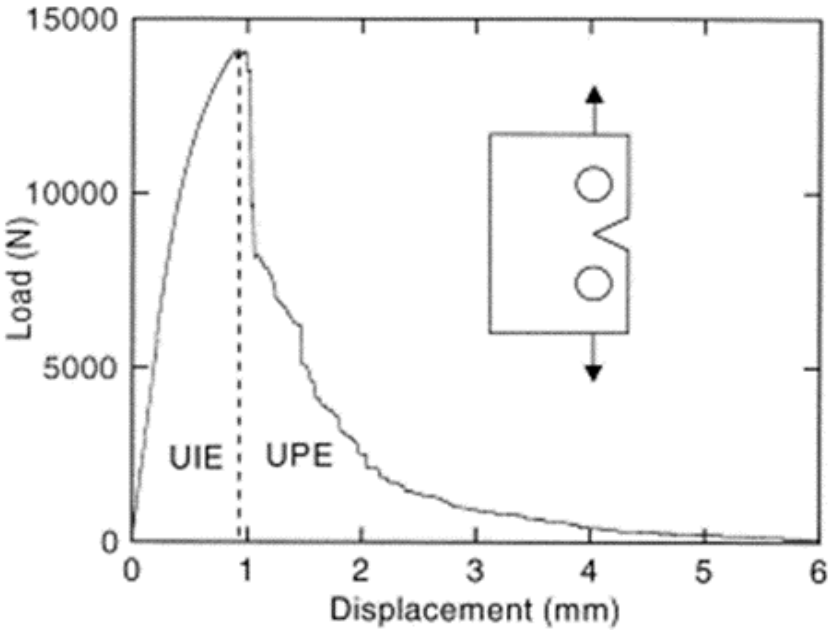

Figure 1.39. Typical specimen geometry and load–displacement curve of a Kahn Tear Test.

Table 1.5. *UIE* and *UPE* values for different aluminium alloy and steel sheets.

Material	***UIE* [kJ/m²]**	***UPE* [kJ/m²]**
AA7050 Al alloy [129]	20-160	Not reported
EN AW-6xxx C [130]	Not reported	280
EN AW-6xxx HS [130]	Not reported	115
Hot stamped 22MnB5 [131]	400-480	Not reported
TWIP steel [132]	400-440	1180-1350

1.4.8.4. Essential Work of Fracture

The Essential Work of Fracture (EWF) methodology was developed by Cotterel and Reddel [133] as an alternative to characterize the tearing resistance of ductile thin sheet materials under plane stress conditions. The method is based on the idea of Broberg [134], who suggested that ductile fracture energy can be separated in two terms: one related to the plastic work dissipated in an outer region surrounding the crack plane, W_p, and another one related to the fracture and developed in the fracture process zone (FPZ, Figure 1.40), W_e. The total work of fracture (W_f) can be expressed as follows:

$$W_f = We + Wp = w_e l_0 t_0 + w_p \beta {l_0}^2 t_0 \quad (30)$$

where w_e is the specific essential work of fracture per unit area, l_0 is the ligament length, t_0 is the specimen thickness, w_p is the specific non-essential plastic work per unit volume and β is a shape factor that depends on the shape of the plastic zone. Dividing Equation (30) by the cross-section area ($l_0 t_0$) allows determining the specific essential work of fracture (w_e) according to:

$$\frac{W_f}{l_0 t_0} = w_f = w_e + w_p \beta l_0 \tag{31}$$

Using Equation (31), w_e is determined by testing up to fracture a series of specimens with different ligament lengths (l_0) and plotting w_f values as a function of l_0. w_e and $w_p\beta$ can be obtained by linear regression, where w_e is given by the intercept and $w_p\beta$ by the slope, as shown in Figure 1.41. w_f values are obtained by integrating the area under load vs displacement curves (W_f) and dividing by the initial cross-section area. It must be noted that w_e cannot be considered an intrinsic material property since it has an important contribution from necking. Thus, it is a material constant for a given sheet thickness.

w_e has shown to be independent of the specimen geometry and can be obtained from different geometries [135-137]. However, for thin sheets, the EWF test protocol [138] developed by the European Structural Integrity Society (ESIS) recommends the use of Double Edge Notched Tension (DENT) specimens (Figure 1.40) because of its symmetry and minimal specimen rotation and buckling during the test.

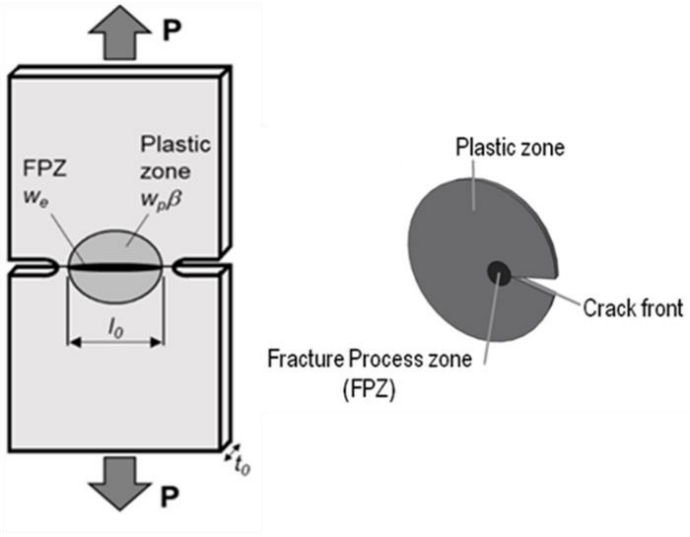

Figure 1.40. DENT specimen used for the evaluation of the EWF (left) and definition of the Fracture Process Zone (right).

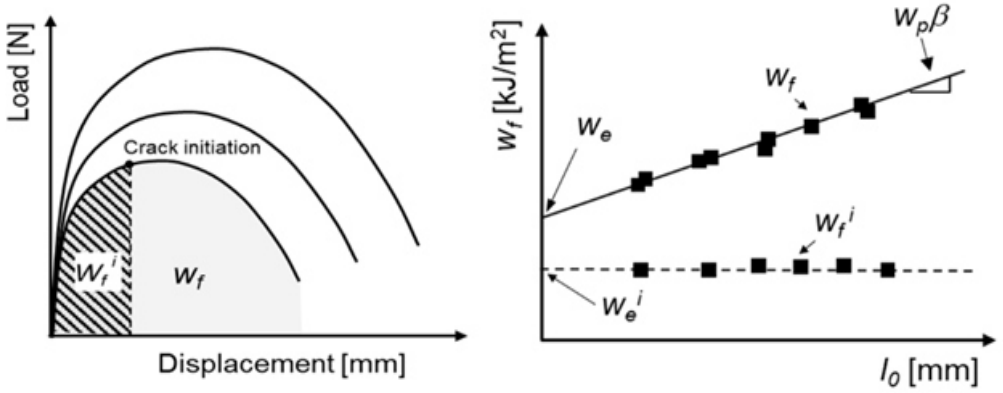

Figure 1.41. Experimental procedure for the determination of the essential work of fracture, w_e and the specific work for fracture initiation, $w_e{}^i$.

Some restrictions must be met to use Equation (31). First, the ligament area must be completely yielded before crack initiation and ligament must be small enough to avoid the spreading of the plastic zone to the boundaries of the specimen. Moreover, ligament length must be large enough to ensure that all specimens present a global plane stress state across the ligament. If the ligament is too small, the process zones at the two crack tips may interact and crack propagation takes place under a mixed plane stress/plane strain state that varies with the ligament length (Figure 1.42). To satisfy these requirements some limitations regarding the ligament length have been proposed. The ESIS protocol [138] recommends a lower ligament length of max (3t or 5 mm), where t is the specimen thickness. This lower boundary is intended to ensure that data is obtained under plane stress conditions. However, it has been found that this transition from plane stress to a mixed stress probably depends on the material characteristics and thickness. Therefore, the recommendation of $3t$ or 5 mm is based on experimental observations [135-137, 140]. For the maximum ligament length, the upper bound min (W/3, $2r_p$) is given. Where W is the specimen width and r_p is the size of the plastic zone, calculated according to Equation (32) [140]:

$$r_p = \frac{1}{2\pi}\frac{Ew_e}{\sigma_{ys}^2} \tag{32}$$

Where E is the Young modulus and σ_{ys} the yield strength. As indicated in the EWF test protocol [138], W/3 is arbitrarily included to avoid edge effects and the condition $2r_p$ is to ensure that the ligament is fully yielded before fracture initiation.

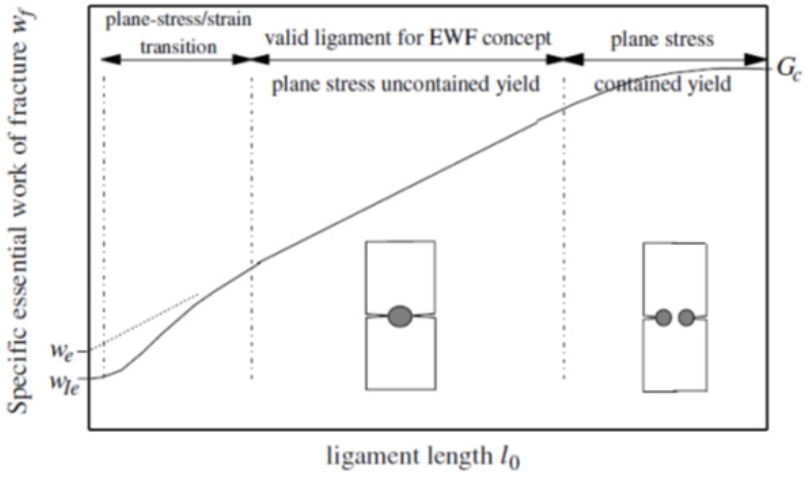

Figure 1.42. Valid ligament lengths for the evaluation of the EWF [139]

As shown by Mai and Cotterell [136], the EWF methodology also allows to separate energetic contributions from crack initiation and crack propagation and determine a crack initiation toughness value, the specific essential work for fracture initiation, w_e^i [136]. The specific work for fracture initiation, $w_f{}^i$ is calculated by integrating the area under the load vs displacement curve until the onset of crack propagation, as illustrated in Figure 1.41. Contrary to w_f, w_f^i is constant and independent of the ligament length.

The EWF methodology has been extensively applied to characterize the fracture toughness of polymers [135-137, 141, 142], ductile metal [118, 119, 139, 143] and high strength steel sheets [20, 26, 84-87, 91]. Table 1.6 shows some published w_e values for thin metal sheets.

Table 1.6. Reported w_e values for metal sheets.

Material	*Thickness (mm)*	*w_e (KJ/m^2)*
TRIP steel (8% austenite vol. fraction) [84]	0.9	270
TRIP steel (24% austenite vol. fraction) [84]	0.9	50
CP steel 1000 MPa UTS [20]	1.4	405
DP steel 1000 MPa UTS [20]	1.4	138
Trip-aided Bainitic Ferritic (TBF) steel [20]	1.4	150
Quenched & Partitioned (Q&P) steel [20]	1.4	194
Press Hardened steel 1500 MPa [20]	1.5	159
Press Hardened steel 1000 MPa [20]	1.5	249

Different authors have addressed the equivalence between w_e and J_c [119, 136, 137]. Mai et al [136, 137] proposed that, under strictly J-controlled crack growth resistance w_e=J_c. The J_R curve is approximately a linear function of crack growth and is given by:

$$J_R = J_c + \frac{dJ}{da}\Delta a \tag{33}$$

The integral of J_R to complete the fracture is the specific work of fracture, w_f, mentioned in equation (31). Equation (33) is very similar in form to the obtained in equation (31) from the energy partitioning, where J_c would correspond to w_e and $\frac{dJ}{da}$ to the $w_p\beta$ term. The equivalence between w_e and J_c is further discussed in this work.

Chapter 2

Objectives and scope

2.1 Objectives of the work

The main objectives of this thesis work are two: first, to assess the applicability of different fracture mechanics testing methods and its derived fracture toughness parameters to characterize the crack initiation and propagation resistance of AHSS sheets and, second, to investigate how fracture toughness can be used to understand and rationalize the cracking behaviour of AHSS. A secondary objective of this research is to gain fundamental knowledge on the influence of microstructure on the fracture toughness of AHSS.

Aimed at reaching these primary goals, the following specific objectives are defined:

1. To define the most suitable experimental methods and specimen geometries for characterizing the fracture toughness of thin AHSS sheets: The first step was to choose the most appropriate fracture mechanics testing procedures. The fracture toughness of the investigated materials was primarily characterized following three methodologies: essential work of fracture (EWF), *J*-integral and Kahn-type tear tests. The EWF method (Papers I-IV) was chosen as the main experimental technique due to its simplicity and reliability. In Paper I, a comparison of the three testing methods is made.

2. To evaluate the influence of experimental variables on the measure of fracture toughness: Different testing variables such as the specimen geometry or the notch radius on fracture toughness measurements are assessed in Paper I. An alternative rapid procedure for specimen notching is also presented in the appended Paper D.

3. To identify the fracture toughness parameters that best describe the crack initiation and propagation resistance of AHSS sheets: The relationship between the different crack initiation and propagation resistance parameters (w_e^i, w_e, J_i, J_c, *UIE*, *UPE*) is discussed in Paper I.

4. To investigate the relationship between fracture toughness and the cracking resistance of AHSS: The correlation of fracture toughness with edge cracking resistance and crash failure behaviour is analysed in Papers II and III, respectively. Further investigations on the correlation fracture toughness-cracking resistance are presented in Papers A-C.

5. To analyse the influence of the microstructure on fracture toughness of AHSS: The effect of the microstructure on the crack propagation resistance of AHSS is discussed in Paper II and Paper IV. Paper II briefly discusses the relation between microstructure and fracture toughness in several 1st and 3rd Generation AHSS grades. Paper IV investigates in detail the influence of the microstructural constituents on fracture resistance of high strength dual-phase steels. Additionally, synchrotron X-Ray Powder Diffraction measurements were performed to investigate the evolution of the retained austenite fraction during the crack propagation of TRIP-assisted steels. Some preliminary results are presented in Chapter 4.

The outcome of this research will contribute to filling the gap of knowledge in fracture toughness properties of thin AHSS sheets. This knowledge will be useful not only to optimize material selection for automotive applications but also to design new AHSS with enhanced mechanical properties and cracking resistance.

2.2 Scope of the research

This thesis work is focused on the experimental evaluation of the mode I plane stress fracture toughness of several AHSS and PHS sheets (thicknesses from 1-1.6) mm and on the application of fracture mechanics to understand their edge formability and cracking behaviour in crash scenario. The numerical modelling of the ductile fracture process is out of the scope of this thesis. The work covers a wide range of AHSS and PHS grades with strengths ranging from 780 to 1500 MPa. Other materials are not considered. However, the findings obtained as a result of the research could be easily extrapolated to other high-strength sheet materials, such as high strength aluminium alloys, stainless steels, etc.

The proposed experimental techniques and their limitations are described below:

Fracture toughness characterization

Fracture toughness is measured in the frame of fracture mechanics using three different experimental methodologies, namely, the EWF, the *J*-integral and the Kahn-type tear test. The different fracture toughness parameters obtained from these tests are compared and discussed.

To avoid the thickness limitations of ASTM E1820 for *J*-integral evaluation, different specimen geometries are proposed. Moreover, alternative methods for direct crack growth measurement by using optical methods are used.

It is important noting that all the fracture toughness parameters evaluated in this work correspond to values of plane stress fracture toughness and, therefore, depend upon specimen thickness. The influence of the sheet thickness on the measured toughness values and the determination of the thickness independent plane strain fracture toughness (J_{Ic}) are not addressed.

Edge cracking resistance and crash failure behaviour

Edge cracking resistance of the investigated materials is characterized by means of ISO 16630 hole expansion tests (HET) and DIC-assisted hole tension tests (HTT). To minimize the inherent scatter of the hole expansion ratio (HER) the onset and propagation of cracks are determined on-line by means of a digital video camera. The use of the DIC in HTT is a valuable tool to determine the fracture strains near the edge of a punched hole. However, these fracture strains are quite sensitive to mesh quality and DIC parameters (camera resolution, facet size, step size, etc.). Other of the experimental drawbacks of these optical strain analysis is the difficulty on accurately measure strains at the edge, due to the poor strain resolution.

Crash fracture behaviour is assessed through laboratory-scale axial and bending impact resistance tests. All the crash tests were performed at voestalpine Stahl laboratories in Linz, Austria. Crashworthiness is determined according to the intrusion level, overall cracking behaviour and energy absorbed. It is worth emphasizing the experimental complexity of these tests, especially of axial crash tests, which can be highly influenced by different extrinsic parameters: crash box geometry, welds, etc.

Microstructural analysis

Basic microstructural investigations for most of the investigated steels include light optical microscopy (LOM) and scanning electron microscopy (SEM) analysis. A detailed microstructural investigation on two GigaPascal DP steels is also performed by means of LOM, SEM, Electron backscatter diffraction (EBSD) and nanoindentation measurements.

Due to the limitations of EBSD in the evaluation of retained austenite (RA) volume fraction, alternative measurements like the saturation magnetization method or synchrotron X-Ray Powder Diffraction measurements were used in some of the investigated materials.

Chapter 3

Materials and experimental methods

The materials investigated and the experimental procedures are described in the appended papers. The following sections provide further experimental details and describe the procedures for the evaluation of additional parameters not included in the papers, such as the critical crack opening displacement (δ_c) from EWF tests or the true major strain at fracture in the notch tip from Kahn-type tear tests ($\varepsilon_{f\ KTT}$). A basic description of the advanced microstructural characterization techniques is also given.

3.1 Materials

A wide range of 1st, 2nd and 3rd generation AHSS were investigated in this work. The mechanical properties and chemical compositions of the studied steels are summarized in Table 3.1 and Table 3.2, respectively. Table 3.1 also indicates the sheet thickness and the paper where they are investigated. The microstructural constituents are described in Table 3.3. The steels can be divided into four main microstructural groups:

- Complex-Phase (CP) like microstructures with homogeneous bainite/tempered martensite matrix: CP1000, Q&P, 3rd Gen Q&P1180, CP1200, TBF/Q&P, PHS1000
- Dual-Phase (DP) like microstructures with soft (ferrite/bainitic ferrite) matrix and hard (martensite) secondary phases: DP1000, TBF, DP780, TRIP780, DP1000A, 3rd Gen DP1180, 3rd Gen TBF1180
- Fully martensitic microstructures obtained by press hardening: PHS1500
- Fully austenitic microstructures (high Mn steel): TWIP

Within these groups, a subgroup of TRIP-assisted microstructures (retained austenite: 6-16%) can be identified: TBF, Q&P, DP780, TRIP780, 3rd Gen steels, TBF/Q&P.

Table 3.1. Mechanical properties of the investigated steels. *YS*= yield strength; *UTS*= ultimate tensile strength, *n*: strain hardening exponent, *UE*: uniform elongation; *TE*: total elongation; *t*=sheet thickness.

Paper	Steel	*t* [mm]	*YS* [MPa]	*UTS* [MPa]	*n* [-]	*UE* [%]	*TE* [%]
Paper I, Paper III	CP1000	1.4	915	1008	0.05	4.8	8.8
	DP1000	1.4	775	1015	0.07	7	11.4
	TBF	1.5	755	1012	0.10	10.5	15.8
	Q&P	1.4	920	1202	0.05	5.3	9.1
Paper II	DP780	1.5	513	823	0.2	14.2	19.9
	TRIP780	1.6	542	851	0.2	20.7	25.8
Paper II/ Paper IV	DP980/DP1000A*	1.35	816	1055	0.13	6.54	9.7
Paper II	3rd Gen DP1180	1.2	895	1212	0.15	10.5	14.3
	3rd Gen TBF1180	1.4	987	1216	0.11	9.2	12.6
	3rd Gen Q&P1180	1.5	1034	1191	0.09	9.2	13.1
Paper III	CP1200	1.6	1041	1218	0.05	3.4	6
	TBF/Q&P	1.4	876	1026	0.09	7.5	11.3
	PHS1500	1.5	1075	1552	0.08	3.7	5.2
	PHS1000	1.5	988	1007	0.05	4.9	7.3
	TWIP	1.4	530	969	0.11	55	59.5
Paper IV	DP1000 B	1.4	773	1040	0.09	5.4	8.7

***** This steel was designated DP980 in Paper II and DP1000 A in Paper IV. Hereinafter, this steel will be referenced as DP1000A.

Table 3.2. Chemical compositions (in weight per cent).

Steel	C	Si	Mn	Cr	B	Al	Ti
CP1000	0.11	0.34	~2.3	0.12	0.0017	0.040	-
DP1000	0.19	0.18	~2.3	0.46	0.0003	0.048	-
TBF	0.20	0.84	>2.4	0.17	0.0003	0.039	-
Q&P	0.12	0.81	>2.4	0.18	0.0002	0.043	-
DP780	~0.1	<0.9	<2.0	<0.7	<0.003	~0.05	<0.0060
TRIP780	~0.20	~1.60	~1.70	~0.02	<0.001	~0.05	~0.0070
DP1000A	~0.15	<0.5	~2.3	<0.7	<0.003	~0.05	<0.0060
3rd Gen DP1180	~0.20	<2.0	~2.5	<0.7	<0.003	~0.05	<0.0060
3rd Gen TBF1180	~0.23	<2.0	<2.9	<0.7	<0.005	~0.04	~0.0070
3rd Gen Q&P1180	~0.18	<2.0	<2.9	<0.7	<0.005	~0.03	~0.0060
CP1200	~0.15	<0.5	1.8-2.2	<0.7	<0.003	-	-
TBF/Q&P	~0.10	0.5-1.0	2.2-2.6	<0.7	<0.003	-	-
PHS1500	~0.20	~0.20	~1.20	<0.7	~0.003	~1.0	-
PHS1000	~0.20	~0.20	~1.20	<0.7	~0.003	~1.0	-
TWIP	~0.50	0.10 -0.15	~15	~0.10	-	~1.0	-
DP1000 B	0.08	0.26	~2.6	0.31	0.0018	0.16	0.0372

Table 3.3. Microstructural constituents. F: ferrite, B: Bainite, BF: Bainitic Ferrite, M: Martensite, TM: Tempered martensite, RA: retained austenite. UB: Upper bainite, LB: Lower bainite.

Steel	Microstructural constituents	RA volume fraction, V_γ [%]
CP1000	B/TM matrix	1.3
DP1000	F/B matrix, TM, M islands, RA	4.3
TBF	F/B matrix, TM, M islands, M/RA	11.2
Q&P	B/TM matrix, RA	6.0
DP780	F/B matrix, M/RA islands	9.8
TRIP780	F/B matrix, M/RA islands	15.6
DP1000A	F/B matrix, TM, M islands, RA	5.5
3rd Gen DP1180	UB/LB matrix, M/RA islands and laths	14.8
3rd Gen TBF1180	Carbide-free B matrix, M/RA islands and laths of RA	15.5
3rd Gen Q&P1180	TM matrix, B, M/RA islands and laths of RA	12.6
CP1200	B/TM	1.4
TBF/Q&P	B/TM matrix, RA	8.4
PHS1500	M	3.3
PHS1000	TM	2.3
TWIP	Austenite	100
DP1000 B	F/B matrix, M islands	2.0

3.2 Fracture toughness measurements

3.2.1 Essential Work of fracture

EWF tests were performed using rectangular Double Edge Notched Tension (DENT) specimens of 240 x 55 mm. Initial notches were machined by electrical discharge machining (EDM). Then, fatigue pre-cracks were nucleated at the notch root following the recommendations of the ASTM E1820. The cracks were extended about 1-1.5 mm per side. All the DENT specimens were machined at 90º with respect to the rolling direction (Figure 3.1a).

For fatigue pre-cracking, a Rumul resonance fatigue machine was used (Figure 3.2a). The machine has a load cell capacity of 150 kN and it is able to work at frequencies up to 250 kHz. Fatigue pre-cracking was conducted under load (P) control in a resonance fatigue machine. Tests were run at room temperature at a constant axial load ratio, R= P_{min}/P_{max}=0.1 (tension–tension).

The ΔK (K_{max}-K_{min}) was kept below 0.3 K_c, where K_{max} and K_{min} are, respectively, the maximum and minimum stress intensity factor applied and K_c is the linear elastic fracture toughness at crack initiation. This condition was verified after the test.

EWF tests were performed at a 250 kN universal testing machine (INSTRON 5585H), equipped with a digital video extensometer (Figure 3.2b). The tests were carried out according to the European Structural Integrity Society (ESIS) protocol for EWF testing [138]. Generally, 5 different ligament lengths (l_0) ranging from 5 to 15 mm were used and about 3 specimens per ligament length were tested. The specimens were tested up to fracture at a constant cross-head speed of 1 mm/min. The load-line displacement was measured by means of the video extensometer using initial extensometer marks separated 50 mm. For the determination of the crack initiation, a high-resolution video camera synchronized with the testing machine was used. w_f^i values were determined for two specimens of each ligament length. Fracture toughness at cracking initiation, w_e^i, was evaluated from the average of w_f^i values.

In order to check whether the ligament was fully yielded before crack initiation and ensure the validity of the EWF measurements, a full field strain analysis was performed at the surface of the ligament area (Figure 3.2c). For this task, a speckle pattern was painted in the specimen surface and a Digital Image Correlation (DIC) equipment was used (Figure 3.2d). Images were recorded at a frame rate of 5 images/second and analysed in GOM Correlate software. For the DIC analysis, a facet size and a step size of 13 and 11 pixels respectively were used.

To determine the strain level from which the material is yielded, DIC-assisted uniaxial tensile tests were previously performed for each material. The DIC was used to evaluate the Equivalent Mises strain at the onset of the plastic region (after σ_{ys}). For all the investigated steels, the plastic regime was found to start approximately at a Mises strain= 0.005.

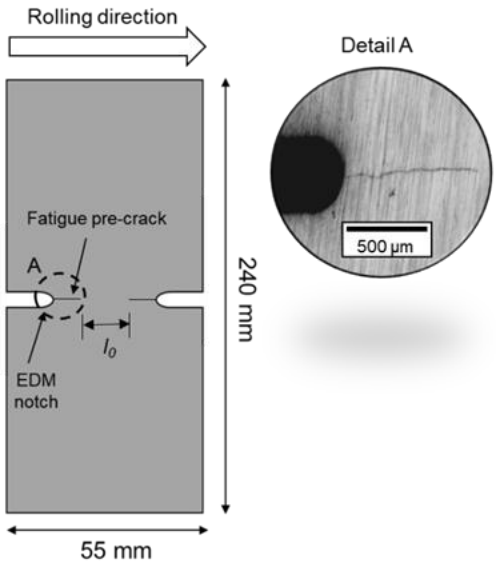

Figure 3.1. DENT specimen used for EWF tests and detail of the fatigue pre-crack at the notch root.

3.2 Fracture toughness measurements

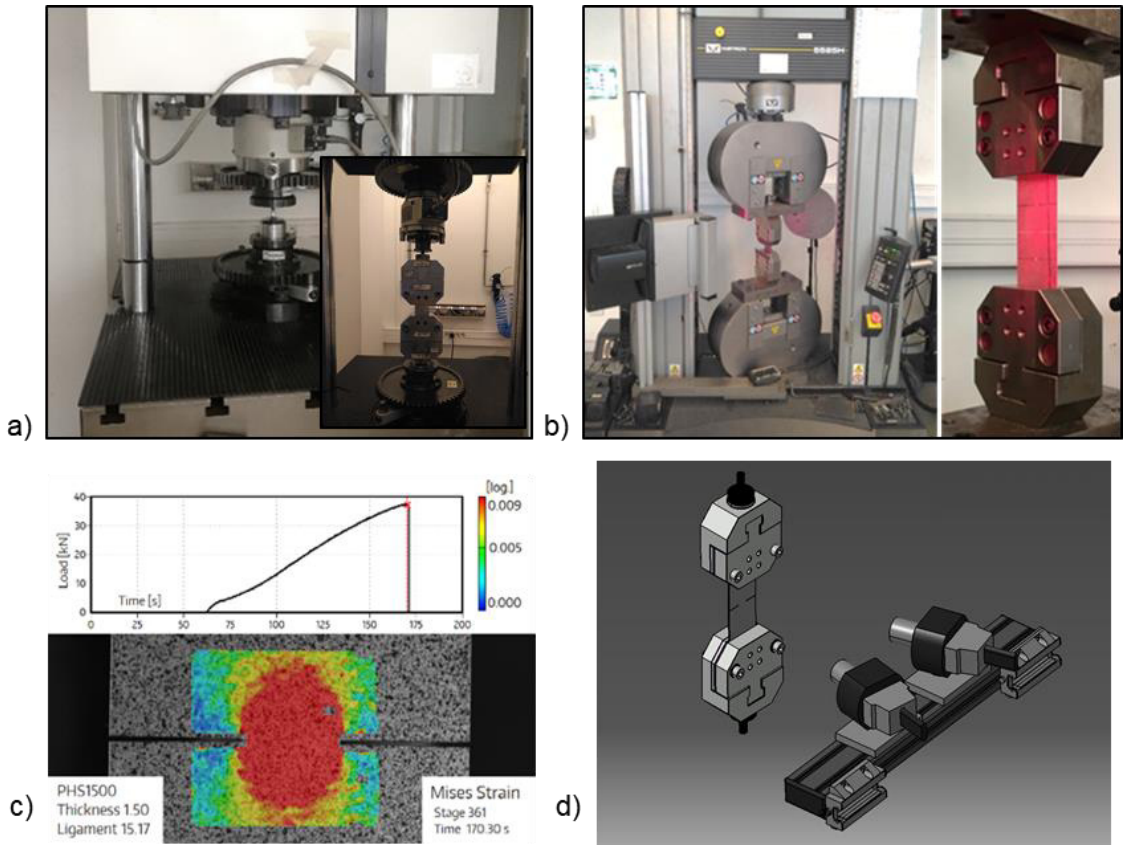

Figure 3.2. a) Resonance fatigue machine. **b)** Universal testing machine INSTRON 5585H used for EWF tests. **c)** Full-field strain analysis in the ligament area of a DENT specimen. **d)** Schematic representation of the experimental setup of the DIC equipment.

3.2.1.1 Notch preparation method

All the EWF tests were performed using fatigue pre-cracked specimens as described above. Additionally, in order to evaluate the influence of notch root radius on fracture toughness, two different notch configurations were investigated: EDM machined notches (notch radius, ρ= 150 μm) and mechanically sheared notches ($\rho\approx$ 2 μm) prepared by a newly developed notching tool (Figure 3.3). Further details about the experimental procedure for specimen notching are given in Paper D.

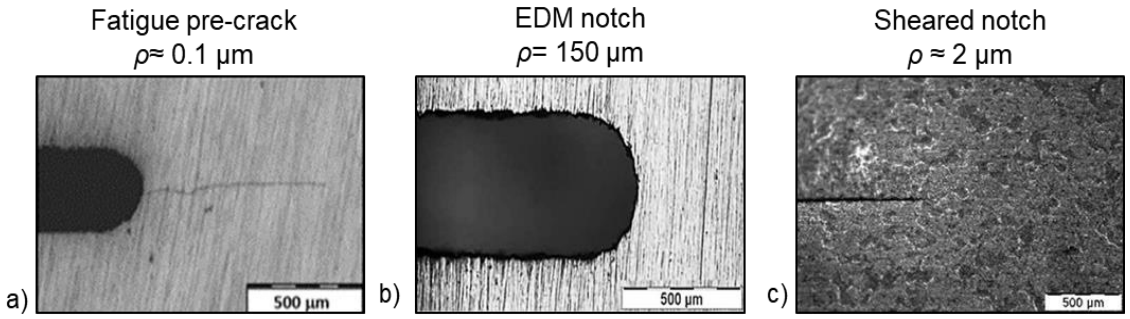

Figure 3.3. Different notch configurations investigated. **a)** Fatigue pre-crack, **b)** EDM notch and **c)** mechanically sheared notches. Optical microscope images.

3.2.1.2 Determination of the critical crack tip opening displacement.

As proposed by Cotterell and Reddel [133] and Hashemi and O'brien [144], the critical crack tip opening displacement (δ_c) was obtained by plotting the displacement at fracture (d_f) against the ligament length (l_0) and extrapolating to zero ligament length (Figure 3.4).

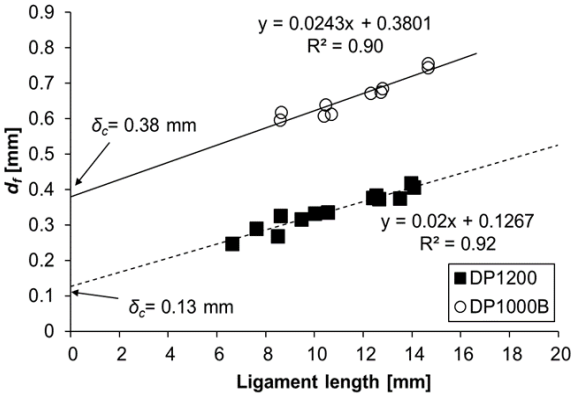

Figure 3.4. Example of determination of the critical crack tip opening displacement (δ_c).

3.2.1.3 Thickness strain measurements in DENT specimens

The true thickness strain in DENT specimens (TTS_{DENT}) was evaluated from the fracture surface according to Equation (9). In this case, t_o is the initial sheet thickness and t_f is the thickness at fracture measured from the fracture surface at a given distance respect to the crack tip. The thickness measurements were performed at different locations and the evolution of TTS_{DENT} as a function of the distance from the crack tip was evaluated. Two different terms were defined: the true thickness strain at crack initiation (TTS_{DENT}^{i}) and the true thickness strain for the stable crack propagation ($TTS_{DENT}{}^{p}$). A detailed description of the experimental procedure for the determination of TTS_{DENT} is available in Paper I, Paper II and Paper IV. Note that in these papers TTS_{DENT} is denoted ε_{3f} (Paper IV), $\varepsilon_{3f\ \text{DENT}}$ (Paper II) or simply ε_3 (Paper I).

3.2.2 J-integral

J-integral measurements were performed in compact tension (CT) specimens following the recommendations of ASTM E1820 [111] with some modifications. To avoid the size constraints of this standard, the specimens were dimensioned following the recommendations of the ASTM E561 [145]. Instead of estimating the current crack length through the elastic compliance technique, the crack advance was measured by means of a high-resolution video camera located in one of the sides of the specimen (Figure 3.5). A *J*-resistance (*J*-R) curve was constructed according to ASTM E1820 and two cracking resistance parameters were obtained: the fracture toughness at crack initiation, J_i, which is the toughness value at the point where first crack extension is detected in the video equipment, and the fracture toughness near the onset of stable crack propagation, J_c, obtained from the intersection of the 0.2 mm offset line with the *R* curve as indicated in ASTM E 1820.

In order to evaluate the effect of the specimen geometry on J_i and J_c determination, *J-integral* measurements were additionally performed with DENT specimens. Paper I describes in detail the dimensions of the specimens and the mathematical expressions used for *J*-integral measurements.

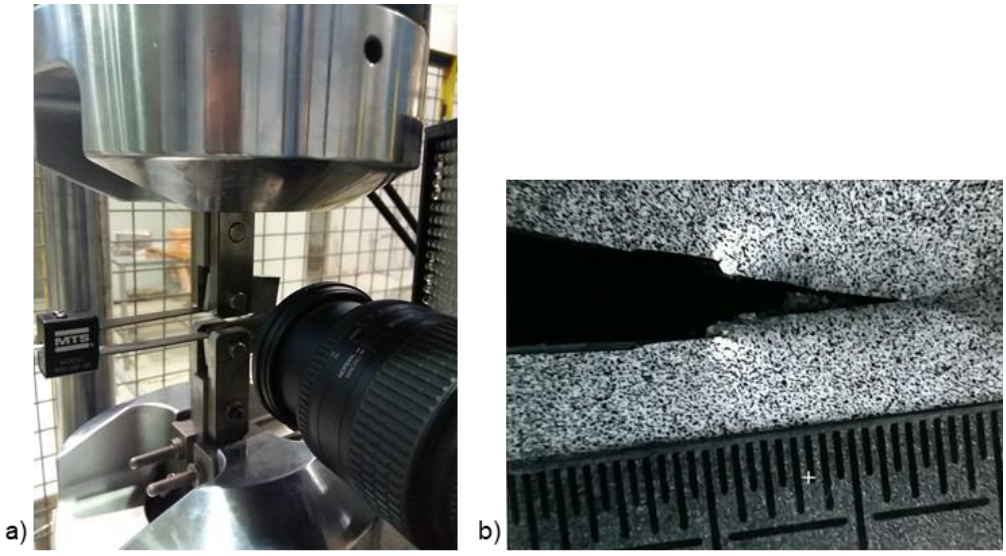

Figure 3.5. a) Experimental setup for the evaluation of the J-integral in CT specimens. **b)** Image from the video camera used for measuring the crack extension.

3.2.3 Kahn-type tear tests

Kahn-type tear tests (KTT) were performed according to ASTM B871 [126]. The specimen geometry is shown in Figure 3.6a. All the specimens were machined with the notch oriented along the rolling direction (T-L specimens). The notch was prepared by EDM ($\rho \approx 150$ µm). The tests were conducted at a constant speed of 1 mm/min. Due to the compression load in the final stage of fracture, the specimens never fractured completely. Therefore, the tests were manually stopped at 10 mm of displacement when the load is steadily decreased to zero. The load-line displacement was measured by a digital video extensometer using extensometer marks separated 10 mm. 3 specimens per material were tested.

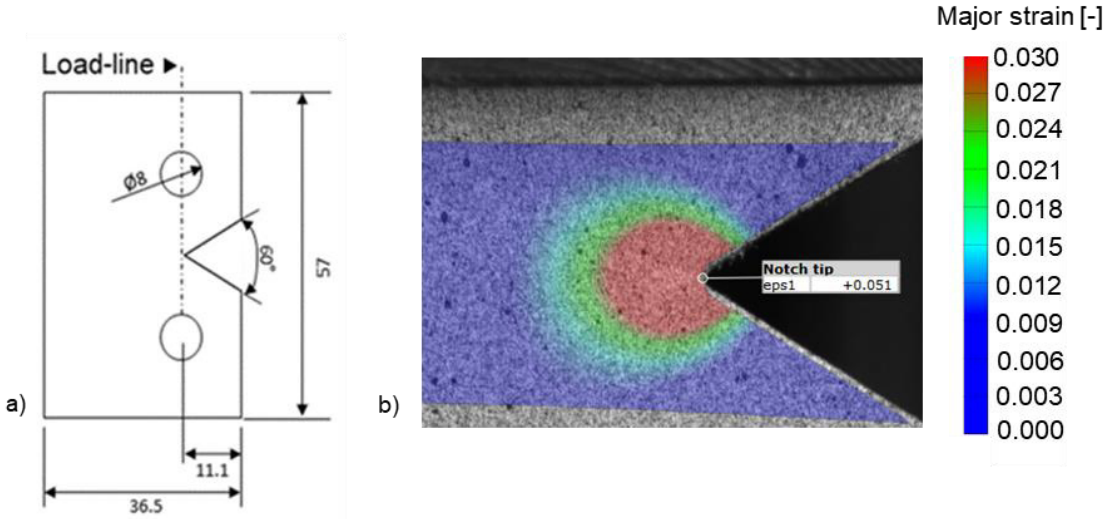

Figure 3.6. a) Specimen geometry used for the Kahn-type tear tests.b) Determination of the true major strain at fracture in the notch tip by means of DIC.

The notch resistance is characterized by the *UIE* (Unit Initiation Energy) and the *UPE* (Unit Propagation Energy). The tear strength was calculated as follows:

$$Tear\ Strength = 4P/bt \tag{34}$$

where P is the maximum load, b is the distance between the notch root and back edge of the specimen and t is the specimen thickness. The tear strength to yield strength ratio (*TYR*) is calculated by dividing the tear strength by the yield strength.

Additionally, a full-field strain analysis was performed on the specimen surface by means of DIC and the true major strain at fracture initiation ($\varepsilon_{f\ KTT}$) was evaluated near the notch tip (Figure 3.6b).

3.3 Edge cracking resistance characterization

3.3.1 Hole Expansion Tests

Hole Expansion Tests (HETs) were performed following the ISO16630 standard [60]. An initial hole 10 mm in diameter was pierced using a cutting clearance of 12%. Figure 3.7 shows the dimensions of specimens used to determine Hole Expansion Ratio (HER) and a picture of the specimen before and after the test.

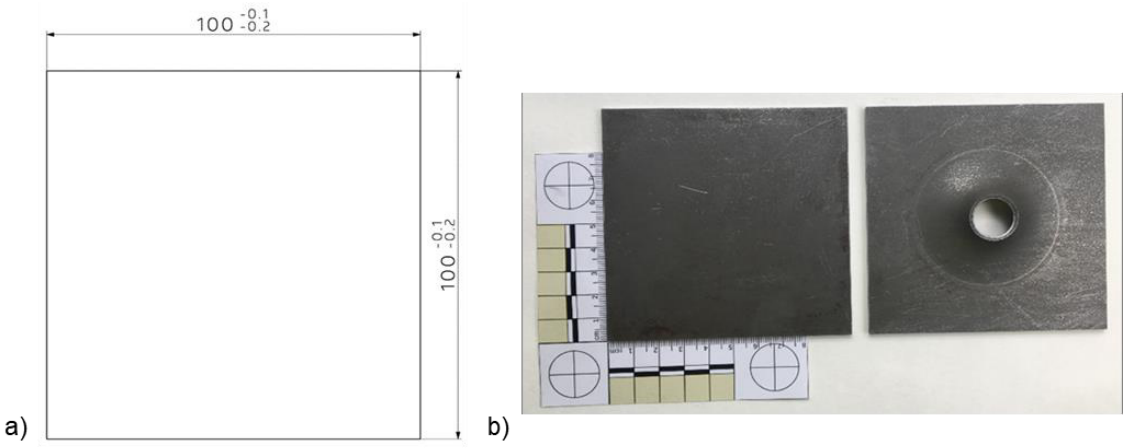

Figure 3.7. a) Specimen geometry used for hole expansion tests. **b)** HER specimen before (left) and after (right) the test.

To determine the Hole Expansion Ratio (HER), a clamping force of 50kN was applied. All the tests were carried out at a temperature of 25°C. The test rate was 1mm/s. To observe the occurrence of cracks in the hole edge, a video camera was located at the bottom of the test tool (Figure 3.8). The final diameter was measured using the images obtained with the video camera when the first through-thickness crack was observed (Figure 3.9). Using this diameter, the limiting hole expansion ratio was calculated according to:

$$\mathrm{HER} = \frac{D_h - D_0}{D_0} x100 \tag{35}$$

Where D_o is the original hole diameter (10mm); and D_h is the hole diameter after rupture, in millimetres.

Figure 3.8. Experimental setup for HER determination.

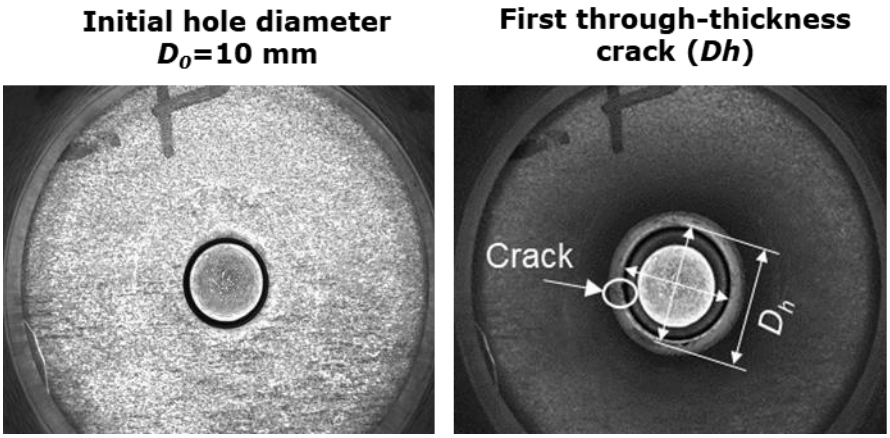

Figure 3.9. Digital images used for the evaluation of the HER.

3.3.1.1 Thickness strain measurements in HET specimens

The true thickness strain in HET specimens (TTS_{HET}) was calculated using Equation (9), where t_0 is the initial sheet thickness and t_f is the thickness at fracture measured in a longitudinal section of an edge crack (Figure 3.10). Thickness measurements were performed at different distances from the punched hole edge. A more detailed explanation of the method for evaluating the TTS_{HET} is available in Paper II.

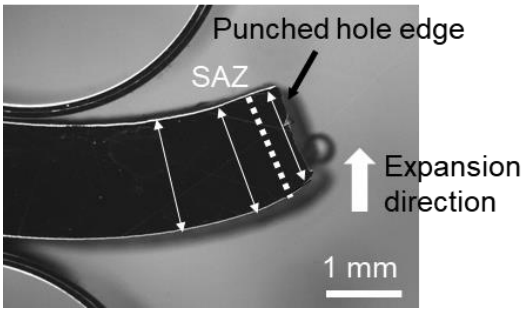

Figure 3.10. Longitudinal section of a crack in a HET specimen after the test and location of the thickness measurements performed. SAZ: shear affected zone.

3.3.2 Hole Tension Tests

For the Hole Tension Tests (HTTs), rectangular specimens of 130 x 25 mm were used (Figure 3.11a). The specimens were machined at the transverse direction and a hole of 10 mm in diameter was punched in the central area. The tests were performed in a tensile machine at a constant cross-head displacement rate of 1 mm/min. The strain at fracture was determined by means of a DIC software. For this purpose, a speckle pattern was applied to all the specimens. The image just before fracture initiation was used for fracture strain ($\varepsilon_{f\ HTT}$) determination (Figure 3.11b). $\varepsilon_{f\ HTT}$ was evaluated by constructing two sections perpendicular to the loading axis crossing through the area of maximum deformation, located in the central region of the hole (Figure 3.12). The maximum strain corresponding to the side of the hole where crack initiates was defined as the $\varepsilon_{f\ HTT}$.

To evaluate the effect of the cutting clearance in edge formability, 4 different punch to die clearances were used for the hole preparation. The punch diameter was kept constant (10 mm) and the inner diameter of the die was varied from 10.3 mm to 10.6 m, resulting in clearances ranging from 11% to 20%. Clearances are calculated according to Equation (36):

$$c = \frac{d_d - d_p}{2t} x100 \tag{36}$$

where c is the clearance as a percentage, d_d is the inside diameter of the die, d_p is the diameter of the punch and t is the sheet thickness. More details about the experimental procedure and the different punch-to-die clearances used can be found in Paper B.

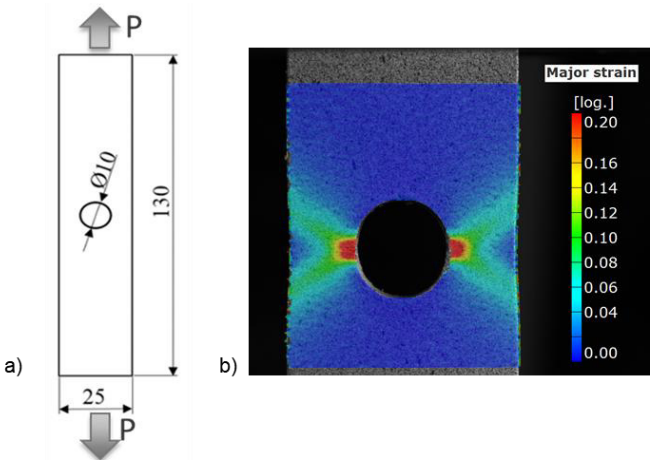

Figure 3.11. a) Specimen geometry used for Hole Tension Tests. **b)** DIC image showing the major strain at fracture.

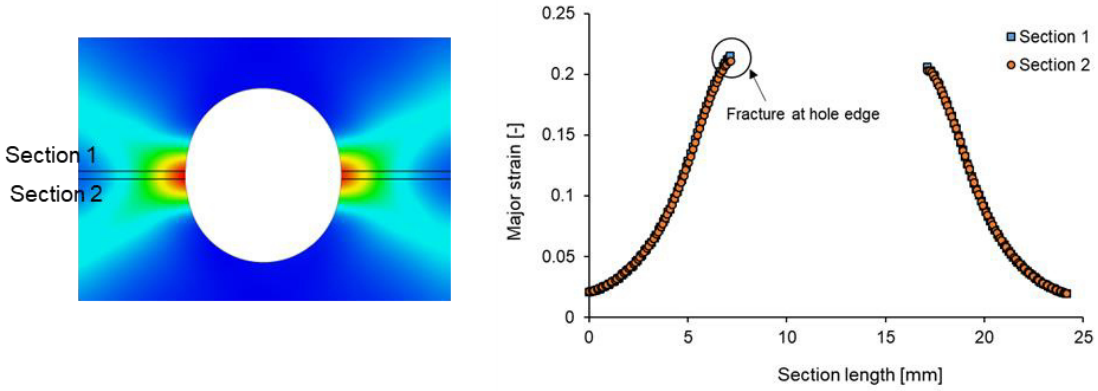

Figure 3.12. DIC strain mapping and sections used for $\varepsilon_{f\,HTT}$ determination

3.4 Crash behaviour characterization

3.4.1 Axial impact resistance tests

Axial impact resistance tests were performed using an impact simulator, which works with a load mass of 283 kg and whose speed can be varied between 10 and 40 km/h. Some images of the experimental setup for axial crash tests at voestalpine Stahl are shown in Figure 1.24a.

Impact tests were performed at different crash speeds and, thus, different intrusion levels. The deformation of axially crashed sample (initial length: 300 mm) was limited to 200 mm shortening For these tests, hat profile specimens were used (Figure 3.13). Profiles were spot-welded to a closing blank of the same steel type. Also at the front and back, closing blanks were welded to the profile. Impact resistance was evaluated by determination of an overall crash index (*CI*, definition in Table 3.4) and the energy absorbed for each deformed crash sample. Intrusions of axial impact tests include only plastic deformation and were determined by the difference in length of unloaded (300 mm) and crashed samples. The energy absorbed during axial impact tests was calculated by integrating the area under the load vs impactor displacement curves (Figure 3.13b). To evaluate the evolution of the *CI* as a function of the intrusion level, a new parameter is introduced, the Crash Index Decreasing Rate (*CIDR*). The *CIDR* quantifies the damage in impact resistance tests and can be understood as a crack propagation rate.

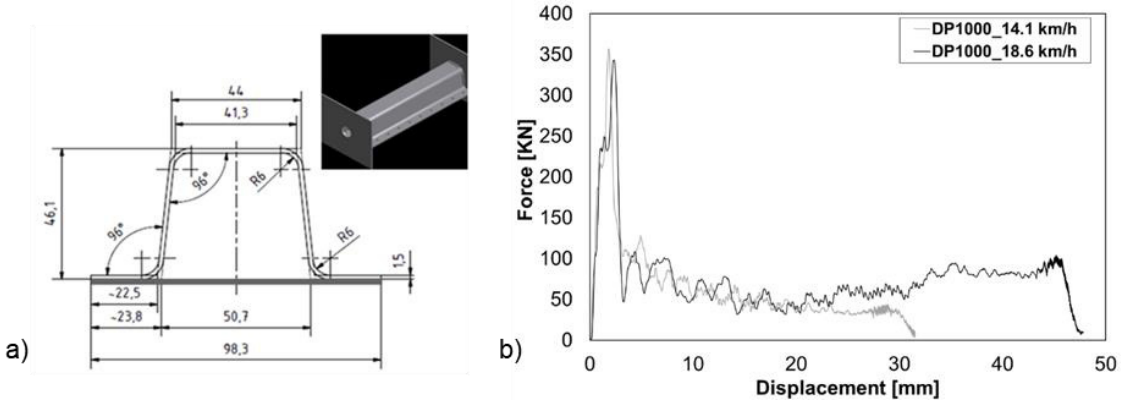

Figure 3.13. a) Geometry of axial crash samples with 1.5 mm blank thickness. **b)** Force vs impactor displacement curves for two axial impact tests with DP1000**.**

Table 3.4. Definition of crash index for axial impact tests [47].

Crash index (*CI*)	Damage
100	no cracks
>75	crack length < 10 mm
50-75	10 mm < crack length < 25 mm
25-50	crack length > 25 mm
<25	"splitting and curling"; multiple breaks

3.4.2 Bending impact resistance tests

The experimental setup for bending crash tests is shown in Figure 1.24b. The geometry of the samples for bending impact tests can be seen in Figure 3.14. A microalloyed steel grade with thickness 1.5 mm was used as a closing blank of the hat profile. The welding spots joining the closing blank and the crash profile are 8 mm in diameter, with a distance of 30 mm between the welding spots for both axial and bending impact resistance tests.

Bending impact tests were conducted at speeds varying from 20 to 30 km/h. The load mass was 86 kg. The maximum bending displacement was limited to 211 mm. Crash index (*CI*) of bending impact samples was derived from the occurring crack length and calculated as defined in [48]. The formula for calculating the crash index is shown in Figure 3.15. The deformation process during the bending impact test was recorded with a high-speed camera. Intrusions of bending impact tests in the following content include plastic and elastic deformation. Bending impact samples do not show any welding spot failure, which means that the corresponding results characterize the behaviour of the base material.

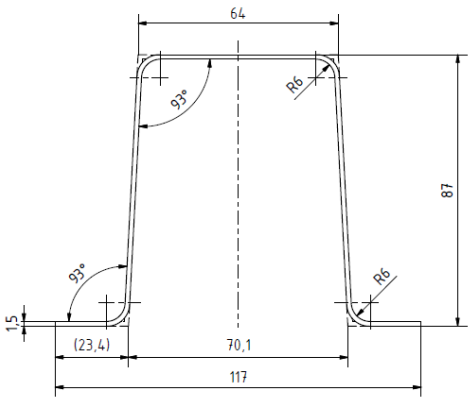

Figure 3.14. Geometry of bending impact test samples with 1.5 mm blank thickness. Length: 900 mm.

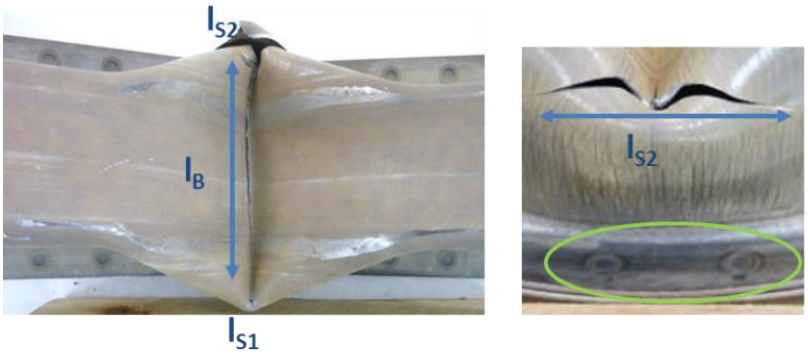

$$Crashindex_{side\ impact} = \left(0.2 \times \left(1 - \frac{l_S}{250}\right) + 1.0 \times \left(1 - \frac{l_B}{250}\right) - 0.2\right) \times 100$$

l_B; the total length of big crack
l_S ; the total length of small crack
*Best case ; no crack, Crash Index = 100%
*Worst case ; l_B = 250mm, Crash Index = 0%

Figure 3.15. Crack location and definition of crash index for bending impact test.

3.5 Microstructural characterization

3.5.1 SEM and EBSD

Microstructural investigations were performed by means of Light Optical Microscopy (LOM) and Scanning Electron Microscopy (SEM). The optical microscope is able to reach up to 1000 magnifications and it is equipped with the image treatment software ANALYSIS. A high-resolution SEM (Figure 3.16a) equipped with a high-resolution electron backscatter diffraction (HR-EBSD) detector was used.

In Paper IV, HR-EBSD measurements were performed to investigate the microstructure of two high strength dual phase steels. In EBSD measurement, a stationary electron beam interacts with a tilted (70º from horizontal) crystalline sample. The diffracted electrons form a pattern (Figure 3.16b) that can be detected with a phosphor screen coupled to a compact lens, which focuses the image from the fluorescent screen onto the CCD camera. The diffraction pattern is characteristic of the crystal structure and orientation. Hence the diffraction pattern provides information about the structure, grain size, grain boundary nature, grain orientation, texture and phase identifications.

For HR-EBSD measurements, the samples were mechanically polished to mirror surface finish with a 0.05 µm colloidal silica suspension. HR-EBSD measurements were performed at 20 kV with a step size of 0.15 µm. The analysed areas were 311 x 231 μm^2. From these measurements, the inverse pole figure (IPF) map, the phase map and the mean angular deviation (MAD) map were used to characterize the microstructure.

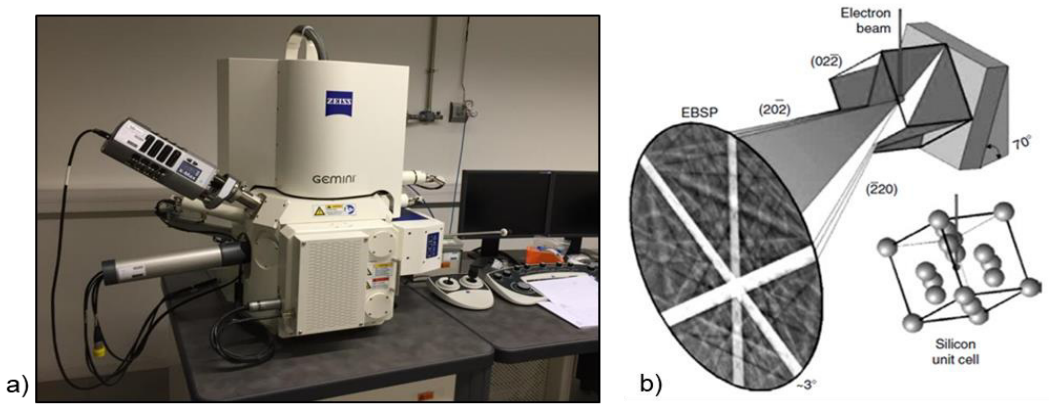

Figure 3.16. a) Scanning Electron Microscope (SEM). **b)** Formation of diffraction patterns (EBSP).

3.5.2 Nanoindentation tests

Nanoindentation technique was used in Paper IV to investigate the distribution of hard secondary phases in the two investigated dual phase steels. Nanoindentation measurements were performed using an iNano nanoindenter (Figure 3.17a) and a Berkovich indenter. In each sample, three arrays of 25x25 indentations were performed. An indentation separation of 6 µm was chosen, covering an area of 150x150 μm^2 (Figure 3.17b). The indentations were performed at an applied load of 20 mN. Hardness values were evaluated using the Oliver and Pharr methodology [146].

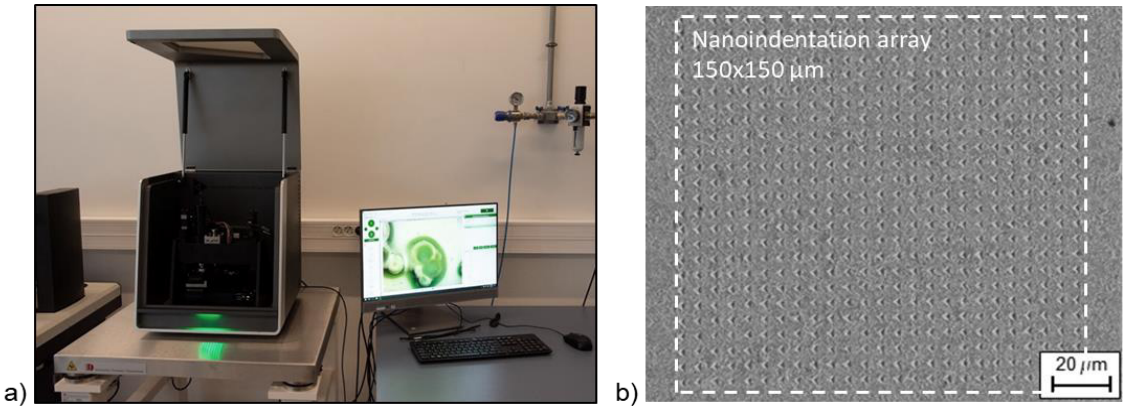

Figure 3.17. a) iNano nanoindenter**. b)** SEM image showing a nanoindentation array.

3.5.3 Synchrotron X-Ray Powder Diffraction

X-ray powder diffraction measurements were performed in three 3rd Generation TRIP-assisted steels with different retained austenite content and mechanical stability (TBF, TBF/Q&P, Q&P). The experiments were performed at the powder diffraction endstation of the Materials Science and Powder Diffraction beamline (BL04-MSPD) at ALBA Synchrotron (Figure 3.18a). Data were collected in transmission mode in the high-angular resolution setup using the Multicrystal Analyser Detector (MAD). This detector allows the exact determination of the diffraction peaks angles with no effects due to small displacements in sample positioning. More detailed information about the BL04-MPSD beamline and the MAD detector can be found in [147,148]. The measurements were performed directly by placing the interest zones in the X-ray beam of 3 x 1.5 mm^2 (width x height, Figure 3.18b). The selected energy for the incident beam was 38keV (0.32622 Å wavelength, determined from NIST640D silicon standard data), high enough to

minimize the absorption due to the sample thickness (1.4-1.5 mm). To evaluate the evolution of the retained austenite transformation during crack propagation, 4 different deformation stages were investigated (Figure 3.18c). For each stage, one sample was analyzed. Three consecutive zones (separated by 3.5 mm) were measured in each of the samples, from the crack tip ("zone 1") to the centre of the ligament ("zone 3) (Figure 3.18b). In each zone, diffraction data were collected from -1º to 44º (2-theta) by scanning the detector at 1º/min, repeating the last 15º twice to increase the statistics, with a total measurement time of 1h. By using this scanning range referenced at the detector central channel and considering the distribution of the 13 channels of the detector with a 1.5º offset, it is ensured that all the channels collected the data in the 8 to 35º (2-theta) range.

Rietveld refinements were performed with the FullProf program [149] using a pseudo-Voigt function and refining the scale factor, zero offset, isotropic thermal factor of Fe, cell parameters, the pseudo-Voigt coefficients considering an anisotropic strain broadening (modelled using the quartic form expression in reciprocal space implemented in FullProf) and one March coefficient for the preferred orientation considering an [hkl]* of [111] for the retained austenite and [110] for martensite.

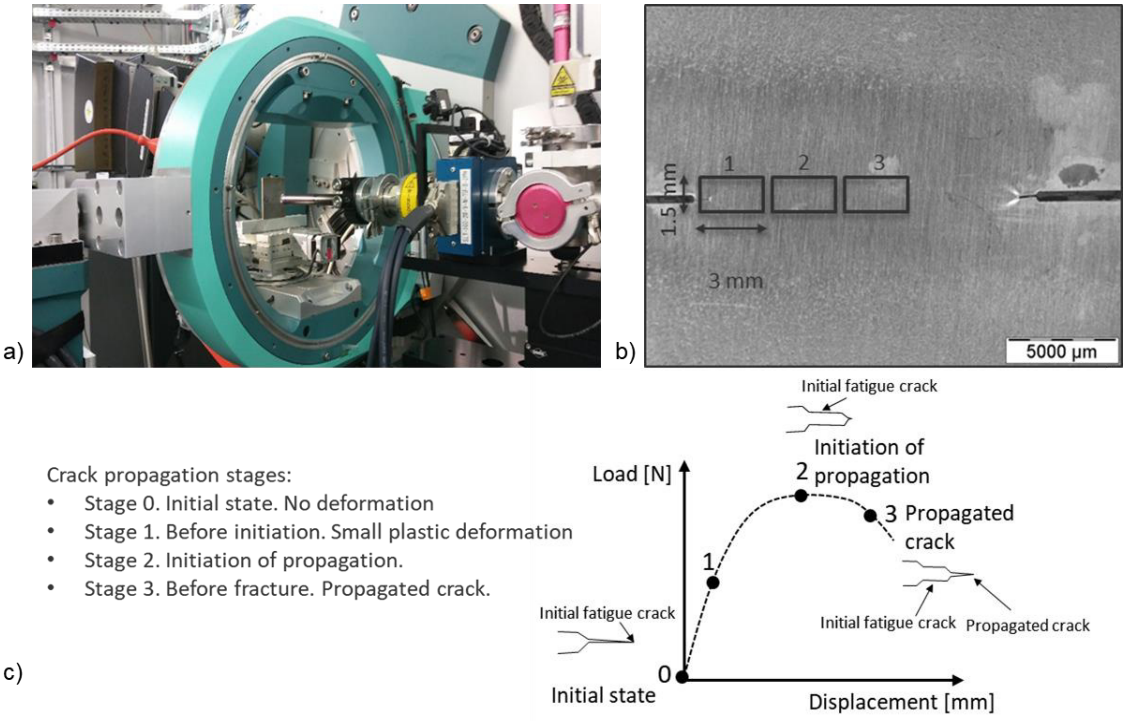

Figure 3.18. a) Experimental setup for Synchrotron X-Ray Powder Diffraction measurements in the MSPD line of Alba Synchrotron**. b)** Location of the measurements in the specimen surface**. c)** Different stages of deformation investigated.

Chapter 4

Results

This chapter summarizes the main results obtained in Papers I-IV. Additional findings presented in appended papers A-D and other unpublished results are also included. In order to provide a global overview of the work, the presentation of the results is divided into three categories: fracture toughness, edge cracking resistance and crash failure behaviour.

The results of microstructural characterizations are not included here. They will be used in the next chapter to discuss the influence of microstructure on fracture toughness. SEM micrographs and microstructural descriptions of the different AHSS grades are available in Papers I-IV. Paper IV, also includes results of HR-EBSD and nanoindentation measurements for the two DP steels investigated (DP1000A and DP1000B). The results of synchrotron X-ray diffraction measurements will be used in Chapter 5 to evaluate the evolution of the retained austenite-to-martensite transformation during crack propagation in TRIP-assisted steels. These results are not published yet. A publication on this topic is currently being prepared.

4.1 Fracture toughness results

4.1.1 Essential Work of Fracture

4.1.1.1. Specific essential work of fracture, w_e

The results of EWF tests are shown in Figure 4.1 to Figure 4.3. The figures show the values of w_f as a function of the initial ligament length (l_0). In all cases, w_f scales linearly with the ligament length and the specific essential work of fracture, w_e, can be obtained by extrapolation to ligament zero. Numerical values of w_e and non-essential plastic work βw_p are given in Table 4.1. Overall, the results showed a good repeatability and a good linear data fitting was obtained for most of the steels (R^2=0.87-0.99, see Table 4.1).

w_e values range from 104 kJ/m^2 to 405 kJ/m^2. In general, CP-like microstructures (CP1000, TBF/Q&P, PHS1000, Q&P, CP1200) show higher w_e than DP-like (DP780, TRIP780, DP1000, TBF) or fully martensitic microstructures (PHS1500). CP1000 shows the highest w_e of the investigated steels, followed by TWIP, which has a fully austenitic microstructure, PHS1000, TBF/Q&P and DP1000B. Q&P steels and CP1200 lie in an intermediate range of w_e values (≈ 200 kJ/m^2). On the other hand, TRIP780, 3rd Gen DP1180 and 3rd Gen TBF1180 exhibits the lowest crack propagation resistance. The rest of steels (DP780, DP1000, DP1000A, TBF) show similar toughness with w_e values around 150 kJ/m^2.

Concerning the non-essential plastic work, βw_p, the trend is rather the contrary than the observed in w_e, i.e. DP-like and TRIP-assisted steels show higher plastic work than CP-like steels. TWIP steel shows by far the highest non-essential plastic work (βw_p= 65 ± 2 MJ/m^3).

Figure 4.4 to Figure 4.6 shows the results of the DIC analysis in the ligament area for three different steel grades. The images show the Equivalent Mises Strain just before crack initiation for the smallest and the largest ligament. In all cases, the ligament area is completely yielded (Mises strain above 0.005-0.006) before crack initiation, which is one of the requirements for the application of the EWF methodology. This analysis was performed in all the investigated materials. All the steels satisfied this requirement.

4.1 Fracture toughness results

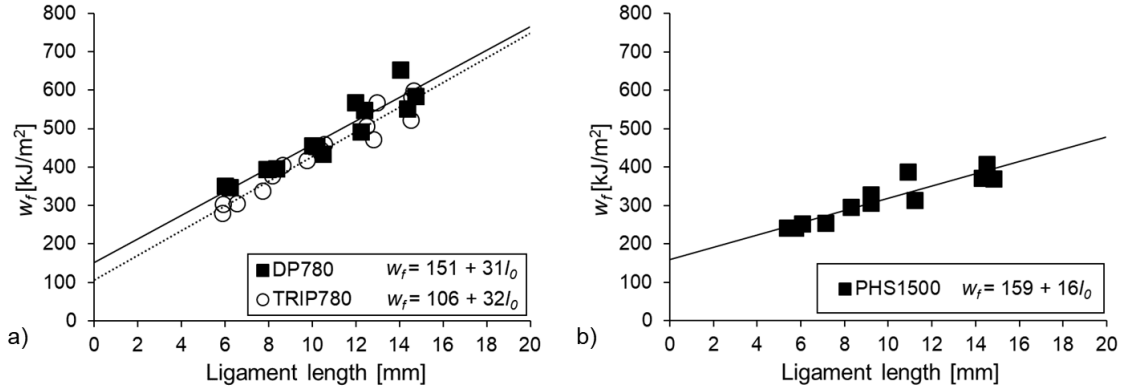

Figure 4.1. w_f as a function of the initial ligament length (l_0). **a)** 780 MPa steel grades. **b)** 1500 MPa steel.

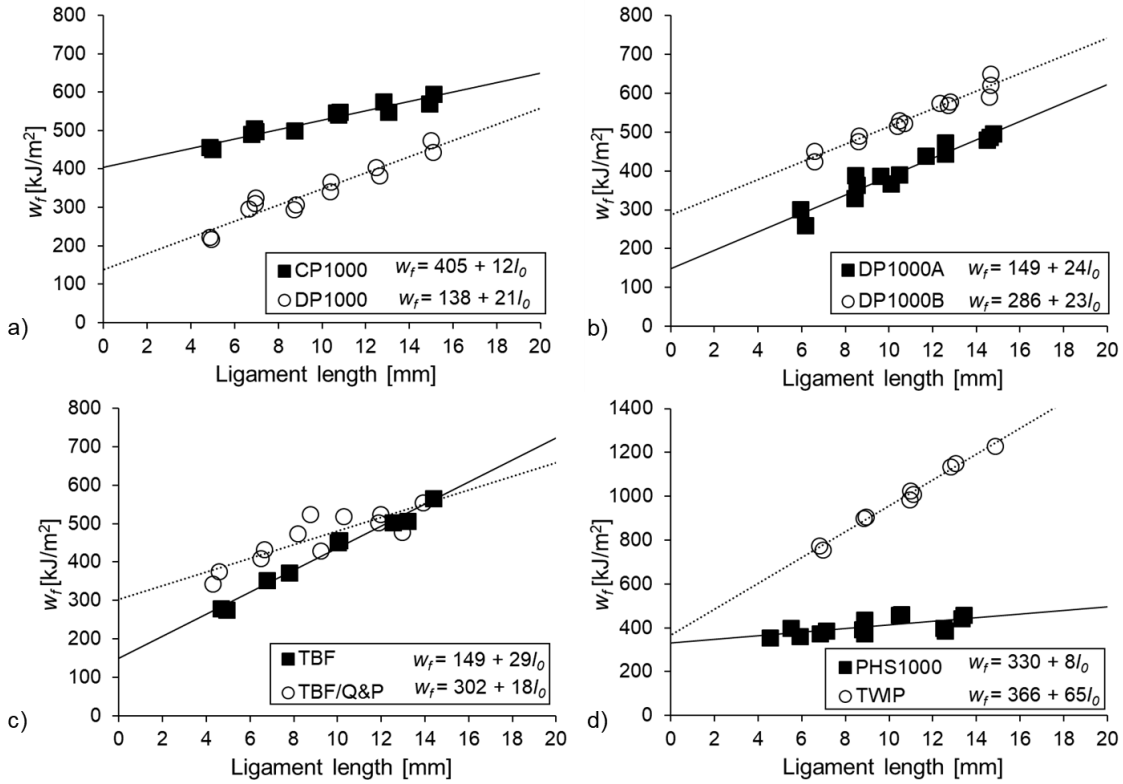

Figure 4.2. w_f as a function of the initial ligament length (l_0). Results for 1000 MPa steel grades.

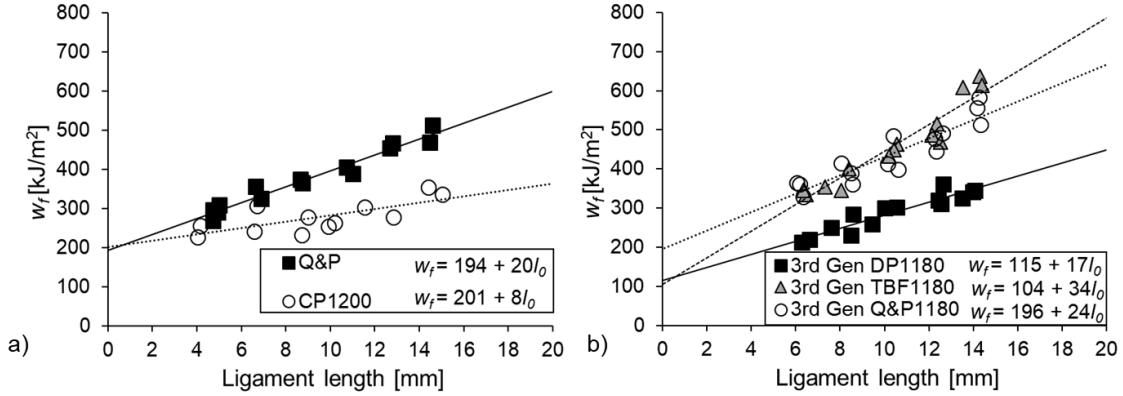

Figure 4.3. w_f as a function of the initial ligament length (l_0). Results for 1200 MPa steel grades.

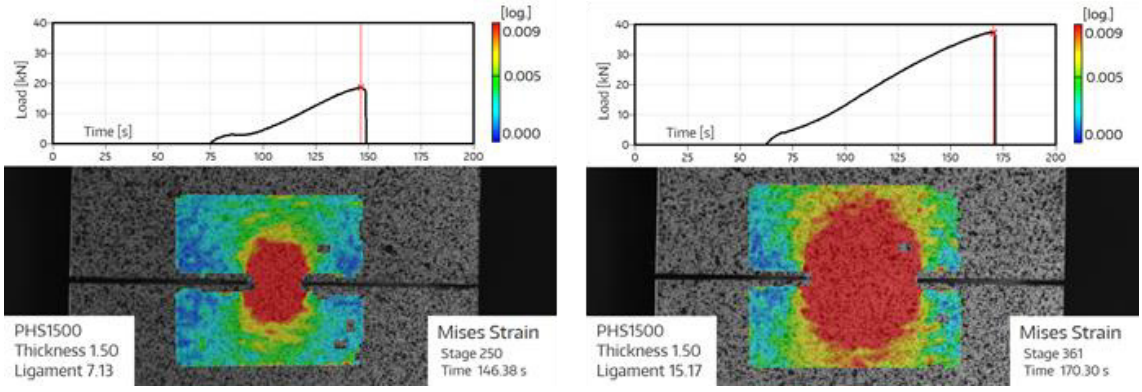

Figure 4.4. PHS1500. Equivalent Mises strain at crack initiation. Small (left) and large (right) ligament length.

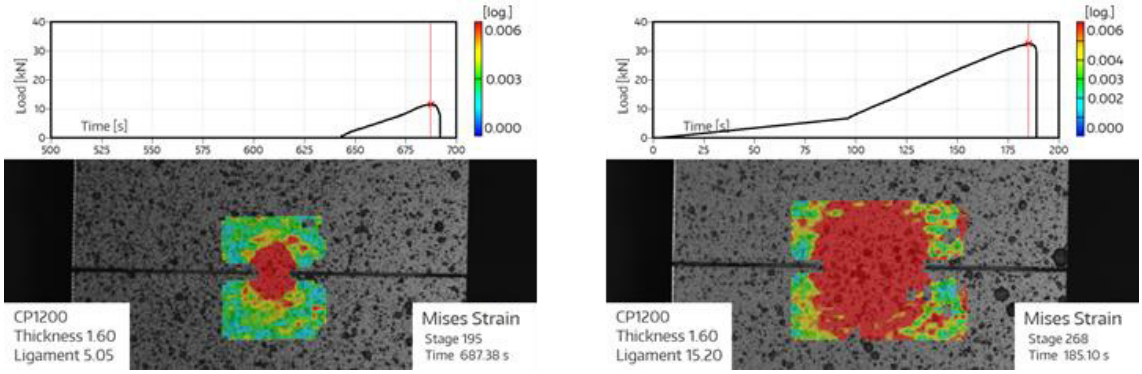

Figure 4.5. CP1200. Equivalent Mises strain at crack initiation. Small (left) and large (right) ligament length.

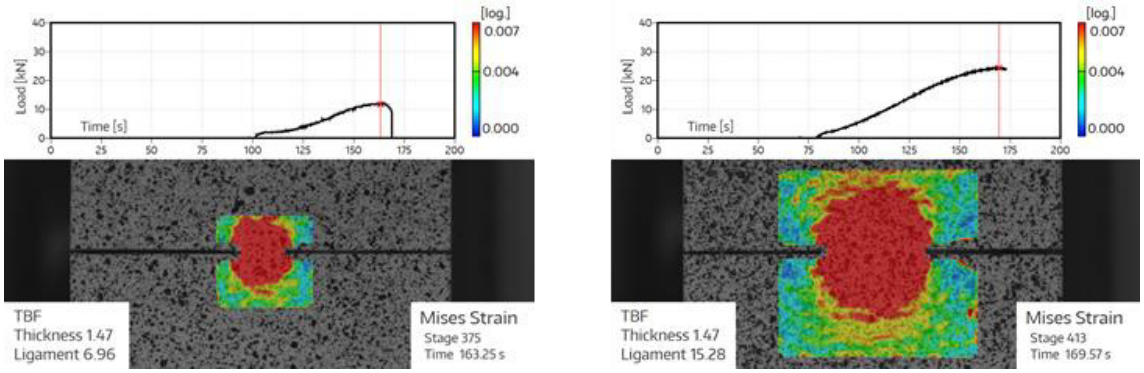

Figure 4.6. TBF. Equivalent Mises strain at crack initiation. Small (left) and large (right) ligament length

4.1.1.2. Fracture toughness at crack initiation, w_e^i

The values of fracture toughness at crack initiation, w_e^i, are summarized in Figure 4.7. w_e^i values are also given in Table 4.1.

Initiation toughness values can be roughly divided into 4 different groups or ranges:

- very high w_e^i (>250 kJ/m^2): TWIP
- high w_e^i (180-200 kJ/m^2): 3rd Gen Q&P1180, DP1000B
- medium w_e^i (≈150 kJ/m^2): CP1000, Q&P, CP1200, TBF/Q&P, PHS1500, PHS1000
- low w_e^i (≈100 kJ/m^2): DP1000, TBF, DP780, TRIP780, DP1000A, 3rd Gen DP1180, 3rd Gen TBF1180.

Similarly to the observed in w_e, DP-like steel grades show the lowest toughness at crack initiation. It is worth noting that CP1000, which has the highest w_e, shows a crack initiation resistance comparable to PHS1500, Q&P or CP1200. In this case, TWIP steel shows the highest toughness at crack initiation.

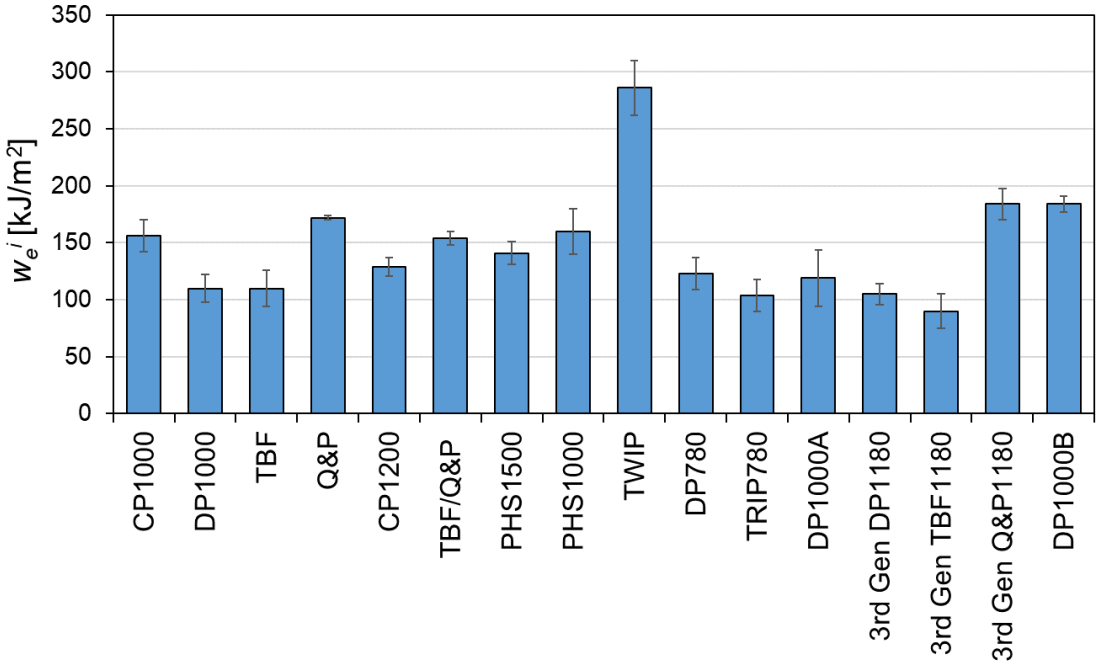

Figure 4.7. w_e^i results for all the studied steel grades.

4.1.1.3. Critical crack tip opening displacement, δ_c

In Figure 4.8 to Figure 4.10, the displacement at fracture (d_f) is plotted as a function of the ligament length. It can be observed that these graphs are very similar to the plots of w_f vs l_0 (Figure 4.1 to Figure 4.3) and the critical crack opening displacement (δ_c) can be obtained by extrapolation to zero ligament length. The values of δ_c are summarized in Table 4.1.

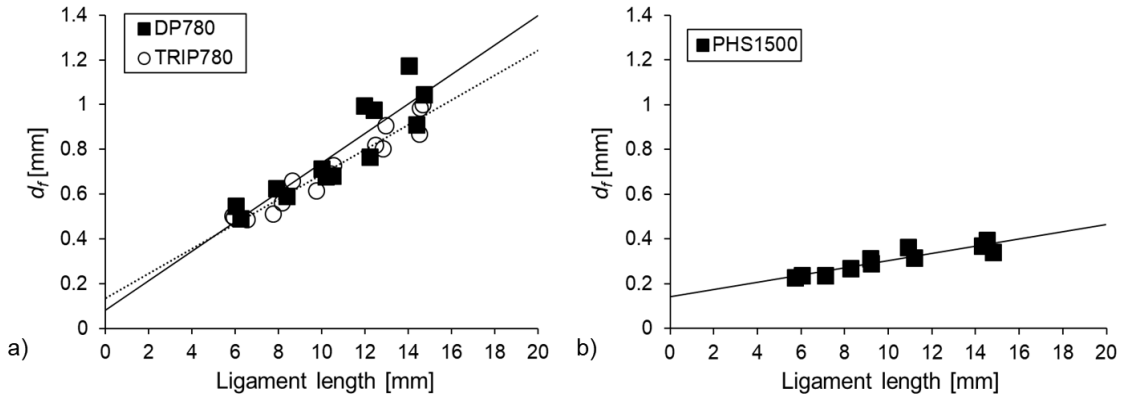

Figure 4.8. d_f as a function of the initial ligament length (l_0). a) 780 MPa steel grades. b) 1500 MPa steel

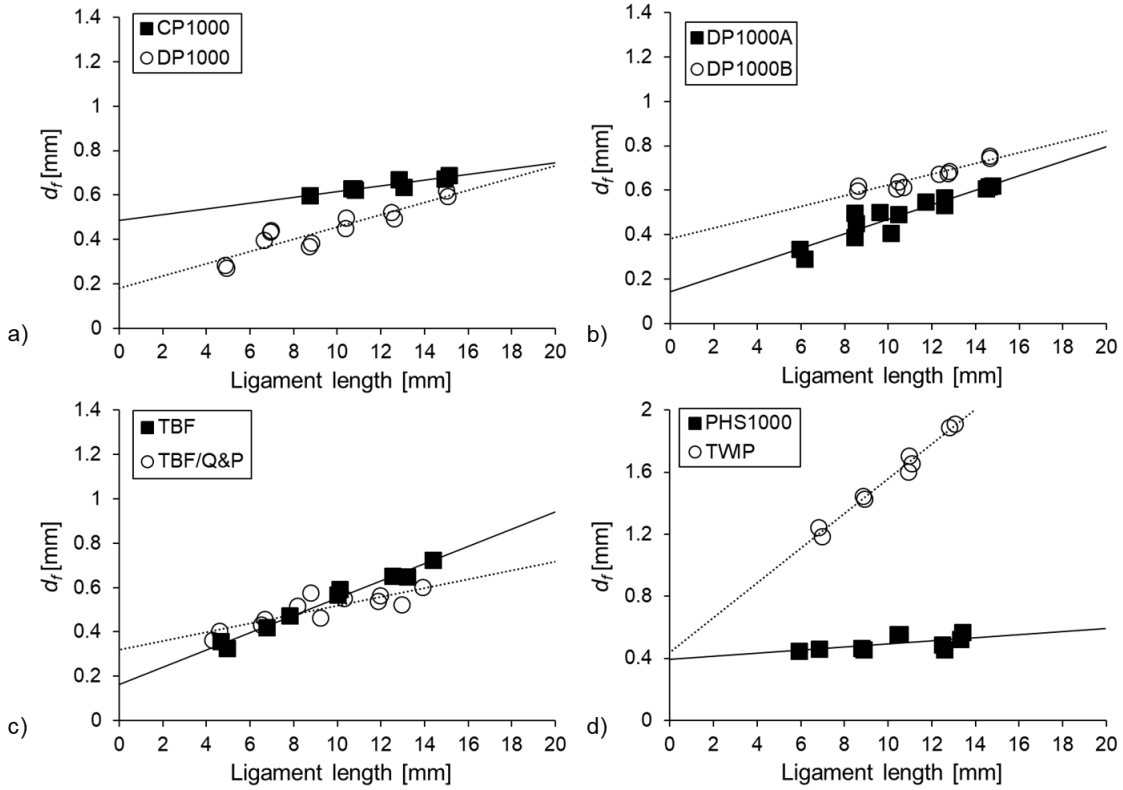

Figure 4.9. d_f as a function of the initial ligament length (l_0). Results for 1000 MPa steel grades.

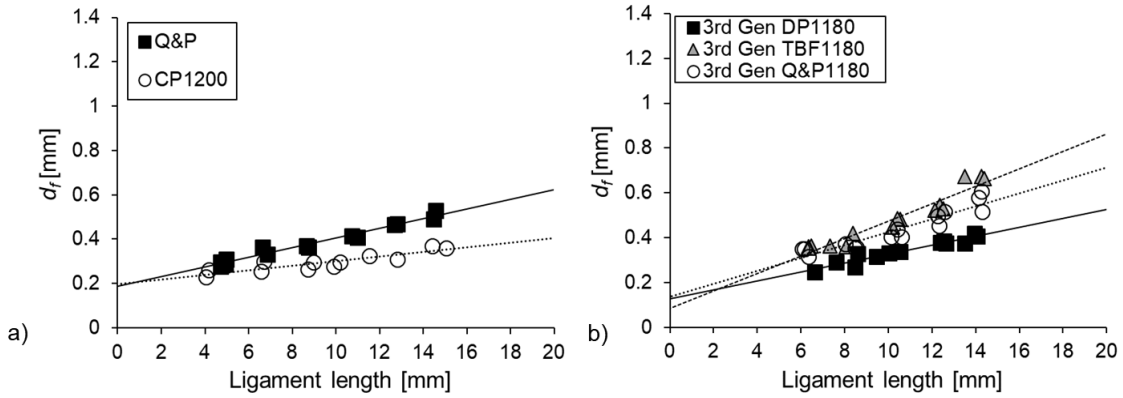

Figure 4.10. d_f as a function of the initial ligament length (l_0). Results for 1200 MPa steel grades.

4.1.1.4. Thickness strain at crack initiation and propagation

Figure 4.11 shows optical microscope images of the fracture surface of different steels, where thickness strain (TTS_{DENT}) measurements were performed. The values of TTS_{DENT} are plotted as a function of the distance from the crack tip in Figure 4.12 to Figure 4.14. ${TTS_{DENT}}^{i}$ and ${TTS_{DENT}}^{p}$ values are given in Table 4.1.

In most cases, the thickness strain gradually increases with increasing the distance from the crack tip until a constant value is reached for a distance of about 0.4-0.6 mm. ${TTS_{DENT}}^{p}$ is the average of thickness strains in this constant region.

The increase in TTS_{DENT} during crack growth illustrates the contribution of necking to the crack propagation resistance. The steels that develop a larger degree of necking during crack

propagation, such as CP1000, show higher contribution from crack propagation after crack initiation. This contribution is less significant in the rest of the steel grades investigated.

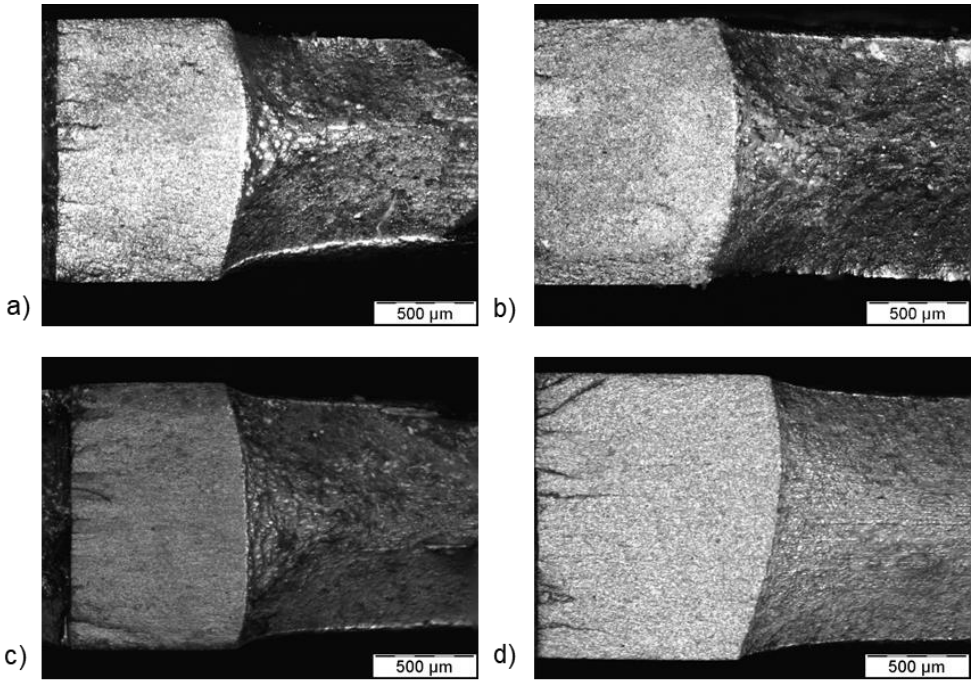

Figure 4.11. Fracture surface of DENT specimens. Images from optical microscope. **a)** CP1000, **b)** Q&P, **c)** DP1000B, **d)** DP780.

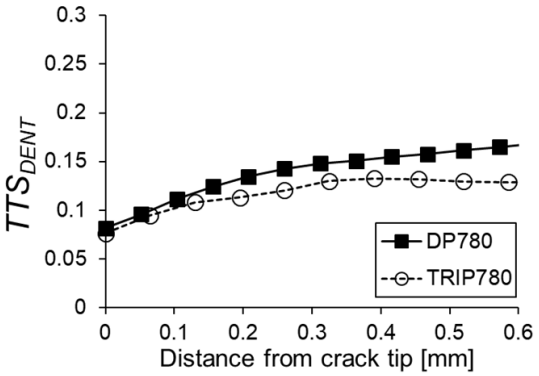

Figure 4.12. True thickness strain (TTS_{DENT}) as a function of the distance from the crack tip. 780 MPa steel grades

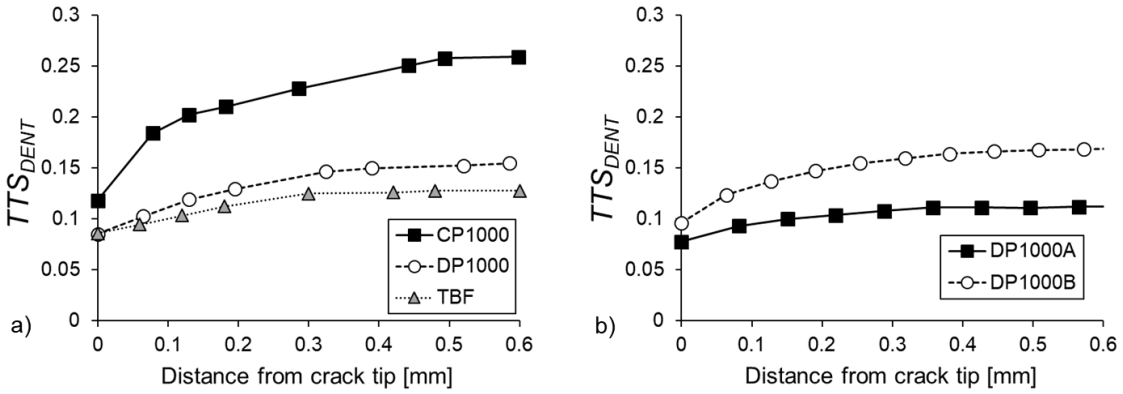

Figure 4.13. True thickness strain (TTS_{DENT}) as a function of the distance from the crack tip. 1000 MPa steel grades.

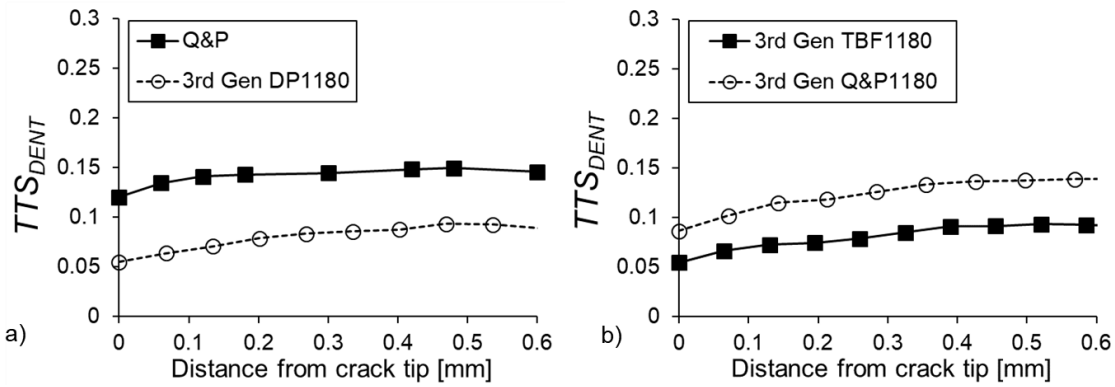

Figure 4.14. True thickness strain (TTS_{DENT}) as a function of the distance from the crack tip. 1200 MPa steel grades.

Table 4.1. Summary of fracture toughness parameters obtained from EWF tests. Results for fatigue pre-cracked specimens machined at 90º with respect to the rolling direction.

Steel	w_e [kJ/m^2]	βw_p [MJ/m^3]	R^2	w_e^i [kJ/m^2]	δ_c [mm]	$TTS_{DENT}{}^i$ [-]	$TTS_{DENT}{}^P$ [-]
CP1000	405 ± 11	12 ± 1	0.93	156 ± 14	0.49 ± 0.02	0.12	0.26
DP1000	138 ± 20	21 ± 2	0.91	110 ± 12	0.18 ± 0.04	0.09	0.15
TBF	149 ± 13	29 ± 1	0.98	110 ± 16	0.16 ± 0.02	0.09	0.13
Q&P	194 ± 12	20 ± 1	0.96	172 ± 2	0.19 ± 0.01	0.12	0.15
DP780	151 ± 31	31 ± 3	0.88	123 ± 14	0.20 ± 0.10	0.08	0.17
TRIP780	106 ± 24	32 ± 2	0.94	104 ± 14	0.13 ± 0.04	0.07	0.14
DP1000A	149 ± 21	24 ± 2	0.93	119 ± 25	0.14 ± 0.04	0.08	0.11
3rd Gen DP1180	115 ± 20	17 ± 2	0.87	105 ± 9	0.13 ± 0.02	0.06	0.09
3rd Gen TBF1180	104 ± 30	34 ± 3	0.92	90 ± 15	0.08 ± 0.03	0.06	0.10
3rd Gen Q&P1180	196 ± 31	24 ± 3	0.83	184 ± 14	0.14 ± 0.03	0.09	0.14
CP1200	201 ± 24	8 ± 2	0.53	129 ± 8	0.20 ± 0.02	-	-
TBF/Q&P	302 ± 32	18 ± 3	0.74	154 ± 6	0.32 ± 0.04	-	-
PHS1500	159 ± 18	16 ± 2	0.85	141 ± 10	0.14 ± 0.02	-	-
PHS1000	330 ± 21	8 ± 3	0.42	160 ± 20	0.32 ± 0.04	-	-
TWIP	366 ± 24	65 ± 2	0.99	286 ± 24	0.44 ± 0.10	-	-
DP1000 B	286 ± 17	23 ± 1	0.96	184 ± 7	0.38 ± 0.03	0.10	0.17

4.1.1.5. Specimens with EDM notches

EWF results for specimens with notches machined by electrical discharge machining (ρ= 150 µm) are shown in Figure 4.15 and Figure 4.16. w_e, w_e^i and βw_p values are given in Table 4.2. Correlation coefficients for linear regression of w_f vs l_0 data are also indicated.

As previously observed for EWF results with fatigue pre-cracked specimens, DP1000 and TBF show lower w_e values than CP1000 and Q&P. However, in this case, CP1000 and Q&P show similar w_e, which contrasts with the high differences observed for pre-cracked specimens.

CP1000 and Q&P also have the highest toughness at crack initiation, w_e^i. In most of the steels, except in CP1000, the non-essential plastic work, βw_p, is drastically reduced if compared with EWF results with fatigue pre-cracks.

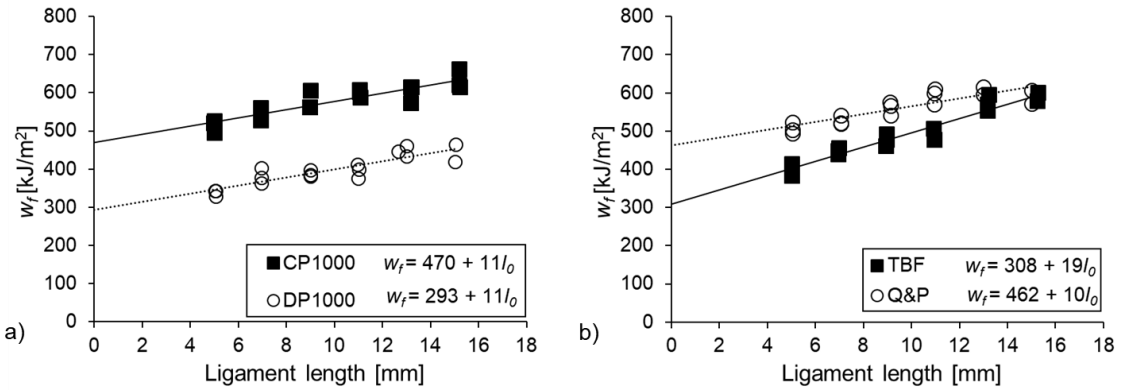

Figure 4.15. EWF results for specimens with EDM notches (ρ= 150 µm). w_f as a function of the initial ligament length (l_0).

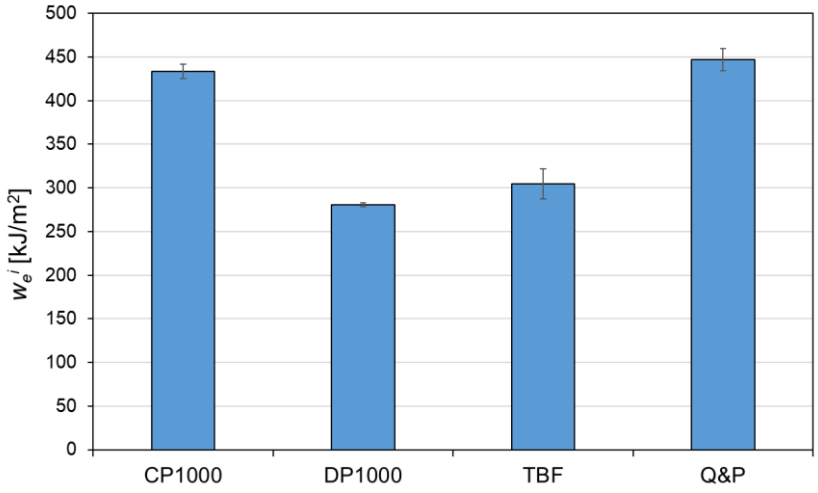

Figure 4.16. w_e^i results for the 4 investigated steel grades. Results for EDM notched specimens.

Table 4.2. EWF results with EDM notched specimens

Steel	w_e notch [kJ/m²]	βw_p notch [MJ/m³]	R^2	w_e^i notch [kJ/m²]
CP1000	470 ± 14	11 ± 1	0.81	433 ± 8
DP1000	293 ± 15	11 ± 1	0.78	281 ± 2
TBF	308 ± 15	19 ± 1	0.92	305 ± 17
Q&P	462 ± 16	10 ± 2	0.74	462 ± 16

4.1.1.6. Specimens with sheared notches

Figure 4.17 shows the EWF results for specimens with mechanically sheared notches ($\rho\approx$ 2-3 µm). w_e and βw_p values are shown in Table 4.3. In all cases, the results are in good agreement with the previously shown for fatigue pre-cracked specimens, as indicated by the almost identical values of w_e and βw_p. A good linear fitting was obtained in the four investigated steels (Table 4.3).

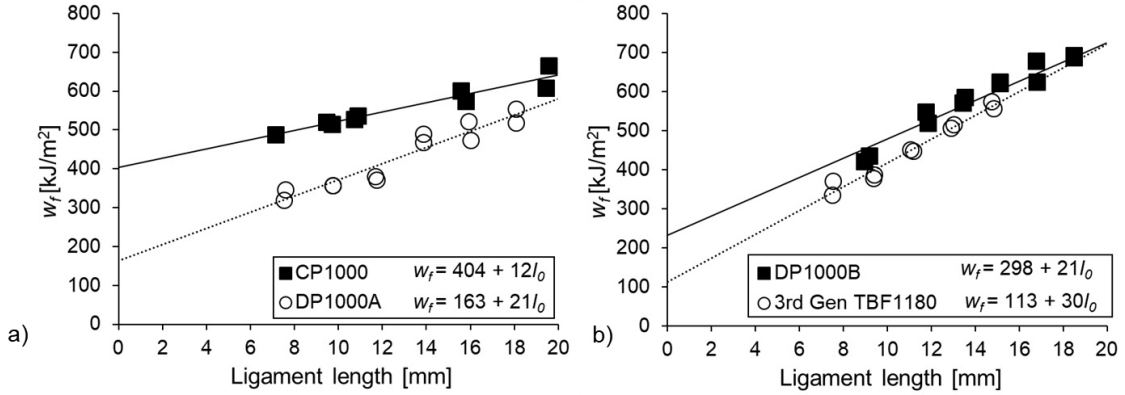

Figure 4.17. EWF results for specimens with sheared notches ($\rho \approx$ 2-3 µm). w_f as a function of the initial ligament length (l_0).

Table 4.3. EWF results from specimens with sheared notches.

Steel	$w_{e\ shear}$ [kJ/m²]	$\beta w_{p\ shear}$ [MJ/m³]	R^2
CP1000	404 ± 19	12 ± 1	0.92
DP1000A	163 ± 27	21 ± 2	0.91
DP1000B	298 ± 32	21 ± 2	0.94
3rd Gen TBF1180	113 ± 21	30 ± 2	0.97

4.1.2 J-integral

Figure 4.18 shows the *J*-R curves obtained for the four AHSS grades investigated in Paper I. The values of J_i and J_c, as well as the slope of the R curve (d*J*/da) and the tearing modulus (T_R), are given in Table 4.4. The slope of the resistance curve is an indicator of the relative stability of the crack growth, i.e. materials showing a lower slope are more likely to experience unstable crack propagation. For *J*-R curves, this slope is usually defined by the T_R, which is determined according to:

$$T_R = \frac{E}{\sigma_{YS}^2}\frac{dJ}{da} \tag{37}$$

where E is the Young's modulus and σ_{YS} is the yield strength. The steels CP1000 and Q&P show the highest *J*-integral values, both at crack initiation (J_i) and near the onset of stable crack propagation (J_c). They also show similar tearing modulus, which indicates very similar crack propagation behaviour. DP1000 and TBF show lower *J* values and tearing modulus. TBF exhibits higher tearing modulus, which leads to greater *J* values for relatively large crack extensions.

J_i and J_c are similar for both CT and DENT specimens. However, the slope of the resistance curve is higher for DENT specimens, as indicated by the higher T_R.

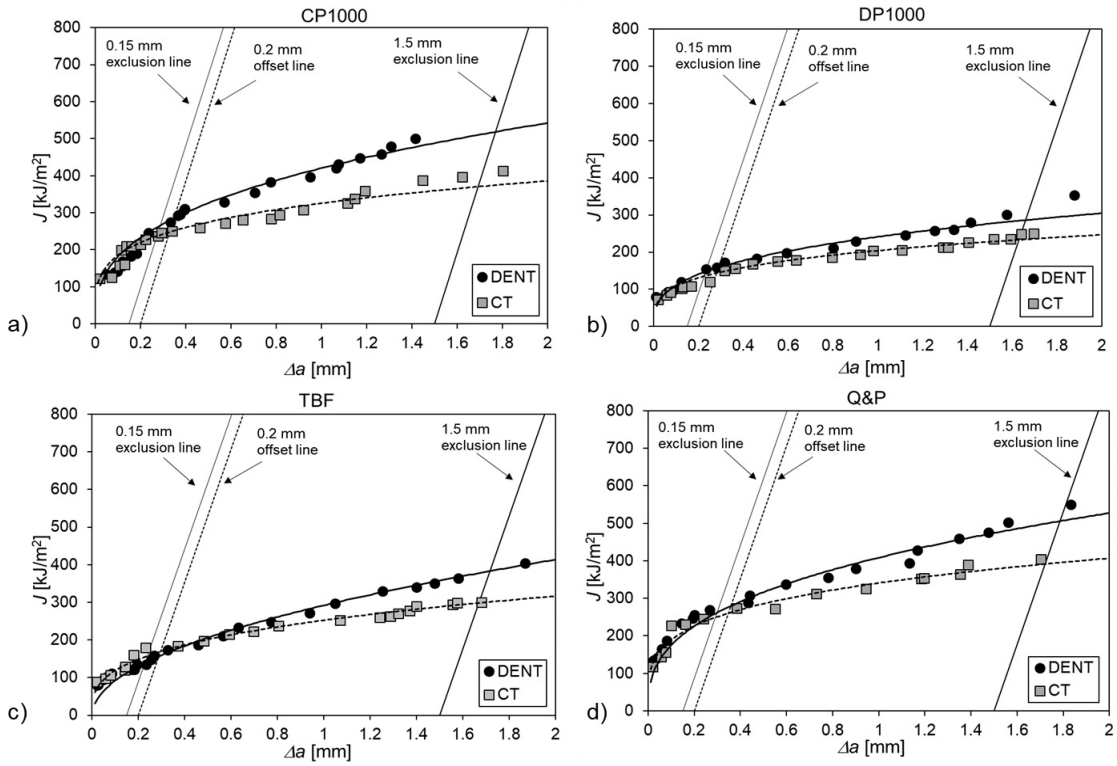

Figure 4.18. J-R curves for the 4 investigated AHSS grades: a) CP, b) DP, c) TBF and d) Q&P. Figure from Paper I.

Table 4.4. Summary of J-integral results

Steel	CT				DENT			
	$J_{i\ CT}$ [kJ/m²]	$J_{c\ CT}$ [kJ/m²]	dJ/da [-]	$T_{R\ CT}$ [-]	$J_{i\ DENT}$ [kJ/m²]	$J_{c\ DENT}$ [kJ/m²]	dJ/da [-]	$T_{R\ DENT}$ [-]
CP1000	125	248	120	30	135	286	186	47
DP1000	84	144	71	25	84	158	109	38
TBF	89	169	87	32	81	157	161	59
Q&P	118	260	112	28	135	280	173	43

4.1.3 Kahn-type tear tests

The load-displacement curves obtained from Kahn-type tear tests (KTT) are shown in Figure 4.19. The results are summarized in Figure 4.20 and Table 4.5. CP1000, Q&P and TBF/Q&P exhibit the highest initiation energy. On the other hand, DP1000 and TBF show the lowest *UIE*. CP1200, PHS1000 and PHS1500 show very similar *UIE* (≈120kJ/m²). Regarding propagation energy, TBF/Q&P has the highest *UPE*, followed by CP1000, TBF and Q&P. CP1200 shows the lowest *UPE*. No clear relationship is observed between *UIE* and *UPE* values. No direct link can be established either with *UIE* or *UPE* and the values of major strain at fracture ($\varepsilon_{f\ KTT}$).

Looking at the tear strength and the tear strength to yield strength ratio (*TYR*), small differences can be observed between the investigated steels. The values of tear strength can be classified according to the strength level of the steel, i.e. PHS1500 shows the highest tear strength followed by the 1200 MPa grades (Q&P and CP1200). Most of the 1000 MPa steels show similar tear strength (≈1700 MPa), except DP1000 and TBF, with the lowest tear strength (≈1550 MPa). No large differences are observed in the *TYR*, which ranges from 1.9 to 2.1 for most of the steels. PHS1000 and CP1200 present the lowest *TYR* (*TYR*= 1.67 and 1.78, respectively).

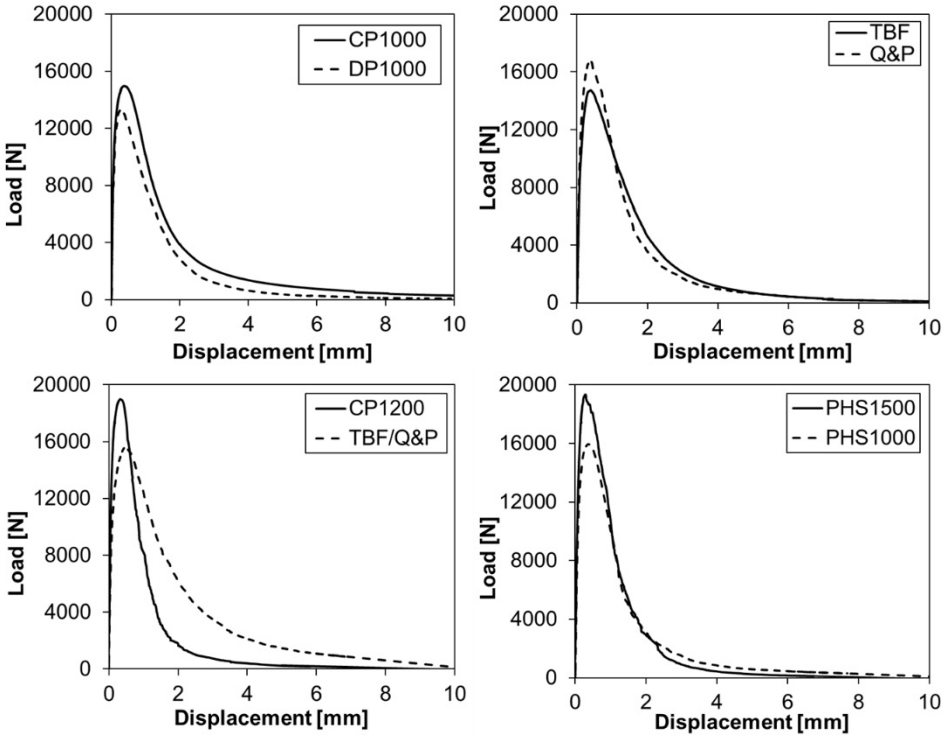

Figure 4.19. Load-displacement curves from KTT. Only one representative curve for each material is shown.

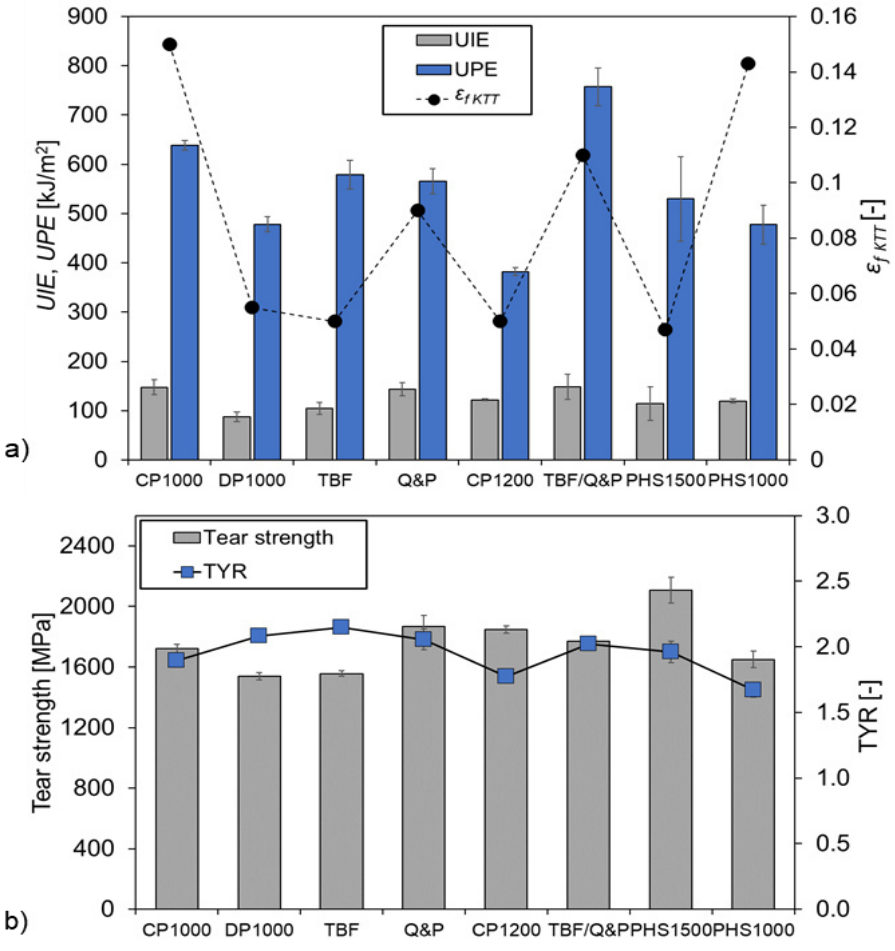

Figure 4.20. Results of KTT. **a)** *UIE*, *UPE* and $\varepsilon_{f\,KTT}$. **b)** Tear strength and *TYR*.

Table 4.5. Summary of fracture resistance parameters obtained from KTTs.

Steel	*UIE* [kJ/m^2]	*UPE* [MJ/m^3]	*Tear strength* [MPa]	*TYR* [-]	$\varepsilon_{f\ KTT}$ [-]
CP1000	147 ± 15	639 ± 10	1720	1.89	0.15
DP1000	87 ± 9	479 ± 15	1538	2.08	0.06
TBF	104 ± 12	579 ± 30	1557	2.15	0.05
Q&P	144 ± 13	566 ± 26	1870	2.06	0.09
CP1200	122 ± 2	382 ± 8	1849	1.78	0.05
TBF/Q&P	148 ± 25	757 ± 38	1770	2.02	0.11
PHS1500	114 ± 34	530 ± 86	2108	1.96	0.05
PHS1000	120 ± 4	477 ± 40	1651	1.67	0.14

4.2 Local ductility parameters from uniaxial tensile tests

Figure 4.21 shows the values of true fracture strain (*TFS*) for the AHSS grades investigated in Paper I and Paper II. The values of true thickness strain (*TTS*) evaluated in Paper II are also shown.

CP1000 shows the highest *TFS* amongst the investigated steels (*TFS*= 1.21), followed by Q&P (*TFS*= 1.05). The rest of the steel grades show similar values of *TFS* ranging from 0.5 to 0.6. In general, for the six steels investigated in Paper II, the *TTS* is almost identical to the *TFS*, except in the case of TRIP 780, where the *TTS* is about half of the *TFS* (*TFS*=0.49 and *TTS*= 0.25). It indicates that in most of the steels the major contribution to the fracture strain comes from localized necking (thickness strain) and width strain is almost negligible. On the other hand, TRIP780 has a similar contribution from both local and diffuse (width strain) necking.

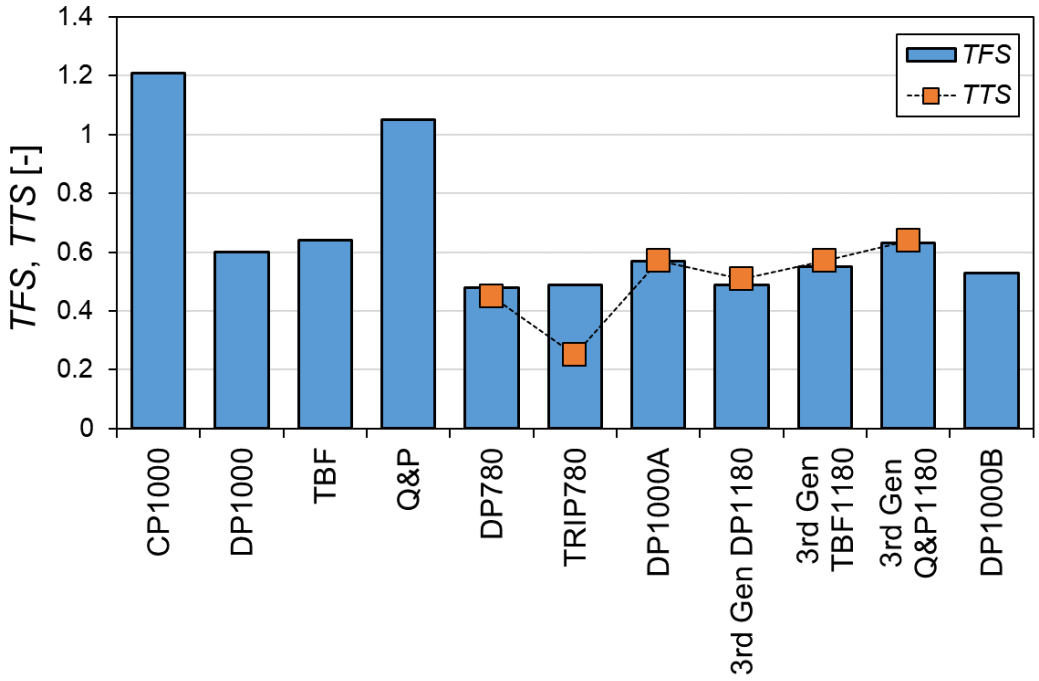

Figure 4.21. True fracture strain (*TFS*) and true thickness strain (*TTS*) measured from the fracture surface of uniaxial tensile specimens.

4.3 Edge cracking resistance

4.3.1 Hole Expansion Tests

4.3.1.1 Hole Expansion Ratio

HER values are shown in Figure 4.22 and Table 4.6. As a rule, and in line with the observations from fracture toughness tests, more homogeneous CP-like microstructures show higher HER than DP-like, TRIP-assisted and fully martensitic microstructures. CP1000 shows the highest HER, followed by TBF/Q&P, Q&P and PHS1000. The lowest HER value is shown by TRIP780. PHS1500, DP1000, TBF, DP780, 3rd Gen DP1180 and 3rd Gen TBF1180 show similar HER (≈30 %). DP1000A and 3rd Gen Q&P1180 present slightly higher HER (≈40 %).

The poorer stretch flangeability of DP-like steels is associated to the hardness differences between soft (ferrite) and hard (bainite/martensite) microstructural constituents, which contribute to the rapid generation of microvoids or decohesion of the soft/hard phase interfaces [19,50].

4.3.1.2 Thickness strain

The values of true thickness strain measured in hole expansion test specimens (TTS_{HET}) for the six steel grades investigated in Paper II are plotted in Figure 4.22. Numerical values are summarized in Table 4.6. TTS_{HET} values follow a similar trend to *TTS* from uniaxial tensile tests shown in Figure 4.21. Most of the steels show similar TTS_{HET} (0.10-0.12), except TRIP780, which presents the lowest thinning (TTS_{HET} =0.08)

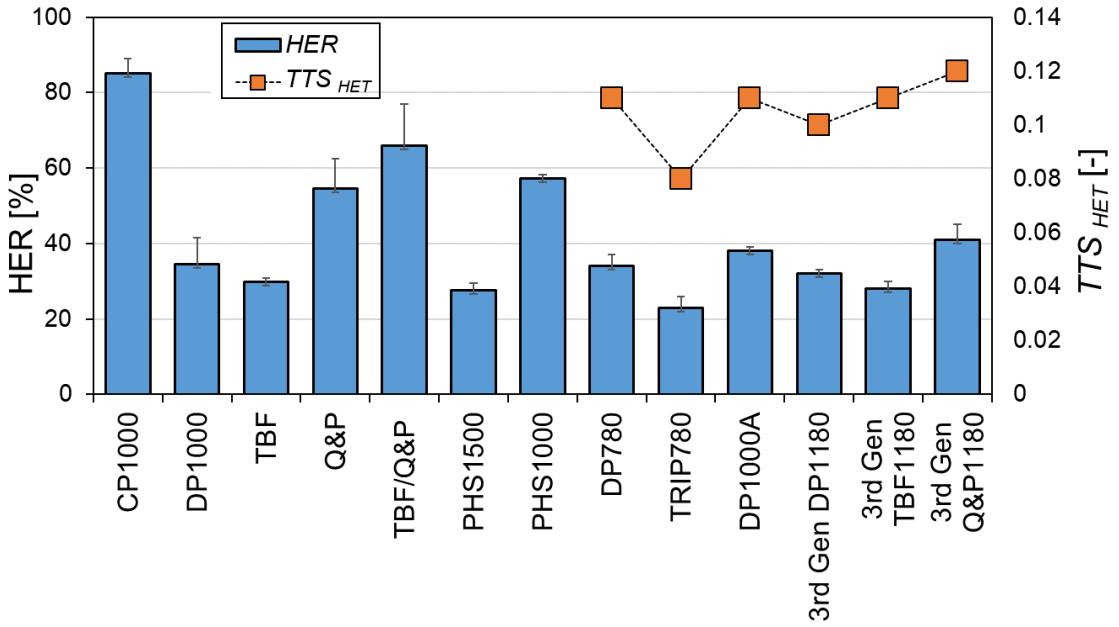

Figure 4.22. HER for the studied AHSS grades. True thickness strain measured from hole expansion test specimens (TTS_{HET}) is also indicated for the steels investigated in Paper II.

4.3.2 Hole Tension tests

The values of major strain at fracture at the hole edge obtained from Hole Tension Tests (HTT) are represented in Figure 4.23. The figure shows the results for the four AHSS grades and the different punching clearances (*c*) investigated in Paper B. The results are also given in Table 4.6.

4.3 Edge cracking resistance

Due to the higher thickness of TBF (t=1.5 mm) compared to the other steels (t=1.4 mm), the resulting clearances were slightly different. The investigated clearances for DP1000, CP1000 and TBF/Q&P were 11%, 14%,18% and 21%. In the case of TBF, the clearances were 10%,13%,17% and 20%.

As expected, the results are in good agreement with hole expansion tests. DP1000 and TBF have significantly lower edge formability (lower $\varepsilon_{f\ HTT}$) than CP1000 and TBF/Q&P. These results also show the great influence of cutting clearance on edge formability, especially in DP1000 and TBF. In all cases, the highest $\varepsilon_{f\ HTT}$ is attained for a punching clearance of 13-14%. For DP1000 and TBF, the fracture strain decreases by up to 38% and 28% respectively for clearances above 14%. On the other hand, CP1000 and TBF/Q&P are less sensitive to punch-to-die clearance. This suggests that materials with higher damage tolerance (fracture toughness) are less sensitive to edge damage, while in the case of low toughness materials (DP-like), edge fracture is strongly affected by the edge quality.

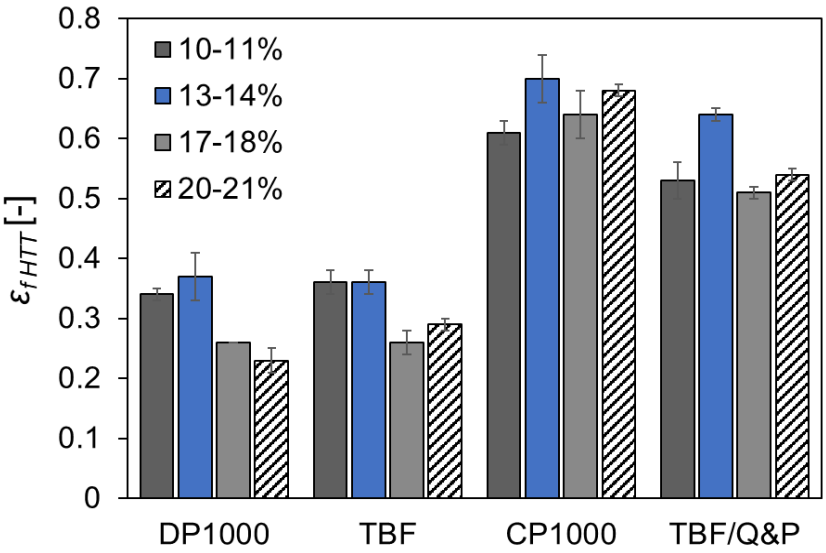

Figure 4.23. Major strain at fracture at the hole edge ($\varepsilon_{f\ HTT}$) for the four investigated steel grades. Results for different punch-to-die clearances.

Table 4.6. Summary of results from edge cracking resistance tests

	Hole Expansion tests		Hole Tension tests, $\varepsilon_{f\ HTT}$			
Steel	*HER* [%]	TTS_{HET} [-]	*c*=10-11%	*c*=13-14%	*c*=17-18%	*c*=20-21%
CP1000	85 ± 4	-	0.61 ± 0.02	0.70 ± 0.04	0.64 ± 0.04	0.68 ± 0.01
DP1000	35 ± 4	-	0.34 ± 0.01	0.37 ± 0.04	0.26 ± 0.00	0.23 ± 0.02
TBF	30 ± 1	-	0.36 ± 0.02	0.36 ± 0.02	0.26 ± 0.02	0.29 ± 0.01
Q&P	55 ± 8	-	-	-	-	-
TBF/Q&P	66 ± 11	-	0.53 ± 0.03	0.64 ± 0.01	0.51 ± 0.01	0.54 ± 0.01
PHS1500	28 ± 2	-	-	-	-	-
PHS1000	57 ± 1	-	-	-	-	-
DP780	34 ± 3	0.11 ± 0.03	-	-	-	-
TRIP780	23 ± 3	0.08 ± 0.00	-	-	-	-
DP1000A	38 ± 1	0.11 ± 0.02	-	-	-	-
3rd Gen DP1180	32 ± 1	0.10 ± 0.02	-	-	-	-
3rd Gen TBF1180	28 ± 2	0.11 ± 0.02	-	-	-	-
3rd Gen Q&P1180	41 ± 4	0.12 ± 0.01	-	-	-	-

4.4 Crash fracture behaviour

4.4.1 Axial impact resistance

Figure 4.24 shows some examples of tested crash boxes and the location of the crack observed during axial impact resistance tests. The results of axial impact resistance tests are described in detail in Paper III.

The evolution of the Crash Index (*CI*) as a function of the intrusion level is illustrated in Figure 4.25. The slope defined by the decrease of *CI* as a function of the intrusion level (dashed lines in Figure 4.25) is defined as the Crash Index Decreasing Rate (CIDR). The CIDR quantifies the growth rate of cracks through the sample under axial impact loading, independently of the crack origin. Thus, the *CIDR* is related to the evolution of damage and can be used to quantify the crash resistance of the material; the lower the *CIDR*, the better the crash resistance. The values of *CIDR* obtained for the nine investigated steel grades are shown in Table 4.7 together with the critical intrusion and the energy absorbed at the maximum intrusion. The critical intrusion refers to the transition from uncracked to cracked samples, i.e. the first CI<100.

The best crash resistance (lower CIDR) is shown by CP1000, PHS1000, TWIP and TBF/Q&P steels. On the other hand, DP1000, TBF and PHS1500 exhibit the worst crash resistance, as indicated by their high *CIDR* (2.2-2.5) and their low *CI* for high intrusion levels. CP1200 and Q&P show slightly better crash performance (*CIDR* ≈1.3-1.8).

The energy absorbed at maximum intrusion represents the crash energy absorption capacity of the material. This energy directly depends on the maximum intrusion allowable by the material and, therefore, it is closely related to the *CIDR*. The maximum intrusion was defined for a *CI* of 20% (specimen severely damaged). The trend observed for energy at maximum intrusion is similar to the one observed for *CIDR* values.

The definition of a single critical intrusion level was difficult in most cases since fracture initiation in axial crash tests can be highly influenced by damage induced at the welding spots. The range of critical intrusions for the different steels is indicated in Table 4.7. Most of the steels show similar ranges of critical intrusion ranging from 20 to 40 mm. The lowest ranges of critical intrusion are shown by Q&P, CP1200 and PHS1500.

Table 4.7. Results from axial impact resistance tests

Steel	Critical intrusion [mm]	*CIDR* [-%/mm]	Energy at maximum intrusion [kJ]
CP1000	27-32	0.29	13.7
DP1000	18-27	2.18	3.6
TBF	25-33	2.54	4.9
Q&P	6-15	1.81	5.3
CP1200	9-18	1.28	6.1
TBF/Q&P	30-45	0.71	9.4
PHS1500	12-13	2.45	3.0
PHS1000	16-20	0.36	9.5
TWIP	99-100	0.11	10.7

4.4 Crash fracture behaviour

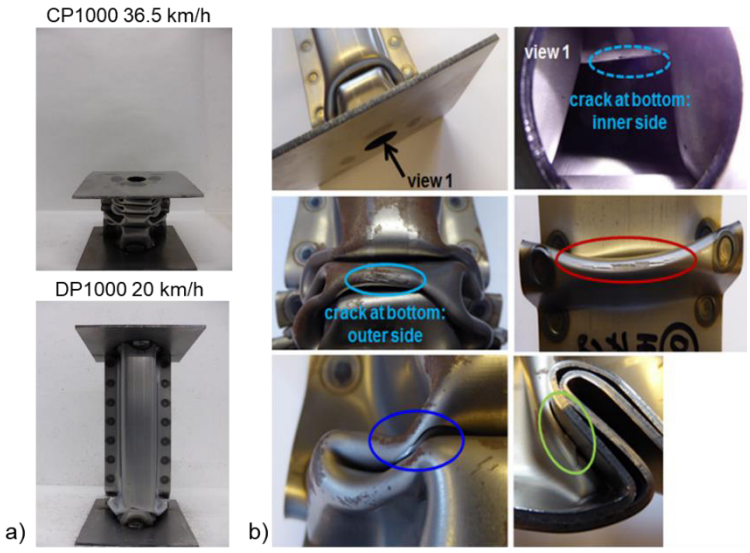

Figure 4.24. a) Crash boxes of CP1000 (top) and DP1000 (bottom) after axial impact resistance tests at different speeds. **b)** Examples and location of cracks observed in axial crash tests.

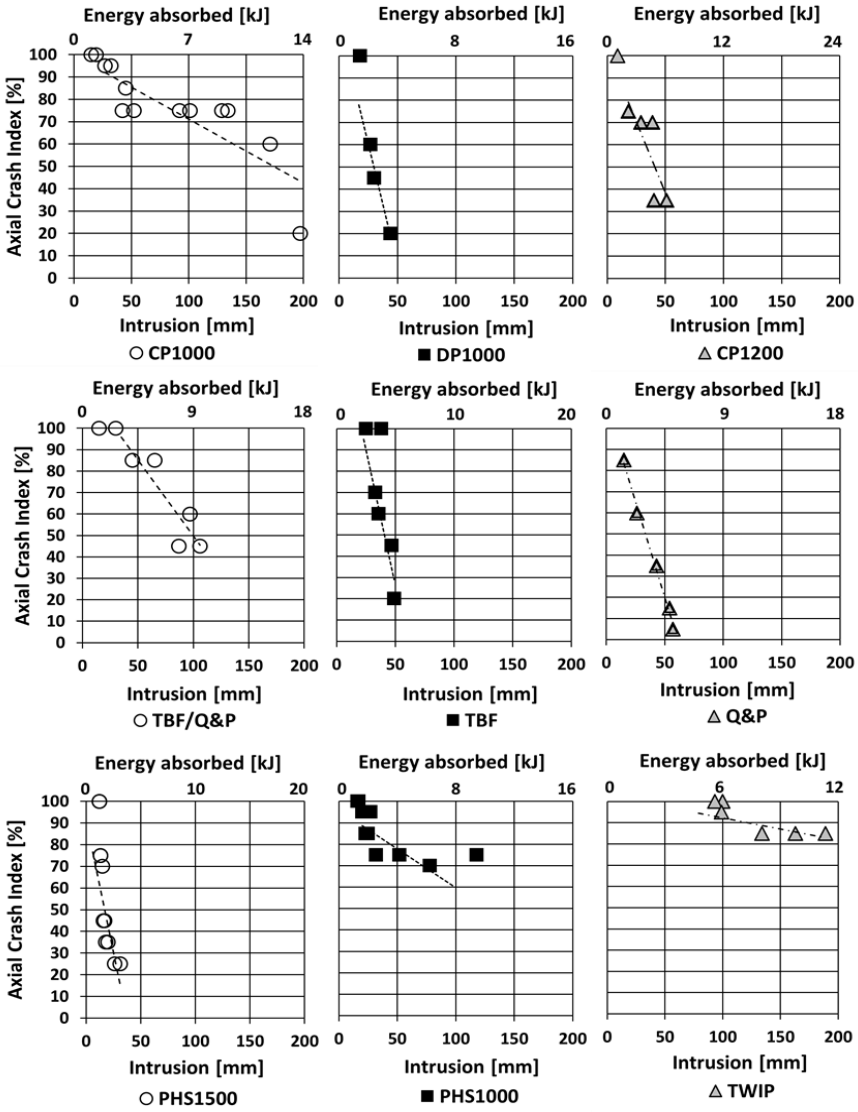

Figure 4.25. Variation of Crash Index (*CI*) as a function of the intrusion in axial impact tests for the studied steels. Energy absorbed is also indicated in the upper x-axis. Figure from Paper III.

4.4.2 Bending impact resistance

The evolution of the *CI* as a function of the intrusion level in bending impact tests is investigated in Figure 4.26. The values of *CIDR* and critical intrusion are shown in Table 4.8. The energy absorbed at maximum intrusion was not considered in bending impact tests. Maximum intrusion level was limited by the test equipment configuration (211 mm) and not by the material behaviour. Therefore, the energy at maximum intrusion was the same for all the steel grades.

Due to the limited maximum intrusion, it was not possible to reach the failure of the sample in all investigated steel grades. In the event that no damage was observed, which was the case for CP1000, TBF/Q&P, PHS1000 and TWIP, at least 3 samples were crashed to the maximum possible intrusion. For these steels, it was not possible to determine a *CIDR*, because of the absence of cracking.

For the rest of steels, the point of the first decrease in *CI* was used to determine the *CIDR*. PHS1500 and TBF present the highest *CIDR*, which indicates a rapid increase in the degree of cracking with the intrusion level. DP1000 and Q&P show slightly better cracking performance (*CIDR*= 0.26-0.28).

PHS1500 shows the lowest intrusion level for crack initiation. On the other hand, DP1000 and TBF exhibit the highest critical intrusion, followed by Q&P with slightly lower values.

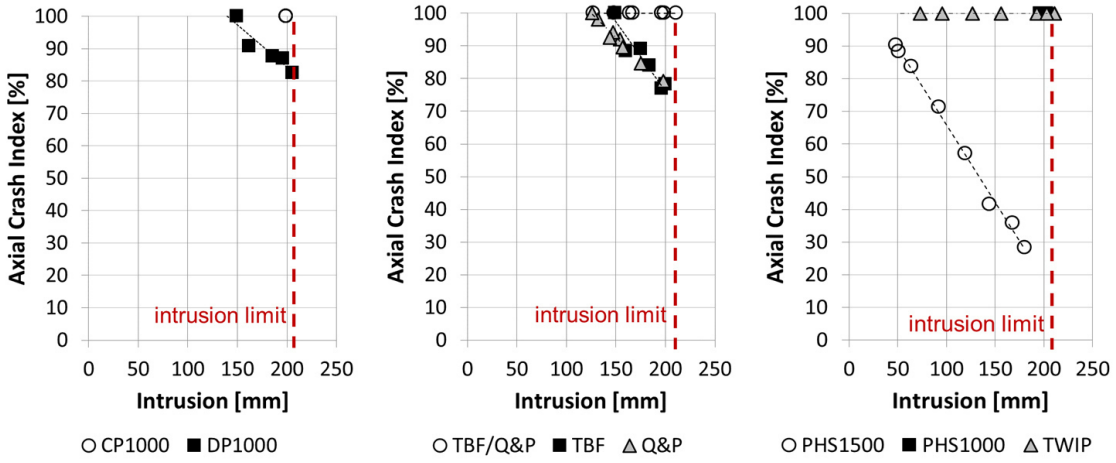

Figure 4.26. Variation of Crash Index (CI) as a function of the intrusion in bending impact tests.

Table 4.8. Results from bending impact resistance tests

Steel	Critical intrusion [mm]	*CIDR* [-%/mm]
CP1000	-	-
DP1000	150-160	0.26
TBF	150-160	0.40
Q&P	125-130	0.28
TBF/Q&P	-	-
PHS1500	45-50	0.49
PHS1000	-	-
TWIP	-	-

Chapter 5

Discussion

5.1 Fracture toughness characterization of AHSS sheets

5.1.1 Essential Work of Fracture

The Essential Work of Fracture (EWF) methodology has been established as one of the most interesting methods to characterize the fracture resistance of thin ductile sheets. The main advantage of this technique is its relative experimental simplicity compared to other conventional fracture mechanics procedures, since it does not require crack growth monitoring and data post-processing is rather simple. The EWF method was originally developed by Cotterell and Redell for ductile metals [133] and was rapidly extended for the characterization of ductile polymers [135-137]. Over the years, the methodology has been widely used for evaluating the fracture resistance of polymer films [150-153] and metallic materials: low carbon steels [133, 154,155], aluminium alloys [119, 139, 140, 156], zinc [140, 143], copper [157] and brass [158]. More recently, the method has gained increasing interest to characterize the fracture resistance of high strength steel sheets. Lacroix et al. [84] used the EWF to evaluate the fracture toughness of different TRIP-assisted steels and to investigate the influence of the TRIP effect in their crack propagation resistance. Later, Muñoz et al. [159] and Gutiérrez et al. [160] studied the applicability of the method in various AHSS steel sheets. Since these works, a number of researchers have used the EWF metholodogy to characterize the fracture properties of several AHSS (DP [20, 86, 91, 161], TWIP [85, 87], Q&P [20, 85]) and PHS [20, 26] sheets.

In spite of the great potential of the EWF method to readily measure the fracture resistance of thin ductile sheets under plane stress conditions, there is not a standard procedure developed yet. One of the main challenges in EWF standardisation is the sensitivity of the method to different testing variables: notch quality (sharpness, alignment), number of specimens, ligament length range, etc. [142]. Different attempts have been made to standardise the EWF methodology [138, 162-164]. The last version of the ESIS protocol for EWF testing was revised in 2001 [138]. This protocol, developed by the ESIS TC4 committee (TC04- Polymers, Polymer composites and adhesives), is based on a series of round robin tests during a seven-year period, with the participation of 23 laboratories, and it is currently the most extended for the evaluation of the EWF. The protocol provides the guidelines for the evaluation of the EWF by using DENT specimens and discuss some of the most critical points related to specimen preparation, testing and data analysis.

In this thesis work, the EWF method was applied to a wide range of advanced high strength sheet steels (t =1.2-1.6 mm), following the recommendations of the ESIS protocol [138]. However, this protocol is focused on the fracture testing of polymers and composites. Therefore, no recommendations are given about the notch preparation in metallic materials. In order to obtain the sharpest possible notch and avoid the influence of notch root radius on fracture toughness measurements, fracture mechanics standard procedures for metals recommend the nucleation of fatigue pre-cracks at the notch root [104, 111]. Accordingly, in the present work, all the DENT specimens used for EWF tests were fatigue pre-cracked according to the recommendations of ASTM E1820 [111], as explained in *Section 3.2*.

All the investigated steels showed to satisfy the requirements for the validity of the EWF methodology. One of the basic requisites for the applicability of the energy partitioning concept is that the ligament is fully yielded before fracture initiation. This was validated in all the steel

grades by means of DIC analysis (Figure 4.4 to Figure 4.6). Such analysis also showed that the shape of the plastic zone is almost circular with a diameter of approximately the ligament length, as previously shown by other authors [133, 161]. Some of the main validation criteria described in the ESIS protocol are briefly discussed below. For the sake of brevity, only one steel per strength class (800 MPa, 1000MPa, 1200 MPa and 1500 MPa) is shown.

Similarity of load-displacement curves and linearity of w_f vs l_0 data

The self-similarity between the load-displacement curves for a set of specimens with different ligament lengths is other of the criteria used for data validation [138, 142, 153]. The AHSS grades investigated in this work accomplished this requirement, as illustrated in Figure 5.1. It can be seen that the shape of the load-displacement curves is similar for the different ligament lengths and maximum load (P_{max}) and displacement at fracture (d_f) scale with the ligament length (Figure 4.8 to Figure 4.10).

As explained before, the specific essential work of fracture (w_e) is obtained by linear regression of w_f vs l_0 data. Therefore, w_f should linearly increase with increasing the ligament length, as evidenced in Figure 4.1 to Figure 4.3. That behaviour may also be an indicator of the EWF applicability. It was found that in materials not accomplishing the ligament yielding criterion (materials not investigated in this work), the w_f remained almost constant independently of the ligament length and, thus, the determination of w_e from extrapolation to zero ligament length was not possible.

The linearity of the w_f vs l_0 data can be used as a data qualification criterion. Marchal et al. [140] proposed a statistical procedure to detect the loss of linearity and improve the accuracy of w_e. The loss of linearity may indicate a change in the fracture mechanisms or the stress state. It is especially critical in the small ligament region, where the transition from plane stress to a mixed plane strain/plane stress mode is more likely to occur [139] (Figure 1.42). For the steels investigated in this work, in general, a good linearity was observed, as indicate the high regression coefficients (R^2>0.90). Only some exceptions with rather low linearity were observed, such as the case of PHS1000 (R^2=0.42) or CP1200 (R^2=0.53).

Ligament length range

The definition of a valid ligament range is a key point to obtain an accurate plane stress fracture toughness value. As mentioned before, the ligament should be small enough to ensure that the ligament is fully yielded before fracture but sufficiently large to ensure a global plane stress state. If the ligament is too small, the fracture may take place under a mixed plane strain/plane stress mode and w_f does not linearly scale with l_0 anymore (Figure 1.42). This transition region is often given by $3t$ [141], where t is the sheet thickness. However, this lower boundary is material dependent. For instance, Wu and Mai [135] found that this transition occurred for l_0=$14t$ in a linear low-density polyethylene (LLDPE) film. On the other hand, Cotterell and Reddel [133], suggested that the lower ligament length should be of the order of $5t$. They also show that the transition zone from plane strain to plane stress, and thus the minimum ligament length, could be determined by observation of the fracture surface after the test. The ESIS protocol also includes an arbitrary value of 5 mm, being the criterion for lower boundary the maximum of 3t or 5 mm. This criterion has been the most extensively used and it has shown to be adequate for most of the materials investigated in the literature.

Regarding the upper boundary, the conditions of $W/3$ and $2r_p$ are given, respectively, to avoid the spreading of the plastic zone to the edges of the specimen and to ensure that the ligament is fully

yielded. However, the ESIS TC4 protocol points out that some research works have shown that the data is often linear beyond this limit. An arbitrary upper limit of l_0=15 mm is proposed for practical purposes.

Table 5.1 shows the ligament limits for the steels investigated in this work, according to the recommendations of the EWF testing protocol. r_p was evaluated according to Equation (32), a Young's modulus of 210 GPa was used for calculation. Overall, the ligament length ranges used are within the limits established in the protocol, except for the 1200 MPa (3rd Gen DP1180, 3rd Gen TBF1180, 3rd Gen Q&P 1180, CP1200) and 1500 MPa steels. For these materials, the criterion of $2r_p$ for the upper limit seems to be too restrictive, which is in line with the mentioned in the protocol, and an upper limit of l_0=15 mm is more appropriate.

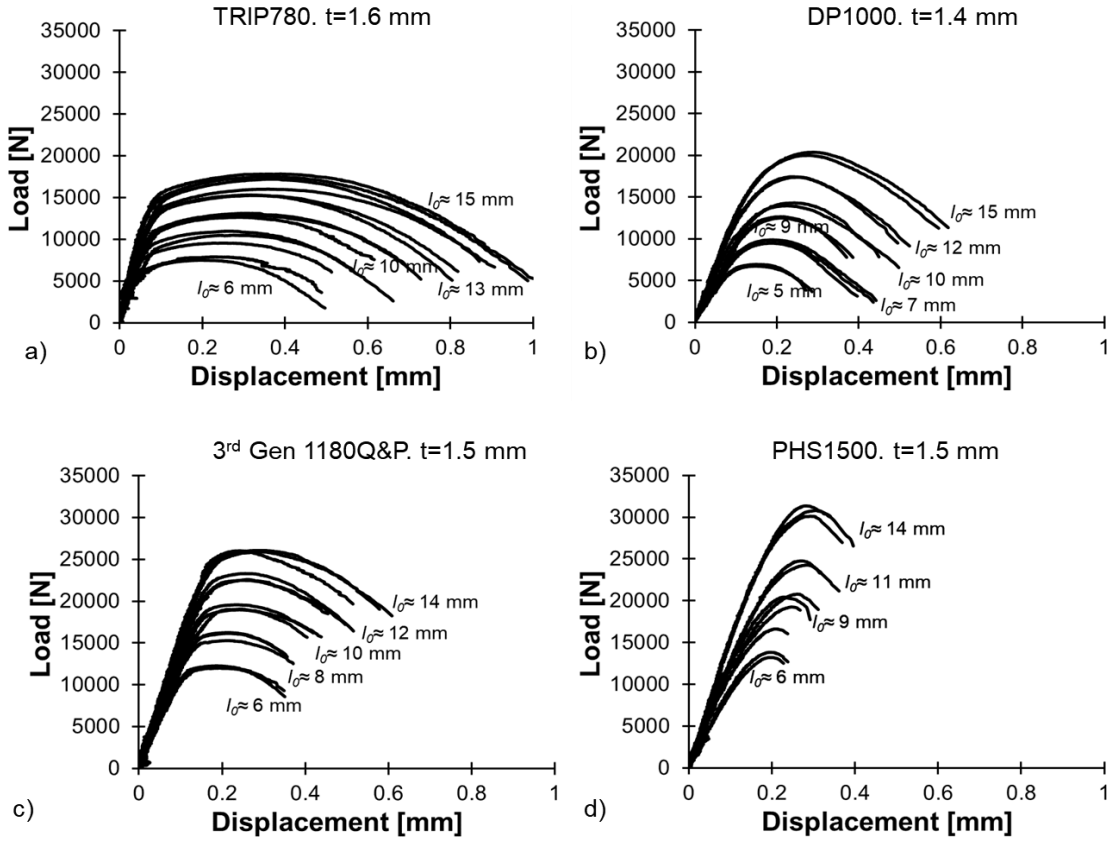

Figure 5.1. Typical load-displacement curves obtained from EWF tests. **a)**TRIP780, **b)** DP1000, **c)** 3rd Gen 1180Q&P, **d)** PHS1500.

Table 5.1. Definition of upper and lower ligament length boundaries according to the ESIS protocol recommendations. $l_{0\ min}$ max(3t, 5mm). $l_{0\ max}$ min(W/3, 2r_p).W is the specimen width, W= 55 mm. Values in parenthesis correspond to the ligament lengths used in the present work.

Steel	t [mm]	σ_{YS} [MPa]	$3t$ [mm]	$2\ r_p$ [mm]	$l_{0\ min}$ [mm]	$l_{0\ max}$ [mm]
CP1000	1.4	915	4.2	32	5 (5)	18 (15)
DP1000	1.4	775	4.2	15	5 (5)	15 (15)
TBF	1.5	755	4.5	17	5 (5)	17 (14)
Q&P	1.4	920	4.2	15	5 (4)	15 (14)
DP780	1.5	513	4.5	38	5 (6)	18 (15)
TRIP780	1.6	542	4.8	24	5 (6)	18 (15)
DP1000A	1.35	816	4.1	15	5 (6)	15 (15)
3rd Gen DP1180	1.2	895	3.6	10	5 (6)	10 (14)
3rd Gen TBF1180	1.4	987	4.2	7	5 (6)	7 (14)
3rd Gen Q&P1180	1.5	1034	4.5	12	5 (6)	12 (14)
CP1200	1.6	1041	4.8	12	5 (4)	12 (15)
TBF/Q&P	1.4	1026	4.2	19	5 (4)	18 (14)
PHS1500	1.5	1075	4.5	9	5 (5)	9 (15)
PHS1000	1.5	988	4.5	23	5 (5)	18 (13)
TWIP	1.4	530	4.2	87	5 (7)	18 (15)
DP1000 B	1.4	773	4.2	32	5 (6)	18 (15)

Stress analysis

Two different stress analyses for EWF data are proposed in the ESIS protocol. The firt is the Hill's criterion. Hill [168] suggested that the maximum stress in a DENT specimen in plane stress is given by:

$$\sigma_{max} = 1.15\sigma_{YS} \tag{38}$$

where σ_{max} is the peak load divided by the initial cross-section area (P/l_0*t) and σ_{YS} is the yield stress of the material obtained from tensile tests.

It has been observed that, generally, the maximum stress is of the same order as given in Equation (38) [138]. However, as shown in Figure 5.2, it is not the case of the steels investigated in this work. For the investigated steel grades, the maximum stress exceeds the stress predicted by Hill's criterion. A similar behaviour has been previously observed by Wu and Mai in a LLDPE film [135]. A better prediction of the maximum stress level is given by 1.15 σ_Y (red dashed line in Figure 5.2), where σ_Y is the effective yield strength, defined in the ASTM E1820 [111] as "an assumed value of uniaxial yield strength that represents the influence of plastic yielding upon fracture test parameters" and calculated according to Equation (24). It is observed that σ_{max} values lie near the red line representing 1.15 σ_Y. The values of σ_{max} tend to decrease with increasing the ligament length and are higher for the shorter ligaments, with is in good agreement with the observations made by different authors [135, 138, 161].

Due to the difficulty in establishing the transition from plane stress to mixed stress mode using Equation (38), Clutton [138] proposed an alternative stress criterion, based on the mean value of σ_{max}, which is denoted σ_{mean} in this work. The criterion is to remove all the data above 1.1σ_{mean} or below 0.9σ_{mean}. This criterion showed to be useful to define the transition from plane stress to mixed stress state and to reject outlying data due to possible experimental errors. This stress criterion was verified in all the AHSS grades investigated (Figure 5.3). In case any data point outlied the limits, the point was removed and w_e was recalculated.

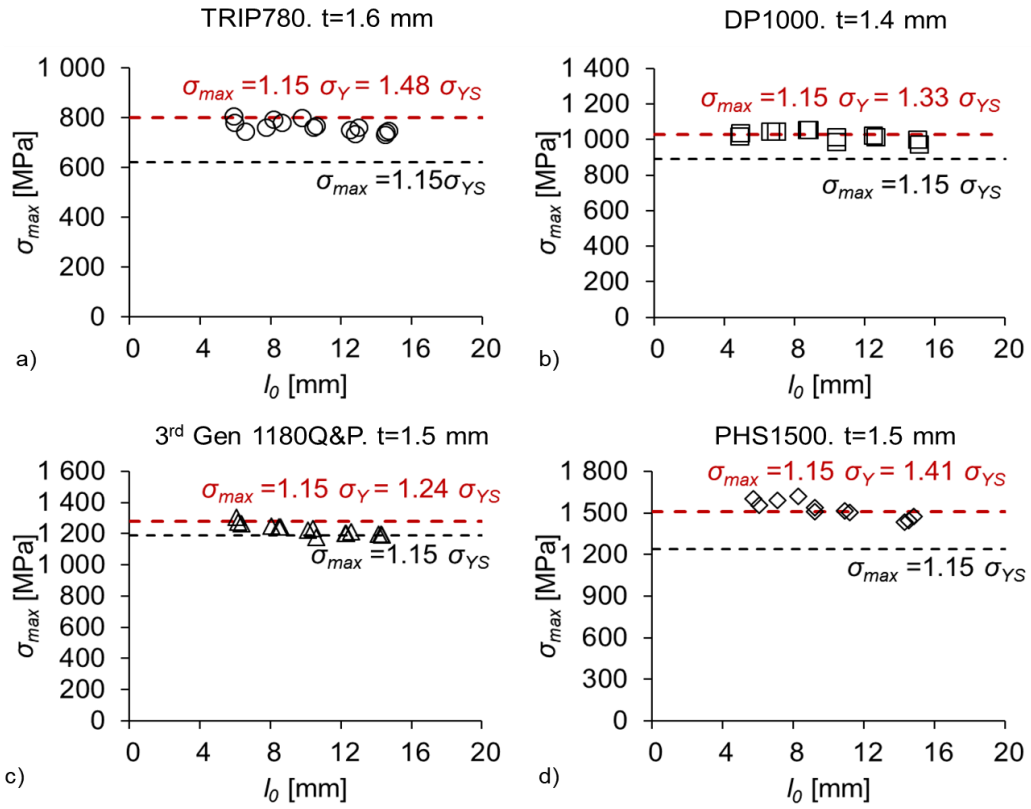

Figure 5.2. σ_{max} as a function of the ligament length for: **a)** TRIP780, **b)** DP1000, **c)** 3rd Gen 1180Q&P, **d)** PHS1500. The black dashed line represents the Hill's criterion, 1.15 σ_{YS}. The red dashed line represents 1.15σ_Y

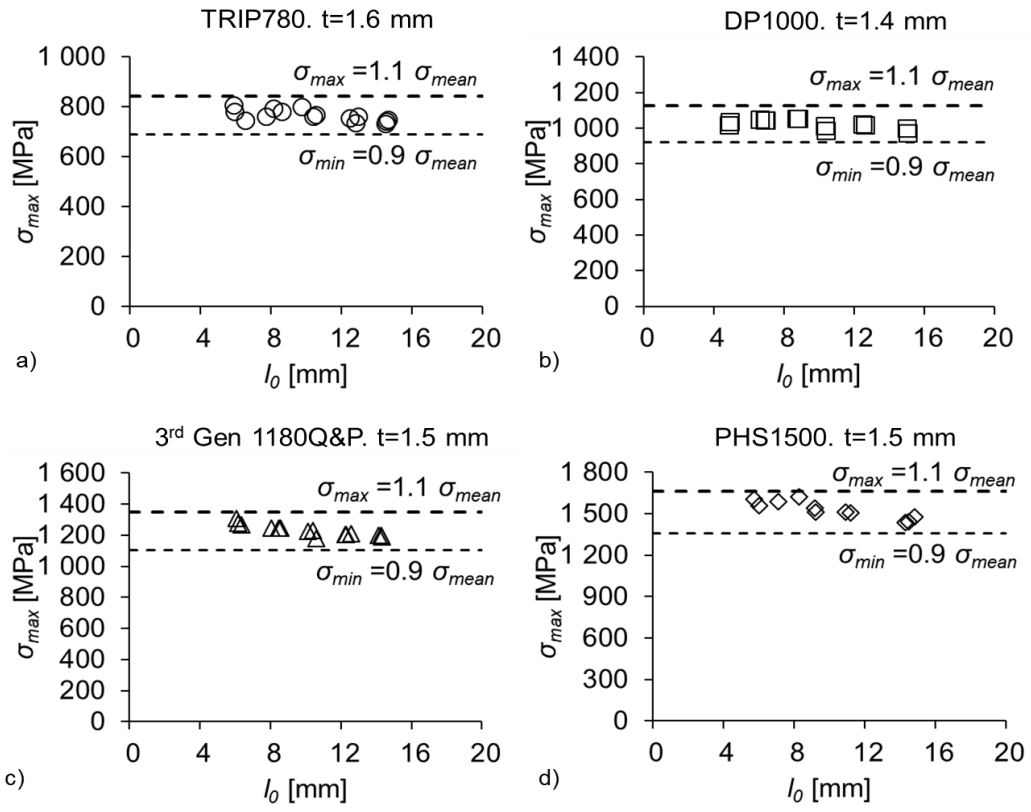

Figure 5.3. Stress criterion based on an average value of σ_{max} (σ_{mean}). The data below 0.9σ_{mean} and above 1.1σ_{mean} are excluded for EWF calculation.

5.1.1.1 Crack initiation and propagation resistance, w_e^i and w_e.

The specific essential work of fracture, w_e, is obtained from an average of w_f values for the complete fracture resistance and, therefore, it contains energetic contributions from both crack initiation and propagation resistance. Mai and Cotterell [136] showed that the EWF methodology also permits to separate from both contributions and determine a fracture toughness value for crack initiation. As shown in Figure 1.41, for each ligament length the work of fracture at crack initiation (w_f^i) can be obtained by integrating the area under the load-displacement curve up to the point of crack growth initiation. Since w_f^i is independent of the ligament length [136], an specific essential work for fracture initiation, w_e^i can be calculated from an average of w_f^i values. Usually, w_e^i is lower than w_e, however, the differences between w_e and w_e^i can significantly vary from one material to another. This is illustrated in Figure 5.4. Most of the investigated AHSS grades, DP780, TRIP780, DP1000, DP1000A, Q&P, 3rd Gen DP1180, 3rd Gen 1180TBF, 3rd Gen 1180Q&P and PHS1500, show very small differences between w_e^i and w_e. It means that, in these steels, the contribution from crack propagation resistance after initiation is small and, thus, $w_e^i \approx w_e$. On the other hand, some steel grades, such as CP1000, DP1000B, TBF/Q&P, PHS1000, TWIP and CP1200, present an important contribution from crack propagation resistance and w_e significantly differs from w_e^i ($w_e >> w_e^i$). For these materials, a single initiation toughness is not suitable enough to describe the overall crack propagation resistance.

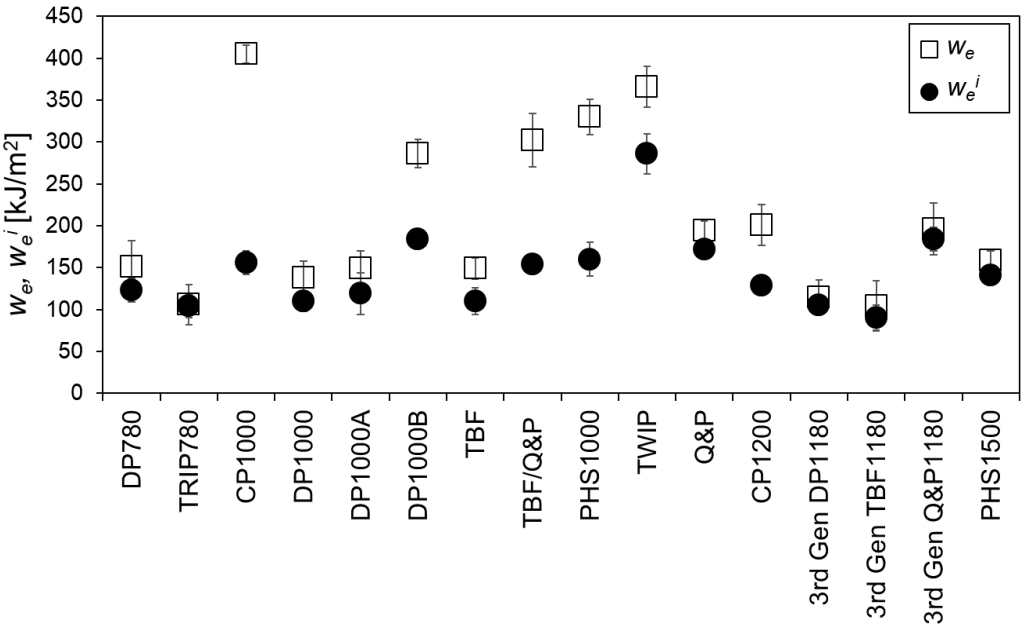

Figure 5.4. w_e and w_e^i for the AHSS investigated in this work.

5.1.1.2 Necking contribution to w_e

As mentioned before, plane stress ductile fracture has an important energetic contribution from necking [84, 133, 119, 166]. Pardoen et a. [166] expressed the specific essential work of fracture as the sum of two contributions:

$$w_e = \Gamma_0 + \Gamma_n \tag{39}$$

where Γ_0 is the energy spent on the creation of new surfaces at the front of the crack tip (intrinsic fracture resistance) and Γ_n is the work of necking, which depends on sheet thickness. This explains the thickness dependence of w_e (and of plane stress fracture toughness in general).

The necking contribution to the essential work of fracture was investigated in Paper I, Paper II and Paper IV. The results showed that, in general, steels presenting lower true thickness strain (TTS_{DENT}), also exhibit lower fracture toughness. Clear evidence of this is found in Paper I, where the fracture behaviour of CP1000 is compared to that of DP1000, TBF and Q&P (Figure 5.5). It can be observed that steels with lower toughness at crack initiation (DP and TBF) show a lower degree of necking at the crack tip. Furthermore, the evolution of TTS_{DENT} with crack growth explains the relative differences between w_e and w_e^i. It is clearly seen that CP1000, which shows the highest difference between w_e and w_e^i, present a greater increase of TTS_{DENT} as a function of the distance from the crack tip. On the other hand, steels with low increase of TTS_{DENT} after crack initiation, show small variation between w_e and w_e^i. These observations confirm that one of the main contributions to the crack propagation resistance of high strength steel sheets comes from necking. This is also illustrated in Figure 5.6 for the rest of steel grades investigated in Papers II and IV. The figure compares the values of fracture toughness at crack initiation (w_e^i) and specific essential work of fracture (w_e) with the true thickness strain for crack initiation ($TTS_{DENT}{}^i$) and propagation ($TTS_{DENT}{}^p$). Overall, a very good agreement is observed between w_e^i and $TTS_{DENT}{}^i$ on the one hand and between w_e and $TTS_{DENT}{}^p$ on the other, especially for 1000 MPa and 1200 MPa steel grades. For the 780 MPa steels, the values $TTS_{DENT}{}^p$ are higher if compared to other steels of similar toughness and superior strength (see for example the TBF of 1000 MPa or the 3rd Gen steels of 1200 MPa). Taking a closer look at these values it can be observed that differences in w_e for DP780 and TRIP780 are also reflected in $TTS_{DENT}{}^p$.

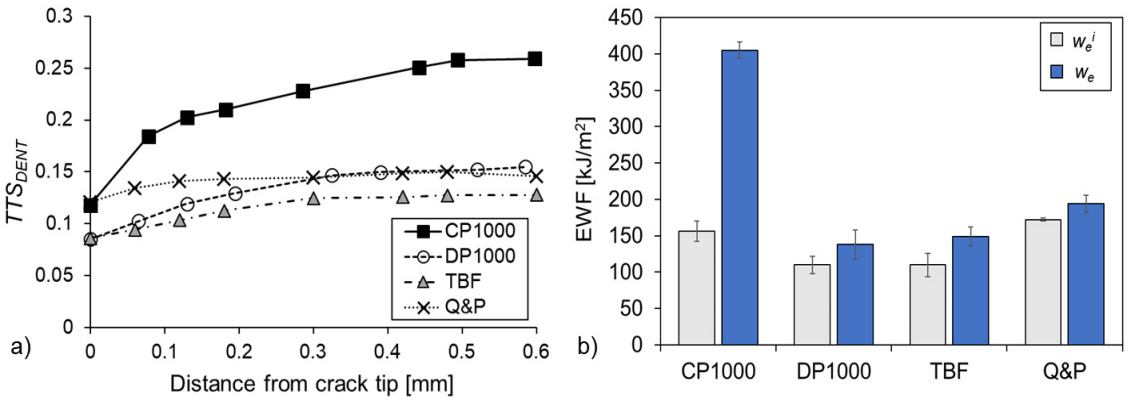

Figure 5.5. a) True thickness strain (TTS_{DENT}) as a function of the distance from the crack tip (image from Paper I). b**)** *w_e and w_e^i.*

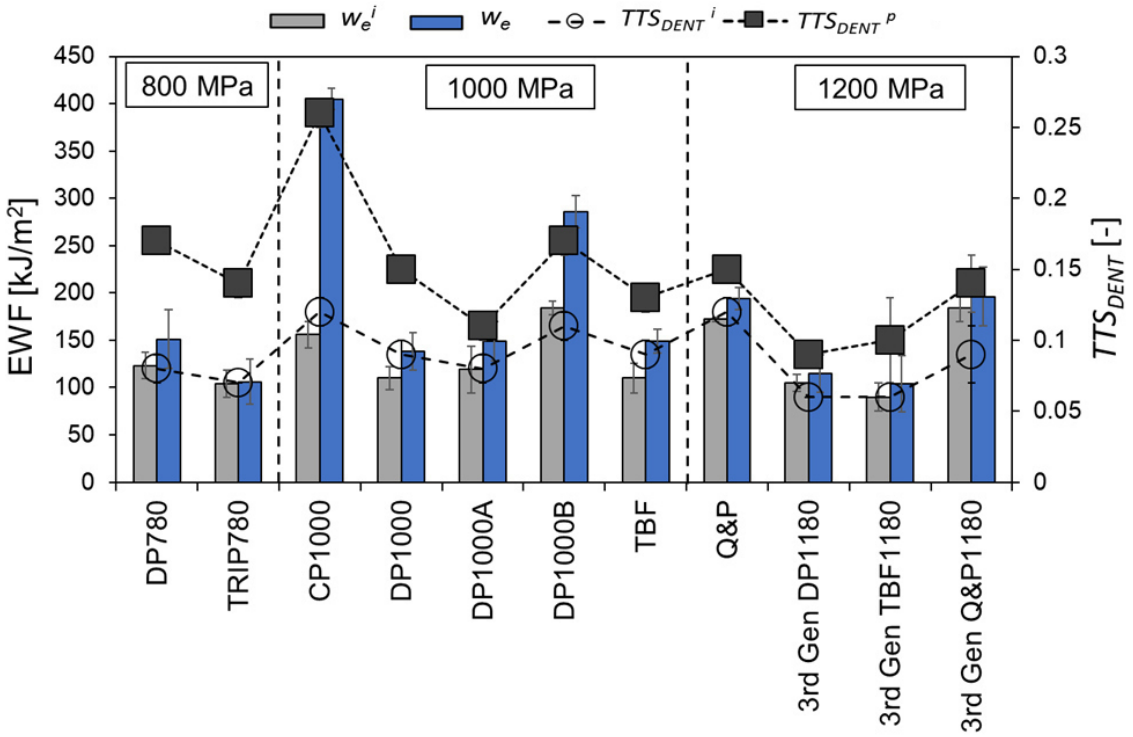

Figure 5.6. Comparison of essential work of fracture (w_e) and fracture toughness at crack initiation (w_e^i) with true thickness strain measured in DENT specimens (TTS_{DENT})

5.1.1.3 Relationship between w_e and δ_c

Similarly to the relationship between J and the crack tip opening displacement proposed by Shih [110] (see Equation 20), the relationship between the specific essential work of fracture and the critical crack opening displacement (δ) can be expressed as follows:

$$\delta = m\frac{w_e}{\sigma_{YS}} \tag{40}$$

where w_e is the specific essential work of fracture, σ_{YS} is the yield stress and m is a material constant dependent on mechanical properties. This relation is investigated in Figure 5.7. The figure plots results obtained in this work together with results from reference [26]. Figure 5.7a shows a linear dependence between w_e/σ_{YS} and δ_c with slope m=0.81 and a quite good correlation coefficient (R^2=0.87). This linear relationship is improved (R^2=0.94) when substituting σ_{YS} by the effective yield strength σ_Y as defined in ASTME1820 [111]. Therefore, rewriting Equation (40), an empirical relationship between δ_c, w_e and flow properties is established according to:

$$\delta_c = m\frac{w_e}{\sigma_Y} \tag{41}$$

where σ_Y is the effective yield strength and m is the material constant which, in this case, is close to 1 (m≈1.05).

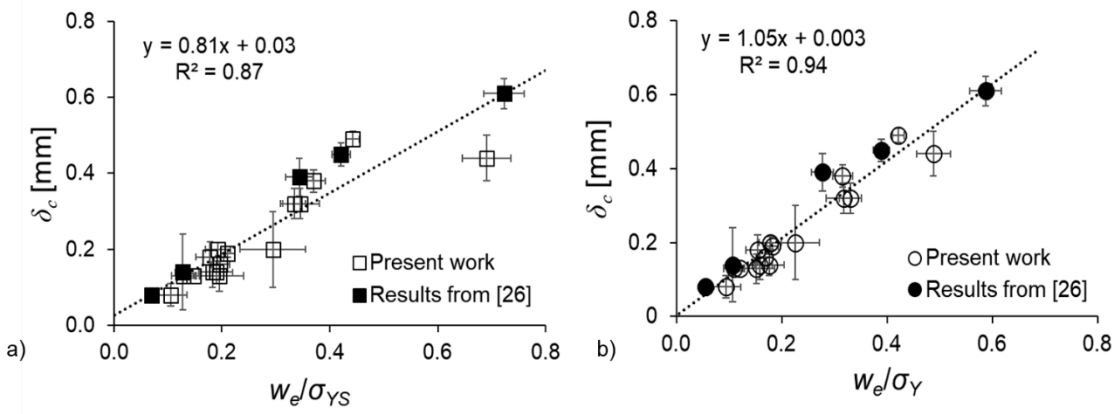

Figure 5.7. Relationship of δ_c with w_e and flow properties.

5.1.1.4 Influence of notch preparation method on EWF

It is well established that fracture toughness is affected by the notch root radius, ρ [88, 129,160, 167, 168]. The apparent increase of fracture toughness with increasing ρ is ascribed to a change in stress triaxiality, i.e. stress triaxiality increases with decreasing the notch radius. Usually, fracture toughness presents a linear dependence with the notch root radius until a minimum critical notch radius ρ_c is reached. Below ρ_c, fracture toughness is found to be independent of the notch radius. However, ρ_c is material dependent and, thus, the determination of fracture toughness for a given notch radius may not be appropriate to accurately measure the crack propagation resistance of the material. According to this, fracture mechanics standard procedures recommend the nucleation of fatigue pre-cracks in the notch root.

In Paper I, the influence of notch radius on essential work of fracture was assessed in four AHSS grades (CP1000, DP1000, TBF, Q&P). For this purpose, two notch configurations were investigated: DENT specimens with notches machined by EDM (ρ= 150 μm) and DENT specimens with fatigue pre-cracks ($\rho\approx$ 0.1 μm). The results are shown in Figure 5.8.

For most of the investigated steel grades, w_e is significantly higher for notched specimens than for specimens with fatigue pre-cracks, which evidences the great influence of notch radius on w_e. Q&P shows the highest notch sensitivity ($w_{e\ crack}/w_{e\ notch}$=0.42) together with DP and TBF ($w_{e\ crack}/w_{e\ notch}$=0.47 and 0.48, respectively). On the other hand, CP1000 is the less sensitive to notch radius ($w_{e\ crack}/w_{e\ notch}$=0.86). Comparing the results of CP1000 and Q&P, it can be observed that fracture toughness values obtained with notched specimens may overestimate the material's fracture resistance. For notched specimens, both steel grades present almost identical fracture behaviour. However, for fatigue pre-cracked specimens, the w_e drastically drops in Q&P, being of the order of the half of CP1000. It is important to keep this in mind when measuring the fracture toughness of different materials, even for comparison purposes, since results can be misleading. Accordingly, only fracture toughness values obtained from fatigue pre-cracked specimens are considered to be representative of *real* fracture toughness of the material.

This is precisely one of the main obstacles that prevent the implementation of fracture toughness measurements as routine testing in automotive industry, since fatigue pre-cracking procedures are expensive and very time-consuming. In this sense, a new rapid notching procedure is proposed in Paper D as an alternative to fatigue pre-cracking. The method consists in introducing two sharp notches ($\rho\approx$ 2-3 μm) in rectangular specimens by means of a simple shearing process. For this purpose, a newly developed tool consisting of a cutting die and a bevelled punch was used (see

Paper D for more details about the tool and the notching procedure). This method was validated for four different AHSS grades: CP1000, DP1000A, DP1000B and 3rd Gen TBF1180. The EWF results for specimens with sheared notches are shown, and compared to the obtained with fatigue pre-cracked specimens, in Figure 5.8a (CP1000) and Figure 5.9 (DP1000A, DP1000B and 3rd Gen TBF1180). For similar ligament length, the four investigated steel grades show practically identical w_f for both fatigue pre-cracked and sheared specimens, which lead to very similar w_e and βw_p.

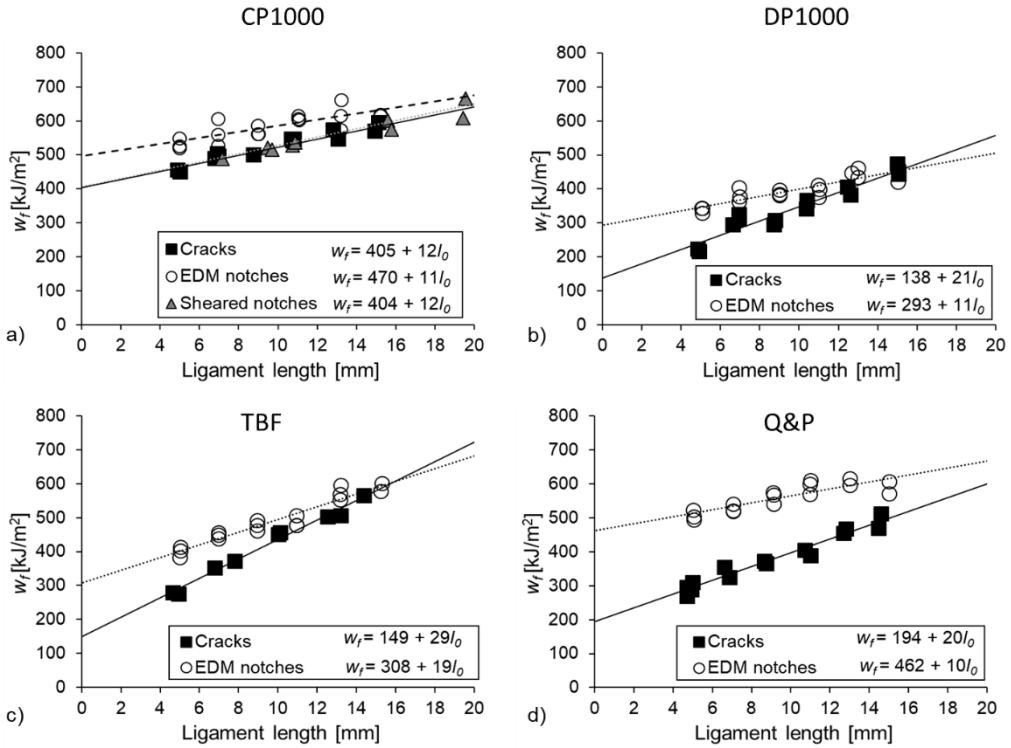

Figure 5.8. EWF results for specimens with EDM notches (open symbols) and specimens with fatigue pre-cracks (black squares)**. a)** CP1000 (results of specimens with sheared notches are also given, grey triangles)**. b)** DP1000**. c)** TBF and **d)** Q&P**.**

One of the major concerns that can arise when preparing notches with mechanical methods, is the accumulation of plastic deformation around the crack tip, which has shown to be critical, for example, in polymer films [152, 169]. Martínez et al. [169] observed a significant variation on the w_e of an ethylene-propylene block copolymer (EPBC) film with DENT specimens prepared using different notch sharpening methods. The w_e increased from 60±7 kJ/m^2 for specimens prepared using femtosecond pulsed laser ablation (Femtolaser) to 134±7 kJ/m^2 for specimens with notches sharpened by a diamond edged razor blade. This large variation of w_e was attributed to the plastic deformation ahead of the crack tip produced during notch sharpening. Similar observations were made by León et al. [155]. However, for the AHSS grades investigated in this project, it seems that the possible plastic deformation introduced during the shearing process has no significant influence on w_e. In fact, the load-displacement curves obtained for specimens prepared with this method are practically identical to the ones for specimens with fatigue pre-cracks (see Paper D, figure 6), which suggests that this effect is almost negligible.

It must be noted that this notching preparation procedure is currently under study and further investigations are needed to quantify the influence of different variables affecting the process

(cutting clearance, punch wear, etc.) and to define its limitations (material strength, thickness, etc.). However, the method has shown to be reliable enough to accurately evaluate the fracture toughness of the four AHSS investigated in this work. These results show the great potential of the method, which can be established as an attractive alternative to fatigue pre-cracking operations in high strength metal sheets.

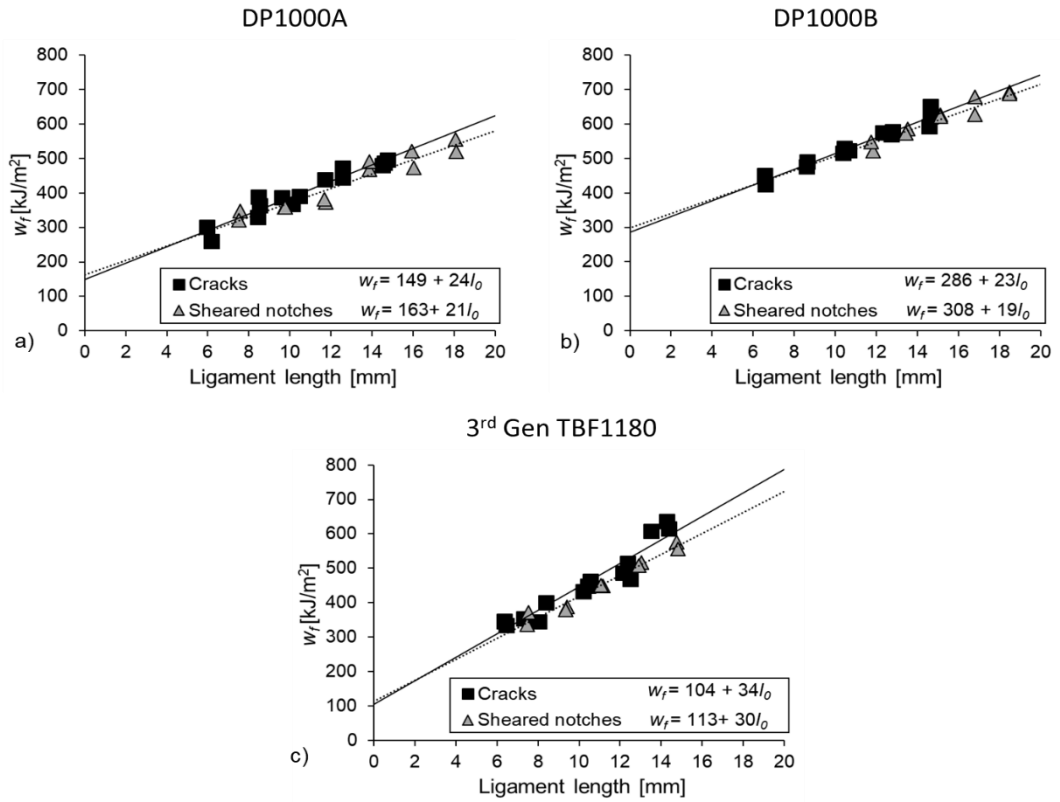

Figure 5.9. EWF results for specimens with sheared notches (grey triangles) and specimens with fatigue pre-cracks (black squares)**. a)** DP1000A, **b)** DP1000B and **c)** 3rd GenTBF1180.

5.1.2 J-integral

The *J*-integral has been the most extended parameter to characterize the fracture toughness of elastic-plastic materials. The *J*-integral procedure is used to evaluate the critical *J*-integral (J_c) for stationary cracks and the *J*-Resistance (*J*-R) curves for growing cracks. Note that the notation J_c has ben used in this work instead of J_{Ic}, which is used to define the thickness independent plane-strain fracture toughness. As defined in ASTM E1820 [111], J_c is a measure of fracture toughness independent of the in-plane dimensions. However, it may depend on specimen thickness. To qualify J_c as a thickness independent fracture toughness parameter, J_{Ic}, the following conditions must be met:

$$B, b_0 > 10\frac{J_c}{\sigma_Y} \tag{42}$$

where B is the specimen thickness, b_0 is the uncracked ligament length and σ_Y is the effective yield strength. J_c represents the fracture toughness near the onset of stable crack propagation. However, many tough materials do not fail catastrophically at *Jc* but they show a rising *R* curve, where *J*

increases with crack growth. In these materials, the *J-R* curve provides a more complete description of the stable crack propagation resistance.

Unfortunately, no standard methods are available to evaluate the *J*-integral in thin gauge materials. The ASTME1820 was developed to characterize the fracture toughness of metallic materials under plane strain conditions and, therefore, specimen size requirements cannot be satisfied by relatively thin sheets. For this reason, some researchers have proposed alternative non-standard methods for *J*-integral measurements in thin ductile sheets. Pardoen et al. [119] used the *J*-integral expression proposed by Rice et al. [170] to evaluate J_c in DENT specimens:

$$J = \frac{K^2}{E} + \frac{1}{t_0 l_0}\left(2\int P du_p - P u_p\right) \tag{43}$$

Where K is the stress intensity factor, which for a DENT specimen is given by Equation (44) [171]:

$$K = \frac{P\sqrt{\pi a}}{t_0 \cdot 2W\sqrt{1-\frac{a}{W}}}\left[1.122 - 0.561\left(\frac{a}{W}\right) - 0.205\left(\frac{a}{W}\right)^2 + 0.471\left(\frac{a}{W}\right)^3 - 0.190\left(\frac{a}{W}\right)^4\right] \tag{44}$$

E is the elastic modulus, t_0 is the specimen thickness, l_0 is the uncracked ligament length, P is the actual load and u_p is the actual plastic displacement. In Equation (44), W is the half of the specimen width.

This approach has been also used in different research works to evaluate the initiation toughness (J_c) of high strength steels [84, 87, 88, 90]. Other of the methods commonly used for *J*-integral evaluation in thin polymer films [152] is the Begley and Landes method [108]. In the appended Paper I, a different approach is investigated. The *J*-integral of the investigated AHSS grades was evaluated following the experimental procedure described in ASTM E1820 for CT specimens introducing some variations. First, the specimen geometry was machined according to the proportions described in ASTM E561 [145], which does not present any restriction regarding specimen thickness. On the other hand, instead of using the compliance technique for actual crack length estimation, crack extension was directly measured on the specimen by means of a high resolution video camera located in one of the specimen sides. For each material, a *J*-R curve was constructed according to ASTM E1820. The results are shown in *Section 4.1.2*.

As observed by Zhu and Leis [117], the results show that if the thickness requirements described in the ASTM E1820 are disregarded the methodology can be applied to evaluate a *J*-R curve in a thin ductile material. Furthermore, the use of a digital video equipment in combination with a digital image analysis software has shown to be accurate enough to follow the evolution of crack extension during the test. In combination with a DIC software, this can be an interesting approach to investigate the crack propagation behavior of thin metal sheets.

In this work, two fracture resistance parameters were defined from the *J*-R curves: the *J* value at at crack initiation, J_i , which is the value for crack growth initiation detected in the video equipment, and J_c, which is defined as the fracture toughness near the onset of stable crack propagation obtained from the intersection of the 0.2 mm offset line with the *R* curve as indicated in ASTM E 1820. In steels with higher toughness, such as CP1000 and Q&P, the initial part of the resistance curve shows a more pronounced slope and the difference between J_i and J_c is greater.

This difference is lower for steels with lower toughness (DP1000 and TBF). These steels also show flatter R curves indicating lower contribution to crack propagation resistance.

5.1.2.1 Influence of specimen geometry

To investigate the influence of specimen geometry on *J*-R curve, *J*-integral measurements were performed using CT and DENT specimens. For DENT specimens, the *J*-integral at crack initiation (J_i) was evaluated from the load-line displacement curve according to Equation (43). To account for the crack growth the *J* values for the different crack extensions were evaluated using an incremental equation as detailed in Paper I.

As illustrated in Figure 4.18, specimen geometry has a significant influence on the resistance curve. However, the R curves converge in the initial part of the graph, providing similar values of J_i and J_c. This is in good agreement with the findings of Xia et al. [172] and Zhu et al. [173]. They showed that constraint level, while has little influence on J_c, has a significant effect on the slope of the R curve. Since constraint level is higher in CT than in DENT specimens, they show lower tearing modulus.

5.1.2.2 Relationship between w_e and J_c

The relationship between w_e and J_c was discussed in Paper I. As mentioned in the introduction (*Section 1.4.8.4*), this topic has been recurrently investigated in literature [119, 135-137, 166, 174]. Different authors showed the equivalence between w_e and J_c in ductile polymers [135,136]. Furthermore, Mai and Cotterell [174] differentiated between J_i and J_c (they called it J_p) and found that J_i and J_c were equivalent to w_e^i and w_e respectively. The results of EWF and *J*-integral measurements performed in Paper I are summarized in Figure 5.10. Although the values of J_i are slightly lower than w_e^i, a quite good agreement can be observed between both parameters in the four investigated steels. It must be noted that the results of *J*-integral measurements are obtained from one single specimen. Therefore, no standard deviation is given. In order to obtain more accurate toughness values and better statistical confidence, it is recommended to test additional specimens. Regarding w_e and J_c, some differences can be discerned between w_e and J_c. On the one hand, some steel grades like DP1000 and TBF show a very good equivalence but, on the contrary, significant deviations are observed between these two parameters in CP1000 and Q&P.

The differences between w_e and J_c are discussed on the basis of their conceptual differences. By definition, the specific essential work of fracture (w_e) contains energetic contributions from crack initiation and propagation resistance since it is derived from a linear regression of w_f for the complete fracture [166]. On the other hand, J_c, as defined by the ASTM E1820, is a toughness value for a small crack advance, determined by the intersection of the *J*-R curve and the 0.2 mm offset line parallel to the construction line. Therefore, as suggested by Pardoen et al. [166], when there is a small contribution from crack propagation after initiation (DP1000, TBF, Q&P), J_C is similar to w_e. On the contrary, for steels having a large contribution from crack propagation resistance, such as the case of CP1000, w_e and J_c differ. In the case of Q&P, as discussed in Paper I , the fact that it shows greater J_c than w_e is probably attributed to the additional energy associated with the 0.2 mm of crack advance. The similarities in *J*-R curves of CP1000 and Q&P are explained by the difference in energetic contributions from necking and plastic work to the ductile fracture process. In CP1000, a large part of the crack propagation resistance energy comes from the necking developed at the crack tip, and it is well captured by w_e. On the other hand, in Q&P this contribution is minimum and the major part of the energetic increase observed in *J*-R curve

comes from the non-essential plastic work developed in a region outside the fracture process zone, which as derived from EWF tests (Figure 4.2 and Figure 4.3), is about the double than for CP1000 (βw_p= 20± 1 MJ/m^3 and 12±1 MJ/m^3 for Q&P and CP1000, respectively). The findings obtained in this work, suggests that when the fracture process has an important contribution from the crack propagation, w_e better represents the tearing resistance of thin ductile sheets than J_c, which is line with previous observations [119].

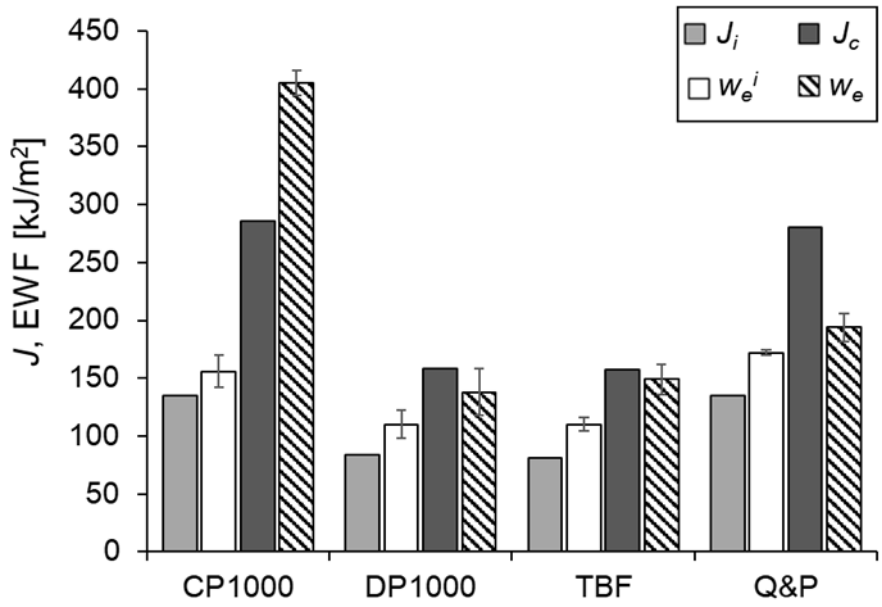

Figure 5.10. Comparison of EWF and *J*-integral results. *J* values obtained from DENT specimens.

5.1.2.3 Thickness independent fracture toughness validation criterion

As mentioned above, according to the ASTM E1820 the measured J_c value can be considered as a plane-strain thickness independent fracture toughness value (J_{Ic}), when the conditions given in Equation (42) are met. The same criterion can be extrapolated to w_e. In this case, the plane-strain specific essential work of fracture is denoted w_{Ie}. The fulfilment of these conditions for all the AHSS studied in this work is investigated in Table 5.2.

As expected, most of the steel grades do not satisfy the minimum thickness requirements suggested by ASTM E1820 to be considered as thickness independent fracture toughness values. However, for some of them (TRIP780, 3rd Gen DP1180, 3rd Gen TBF1180 and PHS1500) the minimum thickness required is below the actual sheet thickness, which suggests that the obtained specific essential work of fracture could be considered as the plane-strain essential work of fracture (w_e=w_{Ie}). Further investigations on the effect of specimen thickness on w_e must be performed to validate these assumptions.

Table 5.2. Validation criteria for considering J_c and w_e as thickness independent plane-strain fracture toughness values, J_{IC} and w_{Ie}, respectively. Values in parenthesis are the minimum thickness values corresponding to J_c values.

Steel	t [mm]	σ_Y [MPa]	J_c [kJ/m^2]	w_e [kJ/m^2]	*Minimum thickness* [mm]	Qualification of J_c and w_e as $J_c = J_{Ic}$, $w_e = w_{Ie}$
CP1000	1.4	962	286	405 ± 11	(3.0) 4.2	NO
DP1000	1.4	895	158	138 ± 20	(1.8) 1.5	NO
TBF	1.5	884	157	149 ± 13	(1.8) 1.7	NO
Q&P	1.4	1061	280	194 ± 12	(2.6) 1.8	NO
DP780	1.5	668	-	151 ± 31	2.3	NO
TRIP780	1.6	697	-	106 ± 24	1.5	YES
DP1000A	1.35	936	-	149 ± 21	1.6	NO
3rd Gen DP1180	1.2	1054	-	115 ± 20	1.1	YES
3rd Gen TBF1180	1.4	1102	-	104 ± 30	0.9	YES
3rd Gen Q&P1180	1.5	1113	-	196 ± 31	1.8	NO
CP1200	1.6	1130	-	201 ± 24	1.8	NO
TBF/Q&P	1.4	951	-	302 ± 32	3.2	NO
PHS1500	1.5	1314	-	159 ± 18	1.2	YES
PHS1000	1.5	998	-	330 ± 21	3.3	NO
TWIP	1.4	750	-	366 ± 24	4.9	NO
DP1000 B	1.4	907	-	286 ± 17	3.2	NO

5.1.3 Kahn-type tear tests

The application of the Kahn-type tear tests (KTT) to characterize the tearing resistance of sheet materials has been mainly focused on thin aluminium alloy sheets [12,127-130]. In fact, the standard method (ASTM B871) that describes the experimental procedure and the specimen proportions for tear testing using the KTT is specific for aluminium alloy products [126]. However, some researchers have adapted the method to readily evaluate the fracture resistance of thin PHS [131] and TWIP [132] sheets. Ying et al. [131] used the KTT to investigate the influence of austenitization temperature, soaking time and start deformation temperature on strength and toughness of 22MnB5 press hardened sheets (t=1.6 mm). Lorthios et al. [132] also applied this method to study the tearing behaviour of a high Mn TWIP steel.

In this work (Paper I and Paper C), the applicability of the KTT to characterize the fracture resistance of thin AHSS sheet was further investigated. The results showed that the specifications described in the ASTM B871 [126] regarding specimen geometry and experimental testing can be directly applied to high strength metal sheets in the range of 1.4-1.6 mm thickness and 1000-1500 MPa. This simplistic energy-based method can be an interesting approach for indexing the tearing resistance of ductile metal sheets and evaluating the effect of processing parameters and microstructural constituents on overall toughness. However, as discussed in Paper I and Paper C, the results must be taken with caution.

As shown in Figure 5.11, *UIE* values are in good agreement with initiation toughness values from EWF tests (w_e^i). It is worth noting that despite the larger notch radius of KTT specimens (ρ= 150 μm) compared to fatigue pre-cracked DENT specimens used for EWF tests (ρ= 0.1 μm), the results for crack initiation resistance are very similar for both test configurations. This behaviour suggests that stress concentration ahead of the notch tip in KTT specimen closely resembles that of a crack and, thus, a machined sharp notch is suitable enough to obtain representative initiation toughness values. On the other hand, large differences are observed between w_e and *UPE*. In

general, *UPE* values are much higher than w_e, which results in an overestimation of the crack propagation resistance. As explained in Paper I, *UPE*, similarly to *J*-resistance curves [175], contains not only the energy for creating new surfaces in the front of the crack tip but also includes an additional contribution from the non-essential plastic work dissipated in the outer region. On the contrary, w_e only quantifies the energy dissipated in the fracture process zone since the contribution from the plastic work is removed when extrapolating w_f vs l_0 data to ligament zero. This explanation can be used to understand the differences between w_e and *UPE* and demonstrates that *UPE* is not a material property that can be only used as a relative index of toughness.

Nevertheless, as the poor correlation between w_e and *UPE* indicates (Figure 5.12a), *UPE* values from KTT may lead to wrong toughness estimations and misleading material ranking. As described in *Section 3.2.3*, an alternative approach, based on the measurement of the major strain at fracture in the notch tip ($\varepsilon_{f\ KTT}$) by means of DIC, is investigated in this work. This parameter shows a much better correlation with w_e (Figure 5.12b) and provides a quite good estimation of fracture toughness.

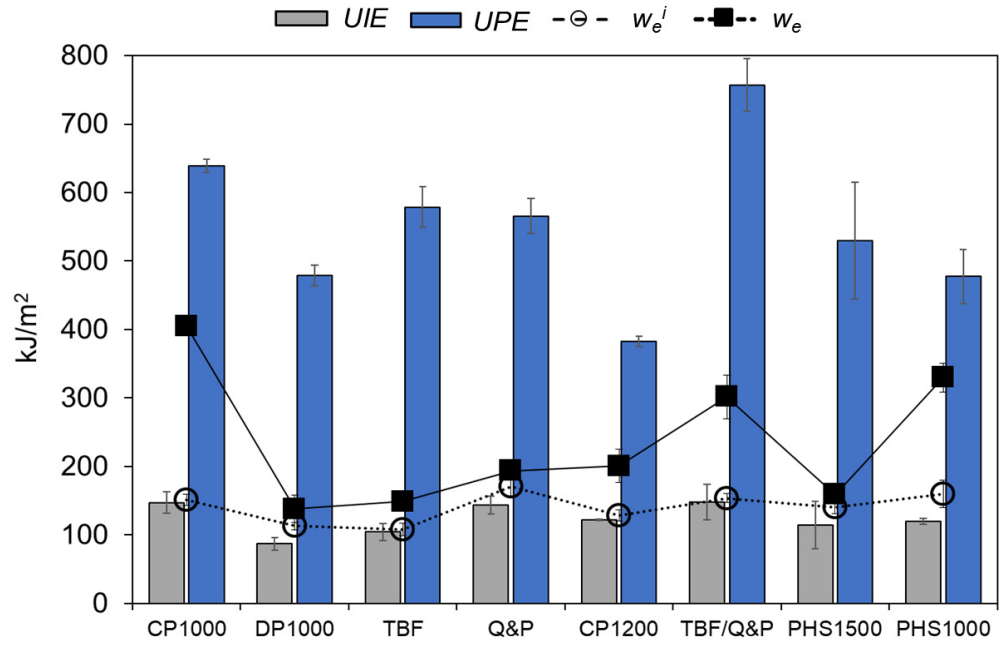

Figure 5.11. Comparison between KTT and EWF results.

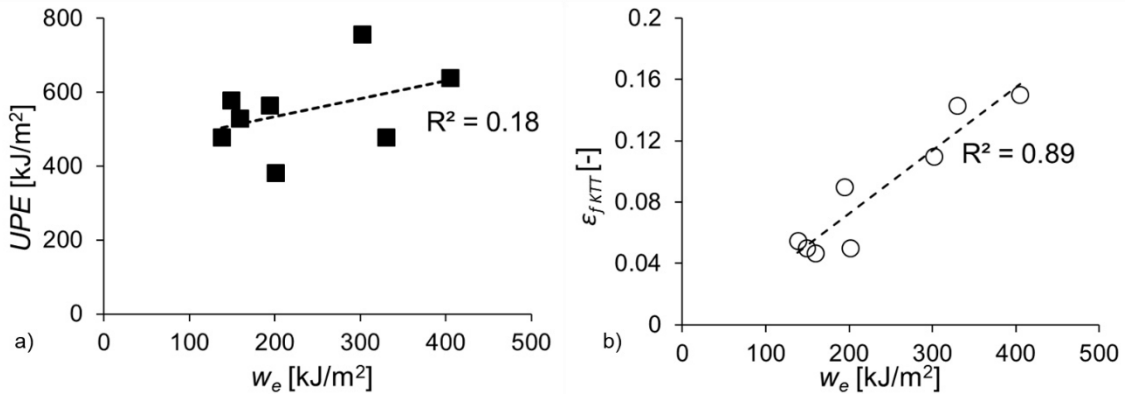

Figure 5.12. Correlation between w_e and: **a)** UPE, **b)** $\varepsilon_{f\ KTT}$.

5.1.4 Relationship between fracture toughness and tensile properties

The relationship between the specific essential work of fracture and uniaxial tensile properties for all the AHSS grades investigated in this work is shown in Figure 5.13. Values of true fracture strain (TFS) and true thickness strain (*TTS*) are only available for the steels studied in Paper I and Paper II. As discussed in these two papers, no direct relationship can be discerned between fracture toughness and any of the conventional uniaxial tensile properties. The results evidence that greater elongation, both uniform (UE) or total (TE), or greater strain hardening exponent (n), which are used to define ductility and formability, do not indicate greater fracture toughness. Rather, on the contrary, steels showing the largest strain hardening and elongation values show relatively low fracture toughness. In the same line, no link is observed between the ultimate tensile strength by total elongation (UTSxTE) product and w_e. The UTSxTE product is often used in literature as a toughness indicator. However, this is in contradiction to the observed in Figure 5.13, which shows that this parameter is not suitable to estimate the cracking resistance of AHSS.

On the other hand, local strain measurements from uniaxial tensile tests (*TFS*, *TTS*) give a better estimation of fracture toughness. Nevertheless, as shown by Xiong et al. [90], these fracture-related parameters often are not accurate enough to describe the fracture behaviour of high strength sheet materials in the presence of existing cracks or defects. Therefore, to better understand the fracture performance of AHSS sheets, including crack initiation and propagation resistance, fracture toughness should be properly measured in the frame of fracture mechanics.

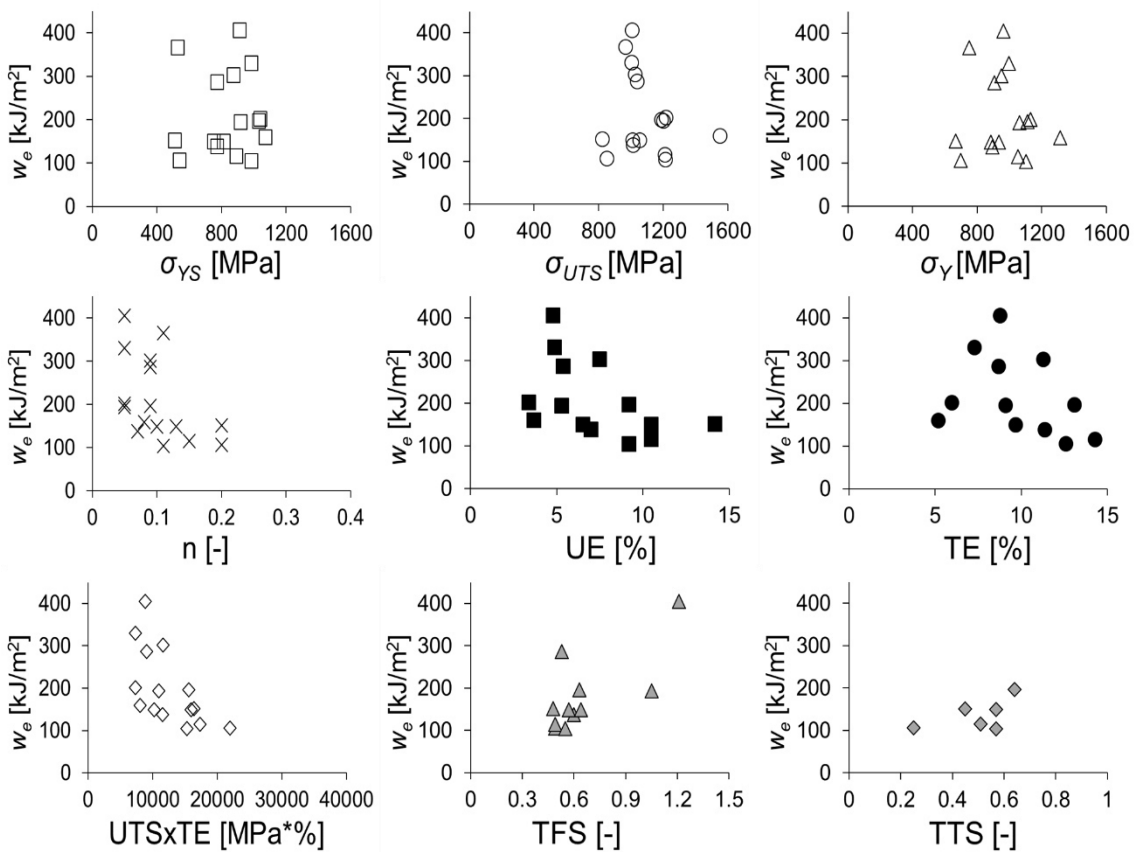

Figure 5.13. Relationship between w_e and different tensile parameters.

5.2 Fracture toughness to understand edge cracking resistance

5.2.1 Correlation between fracture toughness and edge formability

As mentioned in the introduction, the relationship between edge fracture resistance and fracture toughness in high strength metal sheets has been addressed by different authors [20, 23, 26, 76, 80]. These works evidenced that sheared edge formability is governed by the material's resistance against the propagation of pre-existing crack or defects introduced in the previous forming step (punching, shearing, cutting). Accordingly, different fracture mechanics approaches, such as *J*-integral [76, 80] or essential work of fracture measurements [20] have been proposed to understand edge fracture resistance. Takahashi et al. [76] used the critical *J*-integral value (J_c) to rationalize the differences in the edge fracture behaviour of different hot rolled dual phase steels (ferrite + martensite and ferrite+bainite). They observed that the fracture mechanisms present in fracture mechanics and hole expansion tests were very similar, which explained the good correlation between J_c and the limiting hole expansion ratio (HER). Similar conclusions were reached by Yoon et al. [80]. In that case, *J*-integral measurements were performed in various AHSS grades by using Single Edge Notched Tension (SENT) specimens and the parameter K_{Jc} was used as a measure of fracture toughness. K_{Jc} is derived from J_c as indicated in ASTM E18120 [111]:

$$K_{Jc} = \sqrt{\frac{J_c E}{(1-\nu^2)}} \tag{45}$$

where E is the Young'smodulus and ν is the Poisson's ratio.

Alternatively, Casellas et al. [20] proposed the use of the specific essential work of fracture (w_e) to understand the stretch flangeability of several AHSS sheets. They found that steels with higher w_e showed higher HER and established a linear relationship between these two parameters. This approach was further investigated in Paper II and Paper B. The results from these investigations are summarized in Figure 5.14.

Figure 5.14a shows the correlation between w_e and HER for the AHSS grades investigated in this work. Results for CP1000 and DP1000 steels (sheet thickness, t=1.2 mm) studied in Paper A are also included. The very good linear fitting for different AHSS families (R^2=0.90) confirms the close relationship between fracture toughness and stretch flangeability of AHSS and demonstrate that w_e is a suitable property to understand edge fracture resistance.

As discussed in Paper I, the values of HER are well correlated with w_e but not with crack initiation resistance (w_e^i). This is because, phenomenologically, the limiting hole expansion ratio is related to the overall crack propagation resistance rather than to initiation. It must be noted that the HER is determined when a crack has propagated through the full sheet thickness, i.e. a crack extension of about 1-1.6 mm. This argumentation also explains the better correlation between HER and *we* instead of J_c, which, as defined above, is a toughness value for a very small crack extension (0.2-0.3 mm) and, thus, is not suitable enough to describe the full fracture resistance when there is significant crack propagation prior to final failure.

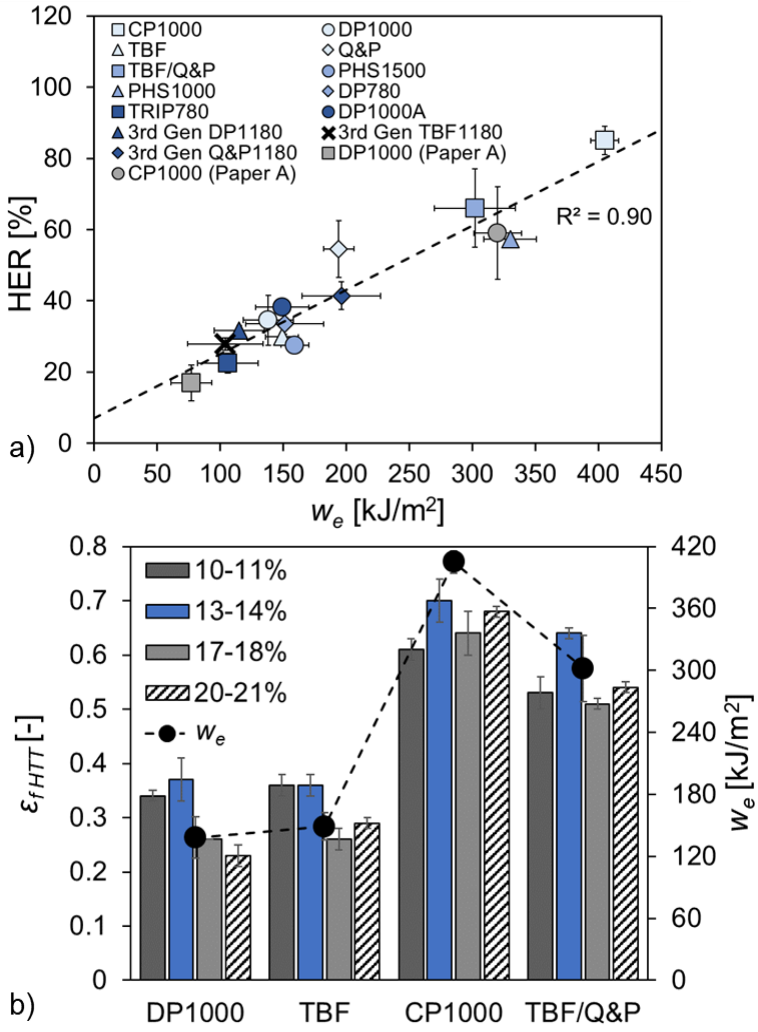

Figure 5.14. a) Correlation between w_e and HER. Figure adapted from Paper II. **b)** Fracture strains measured in HTT specimens (ε_f HTT) for the 4 steel grades investigated in Paper B with different punch to die clearance. w_e are also plotted. Figure from Paper B.

It is important to remark again that edge fracture does not only depend on material properties but also on the hole preparation method, edge quality, etc. The influence of punching clearance on the edge formability of different DP-like (DP1000, TBF) and CP-like (CP1000, TBF/Q&P) was studied in Paper B by means of hole tension tests (HTT) and DIC analysis, as described in previous sections. Figure 5.14b shows the fracture strain values measured on the surface of HTT specimens ($\varepsilon_{f\,HTT}$) for different punch-to-die clearances. The trend observed in Figure 5.14a can be also seen here, i.e steels with higher we present better edge formability, independently of the punching clearance. The results also suggest that tougher steels (CP1000 and TBF/Q&P) are much less sensitive to the edge quality than steels with low fracture toughness (DP1000 and TBF). This phenomenon may be related to the fact that, independently on the damage induced during punching or shearing, these steel grades show greater damage tolerance.

As a conclusion, and based on the good correlation observed between w_e and the results from edge cracking resistance tests, it can be stated that w_e is a key property to understand the edge fracture resistance of AHSS sheets.

5.2.2 Comparison of thickness strain measurements

The similarities between the fracture mechanisms involved in hole expansion tests (HETs) and fracture toughness tests with DENT specimens are further discussed in Paper II. There, the comparison between thickness strain measurements in HET and DENT specimens revealed that the thinning at fracture and, therefore, the crack propagation behaviour is very similar in both tests. This is illustrated in Figure 5.15. As observed, the values of TTS_{HET} coincide with the values of $TTS_{DENT}{}^{p}$ in most of the investigated steels, except in DP780 and TRIP780, where they are closer to the values of thinning at crack initiation $TTS_{DENT}{}^{i}$. According to this, an edge fracture criterion based on the measurement of thickness strain in DENT specimens is proposed. The values of TTS_{DENT} define the limit edge-crack thickness strain. When the critical thinning for crack propagation is exceeded, edge fracture occurs.

As mentioned in Paper II, this criterion might be useful for defining edge fracture limits in FEM modelling. However, other factors such as the influence of edge quality on limit edge thinning values should be investigated in further detail to define a reliable fracture criterion for edge cracking prediction.

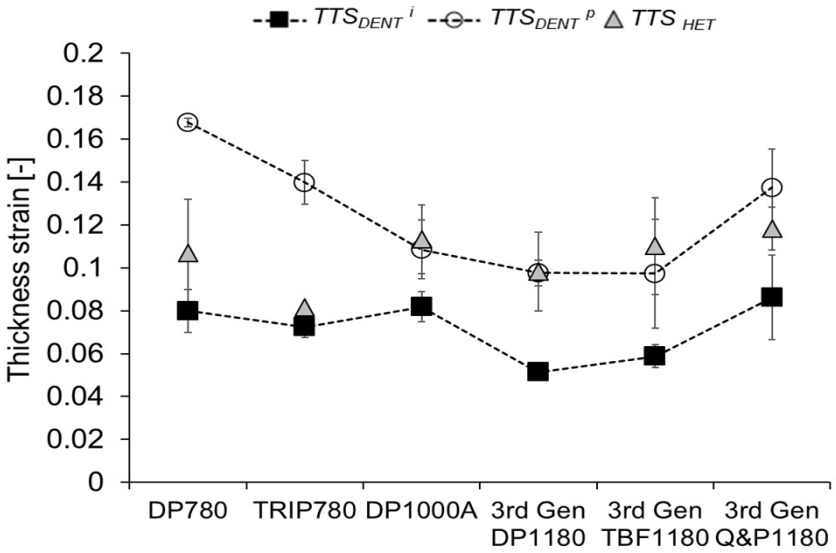

Figure 5.15. Thickness strain measurements performed in DENT and HET specimens.

5.2.3 Industrial case study

A case of industrial applicability of the EWF methodology for edge cracking predictions is presented in Paper A. The study was performed in collaboration with Centro Ricerche Fiat (CRF). In that work, a serial production automotive component that presented multiple edge cracks, was investigated (Figure 5.16). The component was originally manufactured using a 1000 MPa Dual Phase (DP) steel of 1.2 mm thickness. After several production problems, it was decided to substitute this material by a Complex Phase (CP) steel of similar characteristics (same strength and thickness). With the new steel grade, the problems of edge cracking were solved. A first examination of material specifications, including tensile properties and Forming Limit Curves (FLC), did not reveal any apparent cause for the edge cracking problems presented by the DP steel. On the contrary, the material satisfied all the quality requirements and mechanical properties (n value, elongation) and FLC suggested that the DP steel had superior formability (Figure 5.17a and b). A more detailed investigation was performed to identify the origin of the poor edge formability of the DP steel. This investigation included hole expansion tests according to ISO

16630 [60] and EWF tests. The results (Figure 5.17c and d) confirmed the low fracture toughness of DP1000 compared to CP1000 and the consequent low stretch flangeability, measured by the HER.

The investigations carried out in this work show the potential of the EWF methodology as a tool to select cold forming AHSS grades with improved stretch flangeability and avoid unexpected edge fractures that can slow down the productivity and result in great losses and complications.

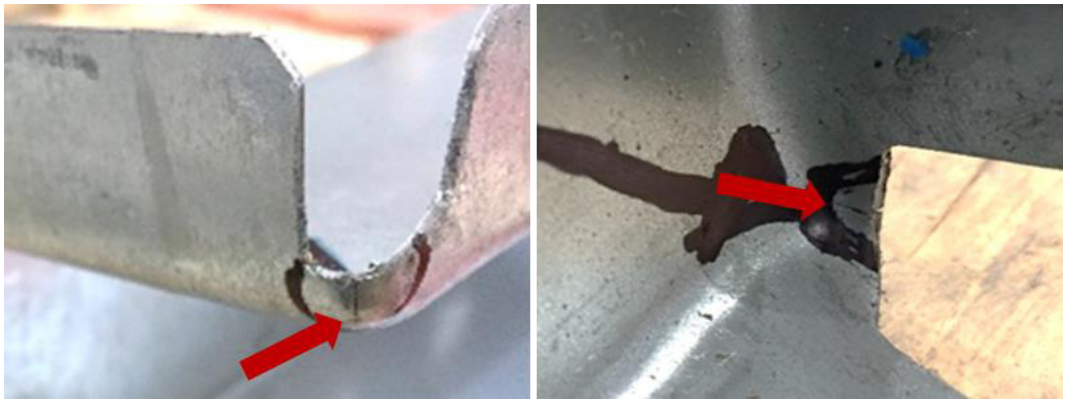

Figure 5.16. Edge cracks observed in the component manufactured with DP steel grade (Paper A)

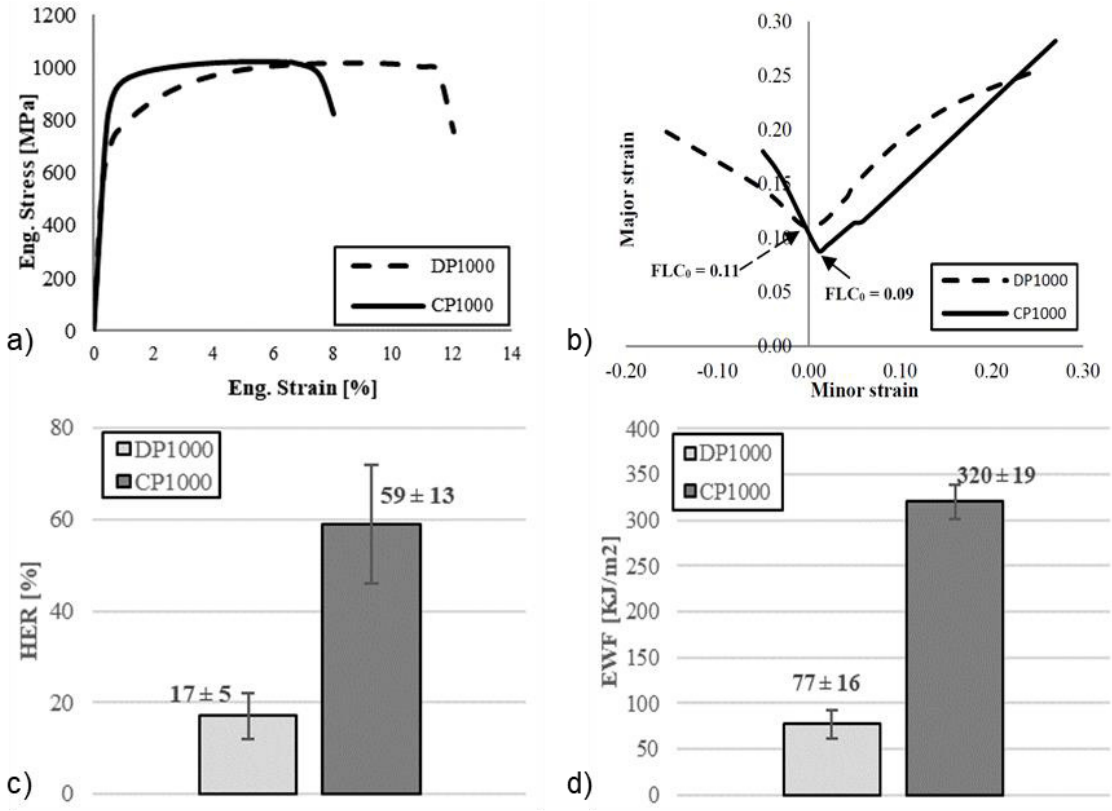

Figure 5.17. Results from mechanical characterizations for the investigated CP and DP grades. **a)** Engineering stress-strain curves, **b)** FLCs, **c)** HER and **d)** EWF. Image from Paper A.

5.3 Correlation between fracture toughness and crash resistance

5.3.1 Axial crash fracture behaviour

The correlation between fracture toughness measurements and the fracture behaviour of AHSS under axial impact conditions is investigated in Paper III. As described in *Section 3.4*, the fracture behaviour of AHSS can be assessed according to an overall crack length and the energy absorbed during impact. The overall cracking of the test sample is evaluated according to a Crash Index (CI) defined in Table 3.4. In this work, a new parameter has been introduced to describe the evolution of the CI with the intrusion level, the Crash Index Decreasing Rate (CIDR). The CIDR quantifies the crack propagation rate in crash-tested samples, i.e. a high CIDR indicates that the CI rapidly decreases with the intrusion level and, thus, that cracks rapidly propagate through the sample. This is translated into a poorer crash foldability and overall fracture performance. On the other hand, a low CIDR means that the material has a higher resistance to crack propagation with increasing intrusion level.

A comparison between specific essential work of fracture and the values of CIDR and Energy absorbed at the maximum intrusion is made in Figure 5.18. In Paper III, the maximum intrusion is established for a CI=20% (sample severely damaged). A very good correlation of w_e with both crash resistance parameters is observed, which shows the relevant role of fracture toughness in crash resistance of AHSS and PHS.

As previously pointed out for edge fracture resistance prediction, crack initiation resistance (w_e^i) provided no good estimation of the overall crash behaviour (see Paper III for more details). These observations allow stating that the axial crash fracture behaviour of AHSS and PHS is strongly dictated by the crack propagation resistance of the material, which is well described by w_e.

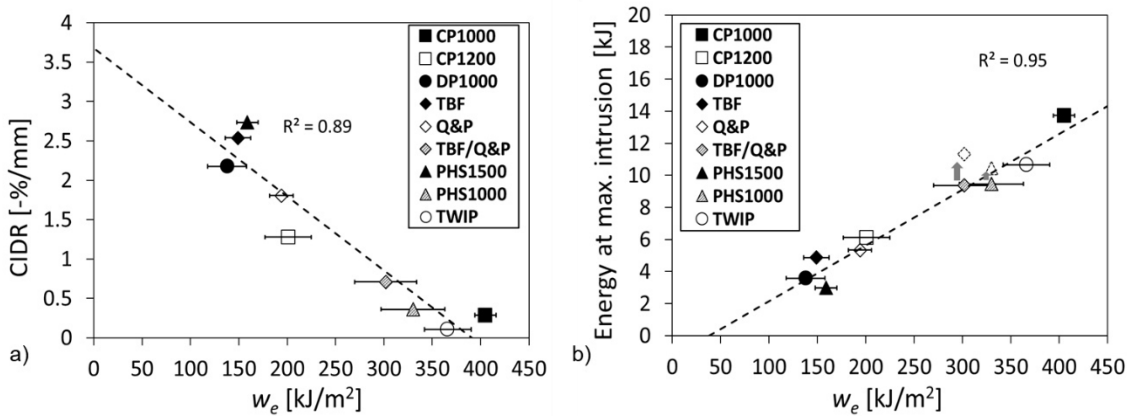

Figure 5.18. Results of essential work of fracture (w_e) against CIDR and energy absorbed at maximum intrusion (CI=20%). Image from Paper III.

5.3.2 Bending impact resistance

A similar strategy was followed to investigate the correlation between cracking behaviour and fracture toughness in bending impact resistance tests. However, as described in *Section 4.4.2*, the fracture behaviour of bending crash samples was slightly different from the observed in axial impact tests. Not all the investigated steel grades presented cracks after testing. This is the case of CP1000, PHS1000, TBF/Q&P and TWIP. Therefore, for these steels, it was not possible to evaluate the damage evolution according to a cracking pattern. For the rest of steel grades, the evolution of an overall crack length with the intrusion level was investigated by using the CIDR

defined above. In any case, the degree of cracking in bending impact samples was, generally, much lower than in axially crash-tested specimens (minimum CI reached ≈ 80%). Only PHS1500 showed a significant amount of cracking (minimum CI ≈ 30%).

As shown in Figure 5.19, and contrary to the observed in axial crash tests, no clear correlation is discerned between w_e and CIDR for the steels presenting cracking. However, it is shown that the steels that did not show damage during crash tests are those with higher fracture toughness (w_e>250 kJ/m^2), which allows defining a threshold toughness value from which bending crash-tested specimens are safe of cracks.

This is an important consideration to keep in mind since in case of a side impact the occurrence of cracks might compromise the structural integrity of the component. Therefore, it should be considered as a high risk factor in the design of crash-relevant parts, which should pursue the optimum combination between high strength (anti-intrusion) and high cracking resistance (structural integrity).

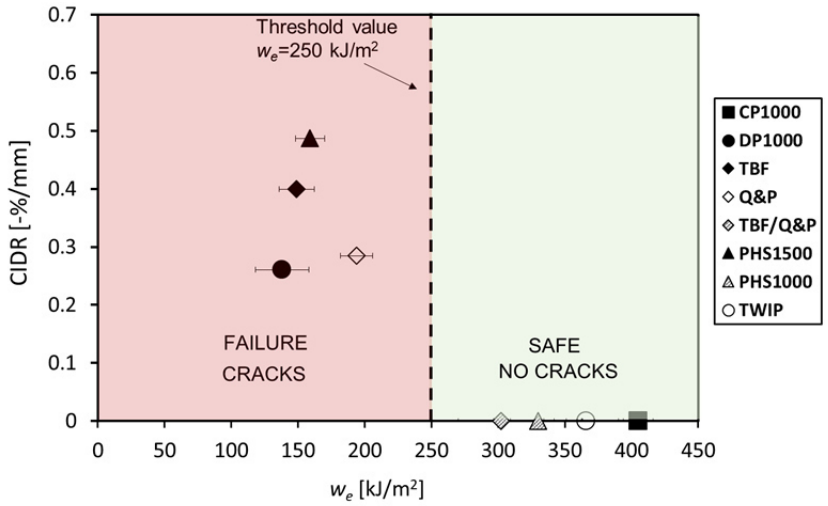

Figure 5.19. Correlation between fracture toughness (w_e) and cracking behaviour in bending impact resistance tests (CIDR). CIDR values of 0 correspond to steel grades that did not showed cracking during crash tests.

5.4 Influence of microstructure on fracture toughness

5.4.1 General discussion

The mechanical behaviour of AHSS is closely linked to their complex multiphase microstructures. In this work, the influence of microstructure on mechanical properties and fracture resistance are discussed. Broadly speaking, most of the investigated AHSS grades can be divided into three big microstructural groups: Complex Phase (CP)-like, Dual Phase (DP)-like and TRIP-assisted microstructures. CP-like microstructures basically consist of a homogeneous bainite/tempered martensite matrix with small amounts of secondary phases in different proportions (martensite, ferrite, austenite). These steels are characterized by moderated strain hardening and uniform elongation but good hole expansion [20, 50] and fracture toughness compared to DP steels (Figure 5.20). DP-like steels present more heterogeneous microstructures consisting of a soft ferrite/bainitic ferrite with the presence of hard secondary phases (martensite)

embedded in the matrix. The strain gradients between the soft matrix and the hard secondary phases contribute to increase the strain hardening rate and to delay the onset of localized necking. Accordingly, DP-microstructures usually present higher strain hardening and elongation values (both uniform and total) than CP-like ones. On the other hand, the same fracture mechanisms that contribute to increasing global ductility have a detrimental effect on local formability (HER) and fracture toughness (Figure 5.20). The hardness differences between phases generate internal stresses during deformation that contribute to the rapid generation of microvoids and/or decohesion of the ferrite/martensite interfaces. In the presence of a crack or defect, such microvoid coalescence rapidly contributes to the crack propagation and final fracture of the sample [50]. The influence of microstructural constituents on fracture toughness and the fracture mechanisms of DP steels are further investigated in Paper IV (see *Section 5.4.2*).

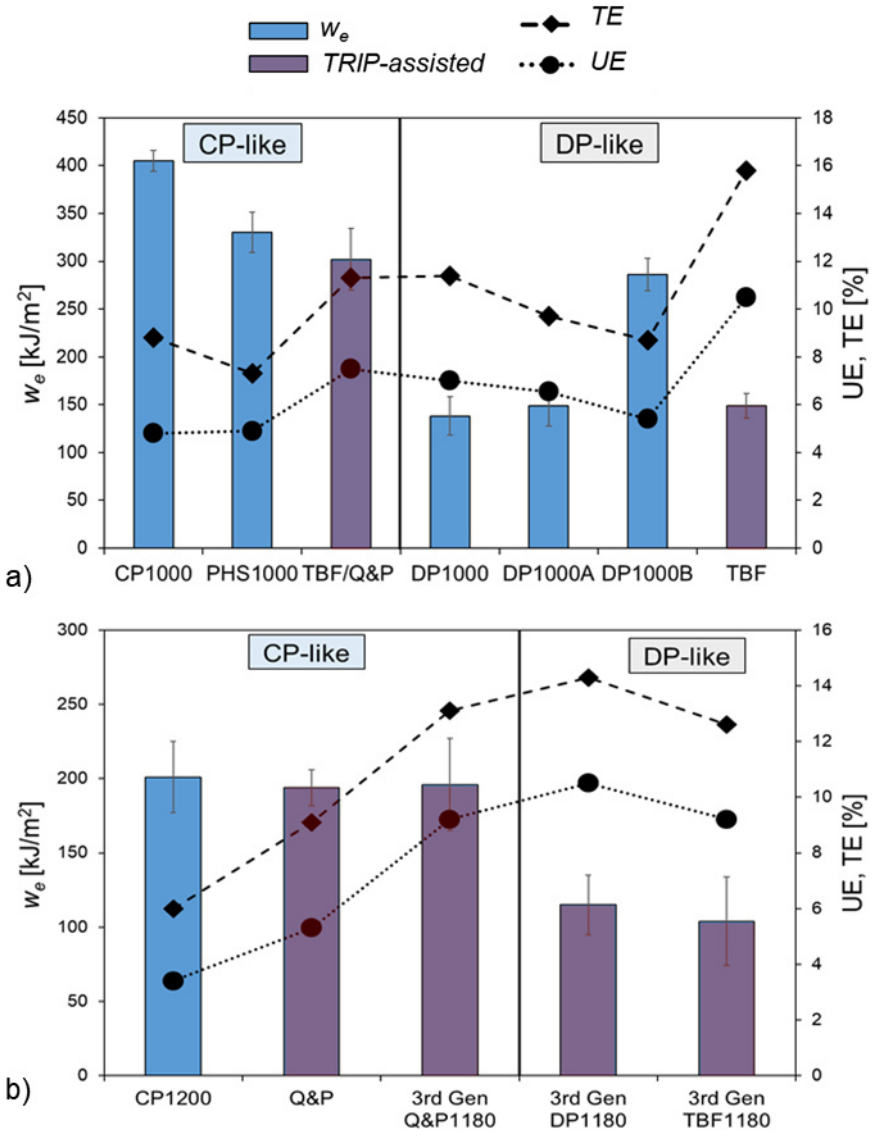

Figure 5.20. Fracture toughness (w_e) and elongation values for some of the steels investigated in this work. **a)** 1000 MPa steel grades. **b)** 1200 MPa steel grades.

TRIP-assisted microstructures can be divided into two categories: 1st Generation TRIP-assisted steels (TRIP780) and 3rd Generation TRIP-assisted microstructures (TBF, Q&P, etc.). As defined

in the introduction, 1st Generation TRIP-assisted or TRIP steels have a ferritic matrix with small amounts of bainite and a significant retained austenite (RA) volume fraction. The austenite to martensite transformation during deformation (TRIP effect) contributes to improving ductility and strength by a similar mechanism than the described for DP steels. The formation of additional mobile dislocations in ferrite in the vicinity of strain-induced fresh martensite increases work hardening and improve uniform elongation. In 3rd Generation TRIP-assisted steels, the soft ferritic matrix is replaced by bainite or tempered martensite. The harder matrix allows attainment of higher strength, while the TRIP effect, helps to maintain good global ductility levels. The beneficial influence of the TRIP effect on mechanical properties is observed when comparing steel grades of similar strength level and matrix characteristics. For example, TBF/Q&P compared to CP1000 and PHS1000 or TBF compared to 1st generation DP steels. For 1200 MPa grades, the superior elongation values of Q&P and 3rd Gen Q&P1180 compared to CP1200 also show the improvement in global formability.

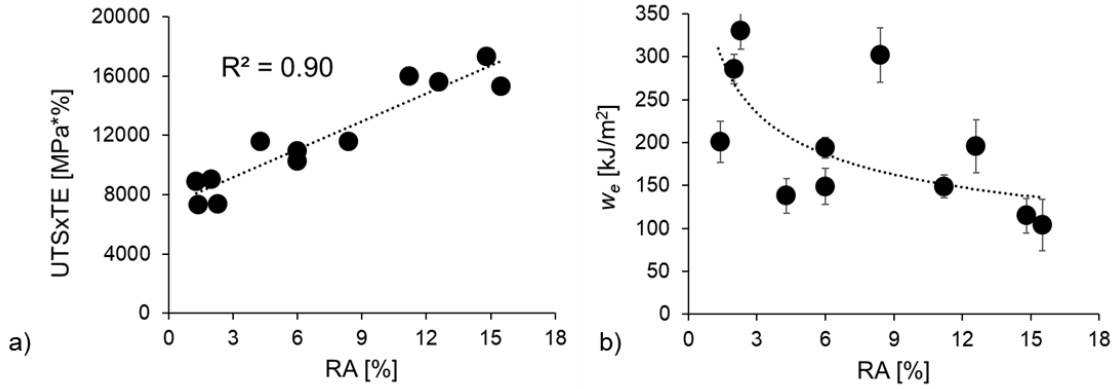

Figure 5.21. Relationship between RA content and **a)** UTSXTE product, **b)** fracture toughness.

The relation between RA content and tensile strength and ductility is more evident in Figure 5.21a. The figure shows a linear increase of UTSxTE product with increasing the RA volume fraction (results for the steels shown in Figure 5.20). However, as discussed in Paper III, no clear relationship can be established between RA content and fracture toughness (Figure 5.21b). In fact, the data plotted in Figure 5.21b suggests a negative influence of RA in overall fracture toughness, i.e. steels with the greatest amount of RA show the lowest w_e.

The influence of RA and matrix characteristics in crack propagation resistance of TRIP-assisted steels has been investigated by different researchers [84, 90, 176, 177]. Jacques et al. [176] stated that a large amount of RA can lead to premature cracking due to the formation of a "brittle" network of strain-induced fresh martensite ahead of the crack tip. Thus, to improve the cracking resistance, the RA volume fraction must be limited. This is in good agreement with the observed in Figure 5.21 and will be further discussed in the next section to explain the different crack propagation resistance of the two DP steels investigated in Paper IV. On the other hand, Lacroix et al. [84] concluded that the TRIP effect can improve crack propagation resistance due to the additional strain hardening contributing to necking in the crack front. Xiong et al. [90] also observed that the fracture toughness of a Q&P steel with different quenching temperatures decreased with increasing the RA content. As previously stated by Jacques et al. [176], this effect was associated with the high RA to martensite transformation rate, influenced by the high stress triaxiality present in the crack tip. According to these observations, it is concluded that to obtain an optimum balance between fracture resistance and global formability, the RA volume fraction

and stability, as well as the matrix characteristics, should be carefully controlled. In this sense, the EWF is proposed as a suitable methodology to investigate the influence of these microstructural features on crack initiation and propagation resistance.

5.4.2 Microstructural investigations on DP steels

In Paper IV, the influence of microstructure on the crack propagation resistance of two industrially processed high strength dual phase sheet steels (DP1000A and DP1000B) is investigated. Microstructural investigations were performed by SEM, HR-EBSD and nanoindention measurements.

The microstructure of DP1000A consists of a matrix containing ferrite (α) and bainite/tempered martensite (α_b) with some dispersed martensite and fresh martensite/retained austenite (M/RA) islands. The SEM images show a large presence of carbide precipitates within B/TM grains (Figure 5.22a). According to magnetization saturation measurements, the RA volume fraction for DP1000A is 6%, which is much higher than the obtained by EBSD analysis (Figure 5.22a). The reasoning to justify the large differences between the two measuring techniques is further explained in Paper IV.

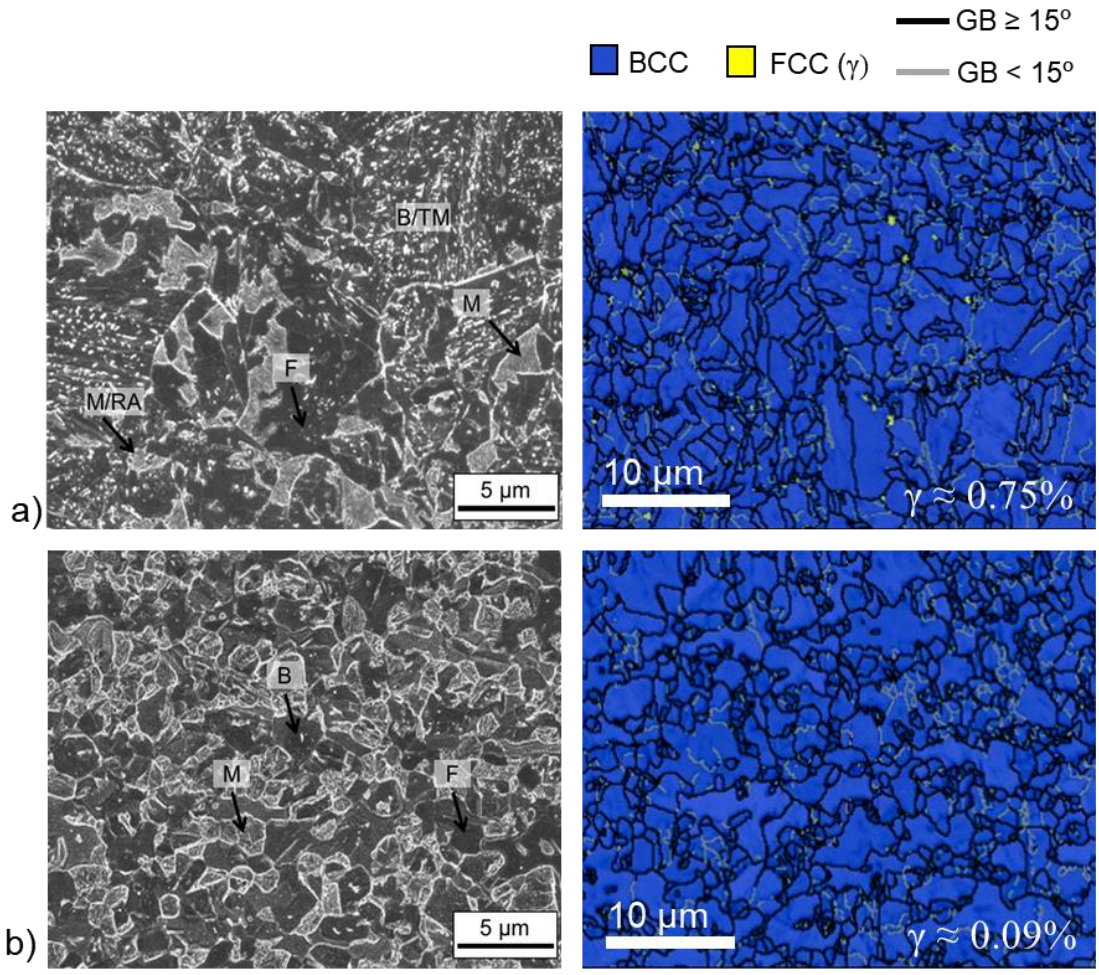

Figure 5.22. SEM micrographs (left) and EBSD phase maps (right) for **a)** DP1000A, **b)** DP1000B.

DP1000B has a ferritic-bainitic matrix with a slightly lower amount of martensite islands (≈27%), which are homogeneously distributed. Contrary to the observed in DP1000-A, carbide precipitation is hardly seen in bainitic (B) areas (Figure 5.22b). For this steel, an almost negligible amount of RA was detected by EBSD (0.09%, Figure 5.22b). The RA volume fraction obtained from magnetic measurements was 2%.

Regarding the proportions of different phases, the differences between the two steel grades are not very large. Both steels show a similar distribution of bainite (harder in the case of DP1000-A). Optical micrographs and EBSD analysis revealed a larger proportion of ferrite in DP1000B (see Paper IV). The grain size is also similar for DP1000A and DP1000B. It is worth noting that the identification of phases volume fraction is a complex and challenging task that required the combination of multiple characterization techniques. A comparison of results from the different techniques led to similar estimations.

The distribution of soft/hard phases is also illustrated by the nanoindentation mappings (Figure 5.23). These images confirm the larger fraction of softer regions (green) in DP1000B. Also, a greater presence of very hard (H>5.5 GPa, colour red) secondary phases is observed in DP1000-A, which can be associated with M/RA islands.

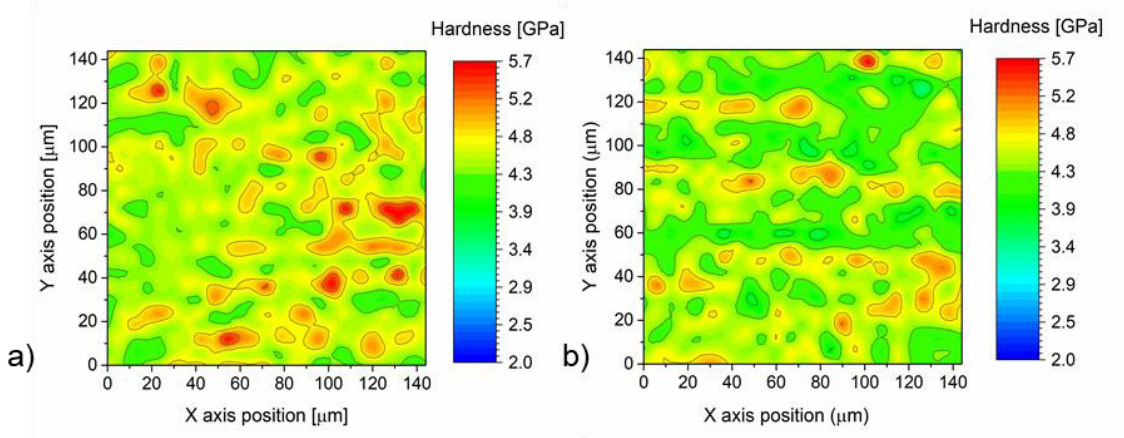

Figure 5.23. Nanohardness mappings. **a)** DP1000-A and **b)** DP1000-B.

The tensile curves and the results from EWF tests are shown in Figure 5.24 and Figure 5.25, respectively. Figure 5.24b also shows the evolution of the RA volume fraction as a function of the true strain. This image evidences the significant austenite to martensite transformation rate in DP1000A (TRIP effect), while this effect is barely seen in DP1000B. Both steel present quite similar mechanical properties in terms of strength and elongation, being slightly superior for DP1000A. As shown in Paper IV, DP1000A also shows superior strain hardening behaviour. On the other hand, they show very different cracking behaviour. DP1000B exhibits significantly higher fracture toughness at crack initiation (w_e^i) and the overall fracture toughness (w_e) is practically the double than for DP1000A.

These differences between the tensile properties and the crack propagation resistance of these two steels are mainly attributed to three factors: 1) volume fraction of fresh martensite/retained austenite, 2) proportion of ferrite in the matrix and 3) connectivity of the hard secondary phases. The larger RA volume fraction in DP1000A and the TRIP effect (Figure 5.24b) improves the strain-hardening behaviour and contribute to increase strength and elongation. On the other hand, as mentioned in the previous section, the transformation of austenite to martensite in DP1000A

can have a detrimental effect on fracture toughness due to the formation of a continuous network of hard bainite/tempered martensite and untempered fresh martensite ahead of the crack tip. This effect increases the connectivity of the hard phases and facilitates crack propagation. In the case of DP1000B, the greater presence of soft regions which a greater ability to accommodate plastic deformation slow down the crack propagation and increase the fracture toughness.

More details about the fracture mechanisms and the crack propagation path in both DP steels are available in Paper IV. A fractographic analysis is also included.

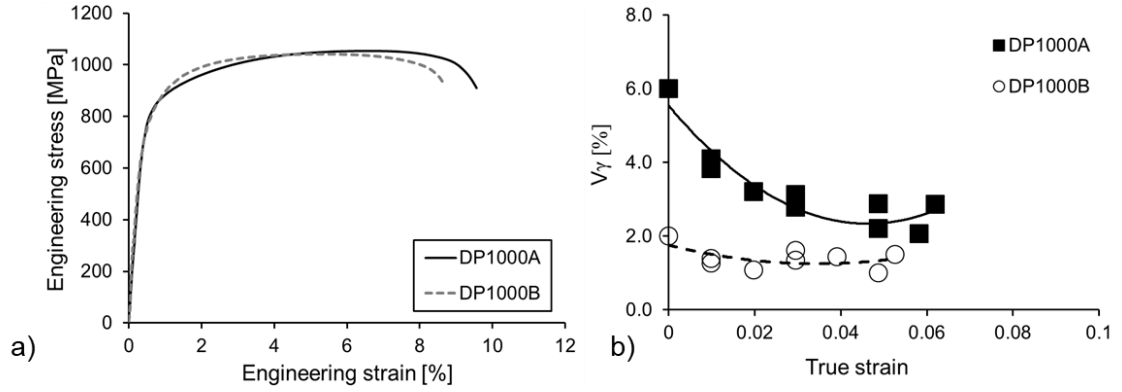

Figure 5.24. a) Engineering stress-strain curves and **b)** evolution of the RA volume fraction with deformation.

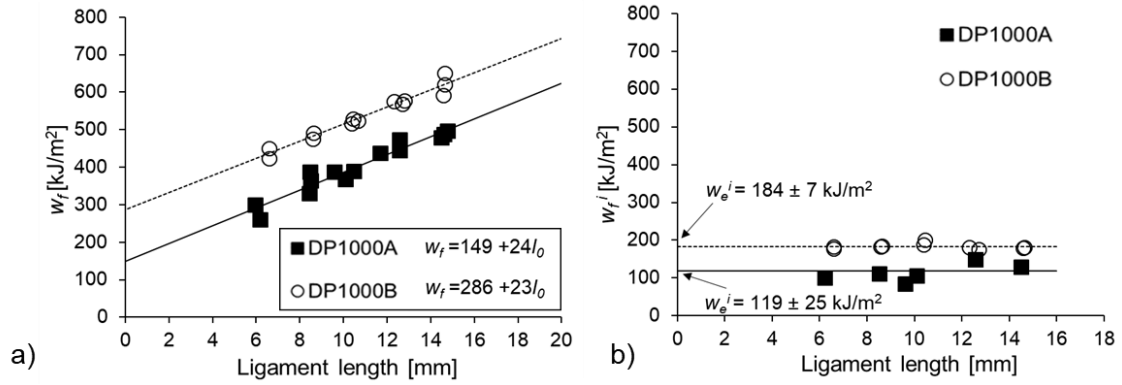

Figure 5.25. EWF results. **a)** w_f as a function of the ligament length. b) w_f^i for different ligament lengths and average w_e^i value.

5.4.2 Retained austenite transformation during crack propagation in TRIP-assisted steels

Owing to their superior strength and formability, 3rd Generation TRIP-assisted steels containing RA have become excellent candidates for substituting 1st Generation AHSS. This fact has focused the research efforts in the development of new steel grades belonging to this family. However, as evidenced in previous sections, understanding the role of the martensitic transformation on cracking resistance is of high importance.

To accurately evaluate the evolution of the RA volume fraction with deformation is important to select the most adequate technique. RA volume fraction can be evaluated by different techniques such as EBSD or magnetization saturation measurements. However, in EBSD measurements, specimen preparation is critical and, as observed in the previous section and reported in different works [178.179], often the RA content is underestimated. In highly deformed zones, like in the areas surrounding the crack tip, this differentiation is even more difficult. On the other hand,

magnetic measurements provide more accurate quantification of RA volume fraction. Nevertheless, whereas they are very useful to evaluate an overall RA content in relatively large areas (such as in tensile specimens), they are not suitable enough to evaluate local variations in RA volume fraction.

In this work, the RA to martensite transformation during crack propagation has been investigated in three 3rd Generation TRIP-assisted steels (TBF, TBF/Q&P and Q&P) by means of ex-situ X-ray powder diffraction measurements performed at ALBA Synchrotron. As explained in *Section 3.5.3*, the measurements were performed in DENT specimens tested to different load-line displacements (1 specimen per deformation level). 4 deformation stages were defined as indicated in Table 5.3 (a schematic representation is given in Figure 3.18). Table 5.3 also shows the specimen designations used and the corresponding load-line displacement and load.

Table 5.3. Definition of the different deformation stages studied.

Material	Specimen designation	Stage definition	Load-line displacement [mm]	Load [N]
TBF	TBF St 0	No deformation	0.00	0
	TBF St 1	Before initiation	0.09	14444
	TBF St 2	Initiation	0.195	20826
	TBF St 3	Before fracture	0.513	17730
TBF/Q&P	TBF/Q&P St 0	No deformation	0.00	0
	TBF/Q&P St 1	Before initiation	0.098	16592
	TBF/Q&P St 2	Initiation	0.251	25090
	TBF/Q&P St 3	Before fracture	0.426	23130
Q&P	Q&P St 0	No deformation	0.00	0
	Q&P St 1	Before initiation	0.117	14781
	Q&P St 2	Initiation	0.250	21923
	Q&P St 3	Before fracture	0.408	21383

For each specimen, 3 consecutive measurements separated 3.5 mm were performed close to the crack tip. Each measurement corresponds to a region identified as Zone I (crack tip), Zone II (≈ 5 mm ahead of the crack tip) and Zone III (centre of the ligament). These consecutive measurements allow detecting small variations in the martensitic transformation rate due to the strain gradients generated at the crack tip (Figure 5.26). Since the stress is higher at the crack tip and decreases with increasing the distance from the crack tip, the transformation rate should also increase in the near tip region.

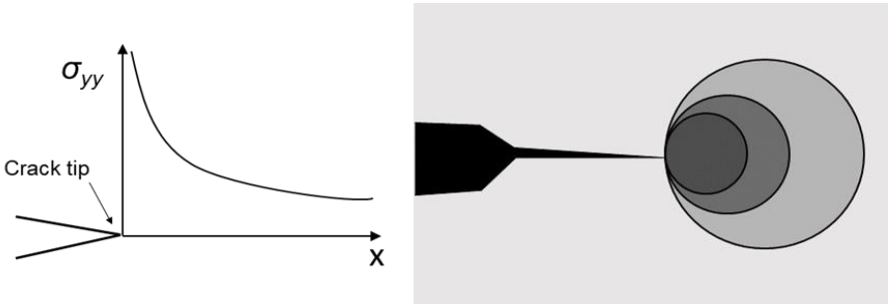

Figure 5.26. Schematic representation of the stress field at crack tip (left) and strain gradients near the crack tip (right).

The results obtained in this study are part of a publication currently under preparation. Some of the main results are shown and discussed below. Figure 5.27 to Figure 5.29 show the diffraction patterns obtained for the TBF, TBF/Q&P and Q&P at the different stages of deformation. The Miller indices (hkl) of planes corresponding to the austenite phase are indicated. For better visualization, an offset has been applied to the diffractograms of the different stages. The austenite phase fraction was derived from Rietveld refinements of the diffraction data, as described in *Section 3.5.3*.

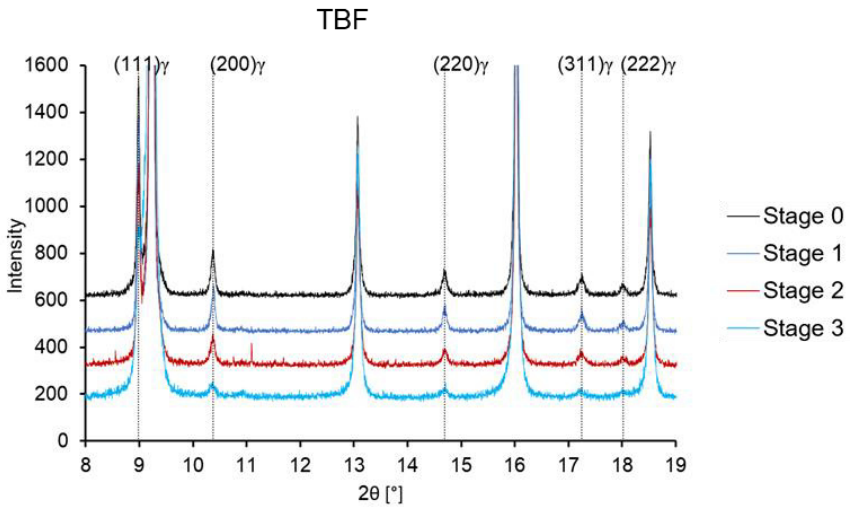

Figure 5.27. X-ray diffraction patterns for TBF. Results for Zone I.

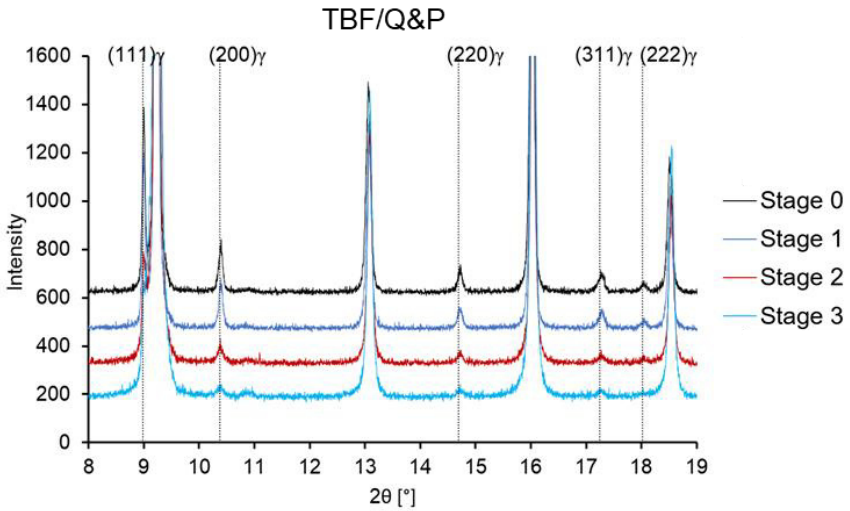

Figure 5.28. X-ray diffraction patterns for TBF/Q&P. Results for Zone I.

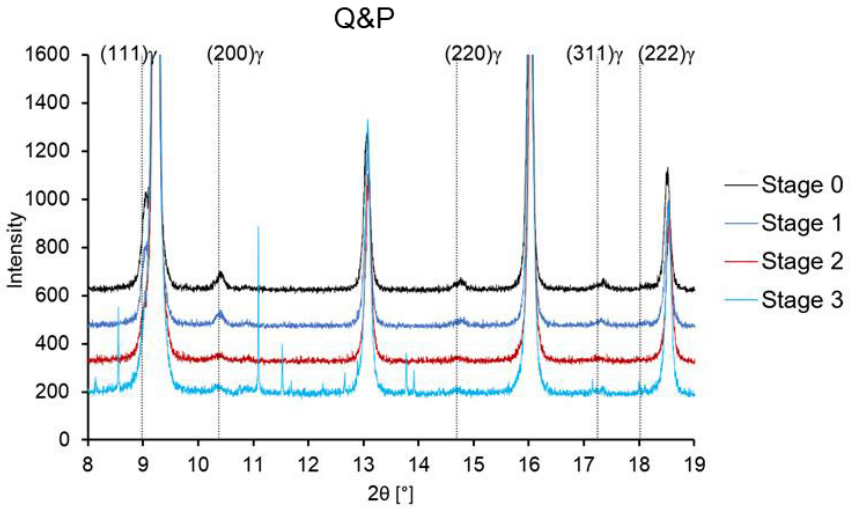

Figure 5.29. X-ray diffraction patterns for Q&P. Results for Zone I.

The RA volume fractions obtained for the different stages and for the different positions respect to the crack tip are shown in Figure 5.30 to Figure 5.32. At stage 1, only Q&P shows a slight decrease in RA volume fraction respect to the initial RA content ($V_{\gamma 0}$). The Q&P steel shows the highest transformation rate (i.e. lower RA stability) and most of the RA is consumed before crack initiation (Stage 2). In TBF/Q&P, also a great part of the RA is transformed at Stage 2. However, TBF is still showing a significant amount of untransformed RA (7.5%), which indicates greater mechanical stability of RA. At the end of the propagation (Stage 3), most of the RA has been transformed in the 3 steels. As mentioned before, it can be observed that the transformation rate decreases with increasing the distance from the crack tip (from Zone 1 to Zone 3).

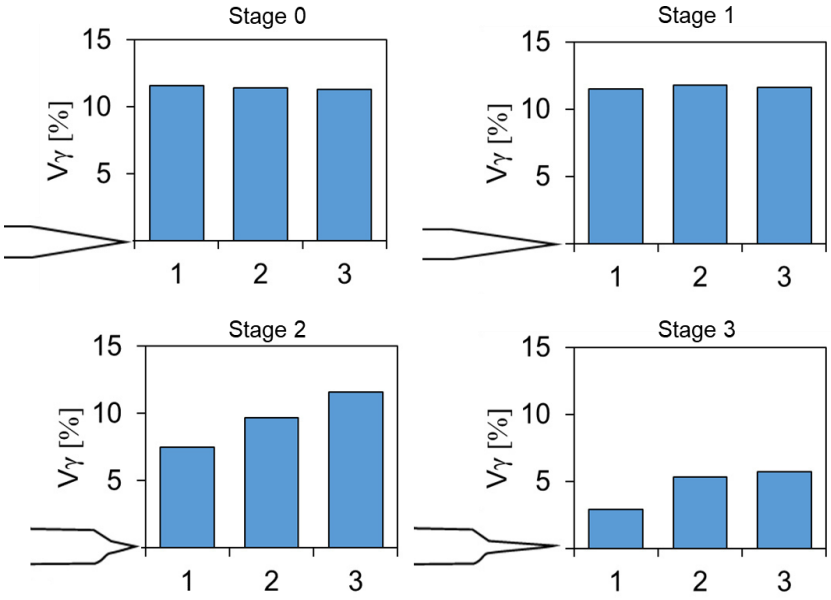

Figure 5.30. TBF.RA volume fraction obtained for the different stages. The positions 1,2 and 3 correspond to the different measurement Zones (see the text for details).

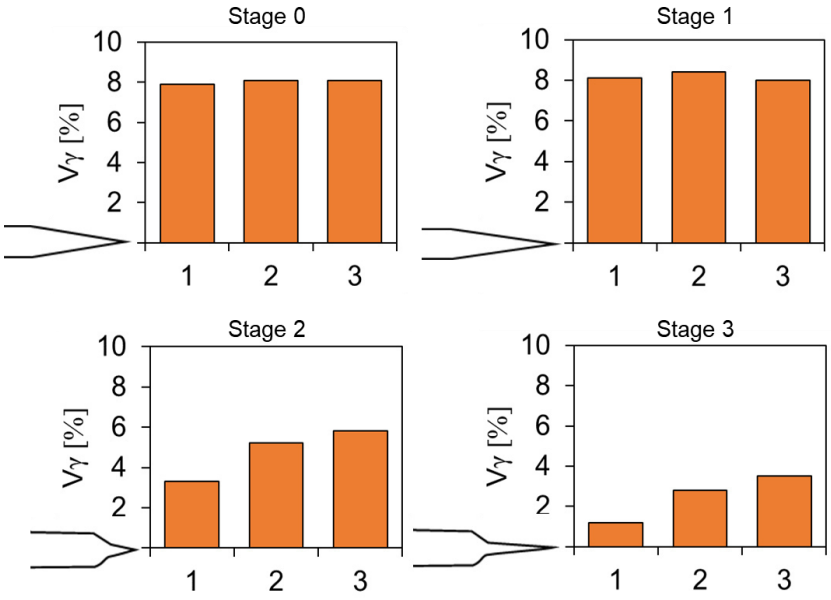

Figure 5.31. TBF/Q&P.RA volume fraction obtained for the different stages. The position 1,2 and 3 correspond to the different measurement Zones (see the text for details).

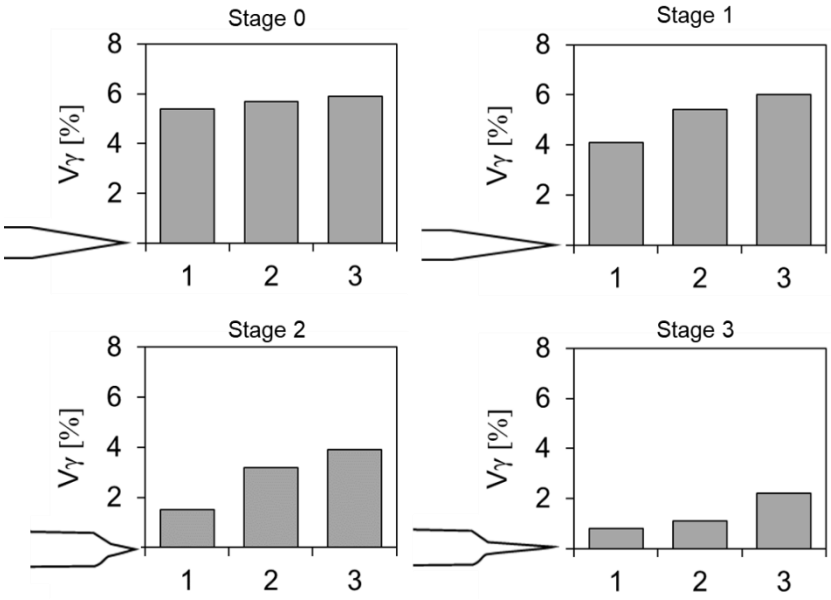

Figure 5.32. Q&P.RA volume fraction obtained for the different stages. The positions 1,2 and 3 correspond to the different measurement Zones (see the text for details).

The different RA to martensite transformation rates observed in the three steels are in good agreement with the RA mechanical stability determined from uniaxial tensile tests (Figure 5.33a), i.e. TBF has the highest stability, Q&P the lowest and TBF/Q&P is an intermediate range. However, comparing the RA volume fraction as a function of the deformation in tensile and DENT specimens (Figure 5.33 b-d), it can be observed that the transformation rate is much higher in DENT specimens. This is caused by the large stress triaxiality at the crack tip, which promotes the mechanically-induced transformation at much lower levels of deformation [176].

From the analysis of the contribution of RA transformation to crack propagation resistance (Figure 5.34), no relation is observed between the amount of RA consumed during crack propagation and the difference between w_e^i and w_e. The TBF steel shows a significant amount of

untransformed RA at crack initiation (stage 2) that progressively transforms during propagation (stage 3). However, looking at fracture toughness results, no significant contribution from crack propagation resistance after crack initiation is observed. On the other hand, TBF/Q&P shows the largest differences between w_e and w_e^i but the amount of RA transformed during the propagation is much lower than in TBF.

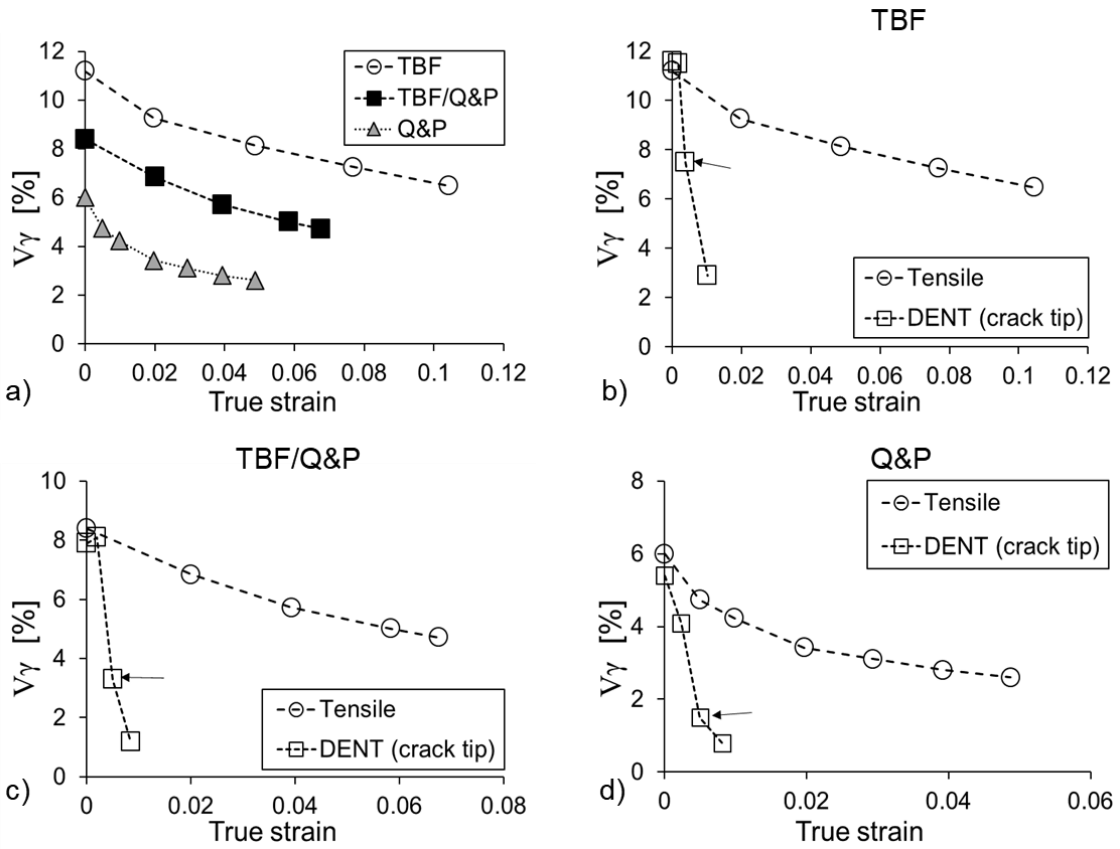

Figure 5.33. a) Evolution of RA volume fraction (Vγ) with deformation in tensile tests (results from magnetic measurements). **b-d)** Comparison of the evolution of RA content with deformation in tensile and DENT specimens (Zone I). The arrows indicate the strain corresponding to crack initiation.

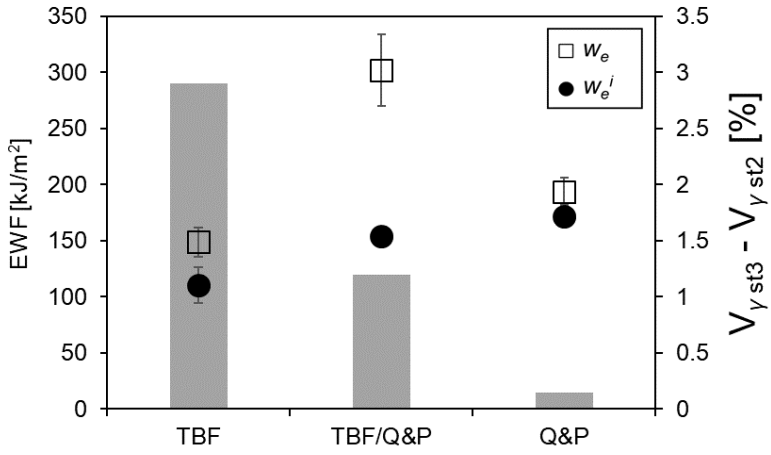

Figure 5.34. RA volume fraction transformed during crack propagation (Vγ st3- Vγ st2) and difference between crack initiation (w_e^i) and crack propagation resistance (w_e).

5.5 AHSS classification according to cracking resistance

The findings obtained in this work evidence that new failure criteria accounting for crack propagation resistance are increasingly necessary to better understand the overall fracture performance of AHSS sheets. According to this, and analogously to the global/local formability maps proposed by Hance and Davenport [52] or Heibel et al. [66], an alternative classification map is proposed in Paper II (Figure 5.35a). In this diagram, uniform elongation (*UE*) is plotted in the horizontal axis and the specific essential work of fracture (w_e) in the vertical axis. *UE* and w_e are used, respectively, as global formability and cracking resistance indices. On that basis, the diagram is divided into different quadrants according to the global formability and cracking resistance level. The more to the right the greater the global formability while upper quadrants indicate superior fracture resistance and damage tolerance.

Additionally, an alternative diagram to the traditional "banana" plot (Figure 1.3) is also shown in Figure 5.35b. This classification system provides a more precise description of the fracture resistance of AHSS as a function of their strength level and can serve as a guide for future steel development and material selection.

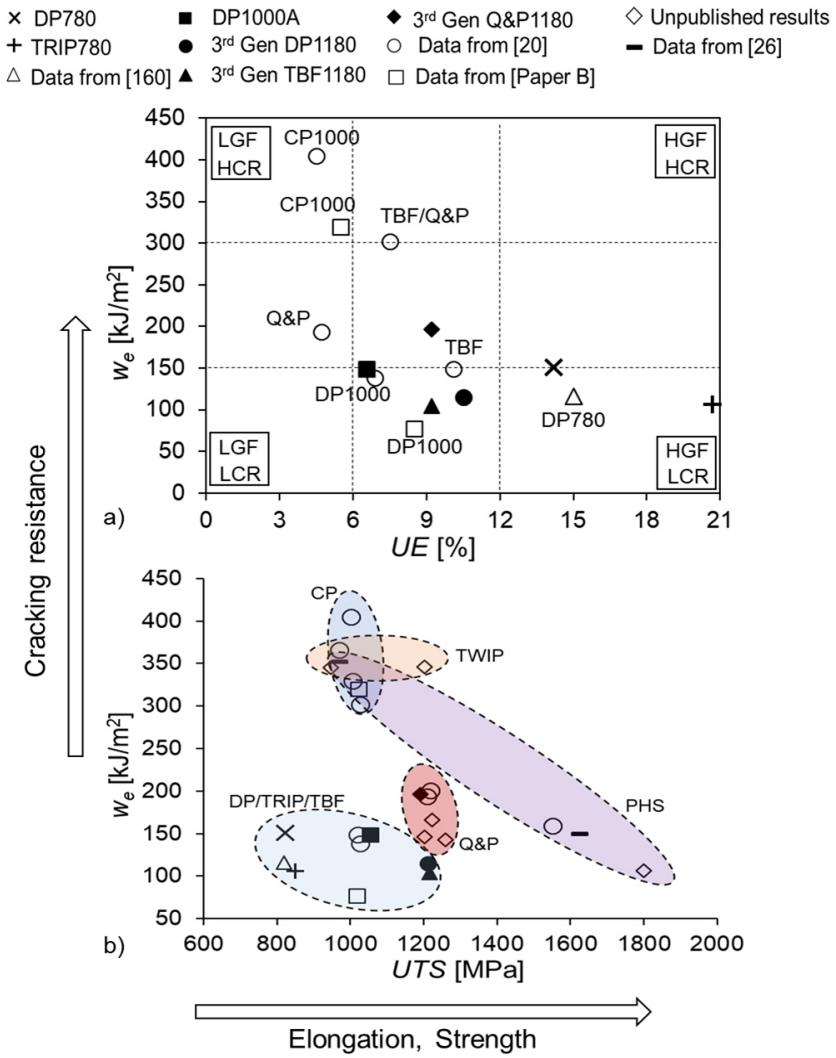

Figure 5.35. a) AHSS classification based on global formability (*UE*) and fracture resistance (w_e). LGF: low global formability, LCR: low cracking resistance, HGF: high global formability, HCR: high cracking resistance. **b)** Proposed diagram for classification of AHSS according to their strength level (*UTS*) and fracture resistance (w_e).

Chapter 6

Conclusions and future work

6.1 Conclusions

In this thesis, the crack initiation and propagation resistance of a wide range of advanced high strength steel sheets has been studied in the frame of fracture mechanics. The relationship between fracture toughness results and fracture behaviour in cold forming (edge cracking) and during crash has been investigated. The conclusions reached from these investigations are listed below.

Plane stress fracture toughness characterization methods

Different fracture toughness testing methods including the Essential Work of Fracture (EWF) methodology, *J*-integral measurements according to ASTM E1820 and Kahn-type tear tests (KTT) have been used to evaluate the crack initiation and propagation resistance of AHSS sheets. From the comparison of the different fracture toughness methodologies and the obtained parameters, it is concluded that:

- The EWF method is applicable to evaluate the crack initiation and propagation resistance of AHSS. The fulfilment of the conditions for obtaining a valid specific essential work of fracture (w_e) has been validated by means of DIC and stress analysis.
- The estimation of stress levels in DENT specimens and the relationship between w_e and δ_c are significantly improved using an effective yield strength (σ_Y) as defined in ASTM E1820 instead of the conventionally defined yield stress (σ_{YS}).
- The ASTM E1820 can be applied to evaluate the *J*-integral of thin AHSS sheets if the thickness restrictions described in the standard are dismissed. An alternative method for online crack growth measurement based on high-resolution video extensometry is proposed. With this method, crack length estimation from compliance technique is avoided.
- The ASTM B871, developed for tear testing of aluminium alloys by using Kahn-type tear tests, has shown to be applicable to characterize the tearing resistance of thin AHSS sheets.
- The values of fracture toughness at crack initiation are shown to be independent of the testing methodology and the specimen geometry used. The identified crack initiation resistance parameters w_e^i, J_i and *UIE* are found to be equivalent.
- w_e has been shown to better quantify the crack propagation resistance of thin high strength sheets than J_c. w_e contains both the energy dissipated during crack initiation and crack propagation to failure, whereas J_c only has an energetic contribution from small crack extension and does not account for the complete fracture resistance. *J*-R curves are also unsuitable to represent the intrinsic fracture toughness of the material because they also include an extrinsic contribution from the plastic work dissipated out of the FPZ.
- The additional contribution to the essential work of fracture developed in the FPZ after crack initiation comes mainly from necking. Thus, materials developing remarkable necking during crack propagation have greater crack propagation resistance. This has been verified by means of thickness strain measurements in the fracture surface of DENT specimens.

- This necking contribution to fracture resistance explains the thickness dependence of w_e (and of plane stress fracture toughness in general).
- For materials that show a large contribution of crack propagation resistance after initiation, a single crack initiation resistance parameter is very conservative and clearly underestimates the overall fracture resistance
- *UPE* values from KTT completely overestimate crack propagation resistance, since they include an energetic contribution from the plastic work dissipated in the outer zone of the FPZ. Therefore, *UPE* cannot be considered a material property and gives inappropriate toughness ranking. On the other hand, the major strain at fracture in the notch tip ($\varepsilon_{f\,KTT}$) measured by DIC has shown to better correlate with toughness values from essential work of fracture.

Influence of testing variables on fracture toughness

The analysis of the effect of notch radius on EWF and the influence of specimen geometry in *J*-integral measurements lead to the following conclusions:

- Notch root radius has a significant influence on EWF measurements. In order to obtain accurate and reliable fracture toughness values, fatigue pre-cracked specimens must be used. Otherwise, the measured toughness values overestimate the real crack initiation and propagation resistance of the material.
- Alternatively, a new rapid notching procedure for obtaining crack-like sharp notches has been introduced. The toughness values obtained from specimens prepared with this method are equivalent to those obtained with fatigue pre-crack specimens. This method is an interesting alternative to avoid fatigue pre-cracking operations for fracture toughness characterization of high strength metal sheets.
- The specimen geometry has no influence on the determination of the *J*-integral at crack initiation (J_i) and near the onset of stable crack propagation (J_c). On the other hand, a significant influence has been observed in the *J*-resistance curves. This is attributed to the different crack tip constraint for the investigated geometries

Relationship between fracture toughness and tensile properties

From the investigation on the relationship between fracture toughness and uniaxial tensile properties, it is observed that:

- Fracture toughness cannot be estimated from conventional uniaxial tensile properties. No correlation is found between the specific essential work of fracture and *UTSxTE* product, which is often used as a toughness indicator, elongation values or strain hardening exponent.
- Local fracture strain measurements (*TFS*, *TTS*) offer a better estimation of fracture resistance. However, they cannot accurately describe the fracture behaviour in the presence of cracks. Therefore, fracture toughness, understood as the material's crack initiation and propagation resistance must be appropriately measured in the frame of fracture mechanics.

Application of fracture toughness to understand fracture performance of AHSS

The correlation between fracture toughness and edge cracking resistance, measured in terms of HER and fracture strains in hole tension tests ($\varepsilon_{f\ HTT}$), has shown that:

- The specific essential work of fracture (w_e) shows a very good linear relationship with HER. Therefore, w_e is a suitable property for edge fracture prediction. This is attributed to the similarity of the fracture mechanisms governing these fracture modes.
- The HER is related to the crack propagation resistance (w_e) rather than to crack initiation (w_e^i, J_i), since it is defined according to a crack that has been grown a distance of the order of the sheet thickness.
- The similar fracture mechanisms present in hole expansion and fracture toughness teste are further evidenced when comparing the true thickness strain in both test configurations (TTS_{DENT} and TTS_{HET}). The equivalence between these parameters allows establishing an objective and physically motivated fracture criterion for edge-cracking prediction.
- Hole Tension Tests (HTT) are suitable to evaluate edge formability and investigate the influence of punching parameters on edge fracture resistance. The results from HTT are in good agreement with the obtained in Hole Expansion Tests (HET) and EWF tests. The trend shows that tougher steels present better edge formability and, overall, they are less sensitive to punching clearance.

EWF results have been correlated to the fracture behaviour of AHSS under impact conditions, evaluated by means of axial and bending impact resistance tests. The investigations have shown that:

- The axial crash resistance of AHSS and PHS can be evaluated according to the cracking behaviour of crash-tested samples. The amount of cracking is defined by the so-called crash index (CI). A new parameter, the crash index decreasing rate (CIDR) has been introduced in this work to describe the overall crack propagation resistance of AHSS under impact loading.
- The evaluated CIDR values for the different investigated steels show a very good correlation with w_e, i.e. steels with higher fracture toughness exhibit a lower degree of cracking during impact tests and, thus, better crash performance.
- Similarly to that observed in edge fracture resistance tests, initiation toughness values are not sufficient to describe the overall crash resistance.
- In bending crash tests, steels showing higher fracture toughness did not present cracking. A threshold toughness value, above which bending crash specimens are safe of cracks, is found.
- According to the above conclusions, w_e is proposed as a relevant material property to rationalize the crash behaviour of AHSS and to design improved crash-resistant microstructures.

Influence of microstructure on fracture toughnes of AHSS

The investigations on the influence of microstructure on the fracture toughness of AHSS revealed that:

- In general, more homogeneous (CP-like) microstructures show higher fracture toughness than DP-like ones. This is attributed to the deformation mechanisms of DP-like steels, which improve strain hardening and elongation (global ductility) but have a negative influence on fracture toughness.
- Something similar occurs in TRIP-assisted steels containing RA. The TRIP effect is known to have a beneficial influence on strength and ductility. However, due to the high stress triaxiality at the front of the crack tip, the RA to martensite transformation rate increases significantly and cracking resistance is reduced due to a "brittle" network effect created by the newly formed martensite.
- The study on the evolution of RA volume fraction during crack propagation resistance confirms that for common ranges of RA content (6-8%) and stability, most of the RA is transformed before crack initiation. For larger RA volume fraction (11%) and stability, a significant amount of RA can be available for crack propagation. However, the transformation of this residual austenite has no contribution to crack propagation resistance. Further investigations should be performed to better understanding the influence of RA content, morphology and stability in crack propagation resistance of TRIP-assisted steels.
- These results highlight that microstructural design must not be only based on tensile properties but also on crack initiation and propagation resistance parameters.

Finally, and based on these findings, a new classification system, considering global ductility (*UE*) and fracture toughness (w_e), is proposed for a more exhaustive description of the overall formability and fracture behaviour of AHSS. The proposed diagram can be useful for improved AHSS performance ranking and can serve as a guide for new material development.

6.2 Future work

The work carried out in this thesis open a wide range of research opportunities in both academic and industrial sectors. Some plausible future research lines are suggested below (some of them are part of ongoing research at Eurecat):

Experimental testing variables

Some of the variables affecting the measurement of fracture toughness have been discussed. The influence of different testing parameters (testing speed, specimen geometry, ligament length range, notch radius etc.) should be evaluated in greater detail.

Alternative standard methods

This work has been mainly focused on the application of the EWF methodology and other methods like the *J*-integral and the Kahn-type tear tests. The use of alternative standard methods and fracture parameters, such as the ISO 22889 and the CTOA, could be also considered in future works.

New rapid notching procedure

The influence of different variables affecting the notch preparation method (punch wear, cutting clearance, etc.) should be further investigated. In addition, the limitations regarding sheet thickness and strength level must be identified.

Thickness dependence of plane stress ductile fracture

Few studies have addressed the influence of sheet thickness on plane stress fracture toughness of ductile materials. Additional investigations should be focused on this topic.

Microstructural and processing effects on fracture resistance

More work is necessary to better understand the effect of different processing parameters (anisotropy, amount and distribution of inclusions, etc.) and microstructural features (phase volume fraction, morphology, distribution, etc.) on crack propagation resistance.

Implementation of fracture toughness criteria for sheet metal fracture modelling

The specific essential work of fracture has shown to be a suitable tool to predict edge formability. Then, the implementation of an EWF-based fracture criterion in FEM modelling for edge fracture simulations could be very interesting to improve the accuracy of currently used models. Some insights have been provided in this work. However, further work is currently ongoing to develop a reliable edge fracture criterion that could be implemented in commercial FEM software.

EWF standardization for metallic materials

As mentioned in the text, there is no specific standard for the evaluation of the EWF and most of the research works found in literature follows the guidelines described in the ESIS protocol developed by the TC4 committee. However, this protocol is focused on the fracture testing of polymers and composites. Therefore, the development of a reference document for evaluating the EWF in thin high strength metal sheets, including limitations, specimen preparation, testing conditions and data processing might be very useful to boost the application of the method.

References

[1] S. Keeler, M. Kimchi, P.J. Mooney: Advanced High-Strength Steels Application Guidelines, version 6.0 2017.

[2] WorldAutoSteel. (2011) FutureSteelVehicle – Final engineering report.https://steel.org/~/media/Files/Autosteel/Programs/FutureSteelVehicle/FSV%20-%20Final%20Engineering%20Report.pdf

[3] WorldAutoSteel. 61% Advanced High-Strength Steel Adds Stability and Safety to the 2021 Kia Seltos. https://www.worldautosteel.org/kia-seltos/

[4] A. Abraham. Metallic Material Trends in North American Light Vehicles. PowerPoint presentation in Great Designs in Steel seminar *2015.*

[5] E. Billur, T. Altan. Three generations of advanced high-strength steels for automotive applications. Part I, The first generation. *Stamping Journal* (2013) 16-17

[6] E. Billur, J. Dykeman, T. Altan. Three generations of advanced high-strength steels for automotive applications. Part II, The second generation. *Stamping Journal* (2014) 12-13.

[7] F. Caballero, M.J. Santofimia, C. García-Mateo, J. Chao, C. García de Andrés. Theoretical design and advanced microstructure in super HSS. *Mater. Des.* 30 (2009) 2077.

[8] C. Garcia-Mateo, F.G. Caballero, T. Sourmail, M. Kuntz, J. Cornide, V. Smanio, R. Elvira. Tensile behaviour of a nanocrystalline bainitic steel containing 3 wt% Si. *Mater. Sci. Eng. A* 549 (2012) 185-192.

[9] D. Krizan, K. Steineder, S. Kaar, T. Hebesberger. Development of third generation advanced high strength steels for automotive applications. 19th international scientific conference Transfer 2018, Trencianske Teplice (Slovakia).

[10] C. Liu, Q. Peng, Z. Xue, S. Wang, C. Yang. Microstructure and Mechanical Properties of Hot-Rolled and Cold-Rolled Medium-Mn TRIP Steels. *Materials* 2018, 11, 2242.

[11] H.L. Yi. Review on δ-Transformation-Induced Plasticity (TRIP) Steels with Low Density: The Concept and Current Progress. *JOM: the journal of the Minerals, Metals & Materials Society* 66 (2014) 1759-1769.

[12] D. Raabe, D. Ponge, O. Dmitrieva, B. Sander. Nanoprecipitate-hardened 1.5 GPa steels with unexpected high ductility. *Scripta Materialia* 60 (2009) 1141–1144.

[13] M.H. Saleh, R. Priestner. Retained austenite in dual–phase silicon steels and its effect on mechanical properties. *J Mater Process Tech* 113 (2001) 587-593.

[14] C.A.N. Lanzillotto, F.Pickering. Structure–property relationships in dual-phase steels. Met Sci 16 (8) (1982) 371-382.

[15] N. Fonstein. Dual Phase steels. In: R.Rana, S.B Singh (Eds.), *Automotive steels*, chapter 7. Woodhead publishing (2017) 169-217.

[16] M.F. Ashby. Work hardening of dispersion-hardened crystals. *Philos Mag* 14 (132) (1966) 1157-1178.

[17] J. Hall, J. Coryell, B. Wendt, D. Adamski. Case Studies of Edge Fracture of Dual Phase Steel Stampings. *SAE Int. J. Mater. Manf.* 8 (2015) 783-788.

[18] C.R.M. Silva, F.J.G. Silva, R.M. Gouveia. Investigations on the edge crack defect in Dual Phase steel stamping process. *Procedia manuf* 17 (2018) 737-745.

[19] A. Karelova, C. Krempaszky, E. Werner, P. Tsipouridis, T. Hebesberger.A. Pichler. Hole Expansion of Dual-phase and Complex-phase AHS Steels - Effect of Edge Conditions. *Steel Res Int* 80 (2009) 71-77.

[20] D. Casellas, A. Lara, D. Frómeta, D. Gutiérrez, S. Molas, Ll. Pérez, J. Rehrl, C. Suppan.

Fracture Toughness to Understand Stretch-Flangeability and Edge Cracking Resistance in AHSS. *Metall Mater Trans A 48* (2017) 86-94.

[21] K. Sugimoto, M. Mukherjee. TRIP aided and complex phase steels. In: R.Rana, S.B Singh (Eds.), *Automotive steels*, chapter 8. Woodhead publishing (2017) 217-257.

[22] T.B.Hilditch, T.de Souza, P.D.Hodgson. Properties and automotive applications of advanced high-strength steels (AHSS). In: M. Shome, M. Tumuluru (Eds.), *Welding and Joining of Advanced High Strength Steels (AHSS)*, chapter 2. Woodhead Publishing (2015) 9-28.

[23] N. Fonstein, H.J. Jun, G. Huang, S. Sriram, B. Yan. Effect of Bainite on Mechanical Properties of Multiphase Ferrite-Bainite-Martensite Steels. *Proceedings from the Materials Science & Technology Conference*, October 16-20, 2011, Columbus, Ohio

[24] A. Nagathan, L. Penter. Hot stamping. In: T.Altan, A. Tekkaya (Eds.), *Sheet Metal Forming Processes and Applications*, chapter 7. ASM International (2012) 133-142.

[25] L. Penter, N. Pierschel. Thermo-mechanical interactions in hot stamping. *Conference on Thermal Issues in Machine Tools* (Dresden, Germany, March 21-23, 2018).

[26] S. Golling, D. Frómeta, D. Casellas, P. Jonsén. Influence of microstructure on the fracture toughness of hot stamped boron steel. *Mat. Sci. and Eng. A* 743 (2019) 529-539.

[27] B. C. De Cooman, Kwang-geun Chin, Jinkyung Kim. High Mn TWIP Steels for Automotive Applications New Trends and Developments in Automotive System Engineering. Prof.Marcello Chiaberge, InTech (2011). https://doi.org/10.5772/14086

[28] R.E. Schramm, R.P. Reed. Stacking fault energies of seven commercial austenitic stainless steels. *Metall Mater Trans A* 6 (1975) 1345-1351.

[29] J.Speer, D.K. Matlock, B.C. De Cooman, J.G. Schroth. Carbon partitioning into austenite after martensite transformation. *Acta Mater*. 51 (2003) 2611–2622.

[30] D.V. Edmonds, K. He, F.C. Rizzo, B.C. De Cooman, D.K. Matlock, J.G. Speer. Quenching and partitioning martensite- A novel steel heat treatment. *Mat. Sci. and Eng.* A 438–440 (2006) 25–34.

[31] R.L. Miller. Ultrafine-grained microstructures and mechanical properties of alloy steels. *Metall Mater Trans* B 3 (1972) 905–912.

[32] H. Luo, J. Shi, C. Wang, W. Cao, X. Sun, H. Dong. Experimental and numerical analysis on formation of stable austenite during the intercritical annealing of 5Mn steel. *Acta Mater.* 59 (2011) 4002.

[33] M.J. Merwin. Low-Carbon Manganese TRIP Steels. *Mater. Sci. Forum*. 539–543 (2007) 4327.

[34] J. Shi, X. Sun, M. Wang, W. Hui, H. Dong, W. Cao. Enhanced work-hardening behavior and mechanical properties in ultrafine-grained steels with large-fractioned metastable austenite. *Scripta Mater*. 63 (2010) 815.

[35] S. Lee, S.J. Lee, B.C. De Cooman. Austenite stability of ultrafine-grained transformation-induced plasticity steel with Mn partitioning. *Scripta Mater*. 65 (2011) 225.

[36] Z.H. Cai, H. Ding, R.D.K. Misra, Z.Y. Ying. Austenite stability and deformation behavior in a cold-rolled transformation-induced plasticity steel with medium manganese content. *Acta Materialia* 84 (2015) 229-236.

[37] C. Liu, Q. Peng, Z. Xue, S. Wang, C. Yang. Microstructure and Mechanical Properties of Hot-Rolled and Cold-Rolled Medium-Mn TRIP Steels. *Materials* 11(11) (2018) 2242.

[38] L. Liu, B. He, M. Huang. The Role of Transformation-Induced Plasticity in the Development of Advanced High Strength Steels. *Adv. Eng. Mater.* (2018) 1701083.

[39] S. Kaar, D. Krizan, J. Schwabe, H. Hofmann, T. Hebesberger, C. Commenda, L. Samek. Influence of the Al and Mn content on the structure-property relationship in density reduced TRIP-assisted sheet steels. *Mat. Sci. and Eng. A* 735 (2018).

[40] H.L.Yi. Review on δ-Transformation-Induced Plasticity (TRIP) Steels with Low Density: The Concept and Current Progress. *JOM: the journal of the Minerals, Metals & Materials Society* 66 (9) 1759-1769.

[41] H. L. Yi, K. Y. Lee, H. K. D. H. Bhadeshia. Extraordinary ductility in Al-bearing δ-TRIP steel. *Proc. R. Soc. A* (2011) 467, 234–243.

[42] S. Chatterjee, M. Murugananth, H. K. D. H. Bhadeshiaet. δ-TRIP steel. *Materials Science and Technology* 23 (20007) No. 7 819-827.

[43] A. Konieczny, T. Henderson. On Formability Limitations in Stamping Involving Sheared Edge Stretching. *SAE Technical Paper 2007-01-0340*, 2007.

[44] K. Mori, Y. Abe, Y. Suzui. Improvement of stretch flangeability of ultra high strength steel sheet by smoothing of sheared edge. *J. Mater. Process. Tech.* 210 (2010) 653–659.

[45] C.R.M Silva, F.J.G. Silva, R.M. Gouveia. Investigations on the edge crack defect in Dual Phase steel stamping process. *Procedia manufacturing* 17 (2018) 737-745.

[46] M.S. Walp MS. Impact Dependent Properties of Advanced and Ultra High Strength Steel. *SAE Technical Paper* 2007-01-0342, 2007.

[47] P. Larour, H. Pauli, T. Kurz, T. Hebseberger. Influence of post uniform tensile and bending properties on the crash behaviour of AHSS and press-hardening steel grades. *Proceedings of the IDDRG2010* (Graz, Austria) 2010.

[48] P. Larour, J. Naito, A. Pichler, T. Kurz, T. Murakami. Side impact crash behavior of press-hardened steels-correlation with mechanical properties. *5th Int. Conf. Hot sheet metal forming of high performance steel (CHS2)* (Toronto, Canada, May 31- June 3 2015) pp 281-289.

[49] T.M. Link, B.M. Hance. Axial and Bending Crash Performance of Advanced High-Strength Steels. *Int. Symp. on New Developments in Advanced High-Strength Steels*. Keystone, Colorado, USA. 2017.

[50] F. Hisker, R. Thiessen, T. Heller. Influence of Microstructure on Damage in Advanced High Strength Steels. *Materials Science Forum* 706–709 (2012) 925–930.

[51] P. Efthymiadis, S. Hazra, A. Clough, R. Lakshmi, A. Alamoudi, R. Dashwood, B. Shollock. Revealing the mechanical and microstructural performance of multiphase steels during tensile, forming and flanging operations. *Mat. Sci. and Eng. A* 701 (2017) 174-186.

[52] B. Hance, M.D. Davenport. Advanced High Strength Steel: Deciphering Local and Global Formability. *Int. Automotive Body Congress 2016*, September 28-29, Dearborn, Michigan, USA.

[53] S. Kalpakjian, S. Schmid. Manufacturing Engineering and Technology, 6th edition. Prentice Hall, 2010.

[54] Y. Bao. Dependence of ductile crack formation in tensile tests on stress triaxiality, stress and strain ratios. *Eng. Frac. Mech.* 72 (2005) 505–522.

[55] Z. Marciniak, J.L. Duncan, S.J. Hu. Mechanics of sheet metal forming, 2nd edition. Butterworth-Heinemann, Oxford 2002.

[56] J. Hu, Z. Guo, N. Saunders. A computational approach for forming limit diagram (FLD) evaluation at elevated temperatures for aluminium alloys. *Proceedings of the 16th International Aluminum Alloys Conference (ICAA16)* (Montréal, Canada) 2018.

[57] ISO 12004-2:2008. Metallic Materials—Sheet and Strip–Determination of Forming-Limit Curves—Part 2: Determination of Forming-Limit Curves in the Laboratory. *International*

Standardization Organization (ISO). Geneva, Switzerland, 2008.

[58] G. Chinouilh, F. Toscan, P. Santacreu, J. Leseux. Forming Limit Diagram Prediction of Stainless Steels Sheets. *SAE Technical Paper* 2007-01-0338, 2007.

[59] M. Abspoel, M. E. Scholting, J. M. M. Droog. A new method for predicting Forming Limit Curves from mechanical properties. *J Mater Process Tech* 213 (2013) 759– 769.

[60] ISO 16630:2017. Metallic materials — Sheet and strip — Hole expanding test. *International Organization for Standardization*.

[61] E. Atzema, M. Borsutzki, M. Braun, S. Brockmann, M. Bülter, B. Carlsson, P. Larour, A. Richter. A European round robin test for the hole expansion test according to ISO 16630. *New Development in Sheet Metal Forming 2012 International Conference*. (Fellbach, Germany, May 23-24, 2012), pp. 171-184.

[62] M. Schneider, U. Eggers. Investigation on punched edge formability. *Proceedings of International Deep Drawing Research Group 2011 conference*. (Bilbao, Spain, June 5-8, 2014).

[63] VDA 238-100, Plate bending test for metallic materials. Verband der Automobilindustrie e.V.(VDA): Berlin, Germany, 2017.

[64] ASTM E8/E8M-15a (2015) Standard Test Methods for Tension Testing of Metallic Materials. ASTM International, West Conshohocken, PA, USA.

[65] P. Larour, J. Freudenthaler, T.Weissböck. Reduction of cross section area at fracture in tensile test: measurement and applications for flat sheet steels. *Journal of Physics: Conf. Series 896* (2017) 012073.

[66] S. Heibel, T. Dettinger, W. Nester, T. Clausmeyer, A.E. Tekkaya. Damage Mechanisms and Mechanical Properties of High-Strength Multiphase Steels. *Materials* 2018, 11, 761.

[67] B. Hance. Practical Application of the Hole Expansion Test. *SAE Int. J. Engines* 10(2):2017

[68] X. Chen, J. Sun, X. Zhu. Simulation Technique for Pre-forming of AHSS Edge Stretching *12th International LS-DYNA® Users Conference* (Michigan, USA, June 03-05) 2012.

[69] P. Larour, J. Freudenthaler, A. Grünsteidl, K.Wang. Evaluation of alternative stretch flangeability testing methods to ISO 16630 standard. *Proceedings of International Deep Drawing Research Group 2014 conference.* (Paris, France, June 1-4, 2014), pp.188-193.

[70] P. Larour, H. Schauer, J. Lackner, E.T. Till. Edge crack simulation with the modular "smiley" forming tool. *Proceedings of International Deep Drawing Research Group 2016 conference*. (Linz, Austria, June 12-15, 2016), pp.457-459.

[71] J. Dykeman, S. Malcolm, B. Yan, J. Chintaman, G.Huang, N. Ramisett, H. Zhu. Characterization of Edge Fracture in Various Types of Advanced High Strength Steel. *SAE Technical Paper* 2011-01-1058, 2011.

[72] K. Watanabe, M. Tachibana, K. Koyanagi and K. Motomura. Simple Prediction Method for the Edge Fracture of Steel Sheet During Vehicle Collision – Evaluation of Fracture Limit from the Edge Using Small-Sized Test Pieces. *5th LS-Dyna User Forum* (Ulm, Germany, October 12, 2006).

[73] M. Feistle, M. Krinninger, I. Pätzold,W.Volk. Edge-Fracture-Tensile-Test. In: Tekkaya A., Homberg W., Brosius A. (Eds.) *60 Excellent Inventions in Metal Forming*. Springer Vieweg, Berlin, Heidelberg (2015) 193-198.

[74] X. Wu, H. Bahmanpour, K. Schmid. Characterization of mechanically sheared edges of dual phase steels. *J. Mat. Proc. Tech.* 212 (2012) 1209-1224

[75] D. Gutiérrez, Ll. Pérez, A. Lara, D. Casellas, J.M. Prado. The influence of fracture toughness in stretch-flangeability in advanced high strength steels sheets. *Proceedings of the IDDRG 2013* (Zurich, Switzerland, June 02-05)

[76] Y. Takahashi, O. Kawano, Y. Tanaka. Fracture Mechanical Study on Edge Flange-ability of High Tensile-strength Steel Sheets. *MS&T 2009: Proceedings from the Materials Science & Technology Conference* (October 25-29, 2009, Pittsburgh, Pennsylvania) pp 1317-1328

[77] P. Larour, H. Pauli, J. Freudenthaler, A. Grünsteidl. Alternative stretch flangeability characterisation methods for AHSS steel grades. *Proceedings of International Deep Drawing Research Group 2011 conference.* (Bilbao, Spain, June 5-8, 2014).

[78] M. Feistle, R. Golle, W. Volk. Determining the influence of shear cutting parameters on the edge cracking susceptibility of high-strength-steels using the edge-fracture-tensile-test. *Procedia CIRP* 41 (2016) 1078 – 1083.

[79] S. Nasheralahkami, S. Golovashchenko, K. Pan, L. Brown, B. Gugnani. Characterization of Trimmed Edge of Advanced High Strength Steel. *SAE Technical Paper* 2016-01-0358, 2016

[80] J.I. Yoon, J. Jung, S.H. Joo, T.J. Song, K.G. Chin, M.H. Seo, S.J. Kim, S. Lee, H.S. Kim. Correlation between fracture toughness and stretch-flangeability of advanced high strength steels. *Matter.Lett.* 180 (2016) 322-326

[81] P. Larour, J. Lackner, L. Wagner. Influence of single hat crash box flange triggering and impactor top plate welding strategy on axial crash foldability of AHSS & UHSS sheets. *IOP Conf. Ser.: Mater. Sci. Eng.* 651 012023

[82] T. Kurz, P. Larour, J. Lackner, T. Steck, G. Jesner. Press-hardening of zinc coated steel – characterization of a new material for a new process. *Proceedings of International Deep Drawing Research Group 2016 Conference* (Linz, Austria, June 12-15, 2016).

[83] P. Dietsch, K. Tihay, S. Cobo, S. Sarkar, D. Hasenpouth, D. Cornette. Predictive approach for crash performance of Press Hardened Steels and its application on new product developments. *6th Int conf hot sheet metal forming of high performance steel (CHS2)* 2017.

[84] G. Lacroix, T. Pardoen, P.J. Jacques. The fracture toughness of TRIP-assisted multiphase steels. *Acta Mater*. 56 (2008) 3900–13.

[85] R. Wu, J. Li, W. Li , X.C. Wu, X. Jin, S. Zhou, L. Wang. Effect of metastable austenite on fracture resistance of quenched and partitioned (Q&P) sheet steels. *Mater. Sci. Eng. A* 657 (2016) 57–63.

[86] S. Sahoo, N. Padmapriya, P. S. De, P.C. Chakraborti, S.K. Ray. Ductile tearing resistance indexing of automotive grade DP590 steel sheets: EWF testing using DENT specimens. *J. Mater. Eng. Perform.* 27 (2018) 2018–23.

[87] Z.C. Luo, R.D. Liu, X. Wang, M.X. Huang. The effect of deformation twins on the quasi-cleavage crack propagation in twinning-induced plasticity steels. *Acta Mater.* 150 (2018) 59–68.

[88] M. Faccoli, G. Cornacchia, M. Gelfi, A. Panvini, R. Roberti. Notch ductility of steels for automotive components. *Eng. Frac. Mech*. 127 (2014) 181–193

[89] Z. Xiong, P.J. Jacques, A. Perlade, T. Pardoen. Ductile and intergranular brittle fracture in a two-step quenching and partitioning steel. *Scripta Mater*. 157 (2018) 6–9.

[90] Z. Xiong, P.J. Jacques, A. Perlade, T. Pardoen. Characterization and Control of the Compromise Between Tensile Properties and Fracture Toughness in a Quenched and Partitioned Steel. *Metall. and Mat. Trans. A* 50 (2019) 3502-3513.

[91] R. Sarkara, S.K. Chandra, P.S. De, P.C. Chakraborti, S.K. Ray. Evaluation of ductile tearing resistance of dual-phase DP 780 grade automotive steel sheet from essential work of fracture (EWF) tests. *Theor Appl Fract Mec* 103 (2019) 102278.

[92] D. Broek. Elementary engineering fracture mechanics. Springer Netherlands 1982. DOI 10.1007/978-94-009-4333-9.

[93] A. Griffith. The Phenomena of Rupture and Flow in Solids. *Philosophical Transactions of Royal Society A* 221 (1921) 163.

[94] C.E. Inglis. Stress in a Plate Due to the Presence of Cracks and Sharp Corners. *Transactions of the Institute of Naval Architects* 55 (1913) 219.

[95] J.R. Rice. A path independent Integral and the Approximate Analysis of Strain Concentrations by Notches and Cracks. *Journal of Applied Mechanics* 34 (1968) 379.

[96] J.R. Rice, G.F. Rosengren. Plane Strain Deformation Near a Crack Tip in a Power-law Hardening Material. *Journal of the Mechanics and Physics of Solids* 16 (1968) 1-12.

[97] J.W. Hutchinson. Singular Behavior at the End of a Tensile Crack in a Hardening Material Journal of the Mechanics and Physics of Solids 16 (1968) 13-31.

[98] G.R. Irwin. Fracture Dynamics. *In: Fracturing of Metals*; American Society of Metals: Cleveland, 1948.

[99] E. Orowan. Fracture strength of solids. *In: Report on Progress in Physics, Vol. 12*; Physical Society of London: London, 1949 185–232.

[100] H.M. Westergaard. Bearing pressures and cracks. *Trans. ASME J. Appl. Mech*. 6 (1939) 49–53

[101] T.L. Anderson. Fracture mechanics: fundamentals and applications. 3rd ed. CRC Press; 2005

[102] C.H.Wang. Introduction to Fracture Mechanics. (1996) DOI:10.13140/RG.2.1.1444.2408

[103] Fracture toughness properties of aerospace materials. In: A. P. Mouritz (Ed.), *Introduction to Aerospace Materials*, chapter 19. Woodhead publishing (2012) 454-468.

[104] ASTM E399-90. Standard test method for fracture toughness of metallic materials. American Society for Testing and Materials. Philadelphia, EEUU 1990.

[105] J.L. Arana, J.J. González. Mecánica de fractura. Servicio editorial Universidad del País Vasco.

[106] A.A. Wells. Unstable Crack Propagation in Metals: Cleavage and Fast Fracture. *Proceedings of the Crack Propagation Symposium*, Vol. 1, Paper 84, Cranfield, UK, 1961.

[107] C.T. Sun, Z.-H. Jin. Elastic-Plastic Fracture Criteria. In: C.T. Sun, Z.-H. Jin (Eds.), *Fracture Mechanics*, chapter 7. Academic Press (2012) 171-187.

[108] J.A. Begley, J.D. Landes. The J-Integral as a Fracture Criterion. ASTM STP 514, American Society for Testing and Materials, Philadelphia, PA, (1972) 1–20.

[109] J.D. Landes, J.A. Begley. The Effect of Specimen Geometry on JIc. ASTM STP 514, American Society for Testing and Materials, Philadelphia, PA, (1972) 24–29.

[110] C.F. Shih. Relationship between the J-Integral and the Crack Opening Displacement for Stationary and Extending Cracks. *Journal of the Mechanics and Physics of Solids*, 29 (1981) 305–326.

[111] ASTM E1820. Standard test method for measurement of fracture toughness. American Society for Testing and Materials.

[112] ASTM E2472. Standard test method for determination of resistance to stable crack extension under low-constraint conditions. American Society for Testing and Materials.

[113] ISO 22889. Metallic materials — Method of test for the determination of resistance to stable crack extension using specimens of low constraint. International Organization for Standardization.

[114] J. Chen, Y. Verreman, J. Lanteigne. On fracture toughness JIC testing of martensitic stainless steels. *13th International Conference on Fracture* June 16–21, 2013, Beijing, China.

[115] S. Zhang, S. Zhou, M. Li, B. Fu. Calculation and comparison on fracture toughness of specific reliability between ASTM and ISO standards. *Mater. Res. Express* 7 (2020) 026529.

[116] N.M. Abd-Allah, M.S. El-Fadaly, M.M. Megahed, A.M. Eleiche. Fracture toughness properties of high-strength martensitic steel within a wide hardness range. *J. of Materi Eng and Perform* 10 (2001) 576–585.

[117] X.K. Zhu, B.N. Leis. Revisit of ASTM round robin test data for determining R curves of thin sheet materials. *J ASTM Int* 2009 [paper ID JAI102510].

[118] Marchal Y, Schmidt K, Pardoen T, Knockaert R, Doghri I and Delannay F 1996 Comparison methods for the measurement of fracture toughness of thin sheets: (ECF 11) Mechanisms and Mechanics of Damage and Failure 2259-2265.

[119] T. Pardoen, Y. Marchal, F. Delannay. Thickness dependence of cracking resistance in thin aluminium plates. *J. of Mech. Sol.* 47 (1999) 2093-2123.

[120] J.C. Newman Jr., M.A. James, U. Zerbst. A review of the CTOA/CTOD fracture criterion. *Eng. Frac. Mech.* 70 (2003) 371–385.

[121] J. Heerens, M.Schödel. On the determination of crack tip opening angle, CTOA, using light microscopy and δ_5 measurement technique. *Eng. Frac. Mech.* 70 (2003) 417–426.

[122] S. Koley, S. Chatterjee, M. Shome. Evaluation of fracture toughness of thin sheet of interstitial free high strength steel through critical crack tip opening angle (CTOAc) measurement. *Int J Fract* 194 (2015) 187–195.

[123] S. Xu, N. Petri, W.R. Tyson. Evaluation of CTOA from load vs. load-line displacement for C(T) specimen. *Eng. Frac. Mech.* 76 (13) (2009) 2126-2134.

[124] M. Ben Amara, G. Pluvinage, J. Capelle, Z. Azari. Crack Tip Opening Angle as a Fracture Resistance Parameter to Describe Ductile Crack Extension and Arrest in Steel Pipes under Service Pressure. *Phys Mesomech* 18 (2015) 355–369.

[125] J.G. Kaufman, A.H. Knoll. Kahn-Type Tear Tests and Crack Toughness of Aluminum Sheet. *Metals Research and Standards* (1964) 151–155.

[126] ASTM B871. Standard Test Method for Tear Testing of Aluminum Alloy Products. American Society for Testing and Materials.

[127] J.G. Kaufman, H. Hunsicker. Fracture Toughness Testing at Alcoa Research Laboratories. *Fracture Toughness Testing and its Applications* (1965) 290-308

[128] G.G. Garret, J.F. Knott. The influence of compositional and microstructural variations on the mechanism of static fracture in aluminum alloys. *Metal. Trans. A* 9 (1978) 1187-1201.

[129] D. Dumont, A. Deschamps, Y. Brechet. On the relationship between microstructure, strength and toughness in AA7050 aluminum alloy. *Mat. Sci. and Eng. A* 356 (2003) 326-336.

[130] P. Henn, M. Liewald, M. Sindel. Investigation on crashworthiness characterisation of 6xxx series aluminium sheet alloys based on local ductility criteria and edge compression tests. *IOP Conf. Ser.: Mater. Sci. Eng.* (2018) 418 012125.

[131] L. Ying, J. Lu, Y. Chang, X. Tang, P. Hu, K. Zhao. Optimization evaluation test of strength and toughness parameters for hot-stamped high strength steels. *J. of Iron and Steel Research Int*. 20 (2013) 51-56.

[132] J. Lorthios, A.F. Gourgues, P. Cugy, C. Scott. Damage of TWIP steels for automotive application. *ICF12 Int. Conference on Fracture*, Ottawa (2009).

[133] B. Cotterell, J.K. Reddell. The Essential Work of Plane Stress Ductile Fracture. *Int. J. Fracture* (1977) 267-277.

[134] K.B. Broberg. On stable crack growth. *J. Mech. Phys. Solids*. 23 (1975) 215-237.

[135] J. Wu, Y.W. Mai. The essential fracture work concept for toughness measurement of ductile polymers. *Polym. Eng. Sci.* 36 (1996) 2275–88.

[136] Y.W. Mai, B. Cotterell. On the essential work of ductile fracture in polymers. *Int. J. Fract.* 32 (1986) 105–25.

[137] Y.W. Mai, P. Powell. Essential work of fracture and J-integral measurements for ductile polymers. *J. Polym. Sci.* 29 (1991) 785–93.

[138] E. Clutton. Essential work of fracture. Moore DR, Pavan A, Williams JG, editors. Fracture mechanics testing methods for polymers, adhesives and composites, vol.28. ESIS Publ.; (2001) 177–95.

[139] B. Cotterell, T. Pardoen, A.G. Atkins. Measuring toughness and the cohesive stress–displacement relationship by the essential work of fracture concept. Eng. Fract. Mech. 72 (2005) 827–48.

[140] Y. Marchal, J.F. Walhin, F. Delannay. Statistical procedure for improving the precision of the measurement of the essential work of fracture of thin sheets. *Int. J. Fract.* 87 (1997) 189–99

[141] A.S. Saleemi A S, J.A. Nairn. The plane-strain essential work of fracture as a measure of the fracture toughness of ductile polymers Polym.Eng. Sci. 30(4) (1990) 211.

[142] A.B. Martínez, J. Gámez-Pérez, M. Sanchez-Soto, J.I.Velasco, O.O. Santana, M.LL. Maspoch. The Essential Work of Fracture method- Analyzing the Post-yielding Fracture Mechanics of polymers. *Eng. Fail. Anal.* 16 2604-2617.

[143] Y. Marchal, F. Delannay. Influence of test parameters on the measurement of the essential work of fracture of zinc sheets. *Int Fract J* 80 (1996) 295–310.

[144] S. Hashemi, D. O'brien. The essential work of plane-stress ductile fracture of poly(ether-ether ketone) thermoplastic. *Journal of Materials Science* 28 (1993) 3977-3982.

[145] ASTM E561. Standard practice for R-curve determination. American Society for Testing and Materials.

[146] W.C. Oliver, G.M. Pharr. An improved technique for determining hardness and elastic modulus using load and displacement sensing indentation experiments. *J Mater Res* 7 (6) (1992) 1564-1583.

[147] F. Fauth, I. Peral, C. Popescu and M. Knapp. The new Materials Science and Powder diffraction beamline at ALBA Synchrotron. *Powder Diffraction* 28 (S2) (2013) pp. S360-S370.

[148] F. Fauth, R. Boer, F. Gil-Ortiz, C. Popescu, O. Vallcorba, I. Peral, D. Fulla, J. Benach, J. Juanhuix. The crystallography stations at the Alba synchrotron. *Eur. Phys. J. Plus* (2015) 130: 160.

[149] J. Rodríguez-Carvajal. Recent advances in magnetic structure determination by neutron powder diffraction. *Physica B: Condensed Matter* 192 (1993) 55-69.

[150] S. Hashemi. Fracture toughness evaluation of ductile polymeric films. *Journal of Materials Science* 32, 1563–1573 (1997).

[151] W.Y.F. Chan, J.G. Williams. Determination of the fracture toughness of polymeric films by the essential work method. *Polymer* 35 (8) (1994) 1666-1672.

[152] N. León, A.B. Martínez, P. Castejón, D. Arencón, P.P. Martínez. The fracture testing of ductile polymer films: Effect of the specimen notching. *Polymer Testing* 63 (2017) 180-193.

[153] A.B. Martínez, N. León, A. Segovia, J. Cailloux, P.P. Martínez. Effect of specimen notch

quality on the essential work of fracture of ductile polymer films. *Engineering Fracture Mechanics* 180 (2017) 296-314.

[154] Y.W. Mai, K.M. Pilko. The essential work of plane stress ductile fracture of a strain-aged steel. *J. Mater. Sci.* 14 (1979) 386 - 394.

[155] Y. Marchal, F. Delannay. Comparison of methods for fracture toughness testing of thin low carbon steel plates. Mater. Sci. Tech. 14 (1998) 1163–1168.

[156] T. Pardoen, F. Hachez, B. Marchioni, P.H. Blyth, A.G. Atkins. Mode I fracture of sheet metal. J. *of the Mech. and Phys. of Sol*. 52 (2004) 423-452.

[157] F. Tuba, L. Oláh, P. Nagy. The role of ultimate elongation in the determination of valid ligament range of essential work of fracture tests. *J. Mater. Sci*. 47 (2012) 2228–2233.

[158] Y.W. Mai, B. Cotterell. Effects of pre-strain on plane-stress ductile fracture in α -brass, *J.Mater.Sci.*13 (1980) 2296-2306.

[159] R. Muñoz, A. Lara, D. Casellas. Fracture toughness characterization of advanced high strength steels. *Int. Deep Drawing Research Group (IDDRG) Conference 2011* (Bilbao, Spain, June 5-8, 2011)

[160] D. Gutiérrez, Ll. Pérez, A. Lara, D. Casellas, J.M. Prado. Toughness evaluation of high strength steels sheets by means of the essential work of fracture. *19th European conference on fracture: fracture mechanics for durability, reliability and safety, ECF* 2012.

[161] S.K. M R, E. Schmidova, P. Konopík, D, Melzer, F. Bozkurt, NV Londe. Fracture Toughness Analysis of Automotive-Grade Dual-Phase Steel Using Essential Work of Fracture (EWF) Method. *Metals* 2020, 10, 1019.

[162] A. Gray. Testing protocol for essential work of fracture. ESIS, editor. 1993, European Structural Integrity Society (ESIS) – TC4.

[163] E. Clutton. Testing protocol for essential work of fracture. ESIS, editor. 1997, European Structural Integrity Society (ESIS) – TC4.

[164] J.G. Williams, M. Rink. The standardisation of the EWF test. *Eng Fract Mech* 74(7) (2007) 1009–1017.

[165] R. Hill. On discontinuous plastic states, with special reference to localized necking in thin sheets. *Journal of Mechanics and Physics of Solids* 1952; 1: 19-30.

[166] T. Pardoen, Y. Marchal, F. Delannay. Essential work of fracture compared to fracture mechanics—towards a thickness independent plane stress toughness. Eng Fract Mech 69 (2002) 617–631.

[167] O. Akourri, M. Louah, A. Kifani, G. Gilgert, G. Pluvinage. The effect of notch radius on fracture toughness JIC. *Eng. Frac. Mech*. 65 (2000) 491-505.

[168] V.V. Chaudhari, D.M. Kulkarni, R. Prakash. Study of influence of notch root radius on fracture behaviour of extra deep drawn steel sheets. *Fatigue Fract. Engng. Mater. Struct.* 32 (2009) 975–986.

[169] A.B. Martínez, A. Segovia, J. Gamez-Perez, M.Ll. Maspoch. Influence of femtolaser notch sharpening technique in the determination of essential work of fracture (EWF) parameters, *Eng. Fract. Mech*. 76 (9) (2009) 1247-1254.

[170] J.R. Rice, P.C. Paris, J.G. Merkle. Some Further Results of J-Integral Analysis and Estimates. Progress in Flaw Growth and Fracture Toughness Testing. STP 536 (1973) 231-245.

[171] H. Tada, P.C. Paris, G.R. Irwin. The stress analysis of cracks handbook. Third edtition. American Society of Mechanical Engineers, New York, 2000.

[172] L. Xia, C.F. Shih, J.W. Hutchinson. A computational approach to ductile crack growth

under large scale yielding conditions. *J. Mech. Phys. Solids* 43 (1995) 389-413.

[173] X.K. Zhu, S.K. Jang. J-R curves corrected by load-independent constraint parameter in dcutile crack growth. *Eng. Frac. Mech*. 68 (2001) 285-301.

[174] Y. Mai, B. Cotterell. Effect of specimen geometry on the essential work of plane stress ductile fracture. *Eng. Frac.Mech.* 21 (1985) 123-128.

[175] B. Cotterell, A.G. Atkins. A review of the J and I integrals and their implications for crack growth resistance and toughness in ductile fracture. *Int. J. Fract.* 81 (1996) 357-372.

[176] P. Jacques, Q. Furnémont, T. Pardoen, F. Delannay. On the role of martensitic transformation on damage and cracking resistance in trip-assisted multiphase steels. *Acta Mater* 49 (2001) 139–152.

[177] I. de Diego-Calderón, I. Sabirov, J.M. Molina-Aldareguia, C. Föjer, R. Thiessen, R.H. Petrov. Microstructural design in quenched and partitioned (Q&P) steels to improve their fracture properties. *Mat. Sci. and Eng. A* 657 (2016) 136.

[178] R. Petrov, L. Kestens, A. Wasilkowska, Y. Houbaert. Microstructure and texture of a lightly deformed TRIP-assisted steel characterized by means of the EBSD technique. *Mat Sci Eng A* 447 (2007) 285–297.

[179] T. Bhattacharyya, S.B. Singh, S. Das, A. Haldar, D. Bhattacharjee. Development and characterisation of C–Mn–Al–Si–Nb TRIP aided steel. *Mat Sci Eng A* 528 (2011) 2394–2400.

Appendix A

Appended publications

Paper I. Identification of fracture toughness parameters to understand the fracture resistance of advanced high strength sheet steels. Engineering Fracture Mechanics 229 (2020) 106949.

Engineering Fracture Mechanics 229 (2020) 106949

Contents lists available at ScienceDirect

Engineering Fracture Mechanics

journal homepage: www.elsevier.com/locate/engfracmech

Identification of fracture toughness parameters to understand the fracture resistance of advanced high strength sheet steels

D. Frómeta[a,*], S. Parareda[a], A. Lara[a], S. Molas[a], D. Casellas[a,b], P. Jonsén[b], J. Calvo[c]

[a] Eurecat, Centre Tecnològic de Catalunya, Unit of Metallic and Ceramic Materials, Plaça de la Ciència, 2, Manresa 08243, Spain
[b] Division of Mechanics of Solid Materials, Luleå University of Technology, 971 87 Luleå, Sweden
[c] Universitat Politècnica de Catalunya, Eduard Maristany 16, 08019 Barcelona, Spain

ARTICLE INFO

Keywords:
Fracture toughness
J-integral
Essential work of fracture
Kahn tear tests
Advanced high strength steel sheets

ABSTRACT

The fracture toughness of four advanced high strength steel (AHSS) thin sheets is evaluated through different characterization methodologies, with the aim of identifying the most relevant toughness parameters to describe their fracture resistance. The investigated steels are: a Complex Phase steel, a Dual Phase steel, a Trip-Aided Bainitic Ferritic steel and a Quenching and Partitioning steel. Their crack initiation and propagation resistance is assessed by means of *J-integral* measurements, essential work of fracture tests and Kahn-type tear tests. The results obtained from the different methodologies are compared and discussed, and the influence of different parameters such as specimen geometry or notch radius is investigated. Crack initiation resistance parameters are shown to be independent of the specimen geometry and the testing method. However, significant differences are found in the crack propagation resistance values. The results show that, when there is a significant energetic contribution from necking during crack propagation, the specific essential work of fracture (w_e) better describes the overall fracture resistance of thin AHSS sheets than J_C. In contrast, energy values obtained from tear tests overestimate the crack propagation resistance and provide a poor estimation of AHSS fracture performance. w_e is concluded to be the most suitable parameter to describe the global fracture behaviour of AHSS sheets and it is presented as a key property for new material design and optimization.

1. Introduction

A vast array of new multiphase advanced high strength steels (AHSS) has been developed in the last two decades in order to fulfil the automotive industry's demands on lightweighting and passive safety. These steels represent one of the best cost-effective, lightweight solutions for auto body and chassis components. Therefore, considerable research efforts are being devoted to the development of optimized microstructures for enhanced structural integrity and impact performance. One of the key steps in material optimization is the establishment of appropriate characterization techniques to understand the role of microstructural constituents on fracture behaviour and predict in-service performance. Nevertheless, with the emergence of AHSS, this task has become even more challenging.

The limited ductility of AHSS compared to conventional mild steels has raised new cracking-related issues that cannot be rationalized via traditional uniaxial tensile testing approaches and classical ductility rankings based on elongation values. For example,

* Corresponding author.
E-mail address: david.frometa@eurecat.org (D. Frómeta).

https://doi.org/10.1016/j.engfracmech.2020.106949
Received 10 December 2019; Received in revised form 10 February 2020; Accepted 21 February 2020
Available online 02 March 2020
0013-7944/ © 2020 The Authors. Published by Elsevier Ltd. This is an open access article under the CC BY-NC-ND license (http://creativecommons.org/licenses/BY-NC-ND/4.0/).

Nomenclature

a	crack length
A_{50}	elongation at fracture (initial gauge length 50 mm)
A_g	uniform elongation
A_{pl}	plastic area under load-displacement curve
β	plastic zone shape factor
δ_5	crack opening displacement measured over an initial gauge length of 5 mm
E	Young's modulus
ε_{ij}	strain tensor
ε_u	true uniform strain
ε_f	true fracture strain
Γ	integration path of the contour integral
J	*J*-integral
J_i	*J*-integral at crack initiation
J_c	*J*-integral near the onset of stable crack propagation
K	stress intensity factor
K_{IC}	mode I plane strain fracture toughness
l_o	initial ligament length
n	strain hardening exponent
P	applied load
R curve	crack growth resistance curve
ρ	notch root radius
σ_{ij}	stress tensor
σ_{YS}	yield stress
σ_{UTS}	ultimate tensile strength
σ_f	fracture stress
t_o	initial thickness
t_f	specimen thickness after fracture
Ti	traction vector components
u_p	actual plastic displacement
w	strain energy density
W	specimen width
W_f	total work of fracture
W_e	essential work of fracture
W_p	non-essential plastic work
w_f	total specific work of fracture
w_f^i	specific work of fracture initiation
w_e	specific essential work of fracture
w_e^i	specific essential work of fracture initiation
w_p	non-essential specific plastic work

Abbreviations

AHSS	advanced high strength steel
CP	complex phase steel
CT	compact tension specimen
CTOA	crack tip opening angle
CTOD	crack tip opening displacement
DENT	double edge notched tension specimen
DP	dual phase steel
EDM	electrical discharge machining
EPFM	elastic plastic fracture mechanics
EWF	essential work of fracture
FPZ	fracture process zone
HER	hole expansion ratio
PHS	press hardened steel
Q&P	quenching and partitioning steel
SENT	single edge notched tension specimen
TE	total elongation
TRIP	transformation induced plasticity steel
TWIP	twinning induced plasticity steel
UIE	unit initiation energy
UPE	unit propagation energy
UTS	ultimate tensile strength

it has been recurrently evidenced in the literature that steels with greater elongation (both uniform and total) can be more susceptible to the appearance of fractures in trimmed, sheared or punched areas during cold forming (edge cracking, hole expansion, stretch flanging) [1–6]. Similar behaviour has been observed in the crash failure behaviour of AHSS and press hardened steels (PHS). It has been shown that steels with higher ductility can exhibit poorer crash ability and a higher amount of cracking during impact loading [7–11]. In this context, fracture toughness, measured in the frame of fracture mechanics, has shown to be the most adequate property to understand this kind of fractures related to the material's crack initiation and propagation resistance [3–6,11].

The contributions of Yoon et al. [3] and Casellas et al. [4] showed a strong correlation between fracture toughness and the edge cracking resistance of multiple AHSS sheets, evaluated in terms of hole expansion ratio (HER). This approach has been further discussed in [5] and [6], where the edge formability of different complex phase (CP) and dual phase (DP) steels is investigated and related to their crack propagation resistance. More recent works have also shown that fracture mechanics can be effectively used to classify and understand the impact performance, as well as other fractures related to the local ductility of AHSS and PHS [11,12]. Therefore, fracture toughness has become a relevant property for new high strength sheet material development and optimization.

However, over the years, little attention has been paid to the cracking resistance of such high strength metal sheets for automotive applications and, thus, limited information is available in the literature. The main reason lies in the intrinsic complexity of elastic plastic fracture mechanics (EPFM) methodologies and the historical absence of standard methods to characterize the fracture toughness of thin ductile sheets under plane stress conditions.

The ASTM E1820 [13] describes the standard procedure for evaluating the fracture toughness of metallic materials by means of the traditional *J-integral* and *Crack Tip Opening Displacement* (*CTOD*) measurements. However, it is intended for plane strain fracture toughness characterization and the defined specimen thickness requirements are not satisfied for thin sheets. Alternative standards were developed later for the evaluation of resistance to stable crack extension of thin-gauge materials, the ASTM E2472 [14] and the ISO 22889 [15]. These standards propose the use of alternative parameters for fracture resistance characterization, the *Crack Tip Opening Angle* (*CTOA*) and the crack opening displacement δ_5, expressed in terms of a resistance curve, δ_5-*R*. However, as pointed out before, such standard EPFM methodologies are experimentally very complex. They require expert technical skill for specimen preparation and the crack advance must be monitored during the whole test, which represents one of the main challenges in fracture mechanics testing procedures. Additionally, they usually involve complex data processing and, such as in the case of the *CTOA*

fracture criterion, the use of finite element method analysis, which makes the application of the methods expensive and time-consuming. Thus, alternative simpler and faster experimental approaches have been developed in order to satisfy the growing need for knowing the fracture properties of thin metallic sheets.

Owing to its experimental simplicity, the essential work of fracture (EWF) method [16] has become one of the most attractive alternatives to assess the ductile tearing resistance of thin metallic sheets [16–27] and polymers [28–31]. Recently, many authors have also used the EWF methodology to characterize the cracking resistance of several AHSS and PHS sheets [4–6,11,12,32–38]. The main advantage of this method is that it is very easy to perform and avoids the need for measurement of the crack extension.

Another testing technique to readily evaluate the fracture resistance of thin metal sheets that has received considerable interest is the Kahn-type tear test [39]. This simple energy-based method offers a valuable tool for indexing the tearing resistance of ductile metal sheets and evaluating the effect of the processing parameters and the microstructural constituents on overall toughness. It has been applied to characterize the toughness of precipitation hardening aluminium alloys [39–42], AHSS [7,12], PHS [43] and twinning-induced plasticity (TWIP) steels [44].

Some researchers have also proposed alternative non-standard single specimen methods based on *J-integral* measurements. For instance, Faccoli et al. [45] used the *J-integral* expressions proposed by Rice et al. [46] for double edge notched tension (DENT) specimens to evaluate the fracture resistance of a TWIP steel, a DP steel and two Quenching and Partitioning (Q&P) steels. A similar approach was used by Luo et al. [37] and Xiong et al. [47,48] to investigate the fracture behavior of different TWIP [37] and Q&P [47,48] microstructures.

According to the number of recent publications dealing with this topic, it is evident that research interest in the fracture behavior of thin AHSS sheets has increased significantly in the last years. However, there are still some uncertainties regarding the effect of different testing variables (specimen geometry, notch radius, etc.) on fracture toughness measurements or which are the most suitable parameters to define the fracture resistance of these sheet materials.

Within this framework, the main aim of the present paper is to briefly review and discuss some of the different existing experimental approaches to evaluating the fracture toughness of thin ductile sheets and to investigate the relevance of the measured toughness parameters to describe the fracture resistance of AHSS sheets. Moreover, it is also aimed at providing a better understanding of the influence of different experimental variables on the obtained toughness values. For this purpose, the fracture toughness of four AHSS sheets typically used in automotive industry is investigated using different EPFM-based characterization techniques. The materials investigated are: a CP, a DP, a Transformation Induced Plasticity (TRIP)-aided Bainitic Ferritic (TBF) and a Q&P steel. Fracture toughness is evaluated through *J-integral* measurements, EWF tests and Kahn-type tear tests. Comparison is made between the different crack initiation and propagation resistance parameters obtained, and their main similarities and differences are discussed. The influence of the notch root radius and the specimen geometry on the measured toughness values is also assessed.

2. Materials

The materials investigated in this work are two conventional first generation AHSS (CP and DP) and two third generation TRIP-aided AHSS grades (TBF and Q&P). The steels were supplied in the form of sheets of 1.4–1.5 mm. The chemical composition of the steels is shown in Table 1. Engineering and true tensile stress-strain curves and mechanical properties for the transverse direction are shown in Fig. 1 and Table 2 respectively. True stress-strain curves are represented up to the uniform strain (ε_u) and extrapolated to the fracture strain (ε_f). The microstructures of the investigated AHSS grades were characterized by means of Scanning Electron Microscopy (SEM). The resulting SEM micrographs are shown in Fig. 2.

The microstructure of the CP steel consists of a homogeneous bainite/tempered martensite matrix (Fig. 2a). These steels are characterized by high yield stress to tensile strength ratio and low strain hardening. They have a great energy absorption capacity and good local formability (hole expansion, bending on tight radius, etc.), which makes them especially suitable for crash resistant parts [11,12]. DP microstructure presents a combination of ferrite/bainitic ferrite and martensite (Fig. 2b). Such mixture of soft (ferrite) and hard (martensite) phases results in great strain hardening and high elongation values. Usually, DP steels exhibit lower yield stress than CP at equal tensile strengths. They show very good global formability but poorer local ductility and fracture toughness than CP steels [11,12]. TBF steel presents a dual-phase like microstructure, basically consisting of ferrite and bainite, with significant amounts (11%) of metastable retained austenite (Fig. 2c). The replacement of the soft single-phase matrix present in first generation TRIP steels by the harder ferrite/bainite matrix allows attainment of higher strengths, while the good ductility and formability is maintained thanks to the TRIP effect. TBF steels generally exhibit greater strain hardening and larger elongation values (both uniform and total) than DP steels, which results in improved global formability. However, they show limited local formability and axial impact energy absorption [11,12]. The Q&P steel (Fig. 2d) has a homogeneous martensite/bainite matrix with retained austenite (6%). The

Table 1
Chemical composition of the investigated steels (in weight per cent).

Steel grade	C	Si	Mn	Cr	B	Al
CP	0.11	0.34	~2.3	0.12	0.0017	0.040
DP	0.19	0.18	~2.3	0.46	0.0003	0.048
TBF	0.20	0.84	> 2.4	0.17	0.0003	0.039
Q&P	0.12	0.81	> 2.4	0.18	0.0002	0.043

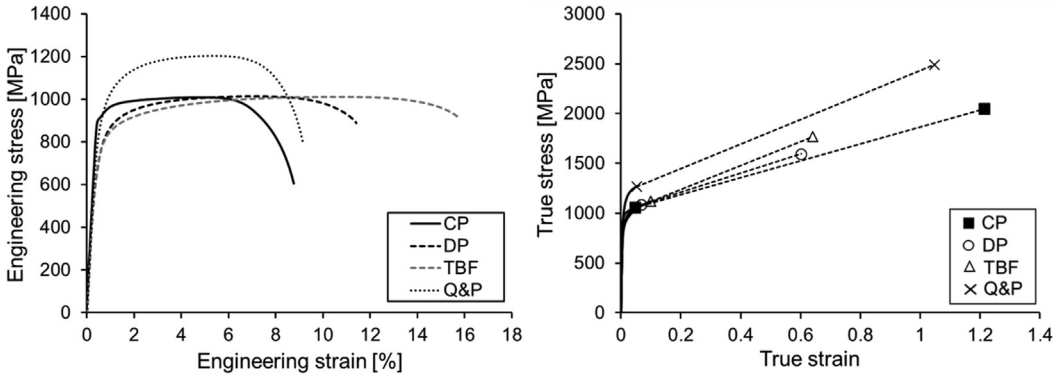

Fig. 1. Engineering and true stress-strain curves. The symbols correspond to the true uniform strain and the true fracture strain.

Table 2
Mechanical properties of the investigated AHSS sheets in transverse direction. t = thickness; σ_{ys} = yield strength; σ_{UTS} = ultimate tensile strength; A_g = uniform elongation (elongation at *UTS*); A_{50} = elongation at fracture (initial gauge length 50 mm); $n_{2\text{-}4}$ = strain hardening exponent between 2 and 4% of deformation; ε_u = true uniform strain; ε_f = true fracture strain; σ_f = fracture stress.

Steel	t [mm]	σ_{ys} [MPa]	σ_{UTS} [MPa]	A_g [%]	A_{50} [%]	$n_{2\text{-}4}$ [–]	ε_u [–]	ε_f [–]	σ_f [MPa]
CP	1.40	915	1008	4.8	8.8	0.05	0.05	1.21	2048
DP	1.40	775	1015	7.0	11.4	0.10	0.07	0.60	1595
TBF	1.50	755	1012	10.5	15.8	0.11	0.10	0.64	1768
Q&P	1.40	920	1202	5.3	9.1	0.10	0.05	1.05	2490

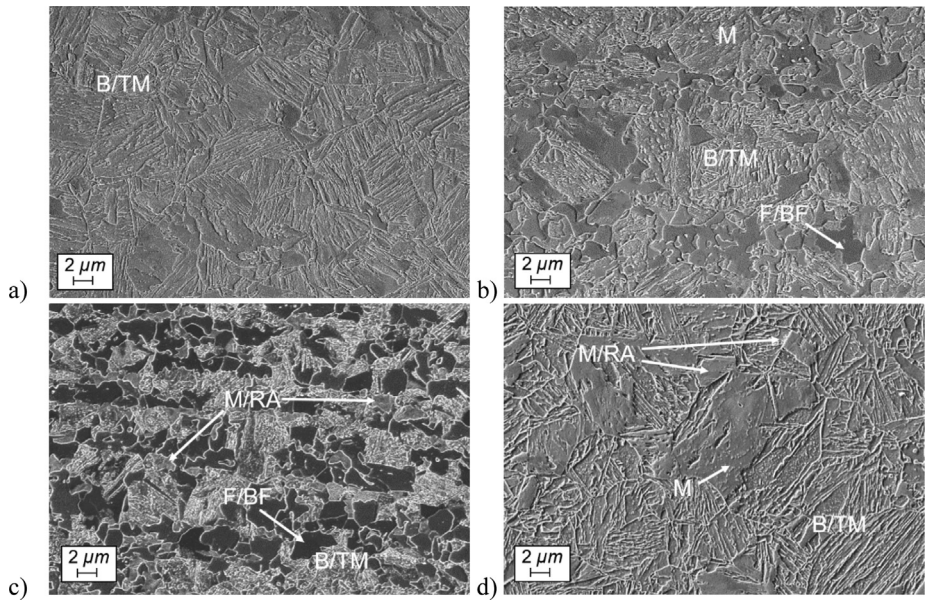

Fig. 2. Microstructures of (a) CP (b) DP (c) TBF and (d) Q&P.

TRIP effect contributes to increased strain hardening, and the presence of hard martensite, rather than bainitic ferrite, leads to higher strength levels than TBF steels, but lower elongation. Q&P steels represent a good option for anti-intrusion structural parts, due to their enhanced bendability and fracture resistance [11,12].

3. Fracture toughness evaluation methods

This section describes the fracture toughness characterization methods used in this work. It is important to note that fracture resistance of thin sheets under plane stress conditions has an extra energetic contribution from necking and, thus, fracture toughness depends on the sheet thickness. Accordingly, all the evaluated fracture toughness parameters shown in the present work are only

representative for the investigated sheet thickness.

3.1. J-integral

The *J-integral* concept was introduced by Rice [49] to characterize the crack tip strain fields in nonlinear elastic materials. The nonlinear energy release rate J can be written as a path independent contour integral:

$$J = \int_{\Gamma} \left(w dx_2 - T_i \frac{\partial u_i}{\partial x_1} ds \right) \tag{1}$$

where Γ is an arbitrary contraclockwise path around the crack tip, w is the strain energy density, T_i are the components of the traction vector, defined according to the outward normal along Γ ($T_i = \sigma_{ij} n_j$), u is the displacement vector and ds is an element of arc length along Γ. The strain energy density w is defined according to Eq. (2):

$$w = \int_0^{\varepsilon_{ij}} \sigma_{ij} d\varepsilon_{ij} \tag{2}$$

where σ_{ij} and ε_{ij} are the stress and strain tensors, respectively.

Since the first works of Begley and Landes [50,51] and Rice et al. [46], the *J*-integral has been the most widely used fracture parameter to characterize the fracture toughness of elastic-plastic materials. It is evaluated in terms of a critical *J*-integral value (*Jc*) for stationary cracks and *J-Resistance* (*J-R*) curves for growing cracks.

The method for the evaluation of J_c and the construction of *J-Resistance (J-R)* curves is described in the standard ASTM E1820 [13]. However, as mentioned above, this standard was developed to evaluate the fracture toughness of metallic materials under plane strain conditions. Thus, specimen size requirements are not fulfilled by many thin sheet materials, as those investigated in this work. For example, considering a thickness of 1.5 mm and the proportions given in the standard for a Compact Tension (CT) specimen ($2 \leq W/B \leq 4$, where W is the distance between the load line and the back end of the specimen and B is the sheet thickness), a specimen with a maximum size of 7.2 × 7.5 mm could be used, which would severely hamper its manipulation and testing.

Nevertheless, Zhu and Leis [52] showed that, if the thickness requirement is not considered, it is possible to apply the ASTM E1820 to evaluate a *J-R* curve in thin sheet ductile materials. To avoid such size constraints, in this study CT specimens for *J-integral* measurements were machined following the recommendations of the ASTM E561 [53]. The ASTM E561 was developed for measuring the *K–R* curve of thin gauge materials and is therefore less restrictive concerning the specimen size. The geometry of the CT specimen used is shown in Fig. 3a. All the specimens were machined with the crack oriented along the rolling direction (T-L). The initial notch was prepared by electrical discharging machining (EDM). A fatigue pre-crack was nucleated from the starting notch and extended 5 mm, resulting in an initial crack size (notch + fatigue pre-crack) of 18 mm ($a/W = 0.64$). For each material, a *J-R* curve was constructed according to ASTM E1820 (Fig. 3b). The crack advance was measured by means of a high resolution video camera located in one of the sides of the specimen (frame rate: 30 images/s). The fracture tests were performed in a universal testing machine under displacement control at a constant cross-head speed of 1 mm/min and the load vs load-line displacement curves were recorded. The load-line displacement was measured by means of a clip-on displacement gage.

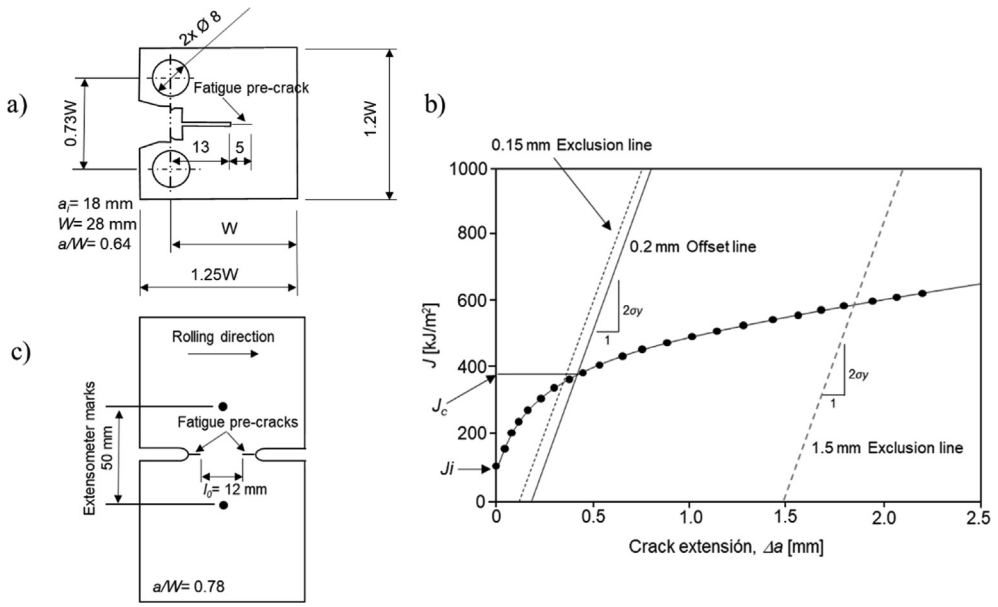

Fig. 3. (a) CT specimen geometry used for *J-integral* measurements. (b) Construction of the J-R curve according to ASTM E1820 and determination of the fracture toughness parameters J_i and J_c. (c) DENT specimen for *J-integral* measurements.

From the *J-R* curves, two cracking resistance parameters were obtained: the fracture toughness at cracking initiation, J_i, which is the toughness value at the point at which first crack extension is detected in the video equipment (subcritical crack initiation), and the fracture toughness near the onset of stable crack propagation, J_c, obtained from the intersection of the 0.2 mm offset line with the *R* curve as indicated in ASTM E 1820.

Additionally, in order to evaluate the effect of the specimen geometry on J_i and J_c determination, *J-integral* measurements were performed with DENT specimens. For the evaluation of J_i, the equation proposed by Rice et al. [46] for a DENT specimen was used:

$$J = \frac{K^2}{E} + \frac{1}{t_0 l_0}\left(2\int P du_p - P u_p\right) \tag{3}$$

where K is the stress intensity factor, which for a DENT specimen is given by Eq. (4) [54]:

$$K = \frac{P\sqrt{\pi a}}{t_0 \cdot 2W\sqrt{1-\frac{a}{W}}}\left[1.122 - 0.561\left(\frac{a}{W}\right) - 0.205\left(\frac{a}{W}\right)^2 + 0.471\left(\frac{a}{W}\right)^3 - 0.190\left(\frac{a}{W}\right)^4\right] \tag{4}$$

E is the elastic modulus, t_0 is the specimen thickness, l_0 is the uncracked ligament length, P is the actual load and u_p is the actual plastic displacement. In Eq. (4), W refers to the half of the specimen width. Eq. (3) is only applicable to stationary cracks. Thus, to account for the crack growth incremental equations must be used as indicated in [55]:

$$J_n = J_{n-1} + \frac{2(A_{pl(n)} - A_{pl(n-1)})}{t_0(l_{n-1} + l_n)} + \frac{2(K_n^2 l_n - K_{n-1}^2 l_{n-1})}{E(l_{n-1} + l_n)} \tag{5}$$

where *n* and *n-1* denote two consecutive points on the recorded load vs load-line displacement curve, A_{pl} refers to the plastic area under the curve and l is the actual ligament length. The parameters E, K and t_0 are defined above.

The geometry of the DENT specimens used for *J-integral* measurements is shown in Fig. 3c. Notches were prepared by EDM and extended by fatigue pre-cracks (≈1.5 mm per side). The initial ligament length (l_0) was of 12 mm (a/W = 0.78). The displacement was measured by means of a videoextensometer using two extensometer marks on the specimen separated 50 mm. The rest of the testing conditions were the same as described above for the CT specimens.

3.2. Essential work of fracture

The idea of the essential work of fracture (EWF) was initially proposed by Broberg [56,57]. He suggested that the ductile fracture process takes place in two different regions: an inner fracture process zone (FPZ) and an outer plastic region. Later, Cotterel and Reddel developed a methodology to experimentally separate these two terms, the EWF methodology [16]. The work developed in the FPZ is called the essential work of fracture (W_e). It represents the energy necessary to create new surfaces at the front of the crack tip and it is proportional to the fractured area. The work dissipated in the outer plastic zone is the non-essential plastic work (W_p), which depends on the volume of the deformed region around the fracture plane. Then, the total work of ductile fracture can be expressed as follows:

$$W_f = W_e + W_p = w_e l_0 t_0 + \beta w_p l_0^2 t_0 \tag{6}$$

where w_e is the specific essential work of fracture per unit area, l_0 is the ligament length, t_0 is the specimen thickness, w_p is the specific non-essential plastic work per unit volume and β is a shape factor that depends on the shape of the plastic zone. Normalizing Eq. (6) by the cross-section area gives:

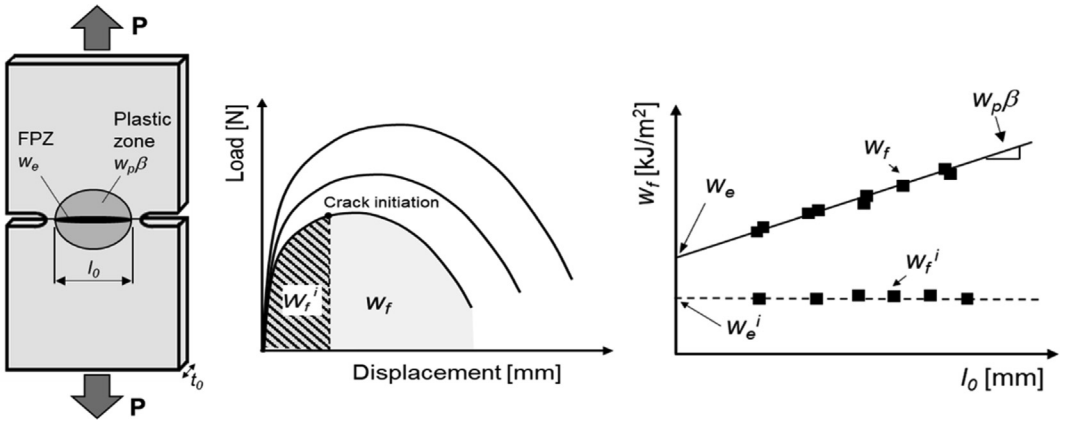

Fig. 4. DENT specimen and experimental procedure for the determination of the essential work of fracture, w_e and the specific work for fracture initiation, w_e^i.

$$\frac{W_f}{l_0 t_0} = w_f = w_e + \beta w_p l_0 \tag{7}$$

Thus, if a series of w_f values are plotted against the ligament length (l_0), w_e and βw_p can be obtained by linear regression, where w_e is given by the intercept and βw_p by the slope, as shown in Fig. 4. w_f values are obtained by integrating the area under load vs displacement curves (W_f) and dividing by $l_0 t_0$. By definition, w_e measures the energy dissipated within the FPZ and, thus, it is a suitable parameter to describe the crack propagation resistance of thin ductile sheets. Many authors have addressed the equivalence between w_e and *J-integral* [21,22,28–30]. Such equivalence is further discussed in Section 4.

The EWF methodology also allows separation of energetic contributions from crack initiation and crack propagation and determination of a crack initiation toughness value, the specific essential work for fracture initiation, w_e^i [29]. The specific work for fracture initiation, w_f^i is calculated by integrating the area under load vs displacement curve until the onset of crack propagation. As shown by Mai and Cotterel [29], w_f^i is independent of the ligament length. Therefore, w_e^i is calculated from an average of w_f^i values from different ligament lengths (Fig. 4).

In this work, w_e and w_e^i have been obtained by testing rectangular DENT specimens of 240 × 55 mm. The specimen geometry and the loading conditions were the same as for *J-integral* measurements (Fig. 3c, Section 3.1). Ligament lengths (l_0) ranging from 5 to 15 mm (a/W: 0.73 ÷ 0.9) were used. Crack initiation was detected by means of a high resolution video camera synchronized with the testing machine. In order to evaluate the effect of the notch radius on the EWF, two different notch conditions were evaluated: notch machined by EDM (ρ ≈ 150 μm) and EDM notch + fatigue pre-crack (ρ ≈ 0.1 μm).

Results for fatigue pre-cracked specimens are extracted from reference [11]. *wf* vs l_0 plots have been included and w_e^i has been recalculated with additional specimens.

3.3. Kahn-type tear tests

The Kahn-type tear tests were originally developed by Kaufman and Knoll [39] to characterize the notch resistance of thin aluminium sheets. The tear test consists in loading up to fracture a single edge notched tensile (SENT) specimen with a very sharp notch at a constant displacement rate and recording the load and displacements required to fracture the specimen (the characteristic load vs load-line displacement curve of the tear test is shown in Fig. 5). Then, the notch resistance is characterized by the *UIE* (Unit Initiation Energy) and the *UPE* (Unit Propagation Energy).

UIE represents the energy necessary (both elastic and plastic) to nucleate a crack and is obtained by integration of the area under the load vs load-line displacement curve up to the displacement corresponding to the maximum load (Fig. 5). *UPE* is the energy per unit area necessary to propagate a crack in a tear specimen up to fracture. *UPE* is the primary result of the tear test and it is obtained by integrating the area of the load vs load-line displacement curve from the point of maximum load to the displacement at fracture (Fig. 5). It represents a measure of the combination of ductility and strength of the material and it can be used as a relative index of toughness. It cannot be considered as an absolute measure of the material's crack propagation resistance since it is geometry dependent. However, the good correlation observed between *UPE* and plane strain fracture toughness, K_{Ic} [39,58], shows that *UPE* can be a suitable parameter for ranking the tearing resistance of thin ductile alloys.

The standard procedure for the tear testing of aluminium alloys products is described in ASTM B871 [59]. Even though the method was developed for aluminium alloys, many authors have shown the suitability of the Kahn-type tear tests to characterize the tearing resistance of AHSS [7,12,43,44]. For example, Ying et al. [43] used the Kahn-type tear tests to investigate the effect of different processing parameters (austenization temperature, soaking time and start deformation temperature) on the strength and toughness of PHS sheets. Lorthios et al. [44] also used these tear tests to study the damage mechanisms of a high Mn TWIP steel.

In the present work, Kahn type tear tests were performed according to ASTM B871 [59]. The notch was prepared by EDM (ρ ≈ 150 μm). All the specimens were machined with the notch oriented along the rolling direction (T-L specimens). The tests were conducted at a constant speed of 1 mm/min. Due to the compression load in the final stage of fracture, the specimens never fractured

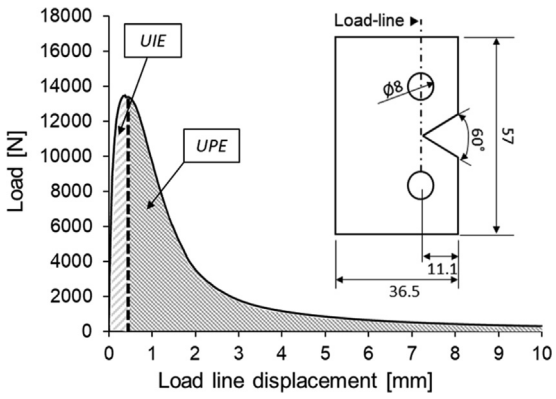

Fig. 5. Load vs load-line displacement curve from Kahn-type tear tests and specimen geometry used for the tear tests.

completely. Therefore, the tests were manually stopped at 10 mm of displacement when load is steadily decreased to zero. For load-line displacement measurement, initial extensometer marks separated 10 mm were placed in the specimen. 3 specimens per material and condition were tested. The high resolution video camera was used to check that crack initiation coincided with the point of maximum load.

4. Results and discussion

4.1. J-integral measurements

Fig. 6 shows the J-R curves obtained for the investigated AHSS grades. J_i and J_c values are given in Table 3. At a first glance, two types of fracture behaviour can be distinguished. On the one hand, CP and Q&P show the highest *J integral* values, both at cracking initiation ($J_{i\ CT}$ = 125 kJ/m^2 and 118 kJ/m^2 respectively) and near the onset of stable crack propagation ($J_{c\ CT}$ = 248 kJ/m^2 and 260 kJ/m^2 for CP and Q&P respectively). Both steel grades exhibit very similar *J-R* curves, characterized by a pronounced slope in the initial part of the curve (blunting line) and a noteworthy increase of *J* values during crack propagation. On the other hand, DP and TBF show substantially lower J_i and J_c values and flatter resistance curves, which indicate that energetic contribution to crack propagation resistance is significantly reduced in these two steels compared to CP and Q&P steels. In this case, DP and TBF have similar *J integral* values at crack initiation ($J_{i\ CT}$ = 84 kJ/m^2 for DP and $J_{i\ CT}$ = 89 kJ/m^2 for TBF) and at the onset of stable crack propagation ($J_{c\ CT}$ = 144 kJ/m^2 and 169 kJ/m^2 for DP and TBF respectively). However, TBF presents a *J-R* curve with a slightly steeper slope, which leads to greater *J* values for relatively large crack extensions.

Specimen geometry is shown to have an important influence on the *J-R* curve, but not on J_i and J_c values. As observed in Fig. 6, the resistance curves obtained with CT and DENT specimens converge in the initial part of the plot, providing similar values of J_i and J_c for all the investigated materials. However, as the crack grows, DENT specimens show higher *J* values than CT specimens, describing a steeper *R* curve. These results are in concordance with the observations of Xia et al. [60] and Zhu et al. [61]. They investigated the effect of the constraint level on *J-R* curve of ductile crack growth by using different specimen geometries. They found that *J-integral* values along the resistance curve decrease with increasing crack tip constraint, whereas little effect of specimen geometry was observed on initiation toughness. They also showed that CT specimens have higher crack tip constraint, and thus lower *J-R* curve, than DENT specimens.

4.2. Essential work of fracture

Fig. 7 and Table 4 show the EWF results obtained for the two investigated notch conditions. The first noticeable thing is the large

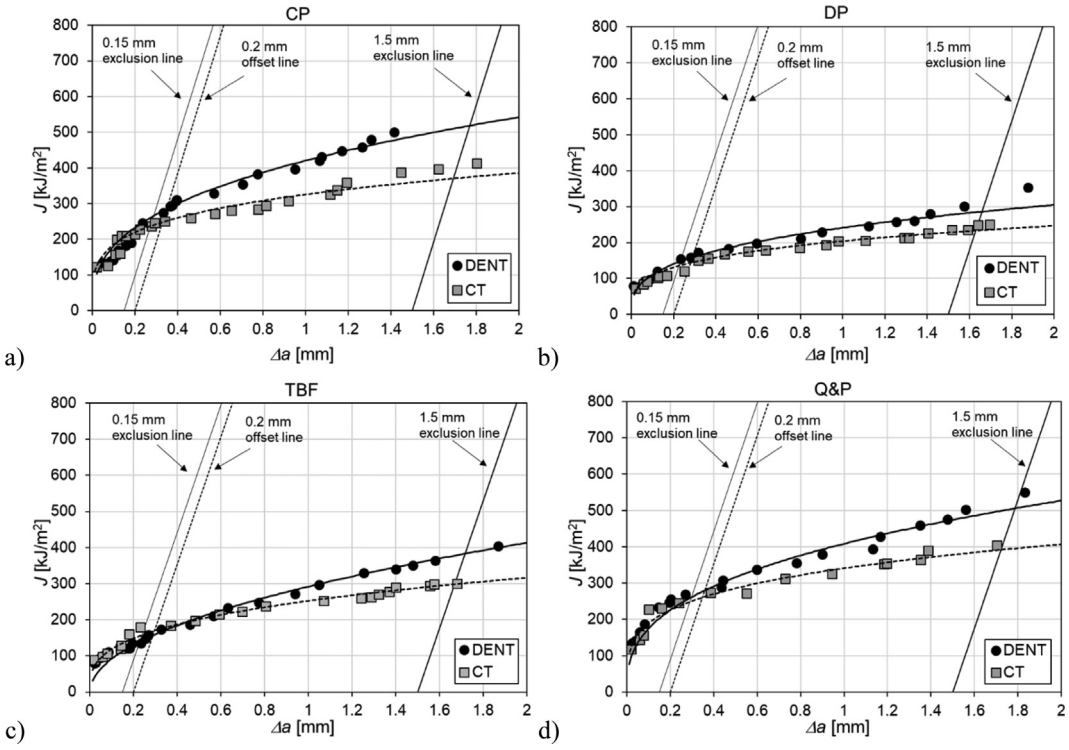

Fig. 6. *J-R* curves for the investigated AHSS grades: (a) CP, (b) DP, (c) TBF and (d) Q&P.

Table 3
Results of *J-integral* measurements with CT and DENT specimens.

	CT		*DENT*	
Steel grade	$J_{i\ CT}$ [kJ/m^2]	$J_{c\ CT}$ [kJ/m^2]	$J_{i\ DENT}$ [kJ/m^2]	$J_{c\ DENT}$ [kJ/m^2]
CP	125	248	135	286
DP	84	144	84	158
TBF	89	169	81	157
Q&P	118	260	135	280

influence of notch root radius on EWF measurements. Values of w_e and w_e^i obtained with notched specimens are much higher than those obtained with fatigue pre-cracked specimens. This effect is particularly relevant for initiation toughness values ($w_{e\ crack}^i / w_{enotch}^i = 0.36$ for CP and TBF and 0.39 for DP and Q&P). w_e also shows a strong notch radius dependency, especially in DP, TBF and Q&P ($w_{e\ crack}/w_{e\ notch} = 0.47$, 0.48 and 0.42 respectively). These results indicate that fracture toughness values obtained with notched specimens overestimate the material's fracture resistance and, thus, may lead to misleading conclusions. This is clearly evidenced when comparing CP (Fig. 7a) and Q&P (Fig. 7d). Both steels exhibit very similar fracture behaviour for notched specimens (almost identical w_e, w_e^i and βw_p). Nevertheless, w_e results for fatigue pre-cracked specimens show that Q&P has significantly lower crack propagation resistance than CP.

The influence of notch root radius on fracture toughness measurements is well known in fracture mechanics testing and it has been addressed by several authors [34,35,45,62–64]. All these works showed a linear increase in fracture toughness with the notch radius, ρ. Such *apparent* increase in fracture toughness is related to the decrease in stress triaxility degree with increasing notch root radius and the additional plastic deformation developed at the notch tip, necessary for crack nucleation. However, it has been found that below a critical radius (ρ_c), fracture toughness becomes independent of ρ. The value of ρ_c depends on the material. Akourri et al. [63] found a ρ_c of ≈0.85 mm for a mild steel, Chaudhari et al. [64] obtained a ρ_c of ≈0.15 mm for extra deep drawing steel sheets. A similar value was observed by Faccoli et al. [45] for a TWIP steel. Muñoz et al. [34] showed that a sharp notch of ρ = 0.01 mm (sharpened by razor blade) provided toughness values close to those obtained with fatigue pre-cracks for a DP780.

As observed, some materials are quite insensitive to notch radius, whereas others show high notch radius sensitivity. Therefore, in general, the determination of fracture toughness for a determined notch radius may not be suitable enough to assess the fracture resistance of the material. For this reason, in order to obtain a more realistic notch-independent toughness value, standard fracture toughness testing procedures recommend the use of fatigue pre-cracked specimens [13–15].

In line with the above comments, only w_e and w_e^i values obtained from fatigue pre-cracked specimens are considered to represent the *real* fracture toughness of the investigated steel sheets in the present study. These will be used from this point forward to discuss their crack initiation and propagation resistance.

The results indicate that CP steel has, by far, the highest crack propagation resistance of the analysed steels ($w_{e\ crack}$ = 405 ± 11 kJ/m^2). Q&P shows significantly lower w_e ($w_{e\ crack}$ = 194 ± 12 kJ/m^2), closer to that of DP and TBF ($w_{e\ crack}$ = 138 ± 20 kJ/m^2 and 149 ± 13 kJ/m^2, respectively). Even though DP and TBF steels have very similar w_e values, they show quite different fracture behaviour. As observed in Fig. 7c, TBF shows greater w_f values (comparable to CP and Q&P) than DP for large ligament lengths. However, these values rapidly decrease for smaller ligament lengths, resulting in low w_e and very high βw_p. In Q&P, similarly to the observed in TBF, there is also a large contribution from the plastic work. On the other hand, CP shows significantly lower βw_p, which indicates that most of the energetic contribution to the ductile fracture process comes from the essential work of fracture developed in the FPZ.

The values of w_e^i also reveal that CP and Q&P have greater crack initiation resistance than DP and TBF. Nonetheless, in this case the differences between the different steels are not as significant as observed for w_e values. Q&P shows the highest w_e^i ($w_{e\ crack}^i$ = 172 ± 2 kJ/m^2), closely followed by CP ($w_{e\ crack}^i$ = 156 ± 14 kJ/m^2). DP and TBF show the lowest toughness at crack initiation ($w_{e\ crack}^i$ = 110 ± 12 kJ/m^2 and 110 ± 16 kJ/m^2, respectively).

It is worth mentioning that, for pre-cracked specimens, crack initiation was detected before the maximum load in all the investigated steels. Accordingly, the (often used) peak load criterion for fracture initiation may result in inappropriate initiation toughness values and, therefore, it must be experimentally assessed for every material.

4.3. Kahn-type tear tests

Fig. 8a shows the load vs load-line displacement curves obtained from the Kahn-type tear tests. *UIE* and *UPE* values are shown in Fig. 8b and Table 5. In this case, the assumption that crack initiation coincided with the point of maximum load was confirmed for all the studied materials. As observed, CP and Q&P show superior *UIE* to DP and TBF. It is interesting to note that, even though Q&P reaches higher load than CP during the tear test (Pmax ≈ 17.1 kN and 14.9 kN respectively), both steels show similar *UIE*. This can be explained by the greater displacement at maximum load shown by CP (dPmax = 0.46 mm for CP and 0.40 mm for Q&P). As illustrated in Fig. 8a, TBF reaches similar P_{max} (≈14.8 kN) to CP but at significantly smaller displacement (d_{Pmax} = 0.34 mm), which results in poorer *UIE*. DP exhibits the lowest *UIE* of the investigated steels. It shows similar displacement at maximum load to TBF (d_{Pmax} = 0.33 mm) and the lowest P_{max} (≈13.6 kN). Looking at *UPE* values, it can be seen that CP has the greatest propagation energy, followed by TBF and Q&P. Finally, DP has the poorest crack propagation resistance.

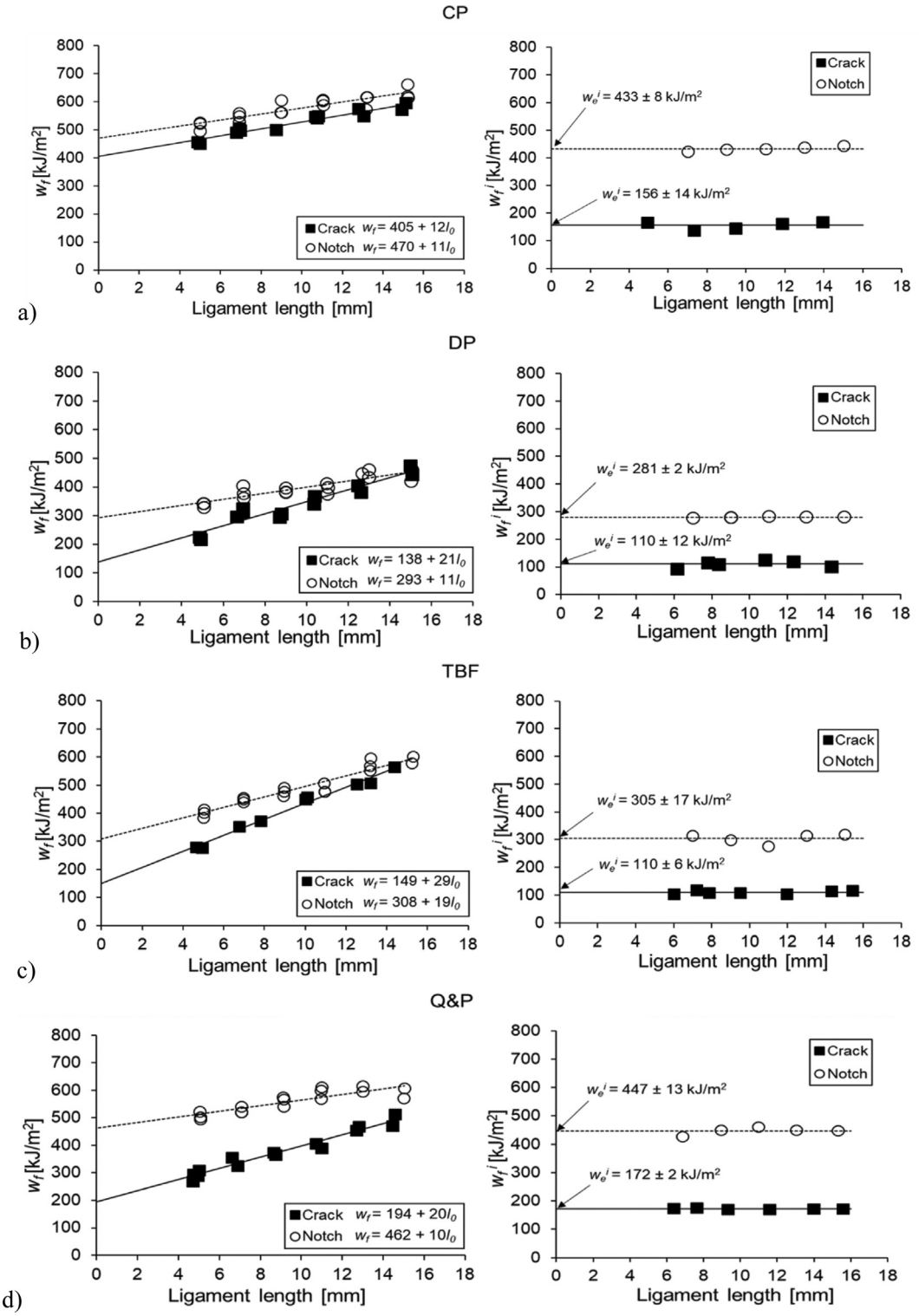

Fig. 7. EWF results for the investigated AHSS grades: (a) CP, (b) DP, (c) TBF and (d) Q&P. Solid symbols correspond to the EWF values obtained with fatigue pre-cracked specimens, open symbols correspond to notched specimens. Left: w_f values as a function of the ligament length. Right: w_f^i values as a function of the ligament length. The average cracking initiation value (w_e^i) is indicated.

The different tearing behavior of the steels can be discerned from their load vs displacement curves. DP, TBF and Q&P show a sudden load drop just after crack initiation (P_{max}) and the load rapidly decreases with increasing displacement. This effect is

Table 4
EWF results. Results for fatigue pre-cracked specimens are extracted from reference [11]. The values of $w_e^{i}{}_{crack}$ can be slightly different, since they have been recalculated.

	Crack (ρ = 0.1 μm)			Notch (ρ = 150 μm)		
Steel grade	$w_e^{i}{}_{crack}$ [kJ/m^2]	$w_{e\ crack}$ [kJ/m^2]	$\beta w_{p\ crack}$ [MJ/m^3]	$w_e^{i}{}_{notch}$ [kJ/m^2]	$w_{e\ notch}$ [kJ/m^2]	$\beta w_{p\ notch}$ [MJ/m^3]
CP	156 ± 14	405 ± 11	12 ± 1	433 ± 8	470 ± 14	11 ± 1
DP	110 ± 12	138 ± 20	21 ± 2	281 ± 2	293 ± 15	11 ± 1
TBF	110 ± 16	149 ± 13	29 ± 1	305 ± 17	308 ± 15	19 ± 1
Q&P	172 ± 2	194 ± 12	20 ± 1	447 ± 13	462 ± 16	10 ± 2

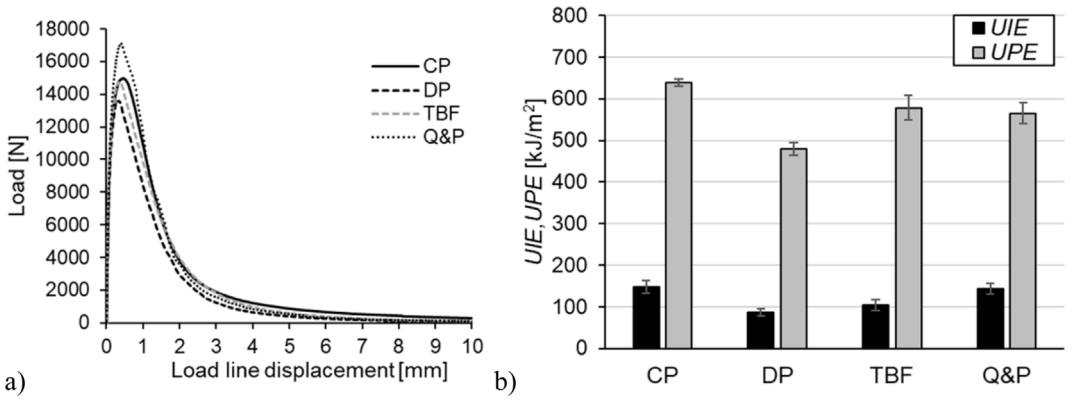

Fig. 8. (a) Load vs load-line displacement curves from Kahn-type tear tests. Only one representative curve per material is plotted. (b) *UIE* and *UPE* for the investigated AHSS.

Table 5
Results of Kahn-type tear tests.

Steel grade	*UIE* [kJ/m^2]	*UPE* [kJ/m^2]
CP	147 ± 15	639 ± 10
DP	87 ± 9	479 ± 15
TBF	104 ± 12	579 ± 30
Q&P	144 ± 13	566 ± 26

especially relevant in Q&P, which shows slightly lower *UPE* than TBF, and DP. CP, in turn, shows a more gradual decrease in the load after P_{max}, which justifies the higher energetic contribution to crack propagation resistance.

4.4. Comparison of fracture toughness parameters

This section is intended to summarize the obtained fracture resistance values according to the different methodologies and to discuss their main differences and similarities.

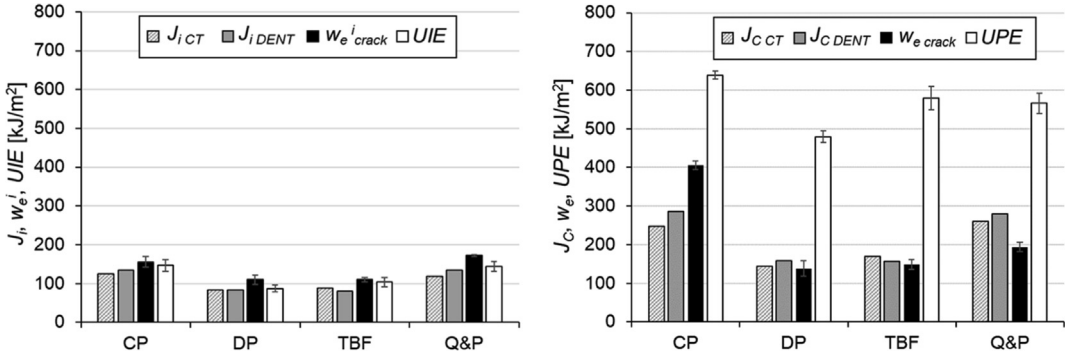

Fig. 9. Summary of crack initiation (left) and crack propagation resistance (right) parameters. Standard deviation is indicated when available.

Fig. 9 shows the different crack initiation and propagation resistance parameters evaluated in this work. The results of EWF measurements with notched specimens are not considered for discussion. It is important to note that J_c, by definition, is not strictly speaking a crack propagation resistance value but it represents the fracture toughness for a small amount of crack extension. Nevertheless, it is plotted together with the crack propagation resistance parameters, w_e and *UPE* to differentiate it from the initiation toughness J_i. This differentiation is important and will be the basis for discussing the relation between J_c and w_e in the following paragraphs.

As shown in Fig. 9 left, crack initiation resistance values are independent of the specimen geometry and the testing methodology used. Surprisingly, in spite of the larger notch radius used in Kahn type specimens, initiation toughness results of tear tests are very similar to those obtained from *J-integral* and EWF measurements with fatigue pre-cracked specimens. It is assumed then, that for this specimen configuration, the stress concentration ahead of the notch tip closely resembles that of a crack and, therefore, a machined sharp notch ($\rho = 150$ μm) is suitable enough to obtain representative toughness values. This contrasts highly with the significant influence of notch root radius observed in DENT specimens for EWF measurements and represents an advantage with respect to the other methods, since the need for time-consuming fatigue pre-cracking procedures is avoided.

However, while *UIE* provides a good estimation of fracture toughness at crack initiation, *UPE* completely overestimates the crack propagation resistance of the material. Fig. 9 right shows that *UPE* is much higher than w_e for all the investigated AHSS grades. Such large discrepancy between *UPE* and w_e can be explained by means of the energy partitioning concept described in Section 3.2, which states that the ductile fracture process has two main energetic contributions: one from the plastic work surrounding the crack plane and other developed in the FPZ, necessary to create new surfaces in the front of the crack tip. In Kahn type tear tests, both contributions are intermingled, i.e. *UPE* contains not only the energy for new surfaces creation but also that of the plastic work. The plastic work is geometry dependent and, therefore, cannot be considered a material property. For this reason, the results from the tear tests must be taken with care and only as a relative index of toughness.

On the other hand, w_e only quantifies the energy dissipated in the FPZ, since the contribution from the plastic work is mathematically removed by extrapolation to ligament zero. As demonstrated by several authors [28,29,66], w_e is an intrinsic material property (for a given sheet thickness) independent of specimen geometry. The relation between w_e and J_c has been repeatedly discussed in literature [21,22,28–30,65]. Wu and Mai [28] and Mai and Cotterell [29] found a very good agreement between w_e and the critical *J-integral* value for different ductile polymers. Mai and Cotterell [65] also differentiated between J_i and J_c (they called it J_p) and showed that w_e^i and w_e were equivalent to J_i and J_c respectively. The correspondence between J_i and w_e^i is corroborated in Fig. 9 left. However, important differences are observed between w_e and J_c. DP and TBF show similar values of w_e ($w_e = 138 \pm 20$ and 149 ± 13 kJ/m^2, respectively) and J_c ($J_{c\ CT} = 144$ and 169 kJ/m^2 respectively). By contrast, in CP and Q&P, w_e ($w_e = 405 \pm 11$ and 194 ± 12 kJ/m^2) significantly differs from J_c ($J_{c\ CT} = 248$ and 260 kJ/m^2, respectively).

Again, it must be kept in mind that J_c and w_e are conceptually different, since J_c is a toughness value for a small crack advance (given by the ASTM E1820) and w_e is an average crack propagation resistance value for the complete fracture process. Furthermore, as shown by Cotterell and Atkins [66], *J-integral* includes, besides the contribution from the essential work of fracture, the plastic work dissipated out of the FPZ. Pardoen et al. [22] suggested that, when there is small contribution from crack propagation after

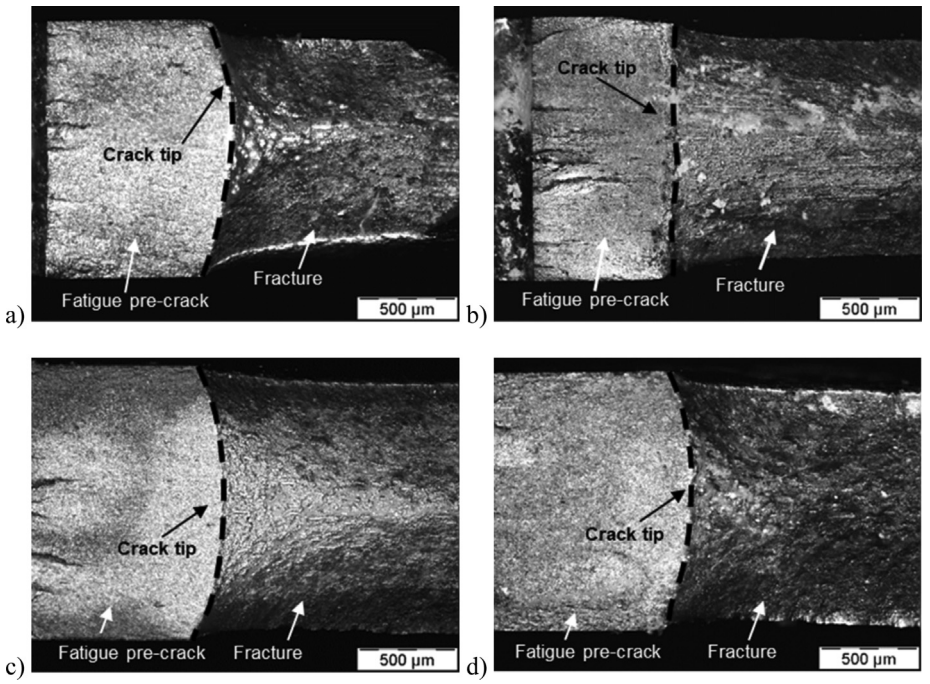

Fig. 10. Fracture surface of DENT specimens: (a) CP (b) DP (c) TBF (d) Q&P.

initiation ($w_e \approx w_e^i$), J_c can be equivalent to w_e. Nevertheless, when there is significant contribution from crack propagation ($w_e \gg w_e^i$), w_e and J_c are different. In plane stress ductile fracture, such contribution to crack propagation resistance developed in the FPZ comes primarily from necking. The evolution of necking during fracture for the studied steel grades is analysed in Figs. 10 and 11. Fig. 10 shows the fracture surface of DENT specimens used for *J-integral* and EWF measurements. In Fig. 11, the true thickness strain (ε_3) is plotted as a function of the distance from the crack tip. True thickness strain is calculated according to Eq. (8):

$$\varepsilon_3 = ln\left(\frac{t_0}{t_f}\right) \tag{8}$$

where t_0 is the initial thickness and t_f is the thickness after fracture. It can be seen that steels with lower w_e^i (DP and TBF) show a lower degree of necking at the crack tip. The differences between w_e and w_e^i can be also explained by the progress of the thickness strain along the FPZ. DP, TBF and Q&P steels, which have $w_e \approx w_e^i$, show small increase of true thickness strain, which is rapidly stabilized at approximately 0.3 mm from the crack tip ($\varepsilon_{3\,ss}/\varepsilon_{3\,tip} \approx 1.7$, 1.5 and 1.2 for DP, TBF and Q&P respectively. $\varepsilon_{3\,ss}$ is the true thickness strain for the steady state and $\varepsilon_{3\,tip}$ is the true thickness strain at crack tip). On the other hand, in CP ($w_e \gg w_e^i$) the degree of necking progressively increases to reach a steady value of $\varepsilon_3 = 0.26$ at approximately 0.5 mm from crack tip ($\varepsilon_{3\,ss}/\varepsilon_{3\,tip} \approx 2.2$).

Such contribution from necking to the ductile fracture process supposes a real increment in the crack propagation resistance of the material [22] and it is effectively measured by w_e. In contrast, in *J-integral* measurements this contribution can be masked due to the additional energy from plastic work. This explains why CP and Q&P have practically identical *J-R* curves (Fig. 6). They show similar energy values for the same crack advance. However, as shown in Section 4.2, this energy comes from different contributions: In CP, it derives from the essential work of fracture dissipated in the FPZ (which justifies the large differences between w_e and J_c) whereas in Q&P, it comes from the non-essential plastic work.

The fact that Q&P shows greater J_c than w_e may be related to the additional energy associated to the 0.2 mm of crack advance. Looking at the resistance curve, it is observed that the transition in the initial slope occurs for a crack advance of approximately 0.1 mm. At this point, J values are in the range of 200–220 kJ/m^2, which are in better agreement with w_e. According to these observations, it can be asserted that when the fracture process has an important contribution from the crack propagation, w_e better represents the tearing resistance of thin ductile sheets than J_c.

4.5. Relation between fracture toughness and tensile strength/fracture properties

Several attempts have been made to correlate fracture properties and uniaxial tensile strength-elongation parameters. For instance, the product of the ultimate tensile strength (*UTS*) by the total elongation (*TE*) has been often used in literature as a toughness indicator. This parameter represents a combination of the material's strength and ductility and it is conventionally used as a performance index of AHSS [67]. The true fracture strain (ε_f) derived from the reduction of area at fracture in tensile tests is also used as a measure of the material's fracture resistance and it has been recently proposed as a relative index of local formability [67]. The common perception is that greater fracture strain or greater $UTS \times TE$ product imply greater fracture toughness. However, as has been proven by different authors [11,32,48], no clear link can be established between fracture toughness of AHSS and these parameters or other related tensile strength/ductility properties. Such assumption is refuted again in Fig. 12. The figure shows no relation between the $UTS \times TE$ product and the different fracture toughness parameters investigated in this study. Furthermore, looking at J_c and w_e, an opposite trend to that expected is observed, i.e. steels with greater $UTS \times TE$ show lower fracture toughness. Similar observations were made by Xiong et al. in various Q&P steels [48]. They also found that the true fracture strain or the product of the fracture stress and the true fracture strain ($\sigma_f \times \varepsilon_f$) were not suitable either to rank toughness. For the steel grades characterized in this study, such tensile fracture parameters seem to provide a better estimation of fracture toughness (Fig. 12), especially in terms of cracking initiation (J_i, w_e^i, *UIE*) and J_c. Nevertheless, they do not capture the large differences in full tearing resistance measured by w_e (Fig. 12b). No clear correlation can be determined either between any of the plotted tensile parameters and *UPE* values from tear tests. Therefore, it is important to highlight again that fracture resistance of high strength sheet materials cannot be estimated from

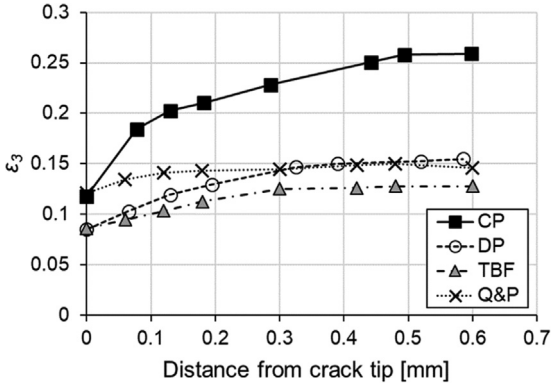

Fig. 11. True thickness strain as a function of the distance from the crack tip.

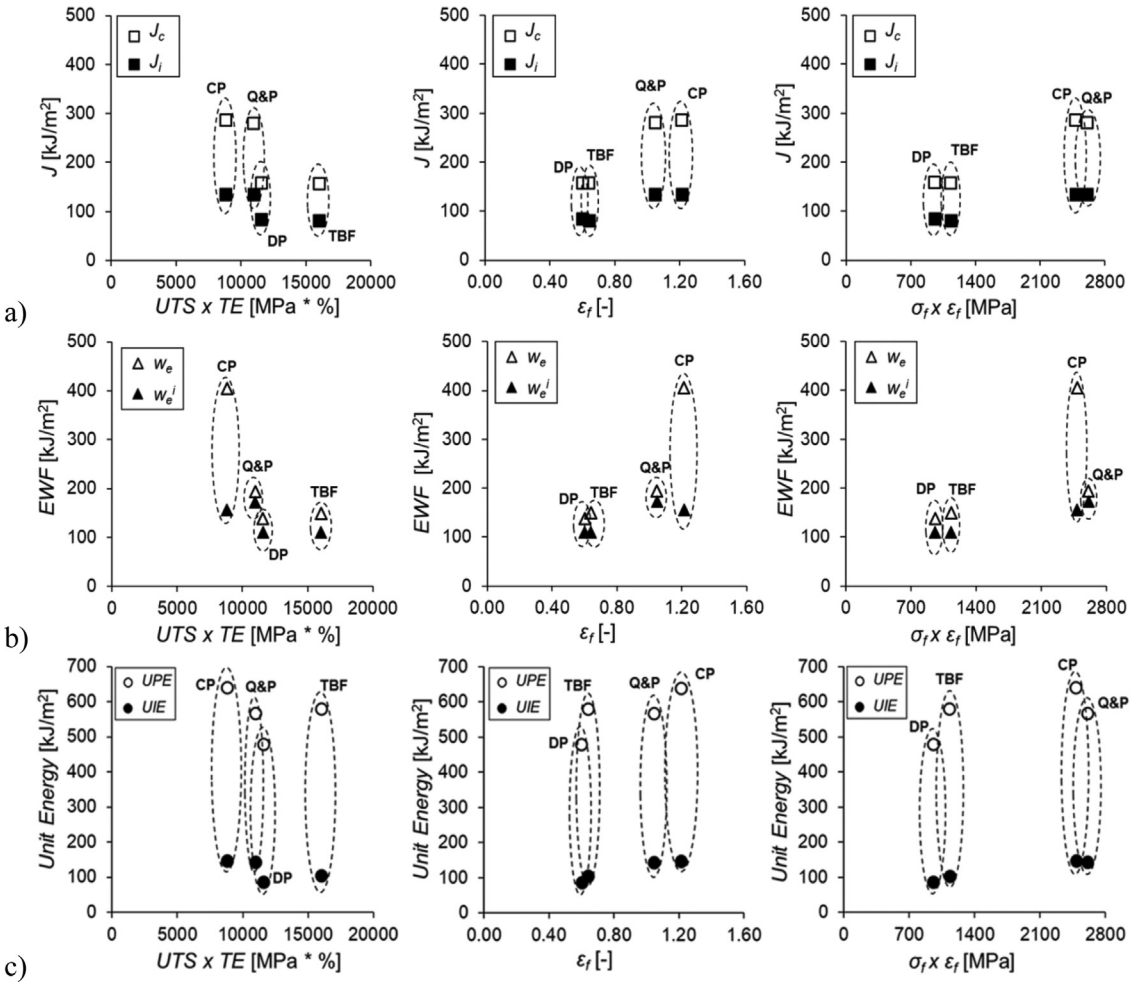

Fig. 12. Fracture toughness as a function of: product of ultimate tensile strength (*UTS*) and total elongation (*TE*); true fracture strain (ε_f); product of fracture stress (σ_f) and true fracture strain (ε_f). (a) J-integral results, (b) EWF results and (c) Kahn-type tear tests results.

tensile properties.

4.6. Application of fracture toughness to understand high strength steel sheet performance

As mentioned before, several research studies have evidenced that fracture toughness is a useful property to rationalize and predict cracking-related phenomena in AHSS sheets, such as edge fractures, crash failure or local formability issues [3–6,11,12]. However, the results obtained in this work show the importance of selecting the adequate toughness parameters to understand the fracture behaviour of these steels and avoid erroneous material rankings. This is illustrated in Fig. 13, where the different crack initiation and propagation resistance values obtained in this work are plotted against edge cracking resistance (in terms of hole expansion ratio), and crashworthiness, expressed as the absorbed energy per unit area in axial impact tests. Published toughness values for AHSS grades of similar thickness and *UTS* are also plotted (data extracted from reference [12]). Detailed information about the experimental procedure for edge cracking and crash resistance characterization is given in [4] and [11] respectively.

As reported in previous works, both edge cracking [4–6] and crash resistance [11,12] of AHSS are strongly related to the specific essential work of fracture, w_e (linear fitting with $R^2 = 0.86$ and 0.95 respectively). In contrast, the investigated crack initiation resistance parameters (J_i, w_e^i, *UIE*) show no clear correlation either with HER or axial impact energy. It indicates that this kind of fractures, as discussed in [11] and [12], is governed by the full tearing resistance of the material rather than by initiation toughness. Therefore, for materials with large contribution from the crack propagation resistance to the complete fracture process, the values of toughness at crack initiation completely underestimate the fracture performance.

CP steel is a clear example of this. As observed in Fig. 13, it shows significantly greater edge cracking resistance and axial impact energy than Q&P (HER = 85 ± 4% and 55 ± 8%; Impact energy per unit area = 36.5 MJ/m^2 and 14.1 MJ/m^2, respectively). Such different fracture behaviour is in good agreement with the differences observed in their overall crack propagation resistance, measured by w_e. Nevertheless, crack initiation resistance is very similar for both steels. Something similar occurs with J_c, which, as

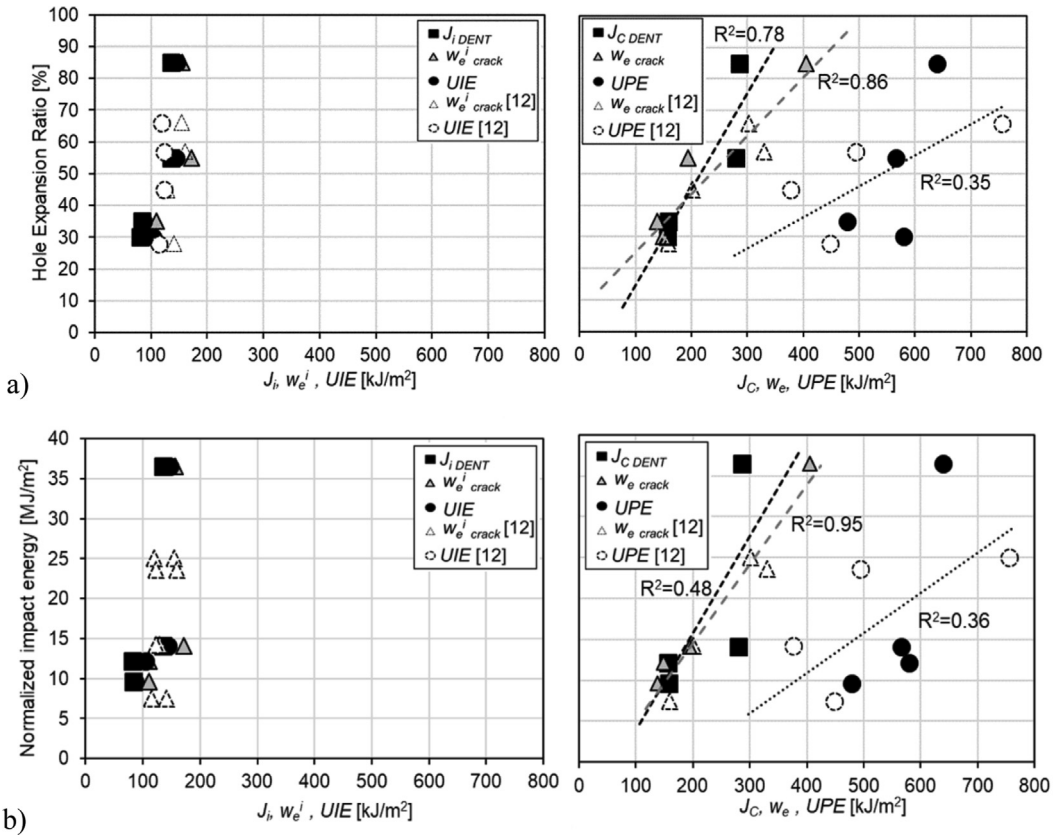

Fig. 13. Correlation between fracture toughness and: (a) edge cracking resistance, expressed as the hole expansion ratio [12]; (b) crashworthiness, in terms of normalized axial impact energy [12]. The fracture toughness parameters investigated in this work (solid symbols) are plotted together other published toughness values (open symbols) [12]. Left: Crack initiation resistance. Right: Crack propagation resistance (correlation coefficient is indicated).

discussed in the previous section, is not suitable enough to describe the full fracture resistance of thin ductile materials with significant crack propagation prior to final failure. *UPE* from tear tests has also been shown to be an unreliable parameter for measuring the crack propagation resistance of thin AHSS sheets. Not only does it overestimate the fracture energy but it can also lead to incorrect toughness estimations, as observed for TBF and Q&P (Fig. 9). This justifies the poor correlation of *UPE* with edge cracking ($R^2 = 0.35$) and axial impact resistance ($R^2 = 0.36$) shown in Fig. 13. The correlation of w_e, *UPE* and local ductility of AHSS sheets is further discussed in [12].

These results indicate that w_e is the most suitable material property to understand the overall fracture performance of thin AHSS sheets. This is a relevant conclusion to take into consideration when using fracture toughness to address the fracture resistance of these steels. Furthermore, it implies w_e as a key property for the development of new AHSS microstructures with enhanced cracking resistance.

5. Conclusions

The fracture toughness of four AHSS sheets for automotive applications has been evaluated through different fracture characterization methodologies and using different specimen geometries and notch conditions. The different tested methodologies, i.e. *J-integral*, EWF and Kahn tear tests, give different values of the energy spent for crack initiation (J_i, w_e^i and *UIE*) and for crack propagation (J_c, w_e and *UPE*). Such differences are discussed below and recommendations for their application to understand the mechanical performance of high strength sheets are given.

Based on the results of the investigations regarding the effect of specimen geometry and notch root radius on fracture toughness measurements, the following conclusions can be drawn:

- The crack initiation resistance (J_i, w_e^i and *UIE*) is independent of the specimen geometry (CT, DENT, Kahn type specimen).
- The specimen geometry has no influence on the determination of the *J-integral* at crack initiation (J_i) and near the onset of stable crack propagation (J_c). However, a significant influence of specimen geometry has been observed in *J* values after a relatively large crack advance. This is attributed to the different crack tip constraint for the investigated geometries.

- Notch root radius has been shown to have a significant influence on EWF measurements. In order to obtain accurate and reliable fracture toughness values, fatigue pre-cracked specimens must be used. Otherwise, the measured toughness values can overestimate the real crack initiation and propagation resistance of the material.

The main differences between the fracture toughness parameters characterized by the three techniques have been discussed and the most relevant conclusions are:

- Kahn type tear tests have been shown to be suitable enough to estimate crack initiation resistance. However, *UPE* values completely overestimate crack propagation resistance, since they include energetic contribution from the plastic work dissipated in the outer zone of the FPZ. Therefore, *UPE* cannot be considered a material property and gives inappropriate toughness ranking.
- Some materials (such as CP steel) may show a large contribution of crack propagation resistance after initiation. In this case, a single crack initiation resistance parameter (J_i, w_e^i or *UIE*) is very conservative and clearly underestimates the overall fracture resistance.
- w_e has been shown to better quantify the crack propagation resistance of thin high strength sheets than J_c. Whereas w_e contains both the energy dissipated during crack initiation and crack propagation to failure, J_c only has energetic contribution from small crack extension and does not account for the complete fracture. *J-R* curves are also unsuitable to represent the *real* crack propagation resistance of the material, because they also include extrinsic contribution from the plastic work dissipated out of the FPZ.
- The additional contribution to the essential work of fracture developed in the FPZ after crack initiation comes mainly from necking. Thus, those materials developing remarkable necking during crack propagation have greater crack propagation resistance.From the analysis of the link between fracture toughness parameters and tensile properties it can be concluded that:
- Conventional toughness estimations based on $UTS \times TE$ product are not suitable to describe the fracture toughness of AHSS. It may lead to wrong material ranking in terms of fracture toughness.
- For the steel grades investigated in this study, tensile fracture parameters, such as the true fracture strain (ε_f) or the product of fracture stress and true fracture strain ($\sigma_f \times \varepsilon_f$), give a better estimation of toughness at cracking initiation and J_c. However, they can underestimate the crack propagation resistance of the material. Therefore, to avoid misleading conclusions about the cracking resistance of high strength sheet metals, fracture toughness must be measured within the framework of fracture mechanics.

Finally, it is concluded that w_e is the most suitable fracture parameter to rationalize crack-related problems in high strength sheets, such as edge fracture or crash behaviour, since they are closely related to the overall energy for the complete fracture rather than to the initiation. Crack initiation parameters, such as w_e^i, *Ji* and *UIE* may underestimate the fracture performance. *UPE* from Kahn type tear tests is not a reliable parameter to predict the kinds of fractures related to the material's crack propagation resistance.

Declaration of Competing Interest

We declare that we have no conflict of interest.

Acknowledgments

The research leading to these results has been partially funded by the EU Horizon 2020 programme under grant agreement H2020-EU.2.1.3. – 814517 (FormPlanet). The authors would like to thank voestalpine Stahl GmbH for supplying the steel sheets. We would also like to acknowledge associate professor Kjell Eriksson at Solid Mechanics, Luleå University of Technology (Sweden), for his good advice and help with editing the manuscript.

Appendix A. Supplementary material

Supplementary data to this article can be found online at https://doi.org/10.1016/j.engfracmech.2020.106949.

References

[1] Konieczny A, Henderson T. On formability limitations in stamping involving sheared edge stretching. SAE technical paper 2007-01-0340; 2007.
[2] Mori K, Abe Y, Suzui Y. Improvement of stretch flangeability of ultra high strength steel sheet by smoothing of sheared edge. J Mater Process Tech 2010;210:653–9.
[3] Yoon JI, Jung J, Joo SH, Song TJ, Chin KG, Seo MH, et al. Correlation between fracture toughness and stretch-flangeability of advanced high strength steels. Matter Lett 2016;180:322–6.
[4] Casellas D, Lara A, Frómeta D, Gutiérrez D, Molas S, Pérez Ll, et al. Fracture toughness to understand stretch-flangeability and edge cracking resistance in AHSS. Metall Mat Trans A 2017;48:86–94.
[5] Frómeta D, Tedesco M, Calvo J, Lara A, Molas S, Casellas D. Assessing edge cracking resistance in AHSS automotive parts by the Essential Work of Fracture methodology. J Phys: Conf Ser 2017;896:012102.
[6] Frómeta D, Lara A, Parareda S, Casellas D. Evaluation of edge formability in high strength sheets through a fracture mechanics approach. AIP Conf Proc 2019;2113:160007.
[7] Walp MS. Impact dependent properties of advanced and ultra high strength steel. SAE technical paper 2007-01-0342; 2007.
[8] Larour P, Pauli H, Kurz T, Hebseberger T. Influence of post uniform tensile and bending properties on the crash behaviour of AHSS and press-hardening steel grades. In: Int deep drawing research group (IDDRG) conference; 2010 (Graz, Austria, May 31-June 2 2010).
[9] Larour P, Naito J, Pichler A, Kurz T, Murakami T. Side impact crash behavior of press-hardened steels-correlation with mechanical properties. In: 5th Int conf hot sheet metal forming of high performance steel (CHS2) (Toronto, Canada, May 31- June 3 2015) p. 281–9.

[10] Link TM, Hance BM. Axial and bending crash performance of advanced high-strength steels. In: Int symp on new developments in advanced high-strength steels. Keystone, Colorado, USA; 2017.
[11] Frómeta D, Lara A, Molas S, Casellas D, Rehrl J, Suppan C, et al. On the correlation between fracture toughness and crash resistance of advanced high strength steels. Eng Frac Mech 2019;205:319–32.
[12] Frómeta D, Lara A, Casas B, Casellas D. Fracture toughness measurements to understand local ductility of advanced high strength steels. IOP Conf Ser: Mater Sci Eng 2019;651:012071.
[13] ASTM E1820. Standard test method for measurement of fracture toughness. American Society for Testing and Materials.
[14] ASTM E2472. Standard test method for determination of resistance to stable crack extension under low-constraint conditions. American Society for Testing and Materials.
[15] ISO 22889. Metallic materials — Method of test for the determination of resistance to stable crack extension using specimens of low constraint. International Organization for Standardization.
[16] Cotterell B, Reddel JK. The essential work of plane stress ductile fracture. Int J Fract 1977;267–277.
[17] Mai YW, Pilko KM. The essential work of plane stress ductile fracture of a strain-aged steel. J Mater Sci 1979;14:386–94.
[18] Marchal Y, Delannay F. Comparison of methods for fracture toughness testing of thin low carbon steel plates. Mater Sci Tech 1998;14:1163–8.
[19] Mai YW, Cotterell B. The essential work of fracture for tearing of ductile metals. Int J Fract 1984;24:229–36.
[20] Pardoen T, Hachez F, Marchioni B, Blyth PH, Atkins AG. Mode I fracture of sheet metal. J Mech Phys Solids 2004;52:423–52.
[21] Pardoen T, Marchal Y, Delannay F. Thickness dependence of cracking resistance in thin aluminium plates. J Mech Sol 1999;47:2093–123.
[22] Pardoen T, Marchal Y, Delannay F. Essential work of fracture compared to fracture mechanics—towards a thickness independent plane stress toughness. Eng Fract Mech 2002;69:617–31.
[23] Marchal Y, Walhin JF, Delannay F. Statistical procedure for improving the precision of the measurement of the essential work of fracture of thin sheets. Int J Fract 1997;87:189–99.
[24] Cotterell B, Pardoen T, Atkins AG. Measuring toughness and the cohesive stress–displacement relationship by the essential work of fracture concept. Eng Fract Mech 2005;72:827–48.
[25] Marchal Y, Delannay F. Influence of test parameters on the measurement of the essential work of fracture of zinc sheets. Int J Fract 1996;80:295–310.
[26] Tuba F, Oláh L, Nagy P. The role of ultimate elongation in the determination of valid ligament range of essential work of fracture tests. J Mater Sci 2012;47:2228–33.
[27] Mai YW, Cotterell B. Effects of pre-strain on plane-stress ductile fracture in α -brass. J Mater Sci 1980;13:2296–306.
[28] Wu J, Mai YW. The essential fracture work concept for toughness measurement of ductile polymers. Polym Eng Sci 1996;36:2275–88.
[29] Mai YW, Cotterell B. On the essential work of ductile fracture in polymers. Int J Fract 1986;32:105–25.
[30] Mai YW, Powell P. Essential work of fracture and J-integral measurements for ductile polymers. J Polym Sci 1991;29:785–93.
[31] Martínez AB, Gamez-Perez J, Sanchez-Soto M, Velasco JI, Santana O, Maspoch MLL. The essential work of fracture method- analyzing the post-yielding fracture mechanics of polymers. Eng Fail Anal 2009;16:2604–17.
[32] Lacroix G, Pardoen T, Jacques PJ. The fracture toughness of TRIP-assisted multiphase steels. Acta Mater 2008;56:3900–13.
[33] Wu R, Li J, Li W, Wu XC, Jin X, Zhou S, et al. Effect of metastable austenite on fracture resistance of quenched and partitioned (Q&P) sheet steels. Mater Sci Eng A 2016;657:57–63.
[34] Muñoz R, Lara A, Casellas D. Fracture toughness characterization of advanced high strength steels. In: Int deep drawing research group (IDDRG) conference; 2011 (Bilbao, Spain, June 5-8, 2011).
[35] Gutiérrez D, Ll Pérez, Lara A, Casellas D, Prado JM. Toughness evaluation of high strength steels sheets by means of the essential work of fracture. In: 19th European conference on fracture: fracture mechanics for durability, reliability and safety, ECF 2012; 2012.
[36] Sahoo S, Padmapriya N, Sarathi De P, Chakraborti PC, Ray SK. Ductile tearing resistance indexing of automotive grade DP590 steel sheets: EWF testing using DENT specimens. J Mater Eng Perform 2018;27:2018–23.
[37] Luo ZC, Liu RD, Wang X, Huang MX. The effect of deformation twins on the quasi-cleavage crack propagation in twinning-induced plasticity steels. Acta Mater 2018;150:59–68.
[38] Golling S, Frómeta D, Casellas D, Jonsén P. Influence of microstructure on the fracture toughness of hot stamped boron steel. Mat Sci Eng A 2019;743:529–39.
[39] Kaufman JG, Knoll AH. Kahn-type tear tests and crack toughness of aluminum sheet. Metals Res Stand 1964:151–5.
[40] Garret GG, Knott JF. The influence of compositional and microstructural variations on the mechanism of static fracture in aluminum alloys. Metal Trans A 1978;9:1187–201.
[41] Dumont D, Deschamps A, Brechet Y. On the relationship between microstructure, strength and toughness in AA7050 aluminum alloy. Mat Sci Eng A 2003;356:326–36.
[42] Henn P, Liewald M, Sindel M. Investigation on crashworthiness characterisation of 6xxx series aluminium sheet alloys based on local ductility criteria and edge compression tests. IOP Conf Ser: Mater Sci Eng 2018;418:012125.
[43] Ying L, Lu J, Chang Y, Tang X, Hu P, Zhao K. Optimization evaluation test of strength and toughness parameters for hot-stamped high strength steels. J Iron Steel Res Int 2013;20:51–6.
[44] Lorthios J, Gourgues A F, Cugy P, Scott C. Damage of TWIP steels for automotive application. In: ICF12 Int conference on fracture, Ottawa; 2009.
[45] Faccoli M, Cornacchia G, Gelfi M, Panvini A, Roberti R. Notch ductility of steels for automotive components. Eng Fract Mech 2014;127:181–93.
[46] Rice JR, Paris PC, Merkle JG. Some Further Results of J-Integral Analysis and Estimates. Progress in Flaw Growth and Fracture Toughness Testing. STP 536; 1973. p. 231–45.
[47] Xiong Z, Jacques PJ, Perlade A, Pardoen T. Ductile and intergranular brittle fracture in a two-step quenching and partitioning steel. Scripta Mater 2018;157:6–9.
[48] Xiong Z, Jacques PJ, Perlade A, Pardoen T. Characterization and control of the compromise between tensile properties and fracture toughness in a quenched and partitioned steel. Metall and Mat Trans A 2019.
[49] Rice JR. A path independent integral and the approximate analysis of strain concentration by notches and cracks. J Appl Mech 1968;35:379–86.
[50] Begley JA, Landes JD. The J-integral as a fracture criterion. ASTM STP 514, American Society for Testing and Materials, Philadelphia, PA; 1972. p. 1–20.
[51] Landes JD, Begley JA. The effect of specimen geometry on JIc. ASTM STP 514, American Society for Testing and Materials, Philadelphia, PA; 1972. p. 24–29.
[52] Zhu XK, Leis BN. Revisit of ASTM round robin test data for determining R curves of thin sheet materials. J ASTM Int 2009 [paper ID JAI102510].
[53] ASTM E561. Standard practice for R-curve determination. American Society for Testing and Materials.
[54] Tada H, Paris PC, Irwin GR. The stress analysis of cracks handbook. New York: Third edition. American Society of Mechanical Engineers; 2000.
[55] Hellman D, Schwalbe KH. R-Curve Behaviour of double edge notched tension specimens in plane stress. Mater Sci Eng Technol 1986;17:280–5.
[56] Broberg KB. Crack-growth criteria and non-linear fracture mechanics. J Mech Phys Solids 1971;19:407–18.
[57] Broberg KB. On stable crack growth. J Mech Phys Solids 1975;23:215–37.
[58] Kaufman JG, Hunsicker H. Fracture toughness testing at alcoa research laboratories. Fracture Toughness Test Appl 1965:290–308.
[59] ASTM B871. Standard Test Method for Tear Testing of Aluminum Alloy Products. American Society for Testing and Materials.
[60] Xia L, Shih CF, Hutchinson JW. A computational approach to ductile crack growth under large scale yielding conditions. J Mech Phys Solids 1995;43:389–413.
[61] Zhu XK, Jang SK. J-R curves corrected by load-independent constraint parameter in dcutile crack growth. Eng Frac Mech 2001;68:285–301.
[62] Landes JD, Begley JA. Experimental methods for elastic-plastic and post-yield fracture toughness measurements. Barking, Post-yield fracture mechanics, Applied Science. Publ; 1979.
[63] Akourri O, Louah M, Kifani A, Gilgert G, Pluvinage G. The effect of notch radius on fracture toughness J_{IC}. Eng Frac Mech 2000;65:491–505.
[64] Chaudhari VV, Kulkarni DM, Prakash R. Study of influence of notch root radius on fracture behaviour of extra deep drawn steel sheets. Fatigue Fract Eng Mater Struct 2009;32:975–86.
[65] Mai Y, Cotterell B. Effect of specimen geometry on the essential work of plane stress ductile fracture. Eng Frac Mech 1985;21:123–8.
[66] Cotterell B, Atkins AG. A review of the J and I integrals and their implications for crack growth resistance and toughness in ductile fracture. Int J Fract 1996;81:357–72.
[67] Hance B. Advanced High Strength Steel (AHSS) Performance Levels. SAE Technical Paper 2018-01-0629; 2018.

Paper II. D. Frómeta, A. Lara, L. Grifé, T. Dieudonné, P. Dietsch, J. Rehrl, C. Suppan, D. Casellas, J. Calvo. Fracture resistance of advanced high strength steel sheets for automotive applications. *Metallurgical and Materials Transactions A,* Accepted manuscript.

Fracture resistance of advanced high strength steel sheets for automotive applications

D. Frómeta[1], A. Lara[1], L. Grifé[1], T. Dieudonné[2], P. Dietsch[2], J. Rehrl[3], C. Suppan[3], D. Casellas[1,4*] and J. Calvo[5]

[1] Eurecat, Centre Tecnològic de Catalunya, Unit of Metallic and Ceramic Materials, Plaça de la Ciència, 2, Manresa 08243, Spain
[2] ArcelorMittal Maizières Research SA, Voie Romaine, BP30320, 57283 Maizières-les-Metz, France
[3] voestalpine Stahl GmbH, voestalpine-Straße 3, 4020 Linz, Austria
[4] Division of Mechanics of Solid Materials, Luleå University of Technology, 971 87 Luleå, Sweden
[5] Universitat Politècnica de Catalunya, Materials Science and Engineering department, Eduard Maristany 16, 08019 Barcelona, Spain

[*]Corresponding author: daniel.casellas@ltu.se

Abstract. The fracture resistance of different advanced high strength steel (AHSS) sheets for automotive applications is investigated through conventional tensile tests, fracture toughness measurements and hole expansion tests. Different fracture-related parameters, such as the true fracture strain (*TFS*), the true thickness strain (*TTS*), the fracture toughness at crack initiation (w_e^i), the specific essential work of fracture (w_e) and the hole expansion ratio (HER) are assessed. The specific essential work of fracture (w_e) is shown to be a suitable parameter to evaluate the local formability and fracture resistance of AHSS. The results reveal that fracture toughness cannot be estimated from any of the parameters derived from tensile tests and show the importance of microstructural features on crack propagation resistance. Based on the relation fracture toughness-local formability, a new AHSS classification mapping accounting for global formability and cracking resistance is proposed. Furthermore, a physically motivated fracture criterion for edge-cracking prediction, based on thickness strain measurements in fatigue pre-cracked DENT specimens, is proposed.

Keywords: **Fracture toughness**, **advanced high strength steel sheets, stretch flangeability, cracking resistance, local formability**

1. Introduction

Advanced high strength steels (AHSS) play a fundamental role in the development of modern lightweight automobiles. The use of these steels for structural and safety related automotive components is undergoing a continuous increase in the last years. The body structure of current passenger cars can have up to 51% of AHSS [1] and this percentage might grow up to 65% in upcoming vehicles [1,2]. The main advantage of AHSS is their excellent combination of high strength and good ductility, which has significantly contributed to reduce the total vehicle mass, while improving crash performance.

The AHSS family comprises a wide variety of complex multiphase microstructures that provide unique combinations of mechanical properties by adjusting their chemical composition and thermomechanical processing routes. AHSS are categorized in three main groups or families: 1st, 2nd and 3rd generation AHSS [1]. Dual Phase (DP), Complex Phase (CP), Martensitic (MS), Press-hardened (PHS) and Transformation-Induced Plasticity (TRIP) steels are part of the 1st generation of AHSS. This generation is characterized by showing higher strength and formability than single-phase high strength low alloyed (HSLA) steels [3]. The 2nd generation includes Twinning-Induced Plasticity (TWIP) and austenitic steels. These steels present excellent ductility compared to the 1st generation AHSS at similar strength levels. However, their high alloy content, which significantly increases production costs, and other problems related to delayed fractures and poor weldability have limited their application [4]. The 3rd generation arose to cover the gap between the 1st and the 2nd generation of AHSS. These steels exhibit higher strength and formability than the 1st generation of steels at significantly lower costs than the 2nd

generation of steels [1]. Some of the steels developed under this classification are TBF (TRIP-aided bainitic ferritic) and Q&P (quenching and partitioning) steels. Other TRIP-assisted steels, such as medium-Mn [5] or δ-TRIP steels [6], and nanoprecipitation steels [7] are under development.

The development of new AHSS with higher strengths has introduced new forming challenges and fracture problems related to their limited cracking resistance, as for example edge fractures, limited hole expandability, etc. [8-10]. Often, these fractures are not coherent with conventional formability criteria based on elongation values from tensile tests or forming limit curves (FLC) [8]. A clear example is the edge formability of DP and CP steels. DP steels usually show lower edge formability and hole expansion ability than CP steels, even though the former have greater uniform and total elongation and higher limit strains in the FLC [9, 11-15]. This inconsistency between fracture resistance and traditional ductility definitions, motivated the development of new formability criteria for AHSS, differentiating between global and local formability [16, 17]. The term global formability refers to the most traditional interpretation of formability, i.e. the resistance against the onset of necking instability, and it is well described by tensile properties (strain hardening exponent, true uniform strain) and FLC. On the other hand, local formability is linked to the material's damage tolerance and cracking resistance (bendability, edge cracking, hole expansion, etc.) and, as mentioned before, has no apparent relation with tensile strength/ductility properties. Consequently, alternative approaches have been developed to experimentally assess the local formability of AHSS. The Hole Expansion Test (HET) according to ISO 16630 [18] is well established as a standard procedure for stretch flangeability evaluation of AHSS sheets and the Hole Expansion Ratio (*HER*) has become an almost mandatory parameter for AHSS products manufacturers. Nevertheless, the *HER* is not a material property and depends on many external factors that can cause large data scattering and compromise its reliability: hole preparation method, edge quality, tool stiffness, test operator, crack detection method, etc. [11,15, 19-24]. In order to overcome such uncertainties and improve the accuracy of edge formability prediction, a series of alternative tests based on optical strain measurements and digital image correlation (DIC) techniques have been proposed [15, 24-29].

More recently, other authors have suggested the use of local fracture strain measurements from uniaxial tensile specimens, such as the true fracture strain (*TFS* or ε_f) [16], the reduction of area (*Z*-value) [30] or the true thickness strain (*TTS*) [17,30], as an indicator of local formability of AHSS. Hance [16] proposed the *TFS* derived from the reduction of area fracture surface to assess the fracture resistance of AHSS sheets and, on the basis of this parameter, developed enhanced formability mappings and defined different performance levels for AHSS [16,31]. Larour et al. [30] and Heibel et al. [17] observed a very good correlation between the *TTS* and the *HER* of several AHSS grades. Following the idea of Hance, Heibel et al. proposed a new classification of AHSS according to their global and local ductility, using the true uniform strain and the *TTS*, respectively [17].

By definition, local formability is related to the material's crack nucleation and propagation resistance, i.e. its fracture toughness. Accordingly, other researchers have used different approaches based on fracture mechanics testing for fracture resistance and local ductility assessment of AHSS [9,14,15, 32-35]. For instance, Takahashi et al. [32] investigated stretch flangeability of different hot rolled high strength steels and found a linear correlation between *Jc* and *HER*. Similar correlation between fracture toughness values and *HER* were observed by Casellas et al. [14], Yoon et al. [33] and Frómeta et al. [9, 15]. In [34] and [35], a link was established between crack propagation resistance and crash folding behavior and other local ductility parameters for several AHSS grades (V-bending, local fracture strain from DIC, etc.).

Following such research, the present work aims at providing further evidence on the relationship between fracture toughness and cracking resistance of AHSS and proposes a new fracture performance classification for AHSS according to their crack propagation resistance. The fracture resistance of

different 1st and 3rd generation AHSS steel grades with ultimate tensile strengths (UTS) from 780 to 1180 MPa is investigated by means of uniaxial tensile tests, essential work of fracture tests and hole expansion tests. The correlation between the different parameters is investigated and the role of the main microstructural characteristics on fracture performance is discussed. The microstructure – material performance relationship is addressed by using the fracture toughness and fracture strain values derived from these tests, because such properties are well correlated to edge cracking and impact crack propagation behavior [9,14,15,34,35]. Based on such analysis, a global ductility vs. fracture toughness diagram is presented to describe the overall formability and fracture resistance of AHSS.

2. Materials and methods

2.1. Materials

Six cold rolled AHSS grades in the range of 780-1180 MPa UTS are investigated. The steels were manufactured and supplied by voestalpine Stahl and ArcelorMittal. Table 1 classifies the 6 AHSS grades according to their strength level and AHSS generation. The steel supplier is also indicated. All the steels were provided in the form of 1.4-1.6 mm thick sheets, except for the 3rd Gen DP1180 (t=1.2 mm). Microstructures are shown in Figure 1 to Figure 3. The figures show optical micrographs after LePera etching and scanning electron microscope (SEM) images. The chemical compositions and the microstructural constituents are given in Table 2 and Table 3, respectively. The retained austenite (RA) volume fraction was measured via the saturation magnetization method, as explained in [36].

780 MPa grades show a matrix mainly consisting of ferrite (F) and bainite (B) with different amounts of martensite (M) and martensite/retained austenite (M/RA) islands. DP780 has a lower amount of RA when compared to the TRIP780 grade. On the other hand, DP980 has a ferritic-bainitic matrix with some amount of tempered martensite and a lower amount of hard martensite islands, which are finely distributed.

3rd Gen DP1180 both consists of a matrix of partly upper bainite (UB) with globular islands of M/RA, and partly of lower bainite/tempered martensite (LB/TM) with globular and lamellar formed islands of M/RA. The 3rd Gen TBF1180 is composed of a matrix of carbide-free bainite with globular islands of M/RA and laths of RA. However, the structure of the 3rd Gen TBF1180 is a bit coarser than the one of 3rd Gen DP1180, which might be attributed to a larger size in prior austenite grains. The microstructure of the grade 3rd Gen Q&P1180 is significantly different when compared to the 3rd Gen DP1180 and TBF1180 steels. It has a matrix consisting of tempered or carbon-depleted martensite, including lath-like retained austenite, globular islands of M/RA and bainite. All three 1180MPa grades show quite high contents of retained austenite (12-16%).

Table 1. Description of the investigated AHSS grades

AHSS generation	Strength level [MPa]	Steel denomination	Thickness [mm]	Supplier
1st GEN	780	DP780	1.5	voestalpine
		TRIP780	1.6	ArcelorMittal
	980	DP980	1.35	voestalpine
3rd GEN	1180	3rd Gen DP1180	1.2	voestalpine
		3rd Gen TBF1180	1.4	ArcelorMittal
		3rd Gen Q&P1180	1.5	ArcelorMittal

Table 2. Chemical composition (in weight per cent, the balance is Fe).

Steel grade	C	Si	Mn	Cr	B	Al	Ti
DP780	~0.15	<0.9	<2.0	<0.7	<0.003	~0.05	<0.0060
TRIP780	~0.20	~1.60	~1.70	~0.02	<0.001	~0.05	~0.0070
DP980	~0.15	<0.5	~2.3	<0.7	<0.003	~0.05	<0.0060
3rd Gen DP1180	~0.20	<2.0	~2.5	<0.7	<0.003	~0.05	<0.0060
3rd Gen TBF1180	~0.23	<2.0	<2.9	<0.7	<0.005	~0.04	~0.0070
3rd Gen Q&P1180	~0.18	<2.0	<2.9	<0.7	<0.005	~0.03	~0.0060

Table 3. Microstructural constituents. F: ferrite, B: Bainite, M: Martensite, TM: Tempered martensite, RA: retained austenite. UB: Upper bainite, LB: Lower bainite.

Steel	Microstructure	RA volume fraction, Vγ [%]
DP780	F/B matrix, M/RA islands	9.8
TRIP780	F/B matrix, M/RA islands	15.6
DP980	F/B matrix, TM, M islands, RA	5.5
3rd Gen DP1180	UB/LB matrix, M/RA islands and laths	14.8
3rd Gen TBF1180	Carbide-free B matrix, M/RA islands and laths of RA	15.5
3rd Gen Q&P1180	TM matrix, B, M/RA islands and laths of RA	12.6

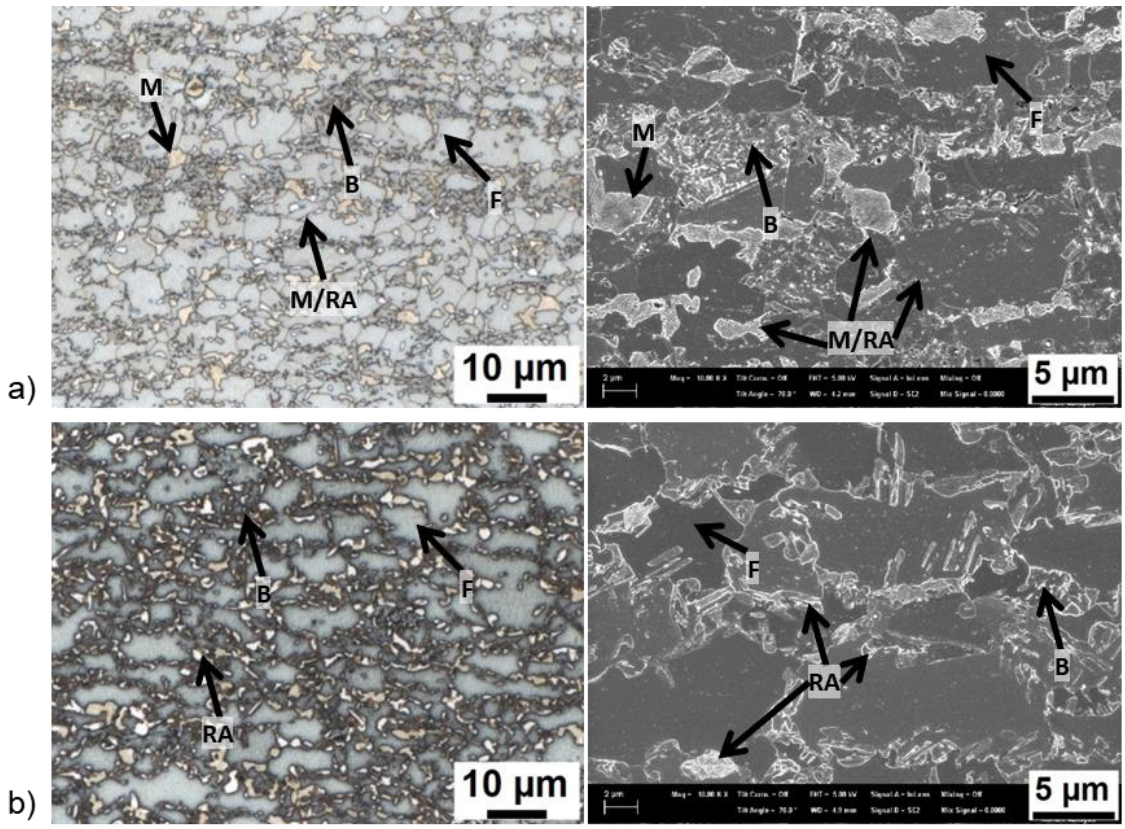

Figure 1. Micrographs of 780 MPa steel grades. Left: Optical microscopy with LePera etching. Right: SEM. a) DP780. b) TRIP780

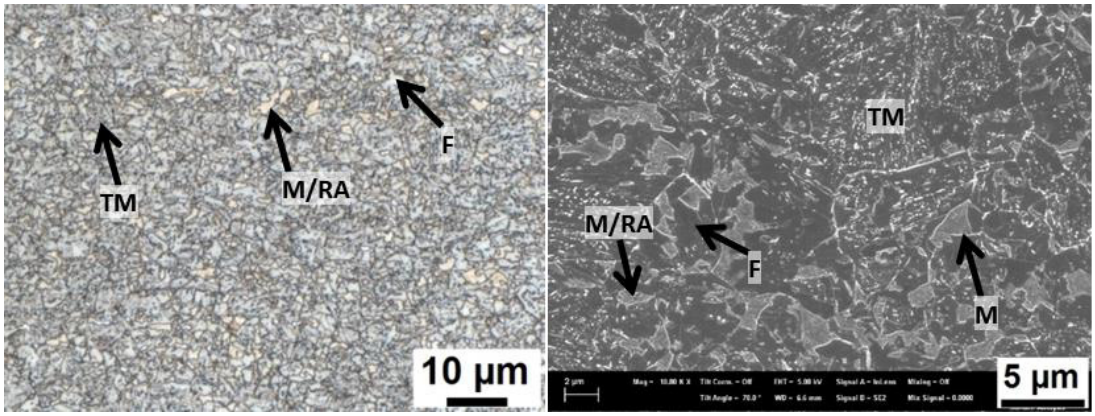

Figure 2. Micrographs of DP980. Left: Optical microscopy with LePera etching. Right: SEM.

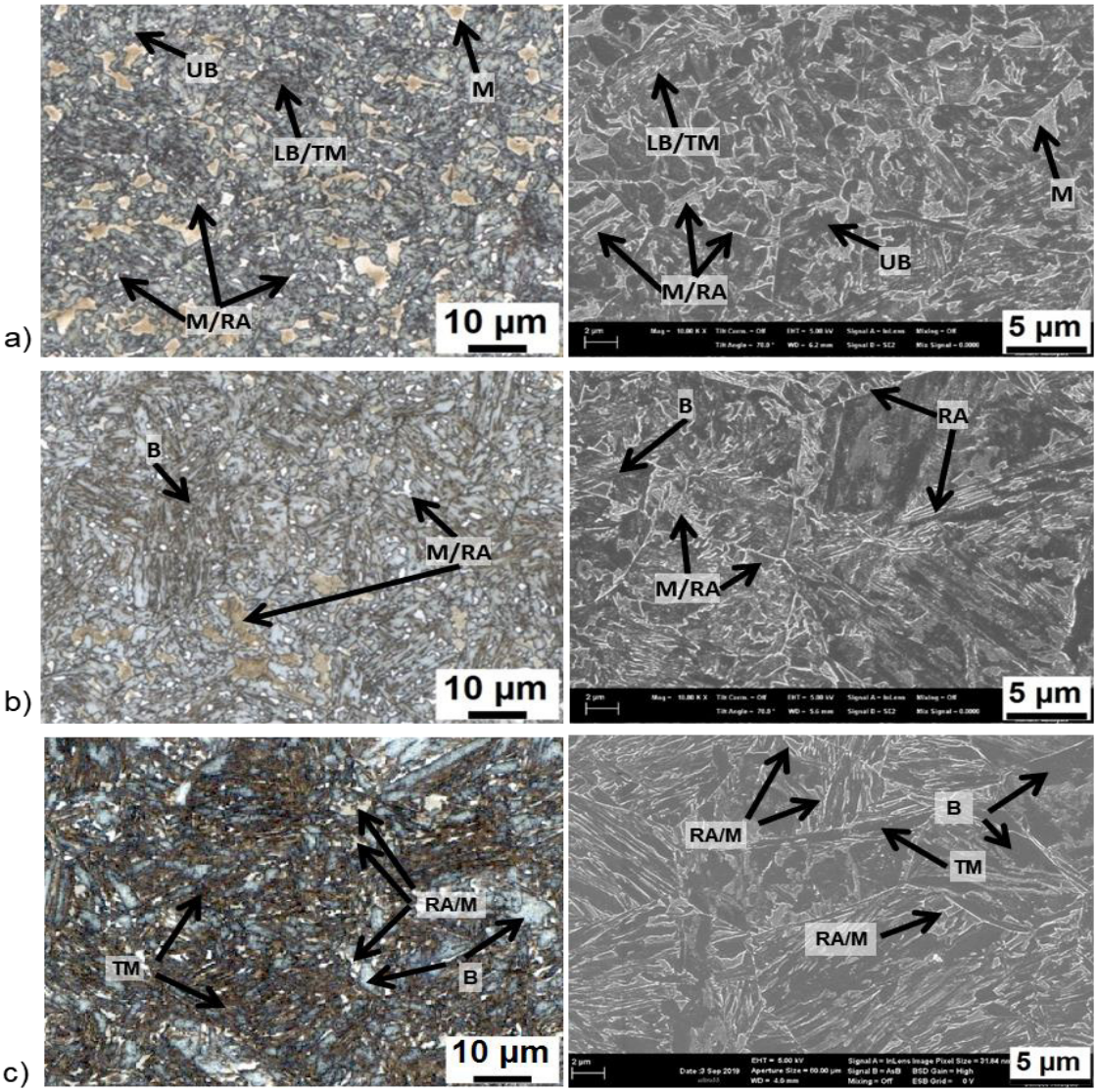

Figure 3. Micrographs of 1180 MPa steel grades. Left: Optical microscopy with LePera etching. Right: SEM. a) 3rd Gen DP1180, b) 3rd Gen TBF1180 and c) 3rd Gen Q&P1180.

2.2. Experimental procedure

2.2.1. Uniaxial tensile tests

Conventional uniaxial tensile tests were performed according to ISO 6892-1 [37]. Standard tensile specimens with a parallel length of 120 mm and a width of 20 mm were machined at transverse orientation respect to the rolling direction. An initial gauge length of 80 mm was used for elongation measurements and 3 specimens per material were tested.

The true fracture strain (*TFS*), derived from the reduction of area at the fracture location was evaluated according to Equation 1:

$$TFS = ln\left(\frac{A_0}{A_f}\right) \quad \text{Equation 1}$$

where A_0 is the initial cross section area and A_f is the area at fracture. The area at fracture was measured from the fracture surface of the tensile specimens according to ASTM E8 [38] with an optical microscope. Thickness measurements were performed on the left (t_{left}) and right (t_{right}) edges and in the middle of the fracture surface (t_{mid}) (Figure 4). From this, the thickness at fracture (t_f) was obtained as follows:

$$t_f = \frac{1}{6}(t_{left} + 4t_{mid} + t_{right}) \quad \text{Equation 2}$$

A_f is calculated according to Equation 3:

$$A_f = width_f * t_f \quad \text{Equation 3}$$

where $width_f$ is the width of the fractured area (Figure 4).

The true thickness strain (*TTS*) was calculated using Equation 4:

$$TTS = ln\left(\frac{t_0}{t_f}\right) \quad \text{Equation 4}$$

where t_o is the initial sheet thickness.

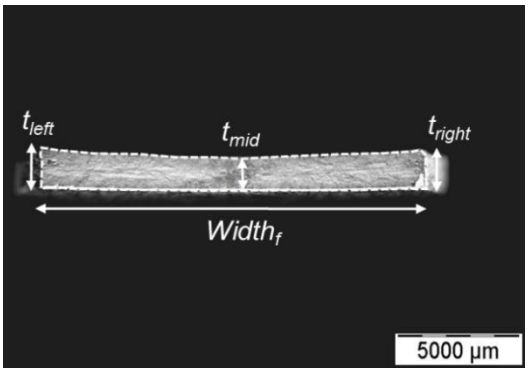

Figure 4. Fracture surface of a uniaxial tensile specimen and location of the thickness and width measurements performed to evaluate the *TFS* and the *TTS*. The dashed line represents the contour of the fractured area.

2.2.2. Fracture toughness

The fracture toughness of the studied AHSS grades was evaluated by means of the essential work of fracture (EWF) methodology [39]. The method allows to experimentally separate the ductile fracture energy (W_f) into two energetic contributions, as shown in Equation 5.

$$W_f = W_e + W_p = w_e l_0 t_0 + w_p \beta {l_0}^2 t_0 \quad \text{Equation 5}$$

where W_e is the essential work of fracture developed in the fracture process zone and W_p is the non-essential plastic work dissipated in an outer region surrounding the crack plane. w_e is the specific work of fracture per unit area, l_0 is the ligament length, t_0 is the specimen thickness, w_p is the specific non-essential plastic work per unit volume and β is a shape factor that depends on the shape of the plastic zone. Dividing Equation 5 by the initial cross section area ($l_0 t_0$) gives:

$$\frac{W_f}{l_0 t_0} = w_f = w_e + w_p \beta l_0 \quad \text{Equation 6}$$

According to Equation 6, if a series of specimens with different ligament lengths is tested up to fracture and w_f is plotted against the ligament length (l_0), a straight line is obtained. Then, w_e can be determined by linear extrapolation to zero ligament length. w_e has shown to be a suitable parameter to describe the crack propagation resistance of thin ductile sheets, including polymers [40-42], metals [43-47] and AHSS [9, 14, 15, 34, 35, 48-52]. It is important to point out that the plane stress fracture toughness of thin ductile sheets has an important contribution from necking and, therefore, the measured w_e cannot be considered an intrinsic material property but a material constant for the given sheet thickness.

Even though w_e has shown to be independent of the specimen geometry and can be obtained from different geometries [40, 42], for thin sheets, the EWF testing protocol [53] developed by the European Structural Integrity Society (ESIS) recommends the use of Double Edge Notched Tension (DENT) specimens because of its symmetry and minimal specimen rotation and buckling during testing.

In the present work, EWF tests were performed by testing rectangular DENT specimens with dimensions of 240 x 55 mm machined in the transverse orientation with respect to the rolling direction (notches aligned in the rolling direction). Five different initial ligament lengths (l_0) ranging from 6 to 14 mm were used and 3 specimens per ligament length were tested. The specimens were tested up to fracture at a constant cross-head speed of 1 mm/min. Initial notches were machined by electrical discharge machining (EDM) and fatigue pre-cracks were nucleated at the notch root to avoid the effect of the notch radius on fracture toughness results (Figure 5a).

The fracture toughness at crack initiation (w_e^i) was also assessed by calculating the energy up to the onset of crack propagation as described in [34] and [51]. Further details about the experimental procedure for the determination of the EWF in AHSS sheets are published in previous works [14, 34, 35,49-51].

The thickness strain of the DENT specimens was evaluated according to Equation 7:

$$\varepsilon_{3f\ DENT} = ln\left(\frac{t_0}{t_f}\right) \quad \text{Equation 7}$$

where t_o is the initial sheet thickness and t_f is the thickness at fracture measured from the fracture surface (Figure 5b). The thickness measurements were performed at different locations and the evolution of $\varepsilon_{3f\ DENT}$ as a function of the distance from the crack tip was evaluated [51]. Two different terms were

identified: the thickness strain at crack initiation ($\varepsilon_{3f\,DENT}{}^{i}$) and the thickness strain for the stable crack propagation ($\varepsilon_{3f\,DENT}{}^{p}$).

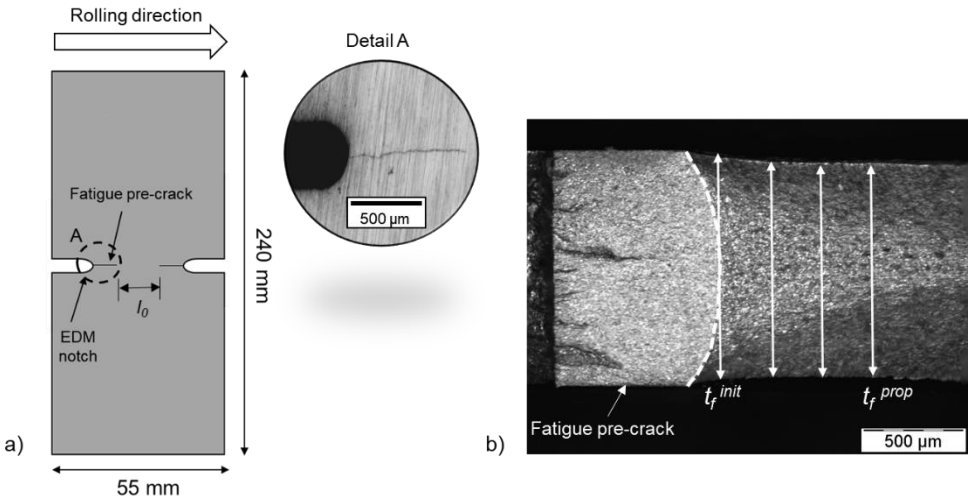

Figure 5. a) DENT specimen used for EWF tests and detail of the fatigue pre-crack at the notch root. b) Fracture surface of a DENT specimen and location of the different thickness measurements. The dashed line indicates the crack tip.

2.2.3. Hole Expansion Tests

Hole expansion tests (HET) were performed according to ISO 16630 [18]. Square samples 100x100 mm with an initial punched hole 10 mm in diameter in the centre were used (Figure 6a). According to standard recommendations, the hole was punched using a punch-to-die clearance of 12 ± 2 %. The hole expansion was performed using a conical expansion tool with a top angle of 60º. The tests were conducted in a universal testing machine at displacement rate of 1 mm/s and were stopped after the first through-thickness crack was observed. Crack formation was detected by using a high resolution video camera (Figure 6). A minimum of 5 specimens per material were tested. The limiting hole expansion ratio (*HER*) was obtained as follows:

$$HER = \frac{D_h - D_0}{D_h} \times 100 \qquad \text{Equation 8}$$

where D_h is the hole diameter after failure and D_0 is the initial hole diameter. D_h was measured from the images of the video camera by using a digital image analysis software (Figure 6d).

Furthermore, thickness measurements at the crack edge were performed by sectioning the cracks of HET specimens after the test, as suggested in [54]. Figure 6e shows a longitudinal section of a crack and the thickness measurements performed at different distances from the punched hole edge. Thickness strains were calculated in the same manner as described above for DENT specimens (Equation 7).

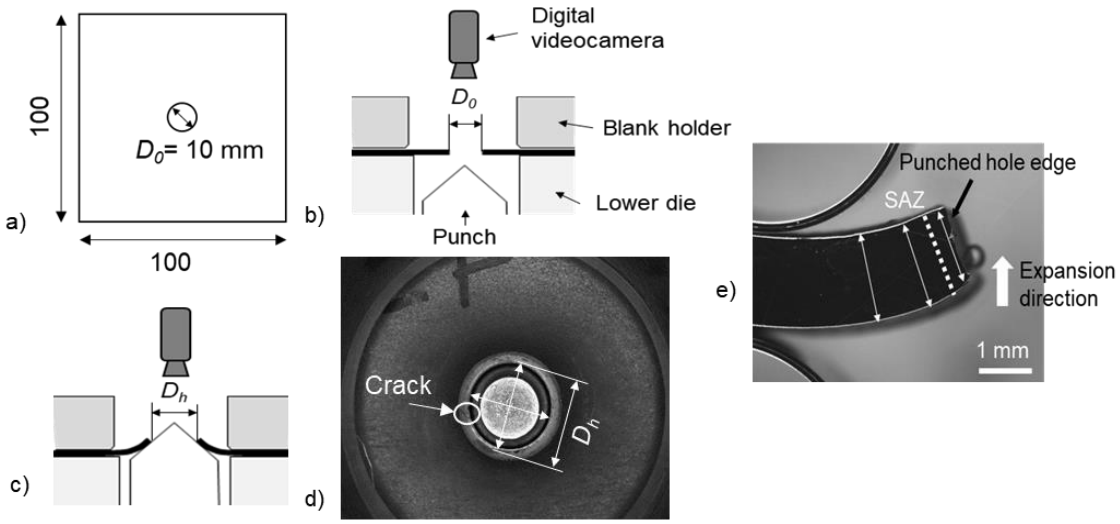

Figure 6. a) Specimen geometry for HET. b, c) Schematic representation of the experimental procedure for the HET. Before (b) and after (c) the test. d) Digital image used for the evaluation of the *HER*. e) Longitudinal section of a crack in a HET specimen after the test and location of the thickness measurements performed. SAZ: shear affected zone.

3. Results

3.1. Uniaxial tensile properties

Figure 7 shows the engineering and true stress-strain curves for the 6 AHSS grades investigated. True stress-strain curves are represented up to the uniform strain and linearly extrapolated to the true fracture strain. The fracture stress was calculated by dividing the load at fracture by the fracture area. The mechanical properties are summarized in Table 4.

DP780 shows comparable YS and UTS but lower elongation (both uniform and total) and *UTSxTE* than TRIP780. Both steels also show similar strain hardening exponent (calculated between 2 and 4% of deformation) and *TFS*. DP980 shows higher strength and lower elongation than 780MPa steel grades. However, it exhibits higher *TFS*. Despite their higher strength, 3rd Gen 1180 MPa steel grades show greater uniform and total elongation values than DP980. The 3rd Gen DP1180 presents lower YS, slightly higher UE/TE and the same UTS level than 3rd Gen TBF1180. 3rd Gen Q&P1180 has similar elongation to 3rd Gen TBF1180 but higher YS and slightly lower UTS. 3rd Gen DP1180 shows the greatest *UTSxTE* product of the three 1180MPa grades. On the other hand, 3rd Gen Q&P1180 shows the greatest *TFS* of the investigated steel grades.

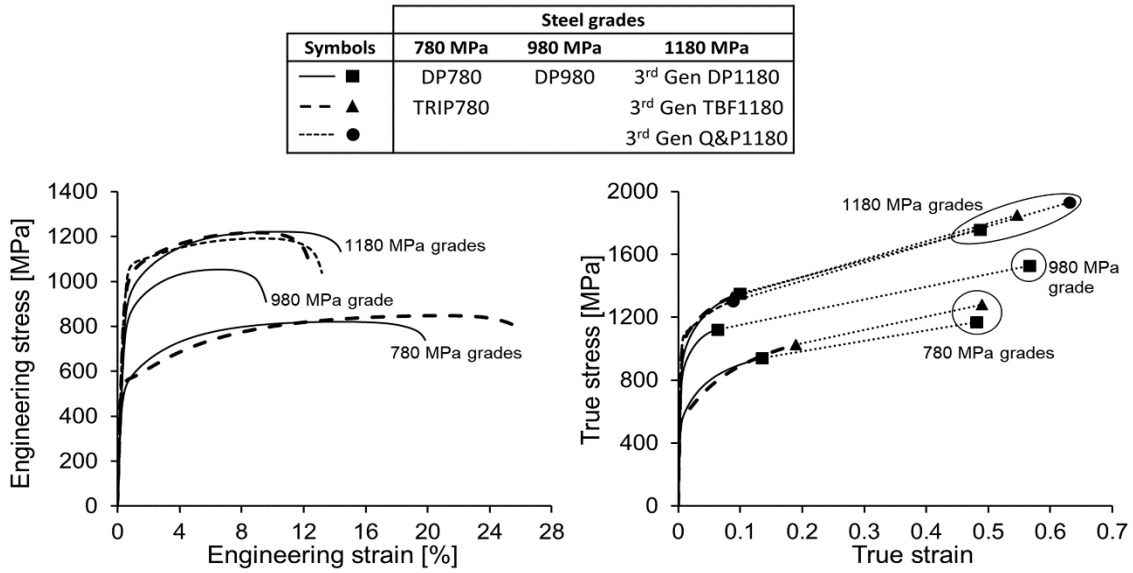

Figure 7. Engineering (left) and true (right) stress-strain curves for the investigated AHSS grades.

Table 4**.** Mechanical properties for the transverse direction. *YS*= yield stress; *UTS* = ultimate tensile strength; *UE* = uniform elongation; *TE* = total elongation (initial gauge length of 80 mm); $n_{2\text{-}4}$ = strain hardening exponent between 2 and 4% deformation; *TUE* = true uniform strain; *TFS* = true fracture strain; *TTS*= true thickness strain.

Steel	*YS* [MPa]	*UTS* [MPa]	*YS/UTS* [-]	*UE* [%]	*TE* [%]	$n_{2\text{-}4}$ [-]	*TUE* [-]	*TFS* [-]	*TTS* [-]	*UTSxTE* [MPa*%]
DP780	513	823	0.62	14.2	19.9	0.20	0.13	0.48	0.45	16378
TRIP780	542	851	0.64	20.7	25.8	0.20	0.19	0.49	0.25	21956
DP980	816	1055	0.77	6.54	9.7	0.13	0.06	0.57	0.57	10234
3rd Gen DP1180	895	1212	0.74	10.5	14.3	0.15	0.10	0.49	0.51	17332
3rd Gen TBF1180	987	1216	0.81	9.2	12.6	0.11	0.09	0.55	0.57	15322
3rd Gen Q&P1180	1034	1191	0.87	9.2	13.1	0.09	0.09	0.63	0.64	15602

3.2. Fracture toughness

3.2.1. Essential Work of Fracture

Figure 8 shows the results from EWF tests. w_e and w_e^i values are given in Table 5. TRIP780 shows one of the lowest w_e of the investigated steels, comparable to that of 3rd Gen DP1180 and 3rd Gen TBF1180. DP780 has slightly greater w_e, similar to DP980 ($w_e \approx 150$ kJ/m^2). 3rd Gen Q&P1180 presents the greatest w_e. Concerning the fracture toughness at crack initiation, the trend is similar to the one observed for w_e. TRIP780, 3rd Gen DP1180 and 3rd Gen TBF1180 have slightly lower w_e^i than DP780 and DP980 while 3rd Gen Q&P1180 shows the greatest w_e^i. DP780 and DP980 present the highest contribution from crack propagation resistance after initiation ($w_e^i/w_e \approx 0.80$). In 3rd Gen DP1180 and 3rd Gen TBF1180 steels, such contribution is lower ($w_e^i/w_e \approx 0.90$). For the steels TRIP780 and 3rd Gen Q&P1180, the energy for crack initiation represents 0.98 and 0.94 of the total fracture energy, respectively.

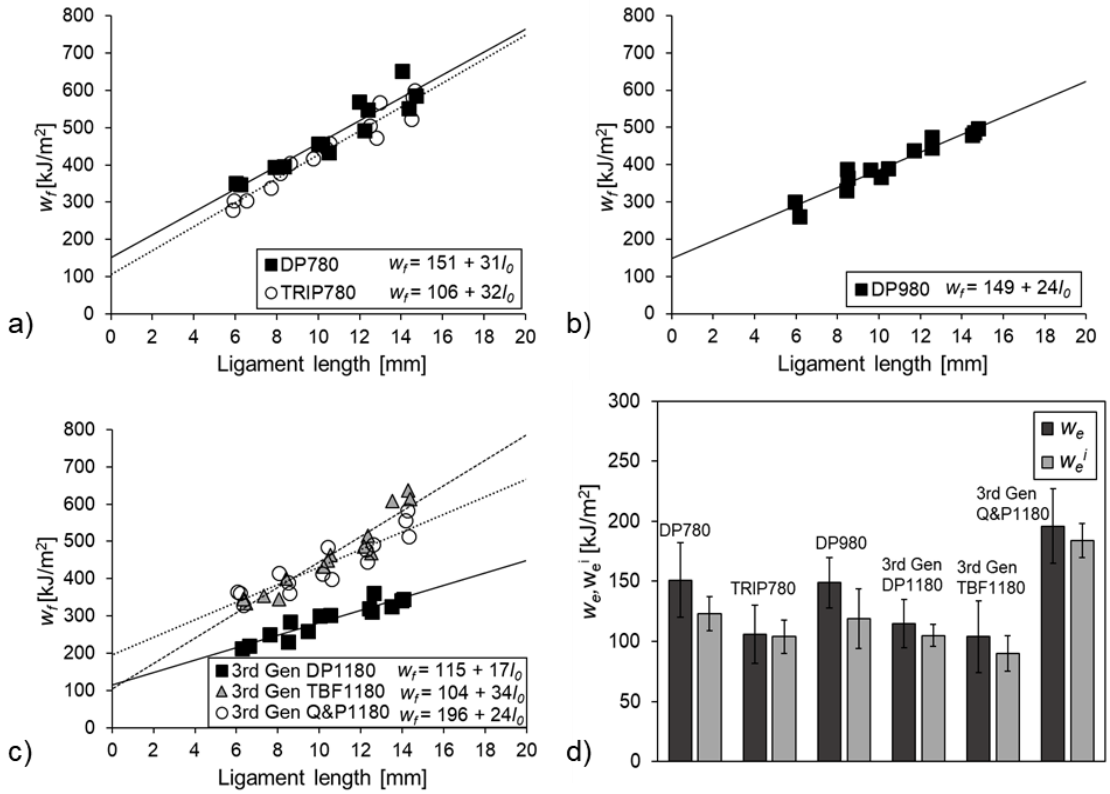

Figure 8. w_f as a function of the ligament length (l_0) for: a) 780 MPa, b) 980 MPa and c) 1180 MPa steel grades. d) w_e and w_e^i for all the investigated AHSS grades.

3.2.2. Fracture thickness strain from DENT specimens

Thickness strain of DENT specimens is plotted in Figure 9 as a function of the distance from the crack tip. $\varepsilon_{3f\,DENT}{}^i$ and $\varepsilon_{3f\,DENT}{}^p$ values are summarized in Figure 9d and Table 5.
$\varepsilon_{3f\,DENT}{}^i$ corresponds to the value of $\varepsilon_{3f\,DENT}$ at the crack tip (distance from crack tip= 0 mm). As observed in Figure 9a-c, $\varepsilon_{3f\,DENT}$ reaches a constant value, corresponding to the stable crack propagation, around 0.4-0.5 mm from the crack tip. $\varepsilon_{3f\,DENT}{}^p$ is an average of $\varepsilon_{3f\,\mathrm{DENT}}$ for a crack tip distance between 0.4 and 0.8 mm.

The steels DP780, TRIP780, DP980 and 3rd Gen Q&P1180 present similar thickness strain at crack initiation ($\varepsilon_{3f\,DENT}{}^i \approx 0.08$). 3rd Gen DP1180 and 3rd Gen TBF1180 show lower $\varepsilon_{3f\,DENT}{}^i$ (≈ 0.05). DP780 also exhibits the greatest thickness strain for the crack propagation, followed by 3rd Gen Q&P1180 and TRIP780. Finally, DP980, 3rd Gen DP1180 and 3rd Gen TBF1180 present the lowest $\varepsilon_{3f\,DENT}{}^p$.

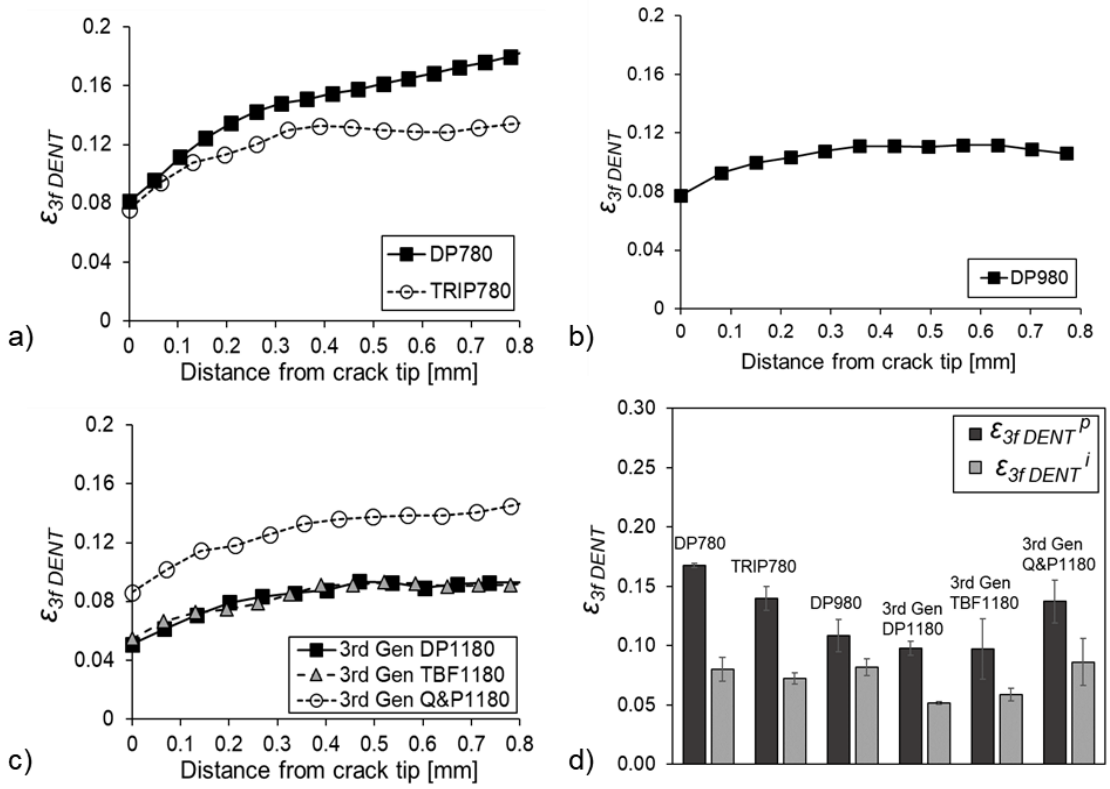

Figure 9. $\varepsilon_{3f\,DENT}$ as a function of the distance from the crack tip for: a) 780 MPa, b) 980 MPa and c) 1180 MPa steel grades. d) $\varepsilon_{3f\,DENT}{}^{i}$ and $\varepsilon_{3f\,DENT}{}^{p}$ for all the investigated AHSS grades.

3.3. Hole Expansion tests

The measured *HER* values are shown in Figure 10a and Table 5. The results are the average of 5 specimens. The standard deviation is indicated (error bars). The Q&P steel exhibits the greatest *HER*, followed by DP980 and DP780. The latter shows very similar *HER* as 3rd Gen DP1180 and 3rd Gen TBF1180. The TRIP780 steel presents the lowest *HER* among the investigated steels.

In Figure 10b-d, the thickness strain measured from HET specimens is plotted as a function of the distance from the punched hole edge. Because of the lower thickness in the shear affected zone (SAZ), the values of thickness strain are higher near the hole edge. After an initial transition, the thickness strain stabilizes at a distance of approximately 0.5-0.6 mm from the edge. To avoid the influence of the SAZ in thickness measurements, thickness strain for HET specimens was determined for a distance between 0.5 and 1.5 mm. The values of true thickness strain in HET specimens (TTS_{HET}) are summarized in Table 5.

Small differences can be appreciated in TTS_{HET} for the investigated AHSS grades. Most of the steels (DP780, DP980, 3rd Gen DP1180 and 3rd Gen TBF1180) present similar thinning at fracture in HET specimens ($TTS_{HET} \approx 0.11$). 3rd Gen Q&P1180 and TRIP780 show the highest and lowest TTS_{HET}, respectively.

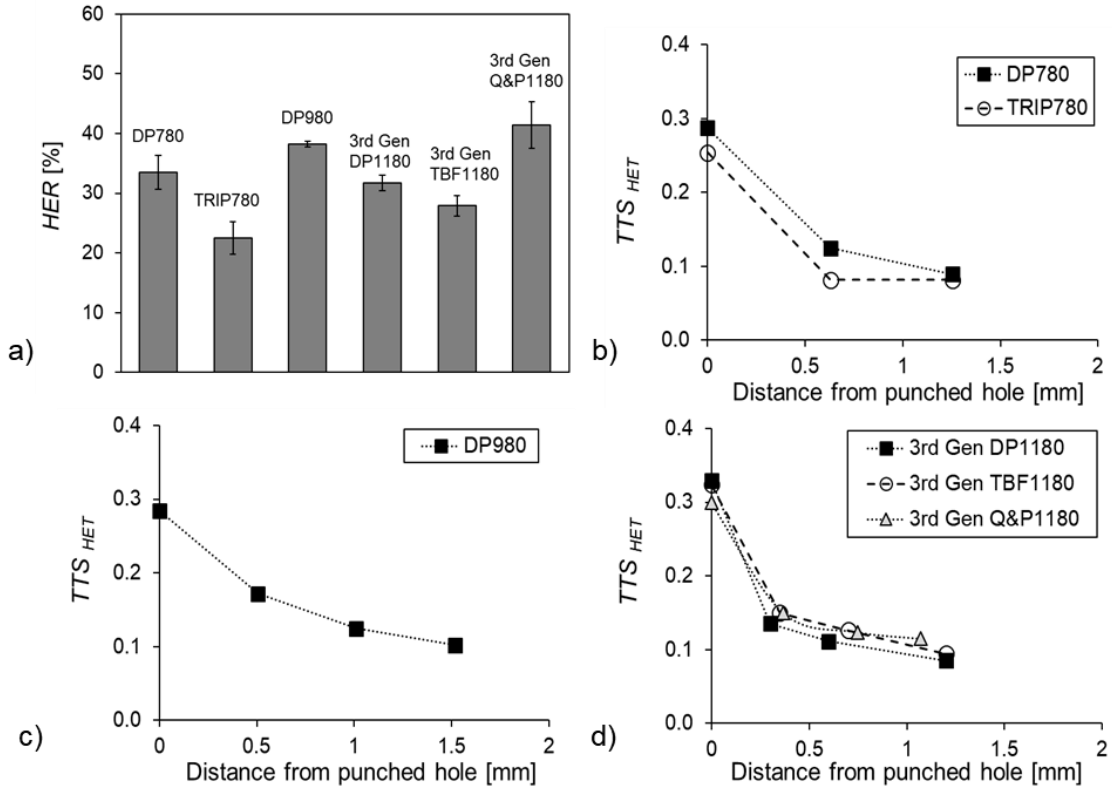

Figure 10. a) Hole expansion ratio values for the investigated AHSS grades. b, c, d) Thickness strain near the crack measured from HET specimens.

Table 5**.** Results from EWF tests and HET

	EWF		Thickness strain DENT		HET	
Steel	w_e^i [kJ/m^2]	w_e [kJ/m^2]	$\varepsilon_{3f\,DENT}{}^i$ [-]	$\varepsilon_{3f\,DENT}{}^p$ [-]	*HER* [%]	TTS_{HET} [-]
DP780	123 ± 14	151 ± 31	0.08 ± 0.01	0.17 ± 0.00	34 ± 3	0.11 ± 0.03
TRIP780	104 ± 14	106 ± 24	0.07 ± 0.00	0.14 ± 0.01	23 ± 3	0.08 ± 0.00
DP980	119 ± 25	149 ± 21	0.08 ± 0.01	0.11 ± 0.01	38 ± 1	0.11 ± 0.02
3rd Gen DP1180	105 ± 9	115 ± 20	0.05 ± 0.00	0.10 ± 0.01	32 ± 1	0.10 ± 0.02
3rd Gen TBF1180	90 ± 15	104 ± 30	0.06 ± 0.01	0.10 ± 0.03	28 ± 2	0.11 ± 0.02
3rd Gen Q&P1180	184 ± 14	196 ± 31	0.09 ± 0.02	0.14 ± 0.02	41 ± 4	0.12 ± 0.01

4. Discussion

4.1. Effect of the microstructure on mechanical properties and fracture resistance

The mechanical properties of AHSS are closely related to their complex multiphase microstructures. The two investigated 780 MPa steel grades, DP780 and TRIP780, have similar microstructures consisting of a ferritic-bainitic matrix with presence of martensite islands and different RA contents. The greater content of RA in TRIP780, leads to higher uniform and total elongation compared to DP780 (Figure 7), thanks to the contribution of the TRIP effect. The beneficial influence of TRIP effect on mechanical properties is associated to the formation of additional geometrically necessary dislocations during the strain-induced martensitic transformation, which increases work hardening and delays the

onset of necking [55,56]. The amount of dislocations generated depends on the amount of the RA transformed. Therefore, a higher RA volume fraction implies a higher contribution of the TRIP effect to the mechanical performance. The relation between the RA content and uniaxial tensile strength and ductility is illustrated in Figure 11; the higher the RA content, the higher the *UTSxTE* product.

In DP980, part of the ferrite is replaced by tempered martensite and the amount of martensite is increased respect to DP780 and TRIP780, resulting in higher strength and lower elongation. DP980 has the lowest amount of RA. Therefore, the contribution of the TRIP effect to the uniform and total elongation is limited compared to the other steel grades. The substitution of the soft ferrite by bainite or tempered martensite in 3rd Gen 1180 MPa steels allows attainment of higher strength levels, while the strain-induced transformation of RA to martensite, significantly improve the ductility compared to DP980.

The advantageous effect of RA and the strain-induced transformation to martensite on strength and ductility has been reported in several works [55, 57-60]. Nevertheless, the contribution of TRIP effect to fracture resistance is not so evident as shown in Figure 11. The figure shows no direct correlation of RA volume fraction with the *TFS* or the fracture toughness (w_e). For instance, looking at 1180 MPa steel grades, it can be seen that the 3rd Gen Q&P1180 shows the highest *TFS* and w_e, whereas it has the lowest amount of RA. The same applies for 780 MPa steel grades. Despite the larger RA content of TRIP780 it shows similar *TFS* and lower w_e than DP780. This finding points out the limited, or even negative, impact of RA on edge formability and crash performance.

Xiong et al. [60] also observed that, for a Q&P steel quenched at different temperatures, the *UTSxTE* product increased with increasing the RA content, while fracture toughness decreased. This detrimental effect of RA on cracking resistance is attributed to the higher stress triaxility present in the crack tip which significantly increases the RA to martensite transformation rate. Consequently, the brittle network of fresh martensite created in the fracture process zone favors damage and rapid crack propagation [59,60]. Different studies revealed that other factors, such as the RA morphology, size or stability also have influence on fracture resistance of TRIP-assisted steels [48,59-61].

However, fracture resistance is not only controlled by RA content and stability but also by matrix characteristics and secondary phases distribution. The work of de Diego-Calderon et al. [61] showed that crack initiation in Q&P steels is mainly controlled by the tempered martensite grain size and volume fraction, which increases the plastic strain energy to form micro-ductile structures and by the untempered martensite island formed during Q&P cycle, which act as cleavage initiation sites. According to this, the larger amount of fresh martensite present in the 3rd Gen DP1180 probably has a negative effect on *TFS* and w_e. On the other hand, the more homogeneous carbon-depleted martensite matrix of 3rd Gen Q&P1180 contributes to increase the fracture resistance. Therefore, to obtain an optimum balance between fracture resistance and global formability, the RA volume fraction and stability as well as the matrix characteristics, should be carefully controlled.

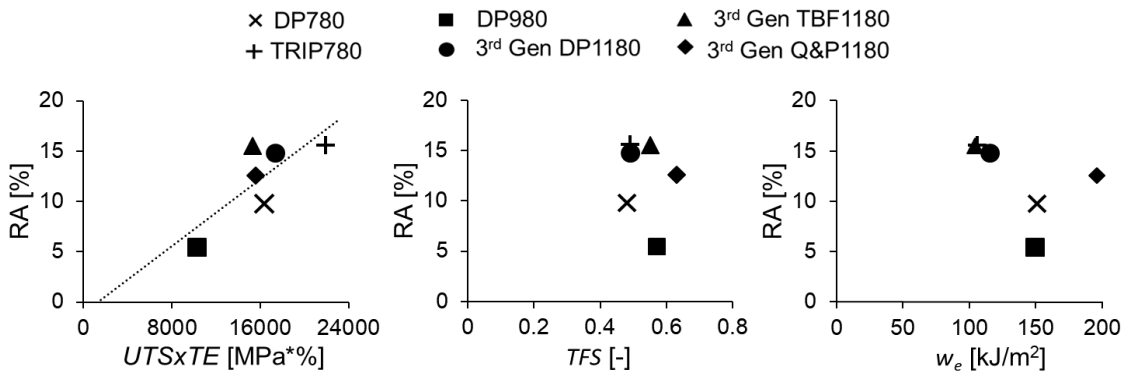

Figure 11. Relation of RA content with strength/ductility and fracture resistance parameters.

4.2. Correlation between stretch flangeability and fracture resistance parameters

The identification of the material properties governing the stretch flangeability of AHSS has been the focus of extensive research [14,17, 28-33,51]. As mentioned before, the *HER* has become the most widespread parameter for stretch flangeability and edge cracking resistance assessment of AHSS. However, while it is a very useful parameter for material ranking, it is not an intrinsic material property and depends on many variables. For this reason, constant efforts are devoted to correlate the *HER* with mechanical properties. Contrary to the observations for low strength steels [62], conventional uniaxial tensile properties such as tensile strength or elongation are not good indicators of *HER*. This is also shown in Figure 12, where the *HER* values measured in this work are plotted against different tensile properties (*UE*, *TE*, *UTSxTE*) and fracture resistance parameters (*TFS*, *TTS*, w_e). The figure shows that the *HER* decreases with increasing *UE*, *TE* and *UTSx UTE* product, which is opposite to the initial expectations. On the other hand, fracture resistance parameters such as the *TFS*, the *TTS* or the w_e are more suitable to rationalize stretch flangeability of AHSS, i.e. the higher the fracture resistance the higher the stretch flangeability. An especially good linear correlation is observed between *HER* and w_e (R^2=0.79), which is in good agreement with the results of Casellas et al. [14] and Frómeta et al. [15]. For the sake of comparison, the w_e and *HER* values obtained in this work are plotted, together with the results of [14] and [15], in Figure 13. Unpublished results for different HSLA steels are also included. The very good linear fitting for different AHSS families (R^2=0.91) strengthen the hypothesis that stretch flangeability of AHSS is mainly dictated by fracture toughness, measured here in terms of w_e, which controls the propagation of the microcracks generated during hole punching (or edge cutting). It is important to remark that *HER* values do not only depend on material properties but also on hole preparation method, edge quality, etc. Consequently, deriving definitive conclusions only from HETs may sometimes lead to misleading material ranking and non-optimum material selection. In turn, fracture toughness is the material property that controls cracking resistance and represents a more objective design parameter for microstructural optimization in terms of fracture resistance.

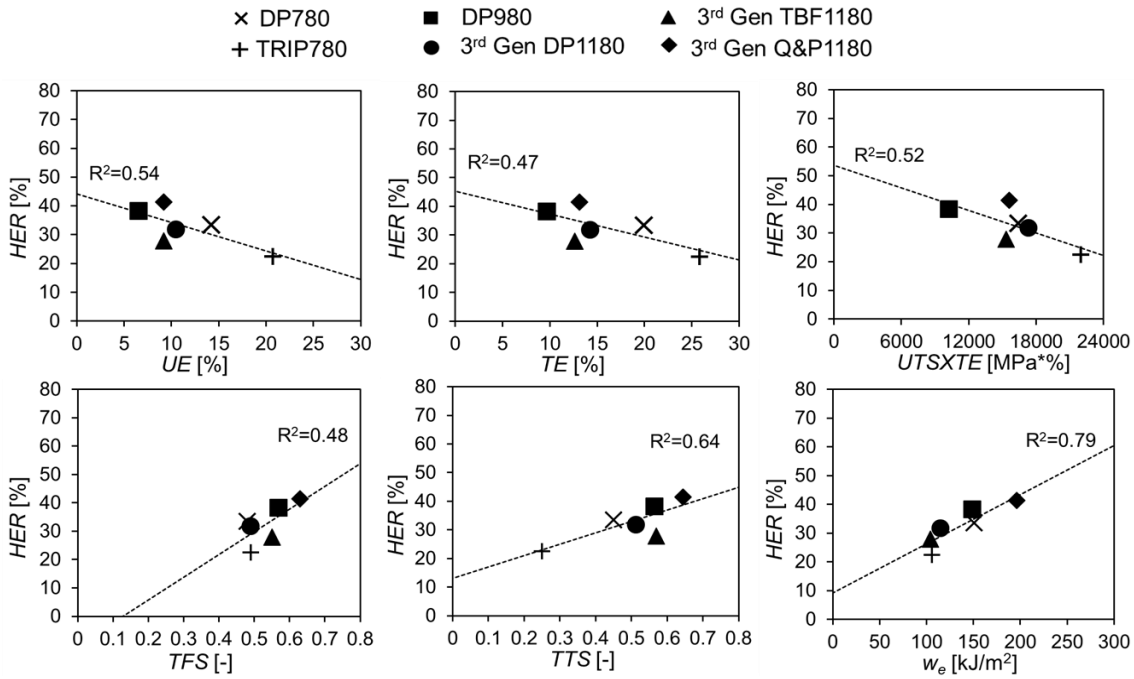

Figure 12. HER values as a function of different uniaxial strength/ductility and fracture resistance parameters

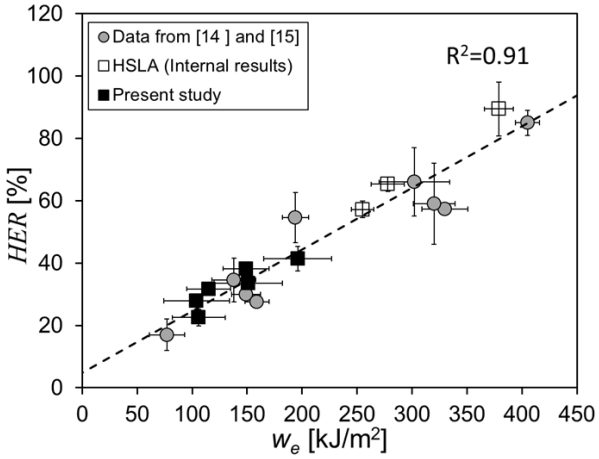

Figure 13.Correlation between *HER* and w_e for the AHSS grades investigated in this work together with previously published results by the authors [14, 15]. Internal unpublished results for HSLA are also plotted. All the *HER* values shown are from HETs according to ISO16630.

4.3. Thickness strain measurements

Figure 14 compares the thickness strains measured in HET, DENT and uniaxial tensile specimens. For all the investigated AHSS grades, the values of thinning measured in HET specimens (TTS_{HET}) are within the range of thickness strain measurements from DENT specimens ($\varepsilon_{3f\,DENT}{}^{i}$ and $\varepsilon_{3f\,DENT}{}^{p}$). It suggests that fracture mechanisms involved in HET and DENT tests are phenomenologically similar; i.e. in both tests, fracture is triggered by the propagation of pre-existing cracks (microcracks around the punched hole in HET [14, 33], and fatigue pre-cracks in DENT specimens). Accordingly, the critical thinning for edge crack propagation can be directly related to the thickness strains measured in pre-cracked DENT specimens, as shown in Figure 14.

This approach can be seen as an alternative to the edge thinning limit (*ETL*) criterion proposed by Hance [54]. The *ETL* is defined as the critical thinning for edge crack propagation and is calculated according to Equation 9:

$$ETL = 1 - \exp\left[\frac{-\ln\left(1+\left(\frac{HER_{LB}}{100}\right)\right)}{R_m+1}\right] \quad \text{Equation 9}$$

where HER_{LB} is the lower-bound *HER* [54] and R_m is the normal anisotropy.

If the *ETL* is exceeded anywhere along the edge of a deformed blank, or a punched hole in this case, then there is high risk of edge cracking. Figure 14 plots the calculated *ETL* values for the steels investigated in the present work. As observed, *ETL* values are in good agreement with TTS_{HET} and $\varepsilon_{3f\,DENT}$. Therefore, thickness strain measurements in pre-cracked DENT specimens can be used to establish a limit edge-crack thickness strain which, like the *ETL* criterion, can be implemented in FEM software as an objective and physically motivated criterion for edge-cracking prediction. Establishing a comparison between this criterion and the edge thinning diagram proposed by Hance [54], the lower safe limit for edge crack prediction would be dictated by the $\varepsilon_{3f\,DENT}{}^{i}$. Below this thickness strain the component would be safe from edge cracking. The upper limit for failure would be given by DENT $\varepsilon_{3f\,DENT}{}^{p}$. The range between $\varepsilon_{3f\,DENT}{}^{i}$ and $\varepsilon_{3f\,DENT}{}^{p}$, would indicate risk of cracking.

As shown in Figure 14, the values of *TTS* from uniaxial tensile specimen completely overestimate the thickness strains from DENT and HET specimens (*TTS*=0.25-0.64). However, looking at the relative differences between the different steel grades, it can be observed that the thickness strain values for the three different test configurations follow a similar trend. This evidences that, whereas the *TTS* cannot be directly used to estimate the thickness reduction in DENT and HET specimens, it can provide a qualitative ranking in terms of fracture toughness and edge fracture resistance.

These observations may help to better understand the relationship between edge fracture and crack propagation resistance in AHSS. However, other factors such as the influence of cutting or punching conditions on limit edge thinning values should be investigated in further detail to define a reliable fracture criterion for edge crack prediction, considering initial edge damage and crack propagation resistance.

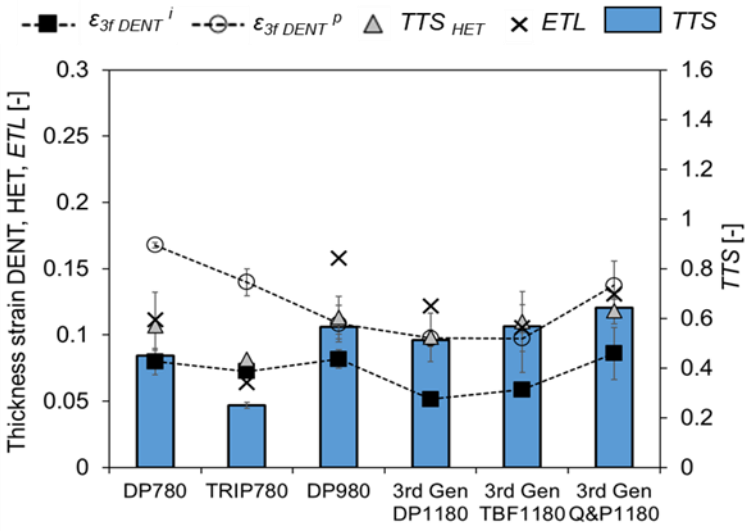

Figure 14. Thickness strain measurements performed in DENT, HET and uniaxial tensile specimens. Edge thinning limit (*ETL*) values are also plotted.

4.4. Relation between tensile properties and fracture toughness

As discussed above, fracture toughness is a relevant property to assess the fracture resistance of AHSS. Unfortunately, as shown in Figure 15, there is no a direct relationship between fracture toughness and conventional uniaxial tensile properties [48,51,60]. It is clearly shown that elongation values (uniform and total) or the *UTSxTE* product, which is usually used as a toughness indicator, are not suitable parameters to estimate the cracking resistance of AHSS. On the other hand, as previously observed for edge fracture resistance (Figure 12), local strain measurements from uniaxial tensile tests (*TFS*, *TTS*) give a better estimation of fracture toughness. Nevertheless, previous works showed that these fracture related parameters often cannot accurately describe the fracture behavior of the material when it is related to the presence of existing cracks or defects [51,60]. Therefore, to better understand the fracture performance of AHSS sheets, including crack initiation and propagation resistance, fracture toughness should be properly measured in the frame of fracture mechanics.

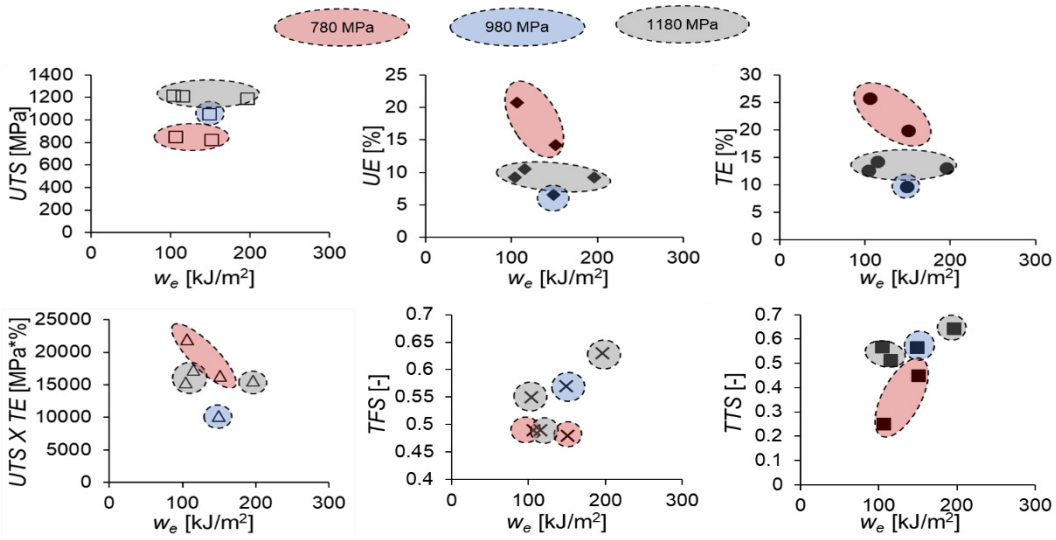

Figure 15. Correlation between fracture toughness and uniaxial tensile properties.

4.5. AHSS classification according to their crack propagation resistance

The need for new classification mappings based on formability and fracture performance of AHSS has become more and more evident in the last years [16,17, 30,31]. The concept of a global/local formability map for AHSS was introduced by Hance [16], who proposed a novel diagram for AHSS performance classification. The global formability was represented in terms of uniform elongation, which is a suitable measure of the material resistance against strain localization or necking, and local formability was indexed on the basis of the *TFS*. The ratio between uniform strain and *TFS* provides a general idea about the overall formability of the material. Alternatively, Larour et al. [30] and Heibel et al. [31], suggested the use of the true thickness strain (*TTS*), for local formability prediction, based on the good correlation between *TTS* and *HER*. Heibel et al. [31] stated that thickness strain measurements are more accurate than fracture strains based on the reduction of area (*TFS* or *Z*-value), since they do not take into account the fracture width, which is only influenced by global formability. They developed a formability mapping using the *TTS* and the true uniform strain (ε_u) as a measure of local and global formability, respectively.

However, none of these classification approaches consider the material's crack propagation resistance which, as shown in the present work and in previous publications [14,15, 34, 35, 51], provides useful information about the overall fracture behavior of AHSS sheets. According to this, an alternative performance mapping approach accounting for the crack propagation resistance is proposed in Figure 16. The figure plots the uniform elongation (*UE*) in the x-axis and the specific essential work of fracture (w_e) in the y-axis. The specific essential work of fracture is raised as an index of local formability or cracking resistance. i.e. the higher the w_e the higher the cracking resistance. The diagram is divided in different quadrants according to global and local formability levels. The more to the right in the plot the greater the global formability, whereas upper quadrants indicate superior fracture resistance and damage tolerance. Compared to traditional classification diagrams based only on tensile strength and elongation values, such as the so-called "banana" plot (Figure 17a), this classification system allows a more complete description of the formability and fracture performance of AHSS (Figure 17b). Moreover, it can serve as a guide for future steel development and optimum material selection for automotive structural parts.

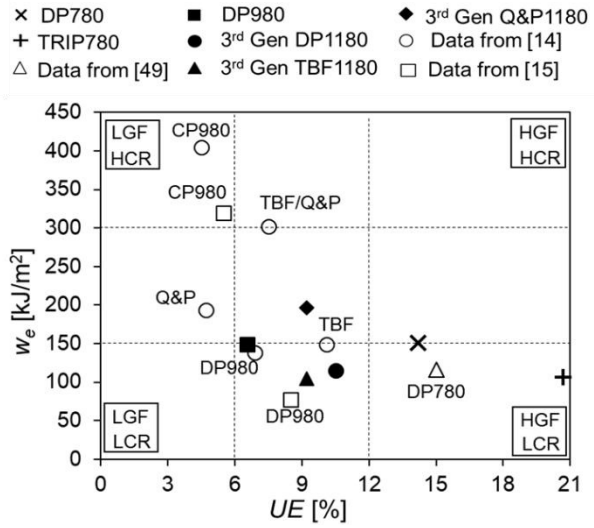

Figure 16. AHSS classification based on global formability (*UE*) and fracture resistance (w_e). LGF: low global formability, LCR: low cracking resistance, HGF: high global formability, HCR: high cracking resistance.

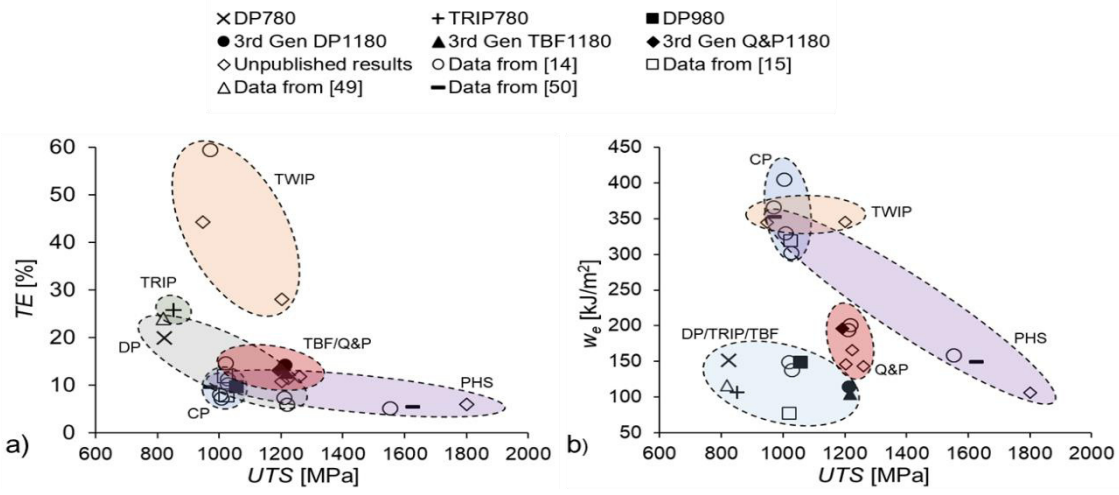

Figure 17. a) Conventional classification diagram of AHSS steels ("banana plot") in terms of *UTS* and *TE*. b) Proposed diagram for classification of AHSS according to their strength level (*UTS*) and fracture resistance (w_e).

5. Conclusions

The mechanical properties and the fracture resistance of different 1st and 3rd generation AHSS grades have been investigated. From the analysis of the obtained results the following conclusions can be drawn:

- Conventional uniaxial tensile properties are not sufficient to describe the local formability and fracture behavior of AHSS. On the other hand, other fracture-related parameters such as the true fracture strain (*TFS)*, the true thickness strain (*TTS*) or the specific essential work of fracture (w_e) provide a better prediction of fracture performance. The very good correlation between w_e and *HER* values for several AHSS and HSLA steels, consolidates the observations made in previous work and confirms the close relationship between fracture toughness and stretch-flangeability in AHSS.

- A new classification mapping considering global ductility (*UE*) and fracture resistance (w_e) is proposed for a more exhaustive description of the overall formability and fracture behavior of AHSS. The proposed diagram can be useful for improved AHSS performance ranking and optimum material selection depending on the requirements of the intended application.

- The true thickness strain (*TTS*) from uniaxial tensile tests significantly overestimates the thickness reduction in punched hole edge and fatigue pre-cracked DENT specimens. However, the relative differences in *TTS* are well reflected in toughness and edge cracking resistance parameters. Therefore, it might be used as a qualitative indicator of fracture toughness and edge fracture resistance.

- The values of thickness strain measured in fatigue pre-cracked DENT specimens ($\varepsilon_{3f\,DENT}$) are similar to edge thinning values measured in HET specimens ($TTS_{\,HET}$). This evidences the similarity between edge fracture and crack propagation mechanisms and allows establishing an objective fracture criterion for edge-cracking prediction. These results highlight the importance of addressing edge cracking phenomena considering the underlying fracture mechanisms, since fracture is governed by crack propagation resistance.

- The essential work of fracture is proposed here as a relevant parameter to assess the fracture resistance of AHSS and to understand the role of microstructural constituents on fracture behavior. The investigation on the correlation between fracture toughness and uniaxial tensile properties has shown that fracture toughness cannot be estimated from traditional ductility or toughness indicators (*UE*, *TE*, *UTSxTE,* etc.). Local strain measurements from tensile tests (*TFS*, *TTS*) offer a better estimation of fracture toughness. However, none of these parameters can accurately describe the fracture behavior in the presence of cracks. Therefore, fracture toughness, understood as the material's crack initiation and propagation resistance, must be measured following a fracture mechanics approach to properly evaluate the microstructural effects on fracture behavior.

- The results obtained from fracture toughness tests revealed that microstructural features that improve global ductility, such as for example the TRIP effect, can have a detrimental effect on fracture toughness. Hence, microstructural design must take into account not only tensile properties but also crack initiation and propagation resistance parameters.

References

[1] S. Keeler, M. Kimchi, P.J. Mooney: Advanced High-Strength Steels Application Guidelines,

version 6.0, 2017.
[2] WorldAutoSteel. (2011) FutureSteelVehicle – Final engineering report. https://steel.org/~/media/Files/Autosteel/Programs/FutureSteelVehicle/FSV%20-%20Final%20Engineering%20Report.pdf
[3] E. Billur, T. Altan: *Stamp. J.,* 2013, pp. 16-17.
[4] E. Billur, J. Dykeman, T. Altan: *Stamp. J.,* 2014, pp. 12-13.
[5] C. Liu, Q. Peng, Z. Xue, S. Wang, C. Yang: *Materials*, 2018, vol.11, 2242.
[6] H.L. Yi: *JOM-J. Min. Met. Mat. S.*, 2014, vol. 66, pp. 1759-1769.
[7] D. Raabe, D. Ponge, O. Dmitrieva, B. Sander: *Scripta Mater.*, 2009, vol. 60, pp. 1141–1144.
[8] K. Mori, Y. Abe, Y. Suzui: *J. Mater. Process. Tech.,* 2010, vol. 210, pp. 653–659.
[9] D. Frómeta, M. Tedesco, J. Calvo, A. Lara, S. Molas, D. Casellas: *J. Phys: Conf. Ser.*, 2017, vol. 896, 012102.
[10] C. R. M. Silva, F. J. G. Silva, R.M. Gouveia: *Procedia manuf.,* 2018, vol. 17, pp. 737-745.
[11] A. Karelova, C. Krempaszky, E. Werner, P. Tsipouridis, T. Hebesberger, A. Pichler: *Steel res. int*., 2009, vol. 80, pp.71-77.
[12] F. Hisker, R. Thiessen, T. Heller: *Mater. Sci. Forum*, 2012, vols. 706–709, pp. 925–930.
[13] P. Efthymiadis, S. Hazra, A. Clough, R. Lakshmi, A. Alamoudi, R. Dashwood, B. Shollock: *Mat. Sci. Eng. A*, 2017, vol. 701, pp. 174-186.
[14] D. Casellas, A. Lara, D. Frómeta, D. Gutiérrez, S. Molas, Ll. Pérez, J. Rehrl, C. Suppan: *Metall.Mater. Trans. A*, 2017, vol. 48, pp. 86-94.
[15] D. Frómeta, A. Lara, S. Parareda, D. Casellas: *AIP Conf. Proc.*, 2019, vol. 2113, 160007.
[16] B. Hance: *Proc. International Automotive Body Congress (IABC*), 2016, Dearborn, Michigan, USA.
[17] S. Heibel, T. Dettinger, W. Nester, T. Clausmeyer, A. E. Tekkaya: *Materials*, 2018, vol. 11, p.761
[18] ISO 16630:2017. Metallic materials — Sheet and strip — Hole expanding test. *International Organization for Standardization.*
[19] M. Schneider, U. Eggers: *Proc. International Deep Drawing Research Group* (IDDRG) conference, 2011, Bilbao, Spain, June 5-8, 2011.
[20] E. Atzema, M. Borsutzki, M. Braun, S. Brockmann, M. Bülter, B. Carlsson, P. Larour, A. Richter: *New Development in Sheet Metal Forming 2012 International Conference*. Fellbach, Germany, May 23-24, 2012, pp. 171-184.
[21] B. Hance, R. Comstock, D. Scherrer: *SAE Technical Paper*, 2013*,* 2013-01-1167.
[22] P. Larour, H. Pauli, J. Freudenthaler, J. Lackner, F. Leomann, G. Schestak: *Proc. International Deep Drawing Research Group (IDDRG) Conference*, 2016, Linz, Austria, June 12-15, 2016, pp. 480-496.
[23] E. Levin, P. Larour, M. Heuse, D. Staupendahl, T. Clausmeyer, A.E. Tekkaya: *IOP Conf. Series: Mat. Sci*., 2018, vol. 418, 012061.
[24] P. Larour, J. Freudenthaler, A. Grünsteidl, K. Wang: *Proc. International Deep Drawing Research Group (IDDRG) conference*, 2014, Paris, France, June 1-4, 2014, pp.188-193.
[25] J. Dykeman, S. Malcolm, B. Yan, J. Chintaman, G. Huang, N. Ramisetti, H. Zhu: *SAE Technical Paper*, *2011,* 2011-01-1058.
[26] P. Larour, H. Schauer, J. Lackner, E.T. Till: *Proc. International Deep Drawing Research Group (IDDRG) 2016 conference*. Linz, Austria, June 12-15, 2016, pp.457-459.
[27] G. Huang, K. Tihay, S. Sriram, B. Weber, P. Dietsch, D. Cornette: *IOP Conf. Ser.: Mater. Sci. Eng*., 2018*,* vol. 418, 012080
[28] S. Westhäuser, M. Schneider, M. Teschner, I.A. Denks: *IOP Conf. Ser.: Mater. Sci. Eng*., 2019, vol. 651, 012049.
[29] I.A. Denks, M. Schneider, S. Westhäuser, C. Lesch: *Steel Res Int*., 2019, vol. 90(6), 1800460.
[30] P. Larour, J. Freudenthaler, T.Weissböck: J. *Phys.: Conf. Ser.*, 2017, vol. 896, 012073.
[31] B. Hance: *SAE Int. J. Mater. Manf.*, 2018, vol. 11(4), pp. 505-516.
[32] Y. Takahashi, O. Kawano, Y. Tanaka: *MS&T 2009: Proc. from the Materials Science &*

Technology Conference. October 25-29, 2009, Pittsburgh, Pennsylvania, pp. 317-1328.
[33] J.I. Yoon, J. Jung, S.H. Joo, T.J. Song, K.G. Chin, M.H. Seo, S.J. Kim, S. Lee S, H.S. Kim: *Matter.Lett.*, 2016, vol. 180, pp. 322-326.
[34] D. Frómeta, A. Lara, S. Molas, D. Casellas, J. Rehrl, C. Suppan, P. Larour, J. Calvo: *Eng. Frac. Mech.*, 2019, vol. 205, pp. 319-332.
[35] D. Frómeta, A. Lara, B. Casas, D. Casellas: *IOP Conf. Ser.: Mater. Sci. Eng.*, 2019, vol. 651, 012071.
[36] E. Wirthl, A. Pichler, R. Angerer, P. Stiaszny, K. Hauzenberger, Y. Titovets, M. Hackl: *Proc. of the International Conference on TRIP-Aided High Strength Ferrous Alloys*, Gent, Belgium, 2002.
[37] ISO 6892-1:2009 (2009) Metallic materials — Tensile testing — Part 1: Method of test at room temperature. *European Committee for Standardization*.
[38] ASTM E8/E8M-15a (2015) Standard Test Methods for Tension Testing of Metallic Materials. *ASTM International*, West Conshohocken, PA, USA.
[39] B. Cotterell, J.K. Reddel: *Int. J. Fract.*, 1977, vol. 13, pp. 267-277.
[40] Y.W. Mai, B. Cotterell: *Int. J. Fract*.,1986, vol. 32, pp. 105–125.
[41] J. Wu, Y.W. Mai: *Polym. Eng. Sci*., 1996, vol. 36, pp. 2275–2288.
[42] A.B. Martínez, J. Gamez-Perez, M. Sanchez-Soto, J.I. Velasco, O. Santana, M.Ll. Maspoch: *Eng. Fail. Anal*., 2009, vol. 16, pp. 2604–2617.
[43] Y.W. Mai, K.M. Pilko: *J. Mater. Sci*., 1979, vol. 14, pp. 386 - 394.
[44] Y.W. Mai, B. Cotterell: *J. Mater. Sci.,* 1980, vol. 13, pp. 2296-2306.
[45] T.Pardoen, Y. Marchal, D. Delannay: *J. of Mech. Sol.*, 1999, vol. 47, pp. 2093-2123.
[46] Y. Marchal, F. Delannay: *Int. Fract. J.,* 1996, vol.80, pp. 295–310.
[47] B. Cotterell, T. Pardoen, A.G. Atkins: *Eng. Fract. Mech*., 2005, vol. 72, pp. 827–48.
[48] G. Lacroix, T. Pardoen, P.J. Jacques: *Acta Mater.*, 2008, vol. 56, pp. 3900–3913.
[49] D. Gutiérrez, Ll. Pérez, A. Lara, D. Casellas, J.M. Prado: *19th European conference on fracture: fracture mechanics for durability, reliability and safety, ECF 2012*.
[50] S. Golling, D. Frómeta, D. Casellas, P. Jonsén: *Mat. Sci. and Eng. A*, 2019, vol. 743, pp. 529-539.
[51] D. Frómeta, S.Parareda, A. Lara, S. Molas, D. Casellas, P. Jonsén, J. Calvo: *Eng. Frac. Mech*., 2020, vol. 229, 106949.
[52] Z. Xiong, P.J. Jacques, A. Perlade, T. Pardoen: *Int. J. Fract.,* 2020, vol. 224, pp. 101–116.
[53] E. Clutton: Essential work of fracture. Moore DR, Pavan A, Williams JG, editors. *Fracture mechanics testing methods for polymers, adhesives and composites*, 2001, ESIS Publ.vol.28*,* pp. 177–195.
[54] B. Hance: *SAE Int. J. Engines,* 2017, vol. 10(2), pp. 247-257.
[55] P. Jacques, Q. Furnémont, A. Mertens, F. Delannay: *Philos. Mag. A*, 2001, vol. 81, pp. 1789-1812.
[56] D. Krizan, K. Steineder, S. Kaar, T. Hebesberger: *19th international scientific conference Transfer 2018*, Trencianske Teplice (Slovakia).
[57] G.B. Olson, M. Cohen: *Metall. Trans. A,* 1975, vol. 6, p.791.
[58] G. B. Olson, M. Azrin: *Metall. Trans. A,*1978, vol. 9, pp. 713–721.
[59] P. Jacques, Q. Furnémont, T. Pardoen, F. Delannay: *Acta mater*., 2001, vol. 49, pp. 139–152.
[60] Z. Xiong, P.J. Jacques, A. Perlade, T. Pardoen: *Metall. Mater. Trans. A*, 2019, vol. 50, pp. 3502-3513.
[61] I. de Diego-Calderón, I. Sabirov, J.M. Molina-Aldareguia, C. Föjer, R. Thiessen, R.H. Petrov: *Mat. Sci. Eng. A*, 2016, vol. 657, pp. 136-146.
[62] X. Chen, H. Jiang, Z. Cui, C. Lian, C. Lu: *Proc. Eng.*, 2014, vol. 81, pp.718–723.

Acknowledgments

This work has been finantially supported by the European Commission, Research Fund for Coal and Steel programme under Grant Agreement 800693 — CrashTough — RFCS-2017.

Paper III. D. Frómeta, A. Lara, S. Molas, D. Casellas, J. Rehrl, C. Suppan, P. Larour, J. Calvo, On the correlation between fracture toughness and crash resistance of advanced high strength steels, *Engineering Fracture Mechanics* 205 (2019) 319-332

Engineering Fracture Mechanics 205 (2019) 319–332

Contents lists available at ScienceDirect

Engineering Fracture Mechanics

journal homepage: www.elsevier.com/locate/engfracmech

On the correlation between fracture toughness and crash resistance of advanced high strength steels

D. Frómeta[a,*], A. Lara[a], S. Molas[a], D. Casellas[a,c], J. Rehrl[b], C. Suppan[b], P. Larour[b], J. Calvo[d]

[a] Fundació CTM Centre Tecnològic, Plaça de la Ciència 2, 08243 Manresa, Spain
[b] voestalpine Stahl GmbH, voestalpine-Straße 3, 4020 Linz, Austria
[c] Luleå University of Technology, 971 87 Luleå, Sweden
[d] Universitat Politècnica de Catalunya, Eduard Maristany 16, 08019 Barcelona, Spain

ARTICLE INFO

Keywords:
Fracture toughness
Crash resistance
Axial impact tests
Advanced high strength steels
Essential work of fracture

ABSTRACT

Automotive industry players have devoted large efforts to identify the material parameters governing the crash resistance of Advanced High Strength Steels (AHSS). Such knowledge is essential to improve impact performance prediction and optimize new steel development. Nevertheless, there is still an open discussion about which are the most relevant properties on AHSS crashworthiness. In this work, the authors investigate the correlation between the fracture toughness of different AHSS and their crash failure behaviour. Fracture toughness is measured in the frame of fracture mechanics, through the essential work of fracture methodology. Two fracture resistance parameters are characterized: the fracture toughness at cracking initiation, w_e^i, and the essential work of fracture, w_e. Toughness values are compared with the results of axial impact tests, which are evaluated according to the energy absorbed and the cracking behaviour observed in crash boxes. Results show that fracture toughness permits to describe different crash events in terms of crack initiation and crack propagation and allows ranking AHSS impact resistance; steels with higher w_e present better crash performance. Therefore, fracture toughness is proposed as a key material property to predict the crash resistance of AHSS and as a relevant design parameter for crash resistant parts.

1. Introduction

The use of advanced high strength steels (AHSS) for chassis and Body-In-White (BIW) components has grown exponentially in the automotive industry in the last two decades aimed at meeting the increasingly demanding safety and fuel consumption requirements [1]. AHSS are especially suitable for lightweight crash resistant automobile parts due to their excellent mechanical properties combining high strength and great energy absorption capacity, which permits reducing the total vehicle mass without compromising the safety of the passengers. For this reason, the characterization of AHSS crashworthiness has become one of the main issues for steelmakers and automotive components manufacturers.

The crash resistance of car parts is a complex property to measure that involves many factors apart from the material properties, such as high strain rates, multiple loading modes, part geometry and welding/joining techniques. Crashworthiness is evaluated at laboratory scale by two different tests: axial and bending (or side) impact resistance tests, where crash resistance is ranked in terms of

* Corresponding author.
E-mail address: david.frometa@ctm.com.es (D. Frómeta).

https://doi.org/10.1016/j.engfracmech.2018.10.005
Received 17 May 2018; Received in revised form 8 September 2018; Accepted 5 October 2018
Available online 17 October 2018
0013-7944/ © 2018 Elsevier Ltd. All rights reserved.

the energy absorbed, deformation, cracking and global appearance of the specimens after crashing. However, such tests are very time-consuming and require significant amounts of material to obtain reliable and reproducible results. Moreover, it is often difficult to extract direct information about the intrinsic crash resistance of the material, since damage can be highly influenced by welding spots, especially in axial impact tests. Thus, the development of experimental small scale laboratory methodologies that permit to foresee crash behavior and determine the effect of material microstructure on crash resistance is essential to optimize material selection and assist new steel grades development.

Great efforts have been taken in the last years to correlate small scale laboratory tests with axial and bending impact tests and identify the material parameters that best describe the crash resistance of AHSS [2–9]. It has been observed that conventional tensile properties, such as tensile strength or fracture elongation, are not valid to classify the crash behaviour of AHSS [2–6]. Fracture elongation, usually associated to the material ductility, is gauge length dependent and totally underestimates the local ductility potential of the material [5]. Therefore, steel grades with poor elongation at fracture may exhibit better crash behaviour than others with greater elongation and vice versa [2–6,9]. Something similar occurs when considering the energy obtained from the area under the engineering stress-strain curves, which is traditionally considered as a rough toughness indicator. Such energy undervalues the post uniform part of energy absorption from necking to fracture and it is not suitable either to predict crash failure behaviour. Alternatively, some authors have shown that local ductility measurements, like the measurement of the local fracture strain in uniaxial and plane strain notched tensile tests or the reduction of the cross-section area at fracture in tensile tests (Z-value), might offer better results for crash performance prediction [2,3,5,10]. Other approaches, such as the bending angle measured from 3-point bending test according to VDA 238-100 [11] or the fracture strain in plane strain tension obtained from these tests, have also shown to be effective to predict bending-dominated failure that occurs with AHSS grades during folding/bending in axial and side crash tests [2–7]. Nevertheless, these parameters by themselves are not enough to describe the overall AHSS crash failure behavior.

Recent works have shown that AHSS crash ability can be evaluated according to their cracking behavior in crash tests by checking the first cracks appearance and further crack propagation at different intrusion levels in impact tested coupons [2–4,6]. Following this approach, it is reasonable to think that crash resistance may be also rationalized in terms of the property that quantifies the crack initiation and propagation resistance of the material, i.e. the fracture toughness. However, fracture toughness is not systematically characterized in thin metal sheets, mainly because of the experimental complexity of conventional elastic-plastic fracture mechanics (EPFM) methodologies, such as *J-integral*, crack-tip opening displacement (CTOD) or crack-tip opening angle (CTOA) measurements. These methods require exhaustive specimen preparation, constant monitoring and rigorous data treatment, not to mention the extra difficulties in crack advance measurement. Moreover, the applicability of some of these methods to thin sheets under plane stress conditions is not well clarified.

An alternative procedure to readily characterize the fracture toughness of thin ductile metal sheets was proposed by Cotterel and Reddel in 1977, the Essential Work of Fracture (EWF) methodology [12]. The method has been extensively used to assess the fracture resistance of thin steel sheets [12–17] and aluminium alloys [16,18–21], among other ductile metals (zinc [16,20,22] copper [23] and brass [16,24]). It has been also successfully applied to evaluate the tearing resistance of ductile polymers [25–28] and more recently the methodology has shown to be appropriate to measure the fracture toughness of AHSS sheets [29–38]. The obtained toughness value, the specific essential work of facture (w_e), quantifies the energy dissipated within the fracture process zone during the ductile tearing process and it is a suitable parameter to describe the crack propagation resistance of thin sheets [12,21,29]. In contrast to the EPFM toughness value, J_C, which is a measure for cracking initiation, w_e contains energetic contributions from both crack initiation and propagation. Nonetheless, as described by Mai and Cotterell [26], the EWF methodology also permits to experimentally separate both contributions and determine a cracking initiation toughness value, the specific work for fracture initiation (w_e^i), which is equivalent to J_C.

The works of Casellas et al. [34] and Frómeta et al. [35] showed that fracture toughness, in terms of w_e, is a suitable material property to rationalize the stretch-flangeability of AHSS and it is expected to be useful to understand other cracking related phenomena in AHSS, such as crack propagation contribution in crash resistance. According to this, the aim of this contribution is to investigate if the EWF can be effectively used to assess AHSS crash behavior at small laboratory scale. For this purpose, the relation between fracture toughness, measured by means of the EWF methodology, and impact behavior, evaluated through laboratory axial impact tests, of different AHSS grades is addressed. Aimed to discern separately the role of crack initiation and crack propagation on AHSS crashworthiness, two cracking resistance parameters were assessed: the overall fracture toughness, w_e, and the energy released for crack initiation, w_e^i.

2. Materials

Nine different AHSS grades on the range of 1.4–1.16 mm thickness were investigated: (a) two commercially available 1st generation AHSS cold forming grades (DP1000 and CP1000); (b) three 3rd generation AHSS grades: Trip-Aided Bainitic Ferritic (TBF) steel (bainitic ferrite matrix with retained austenite), Quenched & Partitioned (Q&P) steel (martensite matrix with retained austenite), and mixed TBF/Q&P microstructure; (c) two hot stamped boron steels: one in-press hardened condition (strength around 1500 MPa) and another one with an additional tempering treatment (strength around 1000 MPa); (d) and finally a Twinning-Induced Plasticity steel, also known as TWIP steel (fully austenitic steel). The chemical compositions of these nine steel grades are shown in Table 1.

A basic investigation of the microstructure of these steel grades was performed by means of scanning electron microscopy (SEM) after electro-polishing. The corresponding microstructures can be seen in Figs. 1–3. CP-like grades (CP1000, CP1200 and TBF/Q&P) show a homogeneous matrix of bainite/tempered martensite (B/TM). Q&P presents a martensitic matrix with bainite and tempered

Table 1
Chemical composition of the investigated materials [mass%]. Balance is Fe.

Steel grade	C	Si	Mn	Cr	B	Al
CP1000	~0.1	< 0.5	1.8–2.2	< 0.7	< 0.003	–
DP1000, CP1200	~0.15					
TBF	~0.2	0.5–1.0	2.2–2.6			
Q&P	~0.1					
TBF/Q&P	~0.1					
PHS1500	~0.2	~0.2	~1.2		~0.003	
PHS1000						
TWIP	~0.5	0.10–0.15	~15	~0.1	–	~1.0

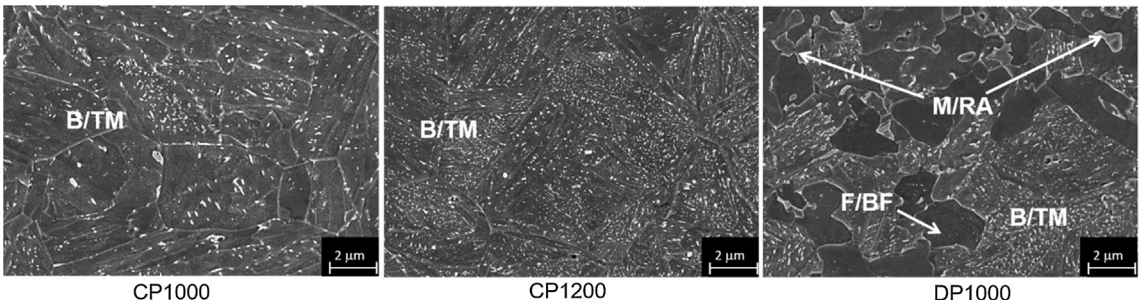

Fig. 1. Microstructure of CP1000, CP1200 and DP1000 grades.

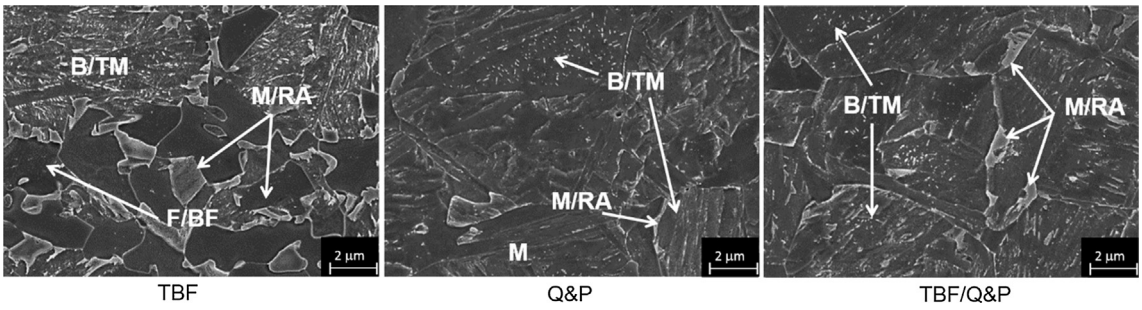

Fig. 2. Microstructure of TBF, Q&P and TBF/Q&P grades.

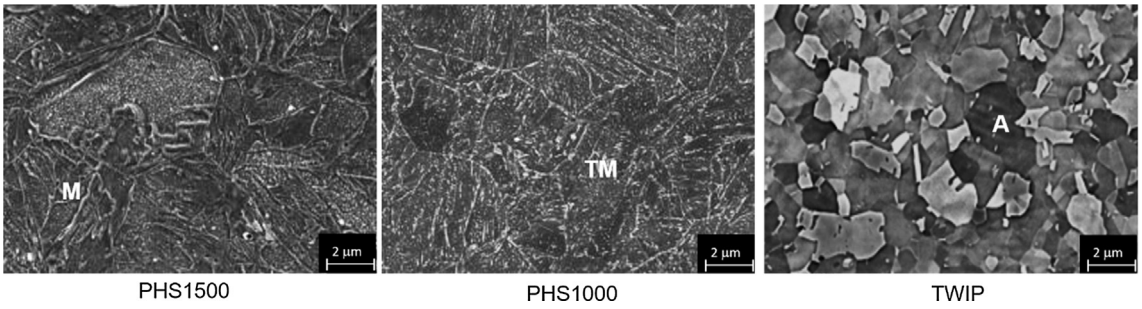

Fig. 3. Microstructure of PHS1500, PHS1000 and TWIP grades.

martensite. In DP1000 and TBF grades the matrix consists of a mixture of ferrite (F), bainitic ferrite (BF), bainite/tempered martensite and martensite (M). DP1000 and TRIP-assisted steel grades (TBF, Q&P and TBF/Q&P) also present moderate amounts of retained austenite (RA). PHS1500 consists of a homogeneous martensitic matrix, which is slightly auto-tempered during cooling. PHS1000 exhibits an homogeneous tempered martensite (TM) matrix. The tempering treatment for PHS1000 basically leads to relaxation of the tetragonal martensite lattice by formation of carbides, which can be observed as white lines and spots in Fig. 3. TWIP steel shows homogeneous austenitic (A) matrix (see Fig. 3).

Conventional axial tensile tests were performed according to EN-ISO6892-1 with specimens oriented at transverse orientation respect to the rolling direction. Table 2 shows the results.

Table 2
Tensile parameters in terms of yield strength (YS), ultimate tensile strength (UTS), elongation at fracture (A80, gauge length 80 mm) and area under stress-strain curve. Thickness (t) of the studied sheets is also given.

Steel grade	t [mm]	YS [MPa]	UTS [MPa]	A80 [%]	$n_{2\text{-}4\%}$	Area under tensile curve [MPa*%]
CP1000	1.4	908	1002	8.1	0.05	7852
CP1200	1.6	1041	1218	6.0	–	7132
DP1000	1.4	738	1027	10.3	0.10	10525
TBF	1.5	725	1019	14.7	0.12	14045
Q&P	1.4	909	1209	7.4	0.09	8643
TBF/Q&P	1.4	876	1026	11.3	0.09	11175
PHS1500	1.5	1075	1552	5.2	0.08	8326
PHS1000	1.5	988	1007	7.3	0.05	5356
TWIP	1.4	530	969	59.5	0.11	47860

3. Experimental procedure

3.1. Crash resistance: axial impact resistance tests

Hat profile specimens were used, as shown in Fig. 4a (length of 300 mm). Profiles were spot-welded to a closing blank of the same steel type. Also at the front and back, closing blanks were welded to the profile. Axial impact resistance tests were conducted for each steel grade at crash speeds from 12 to 36 km/h. The impactor works with a load mass of 283 kg and the speed can be varied between 10 and 40 km/h. The deformation of axially crashed specimen (initial length: 300 mm) is limited to 200 mm shortening.

Impact resistance was evaluated by means of two parameters: the crash index (*CI*) and the energy absorbed for each deformed crash sample. The *CI* is defined according to an overall crack length (Table 3). It does not give information about location or cause of crack initiation. However, it quantifies the damage induced in crashed specimen and determines the crash folding ability for a given intrusion level. This parameter is widely used in the automotive industry and it is a good indicator of crack initiation and propagation resistance in crash samples [2–4]. *CI* was experimentally measured by inspecting every crashed specimen at different intrusion levels and measuring cracks length. In order to discern the influence of welding spots damage and unbuttoning in crack initiation, special attention was paid to detect crack initiation site.

The energy absorbed during axial impact tests was calculated by integrating the area under the load vs impactor displacement curves (Fig. 4b). Intrusions of axial impact tests include only plastic deformation and were determined by the difference in length of unloaded (300 mm) and crashed samples (after elastic recovery).

3.2. Fracture toughness measurements

3.2.1. Essential work of fracture, w_e

The EWF methodology is based on the assumption that the total work of ductile fracture (W_f) can be separated in two terms: an essential work of fracture necessary to create new surfaces in the front of the crack tip (w_e) and a non-essential plastic work dissipated in the outer plastic region surrounding the crack plane (w_p).

In principle, the EWF can be determined from a range of specimen geometries [25] but for thin sheets the Double Edge Notched Tensile (DENT) specimen (Fig. 5) has shown to be the most suitable because the transverse stress between the notches is tensile and there is no buckling. If the ligament is completely yielded and the plastic zone is confined to the notched ligament, then w_p is

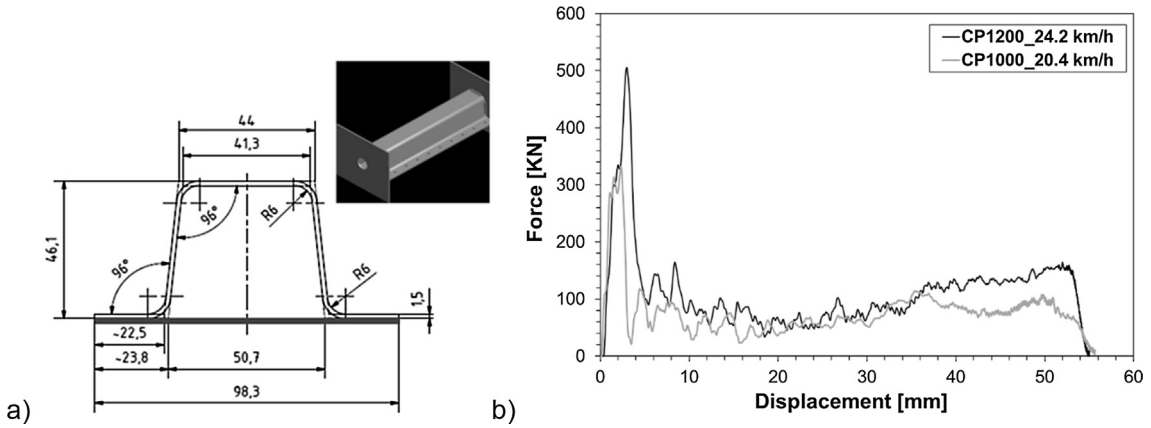

Fig. 4. (a) Geometry of axial crash samples with 1.5 mm blank thickness. (b) Force vs impactor displacement curves for two axial impact tests with CP1200 and CP1000 at different speeds and similar intrusion levels (51 mm and 52 mm, respectively).

Table 3
Definition of crash index for axial impact tests [2].

Crash index (*CI*)	Damage
100	no cracks
> 75	crack length < 10 mm
50–75	10 mm < crack length < 25 mm
25–50	crack length > 25 mm
< 25	"splitting and curling"; multiple breaks

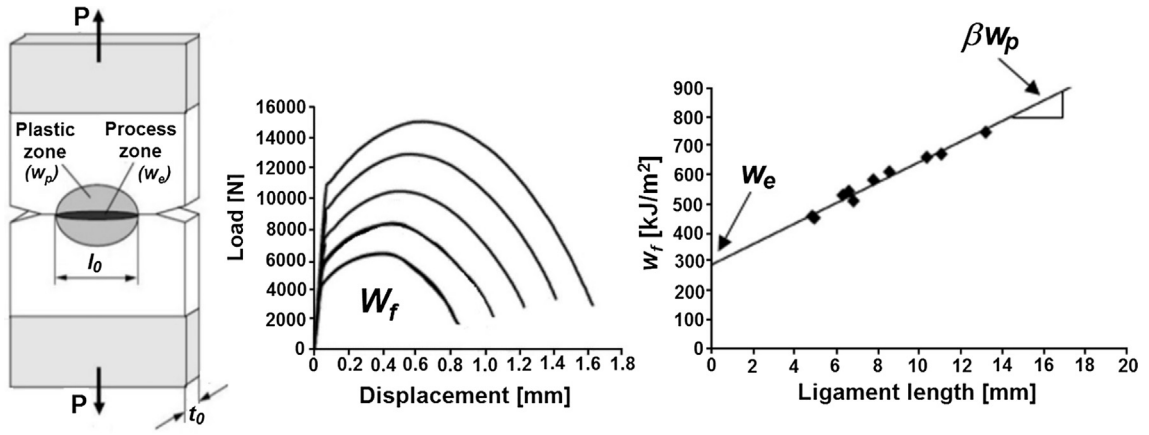

Fig. 5. DENT specimen and experimental determination of the EWF: W_f for different ligament lengths and plot of w_f against l_0, the intercept indicates the specific essential work of fracture, w_e.

proportional to the plastic volume and w_e is proportional to the fractured area:

$$W_f = w_e l_0 t_0 + w_p \beta l_0^2 t_0 \tag{1}$$

β is a shape factor that depends on the shape of the plastic zone, t_0 is the specimen thickness and l_0 is the initial ligament length. Dividing Eq. (1) by the cross section area ($l_0 t_0$) allows the experimental determination of the EWF according to Eq. (2).

$$\frac{W_f}{l_0 t_0} = w_f = w_e + w_p \beta l_0 \tag{2}$$

where w_f is the specific total work of fracture, obtained by testing the DENT specimen at a constant displacement rate, integrating the area under the load vs displacement curve (W_f) and dividing by the initial ligament area:

$$w_f = \frac{1}{l_0 t_0} \int_0^{u_f} P \cdot du \tag{3}$$

Being P the load, u the displacement and u_f the displacement at fracture.

It can be observed that Eq. (2) is the equation of a straight line, where the intercept is the specific essential work of fracture, w_e, and the slope is the specific non-essential plastic work, βw_p. Thus, if a series of DENT specimens with different ligament lengths are tested and w_f is plotted against l_0, both values can be determined (Fig. 5).

In this work, the EWF tests were performed following the procedure stablished in the European Structural Integrity Society (ESIS) protocol [39]. Rectangular DENT specimens of 240 × 55 mm were extracted from AHSS sheets at transverse orientation respect to the rolling direction (Fig. 6). 4 different ligament lengths ranging from 6 to 16 mm were evaluated and about 3 to 5 specimens were tested up to fracture for each ligament length. The tests were performed at a constant cross-head speed of 1 mm/min and a gauge length of 50 mm was used. The displacement was evaluated by means of a video extensometer. In order to avoid the effect of notch root radius in the fracture toughness evaluation, fatigue pre-cracks were introduced on the notch root (Fig. 6), following the recommendations for fatigue pre-cracking given by fracture mechanics standard procedures.

3.2.2. Fracture toughness at initiation, w_e^i

Following the methodology proposed by Mai and Cotterell [26], w_e^i was obtained by calculating the w_f at the initiation of propagation (w_f^i) for different ligament lengths according to Eq. (4):

$$w_f^i = \frac{1}{l_0 \cdot t_0} \int_0^{u_i} P \cdot du \tag{4}$$

Where u_i is the displacement at initiation of propagation (Fig. 7a). Contrary to w_f, w_f^i is constant and independent of the ligament

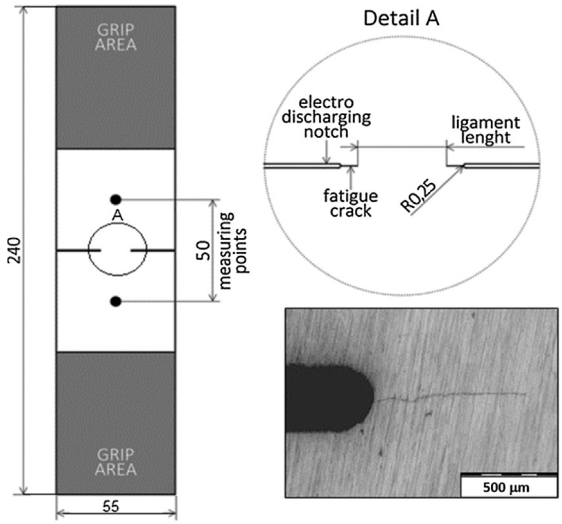

Fig. 6. DENT specimen geometry and detail of fatigue crack at the notch root.

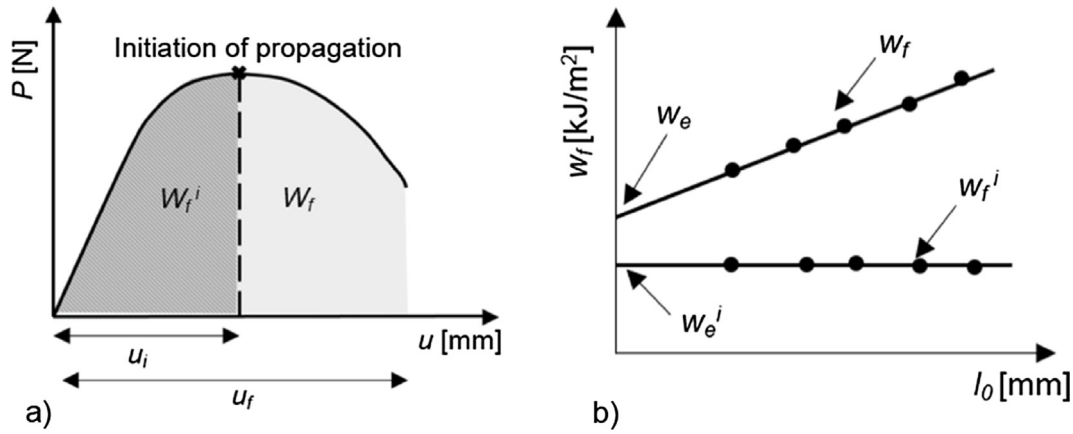

Fig. 7. (a.) Determination of specific work of fracture at initiation of propagation ($w_f{}^i$) (b) Variation of w_f and $w_f{}^i$ in function of ligament length.

length [26], as illustrated in Fig. 7b. Thus, only mean values of $w_f{}^i$ are considered for $w_e{}^i$ calculation. The displacement at which the crack starts to propagate was determined by means of a high-resolution video extensometer synchronized with the testing machine.

It is important to note that fracture toughness of thin ductile sheets has an important contribution from necking and, thus, it is highly influenced by the sheet thickness. Hence, the measured w_e and $w_e{}^i$ values are not fully a material intrinsic property but they are fracture toughness values for the evaluated sheet thickness.

4. Results

4.1. Axial impact resistance tests

The evaluated *CI* values are plotted in Fig. 8 as a function of the intrusion level and the energy absorbed in axial impact tests. Critical intrusion (first $CI < 100$) is defined as the transition from uncracked to cracked specimens. Hence, it is related to the fracture initiation resistance of the material. However, in axial impact tests fracture initiation can result from failure of the bulk material due to the emerging fold geometry, as well as damage induced at the welding spot. Aimed at investigating these influences, five different locations were defined (see Fig. 9a): bottom (outer and inner side), side, closing and complex bending. Bottom and complex bending cracks are considered to show low dependency on welding spot failure. Cracks at the closing bend fold at the side can be influenced by a partial or complete unbuttoning of the welding spot. Fig. 9b shows cracking pattern in different specimen areas, which was used to determine the damage for every steel in terms of *CI*.

A specially significant effect of welding spot failure on critical intrusion was observed in some steel grades. The first appearing cracks on CP1200, DP1000 and Q&P samples coincided with clear unbuttoning of the welding spot and a welding crack propagating from the edge. PHS1500 firstly cracked at the side and bottom inner side position, when the welding spot was already unbuttoned. On

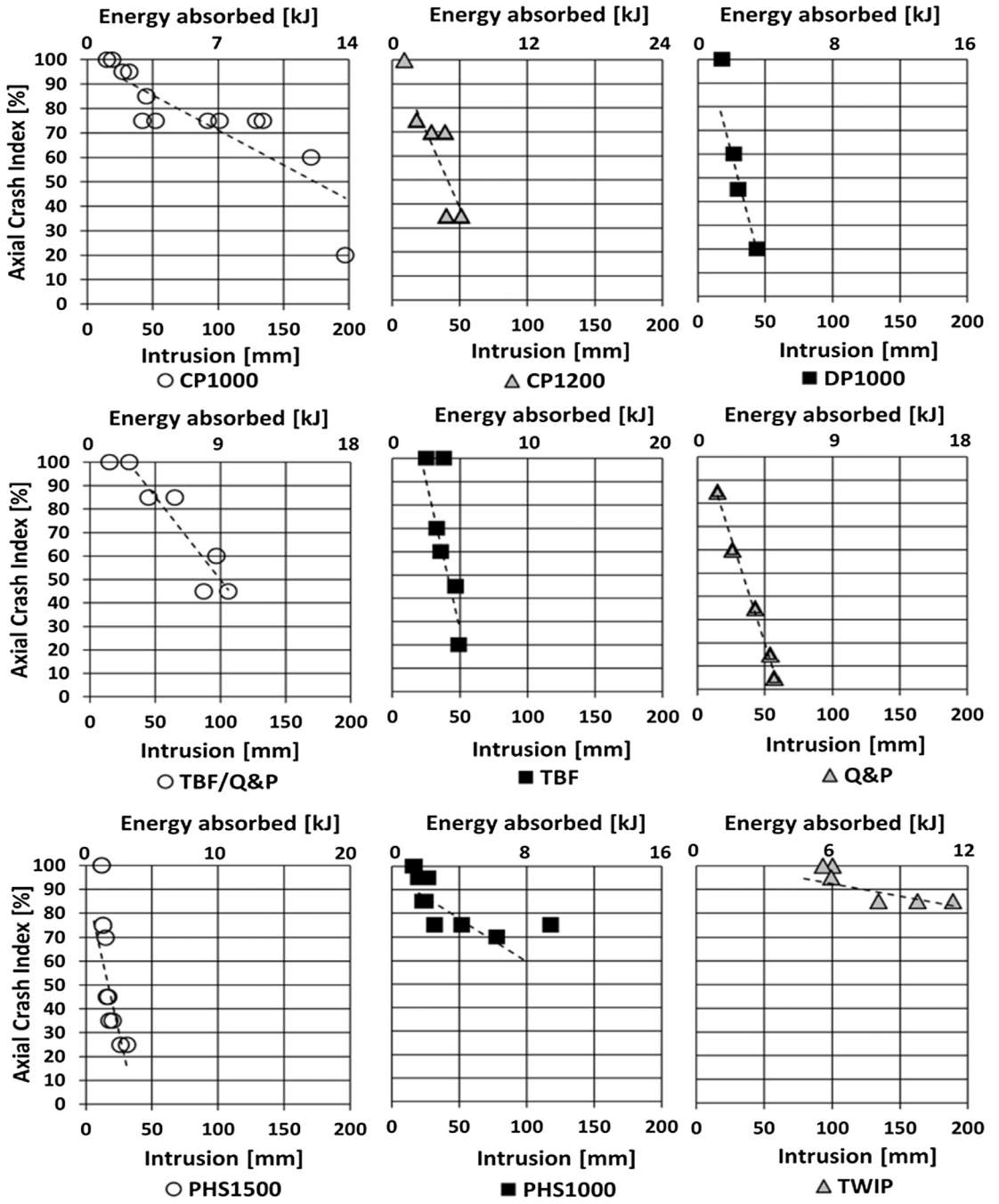

Fig. 8. Variation of Crash Index (*CI*) in function of the intrusion and energy absorbed in axial impact tests for the studied steels. Every data point represents a single test. The values of energy absorbed as a function of intrusion can differ from one material to another. Energy depends not only on the intrusion level but also on the magnitude of the measured force (see force vs displacement curve in Fig. 4b).

PHS1000 samples, small cracks were triggered at complex bending and bottom inner side positions. However, unbuttoning of welding spots occured already at small intrusions. Thus, the determination of a single and reliable critical intrusion level based only on bulk material behaviour was difficult in most cases. These observations must be kept in mind when analyzing critical intrusion results in terms of crack initiation. The range of critical intrusion values determined for the investigated steel grades are indicated in Table 4.

At intrusion levels higher than the critical intrusion for base material cracking, unbuttoning and cracks propagating from unbuttoned welding spots were generally observed in most of the steel grades. Consequently, the damage measured by *CI* does not strictly represent the base material behaviour. However, the Crash Index Decreasing Rate (*CIDR)*, i.e. the slope defined by the decrease of *CI* in function of the intrusion (represented by dashed lines in Fig. 8), describes well the growth of existing cracks through

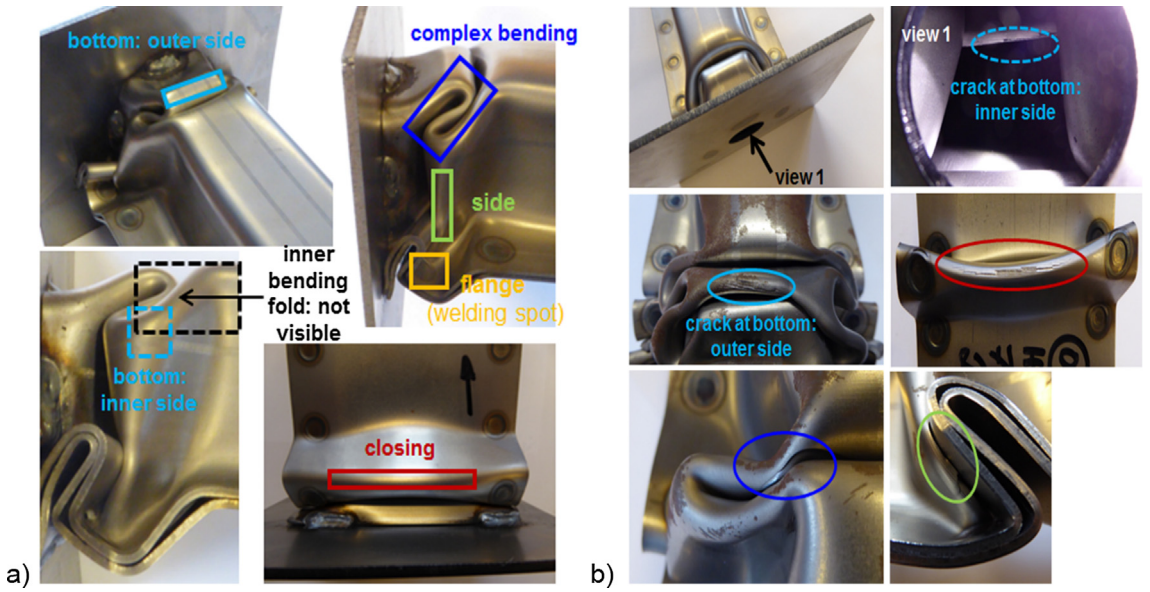

Fig. 9. (a) Observed crack positions on deformed axial crash sample and used nomenclature. (b) Examples for inner and outer side bottom cracks (light blue), closing crack (red), complex bending crack (dark blue) and side crack (green). (For interpretation of the references to colour in this figure legend, the reader is referred to the web version of this article.)

Table 4
Results from axial impact resistance tests and fracture toughness measurements. The values in parenthesis correspond to the extrapolated energy values at *CI* = 20% for PHS1000 and TBF/Q&P.

	Axial impact tests			Fracture toughness	
Steel grade	Critical intrusion [mm]	*CIDR* [-%/mm]	Energy at maximum intrusion [kJ]	w_e [kJ/m^2]	w_e^i [kJ/m^2]
CP1000	27–32	0.29	13.7	405 ± 11	151 ± 8
CP1200	9–18	1.28	6.1	201 ± 24	129 ± 8
DP1000	18–27	2.18	3.6	138 ± 20	113 ± 5
TBF	25–33	2.54	4.9	149 ± 13	108 ± 9
Q&P	6–15	1.81	5.3	194 ± 12	171 ± 15
TBF/Q&P	30–45	0.71	9.4 (11.3)	302 ± 32	154 ± 6
PHS1500	12–13	2.45	3.0	159 ± 11	141 ± 10
PHS1000	16–20	0.36	9.5 (10.4)	330 ± 21	160 ± 20
TWIP	99–100	0.11	10.7	366 ± 24	286 ± 11

the sample under impact loading, independently of the crack origin (base material or spot weld). Therefore, *CIDR* is related to the evolution of damage in axial impact tests and it can be readily used to quantify the crash resistance of the material, i.e. the lower the *CIDR*, the better crash resistance. *CIDR* was determined for all the investigated steel grades making a linear regression from the first *CI* below 100 (first crack appearance) to the lowest *CI*. The obtained values are summarized in Table 4.

Results show that the best crash behavior is achieved for CP1000, PHS1000, TWIP and TBF/Q&P steel grades. They exhibit the lowest *CIDR* values and keep very good *CI* at high intrusions. TWIP steel exhibits the highest crash performance, with *CI* above 85% up to intrusions of 150–200 mm and the lowest slope. CP1000 and PHS1000 show very similar crash behavior, maintaining *CI* about 70–75% at intrusions of 100–120 mm and comparable slopes. In the case of CP1000, small superficial cracks were observed in the inner bottom fold at all crash speeds. However, these cracks do not grow through the sheet thickness until high intrusion levels. Thus, it was not possible to determine a clear slope since no consistent crack propagation was observed until high intrusions and a large scattering was obtained. After the first initial decrease of *CI* up to intrusions of 50 mm, it remains constant at 75% up to 150 mm of intrusion approximately. Finally, a sudden drop of the *CI* is observed until the maximum intrusion (200 mm). Therefore, the defined slope is not strictly a crack propagation rate but it represents an average resistance of the material against the propagation of cracks. PHS1000 shows a more pronounced initial decrease of *CI* up to 50 mm intrusion. However, from 50 mm to 100 mm of intrusion the *CI* remains almost constant at 70–75%. The maximum intrusion achieved for PHS1000 was of 118 mm. TBF/Q&P reaches a *CI* of 40 or more for intrusions up to 100 mm, which indicates that cracks have not propagated through the whole fold. On the other hand, DP1000, TBF and PHS1500 present the worst crash behavior of the investigated steel grades. The high *CIDR* indicates that their *CI* rapidly decrease with increasing intrusion. The slopes of CP1200 and Q&P reveal a slightly better crash performance.

Alternatively to the measurement of the cracking related parameters *CI* and *CIDR,* crashworthiness was also evaluated according

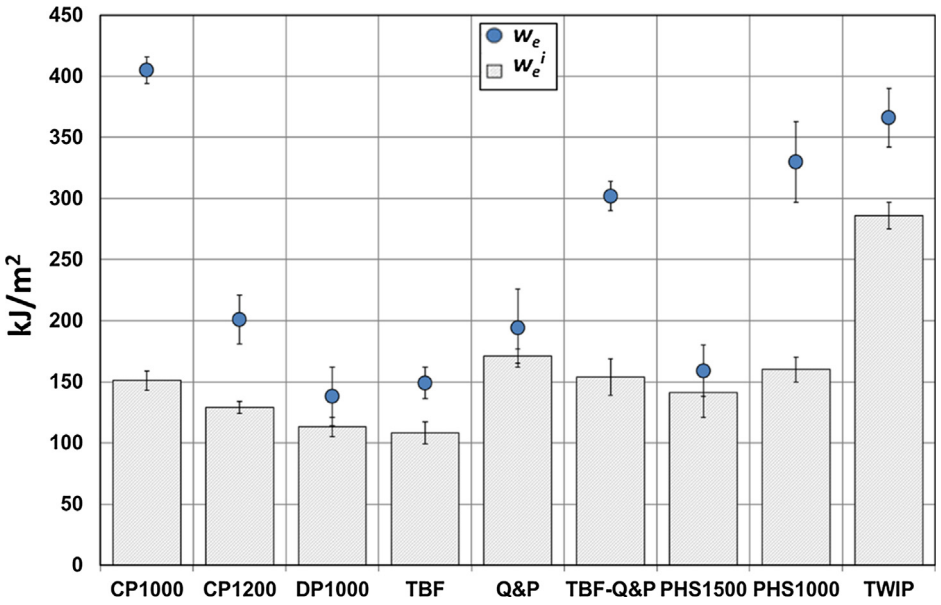

Fig. 10. Fracture toughness at cracking initiation (w_e^i) and essential work of fracture (w_e) for the investigated AHSS grades.

to the energy absorption capacity. Such parameter depends on the maximum intrusion that material can achieve and it contains not only the contribution from plastic deformation but also from crack initiation and propagation resistance. Thus, it also could be directly related to the fracture toughness of the material. A *CI* of 20% (specimen severely damaged) was established to determine the maximum allowable intrusion for each steel. The values of energy absorbed at maximum intrusion are used to quantify the energy absorption capacity of the investigated AHSS grades. Values of energy at maximum intrusion are listed in Table 4.

Results suggest that CP1000 and TWIP steel have the highest energy absorption capacity. However, it is observed that, even though TWIP steel maintains higher *CI* at maximum intrusion (200 mm), the energy absorbed at this point is lower than for CP1000, probably due to its lower yield strength. PHS1000 and TBF/Q&P steel grades also present high energy values at maximum intrusion. It is worth noting that such steels do not reach their maximum possible intrusion and, therefore, these values might be higher. For these steel grades, a possible maximum energy value was obtained by extrapolation of *CI* vs energy data to *CI* = 20%. Values are indicated in parenthesis in Table 4.

PHS1500 and DP1000 exhibit the lowest energy absorption capacity compared with the other steels investigated. TBF, Q&P and CP1200 show intermediate values of energy absorbed.

4.2. Fracture toughness measurements

Fig. 10 shows the values of essential work of fracture (w_e) and fracture toughness at initiation (w_e^i) for the investigated AHSS grades. Numerical values are summarized in Table 4.

4.2.1. Essential work of fracture, w_e

Essential work of fracture results indicate that CP1000, TWIP, PHS1000 and TBF/Q&P present the highest cracking resistance (with w_e ranging between 300 and 400 kJ/m^2), followed by the 1200 MPa steel grades, CP1200 and Q&P (201 ± 24 kJ/m^2 and 194 ± 12 kJ/m^2, respectively). It is important to note that these latter steels present very similar toughness, despite the differences in thickness (1.6 mm for CP12000 and 1.4 mm for Q&P).

The high essential work of fracture obtained for PHS1000 (330 ± 21 kJ/m^2) contrasts with the poor fracture toughness of PHS1500, which shows one of the lowest w_e (159 ± 11 kJ/m^2). These results remark the significant influence of the tempering treatment on fracture resistance of press hardened steels. On the other hand, DP-like steel grades (DP1000 and TBF) present the lowest toughness of the investigated AHSS (w_e = 138 ± 20 kJ/m^2 and 150 ± 13 kJ/m^2 respectively), in contrast to their higher elongation at fracture in tensile tests. This behaviour can be explained by the combination of soft (ferrite) and hard (bainite/martensite) microstructural constituents, which, whereas enhance strain hardening and elongation, has a detrimental effect on fracture toughness. As reported by Hisker et al. [40], local damage mechanisms in DP-steels are highly influenced by the hardness differences between phases. If these differences are high, they give rise to higher internal stresses during deformation, which contribute to the rapid generation of micro voids or decohesion of the soft/hard phase interfaces. Fracture toughness, is very sensitive to local damage, since deformation is concentrated in a very local zone ahead of the crack tip. Thus, microvoid coalescence rapidly contributes to the macroscopic failure of the sample. On the other hand, tensile tests are less sensitive to local damage, since the large work hardening capacity of these steels around the nucleated voids impede that void growth leads directly to macroscopic fracture.

Obtained w_e values are in good agreement with published toughness values for similar steel grades [29–35].

4.2.2. Fracture toughness at initiation, w_e^i

As observed in Fig. 10, most of steel grades exhibit similar values of toughness at cracking initiation ($w_e^i \approx 140–170\ kJ/m^2$), except DP1000, TBF and TWIP. Similarly to the observed in w_e results, DP-like steel grades show again the lowest toughness ($w_e^i = 113 \pm 5\ kJ/m^2$ and $108 \pm 9\ kJ/m^2$ for DP1000 and TBF respectively). However, no clear correlation between w_e^i and microstructural features are observed for the rest of AHSS. It is remarkable that CP1000, which presents the highest essential work of fracture, presents a work for fracture initiation comparable to PHS1500 and lower than other steel grades, such as PHS1000 and Q&P. TWIP steel shows, by far, the highest crack initiation resistance ($w_e^i = 286 \pm 11\ kJ/m^2$).

It is also interesting to note that some steels present a high energetic contribution from crack propagation after initiation, as indicated by the large differences between w_e and w_e^i. In these cases, a single cracking initiation toughness value, w_e^i or the equivalent EPFM toughness value J_C, is not enough to describe the overall fracture resistance of the material. Thus, when there is a significant increase of cracking resistance during propagation, the essential work of fracture (w_e) better defines the steady state crack propagation resistance of the material than w_e^i. In other cases, such as observed in DP1000, PHS1500 and Q&P, this contribution can be negligible and w_e coincide with w_e^i.

5. Discussion

Results of laboratory axial impact resistance tests show that axial impact performance of AHSS grades can be effectively evaluated according to their cracking behaviour (Fig. 8). This approach was firstly proposed by Walp in 2007 [6] and it was successfully applied for characterizing the impact behaviour of aluminium alloys and high strength steels. Later, Larour et al. adapted this methodology and developed the *CI* [2], which has been applied to assess the crash behavior of several AHSS and PHS grades [2–4]. In the present work, a new parameter, the *CIDR*, is proposed to define the damage evolution in axial crash tests according to a growing cracking pattern. This parameter can be understood as a crack propagation rate and it is proposed as an indicator of the crack propagation resistance of the material under impact conditions. Therefore, the presented methodology permits to separate the contributions of crack initiation and crack propagation resistance in AHSS crashworthiness.

The *CIDR* and the energy absorbed at maximum intrusion have been used in this work to characterize the crash performance of different AHSS grades. A close relationship exists between both parameters, as may be discerned in Fig. 11. The energy absorption capacity of the steel is inversely proportional to the *CIDR* since, reasonably, the maximum intrusion achieved depends on how rapid the *CI* decreases. The correlation between mechanical properties and the parameters characterizing the impact behaviour of the steel grades investigated in this work is discussed below.

Tensile properties (elongation at fracture, tensile strength, yield strength and area under engineering curve) are plotted against *CIDR* and energy absorbed at maximum intrusion in Fig. 12. As expected, according to previous works [2–6], no correlation is observed between any of the conventional tensile parameters and crash resistance. Steels with lower elongation at fracture or area under the engineering curve, such as CP1000 or PHS1000, show much better impact performance than other steel grades with greater tensile properties. Other parameters like the yield strength and tensile strength do not also give any relevant information about impact behaviour.

AHSS crash behaviour is shown to be governed by two main factors: the material resistance to crack nucleation, defined by the critical intrusion, and the resistance against the propagation of such cracks, represented by the *CIDR*. As observed in Fig. 8, most of the steel grades investigated, except TWIP, Q&P and PHS1500, present similar critical intrusion levels, in the range of 20–40 mm, i.e.,

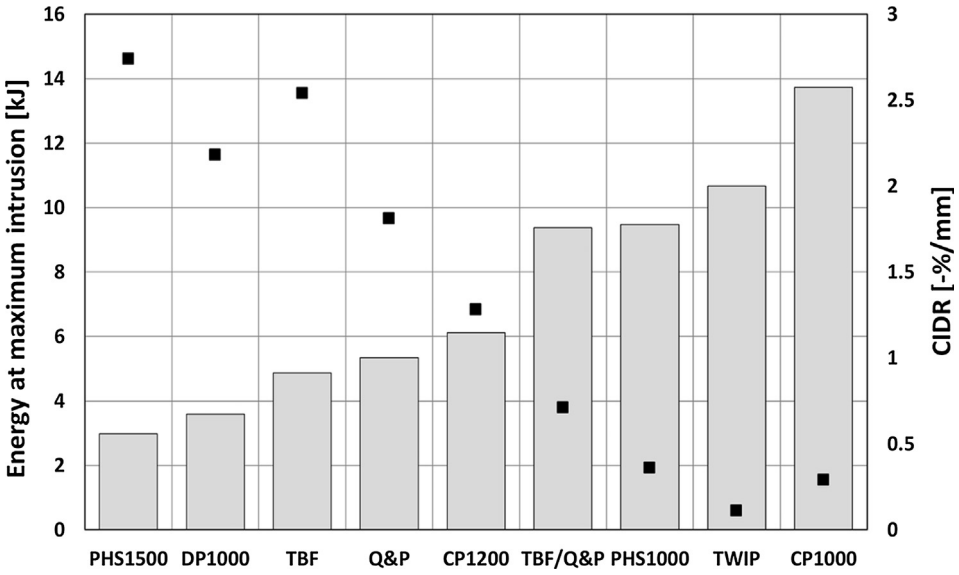

Fig. 11. Correlation between *CIDR* (square points) and maximum energy absorbed (bars).

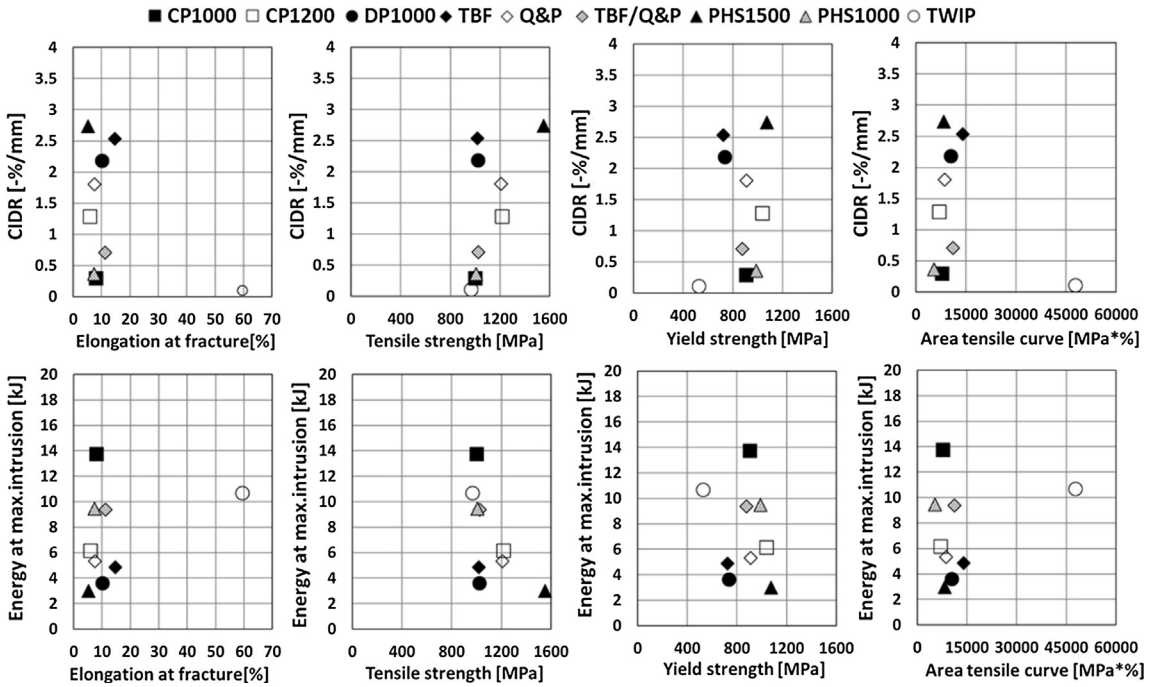

Fig. 12. Tensile properties against axial impact tests results.

they exhibit similar resistance to crack initiation. The major differences, therefore, are observed in the slope represented by the *CIDR*. It means that for the evaluated AHSS grades, crack propagation resistance strongly contributes to increase the crashworthiness. On the basis of these facts, a fracture mechanics based approach could help understanding crash resistance, by using the material resistance to crack initiation (w_e^i) and propagation (w_e). This approach is explained in the following paragraphs.

According to the definition of the critical intrusion as the onset of first cracks, the energy absorbed at that point should be related to the crack initiation energy, w_e^i. Such correlation is shown in Fig. 13. The figure shows the values of energy absorbed at critical intrusion and w_e^i. Energy values were obtained from extrapolation of *CI* vs energy data (Fig. 8), considering a *CI of* 95% as the appearance of first cracks. In general, a good agreement is observed for most of steel grades, except for Q&P, PHS1500 and PHS1000. Such differences may be explained by the effect of the unbuttoning and welding spots cracks, which, as mentioned in Section 4.1, had a high influence on critical intrusion for these steels. The unbuttoning leads to a very small bending radius at the side position and can

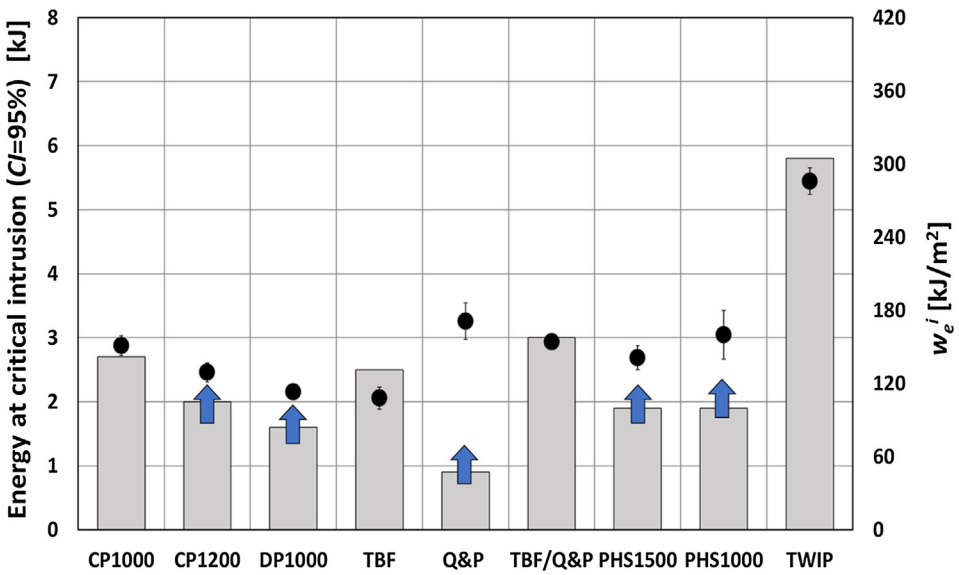

Fig. 13. Values of energy absorbed at critical intrusion (bars) and fracture toughness at initiation, w_e^i (circles). DP1000, CP1200, Q&P, PHS1500 and PHS1000 show effect of spot weld unbuttoning on critical intrusion. Their critical intrusions might be higher, as indicated by arrows.

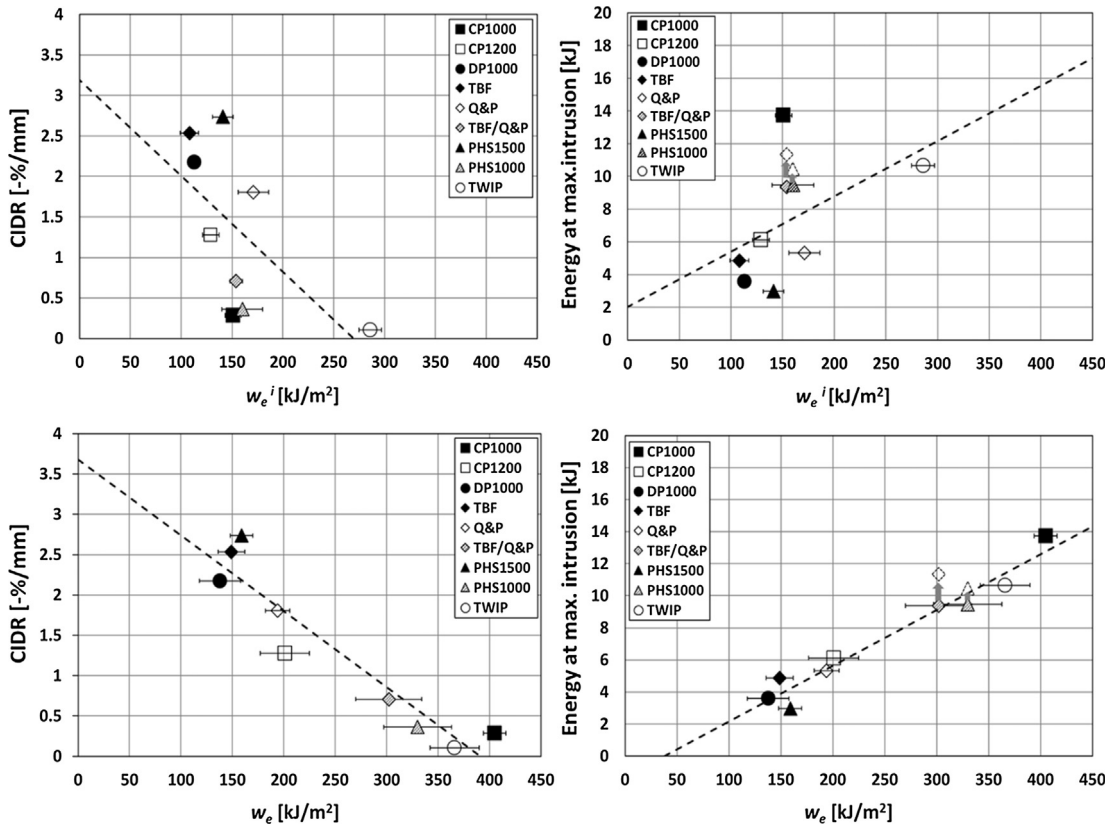

Fig. 14. Results of fracture toughness at initiation (w_e^i) and essential work of fracture (w_e) against *CIDR* and energy absorbed at maximum intrusion. Arrows point out the extrapolated energy values for PHS1000 and TBF/Q&P grades at CI = 20%. Linear regression fitting is represented by a dashed line.

trigger premature crack initiation. Without unbuttoning, the onset of the first cracks might be shifted to a higher crash speed and, thus, critical intrusion for base material should increase. This effect was especially marked for Q&P, but it was also observed, to a lesser extent, in DP1000, CP1200, PHS1500 and PHS1000. For these materials a higher critical intrusion level (and therefore a higher energy) would be expected, as indicated by arrows in Fig. 13. These experimental uncertainties compromise the detailed analysis of the critical intrusions in function of the w_e^i. However, based on the observed experimental trend, w_e^i can be considered as a first indicator of the material resistance against crack nucleation in axial impact tests.

The role of crack initiation and propagation resistance on the overall crash resistance is investigated in Fig. 14. The figure plots w_e^i and w_e against *CIDR* and energy at maximum intrusion. It is observed that w_e^i shows a poor correlation with *CIDR* ($R^2 = 0.38$) and maximum energy ($R^2 = 0.24$), which indicate that material properties related to crack initiation, as w_e^i or J_C, are not sufficient to describe the overall crash failure behaviour. On the other hand, a good correlation is obtained for w_e versus *CIDR* and versus energy absorbed, with very good linear fitting (R^2 of 0.89 and 0.95 respectively). Such good relationship is understood by the relevant role of crack propagation in the crash resistance and it allows stating that crash resistance can be well described by the overall fracture toughness, w_e. According to these observations w_e is postulated as a relevant material property to design high crash resistant alloys.

Nevertheless, one of the questions that can arise is how strain rate affects fracture toughness, since crash can involve strain rates up to 1000 s^{-1}. Recent investigations address the effect of the loading rate on the essential work of fracture of AHSS [41]. The work of Golling *et al.* describes the experimental uncertainties in the evaluation of fracture resistance at high strain rates and shows that fracture energy is very sensitive to the detection of the displacement at final fracture [41]. The work also shows that w_e^i and w_e increase with strain rate: w_e values of 263, 284 and 351 kJ/m^2 at a strain rate of 25 s^{-1} are reported for DP, TBF and Q&P respectively. It is a clear increase with respect to the values showed for these materials in Table 4. However, these values follow a similar trend than the obtained at quasi-static conditions. Therefore, it is expected that the good correlation shown in Fig. 14 will be also maintained for values measured at high strain rate, only shifted to higher values.

6. Conclusions

The work offers a fracture mechanics approach to understand the cracking related phenomena in crash tests and proposes the fracture toughness as a material property to describe crashworthiness in AHSS. After analyzing the experimental results of axial impact resistance tests and the fracture toughness, evaluated by means of the EWF methodology, of different AHSS grades the

following conclusions can be drawn:

- The *CIDR* has been presented as a suitable parameter to describe the axial crash behaviour of AHSS grades. *CIDR* effectively describes the material behavior because it is related to the propagation rate of existing cracks at different intrusion levels, independently of crack origin (base material or spot welds).
- Fracture toughness of thin AHSS sheets can be readily measured by means of the EWF methodology. The methodology permits to separate the energetic contribution from crack initiation, w_e^i and crack propagation, w_e.
- The fracture toughness at initiation, w_e^i, should be correlated with the energy absorbed at critical intrusion. In general, a good correlation was observed between both parameters for most of the steel grades investigated. Critical intrusion is strongly affected by spots welds unbuttoning and/or the detection of cracks initiated at spot welds. Such experimental uncertainties hamper to establish a strong relation between w_e^i and the energy absorbed at critical intrusion. However, the observed experimental trend allows pointing out w_e^i as a relevant material property to understand AHSS crack initiation resistance in impact tests.
- Fracture initiation parameters, such as w_e^i, or the equivalent EPFM toughness value J_C, do not sufficiently explain crash resistance in AHSS. The energetic contribution from crack propagation represents a significant part of the total energy dissipation and it should be considered when correlating to material properties.
- Experimental results of axial crash resistance in terms of *CIDR* and energy at maximum intrusion show a very good correlation with the overall fracture toughness, measured in terms of the essential work of fracture, w_e. Accordingly, fracture toughness of AHSS sheets can be used as a material property to properly rationalize crash behavior in AHSS.
- Thus, fracture toughness becomes a relevant property not only to classify the crashworthiness of commercially available AHSS grades, but also to design new AHSS with improved crash resistance.

Acknowledgements

The authors gratefully acknowledge the funding received from the European Commission, Research Fund for Coal and Steel, under grant agreement RFSR-CT-2014-00015 (Tough-Sheet).

Appendix A. Supplementary material

Supplementary data to this article can be found online at https://doi.org/10.1016/j.engfracmech.2018.10.005.

References

[1] Steel Market Development Institute 2016 Steel Industry Technology Roadmap for Automotive. < www.autosteel.org > .
[2] Larour P, Pauli H, Kurz T, Hebseberger T. Influence of post uniform tensile and bending properties on the crash behaviour of AHSS and press-hardening steel grades. Proceedings of the IDDRG2010 (Graz, Austria). 2010.
[3] Larour P, Naito J, Pichler A, Kurz T, Murakami T. Side impact crash behavior of press-hardened steels-correlation with mechanical properties. 5th Int conf hot sheet metal forming of high performance steel (CHS2) (Toronto, Canada, May 31–June 3, 2015). 2015. p. 281–9.
[4] Kurz T, Larour P, Lackner J, Steck T, Jesner G. Press-hardening of zinc coated steel – characterization of a new material for a new process. Proceedings of the IDDRG2016, Linz, Austria. 2016.
[5] Marten T, Block H, Tröster T, Gerber T, Sikora S, Lenze FJ. Graded Lightweight structures through hot forming. Proceedings of the 4th int conf on hot sheet metal forming of high-performance steel (Lulea, Sweden). 2013.
[6] Walp MS. Impact dependent properties of advanced and ultra high strength steel. SAE Technical Paper 2007-01-0342; 2007.
[7] Dietsch P, Tihay K, Cobo S, Sarkar S, Hasenpouth D, Cornette D. Predictive approach for crash performance of Press Hardened Steels and its application on new product developments. 6th Int conf hot sheet metal forming of high performance steel (CHS2). 2017.
[8] Sato K, Inazumi T, Yoshitake A, Liu SD. Effect of material properties of advanced high strength steels on bending crash performance of hat-shaped structure Int. J Impact Eng 2013;54:1–10.
[9] Laumann T, Pfestorf M. Crash behaviour of various modern steels exposed to high deformation rates. 1st Int conf on hot sheet metal forming of high-performance steel CHS2 (Kassel, Germany Oct. 22–24, 2008). 2008. p. 143–51.
[10] Larour P, Freudenthaler J, Weissböck T. Reduction of cross section area at fracture in tensile test: measurement and applications for flat sheet steels. J Phys: Conf Ser 2017;896:012073.
[11] VDA 238-100 (test specification) Plate bending test for metallic materials; December 2010.
[12] Cotterell B, Reddel JK. The essential work of plane stress ductile fracture Int. J Fract 1977:267–77.
[13] Mai YW, Pilko KM. The essential work of plane stress ductile fracture of a strain-aged steel. J Mater Sci 1979;14:386–94.
[14] Marchal Y, Delannay F. Comparison of methods for fracture toughness testing of thin low carbon steel plates. Mater Sci Tech 1998;14:1163–8.
[15] Mai YW, Cotterell B. The essential work of fracture for tearing of ductile metals. Int J Fract 1984;24:229–36.
[16] Pardoen T, Hachez F, Marchioni B, Blyth PH, Atkins AG. Mode I fracture of sheet metal. J Mech Phys Sol 2004;52:423–52.
[17] Chéhab B, Bréchet Y, Glez JC, Jacques PJ, Mithieux JD, Véron M, et al. Characterization of the high temperature tearing resistance using the essential work of fracture—application to dual phase ferritic stainless steels. Scrip Mater 2006;55:999–1002.
[18] Pardoen T, Marchal Y, Delannay F. Thickness dependence of cracking resistance in thin aluminium plates. J Mech Sol 1999;47:2093–123.
[19] Pardoen T, Marchal Y, Delannay F. Essential work of fracture compared to fracture mechanics—towards a thickness independent plane stress toughness. Eng Fract Mech 2002;69:617–31.
[20] Marchal Y, Walhin JF, Delannay F. Statistical procedure for improving the precision of the measurement of the essential work of fracture of thin sheets. Int Fract J 1997;87:189–99.
[21] Cotterell B, Pardoen T, Atkins AG. Measuring toughness and the cohesive stress–displacement relationship by the essential work of fracture concept. Eng Fract Mech 2005;72:827–48.
[22] Marchal Y, Delannay F. Influence of test parameters on the measurement of the essential work of fracture of zinc sheets. Int Fract J 1996;80:295–310.
[23] Tuba F, Oláh L, Nagy P. The role of ultimate elongation in the determination of valid ligament range of essential work of fracture tests. J Mater Sci 2012;47:2228–33.
[24] Mai YW, Cotterell B. Effects of pre-strain on plane-stress ductile fracture in α -brass. J Mater Sci 1980;13:2296–306.

[25] Wu J, Mai YW. The essential fracture work concept for toughness measurement of ductile polymers. Polym Eng Sci 1996;36:2275–88.
[26] Mai YW, Cotterell B. On the essential work of ductile fracture in polymers Int. J Fract 1986;32:105–25.
[27] Mai YW, Powell P. Essential work of fracture and J-integral measurements for ductile polymers. J Polym Sci 1991;29:785–93.
[28] Martínez AB, Gamez-Perez J, Sanchez-Soto M, Velasco JI, Santana O, Maspoch MLL. The essential work of fracture method- analyzing the post-yielding fracture mechanics of polymers. Eng Fail Anal 2009;16:2604–17.
[29] Lacroix G, Pardoen T, Jacques PJ. The fracture toughness of TRIP-assisted multiphase steels. Acta Mater 2008;56:3900–13.
[30] Muñoz R, Lara A, Casellas D. Fracture toughness characterization of advanced high strength steels. Proceedings of the IDDRG 2011, (Bilbao, Spain). 2011.
[31] Gutiérrez D, Ll Pérez, Lara A, Casellas D, Prado JM. Toughness evaluation of high strength steels sheets by means of the essential work of fracture. 19th European conference on fracture: fracture mechanics for durability, reliability and safety, ECF 2012. 2012.
[32] Casellas D, Madivala M, Lara A, Calvo J, Cabrera JM, Prahl U. Fracture and crack propagation resistance of High Manganese TWIP Steels: experimental evaluation. Proceedings of the 2nd int conf on high Mn steel HMnS2014 (Aachen, Germany). 2014.
[33] Casellas D, Lara A, Molas S, Golling S, Oldenburg M. Fracture resistance of tailor tempered microstructures obtained by different Press Hardening conditions. Proceedings of the 5th int conf on hot sheet metal forming of high-performance steel (Toronto, Canada). 2015.
[34] Casellas D, Lara A, Frómeta D, Gutiérrez D, Molas S, Ll Pérez, Rehrl J, Suppan C. Fracture toughness to understand stretch-flangeability and edge cracking resistance in AHSS. Metall Mater Trans A 2017;48:86–94.
[35] Frómeta D, Tedesco M, Calvo J, Lara A, Molas S, Casellas D. Assessing edge cracking resistance in AHSS automotive parts by the Essential Work of Fracture methodology. J Phys: Conf Ser 2017;896:012102.
[36] Wu R, Li J, Li W, Wu XC, Jin X, Zhou S, et al. Effect of metastable austenite on fracture resistance of quenched and partitioned (Q&P) sheet steels. Mater Sci Eng A 2016;657:57–63.
[37] Luo ZC, Liu RD, Wang X, Huang MX. The effect of deformation twins on the quasi-cleavage crack propagation in twinning-induced plasticity steels. Acta Mater 2018;150:59–68.
[38] Sahoo S, Padmapriya N, Sarathi De P, Chakraborti PC, Ray SK. Ductile tearing resistance indexing of automotive grade DP590 steel sheets: EWF testing using DENT specimens. J Mater Eng Perform 2018;27:2018–23.
[39] Clutton E. Essential work of fracture. Moore DR, Pavan A, Williams JG, editors. Fracture mechanics testing methods for polymers, adhesives and composites, vol. 28. ESIS Publ.; 2001. p. 177–95.
[40] Hisker F, Thiessen R, Heller T. Influence of microstructure on damage in advanced high strength steels. Mater Sci Forum 2012;706–709:925–30.
[41] Golling S, Frómeta D, Casellas D, Jonsén P. Investigation on the influence of loading-rate on fracture toughness of AHSS grades. Mater Sci Eng A 2018;726:332–41.

Paper IV. D. Frómeta, N. Cuadrado, J. Rehrl, C. Suppan, T. Dieudonné, P. Dietsch, J. Calvo, D. Casellas. Microstructural effects on fracture toughness of ultra-high strength dual phase sheet steels. Submitted to *Materials Science and Engineering A* (under review).

Microstructural effects on fracture toughness of ultra-high strength dual phase sheet steels

D. Frómeta[1], N. Cuadrado[1], J. Rehrl[2], C. Suppan[2], T. Dieudonné[3], P. Dietsch[3], J. Calvo[4] and D. Casellas[1,5*]

[1] Eurecat, Centre Tecnològic de Catalunya, Unit of Metallic and Ceramic Materials, Plaça de la Ciència, 2, Manresa 08243, Spain
[2] voestalpine Stahl GmbH, voestalpine-Straße 3, 4020 Linz, Austria
[3] ArcelorMittal Maizières Research SA, Voie Romaine, BP30320, 57283 Maizières-les-Metz, France
[4] Universitat Politècnica de Catalunya, Eduard Maristany 16, 08019 Barcelona, Spain
[5] Division of Mechanics of Solid Materials, Luleå University of Technology, 971 87 Luleå, Sweden

[*]Corresponding author: daniel.casellas@ltu.se

Abstract. The influence of the microstructure on the fracture toughness of two industrially processed 1000 MPa dual-phase (DP) steel grades is investigated. Crack initiation and propagation resistance are evaluated by means of the essential work of fracture (EWF) methodology and the main damage and fracture mechanisms are investigated. The results are discussed in terms of the proportion and distribution of the different microstructural constituents, which is assessed by scanning electron microscopy (SEM), high-resolution electron backscatter diffraction (HR-EBSD) and nanoindentation hardness measurements. The investigations show that strain-induced transformation of retained austenite to martensite (TRIP effect), may be detrimental to cracking resistance, even though it increases tensile properties. This phenomenon is attributed to a brittle network effect generated by the presence of hard fresh martensite islands in the fracture process zone. The connectivity of the hard secondary phases and the proportion of soft phase (ferrite) also have a major role in fracture toughness. The DP steel with larger volume fraction of ferrite and homogeneously distributed martensite islands shows significantly higher crack propagation resistance. The contribution of necking to the ductile fracture process is evaluated by means of thickness measurements in fractured DENT specimens and the correlation between the specific essential work of fracture (w_e) and tensile properties is investigated. It is concluded that the global formability and cracking resistance of high strength DP steels can be balanced through microstructural tailoring.

Keywords: **Dual phase steels, microstructure, fracture toughness, essential work of fracture, TRIP effect.**

1. Introduction

Dual Phase (DP) steels are one of the most extensively used Advanced High Strength Steels (AHSS) for body in white automobile components [1]. Their excellent compromise between high strength and good formability has contributed to their widespread implementation in passenger's car, allowing vehicle weight reduction and enhancing occupant's safety [1, 2]. These steels belong to the first generation of AHSS family and are characterized by showing high strength, low yield strength to tensile strength (YS/TS) ratio, high strain hardening and high ductility compared to other high strength low-alloy steels [1-3]. Such unique combination of mechanical properties is closely linked to their particular microstructure, basically consisting of a soft ferritic matrix with hard martensite islands embedded. In some cases, other secondary phases, such as bainite or retained austenite, can also be present in different proportions [4, 5].

The relationship between microstructure and strength/ductility properties of DP steels has been the focus of extensive research in the last decades [4-14]. Strength level is primarily dictated by the martensite volume fraction; the higher the martensite/ferrite ratio the higher the yield strength and the ultimate tensile strength (typical martensite volume fractions are in the range of 20-50% for tensile strengths of

600-1200 MPa) [5-9]. Generally, such increase of strength is accompanied by a decrease of elongation, both uniform and total [6-8]. Other factors, such as the grain size [10,11], the hardness of the microstructural constituents [12] or their morphology and distribution [13,14] also have influence on mechanical behaviour. Their high strain hardening is caused by the strain gradients between the soft matrix (ferrite) and the hard secondary phases (martensite) during forming, which generate dislocations pile-ups (geometrically necessary dislocations) in the ferritic matrix to accommodate the plastic incompatibility between the two phases [15]. Such deformation mechanism contributes to increase the work-hardening rate and to delay the onset of localized necking, thus improving the formability. Strain hardening behaviour is mostly influenced by the volume fraction, hardness, size and distribution of martensite [1, 5-7,10, 13]. Steels containing retained austenite also have an additional contribution to strain hardening due to the strain-induced transformation of retained austenite to martensite (Transformation Induced Plasticity, or TRIP, effect) in the initial stages of deformation [1, 4].

Owing to their great ductility and strain-hardenability, DP steels are especially suitable for cold forming operations involving large deformations (deep drawing, stretching, hydroforming, etc.). However, in spite of their good formability, several cracking problems during forming, related to their limited edge formability or hole expansion capacity, have been reported [16-18]. The development of DP steel grades with increasingly higher strength (current grades can reach up to 1200 MPa [19,20]) has incremented the frequency of occurrence of these fractures, being a real concern to automotive part manufacturers. Thus, cracking resistance has become a critical factor limiting the applicability of high strength DP steels.

Even though many works have addressed the influence of microstructure on edge formability (or stretch flangeability) of DP steels [12, 21-26], its is still being a topic of debate. Their rather low edge fracture resistance is generally attributed to the heterogeneous microstructure and the differences in hardness between the microstructural constituents [21-25]. Nevertheless, the identification of a singular microstructural parameter controlling the stretch flangeability of DP steels is very complex, since it depends on the interaction of different microstructural features (martensite volume fraction, hardness, size, morphology, distribution of the phases, etc.) [26]. Furthermore, stretch flangeability is standardly measured by means of the Hole Expansion Test (HET) [27]. The value obtained from this test is the Hole Expansion Ratio (HER), which represents the material's ability to resist crack formation from a punched hole. The HER is not a material property and depends on the hole preparation method [22, 28], which sometimes makes difficult to establish clear relationships between microstructure and edge cracking resistance.

Fracture toughness, measured in the frame of fracture mechanics, has shown to be a determinant property governing AHSS edge fracture resistance [17, 26, 29-35]. Hence, understanding the effects of microstructure on fracture toughness is essential to develop DP microstructures with improved cracking resistance. However, few studies have been conducted on the relation microstructure-fracture toughness of DP steels [30, 36-38]. Tkach et al. [36] noticed an increase of K_c with increasing the martensite volume fraction in a 0.06C-1.8Cr-1.6Ni-0.6Mo steel with different heat treatments. They attributed this effect to the higher toughness of the martensite respect to the ferrite and to the lower carbon content of martensite when applying higher annealing temperatures. Fonstein et al. [30] showed that the crack propagation resistance of a cold rolled DP steel was significantly enhanced replacing part of the martensite by bainite. Bayram et al. [37] found that microstructures showing fine needle-like martensite homogeneously distributed in the ferrite matrix exhibited higher K_c than those with equiaxed grains of ferrite and martensite. Lacroix et al. [38] studied the fracture toughness of different TRIP-assisted and DP steels and observed that a decrease in the connectivity of martensite grains significantly increased the crack initiation resistance (J_c).

The present paper aims at better understanding the influence of microstructure on the crack initiation and propagation resistance of high strength DP steels. For this purpose, the fracture toughness and the fracture mechanisms of two industrially processed 1000 MPa DP steel sheets are investigated and correlated to their microstructural features. Fracture toughness is evaluated by means of the essential work of fracture (EWF) methodology [39]. The method allows to readily evaluate the plane stress fracture toughness of thin ductile sheets, separating experimentally the energy consumed during the tearing process in two terms: the energy dissipated in the fracture process zone (FPZ), called specific essential work of fracture (w_e), and the non-essential plastic work (w_p) dissipated in an outer region of the fracture. The first term, w_e, is an average resistance value for the complete fracture (i.e. it contains energetic contributions from crack initiation and crack propagation resistance) and it is a suitable parameter to measure the ductile tearing resistance of thin sheets [38-43]. It is important noting that, even though w_e is independent of specimen geometry and in-plane dimensions [43], plane stress fracture toughness has an additional extrinsic contribution from the necking developed at the crack tip [38-42]. Therefore, it is not strictly a material property but a constant for a given sheet thickness. The non-essential plastic work is a geometry dependent parameter and, thus, cannot be considered a material property. The EWF method has been used in several works to assess the cracking resistance of AHSS sheets [32-35, 38, 42, 44-46]. The mechanical properties and tensile fracture resistance of the two investigated DP steels are evaluated through conventional tensile tests and local fracture strain measurements. Microstructural characteristics are investigated by means of scanning electron microscopy (SEM), high-resolution electron backscatter diffraction (HR-EBSD) analysis and nanoindentation hardness measurements. The results can help to guide microstructural design of high strength DP steels with optimum balance between strength, ductility and fracture resistance.

2. Materials and methods

2.1 Materials

2.1.1. Chemical composition and material processing

Two 1000 MPa DP steels were processed via hot dip galvanizing line (HDGL) at industrial scale. The slabs, obtained by continuous casting, were reheated to a temperature of 1200° C and hot rolled to a thickness of 3-4 mm. After pickling, the steels were cold rolled to the final thickness (1.35-1.4 mm) and annealed on the HDGL.

A schematic representation of the time-temperature cycles of the HDGL is given in Figure 1. DP1000-A was annealed in fully austenitic range. Ferrite was formed during cooling to the overaging temperature. While overaging, stabilization as well as further transformation of the remaining austenite to bainite takes place. After overaging, the steel was dipped in liquid zinc bath. Fresh martensite was formed from remaining austenite during final cooling. DP1000-B was soaked in the intercritical range to have a certain amount of ferrite and austenite in the microstructure. At the end of this soaking step, the steel strip was cooled down to the overaging temperature before dipping in a liquid zinc bath. During this overaging step, a main part of austenite is transformed to bainite. At the exit of the zinc bath, the remaining austenite is transformed to martensite during the final cooling. The chemical compositions of the two DP steels are given in Table 1.

2.1.2. Microstructural characterization

Microstructural analysis was performed by means of SEM and HR-EBSD. After mechanical grinding and polishing, SEM samples were electro-polished. HR-EBSD samples were mechanically polished to mirror surface finish with a 0.05 µm colloidal silica suspension. The HR-EBSD measurements were

performed at 20 kV with a step size of 0.15 μm. The analysed areas were 311 x 231 μm2. The percentage of different phases, as well as the average grain size of ferrite and martensite, was determined by a combination of image analysis, SEM and optical micrographs and EBSD measurements. The amount of retained austenite was validated by means of magnetization saturation measurements [47].

Figure 1 shows the resulting SEM micrographs. HR-EBSD results and volume fraction and size of the different microstructural constituents are shown in Figure 2 and Table 2, respectively. Figure 2 shows the obtained inverse pole figure (IPF) map, the phase map and the mean angular deviation (MAD) map.

The microstructure of DP1000-A consists of a matrix containing ferrite (α) and bainite/tempered martensite (α_b) with some dispersed martensite and fresh martensite/retained austenite (M/RA) islands. The SEM images reveal a great presence of carbide precipitates within B/TM grains (Figure 1a). DP1000-B has a ferritic-bainitic matrix with a slightly lower amount of martensite islands (≈27%), which are homogeneously distributed. Contrary to the observed in DP1000-A, carbide precipitation is hardly seen in bainitic (B) areas (Figure 1b).

Figure 2b shows the HR-EBSD phase constitution map differentiating the BCC phase (ferrite) in blue and the FCC phase (austenite) in yellow. High angle grain boundaries (> 15º) are delimited with black lines and low angle grain boundaries are depicted in grey. The results revealed a 0.75% and 0.09 % of γ phase for DP1000-A and DP1000-B respectively (Figure 2b). However, these values are much lower than the obtained from magnetic measurements (6% and 2 %, respectively). The large differences between the two measuring techniques are probably related to the sample preparation process (most of the retained austenite is transformed to martensite during mechanical polishing) and to the fact that the EBSD measurements are not able to detect very fine grains below 0.15 μm in size (EBSD step size) or thin films of retained austenite. Previous works reported that EBSD measurements may underestimate the volume fraction of retained austenite [48-49]. On the other hand, magnetic measurements provide a more reliable quantification of retained austenite content [48].

The martensite volume fraction was determined from SEM micrographs. However, the differentiation between ferrite and bainite in SEM images was sometimes difficult, especially in DP1000-B. Therefore, the amount of ferrite phase was obtained from Nital etched optical micrographs. The MAD colour map (Figure 2c) was also used as a qualitative indicator of the ferrite fraction. The MAD indicates the degree of misfit between the theoretical and the measured Kikuchi bands. The lower the MAD, the better the match and the higher the indexing quality or the image quality (IQ). The IQ analysis has been often used in literature to differentiate ferrite from bainite or martensite [50-52]. Since bainite and martensite present higher dislocation density than ferrite, the quality of the diffraction pattern is affected by the larger lattice distortion [50-52], leading to lower IQ or higher MAD. However, the differentiation between bainite and martensite is more difficult since the differences in misorientation due to lattice distortions are not so evident. In this work, the MAD analysis was used to provide a general idea on the presence of ferrite in the two investigated DP steels. In Figure 2c, the blue colour indicates a good degree of pattern quality and, thus, it can be associated to the ferrite phase. On the other hand, green colour suggests a deviation of the measured patterns for BCC phase from the theoretical Fe-BCC patterns. These deviations can be associated with the presence of bainite and/or martensite. The MAD colour maps reveal a greater presence of ferrite in DP1000-B compared to DP1000-A, as observed in optical micrographs.

Both steels present very similar grain size distribution for both ferrite and martensite constituents, as shown in Table 2.

Table 1. Chemical composition of the investigated DP steels (in weight per cent).

Steel grade	C	Si	Mn	Cr	B	Al	Ti
DP1000-A	~0.15	<0.5	~2.3	<0.7	<0.003	~0.05	<0.0060
DP1000-B	0.08	0.26	~2.6	0.31	0.0018	0.16	0.0372

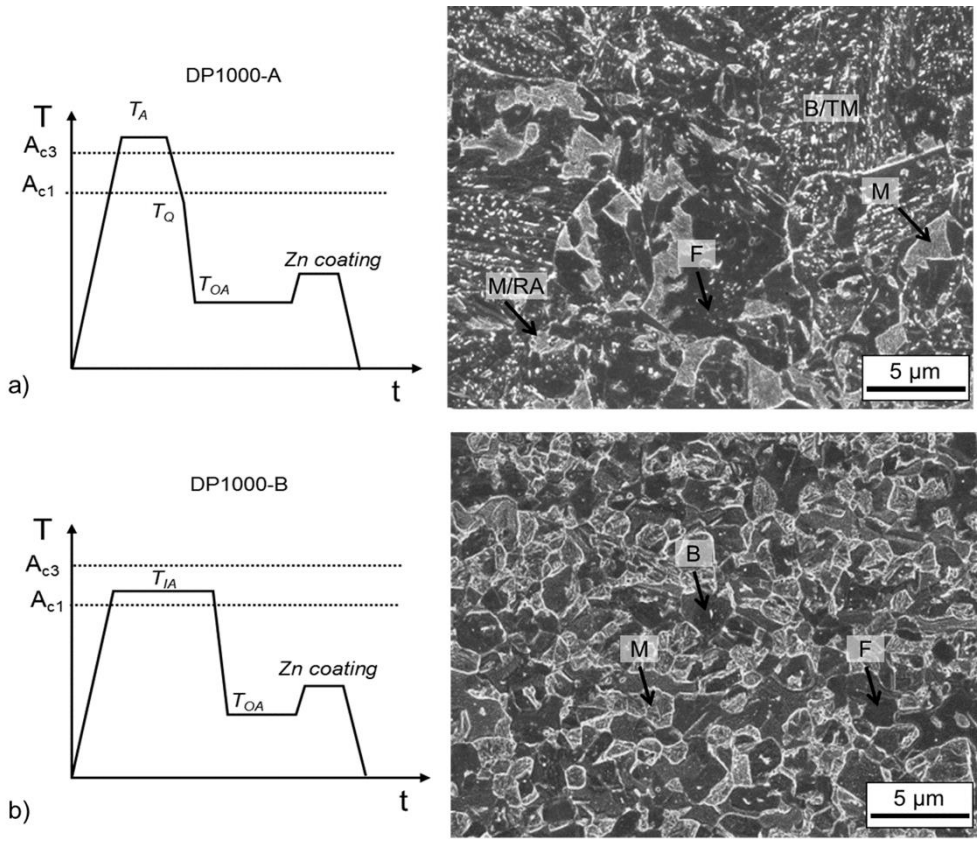

Figure 1. Schematic representation of the time-temperature cycles applied to obtain the DP microstructures and SEM micrographs of a) DP1000-A and b) DP1000-B. T_A: annealing temperature, T_{IA}: Intercritical annealing temperature, T_Q: Quenching temperature, T_{OA}: overaging temperature. F: Ferrite, M: Martensite, TM: Tempered martensite, B: Bainite, RA: Retained austenite.

Table 2. Phase distribution (volume fraction in %) and average grain size (equivalent circle diameter) of the different microstructural constituents

	Phase volume fraction [%]				Grain size [µm]	
Steel	Ferrite (α)	Bainite/Tempered martensite (α_b)	Martensite (α')	Retained Austenite (γ)*	d_α	$d_{\alpha'}$
DP1000-A	23 ± 2	39 ± 1	32 ± 1	6 ± 0.4	1.8 ± 0.6	1.2 ± 0.4
DP1000-B	33 ± 2	37 ± 4	27 ± 1	2 ± 0.3	1.7 ± 0.6	1.3 ± 0.4

*Results from magnetization saturation measurements

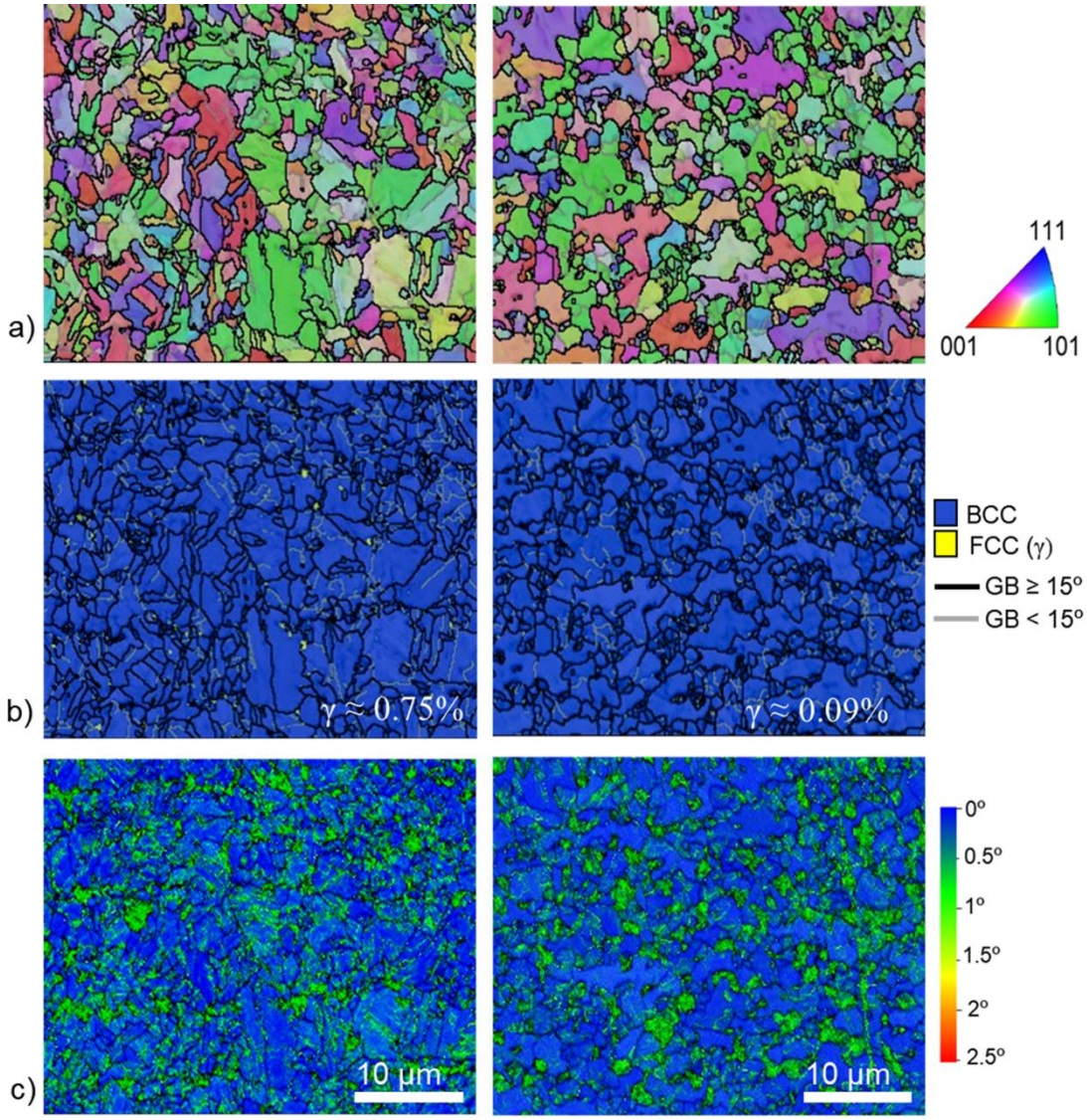

Figure 2. EBSD results for DP1000-A (left) and DP1000-B (Right). a) IPF map, b) phase map and c) MAD map. GB: grain boundary.

2.2. Experimental methods

2.2.1. Uniaxial tensile properties

Conventional tensile tests according to ISO 6892-1 [53] were performed to obtain the tensile properties of the two investigated DP steels for the transverse orientation. Tensile specimens with a width of 20 mm and a parallel length (L_c) of 120 mm were used (specimen type 2 described in ISO 6892-1, Annex B). An initial gauge length of 80 mm was used for strain measurements. The strain rate during the test was 2.5×10^{-4} s^{-1} until the end of the elastic deformation, then 6.7×10^{-3} s^{-1} until the failure of the sample. 3 specimens per material were tested.

The instantaneous strain hardening exponent (n_i) and the strain hardening rate (θ) were calculated according to Equations 1 and 2:

$$n_i = \frac{d(ln\ \sigma)}{d(ln\ \varepsilon)} \quad \text{Equation 1}$$

$$\theta = \frac{d\sigma}{d\varepsilon} \quad \text{Equation 2}$$

where σ and ε are the true stress and the true strain respectively.

The true fracture strain (ε_f), derived from the reduction of area at fracture was also evaluated for all the specimens. ε_f is used as a measure of the material's fracture resistance and it has been recently proposed as a relative index of local formability [54]. It is given by Equation 3:

$$\varepsilon_f = ln\left(\frac{A_0}{A_f}\right) \quad \text{Equation 3}$$

where A_0 is the initial cross-section area and A_f is the area at fracture. The area at fracture was measured from the fracture surface of tensile specimens according to ASTM E8 [55] by using a stereo-light microscope.

To evaluate the evolution of retained austenite-to-martensite transformation with deformation, magnetization saturation measurements [47] were performed in pre-strained uniaxial tensile samples. Five pre-strain levels were selected between zero and uniform strain (ε_u). For each pre-strain level, two specimens were tested.

2.2.2. Nanoindentation

Nanoindentation measurements were performed using an iNano nanoindenter (Nanomechanics). A Berkovich indenter was used. The experimental procedure for sample preparation was the same as described for EBSD measurements. In each sample, three matrices of 25x25 indentations were performed. An indentation separation of 6 μm was chosen, covering an area of 150x150 μm^2. The indentations were performed at an applied load of 20 mN. Hardness values were evaluated using the Oliver and Pharr methodology [56].

2.2.3. Essential Work of Fracture tests

EWF tests were performed using rectangular Double Edge Notched Tension (DENT) specimens of 240 x 55 mm (Figure 3a). The specimens were machined with the notches aligned to the rolling direction (T-L configuration). Starter notches with notch radius ρ=150 μm were machined by electrical discharge machining (EDM). Then, in order to avoid the influence of notch radius on fracture toughness results, fatigue pre-cracks were nucleated at the notch root (Figure 3b) following the recommendations of the ASTM E1820 [57]. Fatigue pre-cracking was conducted under load (P) control in a resonance fatigue machine. Tests were run at room temperature at a constant axial load ratio, R= P_{min}/P_{max}=0.1 (tension–tension). The ΔK (K_{max}-K_{min}) was kept below 0.3 K_c, where K_{max} and K_{min} are, respectively, the maximum and minimum stress intensity factor applied and K_c is the linear elastic fracture toughness at crack initiation. This condition was verified after the test. The cracks were extended about 1-1.5 mm per side. The crack growth was tracked by visual inspection and the final crack length was measured with the aid of an optical microscope. Due to the manual monitoring of the crack growth and the difficulty in propagating the two cracks in a perfectly symmetrical manner, the final crack length usually presented some variations from one side of the specimen to the other (maximum deviation ±0.3 mm).

5 different initial ligament lengths (l_0) ranging from 6 to 14 mm were used and 3 specimens per ligament length were tested. The specimens were tested up to fracture at a constant cross-head speed of 1 mm/min.

The load-line displacement was measured by means of the video extensometer using initial extensometer marks separated 50 mm. The specific total work of fracture (w_f) for each specimen was obtained by integrating the energy under the load vs load-line displacement curve and dividing by the initial cross-section area:

$$w_f = \frac{1}{l_0 t_0} \int_0^{u_f} P \cdot du \qquad \text{Equation 6}$$

where l_0 is the initial ligament length, t_o is the sheet thickness, P is the load, u the load-line displacement and u_f the displacement at fracture (Figure 3c). The specific essential work of fracture, w_e, was then obtained by linear extrapolation of w_f vs l_0 data to ligament zero (Figure 3d). The slope of the linear regression represents the non-essential plastic work (w_p) multiplied by a geometry factor (β). The fracture toughness at crack initiation, w_e^i, was obtained from an average of specific work of fracture initiation (w_f^i) values for different ligament lengths. w_f^i is calculated by integration of the area under load-displacement curves up to the point of crack growth initiation (Figure 3c) according to Equation 7:

$$w_f^i = \frac{1}{l_0 t_0} \int_0^{u_i} P \cdot du \qquad \text{Equation 7}$$

where u_i is the load-line displacement at crack growth initiation (Figure 3c). As observed in Figure 3d, w_f^i remains constant with the ligament length [34,42]. For the determination of the crack growth initiation, a high-resolution video camera synchronized with the testing machine was used. Generally, the crack growth was first initiated in one of the two sides of the specimen. u_i corresponds to the displacement when the first crack starts to grow. w_f^i was calculated for two specimens of each ligament length.

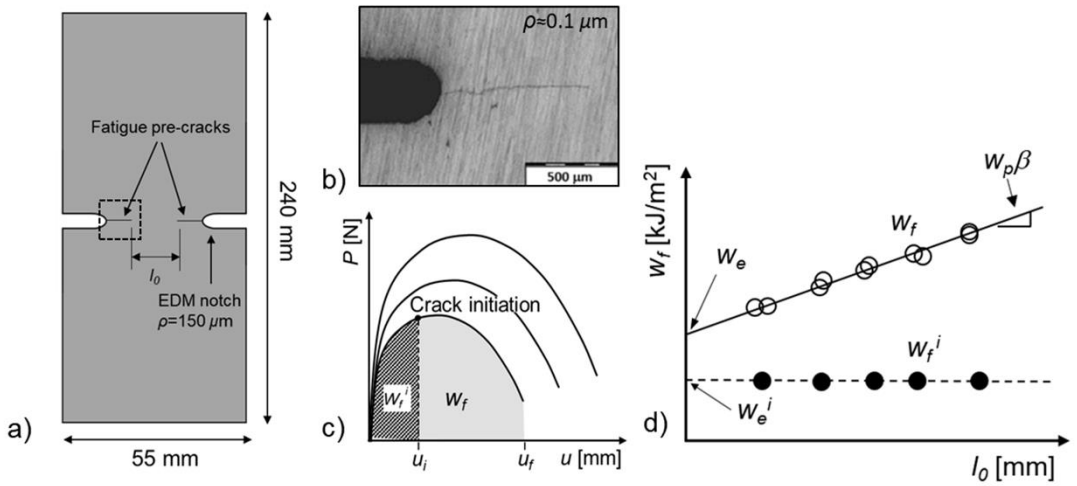

Figure 3. a) DENT geometry used for EWF tests. b) Detail of the fatigue pre-crack at the notch root. c) Typical load-displacement curves obtained from EWF tests. d) Schematic representation of the w_f vs l_o plot and determination of the specific essential work for fracture (w_e) and the fracture toughness at crack initiation.

2.2.4. Fracture surface analysis of DENT specimens

The fracture surface of DENT specimens was investigated by optical microscopy and SEM. To quantify the contribution of necking to the ductile fracture process, thickness strain measurements were performed in different positions of the fracture surface by using an optical microscope and a digital image analysis software (Figure 4a and b). The true fracture thickness strain (ε_{3f}) was then calculated as follows:

$$\varepsilon_{3f} = ln\left(\frac{t_0}{t_f}\right) \qquad \text{Equation 8}$$

where t_o is the initial sheet thickness and t_f is the thickness at fracture measured from the fracture surface. The evolution of ε_{3f} as a function of the crack advance was evaluated and two terms were identified: the fracture thickness strain at crack tip ($\varepsilon_{3f\,tip}$) and the steady-state fracture thickness strain ($\varepsilon_{3f\,SS}$) (Figure 4c).

A fractographic analysis of the fracture surfaces of broken DENT specimens was performed by means of SEM. Void size and distribution and main fracture mechanisms were investigated. The crack path was investigated by SEM observation of DENT specimens tested and stopped after a small amount of crack extension. Metallographic samples were obtained from an area close to the crack tip, polished and etched with a 2% Nital solution to reveal the microstructure.

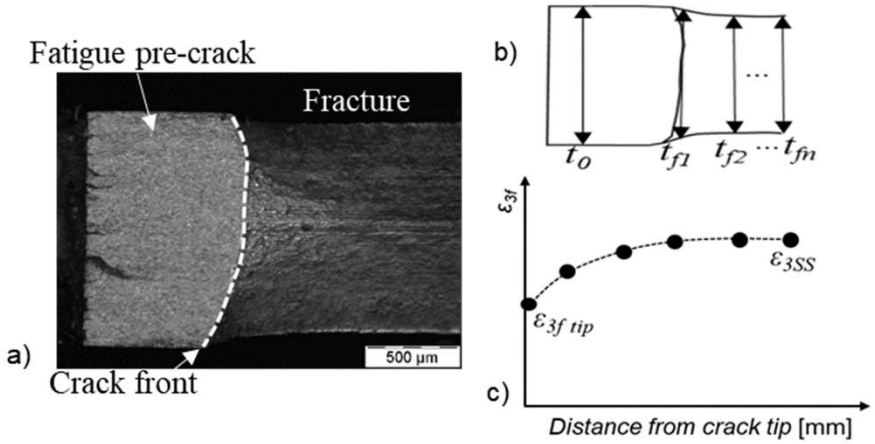

Figure 4. a) Optical microscope image from the fracture surface of a DENT specimen. The dashed line indicates the front of the crack tip. Schematic representation of: b) thickness measurements performed in the fracture surface and c) plot of the true fracture thickness strain (ε_{3f}), as a function of the crack tip distance.

3. Results

3.1. Tensile properties

Figure 5 shows the engineering and true stress-strain curves for the two studied DP steels. True curves are represented up to the uniform elongation (solid lines) and extrapolated to the true fracture strain (ε_f). The true stress at fracture is obtained by dividing the load at fracture by the final cross-section area, A_f. Mechanical properties are given in Table 3. The DP1000-A shows slightly superior strength and elongation values than DP1000-B. DP1000-A also exhibits higher ε_f and UTSxTE. The strain hardening behaviour is shown in Figure 6. Both DP steels are characterized by a high initial strain hardening rate that rapidly decreases with increasing strain, which is typical from DP microstructures. From the onset of the plastic region (ε≈0.02), DP1000-A shows higher strain hardening rate and strain hardening exponent (n) than DP1000-B. Even though DP1000-B has higher initial n, it continuously decreases from the beginning of deformation. On the other hand, in DP1000-A, the strain hardening exponent remains constant at the initial plastic deformation stage (ε≈0.02-0.03) and then linearly decreases up to the true uniform strain. The greater strain hardening behaviour of DP1000-A is probably related to the transformation of retained austenite to martensite, which takes place at the early stages of deformation (see insert in Figure 6a).

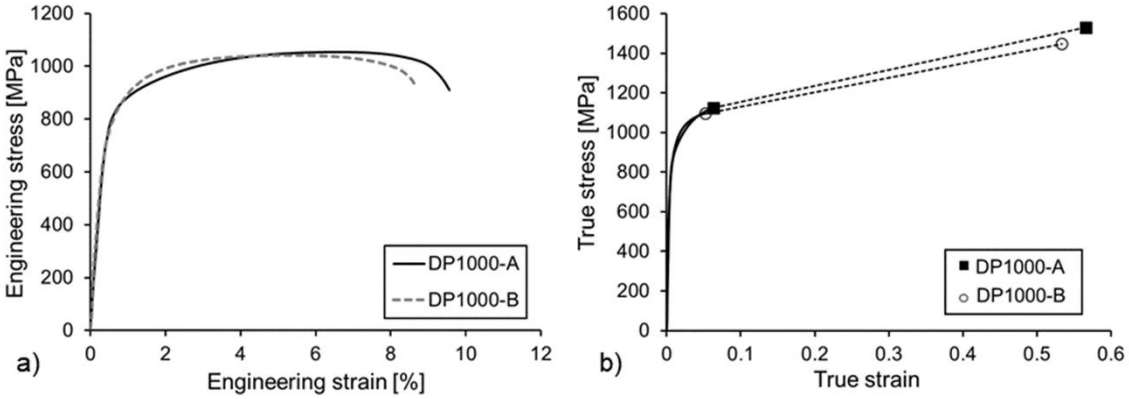

Figure 5. Engineering (a) and true (b) stress-strain curves for the investigated DP steels.

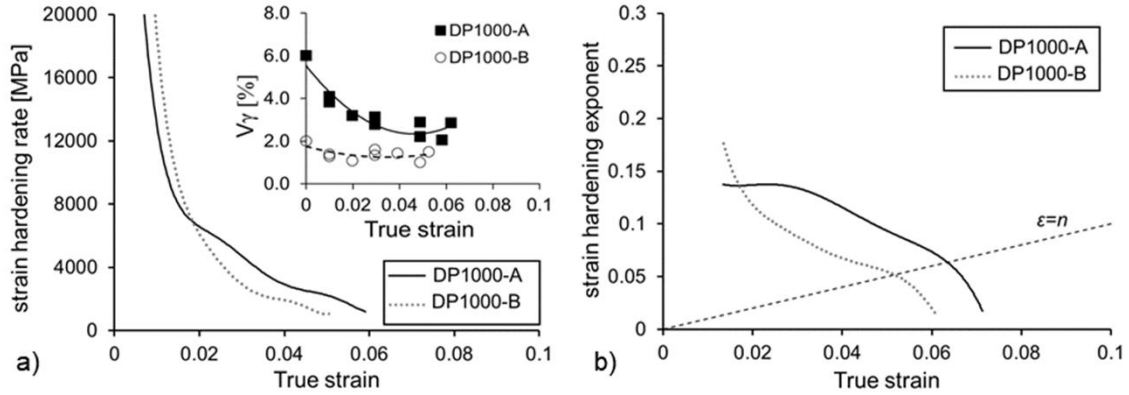

Figure 6. a) Strain hardening rate and volume fraction of retained austenite (Vγ) as a function of the true strain. b) strain hardening exponent as a function of the true strain.

Table 3. Mechanical properties for the transverse direction. *t* = thickness; *YS*= yield stress; *UTS* = ultimate tensile strength; *UE* = uniform elongation; *TE* = total elongation (initial gauge length of 80 mm); $n_{2\text{-}4}$ = strain hardening exponent between 2 and 4% deformation; ε_u = true uniform strain; ε_f = true fracture strain.

Steel	*t* [mm]	*YS* [MPa]	*UTS* [MPa]	*UE* [%]	*TE* [%]	*UTSxTE* [MPa*%]	$n_{2\text{-}4}$ [-]	ε_u [-]	ε_f [-]
DP1000-A	1.35	816	1055	6.5	9.7	10234	0.13	0.06	0.57
DP1000-B	1.40	773	1040	5.4	8.7	9048	0.09	0.05	0.53

3.2. Nanohardness measurements

Figure 7 shows SEM images of the nanoindentation arrays and the resulting nanohardness mappings. Due to the very fine grain size distribution, most of the indentations were located in areas containing more than one single phase, which made difficult the evaluation of the hardness for each individual microstructural constituent. Nevertheless, the results provide an illustrative picture of the hardness distribution in the two studied DP steels.

Hardness histograms are presented in Figure 8. It shows that both steels present a normal distribution of hardness data. The values of hardness can be roughly divided into three groups: $3.25 < H < 4.25$ GPa, $4.25 \leq H < 4.75$ GPa and $H \geq 4.75$ GPa, which might be associated to the ferrite, bainite and martensite phases, respectively. Such range of hardness values for ferrite and martensite are in good agreement with results from the literature [12].

Even though both steels present quite similar distribution of hard phases ($4.75 \leq H < 5.5$ GPa), DP1000-A shows a larger presence of very high hardness values ($H > 5.5$ GPa, colour red in Figure 7). These hard phases showing the highest hardness values may be associated with the carbon enriched fresh martensite/retained austenite islands. The distribution of ferrite (green) and bainite (yellow) in both steels is in concordance with the microstructural description shown in *Section 2.1.2.,* i.e. DP1000-B shows a higher fraction of ferrite than DP1000-A. For the intermediate hardness values, i.e. $4.25 \leq H < 4.75$ GPa, associated with bainite, the histograms in Figure 8 show that steel DP1000-A has a larger proportion of hardness values in the high hardness range than steel DP1000-B. This could be related to the higher amount of carbides observed in the bainite/tempered martensite areas of steel DP1000-A (Figure 1). Even though differences in average hardness, are small, DP1000-A ($H=4.6 \pm 0.3$ GPa) shows slightly greater hardness than DP1000-B ($H=4.4 \pm 0.3$). Applying a *t*-distribution analysis, it can be asserted with a 99% confidence level that both hardness values are significantly different.

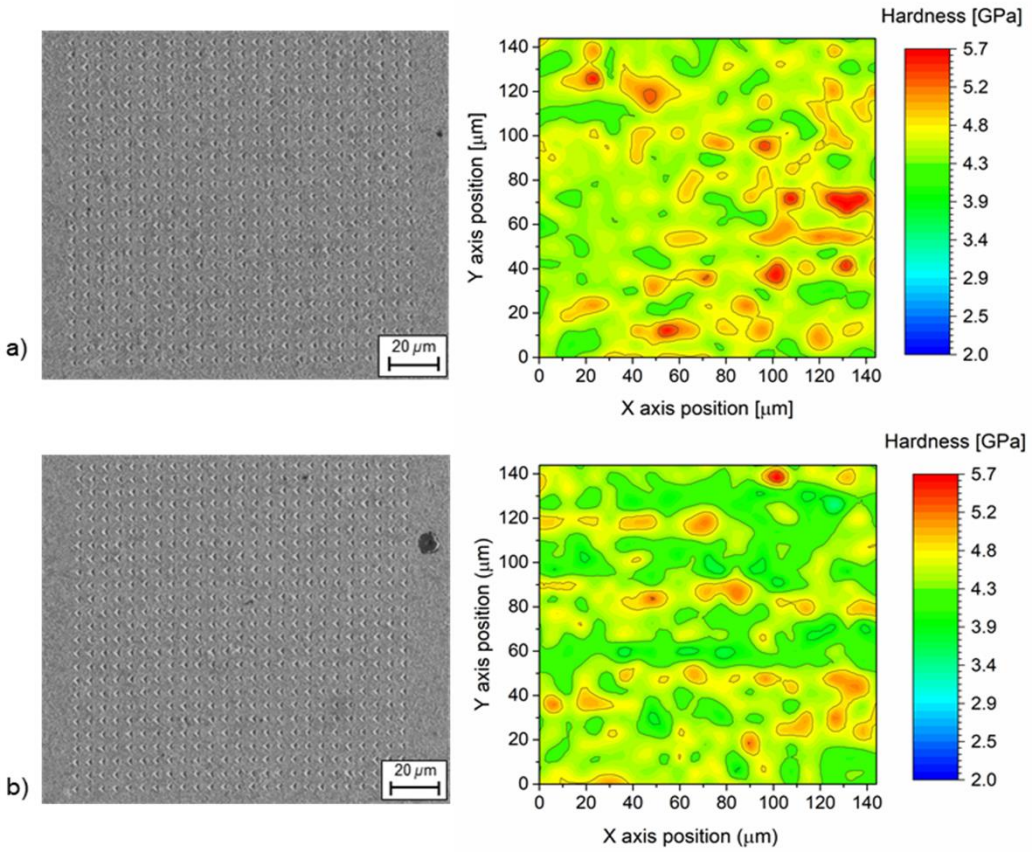

Figure 7. SEM micrographs showing the nanoindentation arrays (left) and obtained nanohardness mappings (right). a) DP1000-A and b) DP1000-B.

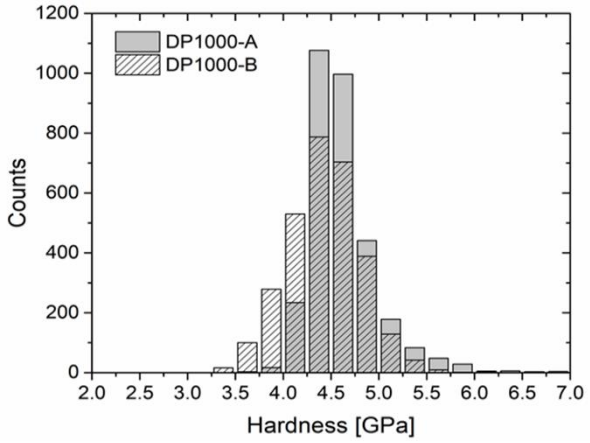

Figure 8. Hardness histograms for the two investigated DP steels.

3.3. Fracture toughness

3.3.1. Essential work of fracture

Figure 9 shows the load vs load-line displacement curves obtained from EWF tests. The values of specific work of fracture (w_f) and specific work of fracture initiation (w_f^i) are plotted as a function of the ligament length in Figure 10a and 10b, respectively. As observed in Figure 9, for similar ligament length, DP1000-B shows greater maximum load and displacement at fracture than DP1000-A. This results in higher *wf* and, consequently, higher w_e (w_e= 286 ± 17 kJ/m^2 for DP1000-B and 149 ± 21 kJ/m^2 for DP1000-A). DP1000-B also presents higher fracture toughness at crack initiation, w_e^i, and greater energetic contribution from crack propagation after initiation (w_e/w_e^i= 1.3 and 1.6 for DP1000-A and DP1000-B respectively).

The similar slope of the w_f vs l_o data regression indicates that both steels have almost identical non-essential plastic work, βw_p. The values of βw_p obtained for DP1000-A and DP1000-B are 24 ± 2 and 23 ± 1 MJ/m^3 respectively.

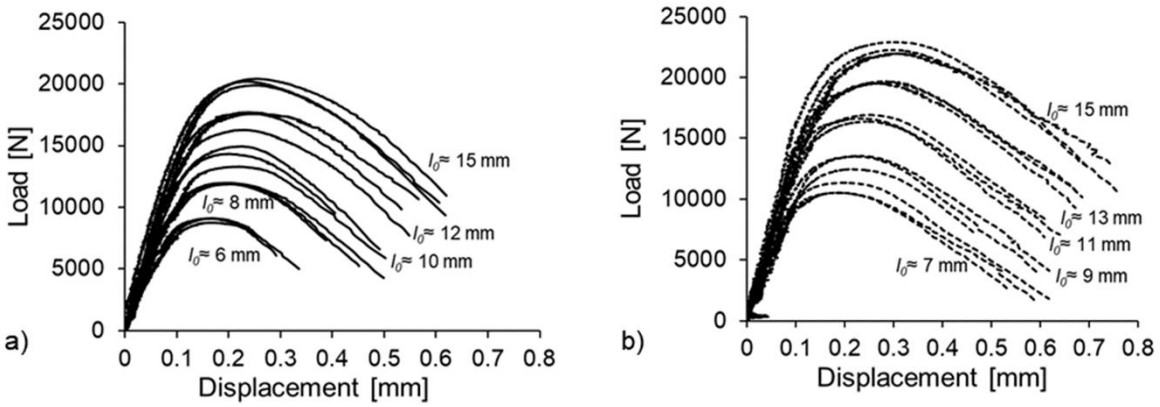

Figure 9. Load-displacement curves from EWF tests. a) DP1000-A and b) DP1000-B.

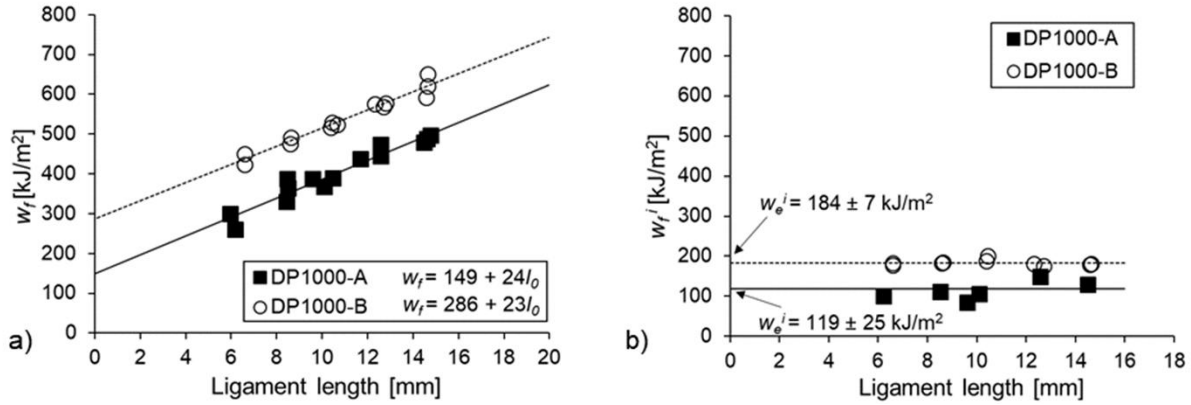

Figure 10.a) w_f as a function of the ligament length. w_e and βw_p are given in the legend. b) w_f^i for different ligament lengths. The average fracture toughness at crack initiation, w_e^i is indicated.

3.3.2. Fracture thickness strain measurements in DENT specimens

Figure 11 shows the evolution of ε_{3f} as a function of the distance from the crack tip. The plotted ε_{3f} values are the average of two specimens. The steel DP1000-B exhibits a higher degree of necking both at crack initiation ($\boldsymbol{\varepsilon_{3f\,\mathrm{tip}}}$) and during crack propagation ($\boldsymbol{\varepsilon_{3f\,\mathrm{SS}}}$). In both steels the crack tip neck stabilizes at a distance of approximately 0.4 mm from the crack tip, reaching a steady fracture strain of $\boldsymbol{\varepsilon_{3f\,\mathrm{SS}}}$= 0.12 and 0.16 for DP1000-A and DP1000-B respectively.

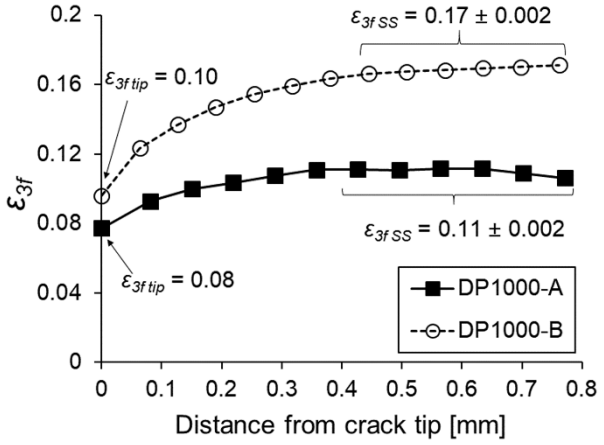

Figure 11. Fracture thickness strain (ε_{3f}) as a function of the distance from crack tip.

3.3.3. Investigation of crack path

Figure 12 shows SEM micrographs taken from an area adjacent to the crack advance. Figures 12a-d show the crack propagation path for DP1000-A and DP1000-B. In both steels, the crack preferentially propagates bordering the martensite grains. DP1000-A shows a straighter crack propagation path, favoured by a greater presence of martensite grains and fresh martensite blocks (M/RA) along the crack path. On the other hand, in DP1000-B the crack follows a zig-zag path, which indicates lower connectivity of the hard secondary phases, caused by a more homogeneous distribution of martensite

islands. As illustrated in Figure 12e and 12f, void nucleation results mainly from decohesion of martensite grains and decohesion of the ferrite-martensite and/or fresh martensite-bainite interface.

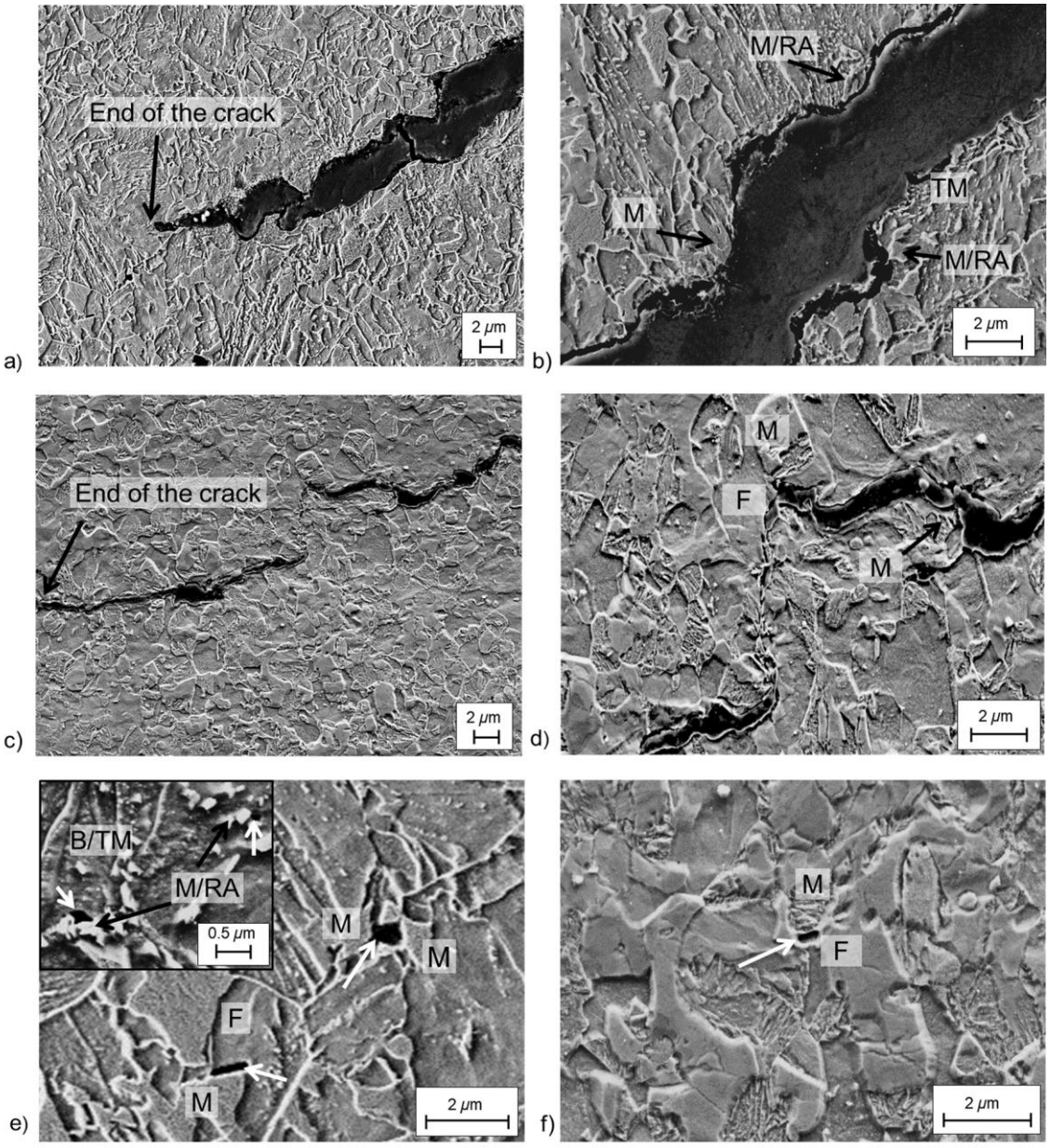

Figure 12. SEM micrographs from a region close to the crack tip. DP1000-A (upper row) and DP1000-B (middle row). a, c) Crack propagation path (2500x magnification). b, d) Closer view of the crack propagation path (6500x magnification). e, f) Void nucleation (white arrows) by decohesion of martensite grains and ferrite-martensite or fresh martensite (M/RA)-bainite interface. DP1000-A (e) and DP1000-B (f).

3.3.4. Fractographic analysis

Figure 13 and Figure 14 show the SEM micrographs of the fracture surface of DENT specimens for the two studied DP steels. Three different regions are identified in the fracture surface: Zone I, Zone II and Zone III. The Zone I corresponds to the flat triangular region ahead of the crack tip (surrounded by a white line in Figure 13a and Figure 14a), where crack initiation takes place. Due to the higher stress

triaxiality in the centre of the plate thickness, the crack initiates following a normal plane respect to the principal tensile stress. After the formation of this initial triangular area, the growing crack rapidly tilts 45º respect to the loading axis and a slant (or shear-induced) fracture occurs. This mode of fracture is commonly observed in thin ductile sheets [58], and it is associated to the formation of shear deformation bands produced by the variation of stress triaxiality through the specimen thickness (triaxiality is lower in the outer free-surfaces of the specimen) [59]. Hence, the stress state in the crack front evolves from plane strain at crack initiation to a biaxial (or plane stress) state during propagation. Zone II and Zone III correspond to different locations in the shear-induced fracture. Zone II is in a region close to the crack tip whereas Zone III is in the stable crack propagation area. The size of the flat triangular region for the two studied DP steels is given in Table 4.

The fracture surface of both steels present a dimpled appearance, typical of a ductile fracture mechanism of void nucleation, growth and coalescence. DP1000-A presents a bimodal dimple size distribution with large (≈7μm) and small (2-3 μm) secondary voids. Some dispersed tearing cracks can be also observed (Figure 13b). In the slant fracture area (Zone II and Zone III), a few smooth zones, where dimples are hardly visible, are detected (indicated by arrows in Figure 13c and 13d). These smooth areas suggest that friction between the two fracture surfaces has occurred during the slant fracture process [60, 61]. Three different void sizes are distinguished in DP1000-B: small (2-3 μm), large (10-12 μm) and very large (18-30 μm) voids. Table 4 shows the average void size distribution for the three different fractures zone investigated. In general, because of the high stress triaxiality, Zone I shows larger spherical voids and dimples elongated in the loading direction [61,62]. In Zone II and Zone III (slant fracture), voids are smaller and oriented at 45º respect to crack advance direction, especially in Zone II. This coalescence mode of small secondary voids is often called void sheeting.

Small voids are predominant in both steels. As shown in Figure 12 and reported in previous studies [38, 63], these voids are primarily generated by martensite cracking or interface decohesion between harder and softer particles. Also, some inclusions were observed within the dimples, which acted as void initiation sites. In the case of DP1000-A, few small (<2 μm) spherical oxide inclusions were present (Figure 15a). In DP1000-B, larger voids are mainly nucleated at coarse TiN (≈3-4 μm) precipitates by particle fragmentation and/or decohesion of the interface particle/matrix [64] (Figure 15b).

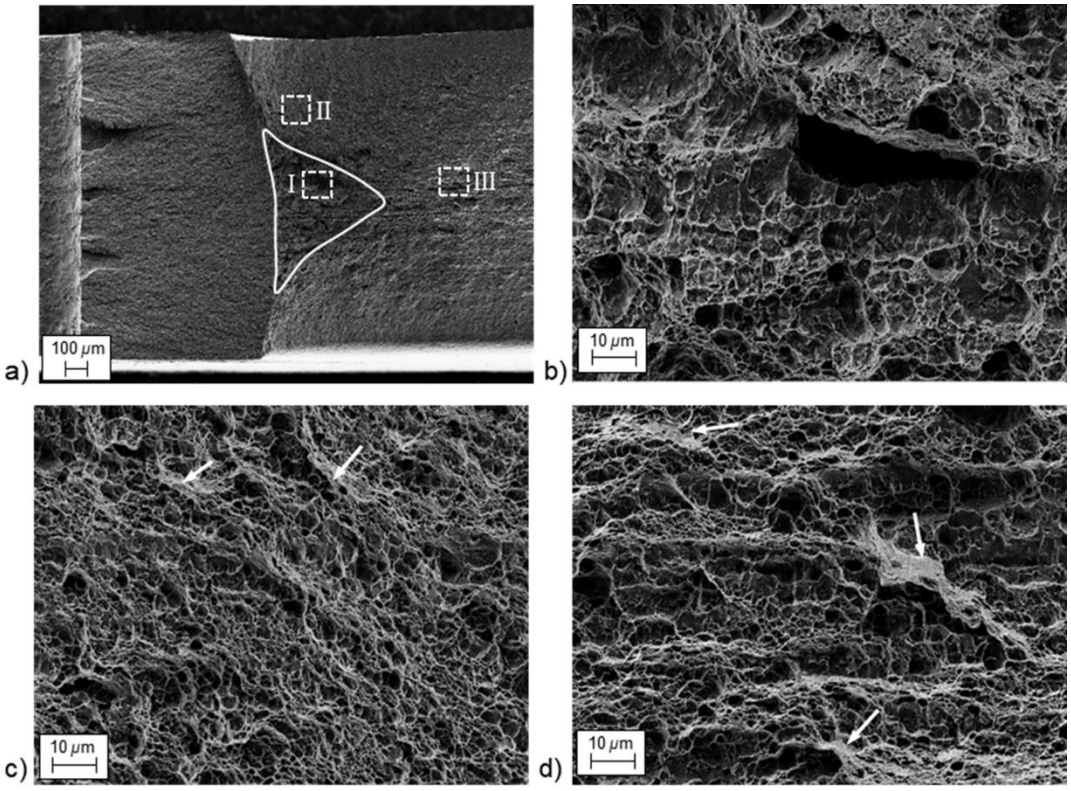

Figure 13. DP1000-A. SEM micrographs of the fracture surface of a DENT specimen. a) General image of the fracture surface (50x magnification). Closer view (1000x magnification) of: b) Zone I, c) Zone II and d) Zone III.

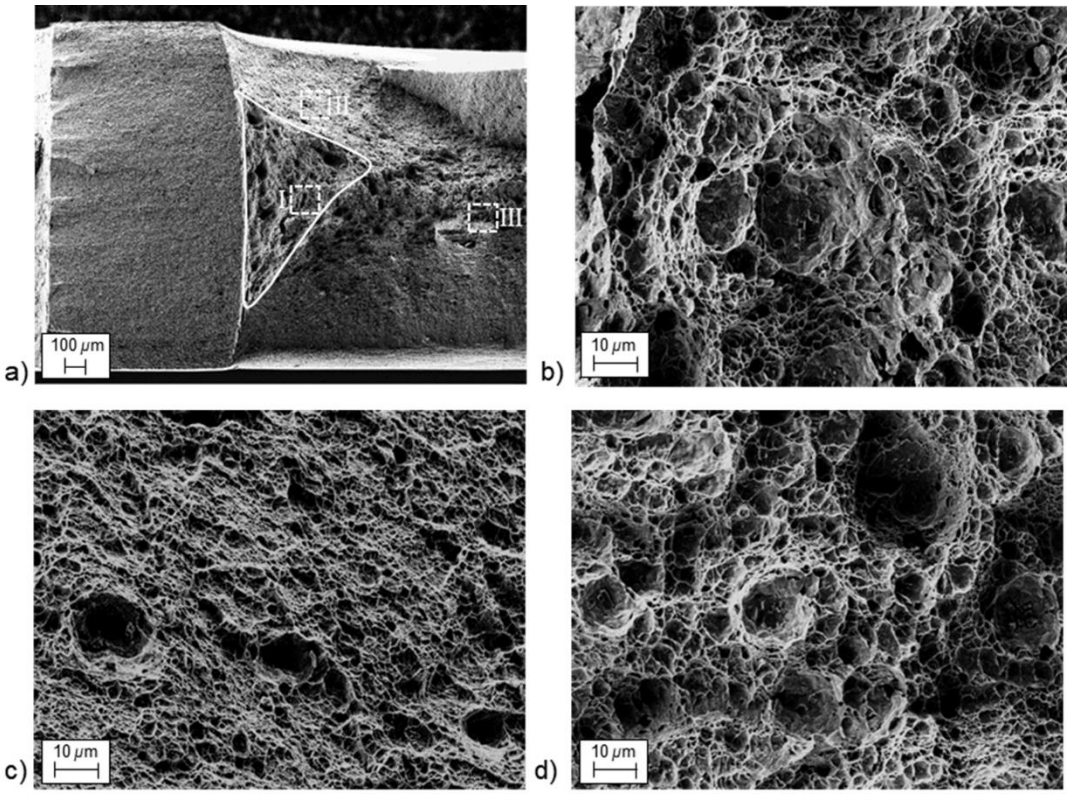

Figure 14. DP1000-B. SEM micrographs of the fracture surface of a DENT specimen. a) General image of the fracture surface (50x magnification). Closer view (1000x magnification) of: b) Zone I, c) Zone II and d) Zone III.

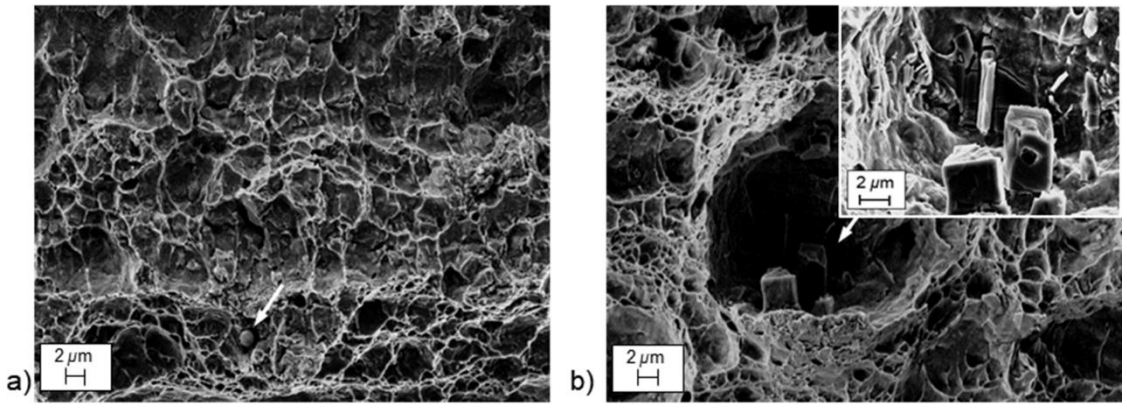

Figure 15. a) Microvoid nucleated at Al_2O_3 inclusion in DP1000-A (Secondary electrons, 2000x magnification). b) Microvoid nucleated at TiN precipitate in DP1000-B (Secondary electrons, 2000x magnification) and detail of the fragmented TiN particle (InLens image, 5000x magnification).

Table 4. Void size distribution at different fracture zones

		Average void size (μm)			
Steel	Void type	Zone I	Zone II	Zone III	Area of flat fracture (μm^2)
DP1000-A	Small	2.6	1.7	1.9	186434
	Large	6.9	6.7	6.9	
DP1000-B	Small	2.7	2.2	2.2	328980
	Large	12.3	9.4	10.3	
	Very large	30.7	17.0	18.5	

4. Discussion

4.1. Influence of microstructure on uniaxial tensile properties

Figure 5 shows that the tensile properties of the two investigated DP steels are quite similar in terms of strength and ductility. However, small differences can be discerned and discussed on the basis of the distribution of their microstructural constituents. The steel having a lower amount of ferrite (DP1000-A) shows slightly higher yield strength (YS). This is in good agreement with observations in previous studies and it is related to the lower dislocation density present in ferrite/ferrite interfaces compared to ferrite/bainite or ferrite/martensite boundaries [65, 66]. The lower density of dislocations facilitates the free movement of existing dislocations due to the lower interaction between them [66]. When increasing the volume fraction of hard phases, the dislocation density is increased due to the major presence of ferrite/bainite or ferrite/martensite interfaces, leading to lower dislocations mobility and thus to higher YS. The differences in the bainite phase, with a higher amount of carbides for DP1000-A than for DP1000-B could also contribute to the higher YS.

Chang et al. [65] showed that yield strength of DP steels is mainly governed by ferrite characteristics and independent of the martensite volume fraction since during yielding the plastic deformation of martensite is practically negligible. On the other hand, they found that tensile strength (UTS) depends

on the amount of martensite. This is confirmed for the steels investigated in this work. DP1000-A, which has higher martensite volume fraction, shows slightly higher UTS. This steel also has an additional influence of the strain-induced transformation of retained austenite to martensite (TRIP effect). The larger fraction of retained austenite present in DP1000-A (6%) compared to DP1000-B (2%) and the TRIP effect significantly improves the strain hardening behaviour (Figure 6) and contributes to increasing strength and elongation [4]. As shown in Figure 5, the true fracture strain (ε_f) is also slightly increased. The beneficial influence of TRIP effect on mechanical properties is associated to the formation of additional mobile dislocations in ferrite and bainite in the vicinity of newly formed strain-induced martensite, which increases strain hardening and delays the onset of necking [67,68].

4.2. Microstructural effects on fracture toughness

The large differences in crack initiation and propagation resistance (Figure 10) also can be explained by the higher volume fraction of retained austenite present in DP1000-A. Contrary to the observed in uniaxial tensile properties, the strain-induced transformation of retained austenite to martensite may have a detrimental effect on fracture toughness. Jacques et al. [69] observed that in TRIP-assisted steels, due to the greater stress triaxiality in the front of the crack tip, most of the retained austenite present in the fracture process zone transforms to martensite before crack initiation. As a consequence, the newly formed martensite is distributed in the form of a brittle network along the fracture process zone. This is corroborated in Figure 12a and b, where the presence of fresh martensite grains along the crack path is confirmed. Therefore, in DP1000-A, the transformation of retained austenite to martensite generates a continuous network of high strength bainite/tempered martensite (harder than the one in DP1000-B due to the higher amount of carbides) and untempered fresh martensite that increases the connectivity of the hard secondary phases (Figure 7a) and triggers unstable crack propagation [38, 69-71]. On the other hand, in DP1000-B the hard martensite islands are more “isolatedly” distributed (Figure 7b), which facilitate crack propagation through the soft ferrite phase (Figure 12c and d). Such crack propagation mode, enables larger plastic deformation and increases crack propagation resistance, giving rise to higher fracture toughness.

In summary, the results show that the fracture toughness of the two 1000 MPa DP steels investigated in this work primarily depends on two main factors: the presence of C-enriched fresh martensite/retained austenite islands and the connectivity of the hard secondary phases. It is shown that even a moderate amount of fresh martensite/retained austenite islands may have a negative influence on fracture resistance. The presence of a lower proportion of ferrite in the matrix has also shown to have a deleterious effect on cracking resistance of ultrahigh strength DP steels. These observations show that, depending on the application, cracking resistance can be enhanced at the cost of elongation and strength by reducing the connectivity and volume fraction of residual austenite/martensite and increasing the ferrite fraction.

4.3. Necking contribution to plane stress fracture toughness

As pointed out before, plane stress ductile fracture has an important energetic contribution from necking [38-42]. Accordingly, the specific essential work of fracture (w_e) developed in the fracture process zone, can be expressed as the sum of two contributions [41]:

$$w_e = \Gamma_0 + \Gamma_n \qquad \text{Equation 9}$$

where Γ_0 is the energy spent on the creation of new surfaces at the front of the crack tip (intrinsic fracture resistance) and Γ_n is the work of necking, which depends on sheet thickness. This explains the thickness dependence of w_e (and of plane stress fracture toughness in general) and states the importance of

comparing fracture toughness values for materials of similar thickness, as the selected in the present study.

The contribution of necking to the ductile fracture process is illustrated in Figure 11. The lower values of true thickness strain both at crack initiation ($\varepsilon_{3f\,tip}$) and during crack propagation ($\varepsilon_{3f\,SS}$) coincides with the lower fracture toughness at crack initiation (w_e^i) and specific essential work of fracture (w_e). When most of the necking work is developed at crack initiation and the neck is rapidly stabilized, the contribution to the total crack propagation resistance is limited, such as the case of DP1000-A ($\varepsilon_{3f\,SS}$ / $\varepsilon_{3f\,tip}$=1.4, w_e/w_e^i= 1.3). On the other hand, as observed in DP1000-B, if the neck developed at the crack tip progressively increases during the crack advance, the crack propagation resistance is significantly increased ($\varepsilon_{3f\,SS}$ / $\varepsilon_{3f\,tip}$=1.8, w_e/w_e^i= 1.6). This confirms that one of the main contributions to the crack propagation resistance of high strength steel sheets comes from necking [42].

4.4. Damage and fracture mechanisms

The two investigated DP steels presented a ductile fracture mechanism of void nucleation, growth and coalescence. The decohesion of martensite grains and ferrite-martensite or martensite-bainite interfaces were identified as the main void nucleation mechanisms (Figure 12e and f). In DP1000-A, the greater presence of fresh strain-induced martensite in a mainly bainitic matrix promotes rapid void nucleation and coalescence, which explains the prevalence of very small dimples and tearing cracks in the fracture surface (Figure 13). DP1000-B showed a more ductile fracture appearance with a greater number of larger dimples. This can be ascribed to the lower hardness of martensite islands and the major proportion of ferrite in the matrix.

The influence of the coarse TiN precipitates (Figure 15b) on the fracture toughness of DP1000-B is not clear and should be studied in further detail. Previous works have reported that coarse TiN particles may act as cleavage initiation sites in steels and have a detrimental effect on toughness [72-74]. Nevertheless, in DP1000-B, these precipitates serve as preferential sites for primary ductile void growth and seem not to have a major influence on cracking resistance. Even though no clear evidence of the effect of TiN precipitates on the fracture behaviour is shown in this work, in general, it is recommended to limit the presence of these particles, since they can also have a negative impact on stretch flangeability [75].

4.5. Relationship between fracture toughness and tensile properties

It is evident that fracture toughness has become a relevant property to understand the cracking resistance of thin AHSS sheets [17, 26, 29-35]. Nevertheless, fracture mechanics testing of thin ductile plates is not straightforward and, therefore, toughness is often inferred from tensile properties. For instance, the product of *UTSxTE*, which represents a combination of the material's strength and ductility, is usually used as a toughness indicator [66]. However, several works have shown that this practice can lead to misleading conclusions on the fracture resistance of AHSS [38, 42, 71]. As shown in the present work, it is especially risky to assume a direct relation between uniaxial tensile properties and cracking resistance on materials containing retained austenite since the TRIP effect, whereas can effectively improve strength and elongation, may have a negative influence on fracture toughness [38, 69, 71].

Figure 16 shows the relation between fracture toughness and uniaxial tensile parameters for different DP and complex phase (CP) steels of similar thickness. No clear correlation can be established between w_e and tensile strength (YS or UTS) or the *UTSxTE* product. This evidences again that *UTSxTE* is not a good indicator of fracture toughness. Especially good linear correlation is observed between w_e and strain hardening exponent (n); w_e linearly decreases with increasing the n value. This can sound

contradictory since, usually, higher n is associated with greater formability. However, as aforementioned, strain hardening mechanisms of AHSS are closely related to microstructure inhomogeneity and strain gradients between soft and hard microstructural constituents, which promotes nucleation and coalescence of microvoids. In fracture toughness testing, due to the large stress triaxiality present in the front of the crack tip and the high plastic localization, this void growth and coalescence process is accelerated and rapidly contribute to macroscopic fracture [23].

These are key factors to keep in mind when developing new AHSS microstructures with an optimum balance between formability and cracking resistance. For example, it is interesting to note that, although previous works showed that DP steels have lower crack propagation resistance than CP ones [33], DP microstructures can be designed to attain high fracture toughness comparable to CP steels of similar strength (Figure 16) at expenses of global formability (strain hardening and elongation).

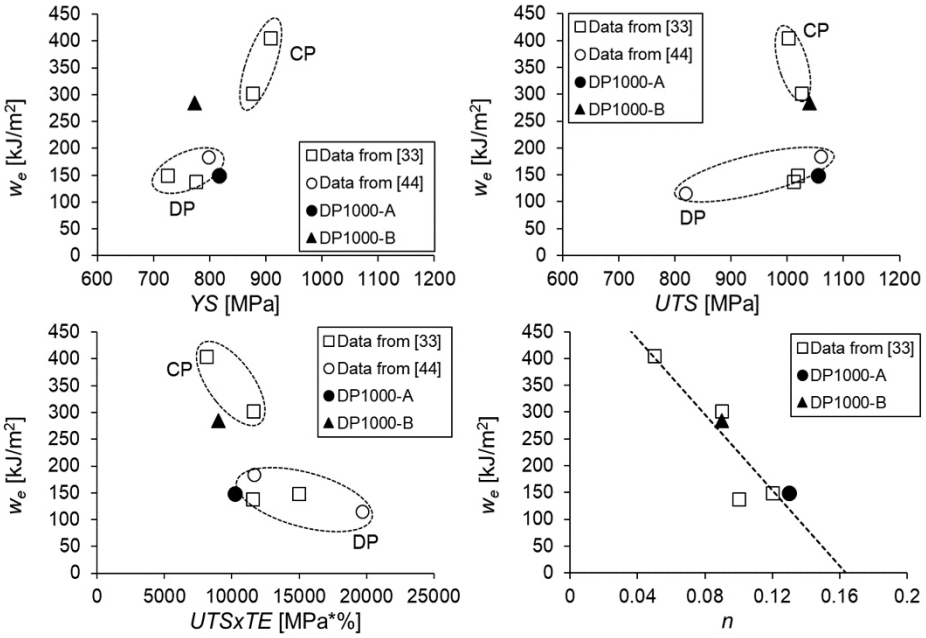

Figure 16. Specific essential work of fracture (w_e) as a function of different uniaxial tensile parameters.

5. Conclusions

The fracture behaviour of two commercial 1000 MPa DP steels processed at industrial scale has been characterized and the influence of microstructural constituents on fracture response has been investigated. From the investigations performed and the obtained results, the following conclusions can be drawn:

- The mechanical properties of DP1000-A in terms of strength and ductility are slightly superior to DP1000-B. The lower amount of ferrite in the matrix leads to an increase in yield strength, whereas the higher martensite volume fraction increases UTS. The presence of a moderated amount of retained austenite (≈6 %) and the strain-induced transformation of austenite to martensite (TRIP effect) contributes to increasing strain-hardening and elongation (both uniform and total).

- Contrary to the observed in uniaxial tensile properties, the presence of fresh martensite/retained austenite (M/RA) islands has a negative effect on cracking resistance of DP1000-A. It is

attributed to the formation of a “brittle” network of hard phases that favours rapid crack propagation.

- The superior crack initiation and propagation resistance of DP1000-B are ascribed to three main factors:1) lower volume fraction of fresh martensite/retained austenite, 2) a higher proportion of ferrite in the matrix and 3) lower connectivity of the hard secondary phases.

- The two DP steels show a ductile fracture mechanism of void growth and coalescence. The main void nucleation mechanisms were identified as: 1) decohesion of martensite grains, 2) decohesion of the ferrite-martensite interface, 3) decohesion of bainite-fresh martensite (M/RA) interface and 4) void nucleation at inclusions (aluminium oxides in DP1000-A and titanium nitrides in DP1000-B). Further investigations are suggested to understand the role of coarse TiN particles on fracture toughness.

- The fracture toughness of high strength DP steel sheets has a significant contribution from necking. The steel showing a higher degree of necking at crack initiation and propagation (DP1000-B) exhibits greater crack initiation and propagation resistance. The differences between crack initiation and crack propagation resistance also can be explained by the evolution of necking during crack propagation. When the neck developed at the crack tip progressively increases during crack propagation, a significant increase on crack propagation resistance is observed.

- Fracture toughness cannot be directly inferred from tensile properties. From the comparison of results obtained in this work with data from the literature, it is shown that w_e does not correlate with YS and UTS. Contrary to the usual perception, fracture toughness does not increase with increasing *UTSxTE* and *n* value, which are generally used as indicators of toughness and formability. Rather, on the contrary, a negative relationship was observed between fracture toughness and *n* value. The inverse proportionality between w_e and strain hardening exponent is related to the nature of strain-hardening mechanisms of AHSS, which are mainly governed by microstructural inhomogeneities that favour local failure.

These results provide a better understanding of the role of the different microstructural constituents on cracking resistance of high strength DP steels and can serve as a guide for new material development

Acknowledgments
This work has been financially supported by the European Commission, Research Fund for Coal and Steel programme under Grant Agreement 800693 — CrashTough — RFCS-2017.

Data availability

The raw/processed data required to reproduce these findings cannot be shared at this time as the data also forms part of an ongoing study.

References

[1] N. Fonstein. Dual Phase steels. In: R.Rana, S.B Singh (Eds.), *Automotive steels*, chapter 7. Woodhead publishing (2017) 169-217.
[2] S. Keeler, M. Kimchi, P.J. Mooney. Advanced High-Strength Steels Application Guidelines, version 6.0 2017.
[3] R. Kuziak, R. Kawalla, S. Waengler. Advanced high strength steels for automotive industry. *Arc Civ Mech Eng* 8 (2008) 103-117.

[4] M.H. Saleh, R. Priestner. Retained austenite in dual–phase silicon steels and its effect on mechanical properties. *J Mater Process Tech* 113 (2001) 587-593.
[5] C.A.N. Lanzillotto, F.Pickering. Structure–property relationships in dual-phase steels. *Met Sci* 16 (8) (1982) 371-382.
[6] R.G. Davies. Influence of martensite composition and content on the properties of dual phase steels. *Metall. Trans. A* 9A (1978) 671-679.
[7] K. Hasegawa, Y. Toji, H. Minami, H. Ikeda, T Morikawa, K. Higashida. Effect of martensite fraction on tensile properties of dual-phase steels. *Tetsu to Hagane* 98 (2012) 320-327.
[8] A. Saai, O.S Hopperstad, Y. Granbom, O.G. Lademo. Influence of volume fraction and distribution of martensite phase on the strain localization in dual phase steels. *Proc Mat Sci* 3 (2014) 900 – 905.
[9] N. Fonstein, M. Kapustin, N. Pottore, I. Gupta, O. Yakubovsky. Factors that Determine the Level of the Yield Strength and the Return of the Yield-Point Elongation in Low-Alloy Ferrite–Martensite Steels. *Phys Met Metallogr* 104 (2007) 315–323.
[10] M. Calcagnotto, Y. Adachi, D. Ponge, D. Raabe. Deformation and fracture mechanisms in fine- and ultrafine-grained ferrite/martensite dual-phase steels and the effect of aging. *Acta Mater* 59 (2011) 658–670.
[11] H. Mohrbacher. Advanced metallurgical concepts for DP steels with improved formability and damage resistance. *International symposyum on new developments in advanced high strength sheet steels*, 23-27 June 2013, Vail, Colorado, USA.
[12] M.D. Taylor, K.S. Choi, X. Sun, D.K. Matlock, C.E. Packard, L. Xuc, F. Barlat. Correlations between nanoindentation hardness and macroscopic mechanical properties in DP980 steels. *Mat Sci Eng* A 597 (2014) 431–439.
[13] K. Park, M. Nishiyama, N. Nakada, T. Tsuchiyama, S. Takaki. Effect of the martensite distribution on the strain hardening and ductile fracture behaviors in dual-phase steel. *Mat Sci Eng A* 604 (2014) 135–141.
[14] F. Zhan, A. Ruimi, P.C. Wo, D.P. Field. Morphology and distribution of martensite in dualphase (DP980) steel and its relation to the multiscale mechanical behavior. *Mat Sci Eng A* 659 (2016) 93–103.
[15] M.F. Ashby. Work hardening of dispersion-hardened crystals. *Philos Mag* 14 (132) (1966) 1157-1178.
[16] J. Hall, J. Coryell, B. Wendt, D. Adamski. Case Studies of Edge Fracture of Dual Phase Steel Stampings. *SAE Int. J. Mater. Manf*. 8 (2015) 783-788.
[17] D. Frómeta, M. Tedesco, J. Calvo, A. Lara, S. Molas, D. Casellas. Assessing edge cracking resistance in AHSS automotive parts by the Essential Work of Fracture methodology. *J. Phys: Conf. Ser.* 2017 896 012102.
[18] C.R.M. Silva, F.J.G. Silva, R.M. Gouveia. Investigations on the edge crack defect in Dual Phase steel stamping process. *Procedia manuf* 17 (2018) 737-745.
[19] D. Bhattacharya. Microalloyed steels for the automotive industry. *Tecnol. Metal. Mater. Min*. 11, (2014) 4 371-383.
[20] Y. Li, R. Song, L. Jiang, Z. Zhao. Strength response of 1200 MPa grade martensite-ferrite dual-phase steel under high strain rates. *Scripta Mater* 164 (2019) 21–24.
[21] K. Hasegawa, K. Kawamura, T. Urabe, Y. Hosoya. Effects of Microstructure on Stretch-flange-formability of 980 MPa Grade Cold-rolled Ultra High Strength Steel Sheets. *ISIJ Int* 44 (2004) 603–609.
[22] A. Karelova, C. Krempaszky, E. Werner, P. Tsipouridis, T. Hebesberger, A. Pichler. Hole Expansion of Dual-phase and Complex-phase AHS Steels - Effect of Edge Conditions. *Steel Res Int* 80 (2009) 71-77.
[23] F. Hisker, R. Thiessen, T. Heller. Influence of Microstructure on Damage in Advanced High Strength Steels. *Mater Sci Forum* 706–709 (2012) 925–930.
[24] I. Pushkareva, S. Allain, C. Scott , A. Redjaïmia, A. Moulin. Relationship between

Microstructure, Mechanical Properties and Damage Mechanisms in High Martensite Fraction Dual Phase Steels. *ISIJ Int* 55 (10) (2015) 10 2237-2246.
[25] O.R. Terrazas, K.O. Findley, C.J. Van Tyne. Influence of Martensite Morphology on Sheared-Edge Formability of Dual-Phase Steels. *ISIJ Int* 57 (2017) 937-944.
[26] J.I. Yoon, J. Jung, H.H. Lee, J.Y. Kim, H.S Kim. Relationships Between Stretch-Flangeability and Microstructure-Mechanical Properties in Ultra-High-Strength Dual-Phase Steels. *Met Mater Int* 25 (2019) 1161–1169.
[27] ISO 16630:2017. Metallic materials — Sheet and strip — Hole expanding test. *International Organization for Standardization*.
[28] K. Mori, Y. Abe, Y. Suzui. Improvement of stretch flangeability of ultra high strength steel sheet by smoothing of sheared edge. *J Mater Process Tech* 210 (2010) 653–659.
[29] Y. Takahashi, O. Kawano, Y. Tanaka. Fracture Mechanical Study on Edge Flange-ability of High Tensile-strength Steel Sheets. *MS&T 2009: Proceedings from the Materials Science & Technology Conference* (October 25-29, 2009, Pittsburgh, Pennsylvania) 317-1328.
[30] N. Fonstein, H.J. Jun, G. Huang, S. Sriram, B. Yan. Effect of Bainite on Mechanical Properties of Multiphase Ferrite-Bainite-Martensite Steels. *Proceedings from the Materials Science & Technology Conference*, October 16-20, 2011, Columbus, Ohio.
[31] J.I. Yoon, J. Jung, S.H. Joo, T.J. Song, K.G. Chin, M.H. Seo, S.J. Kim, S. Lee, H.S. Kim. Correlation between fracture toughness and stretch-flangeability of advanced high strength steels *Matter Lett* (2016) 180 322-326.
[32] D. Casellas, A. Lara, D. Frómeta, D. Gutiérrez, S. Molas, Ll. Pérez, J. Rehrl, C. Suppan. Fracture Toughness to Understand Stretch-Flangeability and Edge Cracking Resistance in AHSS. *Metall Mater Trans A* 48 (2017) 86-94.
[33] D. Frómeta, A. Lara, S. Parareda, D. Casellas. Evaluation of Edge Formability in High Strength Sheets Through a Fracture Mechanics Approach. *AIP Conference Proceedings* 2113, 160007 (2019).
[34] D. Frómeta, A. Lara, S. Molas, D. Casellas, J. Rehrl, C. Suppan, P. Larour, J. Calvo. On the correlation between fracture toughness and crash resistance of advanced high strength steels. *Eng Frac Mech* 205 (2019) 319-332.
[35] D. Frómeta, A. Lara, B. Casas, D. Casellas. Fracture toughness measurements to understand local ductility of advanced high strength steels. *IOP Conf. Ser.: Mater Sci Eng* (2019) 651 012071.
[36] A.N. Tkach, N.M. Fonstein, V.N. Simin'kovich, A.N. Bortsov, Y.N. Lenets. Fatigue crack growth in a dual-phase ferritic-martensitic steel. *Mater Sci* 20 (1985) 448–453.
[37] A. Bayram A, A. Uğuz, M. Ula. Effects of Microstructure and Notches on the Mechanical Properties of Dual-Phase Steels. *Mater charact* 43 (1999) 259–269.
[38] G. Lacroix, T. Pardoen, P.J. Jacques. The fracture toughness of TRIP-assisted multiphase steels. *Acta Mater* 56 (2008) 3900–13.
[39] B. Cotterell, J.K. Reddel. The essential work of plane stress ductile fracture. *Int J Fracture* 13 (1977) 267-277.
[40] T. Pardoen, Y. Marchal, F. Delannay. Thickness dependence of cracking resistance in thin aluminium plates. *J Mech Sol* 47 (1999) 2093–2123.
[41] T. Pardoen, Y. Marchal, F. Delannay. Essential work of fracture compared to fracture mechanics—towards a thickness independent plane stress toughness. *Eng Fract Mech* 69 (2002) 617–631.
[42] D. Frómeta, S. Parareda, A. Lara, S. Molas, D. Casellas, P. Jonsén, J. Calvo. Identification of fracture toughness parameters to understand the fracture resistance of advanced high strength sheet steels. *Eng Frac Mech* 229 (2020) 106949.
[43] J. Wu, Y.W. Mai. The essential fracture work concept for toughness measurement of ductile polymers. *Polym Eng Sci* 36 (1996) 2275 - 2288.
[44] D. Gutiérrez, Ll. Pérez,A. Lara, D. Casellas, J.M. Prado. Toughness evaluation of high strength steels sheets by means of the essential work of fracture. *19th European conference on fracture:*

fracture mechanics for durability, reliability and safety, ECF 2012.
[45] Z.C. Luo, R.D. Liu, X. Wang, M.X. Huang. The effect of deformation twins on the quasi-cleavage crack propagation in twinning-induced plasticity steels. *Acta Mater* 150 (2018) 59–68.
[46] R. Sarkara, S.K. Chandraa, P.S. De, P.C. Chakraborti, S.K. Ray. Evaluation of ductile tearing resistance of dual-phase DP 780 grade automotive steel sheet from essential work of fracture (EWF) tests. *Theor Appl Fract Mec* 103 (2019) 102278.
[47] E. Wirthl, A. Pichler, R. Angerer, P. Stiaszny, K. Hauzenberger, Y.Titovets, M. Hackl. Determination of the volume amount of retained austenite and ferrite in small specimens by magnetic measurements. *Proceedings of the International Conference on TRIP-Aided High Strength Ferrous Alloys*, Gent, Belgium, 2002.
[48] R. Petrov, L. Kestens, A. Wasilkowska, Y. Houbaert. Microstructure and texture of a lightly deformed TRIP-assisted steel characterized by means of the EBSD technique. *Mat Sci Eng A* 447 (2007) 285–297.
[49] T. Bhattacharyya, S.B. Singh, S. Das, A. Haldar, D. Bhattacharjee. Development and characterisation of C–Mn–Al–Si–Nb TRIP aided steel. *Mat Sci Eng A* 528 (2011) 2394–2400.
[50] M. de Meyer, L. Kestens, B.C. de Cooman. Texture development in cold rolled and annealed C-Mn-Si and C-Mn-Al-Si TRIP steels. *Mater Sci and Technol* 17(11) (2001) 1353-1359.
[51] J.Wu, P.J. Ray, C.I. Garcia, M. Hua, A.J. Deardo. Image Quality Analysis: A mew method of Characterizing Microstructures. *ISIJ international*, 45 (2) (2005) 254-262.
[52] P.T. Pinard, A. Schwedt, A. Ramazani, U. Prahl, S. Richter. Characterization of dual phase steel microstructure by combined sub-micrometer EBSD and EPMA carbon measurements. *Microscopy and Microanalysis* 19(4) (2013) 1-11.
[53] ISO 6892-1:2009 (2009) Metallic materials — Tensile testing — Part 1: Method of test at room temperature. *European Committee for Standardization*.
[54] B. Hance. Advanced High Strength Steel (AHSS) Performance Levels. *SAE Technical Paper* 2018-01-0629, 2018.
[55] ASTM E8/E8M-15a (2015) Standard Test Methods for Tension Testing of Metallic Materials. *ASTM International*, West Conshohocken, PA, USA.
[56] W.C. Oliver, G.M. Pharr. An improved technique for determining hardness and elastic modulus using load and displacement sensing indentation experiments *J Mater Res* 7 (6) (1992) 1564-1583.
[57] ASTM E1820. Standard test method for measurement of fracture toughness. *American Society for Testing and Materials.*
[58] W. Lan, X. Deng, M. Sutton, C.S. Cheng. Study of slant fracture in ductile materials. *Int J Fract* 141 (2006) 469–496
[59] T.L. Anderson. Fracture mechanics: fundamentals and applications. 3rd ed. CRC Press; 2005.
[60] F. Bron, J. Besson, A. Pineau. Ductile rupture in thin sheets of two grades of 2024 aluminum alloy. *Mat Sci Eng A* 380 (2004) 356–364.
[61] Z. Xiong, P.J. Jacques, A. Perlade, T. Pardoen. On the sensitivity of fracture mechanism to stress concentration configuration in a two-step quenching and partitioning steel. *Int J Fract* (2020). https://doi.org/10.1007/s10704-020-00448-0.
[62] J.R. Rice, D.M. Tracey. On the ductile enlargement of voids in triaxial stress fields. *J Mech Phys Solids* 17 (1969) 201- 217.
[63] N. Saeidi, F. Ashrafizadeh, B. Niroumand, M.R. Forouzan, F. Barlat. Damage mechanism and modeling of void nucleation process in a ferrite–martensite dual phase steel. *Eng Frac Mech* 127 (2014) 97–103.
[64] O. León-García, R. Petrov, L.A.I. Kestens.Void initiation at TiN precipitates in IF steels during tensile deformation. *Mat Sci Eng A* 527 (2010) 4202–4209.
[65] P.H. Chang, A.G. Preban. The effect of ferrite grain size and martensite volume fraction on the tensile properties of dual phase steel. *Acta Metall* 33 (1985) 897-903.
[66] Z.P. Xiong, A.G. Kostryzhev, N.E. Stanford, E.V. Pereloma. Microstructures and mechanical

properties of dual phase steel produced by laboratory simulated strip casting. *Mater Design* 88 537-549.

[67] D. Krizan, S. Katharina, S. Kaar, T. Hebesberger. Development of third generation advanced high strength steels for automotive applications. *19th international scientific conference Transfer 2018*, Trencianske Teplice (Slovakia).

[68] P. Jacques, Q. Furnémont, A. Mertens, F. Delannay. On the sources of work hardening in multiphase steels assisted by transformation-induced plasticity. *Philos Mag A* 81 (7) (2001) 1789-1812.

[69] P. Jacques, Q. Furnémont, T. Pardoen, F. Delannay. On the role of martensitic transformation on damage and cracking resistance in trip-assisted multiphase steels. *Acta Mater* 49 (2001) 139–152.

[70] Z. Xiong, P.J. Jacques, A. Perlade, T. Pardoen. Ductile and intergranular brittle fracture in a two-step quenching and partitioning steel. *Scripta Mater* 157 (2018) 6–9.

[71] Z. Xiong, P.J. Jacques, A. Perlade, T. Pardoen. Characterization and Control of the Compromise Between Tensile Properties and Fracture Toughness in a Quenched and Partitioned Steel. *Metall Mater Trans A* (2019).

[72] L.P. Zhang, C.L. Davis, M. Strangwood. Effect of TiN particles and microstructure on fracture toughness in simulated heat-affected zones of a structural steel. *Metall Mater Trans A* 30 (1999) 2089-2096.

[73] W. Yan, Y.Y. Shan, K. Yang. Effect of TiN Inclusions on the Impact Toughness of Low-Carbon Microalloyed Steels. *Metall Mater Trans A* 37 (2006) 2147- 2158.

[74] J. Du, M. Strangwood, C.L. Davis. Effect of TiN particles and grain size on the charpy impact transition temperature in steels. *J Mater Sci Technol* 28 (2012) 878–888.

[75] A. Kaijalainen, V. Kesti, R. Vierelä, M. Ylitolva, D. Porter, J. Kömi. The effect of microstructure on the sheared edge quality and hole expansion ratio of hot-rolled 700 MPa steel. *IOP Conf. Ser.: J Phys Conf Ser* 896 (2017) 012103.

Appendix B

Other appended works

Paper A. D. Frómeta, M. Tedesco, J. Calvo, A. Lara, S. Molas, D. Casellas. Assessing edge cracking resistance in AHSS automotive parts by the Essential Work of Fracture methodology, *J. Phys.: Conf. Ser.* 896 (2017) 012102.

IOP Conf. Series: Journal of Physics: Conf. Series **896** (2017) 012102 doi:10.1088/1742-6596/896/1/012102

Assessing edge cracking resistance in AHSS automotive parts by the Essential Work of Fracture methodology

D Frómeta[1], M Tedesco[2], J Calvo[3], A Lara[1], S Molas[1] and D Casellas[1,4]

[1] Fundació CTM Centre Tecnològic, Plaça de la Ciència 2, 08243 Manresa, Spain
[2] Centro Ricerche Fiat, Corso Settembrini 40, 10135 Turin, Italy
[3] Universitat Politècnica de Catalunya, Eduard Maristany 10-14, 08019 Barcelona, Spain
[4] Luleå University of Technology, 971 87 Luleå, Sweden

E-mail: david.frometa@ctm.com.es

Abstract. Lightweight designs and demanding safety requirements in automotive industry are increasingly promoting the use of Advanced High Strength Steel (AHSS) sheets. Such steels present higher strength (above 800 MPa) but lower ductility than conventional steels. Their great properties allow the reduction of the thickness of automobile structural components without compromising the safety, but also introduce new challenges to parts manufacturers. The fabrication of most cold formed components starts from shear cut blanks and, due to the lower ductility of AHSS, edge cracking problems can appear during forming operations, forcing the stop of the production and slowing down the industrial process.

Forming Limit Diagrams (FLD) and FEM simulations are very useful tools to predict fracture problems in zones with high localized strain, but they are not able to predict edge cracking. It has been observed that the fracture toughness, measured through the Essential Work of Fracture (EWF) methodology, is a good indicator of the stretch flangeability in AHSS and can help to foresee this type of fractures.

In this work, a serial production automotive component has been studied. The component showed cracks in some flanged edges when using a dual phase steel. It is shown that the conventional approach to explain formability, based on tensile tests and FLD, fails in the prediction of edge cracking. A new approach, based on fracture mechanics, help to solve the problem by selecting steel grades with higher fracture toughness, measured by means of EWF. Results confirmed that fracture toughness, in terms of EWF, can be readily used as a material parameter to rationalize cracking related problems and select AHSS with improved edge cracking resistance.

1. Introduction

AHSS present excellent mechanical properties that poses them as a great option for safety components, structural parts of the car body and chassis, reducing the total vehicle mass and enhancing crashworthiness. Their use in the automotive industry has been strongly extended in the last two decades in order to fulfill the more and more demanding safety and fuel consumption legislations [1]. The use of this kind of steels has introduced new issues that are not completely solved. One of them is the edge cracking in cold formed sheet components. AHSS present high strength (600-1200 MPa) but limited ductility, compared to conventional mild steels, which makes them more sensitive to premature cracking during cold forming operations, especially in trimmed, sheared or punched areas, where the material is


Content from this work may be used under the terms of the Creative Commons Attribution 3.0 licence. Any further distribution of this work must maintain attribution to the author(s) and the title of the work, journal citation and DOI.
Published under licence by IOP Publishing Ltd

damaged and defects, such as micro cracks can be present [2-4]. These defects can trigger the crack propagation through the sheet thickness during the subsequent cold forming processes and lead to the fracture of the component [4]. Figure 1 shows some examples of cracks in cold formed components.

Figure 1. Examples of edge cracking in cold formed components

Intensive research has been made on this issue and great efforts have been put on the development of failure criteria to predict this type of fractures. It has been shown that conventional approaches, such as FLD or tensile tests are not valid to predict them [5-6]. Hence, additional tests are required to quantify the edge cracking sensitivity of AHSS. In this regard, stretch flangeability, measured by the Hole Expansion Test (HET), has shown to be suitable to foresee edge cracking related problems and has become an important parameter to consider in AHSS sheets formability [7].

Previous works showed that stretch flangeability of AHSS is governed by the crack propagation resistance of the material [8-11]. Casellas et al. analysed the correlation between stretch flangeability and fracture toughness (in terms of *Essential Work of Fracture, EWF*) on several AHSS grades with different microstructure and a quite good correlation between the two parameters was found [10]. AHSS showing higher EWF values presented higher Hole Expansion Ratio (HER), i.e. the tougher the material the greater the stretch flangeability. Other authors found the same trend between HER and J_c values [11]. Thus, fracture toughness, could be used to rationalize edge cracking and rank the stretch flangeability of AHSS.

Nevertheless, within the frame of Elastic Plastic Fracture Mechanics (EPFM), no standard methods are available to readily measure the fracture toughness of thin steel sheets presenting plane stress conditions. Conventional EPFM methodologies (J-Integral, CTOD, J-R curves, etc.) are standardized for plane strain conditions and their implementation requires exhaustive sample preparation, time consuming tests with constant monitoring and rigorous data treatment [12].

The EWF methodology was developed by Cotterell and Reddel [13] in the 80s as an alternative to measure the fracture toughness of thin plates under plane stress and was applied successfully to polymers [14-16] and ductile metals [17-20]. More recently, the methodology has been applied to AHSS sheets and has shown to be appropriate to evaluate the fracture toughness [10, 21-23]. The main advantage of this methodology is the relative easiness of the procedure compared to the other methods.

This work aims to provide a reliable tool, based on fracture mechanics, able to discern the edge cracking sensitivity of AHSS sheets and avoid unexpected fractures in industrial cold formed components. For this purpose, a serial production automotive part has been studied. The component presented multiple cracks in stretched flanges when manufactured with a dual phase (DP) steel (figure 2). The problem was solved replacing the DP steel grade by a complex phase (CP) steel with the same maximum strength and thickness. Different mechanical tests, including an EPFM-based one, were used to assess the edge cracking resistance of AHSS.

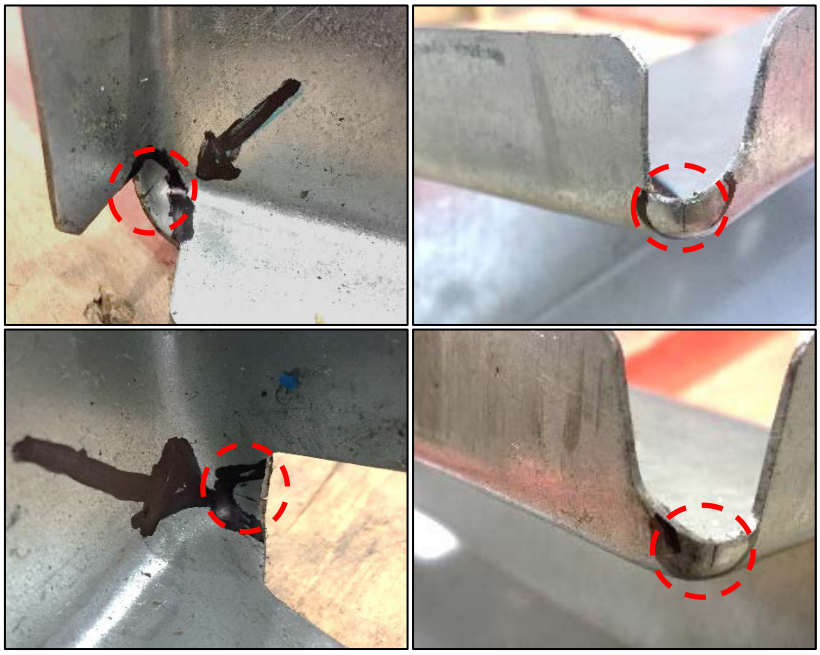

Figure 2. Edge cracks observed in the component manufactured with DP steel grade.

2. Materials

The materials investigated were two 1st generation AHSS grades of 1000 MPa UTS, commonly used for lightweight automotive components: a DP steel and a CP steel. Both steel grades are presented in form of sheets of 1.2 mm thickness. The chemical composition of the steels is shown in table 1. A basic microstructural characterization was performed by means of Scanning Electron Microscopy (SEM). The results are shown in figure 3. DP1000 presents a matrix consisting on a mixture of ferrite and martensite whereas CP1000 exhibits a more homogeneous microstructure, consisting on a bainite/tempered martensite matrix.

Table 1. Chemical composition of the studied steels (in wt%)

Steel grade	C	*Si*	Mn	*Cr*	B	*Al*
CP1000	~0.1	<0.5	1.8-2.2	<0.7	<0.003	-
DP1000	~0.15					

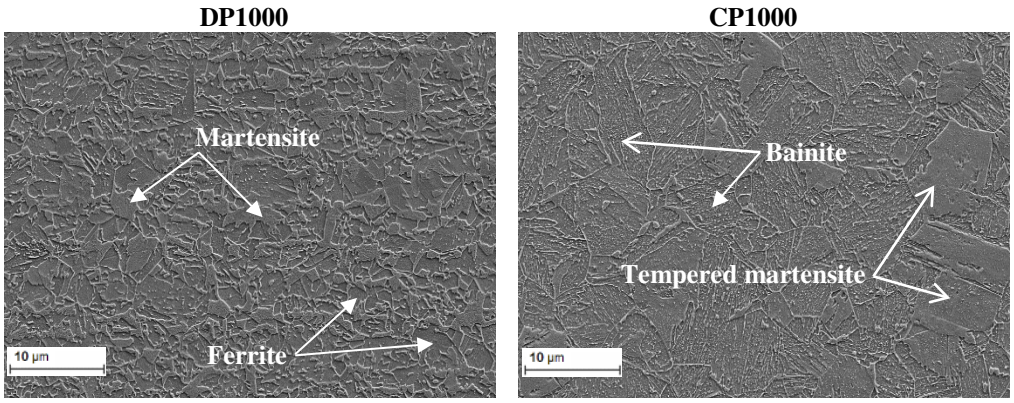

Figure 3. Microstructures of DP1000 (left) and CP1000 (right).

3. Experimental results

In order to characterize the fracture resistance of the studied steel sheets and rationalize the cold forming behaviour, different mechanical tests were performed.

3.1. Tensile tests

Conventional uniaxial tensile tests according EN-ISO 6892 were performed at transverse orientation respect to the rolling direction with an initial gauge length of 80 mm. 3 specimens per material were tested. Engineering stress-strain curves obtained from tensile tests are shown in figure 4a and tensile parameters are summarized in table 2.

Both steel grades present identical maximum strength. DP1000 shows low yield strength, a great strain hardening and large elongation. On the other hand, CP1000 exhibits higher yield strength, but lower work hardening rate and elongation. Such mechanical properties are controlled by their complex microstructures. In DP steels, the combination of a soft ferritic matrix and hard martensitic phases provides good ductility and attain high tensile strength. The great work hardening rate is caused by the limited deformation of ferrite due to the presence of hard martensite islands, which means higher rate of dislocations accumulation. The homogeneous multiphase microstructure of CP steels leads to attain higher yield strength, but the elongation obtained in this kind of steels is smaller than in DP.

Table 2. Tensile parameters at transverse direction: yield strength (σ_{ys}), Ultimate Tensile Strength (σ_{UTS}), elongation at fracture and work hardening coefficient (n).

	t [mm]	**σ_{ys} [MPa]**	**σ_{UTS} [MPa]**	**Elongation at fracture [%]**	**$n_{2\text{-}4\%}$**	**Area under tensile curve [MPa*%]**
DP1000	1.2	697	1018	11.99	0.18	11286
CP1000	1.2	904	1022	7.97	0.07	7677

3.2. Formability tests

Formability of the two steel grades has been assessed through Nakajima stretching tests. They were performed according to ISO 12004 to obtain the Forming Limit Curves (FLC). Grease, Teflon and polyurethane disks were inserted between the punch and the sample to minimize the friction between the parts. Six different geometries were used to obtain the different strain paths and determine the FLCs (figure 4b). 3 specimens for each geometry were evaluated. A blank holder force of 600 kN was applied and the punch speed was set to 90 mm/min.

DP1000 shows higher FLC_0 (plain strain) value and greater formability on the right side of the FLD, corresponding to biaxial strain modes. In the left side of FLD (uniaxial strain paths) CP1000 shows slightly better behaviour. However, the information corresponding to negative minor strains is limited, since the level of minor strain reached with the tested geometries is low, especially for CP1000 (minimum minor strain: 0.03).

3.3. Stretch flangeability tests

HET were performed according to ISO 16630 [7] to evaluate the stretch flangeability of the investigated AHSS. 6 specimens per each material were evaluated. The tests were conducted with a punch speed of 1 mm/s and a clamping force of 600 kN was applied to avoid any material draw-in from the clamping area during the test. The initial hole diameter was 10 mm and the cutting tolerance was set to 12 %.

The value obtained from HET is the HER, which represents the maximum diametric expansion that a circular punched hole can reach when a conical tool is forced into it until a crack in the hole edge extends through the full sheet thickness.

HER values are plotted in figure 4c**.** DP1000 shows HER values from 12 % to 22 % and CP1000 from 47 % to 84 %. Such high variability has been previously reported by other authors [24, 25].

CP1000 shows much larger hole expandability than DP1000. The lower stretch flangeability of DP steels is explained by the hardness difference between the ferrite and martensite phases. On the other hand, the smaller difference in properties between phases and lower internal stresses in CP grades lead to improved hole expansion behaviour [2, 9].

3.4. Essential Work of Fracture tests

The fracture toughness of the studied AHSS grades was evaluated by means of the EWF tests. EWF tests are performed following the procedure stablished in the European Structural Integrity Society (ESIS) protocol [26]. Rectangular Double Edge Notched Tensile (DENT) specimens of 90 x 40 mm were extracted from the cold formed components at 0º respect to the rolling direction. A total of 10 specimens per material were tested with 4 different ligament lengths ranging from 7 to 14 mm. 2 specimens were evaluated for each intermediate ligament (9 and 11 mm), whereas for the extreme ligament lengths (7 and 14 mm) 3 specimens per ligament were tested.

The tests were performed at a constant cross-head speed of 1 mm/min and a gauge length of 25 mm was used. To avoid the effect of notch root radius in the fracture toughness evaluation, fatigue pre-cracks were introduced on the notch root. It must be noted that w_e is not fully a material intrinsic property but it is influenced by the sheet thickness, since plane stress fracture toughness depends on the volume available to deform plastically at the front of crack tip. Hence, w_e is a fracture toughness value for the evaluated sheet thickness.

Figure 4d shows the EWF results obtained for DP1000 and CP1000 steel grades. It is observed that CP grade exhibits much greater fracture toughness than DP. Remarkable differences in toughness between CP and DP steel grades were reported previously by other authors [3, 10].

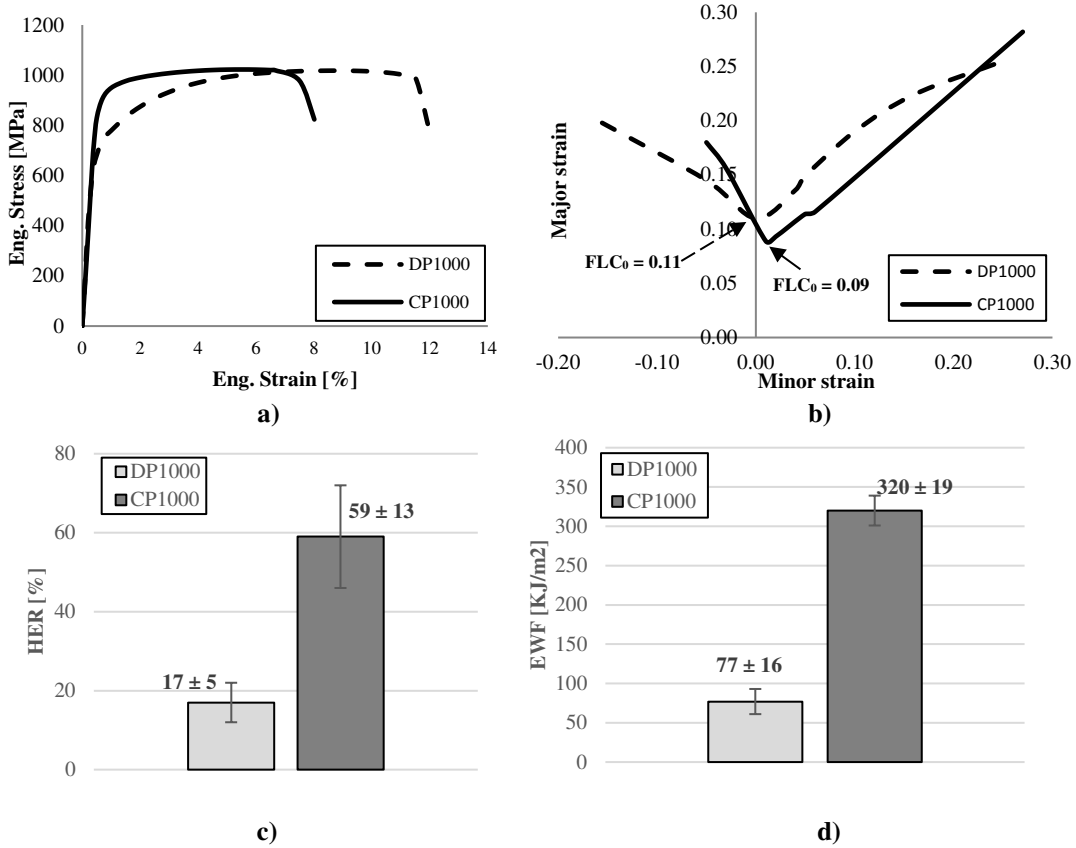

Figure 4. Experimental results obtained with the investigated CP and DP grades. a) Tensile curves, b) FLCs, c) HER values and d) EWF values.

4. Discussion

DP1000 shows much greater elongation than CP1000 in tensile tests, what would indicate higher ductility of the DP grade, and much higher n-value, generally associated to greater formability. However, DP1000 showed extensive edge cracking compared to CP1000. It must be noted that tensile tests evaluate only global damage. The fracture elongation obtained is an average strain along a gauge length and such strain value totally underestimates the local ductility potential of the material. Hisker et al. found that the microstructure of DP-steels is more sensitive to localized damage but it is compensated by the great work-hardening [28]. Thus, DP steels present great tensile properties but poor stretch-flangeability. However, the homogeneous microstructure of CP-steels is less sensitive to localized damage but has limited capacity for work-hardening, which leads to lower elongation in tensile tests but higher edge stretchability [28].

Fracture energy extracted from tensile test is also not suitable to describe edge cracking. Classical toughness definitions are based on the energy obtained from the area under the engineering curves and, usually, higher energy is associated with higher toughness (figure 4a, table 2). DP1000 shows higher fracture energy than CP1000. Hence, such energy values do not describe edge cracking.

DP1000 also shows higher FLC_0 than CP1000 (figure 4b), but again, this value cannot be used to understand edge cracking. FLD is suitable to evaluate the formability of AHSS when general deformation modes are present, but for shearing or edge stretching a poor correlation is obtained and FLC fails to predict the fracture [6]. The deformation mode for edge stretching is uniaxial tension. The fracture of the specimens in FLD tests at uniaxial tension is preceded by localized necking in the bulk material. Thus, the fracture strain determined overestimates edge cracking, which occurs before considerable necking at a much lower strain level [5, 24].The different edge crack behavior showed by DP1000 and CP1000 cannot be explained by means of conventional approaches, i.e. fracture elongation from tensile tests or FLC.

HET has shown to be suitable to estimate the stretch flangeability of AHSS [5, 24 and 27]. HER values obtained from the investigated steels (figure 4c) highlight the greater edge cracking resistance of CP steel grade against DP steel. The poor stretch flangeability showed by the DP justify the appearance of multiple edge cracks, observed in the cold formed component. However, the big scattering observed in the measurements can lead to question the objectivity of the method to characterize edge cracking sensitivity. Such scatter is attributed to the high number of variables during the test: amount of damage introduced during punching, method of crack detection, etc.

Fracture toughness measured in the frame of EPFM, through the EWF tests, can also be used as a material property to understand edge cracking. The EWF measurements carried out show that the fracture toughness of the CP1000 steel grade is much greater than the DP1000 steel ones (figure 4d) and it is found that higher EWF is related to greater HER values (figure 4c). Hence, the EWF is able to rationalize the poor edge cracking resistance of DP1000 and justify the appearance of multiple cracks at the edges of the cold formed component. This is in agreement with previous works that showed a very good correlation between HER and EWF [3, 10]. Such authors proposed EWF as an alternative method to evaluate the stretch-flangeability of AHSS. The results obtained in the present work are in good agreement with these investigations and support such proposal.

As a matter of comparison, the values of EWF and HET obtained here are plotted together with results from reference [10], in figure 5. It can be observed that results fit quite well in the almost linear correlation, and allows pointing out EWF as a material property and a reliable experimental parameter to evaluate stretch-flangeability of CP and DP steels and predict edge crack sensitivity.

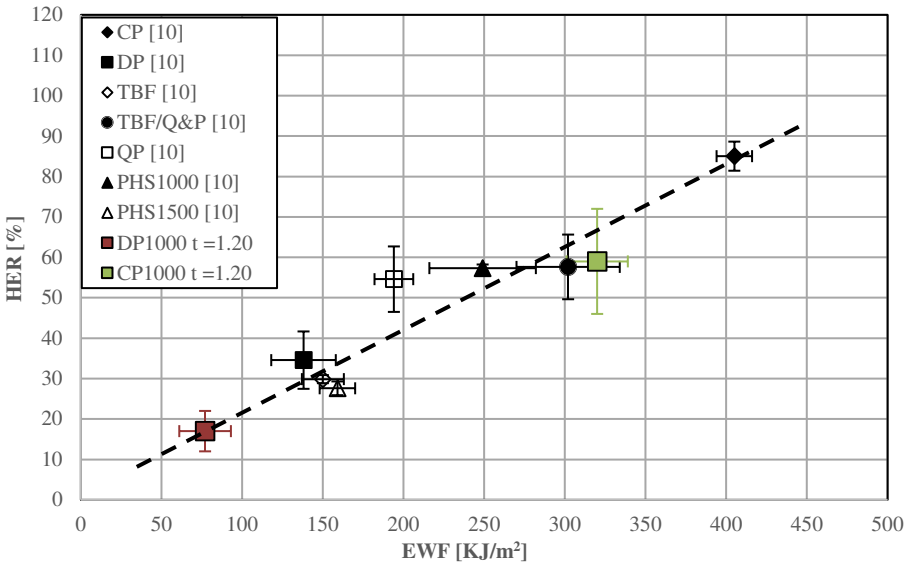

Figure 5. EWF against HER. CP and DP steel grades investigated in this work together with other AHSS grades reported in reference 10.

5. Conclusions

From the investigations carried out in this work with a serial produced AHSS automotive component and with the results of different mechanical tests, the following conclusions can be drawn:

- Conventional approaches, such as FLD or tensile tests are not capable to predict edge cracking sensitivity of DP and CP steels.
- It is shown that EWF methodology is a reliable tool to evaluate the fracture toughness of CP and DP steel grades and can properly rationalize edge cracking related problems.
- EWF is proposed as a parameter to select AHSS grades with improved stretch flangeability and avoid unexpected edge fractures during cold forming processes.

Acknowledgments

The research leading to these results has been partially funded by the European Commission, Research Fund for Coal and Steel, under grant agreement RFSR-CT-2014-00015 (Tough-Sheet).

References

[1] Steel Market Development Institute 2016 *2016 Steel Industry Technology Roadmap for Automotive*. www.autosteel.org

[2] Wu X, Bahmanpour H and Schmid K 2012 Characterization of mechanically sheared edges of dual phase steels *J. Mat. Proc. Tech.* **212** 1209-1224

[3] Gutiérrez D, Pérez LL, Lara A, Casellas D and Prado J M 2013 The influence of fracture toughness in stretch-flangeability in advanced high strength steels sheets *Proceedings of the IDDRG 2013 (Zurich, Switzerland, June 02-05)*

[4] Takahashi Y, Kawano O and Tanaka Y 2009 Fracture Mechanical Study on Edge Flange-ability of High Tensile-strength Steel Sheets *MS&T 2009: Proceedings from the Materials Science & Technology Conference (October 25-29, 2009, Pittsburgh, Pennsylvania)* pp 1317-1328.

[5] Larour P, Pauli H, Freudenthaler J and Grünsteidl A 2011 Alternative stretch flangeability characterisation methods for AHSS steel grades *Proceedings of the IDDRG2011 (Bilbao, Spain, June 05-08)*

[6] Chen X, Sun J and Zhu X 2012 Simulation Technique for Pre-forming of AHSS Edge Stretching *12th International LS-DYNA® Users Conference (Michigan,USA,June 03-05)*

[7] ISO/TS16630. Metallic materials – Method of hole expanding test, 2003

[8] Takahashi Y, Kawano O, Ushioda K and Aihara S 2012 Fracture Mechanical Study on Stretch Flange-Ability of Hot-Rolled High Tensile Strength Steel Sheets *Proceedings of Asia Steel International Conference 2012*
[9] Fonstein N, Jun HJ, Huang G, Sriram S and Yan B 2011 Effect of Bainite on Mechanical Properties of Multiphase Ferrite-Bainite-Martensite Steels *Proceedings from the Materials Science & Technology Conference (October 16-20, 2011, Columbus, Ohio)*
[10] Casellas D, Lara A, Frómeta D, Gutiérrez D, Molas S, Pérez LL, Rehrl J and Suppan C 2017 Fracture Toughness to Understand Stretch-Flangeability and Edge Cracking Resistance in AHSS *Metall and Mat Trans A* **48** 86-94
[11] Yoon J I, Jung J , Joo S H, Song T J, Chin K G, Seo M H, Kim S J, Lee S and Kim H S 2016 Correlation between fracture toughness and stretch-flangeability of advanced high strength steels *Matter.Lett.* **180** 322-326
[12] ASTM E1820. Standard Test Method for Measurement of Fracture Toughness, 2013.
[13] Cotterell B and Reddel JK 1977 The essential work of plane stress ductile fracture *Int.J.Fracture* **13** 267-277
[14] Mai YW and Cotterel B 1986 On the essential work of ductile fracture in polymers *Int.J.Fracture* **32** 105-125
[15] Wu J and Mai YW 1996 The Essential Fracture Work Concept for Toughness Measurement of Ductile Polymers *Polym.Eng. Sci* **36** 2275-2288
[16] Martínez AB, Gámez-Pérez J, Sanchez-Soto M, Velasco JI, santana O.O, and Maspoch MLL 2009 The Essential Work of Fracture method- Analyzing the Post-yielding Fracture Mechanics of polymers *Eng. Fail. Anal.* **16** 2604-2617
[17] Marchal Y and Delannay F 1998 Comparison of methods for fracture toughness testing of thin low carbon steel plates. *Mater Sci Tech Ser* **14** 1163–1168
[18] Cotterell B, Pardoen T and Atkins AG 2005 Measuring toughness and the cohesive stress–displacement relationship by the essential work of fracture concept. *Eng. Fract. Mech.* **72** 827–848
[19] Marchal Y and Delannay F 1996 Influence of test parameters on the measurement of the essential work of fracture of zinc sheets. *Int Fract J* **80** 295–310
[20] Pardoen T, Marchal Y and Delannay F 1999 Thickness dependence of cracking resistance in thin aluminium plates *J.Mech.Phys.Solids* **47** 2093-2123
[21] Llobet A, Casellas D, Riera MD and Prado JM 2008 Fracture toughness characterization of Advanced high strength Steels by means of the Essential Work of Fracture *Proceedings from International Conference on New Developments in Advanced High-Strength Sheet Steels (Orlando,USA,June 15-18)*
[22] Muñoz R, Lara A and Casellas D 2011 Fracture toughness characterization of advanced high strength steels *Proceedings of the IDDRG2011 (Bilbao, Spain, June 05-08)*
[23] Lacroix G, Pardoen T and Jacques PJ 2008 The fracture toughness of TRIP-assisted multiphase steels *Acta Mater.* **56** 3900–3913
[24] Larour P, Freudenthaler J, Grünsteidl A and Wang K 2014 Evaluation of alternative stretch flangeability testing methods to ISO 16630 standard *Proceedings of the IDDRG2014 (Paris, France, June 01-04)*
[25] Larour P, Freudenthaler J, Lackner J, Leomann F and Schestak G 2016 Experimental artefacts on ISO 16630 hole expansion ratio *Proceedings of the IDDRG2016 (Linz, Austria, June 12-15)*
[26] Clutton E, Moore DR 2003 ESIS EWF Protocol: Essential work of fracture and cohesive zone fracture toughness.
[27] Shi M and Chen X 2007 Prediction of Stretch Flangeability Limits of Advanced High Strength Steels using the Hole Expansion Test *SAE Technical Paper 2007-01-1693*
[28] Hisker F, Thiessen R and Heller T 2012 Influence of Microstructure on Damage in Advanced High Strength Steels *Mater. Sci. Forum* **706-79** 925-930

Paper B. D. Frómeta, A. Lara, S. Parareda and D. Casellas. Evaluation of Edge Formability in High Strength Sheets Through a Fracture Mechanics Approach. *AIP Conference Proceedings* 2113 (2019) 160007.

ATTENTION¡¡
Pages 226 to 232 of the thesis, containing the article mentioned above are available at the editor's web

https://aip.scitation.org/doi/abs/10.1063/1.5112704

Paper C. D. Frómeta, A. Lara, B. Casas, D. Casellas. Fracture toughness measurements to understand local ductility of advanced high strength steels. *IOP Conf. Ser.: Mater. Sci. Eng.* 651 (2019) 012071

IOP Conf. Series: Materials Science and Engineering **651** (2019) 012071 doi:10.1088/1757-899X/651/1/012071

Fracture toughness measurements to understand local ductility of advanced high strength steels

D. Frómeta[1*], A. Lara[1], B. Casas[1] and D. Casellas[1,2]

[1] Eurecat, Centre Tecnològic de Catalunya, Unit of Metallic and Ceramic Materials, Plaça de la Ciència, 2, Manresa 08243, Spain
[2] Division of Mechanics of Solid Materials, Luleå University of Technology, 971 87 Luleå, Sweden

[*]Corresponding author: david.frometa@eurecat.org

Abstract. The determination of the material parameters that best predict the local ductility of high strength sheet materials has become the focus of active research. Even though several correlations have been proposed, they can sometimes be not accurate enough and discussion is still open on this topic. This paper investigates the suitability of different fracture toughness measurements for local ductility prediction in multiple advanced high strength steels (AHSS). Fracture toughness is characterized by means of essential work of fracture and Khan tear tests. The results show that the essential work of fracture, w_e, correlates well with different local formability (HER, critical bending angle from V-bending tests and local strain at fracture from uniaxial tensile tests) and crash resistance parameters (energy absorbed in axial impact tests). It confirms that fracture toughness, measured in the frame of fracture mechanics, is a relevant material property to rationalize cracking issues associated to the local ductility of AHSS. On the other hand, it is also shown that Khan tear tests, which are conventionally used to evaluate the fracture resistance of thin metal sheets, can overestimate crack propagation resistance and offer a poor prediction ability for local formability and crash performance.

1. Introduction

A wide variety of new high strength sheet materials have been developed in the last years for automotive lightweight applications. The limited ductility of these materials has posed new forming challenges that cannot be rationalized through conventional fracture characterization criteria. This fact has motivated the development of alternative characterization methodologies and improved formability mappings accounting for global and local formability. Global formability refers to the material resistance against necking instability and is well described by traditional tensile parameters (true uniform strain, elongation at fracture, n-value) and forming limit diagrams. Nevertheless, these tests provide little information regarding local formability issues (edge cracking, fractures occurring during bending on tight radius, crash folding behaviour). Thus, new experimental approaches are necessary to predict this kind of fractures associated to the local ductility of the material.

In this sense, recent research works have demonstrated that fracture toughness, measured within the frame of fracture mechanics, is a relevant material property to describe such cracking related problems in AHSS [1-5]. Many works have shown the suitability of fracture toughness to rationalize and classify the stretch flangeability of high strength steels [1-4]. More recently, the measurement of fracture toughness has been also used in [5] to understand the crash failure behaviour of different AHSS grades. Therefore, it is evident that there is a close relationship between the crack propagation resistance of high

Content from this work may be used under the terms of the Creative Commons Attribution 3.0 licence. Any further distribution of this work must maintain attribution to the author(s) and the title of the work, journal citation and DOI.
Published under licence by IOP Publishing Ltd

strength metal sheets and its local ductility. Nevertheless, the measurement of fracture toughness according to elastic plastic fracture mechanics (EPFM) standards [6] is rather complex and involves exhaustive specimen preparation and test monitoring, which hamper its implementation as a routine testing in automotive industry. There exist alternative simpler methods to characterize the fracture toughness of thin metal sheets, such as the essential work of fracture (EWF) methodology [7].

The EWF methodology is easier than standard methods since it permits to obtain the material crack initiation and propagation resistance without measuring the crack advance during the test, which is one of the main experimental challenges in EPFM procedures. Toughness values obtained from the EWF methodology have shown to be suitable to predict cracking related phenomena in AHSS sheets, such as edge cracking [1, 2] and crack propagation under crash loading [5]. Another method frequently used to characterize the fracture resistance of thin metal sheets is the Khan Tear Test (KTT). It has been extensively used to characterize the notch resistance of precipitation hardening aluminum alloys [8-10] and to evaluate toughness in different microstructures obtained by hot stamping of 22MnB5 steels [11] and in TWIP steels [12]. The main advantage of KTTs is that they are very simple tests and provide an estimation of the crack propagation resistance of the material.

The aim of this work is twofold; firstly, to determine the fracture resistance of several AHSS grades by means of these two methodologies, the EWF and the KTT; and secondly to assess the correlation between fracture toughness and local ductility in AHSS. The ability of the proposed methodologies to predict local ductility, as well as their main advantages and drawbacks, are discussed. Fracture toughness results are compared with different local formability and crash resistance parameters widely applied in the automotive sector:

- HER according to ISO 16630
- Bending angle from V-bending tests according to VDA 238-100
- Local strain at fracture from uniaxial tests obtained by means of Digital Image Correlation (DIC)
- Energy absorbed in axial impact tests

2. Fracture toughness measurements

2.1. Essential Work of Fracture

The Essential Work of Fracture (EWF) methodology was developed as an alternative method to quantify the ductile tearing resistance of thin ductile metal sheets [7]. The methodology permits to partition the total work of ductile fracture (W_f) in two energetic contributions: an essential work of fracture (w_e), spent in the fracture process zone and necessary to create new surfaces in the front of the crack tip and a non-essential plastic work (w_p) surrounding the fracture area. The first term is proportional to the fracture surface and the second is proportional to the plastic volume, according to:

$$W_f = w_e l_0 t_0 + w_p \beta {l_0}^2 t_0 \quad (1)$$

where l_0 is the ligament length (unfractured area ahead of the crack tip), t_0 is the specimen thickness and β is a shape factor that depends on the shape of the plastic zone. W_f is obtained by testing a Double Edge Notched (DENT) specimen (Figure 1) at a constant displacement rate and integrating the area under the load vs displacement curve. The specific work of fracture (w_f) is obtained by dividing W_f by the initial ligament area $l_0 t_0$. Thus, equation (1) can be rewritten as:

$$\frac{W_f}{l_0 t_0} = w_f = w_e + w_p \beta l_0 \quad (2)$$

If DENT specimens with different ligament lengths are tested and w_f is plotted against the ligament length l_0, a straight line with a positive intercept, which is the specific essential work of fracture (w_e), is obtained (Figure 1).

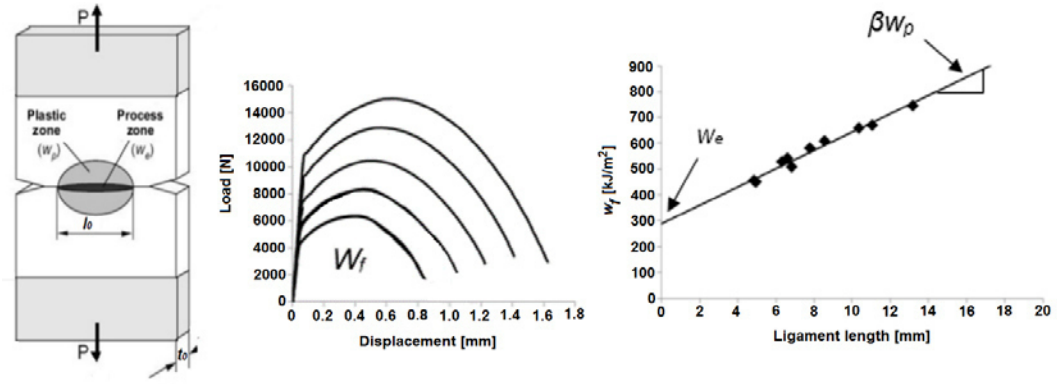

Figure 1. DENT specimen and experimental determination of the EWF: W_f for different ligament lengths and plot of w_f against l_0, the intercept indicates the specific essential work of fracture, w_e [5].

The obtained toughness value, w_e, quantifies the energy dissipated within the fracture process zone during the ductile tearing process and it is a suitable parameter to describe the crack propagation resistance of thin ductile sheets [1, 2, 5, 7]. w_e contains energetic contributions from both crack initiation and propagation since is an average value obtained from a linear regression of w_f values for the complete separation. However, as shown by Mai and Cotterell [13], the EWF methodology also permits to separate both contributions and determine a cracking initiation toughness value, the specific work for fracture initiation. w_e^i. The specific work for fracture initiation, w_f^i is calculated by integrating the area under load vs displacement curve until the onset of crack propagation (Figure 2, left). As observed in Figure 2 right, w_f^i is independent of the ligament length. Therefore, w_e^i is calculated from the average of w_f^i values.

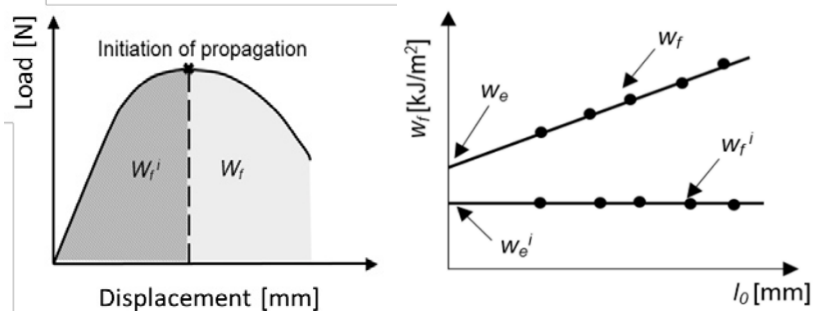

Figure 2. Left: Determination of specific work of fracture at initiation of propagation ($w_f{}^i$). Right: Variation of w_f^i in function of ligament length and determination of the specific essential work of fracture at cracking initiation, w_e^i [5].

For the evaluation of the EWF, rectangular DENT specimens of 240 x 55 mm (machined at 90º respect to the rolling direction) with ligament lengths ranging from 6 to 16 mm were tested up to fracture at a constant speed of 1 mm/min. In order to obtain toughness values independent of the notch radius fatigue pre-cracks were nucleated on the notch root (notch radius, $\rho \approx 0{,}1\ \mu$m). More detailed information about the specimen geometry and test conditions is given in [5].

2.2. Khan Tear Tests

Khan Tear Tests (KTT) were originally developed to characterize the notch resistance of thin aluminum sheets [8]. The experimental procedure for KTT is described in ASTM B871 [14]. It consists in pulling at constant speed a single edge notched tensile (SENT) specimen with no prior fatigue pre-crack but a sharp notch. In this case, the notch radius was of 150 µm, obtained by electrical discharge machining (EDM). The specimens were machined at transverse direction and KTTs were conducted at a constant displacement rate of 1 mm/min. An initial gauge length of 10 mm was used for load-line displacement

measurement. The specimen geometry and the characteristic load vs displacement curve are shown in Figure 3.

The notch resistance is characterized by the unit initiation energy (UIE) and the unit propagation energy (UPE). UIE represents the notch resistance to nucleate a crack and is calculated from the area under the load-displacement curve at maximum load. UPE is the primary result of the tear test and it is calculated from the area after the maximum load. It provides a measure of the combination of strength and ductility that permits a material to resist crack growth and it has significance as a relative index of fracture toughness. As indicated in the standard ASTM B871 [14], the method does not provide an absolute measure of the material resistance against crack propagation but a comparative measure of resistance to unstable fracture in the presence of crack-like stress concentrators.

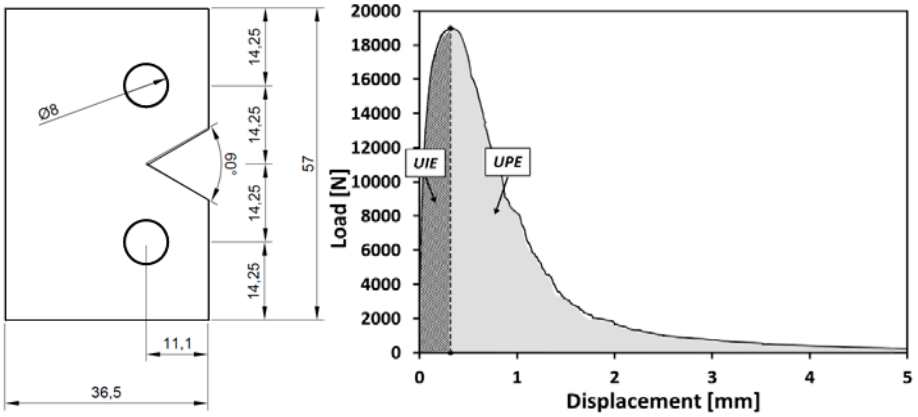

Figure 3. SENT specimen for tear tests (left). Load–displacement curve for a Kahn Tear Test (right). The UIE is calculated from the area under the curve before maximum load, and the UPE after maximum load.

2.3. Comparison between EWF and KTT

Figure 4 compares fracture toughness results obtained by means of the EWF methodology and KTT. On the one hand, it is interesting to note that, even though the difference in notch radius between the two test configurations, there is a good correspondence between the values of crack initiation resistance, w_e^i and UIE. It means that for the SENT specimen the machined sharp notch (ρ= 150 µm) closely represents the stress singularity of a crack. It supposes an advantage respect to the EWF tests since, it avoids the propagation of fatigue pre-cracks in the notch root, which is the most time consuming part in fracture mechanical characterizations.

However, whereas results for crack initiation resistance are very similar, large differences are observed in the values associated to the crack propagation resistance, w_e and UPE. For example, DP1000 and TBF show UPE values (464 and 493 kJ/m^2 respectively) comparable to PHS1000 (494 kJ/m^2), which contrasts with the large differences observed in w_e: DP1000 and TBF shows the lowest w_e (138 ± 20 and 149 ± 13 kJ/m^2), whereas PHS1000 exhibits a much greater w_e value (330 ± 21 kJ/m^2). It is also observed that, according to UPE values, TBF/Q&P presents the greatest crack propagation resistance (755 kJ/m^2). On the contrary, CP1000 shows the higher w_e (405 ± 11 kJ/m^2). These differences can be associated to both the effect of the specimen geometry during crack propagation in KTT and to the conceptual dissimilarities between the two methodologies. It must be noted that after crack initiation, the load rapidly evolves from uniaxial tensile to bending and, therefore, crack propagates under a complex mixed loading mode. It give rise to UPE values that cannot be directly compared with pure Mode I fracture resistance, as given by w_e. Moreover, the energy calculated in the UPE is not only an energy for new fracture surface creation but it also contains the energetic contribution of the dissipated plastic work, which depends on the specimen geometry. In this regard, the EWF methodology separates both contributions and the toughness value w_e only quantifies the work spent in the fracture process zone to create new surfaces at the crack tip. Therefore, w_e better represents the steady state crack propagation resistance and it can be considered a material property, equivalent to the elastic plastic fracture

mechanics toughness value J_C [13]. On the contrary, as mentioned before, UPE can be only used as a comparative value for crack propagation resistance for a given material. It is not a material property and it should be only used to rank materials crack propagation resistance. However, as observed in Figure 4, UPE can significantly overestimate such property.

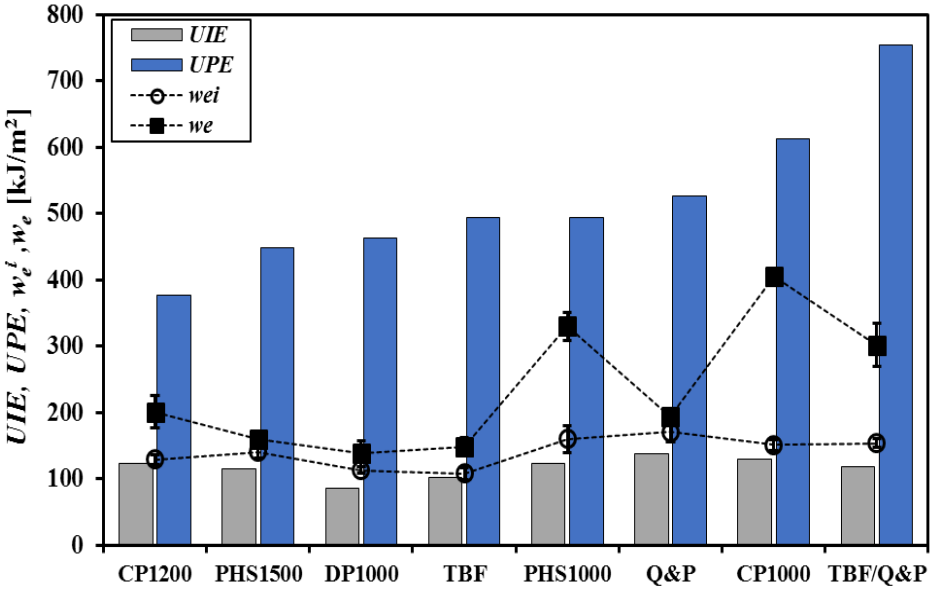

Figure 4. Results of EWF and KTT for different AHSS grades. EWF results taken from reference [5].

3. Local formability and crash behaviour

3.1. Stretch flangeability

The results of Hole Expansion Tests (HET) according to ISO 16630 for the investigated AHSS grades are summarized in Table 1. Initial punched holes of 10 mm in diameter were used for the expansion tests (punch to die clearance of 12 ± 2 %). Hole Expansion Ratio (HER) values are taken from reference [1].

3.2. Bendability

3-point V-bending tests according to VDA 238-100 were performed at voestalpine Stahl following the procedure described in the work of Suppan et al. [15]. Specimens were bent with a sharp punch (r=0.4 mm) at a speed of 20 mm/min with the bending line lying parallel to rolling direction (bending strain in transverse direction). Free rotating rollers with a radius R=15 mm were used as shoulders and were separated according to:

$$d = 2t + 0.5 \quad (3)$$

where d is the free space between the rolls and t is the specimen thickness. All values are in mm.

The punch force and displacement was recorded and the test was stopped when the maximum punch stroke at around 160° bending angle was reached. Bending angle was indirectly calculated from the punch displacement as indicated in [16]. In the present work, the bendability was characterized by means of the critical angle (α_{Crit}), defined as the angle at which the first visible crack was detected. In most cases, the critical angle coincided with the bending angle at maximum force ($\alpha_{Crit} = \alpha_{Fmax}$), except for CP1000, where first visible cracks were detected up to 30° after the maximum load. Values of α_{Crit} are reported in Table 1.

3.3. Local strain at fracture from uniaxial tensile tests assisted by digital image correlation

Uniaxial tensile tests according to EN-ISO 6892 were performed in transverse direction. A Digital Image Correlation (DIC) equipment was used to monitor and determine the strain during the whole test. The

DIC equipment permits to measure local strains within the necking area. The local strain level after necking is much greater than the obtained by conventional extensometry with much larger 80 mm gage length and it better defines the local ductility potential of the material. Images were recorded at a frame rate of 10 images/second. A facet size and a step size of 11 and 9 pixels respectively were used. The local strain at fracture (*Local* ε_f) was determined from the point of maximum deformation (major logarithmic strain) at the stage before fracture (Figure 5a). *Local* ε_f values are summarized in Table 1.

3.4. Maximum energy absorbed in axial impact tests

Crash resistance of AHSS is usually evaluated according to the energy absorbed, deformation, cracking and global appearance of the specimens after crash testing. In this work, the maximum energy absorbed in axial crash tests was used to characterize the impact resistance of the investigated steel grades. The energy absorbed during crash loading was calculated by integrating the area under the force vs impactor displacement (Figure 5b). To avoid the influence of the specimen thickness, the energy values from [5] were normalized by the cross-section area of the crashed sample. The values of impact energy absorbed per unit area are shown in Table 1. Details about crash specimen geometry and the experimental procedure followed for crash characterization can be found in reference [5].

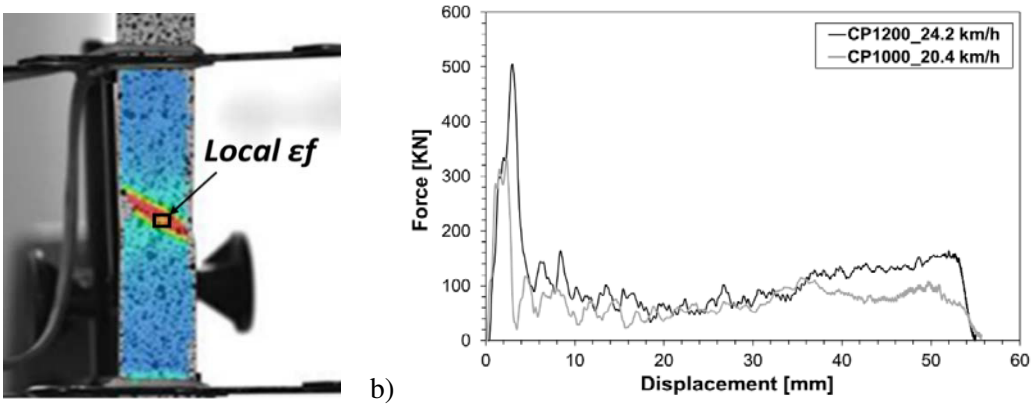

a) b)

Figure 5. a) Determination of local strain at fracture (*Local* ε_f) from uniaxial tensile tests with DIC. **b)** Force vs impactor displacement curves obtained from axial impact tests [5].

Table 1. Local formability measurements and crash behaviour for the investigated AHSS grades. Standard deviation is indicated when available. HER values and energy absorbed in axial impact tests are extracted from references [1] and [5] respectively. Mechanical properties for the transverse direction and sheet thickness are also given.

	Thickness, t [mm]	HER [%]	α_{Crit} [°]	*Local* ε_f [log.]	Axial impact energy per unit area [kJ/m^2]	Yield stress, σ_{ys} [MPa]	Ultimate tensile strength, σ_{UTS} [MPa]	Elongation at fracture, A_{80} [%]
CP1200	1.6	45 ± 10	77	0.48	14229	1041	1218	6.0
PHS1500	1.5	28 ± 2	55	0.42	7461	1075	1552	5.2
DP1000	1.4	35 ± 8	62	0.45	9592	738	1027	10.3
TBF	1.5	30 ± 1	80	0.45	12186	725	1019	14.7
PHS1000	1.5	57 ± 1	90	0.48	23626	988	1007	7.3
Q&P	1.4	55 ± 8	71	0.52	14122	909	1209	7.4
CP1000	1.4	85 ± 4	120	0.57	36504	908	1002	8.1
TBF/Q&P	1.4	66 ± 11	95	0.57	25047	876	1026	11.3

4. Fracture toughness vs local ductility

Figure 6 plots fracture resistance results (w_e and UPE) against local formability and crash resistance parameters. It is observed that w_e shows a good correlation with all the different local ductility measurements, especially with ISO 16630 HER and maximum energy absorbed in axial impact tests

(R^2=0.86 and 0.95 respectively), as previously reported and discussed by Casellas et al. [1] and Frómeta et al. [5]. It is also found a quite good correlation with the critical bending angle, α_{Crit} (R^2=0.83) and the local strain at fracture from uniaxial tensile tests (R^2=0.60). Such results confirm the straight relationship between fracture toughness and the local ductility of AHSS and pose the essential work of fracture as a suitable material property to predict local formability and crash resistance. On the other hand, crack propagation resistance results from KTT (UPE), overall, show a low prediction ability for local formability and crash performance assessment. UPE shows a poor correlation with HER (R^2=0.44), bending angle (R^2=0.37) and impact energy per unit area (R^2=0.42). Such correlation is improved for local strain at fracture (R^2=0.64), which is comparable to the observed with w_e. Therefore, it is shown that, even though the UPE can give an estimation of the crack propagation resistance of the material, it is not a reliable parameter to predict cracking phenomena related to the material's fracture toughness.

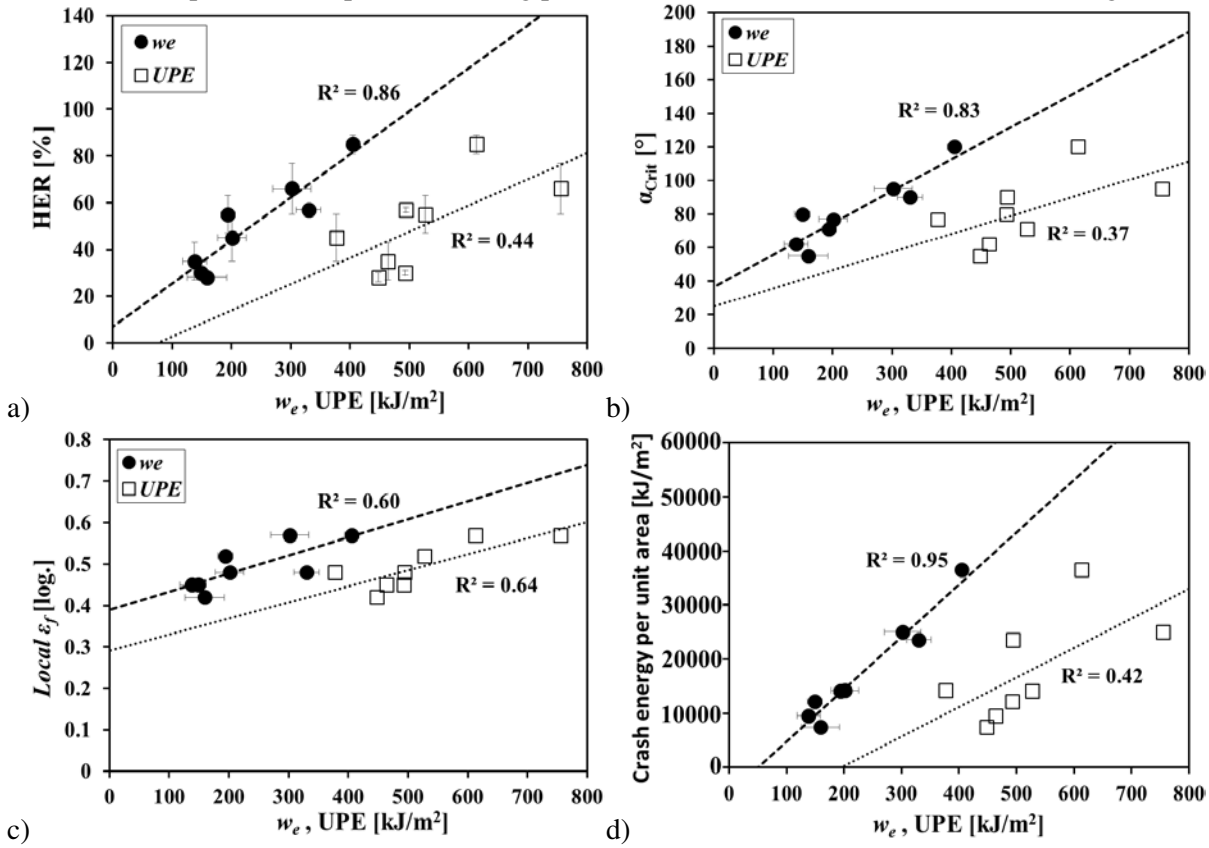

Figure 6. Fracture toughness results (w_e and UPE) against different local ductility parameters: **a)** HER according to ISO 16630 [1]. **b)** Critical bending angle (α_{Crit}) from V-bending tests. **c)** local strain at fracture (*Local εf*) from uniaxial tensile tests with DIC. d) Maximum energy absorbed in axial impact tests per unit area.

5. Summary and conclusions

The experimental investigations carried out in this work allow pointing out fracture toughness, in terms of essential work of fracture, as a suitable material property to estimate the local ductility of AHSS sheets. This conclusion is based on the good correlation observed between w_e and the different local ductility parameters for a wide range of AHSS grades.

This work compared the ability of fracture resistance values from the EWF methodology and KTT to understand crack-related problems in AHSS, as local formability or crashworthiness. Even though crack initiation values from KTT are quite reliable and very similar to the obtained by means of the EWF methodology, the crack propagation resistance in such tests is strongly influenced by the changing load mode during the test. UPE values show a poor correlation with the evaluated local ductility and

crash resistance parameters. The good prediction capability of w_e compared with UPE can be understood considering their intrinsic differences, i.e. w_e accounts for the dissipated energy to create new surfaces in Mode I during crack propagation whereas UPE contains the contribution from plastic work during crack propagation in a mixed loading mode. Local ductility and crashworthiness are more related to crack propagation than to first crack nucleation, which explains their good correspondence with essential work of fracture values, w_e.

Acknowledgments
The authors would like to thank Dr. Clemens Suppan, Dr. Johannes Rehrl and Dr. Patrick Larour from voestalpine Stahl GmbH for providing the results of V-bending tests and for the support in the analysis of results and useful discussions.

References

[1] Casellas D, Lara A, Frómeta D, Gutiérrez D, Molas S, Pérez Ll , Rehrl J and Suppan C 2017 Fracture Toughness to Understand Stretch-Flangeability and Edge Cracking Resistance in AHSS *Metall and Mat Trans A* **48** 86-94.
[2] Frómeta D, Tedesco M, Calvo J, Lara A, Molas S and Casellas D 2017 Assessing edge cracking resistance in AHSS automotive parts by the Essential Work of Fracture methodology *J Phys: Conf Ser* 2017 **896** 012102.
[3] Yoon J I, Jung J , Joo S H, Song T J, Chin K G, Seo M H, Kim S J, Lee S and Kim H S 2016 Correlation between fracture toughness and stretch-flangeability of advanced high strength steels *Matter.Lett.* **180** 322-326
[4] Takahashi Y, Kawano O, Ushioda K and Aihara S 2012 Fracture Mechanical Study on Stretch Flange-Ability of Hot-Rolled High Tensile Strength Steel Sheets *Proceedings of Asia Steel International Conference 2012*
[5] Frómeta D, Lara A, Molas S, Casellas D, Rehrl J, Suppan C, Larour P and Calvo J 2019 On the correlation between fracture toughness and crash resistance of advanced high strength steels *Eng. Frac. Mech.* **205** 319-332.
[6] ASTM E1820. Standard Test Method for measurement of fracture toughness.
[7] Cotterell B and Reddel JK 1977 The essential work of plane stress ductile fracture *Int. J. Fracture* 267-277.
[8] Kaufman JG and Knoll AH 1964 Kahn-type tear tests and crack toughness of aluminium alloy sheets *Mater. Res. Std.* **4** 151.
[9] Garret GG and Knott JF 1978 The influence of compositional and microstructural variations on the mechanism of static fracture in aluminum alloys. *Metal. Trans. A* **9** 1187-1201.
[10] Dumont D, Deschamps A and Brechet Y 2003 On the relationship between microstructure, strength and toughness in AA7050 aluminum alloy. *Mat. Sci. and Eng. A* **356** 326-336.
[11] Ying L, Lu J, Chang Y, Tang X, Hu P and Zhao K 2013 Optimization evaluation test of strength and toughness parameters for hot-stamped high strength steels *J. of Iron and Steel Research Int.* **20** 51
[12] Lorthios J, Gourgues A, Cugy P, Scott CP 2009 Damage of TWIP steels for automotive application, In *ICF12 Int. Conf. Fracture* Ottawa
[13] Mai YW and Cotterell B 1986 On the essential work of ductile fracture in polymers *Int. J. Fract.* **32** 105-125.
[14] ASTM B871. Standard Test Method for Tear Testing of Aluminum Alloy Products.
[15] Suppan C, Hebesberger T, Pichler A, Rehrl J and Kolednik O 2018 On the microstructure control of the bendability of advanced high strength steels *Mat. Sci.and Eng. A* **735** 89–98
[16] Larour P, Hackl B, Leomann F and Benedyk K 2012 Bending angle calculation in the instrumented three-point bending test *Proceedings IDDRG 2012*, Mumbai, India.

Paper D. D Frómeta, A. Lara, S. Parareda, L. Grifé, D. Casellas. New tool to evaluate the fracture resistance of thin high strength metal sheets. *IOP Conf. Ser.: Mater. Sci. Eng.* 967 (2020) 012088.

New tool to evaluate the fracture resistance of thin high strength metal sheets

D Frómeta[1], A Lara[1] S Parareda[1], L. Grifé[1] and D Casellas[1,2]
[1] Eurecat, Centre Tecnològic de Catalunya, Unit of Metallic and Ceramic Materials, Plaça de la Ciència 2, 08243 Manresa, Spain
[2] Division of Mechanics of Solid Materials, Luleå University of Technology, 971 87 Luleå, Sweden

Abstract. Fracture toughness has become a key property to predict the fracture performance of high strength metal sheets (edge cracking resistance, crash failure behaviour, local formability, etc.). However, the measurement of the fracture toughness of thin sheets still being challenging, mainly because of complex, expensive and time-consuming specimen preparation. In this work, an innovative tool to readily assess the fracture resistance of thin advanced high strength metal sheets is presented. The device consists of a special cutting tool (punch and die) designed to introduce sharp notches in sheet specimens through a simple shearing process. This new method avoids the need for fatigue pre-cracking procedures and allows measuring the fracture toughness of thin metal sheets with easy and cheap specimen preparation. It has been used in this work to evaluate the crack propagation resistance of four different advanced high strength steel sheets. The obtained toughness values are in good agreement with those measured with fatigue pre-cracked specimens and they show to be suitable to predict edge formability of AHSS sheets.

1. Introduction

Recent developments in new high strength sheet materials for automotive lightweight construction has brought new challenges to the sheet manufacturing sector: the need for accurate characterization techniques and methods to avoid sheet cracking occurrence during forming and to predict in-service performance. The high strength and limited ductility of such alloys increase their cracking susceptibility and reduce their formability. Thus, end-use industries and their suppliers are currently facing serious productivity losses due to the occurrence of unexpected fractures during forming. Moreover, end-users are continuously asking for high-performance materials and reliable methods to predict crashworthiness in the transport sector and long-life performance in other engineering applications. In this regard, fracture toughness measured in the frame of fracture mechanics has shown to be a suitable material property to understand crack-related problems in high strength metal sheets [1-5]. Unfortunately, the experimental evaluation of fracture toughness in thin sheets is not straightforward. It involves tedious specimen preparation, including expensive and time-consuming fatigue pre-cracking operations, and complex crack growth measuring techniques. Furthermore, the thickness of these sheets (usually 1-3 mm), do not satisfy the size requirements described in fracture mechanics standard procedures [6,7]. As a consequence, the knowledge of the fracture properties of such high strength sheet materials is very limited.

The Essential Work of Fracture (EWF) methodology [8] has shown to be a suitable alternative to readily characterize the fracture toughness of such thin high strength metal sheets [2-5, 9]. The method is very simple and does not require the measurement of the current crack advance during the test, which

Content from this work may be used under the terms of the Creative Commons Attribution 3.0 licence. Any further distribution of this work must maintain attribution to the author(s) and the title of the work, journal citation and DOI.
Published under licence by IOP Publishing Ltd

supposes great advantage respect to traditional elastic-plastic fracture mechanics (EPFM) procedures. However, as it is well known in fracture mechanics testing, EWF measurements are strongly affected by the notch root radius [9]. Therefore, to obtain reliable notch-independent toughness values, it is necessary the use of fatigue pre-cracked specimens as recommended by standard procedures [6, 7]. This significantly increases the cost and time of the tests. Moreover, specialized equipment and skilled staff are required. To overcome such experimental difficulties in specimen preparation for fracture toughness characterization of thin metal sheets and to promote its application as routine testing for quality control and material selection, an innovative tool is presented in this work. The device, developed at the Unit of Metallic and Ceramic Materials of Eurecat and registered under European patent EP 3567364A1, consists of a two-pillar modular cutting die, equipped with a bevelled punch (Figure 1 left) designed to introduce crack-like sharp notches in the sheet specimens. The tool allows obtaining rectangular Double Edge Notched Tension (DENT) specimens (Figure 1 right) by means of a simple shearing process. It works with sheet blanks between 0.5 and 2 mm thickness approximately (its application to thicknesses above 2 mm is under study). In the present work, the new device has been used to evaluate the EWF of 4 different Advanced High Strength (AHSS) sheets of 1000-1200 MPa strength and ≈1.4 mm thickness. In order to validate the obtained fracture toughness results, they are compared to those obtained with conventional fatigue pre-cracked specimens.

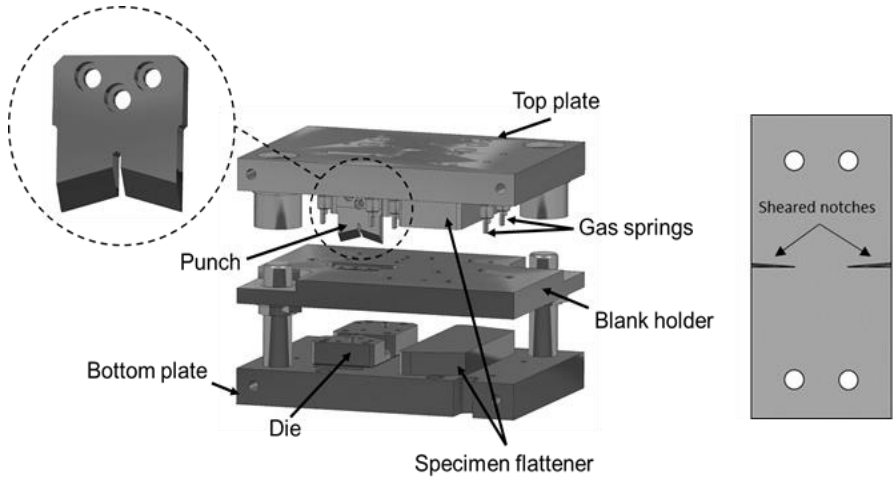

Figure 1. Left: Tool for introducing sharp notches in sheet metal specimens and detail of the bevelled punch. Right: DENT specimen with sheared sharp notches

2. Materials and methods

2.1. Materials

The materials investigated in this work are 4 AHSS grades in the form of 1.35-1.4 mm thickness sheets. The steels are a Complex Phase (CP) steel, two Dual Phase (DP) steels and a 3rd GEN Transformation Induced Plasticity (TRIP)-assisted steel. The mechanical properties of the studied steels for the transverse direction are indicated in Table 1. Sheet thickness is also given. CP steel has a homogeneous bainite/tempered martensite matrix and it is characterized by low strain hardening and high yield stress to tensile strength ratio. DP-A has a ferritic-bainitic matrix with some amount of tempered martensite and a lower amount of hard martensite islands. It shows higher strain hardening and greater elongation values than CP steel. DP-B has a more homogeneous ferrite-martensite distribution. It shows slightly lower elongation than DP-A and higher strain hardening than CP. The microstructure of the 3rd Gen TRIP-assisted steel consists of a bainitic matrix with islands of martensite/retained austenite. It has a considerable amount of retained austenite (≈15%). The strain-induced transformation of retained austenite to martensite (TRIP effect) enhances strain hardening and elongation values (both uniform and total).

Table 1. Mechanical properties of the investigated materials for the transverse direction

Material	Thickness, t [mm]	Yield strength, σ_{ys} [MPa]	Ultimate Tensile Strength, σ_{UTS} [MPa]	Uniform elongation, A_g [%]	Elongation at fracture, A_{80} [%]	Strain hardening exponent, $n_{2\text{-}4\%}$
CP	1.4	915	1008	4.8	8.8	0.05
DP-A	1.35	807	1057	6.6	9.6	0.13
DP-B	1.4	769	1040	5.3	8.7	0.09
3rd Gen	1.4	987	1216	9.2	12.6	0.11

2.2. Fracture toughness measurements: Essential Work of Fracture methodology

The Essential Work of Fracture (EWF) methodology was developed to quantify the ductile tearing resistance of thin ductile metal sheets [8]. The methodology permits to separate the total work of ductile fracture (W_f) in two energetic contributions: an essential work of fracture (w_e), developed in the fracture process zone and necessary to create new surfaces in the front of the crack tip and a non-essential plastic work (w_p) surrounding the fracture area. The first term is proportional to the fracture surface and the second to the plastic volume, according to:

$$W_f = w_e l_0 t_0 + w_p \beta {l_0}^2 t_0 \tag{1}$$

where l_0 is the ligament length (the non-fractured section between the two edge notches, see Figure 2), t_0 is the specimen thickness and β is a shape factor that depends on the shape of the plastic zone. Even though different specimen geometries can be used to obtain the EWF, the DENT specimen has shown to be the most suitable geometry for thin sheets since there is no buckling during the test. The experimental procedure for the determination of the EWF is schematized in Figure 2. W_f is obtained by testing a DENT specimen (Figure 2 left) up to fracture at a constant displacement rate and integrating the area under the load vs displacement curve. The specific work of fracture (w_f) is obtained by dividing W_f by the initial ligament area $l_0 t_0$. Thus, equation (1) can be rewritten as:

$$\frac{W_f}{l_0 t_0} = w_f = w_e + w_p \beta l_0 \tag{2}$$

If DENT specimens with different ligament lengths are tested and w_f is plotted against the ligament length l_0, a straight line with a positive intercept, which is the specific essential work of fracture (w_e), is obtained (Figure 2 right).

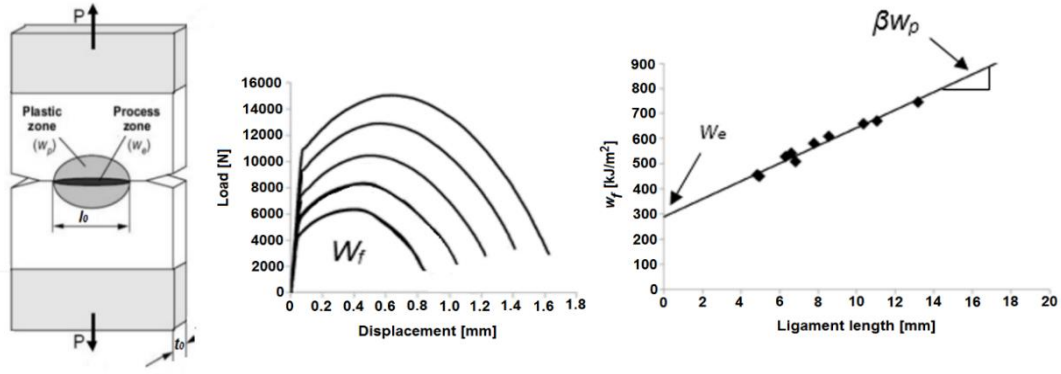

Figure 2. DENT specimen and experimental determination of the EWF: W_f for different ligament lengths (l_0) and plot of w_f against l_0. The y-intercept indicates the specific essential work of fracture, w_e [4].

2.3. Specimen preparation

In the present work, EWF tests have been performed with two different notch configurations: 1) fatigue pre-cracks according to standard procedures recommendations and 2) mechanically sheared notches obtained with the new tool. The experimental procedure for the preparation of both notch conditions is described in *Section 2.3.1* and *2.3.2*.

2.3.1. Fatigue pre-cracked specimens. For EWF tests with fatigue pre-cracked specimens, rectangular DENT specimens of 240 x 55 mm were used (Figure 3 left). Initial notches were machined by electrical discharging machining (EDM). Then, fatigue pre-cracks were nucleated at the notch root following the recommendations of the ASTM E1820 standard [7]. For fatigue pre-cracking, a resonance fatigue machine was used (Figure 3 right). The cracks were extended about 1-1.5 mm per side. All the specimens were machined at transverse orientation respect to the rolling direction. The final notch radius (ρ) at the crack tip is approximately 0.1 µm. Ligament lengths (l_0) from 5 to 15 mm were used and 3 specimens per ligament length were tested.

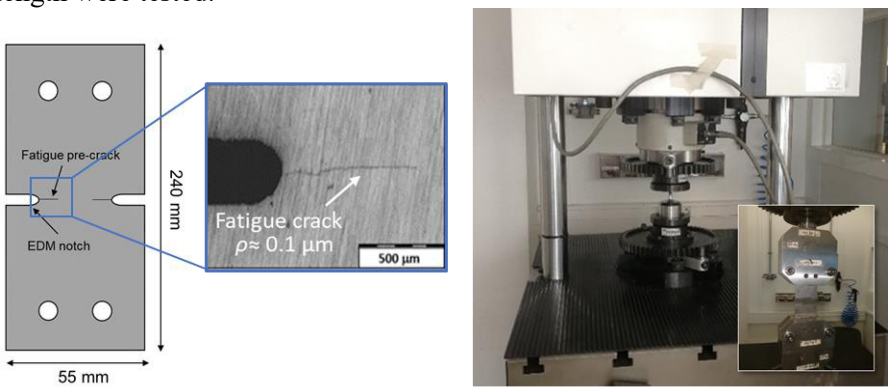

Figure 3. Left: DENT specimen and detail of the fatigue pre-crack. Right: Resonance fatigue machine.

2.3.2. Specimens with sheared notches. The new notching device (Figure 1) was used to prepare DENT specimens with different ligament lengths. Figure 4 shows some images of the experimental setup. The tool was mounted in a Zwick Roell 50 kN AllroundLine testing machine. The machine has two working areas, which permits to perform the notching and the subsequent tensile testing with a single testing equipment and easily switch from one operation to another (Figure 4a). The experimental procedure for specimen notching is schematized in Figure 5. The process is described as follows: first, a rectangular specimen of 200 x 55 mm (cut at transverse orientation respect to the rolling direction) is placed at the die and fixed using 2 pins (Figure 4c). This fixation system ensures the alignment of the specimen and that notches are always centred respect to the pinning holes. Then, the punch is moved downwards and, by means of a shearing process, two sharp notches (notch radius, ρ≈2 µm) are introduced in the specimen (notches symmetrical respect to the longitudinal axis of the specimen). The ligament length is modified by controlling the punch displacement, i.e. the greater the punch displacement the smaller the ligament between the two notches. After cutting, the punch returns to the initial position and the specimen can be extracted. Due to the shearing operation, the specimen is slightly bent at the end of the process. Therefore, a final flattening operation is performed before tensile testing. The specimen is placed in the base intended for that purpose (base for specimen flattening, Figure 4b) and pressed with the blank holder. This final step is optional and it does not affect the final result. However, it is highly recommendable since it facilitates the specimen manipulation and the fitting in the testing grips.

Due to the difficulty of measuring the length of the ligaments directly on the specimen, they were measured from the fracture surface after testing. Ligament lengths (l_0) from 8 to 20 mm were obtained and 2 specimens per ligament length were used. In total, 8 to 12 specimens per material were tested.

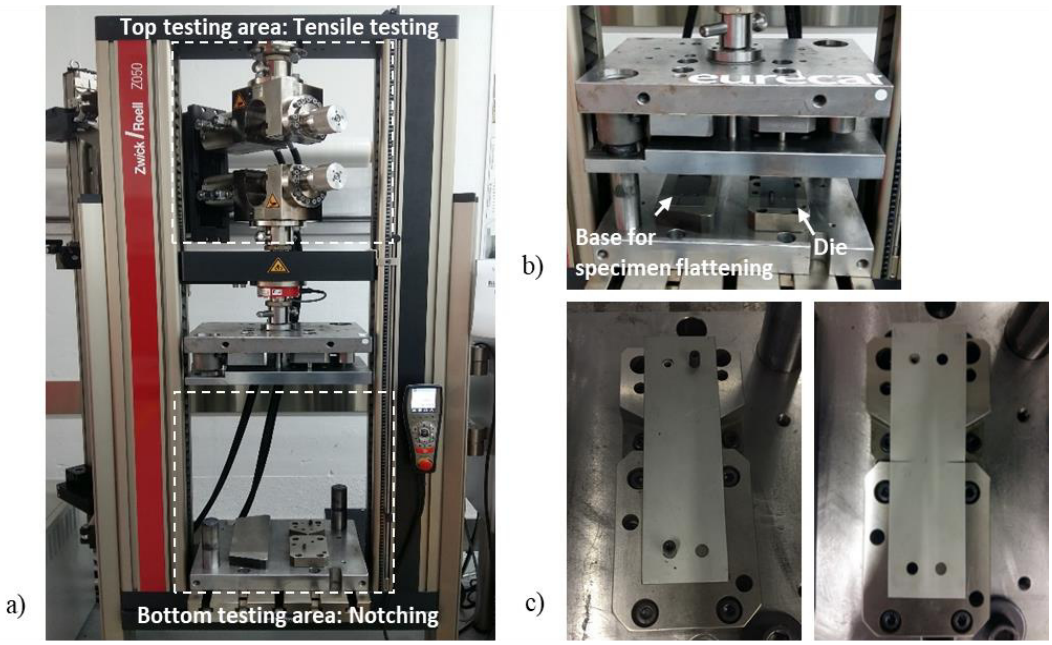

Figure 4. Images of the experimental setup for the notching process. a) Setup of the tool in the testing machine. b) Detail of the cutting tool. c) Specimen before (left) and after (right) the notching process.

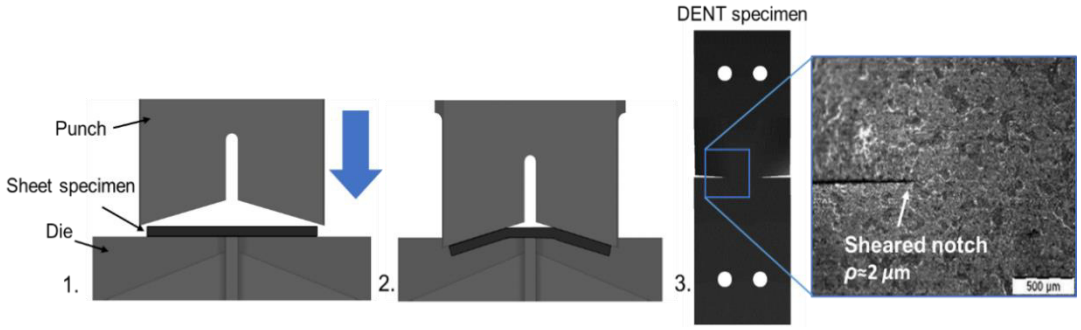

Figure 5. Schematization of the experimental procedure for the preparation of sheared notches in sheet specimens.

2.4. EWF tests

After notch preparation, the DENT specimens were tested up to fracture according to the European Structural Integrity Society (ESIS) protocol for EWF testing [10]. The tests were conducted at a constant displacement rate of 1 mm/min. The load-line displacement was measured by means of the video extensometer using initial extensometer marks separated 25 mm.

3. Results and discussion

3.1. EWF results

Figure 6 shows the load vs load-line displacement curves for the two specimen configurations. Figure 7 plots the values of w_f as a function of the ligament length. Numerical values of w_e and βw_p are given in Table 2 and Figure 8. As observed, for the same ligament length, both fatigue pre-cracked and sheared specimens show very similar load vs displacement curves (similar maximum load and displacement at fracture) in the four investigated materials. It explains the good agreement between w_f values for the two notch conditions (Figure 7) and the practically identical specific essential work of fracture, w_e and plastic work, βw_p (Figure 8). In general, very good repeatability is observed for sheared specimens, which

enhance the reliability of the obtained toughness values and confirms the robustness of the new process. It is worth noting that the similarity between specimens of the same ligament length is improved in sheared specimens. This is because the notch length is precisely defined by the punch displacement and, therefore, is easier to obtain multiple specimens with the same ligament. On the other hand, the ligament size in fatigue pre-cracked specimens is determined by the length of the fatigue cracks, which makes difficult to have two specimens with identical ligament.

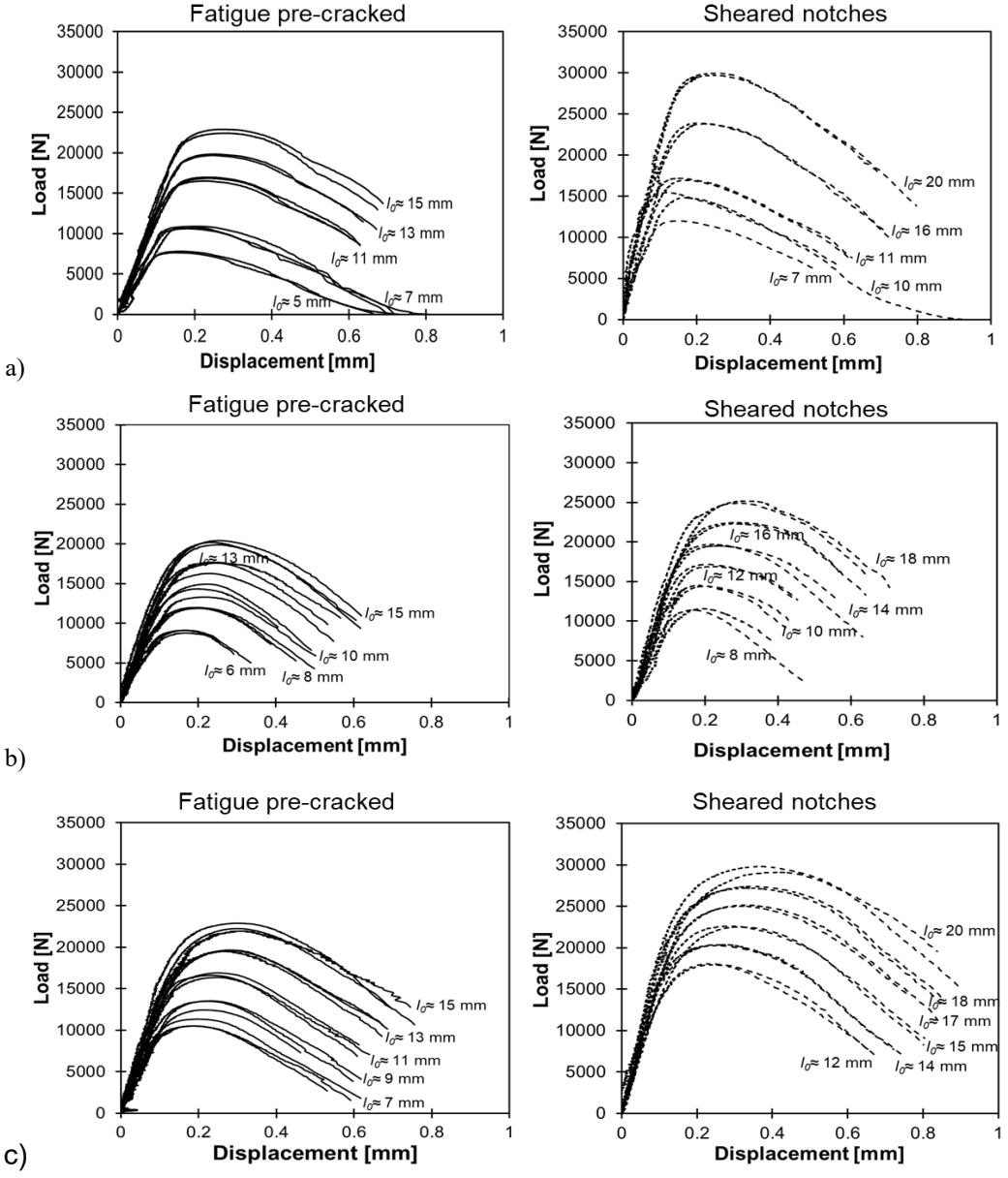

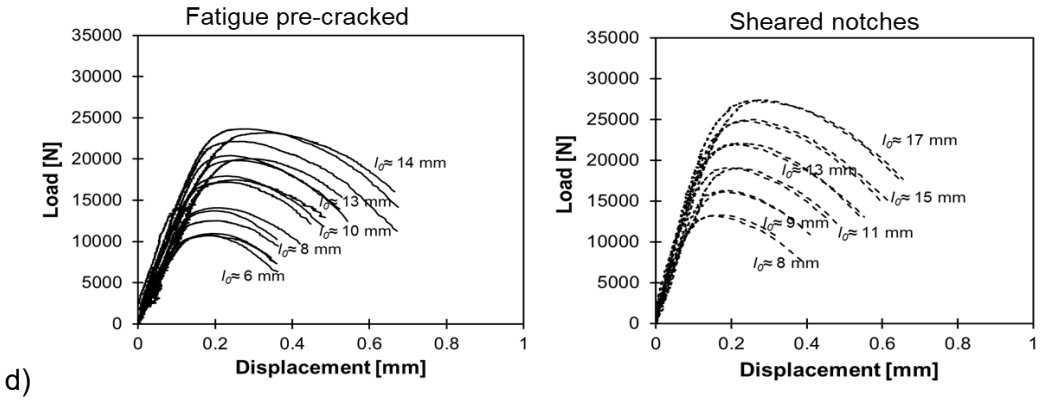

d)

Figure 6. Load-displacement curves obtained from EWF tests with fatigue pre-cracked specimens (left) and specimens with sheared notches (right). a) CP, b) DP-A, c) DP-B and d) 3rd Gen AHSS.

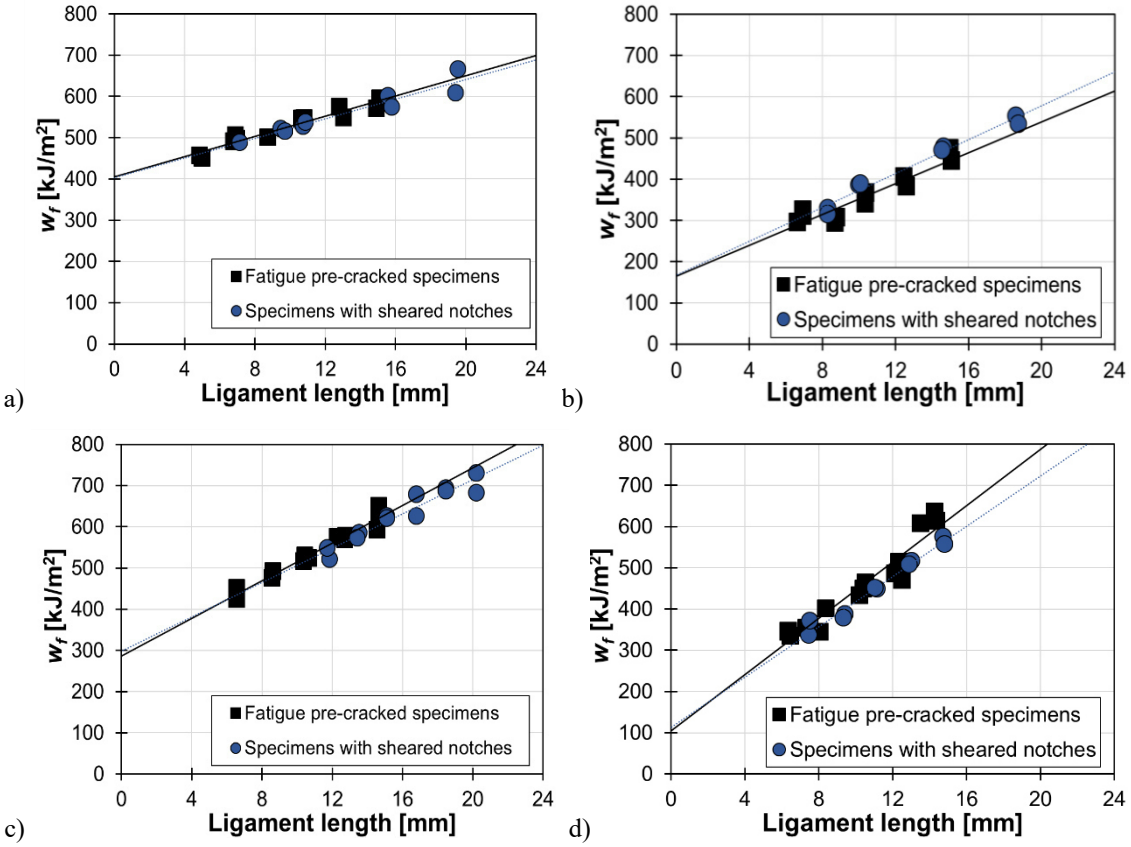

a) b) c) d)

Figure 7. w_f values against ligament length for the two investigated specimen configurations. **a)** CP, **b)** DP-A, **c)** DP-B and **d)** 3rd Gen TRIP-assisted.

Table 2. EWF results obtained with fatigue pre-cracked specimens and specimens with sheared notches

	Fatigue pre-cracked		*Sheared notches*	
Material	w_e [kJ/m^2]	βw_p [MJ/m^3]	w_e [kJ/m^2]	βw_p [MJ/m^3]
CP	405 ± 11	12 ± 1	404 ± 19	12 ± 1
DP-A	149 ± 21	24 ± 2	163 ± 27	21 ± 2
DP-B	286 ± 17	23 ± 1	298 ± 32	21 ± 2
3rd GEN	104 ± 30	34 ± 3	113 ± 21	30 ± 2

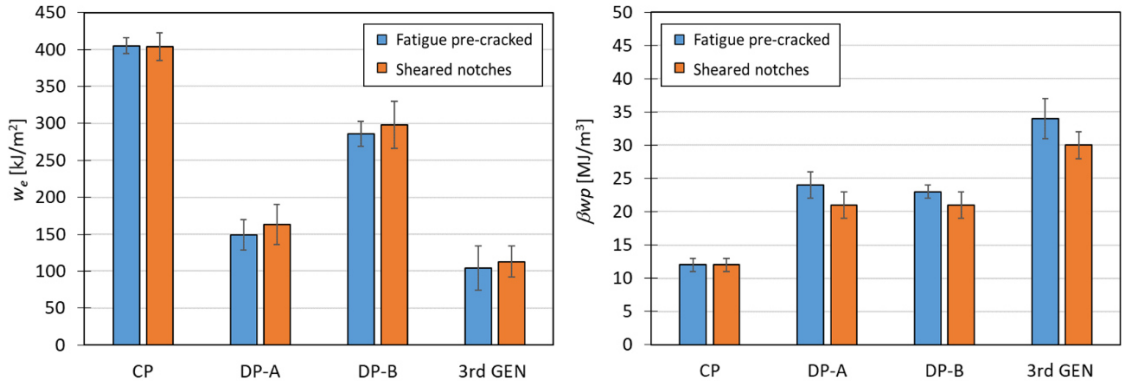

Figure 8. Results from EWF tests with fatigue pre-cracked (blue) and sheared (orange) specimens. Left: specific essential work of fracture, w_e. Right: non-essential plastic work, βw_p.

3.2. Fracture surface of DENT specimens

Figure 9 shows the fracture surfaces of different sheared and fatigue pre-cracked DENT specimens. It can be observed that for both specimen configurations the fracture aspect is quite similar and the ligament is well defined between the two notches. The major difference between the two notch types is the shape of the crack front (concave for the sheared notch and convex for the fatigue pre-crack). Overall, it was found that the morphology of the sheared notches is similar in the four investigated AHSS grades and independent of the ligament length.

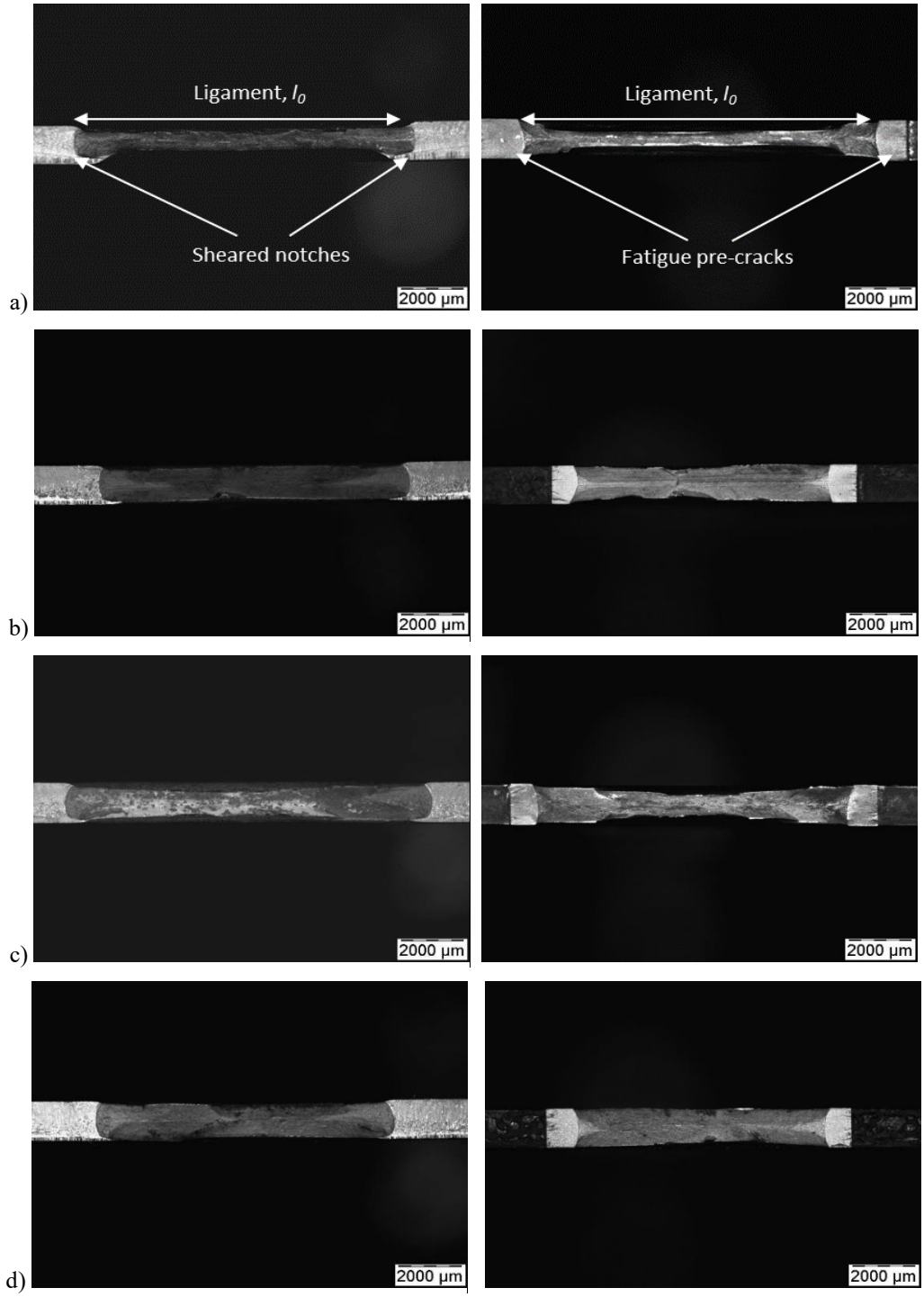

Figure 9. Fracture surfaces of DENT specimens with sheared notches (left) and fatigue pre-cracks (right). a) CP, b) DP-A, c) DP-B and d) 3rd GEN. The different areas (fractured ligament, sheared notch and fatigue pre-crack) are indicated in the first images.

4. Applications

As mentioned before, fracture toughness has shown to be a useful material property to predict crack-related problems in high strength metal sheets, such as edge fractures [1-3], crack formation during crash [4] or other fractures related to their local ductility [5]. It is illustrated in Figure 10, where w_e values of several AHSS grades are plotted against HER [2-3] and the maximum energy absorbed in axial crash tests [4]. As already discussed in [2-5], w_e shows a very good correlation with HER and crash resistance.

Therefore, w_e can be used to estimate the fracture resistance of AHSSs and predict their cracking behaviour during forming or crash. According to the linear data fittings depicted in Figure 10, expected values of HER and impact energy for the steel grades investigated in this work are plotted as a function of the obtained specific essential work of fracture values (results from EWF tests with sheared specimens). In the case of DP-A and 3rd GEN steel, the HER was experimentally evaluated according to ISO16630. As observed, the measured HER fits very well in the linear w_e vs HER data fitting, which validates the suitability of w_e for edge cracking resistance prediction. Therefore, the new testing procedure presented, can be used as a fast and cost-effective tool to readily assess the fracture performance of AHSS sheets.

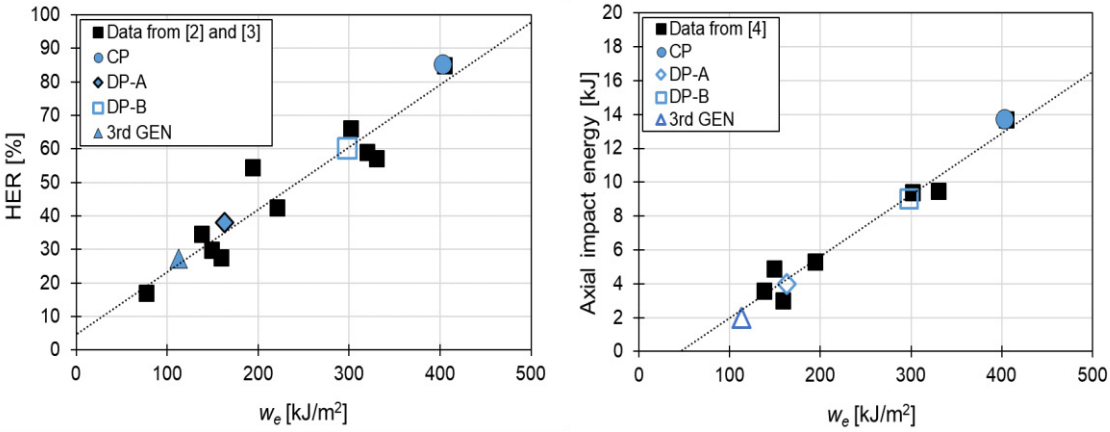

Figure 10. Correlation of w_e with HER (left) and axial impact energy (right). The data represented by black squares is extracted from references [2-4]. Blue symbols correspond to w_e values obtained in this work. Solid symbols represent experimentally evaluated values of HER and axial impact energy. Open symbols are expected values according to the linear data fitting (dashed line).

5. Conclusions

In the present work, an innovative device to prepare high strength metal sheet specimens for fracture toughness characterization has been presented. The tool can be easily mounted in a universal testing machine and offers an easy and cheap alternative to fatigue pre-cracking procedures. The new process has shown to be robust and reliable enough to evaluate the fracture toughness of four different AHSS sheets. It supposes a great time-saving in specimen preparation and it can be very useful to boost the use of fracture toughness measurements as routine testing for coil quality determination or for the selection of high strength sheet materials with enhanced cracking resistance.

6. References

[1] Yoon J I, Jung J, Joo S H, Song T J, Chin K G, Seo M H, Kim S J, Lee S and Kim H S Correlation between fracture toughness and stretch-flangeability of advanced high strength steels *Matter.Lett.* 180 (2016) 322-326.

[2] Casellas D, Lara A, Frómeta D, Gutiérrez D, Molas S, Pérez Ll, Rehrl J and Suppan C. Fracture Toughness to Understand Stretch-Flangeability and Edge Cracking Resistance in AHSS. *Metall. and Mat. Trans.* A 48 (2017) 86-94.

[3] Frómeta D, Lara A, Parareda S and Casellas D. Evaluation of Edge Formability in High Strength Sheets Through a Fracture Mechanics Approach. *AIP Conference Proceedings* 2113, 160007 (2019).

[4] Frómeta D, Lara A, Molas S, Casellas D, Rehrl J, Suppan C, Larour P and Calvo J. On the correlation between fracture toughness and crash resistance of advanced high strength steels. *Eng.*

Frac. Mech. 205 (2019) 319-332.
[5] Frómeta D, Lara A, Casas B, and Casellas D. Fracture toughness measurements to understand local ductility of advanced high strength steels. *IOP Conf. Ser.: Mater. Sci. Eng.* (2019) 651 012071
[6] ASTM E1820. Standard test method for measurement of fracture toughness. American Society for Testing and Materials
[7] ASTM E399. Standard test method for plane-strain fracture toughness of metallic materials. American Society for Testing and Materials
[8] Cotterell B and Reddel JK. The essential work of plane stress ductile fracture. *Int. J. Fract.* (1977) 267-277.
[9] Muñoz R, Lara A and Casellas D. Fracture toughness characterization of advanced high strength steels. *Int. Deep Drawing Research Group (IDDRG) Conference 2011* (Bilbao, Spain, June 5-8, 2011)
[10] Clutton E. Essential work of fracture. Moore DR, Pavan A, Williams JG, editors. Fracture mechanics testing methods for polymers, adhesives and composites, vol.28. ESIS Publ.; (2001) 177–95.

Acknowledgements
The present research work has been partially funded by the EU Horizon 2020 programme under grant agreement H2020-EU.2.1.3. – 814517 (FormPlanet).

UNIVERSITAT POLITÈCNICA DE CATALUNYA
BARCELONATECH
Escola d'Enginyeria de Barcelona Est

eurecat